UNIVERSITY OF SOUTHAMPTON
INSTITUTE OF SOUND AND VIBRATION RESEARCH

A NUMERICAL STUDY OF MULTICHANNEL SYSTEMS FOR THE PRESENTATION OF VIRTUAL ACOUSTIC ENVIRONMENTS

by

Ingyu Chun

A thesis submitted for the degree of
Doctor of Philosophy

JUNE 2004

To my dear wife

UNIVERSITY OF SOUTHAMPTON

ABSTRACT

INSTITUTE OF SOUND AND VIBRATION RESEARCH

Doctor of Philosophy

A NUMERICAL STUDY OF MULTICHANNEL SYSTEMS FOR THE PRESENTATION OF VIRTUAL ACOUSTIC ENVIRONMENTS

by Ingyu Chun

The performance of virtual acoustic systems using binaural technology is highly sensitive to the geometry of the listener's ears at relatively high frequencies since the acoustical features of the listener's ears are peculiar to that listener. The objective of this thesis is to undertake a numerical study of virtual acoustic imaging systems of which performance may be nearly independent of individual ear shape. The system developed aims to reproduce the incident sound field on the ear using a multichannel headphone. This has been called the RISE (Reproduction of the Incident Sound on the Ear) system in this thesis. The multichannel headphone reproduction uses the boundary surface control principle derived from the Kirchhoff-Helmholtz integral equation. The performance of the system using the incident sound field reproduction method can be made to be independent of the geometry and boundary condition of the scattering body within the control volume. The results of computer simulations show that the desired sound pressure at the eardrum of an arbitrary listener can be successfully replicated in the virtual acoustic environment by using the RISE system. The optimal strengths of headphone sources can be evaluated by using a dummy head model without the ears. This implies that anyone can experience nearly the same quality of the virtual sound field that can be created inside the multichannel headphone of the RISE system. The optimization of the multichannel headphone has been studied in terms of the size of the control volume and headphone, the number of headphone sources, and the boundary condition of the headphone surface. For example, 17 evenly distributed headphone sources per ear can reproduce any angle of incident sound on the ear reasonably well in three-dimensional space up to at least 10kHz. Highly absorbent inner surfaces of the headphone are required. Some practical guidelines for the design of a multichannel headphone are also suggested.

JUNE 2004

LIST OF CONTENTS

ACKNOWLEDGEMENTS

I would like to thank my supervisor Prof. P. A. Nelson for his thorough guidance and helpful support. He has given me many creative ideas for my research. Without his help, I could not have completed my thesis. I also want to thank Dr. Phil Joseph and Dr. Boaz Rafaely for the helpful advice and encouragement. I am indebted to Prof. A. J. Keane who assisted in the provision of the computing resources. I would also like to acknowledge my many colleagues with whom I have discussed my studies. I am grateful to Dr. Geun-tae Yim for helpful suggestions and help too. I would also like to express sincere appreciation to my parents for their support and encouragement. My special thanks go to my wife Wookyoung Chun for her everlasting love and utmost support.

LIST OF SYMBOLS

A = cross sectional area [m^2]

$C(\mathbf{x})$ = coefficient for an exterior acoustic problem

$C^0(\mathbf{x})$ = coefficient for an interior acoustic problem

c_0 = speed of sound [m/s]

e = base of natural logarithm, 2.71828…

f = frequency [Hz]

$G(\mathbf{x}|\mathbf{y})$ = Green's function , field at **x** due to source at **y**

$g(\mathbf{x}|\mathbf{y})$ = free space Green's function, field at **x** due to source at **y**

H = transfer function from surface pressure to field pressure

H' = transfer function from surface normal velocity to field pressure

j = $\sqrt{-1}$, imaginary unit

k = wave number = ω / c_0

N = linear shape functions defined on a master element

$\mathbf{n}$ = unit vector normal to surface

n = distance in the direction of **n**

n_e = the number of elements

n_j = the number of nodes (3 or 4) on an element

n_n = the total number of nodes in all elements

p = acoustic contribution to pressure [Pa]

R = reflection coefficient

S = surface

Q_{vol} = acoustic source strength distribution [m^3/s]

q = complex acoustic source strength [m^3/s]

V = volume

v = particle velocity [m/s]

v_n = normal particle velocity [m/s]

$\mathbf{x}$ = position vector from origin to a point

$\mathbf{y}$ = position vector on the surface S

$\mathbf{y}_v$ = position vector in the volume V

z = specific acoustic impedance

α = primary sound field

β = secondary sound field to reproduce the sound field α

γ = another primary sound field

δ = secondary sound field to reproduce the sound field γ

ε = radius of infinitesimal volume V_ε

ϕ = differentiable scalar function

ρ_0 = ambient density [kg/m^3]

$\rho_0 c_0$ = characteristic acoustic impedance of a fluid

ω = angular frequency [rad/s]

ξ = a local coordinate on a master element

ψ_L = fundamental solution of the Laplace equation

CHAPTER 1
INTRODUCTION

1.1 Introduction

In everyday life, we can easily locate and interact with auditory events in three-dimensional (3-D) space. Virtual acoustic systems or 3-D audio systems try to control and manipulate the spatial auditory perception of a listener. Virtual acoustics can be defined as the technology to produce virtual acoustic sources perceived by a listener as being in a position where no actual source is present (Morfey, 2001). The terms "virtual acoustics", "3-D audio", "binaural audio" and "spatialized sound" have all been used to describe the simulation of this process. 3-D audio systems have been developed since monophonic gramophones came into being. However, 3-D audio technology has been developed relatively slowly due to the complexity of the human sound localization system. The 3-D audio technology is now in increasing demand as a result of people's enthusiasm for multi-media and virtual reality.

1.2 Applications

There are many applications related to virtual acoustic systems. For example, interactive virtual reality systems combine 3-D audio technology with 3-D video technology (Blauert *et al.*, 2000). These systems try to control and manipulate audio-visual-tactile stimuli using movement-tracking devices. In the case of flight simulation, vibro-acoustic interaction is also considered. Teleconferencing systems also use virtual reality systems with a limited bandwidth of signals for the transmission of human voices (Begault, 1999). A major problem with current teleconferencing systems comes from audio-visual-temporal asynchrony. Architectural acousticians often use auralization systems to hear the acoustics of designed rooms or auditoria. Virtual acoustics can be also essential for home theatre

systems and 3-D games. The performance of home theatre systems depends on listening position, the condition and geometry of the listening room, and the level of background noise. Virtual acoustic presentations for 3-D games should be implemented very fast even in cases of multiple fast moving virtual sources.

1.3 Progress and Trends

The history of spatial audio systems starts from about one hundred years ago. The first monophonic record player was developed in the late 1800s. The first experiment introducing the stereophonic transmission of music was undertaken by Clement Ader at the Paris exhibition of 1881 (Hertz, 1981). Steinberg and Snow at Bell Labs in the 1930s tried to reproduce the sound field in auditorium by using three microphone/loudspeaker channels and got quite convincing results. This work was intended for cinema sound reproduction. Alan Blumlein showed that it would be possible to create phase differences between the ears in natural listening by introducing only amplitude differences between a pair of loudspeakers (Blumlein, 1931). Two channel stereo sound systems were introduced commercially in the late 1950s in a manner similar to that proposed by Blumlein and became widely available to the public in the 1960s. Multichannel stereo formats for the cinema became popular in the late 1950s and 1960s. Dolby Stereo for cinema sound enabled a four channel surround sound signal to be matrix encoded into two optical sound tracks and Dolby surround has been released for home cinema applications (Rumsey, 2001). The quadraphonic sound system was configured for a square arrangement of four loudspeakers but failed to impress consumers. It gave poor front images, often with a "hole in the middle". Ambisonic sound was developed in the 1970s and tried to reproduce directional sounds by using multichannel loudspeakers. In recent years, home theatre systems using the ITU (International Telecommunication Union) 5.1 channel configuration have been very successful and are becoming widespread. People get used to surround sound in the cinema and want to experience it at home. Thanks to the thriving movie and game industry, spatial audio systems are likely to be advanced and become more popular. Current virtual acoustic systems that are

actively researched in various laboratories use a binaural technology with individualized head-related transfer functions, head tracking devices, and auralization techniques using artificial reverberation (Begault *et al.*, 2000). Binaural recording technology uses the following principle: if sound pressures at the listener's eardrums are recorded and reproduced exactly as they were, then the complete aural experience including timbre and spatial aspects is assumed to be reproduced (Møller, 1992). Binaural recordings can be made with small two microphones placed in the ear canals of a real or dummy head. Although binaural signals are intended for headphone reproduction, they can be reproduced by two loudspeakers through crosstalk cancellation. In recent psychoacoustic experimentation, the interactive virtual environment generator using the above technologies shows convincing performance of virtual sound localization (Djelani *et al.*, 2000).

1.4 Objectives

The goal of virtual acoustic systems is to improve the ability of audio systems to produce virtual acoustic environments such that listeners cannot tell the difference between real sound images and the virtual sound images that are produced by such systems. However, the performance of the current virtual acoustic systems is highly sensitive to the geometry of individual ears at high frequencies. Therefore, an individualized Head-Related-Transfer-Function (HRTF) should be used to produce a virtual acoustic environment. However, each person has such different individualized HRTF and the calculation of the individualized HRTF is a very time-consuming and expensive process. This is one of the most critical problems associated with virtual acoustic systems. The objective of this study is to investigate virtual acoustic systems using multi-channel headphones, which are not sensitive to the geometry of individual ears even at high frequencies, and to investigate the optimal virtual acoustic systems for headphone listening.

1.5 Overview and the contribution of the thesis

Chapter 1 introduces the concept of virtual acoustics and its applications. Progress and trends of virtual acoustic systems are also introduced. The objectives of the thesis are described. Chapter 2 describes how humans can localize sound events in the natural hearing environment by introducing monaural cues, binaural cues, and other cues such as head movement and reverberation. Acoustical features of the human ear and acoustical coupling between the ear and the headphone are also described. Chapter 3 describes various kinds of spatial audio systems from two-channel stereo to multichannel surround reproduction. Loudspeakers are compared with headphones. Reproduction systems using the wave field synthesis method are also described. Chapter 4 describes how sound fields can be numerically calculated by introducing the Kirchhoff-Helmholtz integral equation. The non-uniqueness problem for exterior acoustic problems is also described. The number of over-determination points to solve the non-uniqueness problem is discussed. Chapter 5 explains the incident sound field reproduction method by introducing simple cases of a one-dimensional tube and a single scattering body in three-dimensional space, and explains the boundary surface control principle upon which a virtual acoustic system can be based. The basic theory of inverting non-square matrices is introduced in order to deduce the optimal acoustic source strengths for reproducing a given desired sound field. Numerical simulations for the incident sound field reproduction system are presented in case of a single scattering body. Chapter 6 further develops the theory of the virtual acoustic systems for reproducing the incident sound field on the ear with multichannel headphones by introducing the case of two scattering bodies and the human head. The validity of the assumptions of the theory is also discussed. Numerical simulations for the incident sound field reproduction system are also presented in case of two scattering bodies. Chapter 7 introduces the numerical models of ears, heads, and headphones, and explains the numerical modelling procedure and some important design factors. Chapter 8 describes the procedure used in the numerical simulation and introduces an example of the numerical simulation of a virtual acoustic system. Some causes of reproduction error and validity of the assumptions of the theory regarding the human head are discussed. Chapter 9 describes the performance of the virtual acoustic

system for various positions of the primary source relative to the listener. The design of the geometry of control surfaces is discussed. Chapter 10 presents the results of a study of the optimization of the headphone in terms of the number of headphone sources, the boundary conditions of the headphone, and the size of the headphone. Chapter 11 concludes the thesis.

The major original contributions of the thesis are as follows. First, theory of the incident sound field reproduction method is explained. The theory proves that sound field inside the control volume can be exactly reproduced regardless of the geometry and boundary condition of the scattering body inside the control volume in a free field. This theory can be used for the reproduction system for an arbitrary listener. Second, the theory of virtual acoustic systems related to the human head using headphone reproduction is explained. The theory shows that the sound field inside the control volume can be exactly reproduced if the incident sound field on the control volume is independent of the geometry and boundary condition of the scattering body inside the control volume. Third, the RISE (Reproduction of the Incident Sound on the Ear) system is developed. The RISE system reproduces the incident sound field on the ear using a multichannel headphone. This new virtual acoustic system is a user-independent system and so it does not need to be designed for the individual. Everyone hears the same output signal produced by the RISE system for a given input signal and everyone can feel the same quality of reproduction. Since human hearing is a very individualized process, the performance of the RISE system should be much better than that of the non-individualized binaural system. Fourth, numerical simulations of the RISE system are performed. The results show that virtual acoustics can be successfully produced for any positions of virtual sources and its performance can be independent of the listener's ear for given headphone source strengths. Fifth, various aspects of the optimization of the multichannel headphone are studied and practical guidelines for the design of a multichannel headphone are suggested.

CHAPTER 2
SPATIAL HEARING

2.1 Introduction

Humans can naturally perceive aural events coming from anywhere in three-dimensional space. A listener can recognize the direction of an aural event through body filtering that is caused by scattering from the human torso, head, and pinna. The sound localization ability of the human is influenced by many acoustical cues, such as the interaural time difference (ITD) cue, the interaural level difference (ILD) cue, the monaural spectral cue, head movement, room reverberation, and so on. This chapter describes how these cues affect sound localization in the natural hearing environment and also describes their relative importance. Each human ear has unique acoustical features, such as resonance, which are also described in this chapter. The acoustical coupling between the listener's ear and headphones is also discussed.

2.2 Monaural cues

An acoustic system consisting of a source and a listener in a free field is considered to study monaural cues. The transfer function of this system in the frequency domain is called the Head-Related Transfer Function (HRTF) that describes the sound transmission from a sound source to a point in the ear canal of a human subject in a free field. Its corresponding impulse response function in the time domain is called the Head-Related Impulse Response (HRIR). The definition of the HRTFs is variable since the choice of the reference point in the ear canal where the measurement is made varies (Møller, 1992). One of the definitions of the HRTFs can be given by

$$\text{HRTF} = \frac{\text{sound pressure at the entrance to the blocked ear canal}}{\text{sound pressure in the middle of the head with the listener absent}}. \quad (2.1)$$

In this case, it is assumed that the reference point where sound pressure is recorded is at the entrance to the ear canal when the ear canal is blocked by, for example, an earplug. The reference point can be changed to the listener's eardrum or the entrance to the open ear canal. Figure 2.1 shows an example of (a) the amplitude spectrum of HRTFs and (b) the HRIRs for the two ears of one subject (Møller *et al.*, 1995a). The sound comes from the left side in the horizontal plane. The amplitude spectrum of HRTFs show that the signal at the right ear is much attenuated compared to that at the left ear and has an overall shape of a low-pass filter with a cut-off frequency around 4 kHz due to the shadowing effect of the head in this example. It shows numerous spectral peaks and dips particularly at high frequencies. The HRIRs at the left ear is substantially different from that at the right ear in the temporal fine structure of the impulse response. The signal at the left ear arrives earlier than zero since the left ear is closer to the source than the middle of the head, but the signal at the right ear arrives later than zero.

Monaural acoustical localization cues are based on the fact that the sound pressure at each ear depends on the position of the sound source relative to the listener. The monaural temporal cue results from the change of sound pressure at one ear caused by a change in the HRIR. The temporal fine structure of this impulse response function can contain information relating to the sound source position. Because the HRIRs are short, on the order of about 2 ms, the limited temporal resolving power of the auditory system probably makes the temporal fine structure of the HRIRs undetectable (Green, 1971). Some psychophysical experiments suggest that changes in the temporal fine structures of the HRIRs do not result in the perception of subsequent changes of sound source position (Kistler and Wightman, 1992). Therefore, the monaural temporal cues do not play an important role of sound localization for above reasons. This suggests that monaural phase information is not very important in virtual acoustic systems.

The monaural spectral cue results from the change of the sound pressure at one ear caused by a change in the amplitude spectrum of the HRTF. This spectrum contains much information relating to the sound source position. The HRTF varies for every source position and angle of incidence. The major changes of the HRTFs among source directions are the characteristic spectral peaks and dips above 1 kHz. The

monaural spectral cue plays a dominant role in the sound localization at high frequencies from about 5 kHz (Wightman and Kistler, 1997). However, there are individual differences in the HRTFs due to anatomical differences among people. The monaural spectral cue is highly idiosyncratic. It is highly sensitive to the size and geometrical shape of the listener's pinna at high frequencies (Shaw, 1997). Therefore, it is difficult to generalize the spectral characteristics to non-individualized HRTFs. Møller *et al.* (1995a) measured the HRTFs for 40 subjects and various source directions. The range of amplitude gain is up to 20dB and attenuation is more than 40dB overall. Figure 2.2 shows an example of (a) the amplitude spectrum of HRTFs and (b) the HRIRs for the two ears of 40 subjects, and the sound comes from the left side in the horizontal plane. It shows interindividual variation in the HRTFs, but they observed that differences between 40 subjects' HRTFs were relatively small up to about 8 kHz. Averaging HRTFs across subjects is problematic since it results in flattened curves that cannot represent a typical subject because narrow peaks and dips occurring at slightly different frequencies for each subject are flattened. In general, the use of nonindividualized HRTFs can lead to mislocalizations in elevation, front-back confusions, and nonexternalized source images, especially when head tracking is not employed (Wenzel *et al.*, 1993). Although humans localize sources best with their own HRTFs, the HRTFs of a "good localizer" can be found to be more useful to generalize the details of HRTFs. The subjects can gradually adapt to non-individualized HRTFs by training over a period and localization errors become smaller with familiarity. The ability to resolve spatial locations can be improved by using "supernormal" localization cues with larger ranges of interaural difference than normal cues (Shinn-Cunningham *et al.*, 1998). Although the monaural spectral cue can be useful, it has problematic characteristics. A listener must have *a priori* knowledge about a source spectrum and relevant HRTF features to decode the sound source position from the sound pressure at each ear, since this is the product of the HRTF and the source spectrum. It may be reasonable to assume that listeners know their HRTF features and the spectrum of the most real world sound sources, although this issue is still controversial.

2.3 Binaural cues

Binaural acoustical localization cues are based on the fact that the differences between sound pressures at both ears depend on the position of the sound source relative to the listener. Those can be derived from a ratio of the HRTFs at the two ears. Since the sound pressure in the middle of the head with the listener absent, which reflects the spectrum of the sound source, cancels in the ratio of the HRTFs, the binaural cues do not need *a priori* knowledge of the source spectrum.

The binaural temporal cue results from the change of sound pressure at two ears caused by a change in the phase differences of the HRTFs at two ears. The interaural phase differences (IPDs) show the group delay of the signal due to difference of the propagation length from the source to listener's two ears. They are nearly a pure delay, but the ear is sensitive to IPDs only at low frequencies (Rumsey, 2001). The IPDs can give ambiguous information above about 700 Hz because it is hard to tell which ear is lagging and which is leading. They can also be confusing in reflective environments because room modes and reflective waves may modify the phase cues. The binaural temporal cue is often represented by the interaural time difference (ITD) that is a time difference between the signals arriving at the two ears of the listener. Figure 2.3 shows an example of the interaural time difference for some angle of incidence of the plane wave source when a human head is assumed as a sphere and the source is very far from the head compared to the radius of the spherical head (Blauert, 1997). In this case, the ITD is given by

$$\mathrm{ITD} = \frac{r(\theta + \sin\theta)}{c_0} \tag{2.2}$$

where r is the radius of the head, θ is the angle of incidence of the source, and c_0 is the speed of sound. The maximum time delay between the ears is about 0.65 ms when a sound source is at the side of the head and this is called the binaural delay. The ITD is nearly indistinguishable between front and rear sources, and so it gives front-back confusion to the listener. The contours of constant ITD are roughly

circular because the human head is nearly spherical, and so it gives confusion of exact position of the sound source to the listener. However, the ITD is a more reliable cue than any other cues because it does not depend on source characteristics and it is not highly idiosyncratic. If a broadband sound source has low frequency components below about 1.5 kHz, the ITD cue plays a dominant role in the sound localization at low frequencies below about 1.5 kHz (Wightman and Kistler, 1992).

The binaural spectral cue results from the change of sound pressure at two ears caused by a change in the amplitude differences of the HRTFs at two ears. This binaural spectral cue is often represented by the interaural level difference (ILD) that is the sound pressure level difference between the signals arriving at the two ears of the listener. Note that the ILD is small at frequencies below about 1500 Hz regardless of source position because the dimensions of the head and pinna are small compared to the acoustic wavelength. The ILD is also highly idiosyncratic because the monaural spectral cue is highly idiosyncratic at high frequencies.

Wightman and Kistler (1997) studied the factors that influence the salience of the various sound localization cues. The ITD cue would be the most reliable cue since it does not depend on source characteristics and it is not highly idiosyncratic. The pattern of ILDs across frequency also does not depend critically on source characteristics although they are highly idiosyncratic at high frequencies. The ILDs and monaural spectral cues may be used primarily to resolve front-back confusions that reflect the ambiguity of the ITD cue. The ILDs and monaural spectral cues play a dominant role in sound localization at high frequencies above about 5 kHz. The ITD and ILD do not need *a priori* knowledge about a source spectrum.

2.4 Head rotation and artificial reverberation

People are easy to confuse in localizing a source to the front that should be in the rear or vice versa, and this is called "front-back confusion". Many researchers demonstrated experimentally that head rotations play an important role in the

resolution of front-back confusions (Hill *et al.*, 2000). The head rotations influence the ITDs, ILDs, and monaural spectral cues allowing the hearing mechanism to use this movement to help resolve such errors. But, the changes in the ITD with head rotations appear to be the primary mechanism for resolution of front-back confusions when a broadband sound source has low frequency components below about 1.5 kHz. This head rotation cue or dynamic cue for the resolution of spatial ambiguity in relation to source elevation does not function above 2 kHz (Perrett and Noble, 1997). But head rotation with non-individualized HRTFs can improve localization accuracy in relation to azimuth angle of incidence of the source (Begault *et al.*, 2000). The head rotation cue can be incorporated into virtual acoustic systems by using head tracking devices.

Some spatial cues can be strongly influenced by the visual information. It is normal to rely quite heavily on the visual sense for information about events within the visible field. Most subjects localize aural events primarily behind them rather than in front when playing binaural recordings without accompanying visual information or any form of head tracking. In the absence of the ability to move the head to resolve front-back conflicts, the brain tends to assume a rear sound image if something cannot be seen.

In a free field, the sound level generated by a monopole type source drops off about 6dB for every doubling in distance from the source. However, in reverberant space, the sound level does not drop off as rapidly as one moves from a sound source because the reflected sound builds up to create a relatively steady level of reverberant sound throughout the space. There is a critical distance at which the direct and reflected sound components are equal in level. Distance or depth perception can be easier in reverberant spaces because the reverberation time and the early reflection timing give many clues to its perception although absolute distance perception is very unreliable in a free field. The early reflections in the period after the direct sound up to 50~80ms have been found to contribute to the sense of the size of a sound source, and have the effect of broadening or deepening the spatial attributes of a source. Slightly later reflections after 80ms contribute to the sense of spaciousness or envelopment. Spaciousness is used to describe the sense of open space or room where the listener is located. It is related to the sense of externalization whether the sound

appears to be outside the head rather than constrained to a region inside the head. Envelopment is used to describe the sense of immersivity and involvement in a sound field with sound coming from all around. If artificial reverberation is added to binaural signals, the sound perception can be externalized. Moreover, artificial reverberation can improve localization accuracy of azimuth, but degrade that of elevation (Begault *et al.*, 2000)

2.5 Acoustical features of the human ear

Figure 2.4 shows the descriptive diagram of external ear. The ear canal is an irregular tubular structure and its cross-sectional area is sharply tapered in the region adjoining the eardrum (Stinson and Lawton, 1989). There is no clear boundary between the concha and the ear canal. The ear canal can be modelled as a simple cylindrical cavity having a diameter of 7.5mm, a length of 22.5 mm and a volume of 1 cm^3, which is terminated by a piston-like eardrum that is perpendicular to the axis at low frequencies below 8 kHz (Shaw, 1974). The ear canal model will be discussed further in the section 7.3.

Shaw (1997) measured the frequency response curves for ten human ears at the blocked ear canal position with a progressive wave source at eight angles of incidence in the circumaural plane. The response curves varies greatly with the angle of incidence and their differences for a given angle of incident between subjects are significant particularly at frequencies above 5 kHz. However, they have common characteristics. The frequency response is strong between 6 and 9 kHz but weak above 12 kHz when incident sound waves come from high elevations above 60°, and the situation is reversed when incident waves come from the front. The pattern of the frequency response curves shows parallel sloping lines between 5 and 11 kHz with source elevation and so the ear acts like a low-pass filter system where the cut-off frequency increases with source elevation. Although the patterns of the frequency response curves are similar among listeners, and have several resonances, each listener has a unique frequency response. For example, its resonance frequencies are

different since the HRTFs are largely determined by diffraction and cavity resonance effects associated with the structure of the ear. The concha is a broad shallow open cavity having a volume of about 4 cm^3 with substantial radiation damping and acts as an acoustical resonator. Figure 2.5 shows average characteristics of the first six modes of the human concha under blocked ear canal conditions (Shaw, 1997). In this figure, the mode patterns, resonance frequencies, directions of maximum response, and response levels are averaged over ten subjects. The first mode at 4.2 kHz is a quarter wavelength depth resonance with uniform sound pressure across the base of the concha and it is strongly excited from all directions. The pressure distribution for the first mode has the characteristics of a monopole type of resonance. The second and third mode is a vertical pair, and fourth, fifth, and sixth mode is a horizontal triplet. The second mode at 7.1 kHz has a single nodal surface near the crus helias separating pressure zones that are opposite in phase, and it is excited at a mean source angle of 68° from 53° to 97°. The third mode at 9.6 kHz has two nodal surfaces and its response is relatively weak, and it is excited at a mean source angle of 73° from 57° to 105°. The fourth mode at 12.1 kHz has three nodal surfaces and it is strongly excited from the front at a mean source angle of −6° from −15° to 35°. The pressure distribution for the second mode shows a vertical dipole type of resonance and that for the fourth mode shows that of a horizontal dipole, roughly speaking. The fifth mode at 14.4 kHz has four nodal surfaces and it is excited from the front at a mean source angle of 8° from −7° to 15°. The sixth mode at 16.7 kHz has five nodal surfaces and it is excited from the front at a mean source angle of 7° from −15° to 30°. The pressure distribution for the fifth shows a lateral quadrupole type of resonance and that for the sixth mode shows that of a longitudinal quadrupole, roughly speaking. The broadband directional characteristics are generally common to all subjects. However, there can be substantial acoustical differences between pairs of pinnae that are very similar in apperance, for example, in the case with KEMAR-L and KEMAR-R, due to even minor differences of pinna geometry. This interaural pinna disparity can exist probably because the pinna is a cartilaginous structure that is easily deformed.

2.6 Coupling between the ear and the headphone

When a listener wears a headphone, the external ear is strongly coupled to the headphone and the frequency response of the ear shows different characteristics that depend on the interaction between the individual ear and the headphone (Shaw, 1997). The interaction varies with the type of the headphone. In the case of the circumaural headphone, the transducer does not contact with the pinna. The ear is entirely surrounded by the external part of the circumaural headphone's cushion. The cavity radius and the distance between the eardrum and the transducer are two characteristic dimensions. The intersubject differences of the frequency responses at the eardrum are small and the system can be described in terms of lumped acoustical elements at low frequencies below 1.5 kHz since both characteristic dimensions are small compared to the acoustic wavelength. The coupled frequency response follows the response curve of the individual ear between 1 and 5 kHz since the acoustical coupling between the ear and the headphone is relatively weak. However, since the acoustical coupling becomes stronger and wave effects become predominant at high frequencies above 5 kHz, the intersubject and intrasubject variations in the response above 5 kHz can be very large. In the case of the supra-aural headphone, the transducer contacts with the pinna and the characteristic dimension is the distance between the face of the transducer and the eardrum. The coupled frequency response at the eardrum is well defined and intersubject differences are small between 0.5 and 2 kHz. Below 500 Hz, the response may vary by 5~15 dB depending on the air tightness of the seal and the rigidity of the cartilage. At high frequencies above 5 kHz, the response becomes very different from that of the undistorted open ear. In the case of the insert earphone, the characteristic dimension is the distance between the tip of the ear mould and the centre of the eardrum. The response is well defined below 5 kHz. The free field resonance characteristics of the ears are eliminated with the insert earphone.

When a virtual acoustic field is produced by a headphone using binaural technology, calibration for the generation of the virtual acoustics is needed to compensate for the undesirable spectral coloration introduced by the acoustical coupling between the ear

and the headphone. When a sound source having a spectrum of $S(j\omega)$ is placed in a free field, the sound pressure having a spectrum of $E(j\omega)$ at some point in the ear canal is given by

$$E(j\omega) = H(j\omega)S(j\omega) \tag{2.3}$$

where $H(j\omega)$ is the HRTF from the sound source to the point in the ear canal in a free field. When a headphone source having a spectrum of $Q(j\omega)$ generates sound, the sound pressure having a spectrum of $E'(j\omega)$ at the same point in the ear canal is given by

$$E'(j\omega) = H_H(j\omega)Q(j\omega) \tag{2.4}$$

where $H_H(j\omega)$ is the headphone transfer function (HpTF) from the headphone source to the point in the ear canal. The HpTFs can be much influenced by the acoustic coupling between the ear and the headphone, and it is nondirectional. To create virtual acoustic fields using the headphone, the sound pressure $E'(j\omega)$ should be the same as the sound pressure $E(j\omega)$. Then, the headphone source spectrum $Q(j\omega)$ for generation of the virtual acoustics is given by

$$Q(j\omega) = \frac{H(j\omega)}{H_H(j\omega)}S(j\omega). \tag{2.5}$$

The virtual synthesis filter of the headphone is the HRTFs times the inverse HpTFs. In addition to the highly idiosyncratic features of the HRTFs, the HpTFs are also different for different listeners since the acoustical coupling effect differs for different geometry of the ear. Møller *et al.* (1995b) suggested the individualized equalization of the headphone response is preferable since there is significant intersubject variability among individuals. However, the intrasubject variability in the HpTFs over different placements of a supra-aural headphone is significant, and it arises mainly from the variable coupling of the headphone cushion to the ear for different placements (Kulkarni and Colburn, 2000). Shaw (1966) measured the HpTFs of three

different circumaural headphones and two different supra-aural headphones and they were very sensitive to the headphone position and it may vary by 5~15dB when the headphone is displaced by a few millimeters. This implies that even though the individual HRTFs and HpTFs are used to generate virtual acoustic fields with a headphone, the sound pressure at the listener's eardrum can be unpredictable due to high intrasubject variations at high frequencies above 5 kHz. He also mentioned that appreciable reductions in intrasubject range could be attained by appropriate design changes of headphones. For example, suitably designed circumaural headphones may present coupling situation similar to free field conditions (Shaw and Thiessen, 1962). Pralong and Carlile (1996) measured the HpTFs of a circumaural headphone and a supra-aural headphone for six different placements of the headphones, as shown in Fig. 2.6. They observed that the intrasubject variability of the circumaural headphone was not bad although that of the supra-aural headphone was much worse. Their study also demonstrates that non-individualized HRTFs can be properly reconstructed at a listener's eardrum if individualized HpTFs are used. The use of non-individualized HpTFs can result in a greater disruption of monaural spectral cues compared to binaural spectral differences.

2.7 Conclusion

This chapter described the sound localization cues and their relative importance. Although the monaural temporal cues do not play an important role in sound localization, the monaural spectral cues and the ILDs play a dominant role in the sound localization at high frequencies from about 5 kHz. However, the monaural spectral cues and the ILDs are highly sensitive to the size and geometrical shape of the listener's ear at high frequencies since each listener's ear has a unique frequency response that has several resonances. The ITD cue plays a dominant role in the sound localization at low frequencies below about 1.5 kHz, it does not depend on source characteristics, and it is not highly idiosyncratic. Head rotations play an important role in the resolution of front-back confusions. Sound perception can be externalized with headphone presentation by adding artificial reverberation. In the case of headphone

reproduction using binaural technology, the acoustical coupling between the individual ear and the headphone is significant and wave effects are predominant at high frequencies above 5 kHz. The intersubject and intrasubject variations in the frequency response above 5 kHz can then be very large. Individualized equalization of the headphone response is needed to compensate for the undesirable spectral coloration introduced by this acoustical coupling.

FIGURES

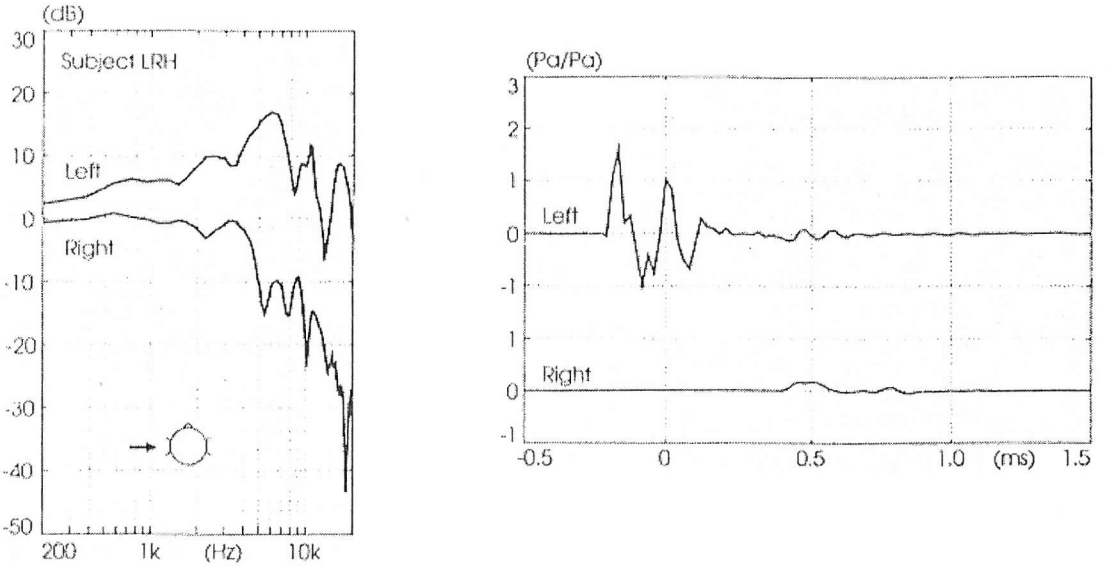

Figure 2.1 (a) The HRTFs and (b) the HRIRs for one subject. The sound comes from the left side in the horizontal plane (after Møller *et al.*, 1995a).

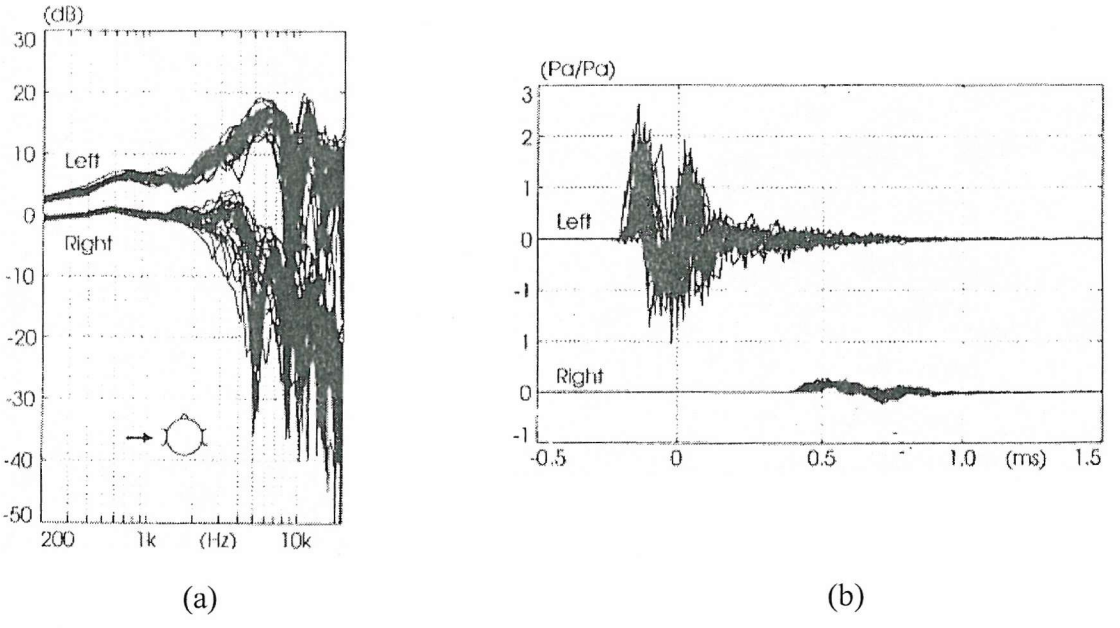

Figure 2.2 (a) The HRTFs and (b) the HRIRs for 40 subjects. The sound comes from the left side in the horizontal plane (after Møller *et al.*, 1995a).

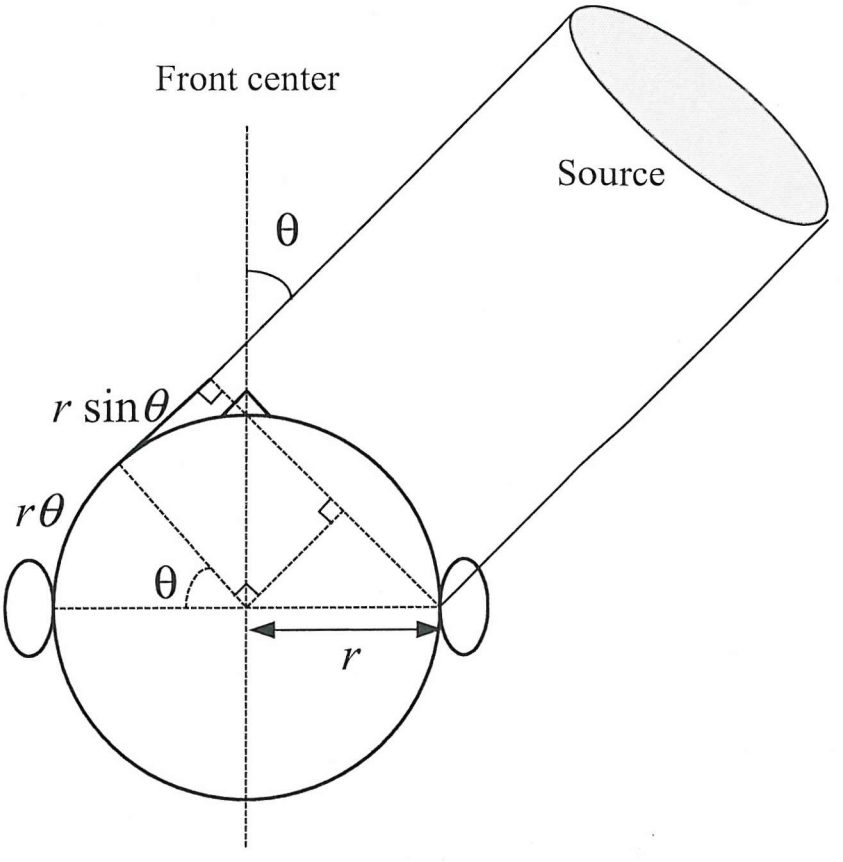

Figure 2.3 The interaural time difference for some angle of incidence of the source.

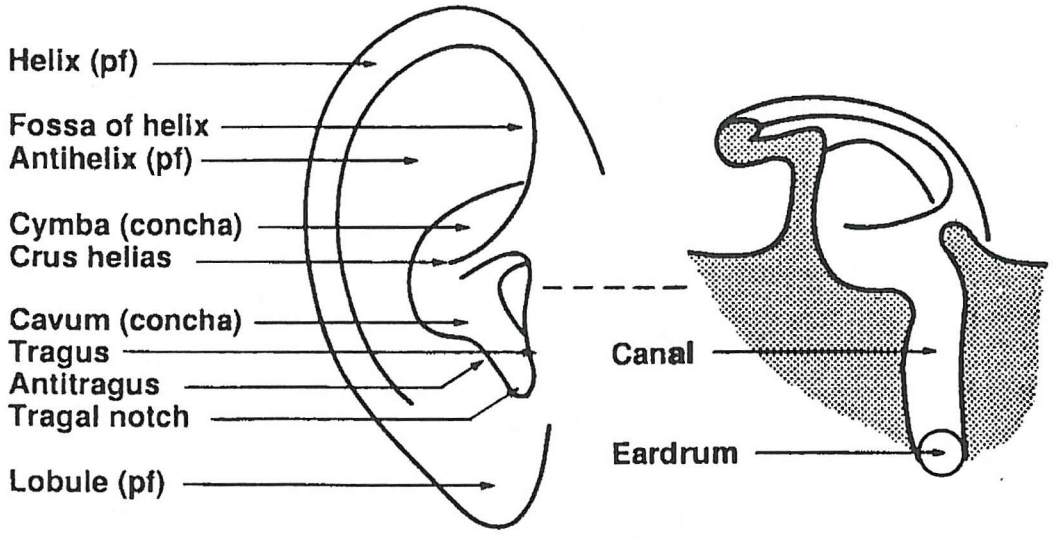

Figure 2.4 Descriptive diagram of external ear (after Shaw, 1997).

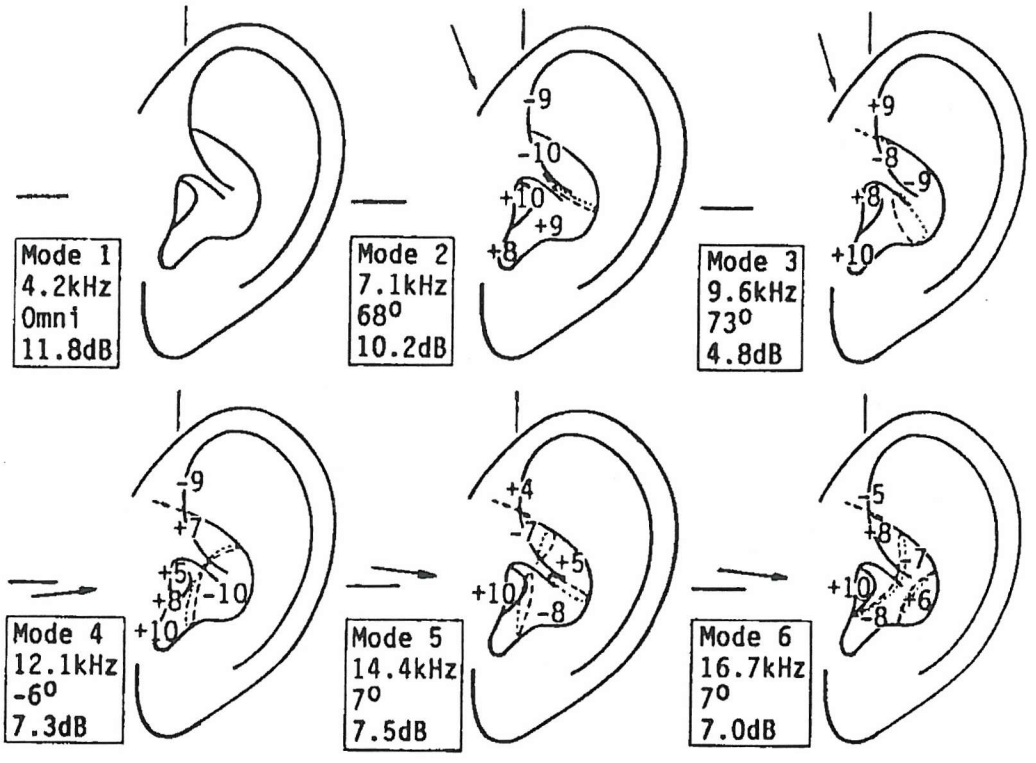

Figure 2.5 Average characteristics of six modes (after Shaw, 1997).

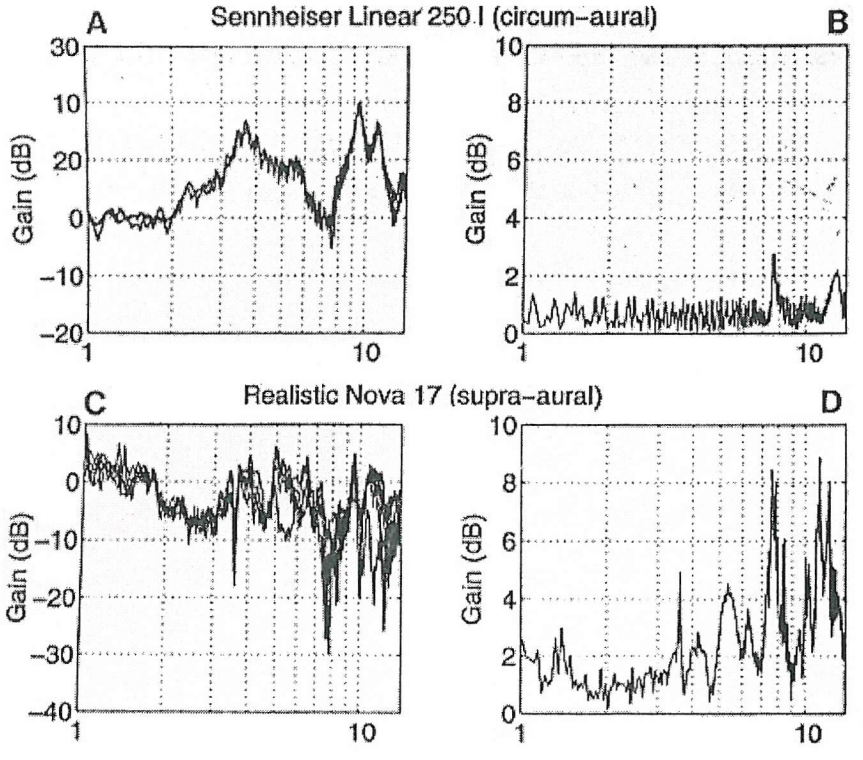

Figure 2.6 (A) Headphone transfer function for Senheiser 250 Linear circumaural headphones for six different placements of the headphones, (B) standard deviations for (A), (C) Headphone transfer function for Realistic Nova 17 supra-aural headphones, (D) standard deviations for (C) (after Pralong and Carlile, 1996)

CHAPTER 3
SPATIAL AUDIO

3.1 Introduction

The primary purpose of spatial audio can vary, depending on whether the application requires accurate rendering of sound sources and reflections over a 360° sphere, or whether it requires the production of an artistic or creative illusion although the distinction is not clear. For example, the applications for accurate 3D rendering can be virtual reality systems, or teleconferencing systems. The systems using binaural technology, "Ambisonics", or "Wave Field Synthesis" may be in this category. The applications for artistic illusion can be home theatre systems, computer games, or auralization systems. The various spatial audio systems from conventional two-channel stereo to modern 5.1 channel surround systems may be in this category. This chapter describes these various spatial audio systems.

3.2 Loudspeakers vs. headphones

The reproduction device of virtual acoustic systems can be either headphones or loudspeakers. Headphone reproduction systems have many advantages for the localization of virtual sound images. First, the influence of background noise can be substantially reduced. Second, headphone reproduction is independent of the condition of the listening room and the sitting position. This means that the "sweet spot" is everywhere for headphone reproduction. The "sweet spot" is the restricted area where a listener can hear spatialized sound that a spatial audio system intends to deliver to a listener. Third, headphone reproduction systems do not need cross-talk cancellation since each ear is fed only with one channel's signal. Fourth, the sound field inside a headphone is easier to control than the sound field from loudspeakers

since the relative position from a listener's eardrum to a headphone's transducer is nearly fixed. However, headphone reproduction systems can have disadvantages as well when acoustic spatial cues are not accurately produced. First, sound images can be localized inside a listener's head, so called "In-head localization". This often happens without any spatial cues, for example, in the case of stereo headphone reproduction for music listening. Second, front sound images can be confused with corresponding back sound images. Third, the undesirable spectral coloration such as resonance of the enclosed space can also occur inside the headphone. The sound field inside the headphone is influenced by the acoustic coupling between the listener's ear and the headphone. One might expect that those problems of headphone reproduction can be solved more effectively than those of loudspeaker reproduction since the headphone reproduction is easier to control. It has been demonstrated that sound images can be externalised by adding artificial reflections, and the front-back confusion can be overcome by allowing the movement of a listener's head by using head tracking devices (Begault *et al.*, 2000). The undesirable spectral coloration from the acoustical coupling between the ear and the headphone can be in principle removed by filtering the inverse headphone transfer function, in a so called equalization process (Møller *et al.*, 1995b).

On the other hand, loudspeaker reproduction systems have different features and advantages. They give a natural auditory environment rather than headphones that may be inconvenient for listeners in some cases. They also show good externalisation of sound images and give good frontal images. However, there is crosstalk between the signals at the two ears of the listener that does not occur with headphone reproduction. Therefore, an additional cross-talk cancellation process is needed for replaying binaural signals on loudspeakers. The condition of the listening room and background noise can influence listener's hearing for loudspeaker reproduction. The "sweet spot" produced by loudspeakers is usually narrow, and a listener should be within the sweet spot to hear spatialized sound that the loudspeakers intends to deliver. This narrowness of the sweet spot may be inconvenient for listeners since the listener is not free to choose where to sit for listening.

3.3 Two-channel spatial audio systems

Two-channel stereophonic reproduction is often called simply 'stereo'. Figure 3.1 shows the optimum arrangement of two loudspeakers and a listener for two-channel stereo listening. The optimum configuration for two-loudspeaker stereo is an equilateral triangle with the listener located just to the rear of the point of the triangle and the loudspeakers forming the baseline. The "phantom" or "virtual" sound source can be created in the angle between the two loudspeakers using only amplitude differences between the loudspeakers, where the time difference between the signals is small (Blumlein, 1931). It would be possible to create the phase and amplitude differences between the ears, similar to those in natural listening, by controlling the amplitude differences (Rumsey, 2001). If a time difference also exists between the channels, then transient sounds will be pulled towards the advanced speaker due to the precedence effect. However, the phantom sound source cannot be created beyond the loudspeakers and has some amount of mid range coloration called "hole in the middle" effect due to the lack of a centre loudspeaker. Sound stages tend to collapse into the nearest loudspeaker quite rapidly as one moves away from the ideal listening position or "sweet spot".

It is sometimes convenient to work with stereo signals in the so-called "sum and difference" format (Rumsey, 2001). The sum signal is denoted "M", and is based on the addition of the left (L) and right (R) signals, which is given by

$$M = (L+R) - 3 \text{ dB} \quad \text{or} \quad (L+R) - 6 \text{ dB}. \tag{3.1}$$

The M signal would be heard by someone listening to a stereo programme in mono. The difference signal is denoted "S", and is based on the subtraction of R from L, which is given by

$$S = (L-R) - 3 \text{ dB} \quad \text{or} \quad (L-R) - 6 \text{ dB}. \tag{3.2}$$

The correction factor ranging between –3 dB and –6dB is applied since overmodulation of the M channel can result from the case where a maximum level signal exists on both L and R signals representing a central image. If identical signals exist on the left and right channels, the –6dB correction factor is applied. If the left and right signals are non-coherent, the –3dB correction factor is applied. The sum and difference format signals can be used to reconstruct the left and right signal, and so it is possible to convert a stereo signal from one format to the other and back again.

Binaural stereo is used for signals that have been recorded or processed to represent the amplitude and timing characteristics of the sound pressures present at two human ears. This is based on the principle that the most accurate reproduction of natural spatial listening cues can be achieved if the ears of the listener can be provided with the same signals that they would have experienced in the natural listening environment. Binaural stereo signals or non-individualzied HRTFs can be recorded by using two microphones located in the ears of a dummy head. This recorded sound is assumed to encode all of the spatial cues received by the human ear. When these recorded binaural stereo signals are reproduced over a two-channel headphone, the listener can experience the virtual acoustic field. However, there are several problems associated with making accurate reproduction of spatial cues using binaural stereo (Begault, 1991). It is difficult to generalize the HRTFs that should be used for commercial systems since individual HRTFs are unique. Head movements that help to resolve front-back confusion in natural listening are not easy to incorporate into binaural stereo. Visual cues are often missing during binaural reproduction. Headphones differ in their equalization and method of mounting, which leads to distortions in the perceived HRTFs on reproduction. Sound images are often localized inside a listener's head. Distortions such as phase and frequency response errors in the signal chain can affect the subtle cues required. If the generalized HRTFs of "good localizers" are used, people can adapt to those HRTFs gradually. Head movements can be incorporated by using head tracking devices. Three-dimensional visual information can be given in full virtual reality systems. Headphones should be equalized to have a flat frequency response at the point in the ear where the binaural recording microphone was originally placed. If artificial reverberation is added to binaurally reproduced signals, the sound images can be externalized. Distortions in

the signal chain have been markedly reduced since the introduction of digital audio systems. When binaural signals are replayed on loudspeakers, additional cross-talk cancelling processing is required. However, the cross-talk-cancelling filters are only valid for a very narrow range of the "sweet spot".

3.4 Multi-channel spatial audio systems

Figure 3.2 shows the optimum arrangement for three-channel stereo listening. Three-channel stereo has three loudspeakers arranged equidistantly across the front sound stage and it requires the use of a left (L), centre (C) and right (R) channel. Although the three-channel stereo alone is rarely used, it forms the basis of many surround sound systems. It allows a wider front sound stage than the two-channel stereo because the centre channel acts to "anchor" the central image and the left and right loudspeakers be placed further out to the sides, for example ±45° (Rumsey, 2001). But, the angle between the outer loudspeakers is 60° in the ITU (International Telecommunications Union) standard configuration for compatibility with two-channel reproduction. It can also allow for a wider range of listening positions than the two-channel stereo because sound stages tend to collapse into the nearest loudspeaker less rapidly. The centre channel has the effect of stabilizing the important central image for off-centre listeners. The centre image does not suffer the timbral modification. However, the centre loudspeaker position is often very inconvenient. The centre loudspeaker should be placed above or below the television monitor in many cases, although it can be placed behind an acoustically transparent screen in cinema reproduction.

Four-channel systems add a surround channel to the three front channels. This was first developed for cinema applications where a large number of surround loudspeakers are fed from the single surround channel to give 'wrap-around' effects. In consumer systems, two surround loudspeakers are often fed from the single surround channel and the gain of the channel is usually reduced by 3dB (Rumsey, 2001). Since the surround channel is mono, the listener cannot hear decorrelated

signals to create a good sense of envelopment or spaciousness without using stereo surround channels. But artificial decorrelation between surround loudspeakers can be used to improve the spaciousness.

The "5.1-channel system" has been standardized for numerous surround sound applications. This system gives stereo effects and room ambience with a front-oriented sound stage. It has three front channels that are intended to be used for a conventional three-channel stereo sound image and two surround channels that are intended for generating supporting ambience or room impression. The system also incorporates an additional low frequency effects channel or sub-bass channel with an upper limit extending to a maximum of 120Hz. This sub-bass channel is not intended for conveying the low frequency component of the main channel signals. ITU-R BS. 775-1 (1994) specifies the channel configuration of the 5.1 surround system as shown in Fig. 3.3. The left and right loudspeakers are located at ±30° for compatibility with two-channel stereo reproduction. The surround loudspeakers are located at ±110° to provide a compromise between the need for effects panning behind the listener and the lateral energy important for good envelopment, but their locations are often inconvenient. The 5.1-channel surround system is not intended for accurate 360° phantom imaging capability. The front sound stage is narrower than it could be if compatibility with two-channel stereo reproduction were not a requirement. The centre channel can be a problem for music balancing designed for two-channel stereo. Two surround loudspeakers lead to a large hole in the potential image behind the listener since there is no loudspeaker behind the listener.

"Ambisonics" aims to offer a complete hierarchical approach to directional sound recording, storage or transmission and reproduction (Gerzon, 1977). The Ambisonics system encodes sound from all directions in terms of pressure and velocity components and decodes these signals to a number of loudspeakers. The inputs to the loudspeakers include psychoacoustically optimized shelf filtering above 700Hz to correct for the shadowing effects of the head and an amplitude matrix that determines the correct levels for each speaker for the layout chosen. The following formats exist for signals in the ambisonic system: the A-format for microphone pickup, the B-format for studio equipment and processing, the C-format for transmission, and the D-

format for decoding and reproduction. The A-format consists of the four signals from a microphone with four sub-cardioid capsules mounted on the four faces of a tetrahedron, and corresponds to left-front, right-front, left-back and right-back. The B-format consists of four signals that between them represent the pressure and velocity components of the sound field in any direction, and is made up of three orthogonal components (X, Y and Z) and an omnicomponent (W). The B-format signal may be derived from the A-format microphone by using a sum and difference technique. The C-format consists of four signals used for mono or stereo-compatible transmission or recording. The D-format signals are those distributed to loudspeakers for reproduction, and are adjusted depending on the selected loudspeaker layout. They may be derived from either B- or C-format signals using an appropriate decoder, and the number of speakers is not limited in theory. The incorporation of additional directional components into the Ambisonic signal structure can improve directional encoding that covers a larger listening area than first order Ambisonics. However, for this higher order Ambisonics, it is much more difficult to design microphones that produce the required polar patterns.

3.5 Wave field reproduction

Berkhout (1993) introduced the concept of electro-acoustic wave field synthesis that is based on the Huygens's principle. If a plane surface separating the listening area from the primary source area is considered in a given room, only knowledge of the sound pressure distribution on the surface is required. Each point on the surface contributes as a secondary source whose strength is given by the sound pressure at that point. Theory proved there were no differences between the electronically generated wave fields and the real wave fields. The wave fields of the sound sources on stage are measured by directional microphones, and then they are electronically extrapolated away from the stage, and finally they are re-emitted in the hall by many loudspeaker arrays, as shown in Fig. 3.4. This system can generate reflections in the same way as direct sound by using the image source concept. There can be a spatial aliasing effect due to spatial sampling above a certain frequency, so a sufficient

number of loudspeakers should be used to avoid this effect. The spacing of the loudspeakers must be less than half of the shortest wavelength of the reproduced sound. There can be also a truncation effects since a linear array has a finite length, and this can be overcome by using the main and side arrays with spatial windowing (Boone *et al.*, 1995). In practice, the loudspeaker array is mainly in the horizontal plane and spaciousness is also mainly observed in the horizontal plane.

Ise (1999) suggested a virtual acoustic system based on the boundary surface control principle that will be explained more in section 5.4. The sound field within a closed region can be reproduced if the sound pressure and its gradient on the boundary of the region are reproduced. The performance of this system is independent of a listener inside the reproduced region. Takane *et al.* (1999) also suggested a similar system to reproduce the boundary sound pressure and local sound intensity with additional control points to avoid the non-uniqueness problem at the eigenfrequencies of the internal control region.

3.6 Conclusion

This chapter described various spatial audio systems. Headphone reproduction systems have advantages for the localization of virtual sound images such as reduced background noise, no "sweet spot", no cross-talk cancellation, and high controllability. But they have disadvantages such as in-head localization, front-back confusion, and spectral coloration. Two-channel stereo systems can create a virtual sound source between two loudspeakers by controlling amplitude differences between two loudspeakers. Binaural stereo systems represent the amplitude and timing characteristics of the sound pressures present at two human ears, and the listener can experience virtual acoustic fields produced by a two-channel headphone using binaural stereo signals. 5.1-channel surround systems give stereo effects and room ambience with a front-oriented sound stage. Ambisonics systems and wave field synthesis systems aim to generate virtual acoustic fields in the control volume with a number of loudspeakers.

FIGURES

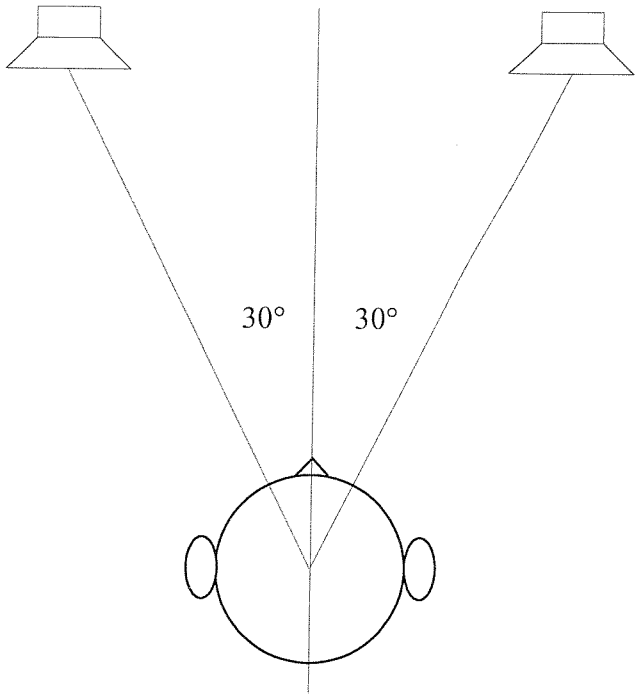

Figure 3.1 Optimum arrangement for two-channel stereo listening

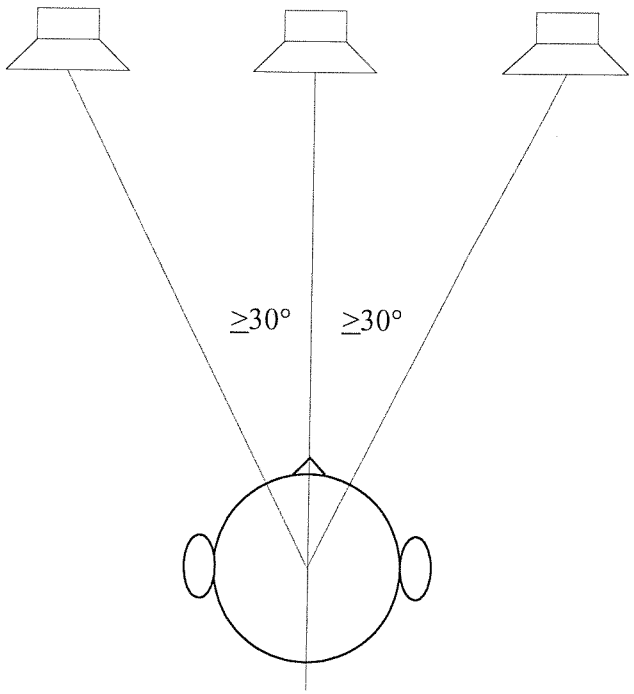

Figure 3.2 Optimum arrangement for three-channel stereo listening

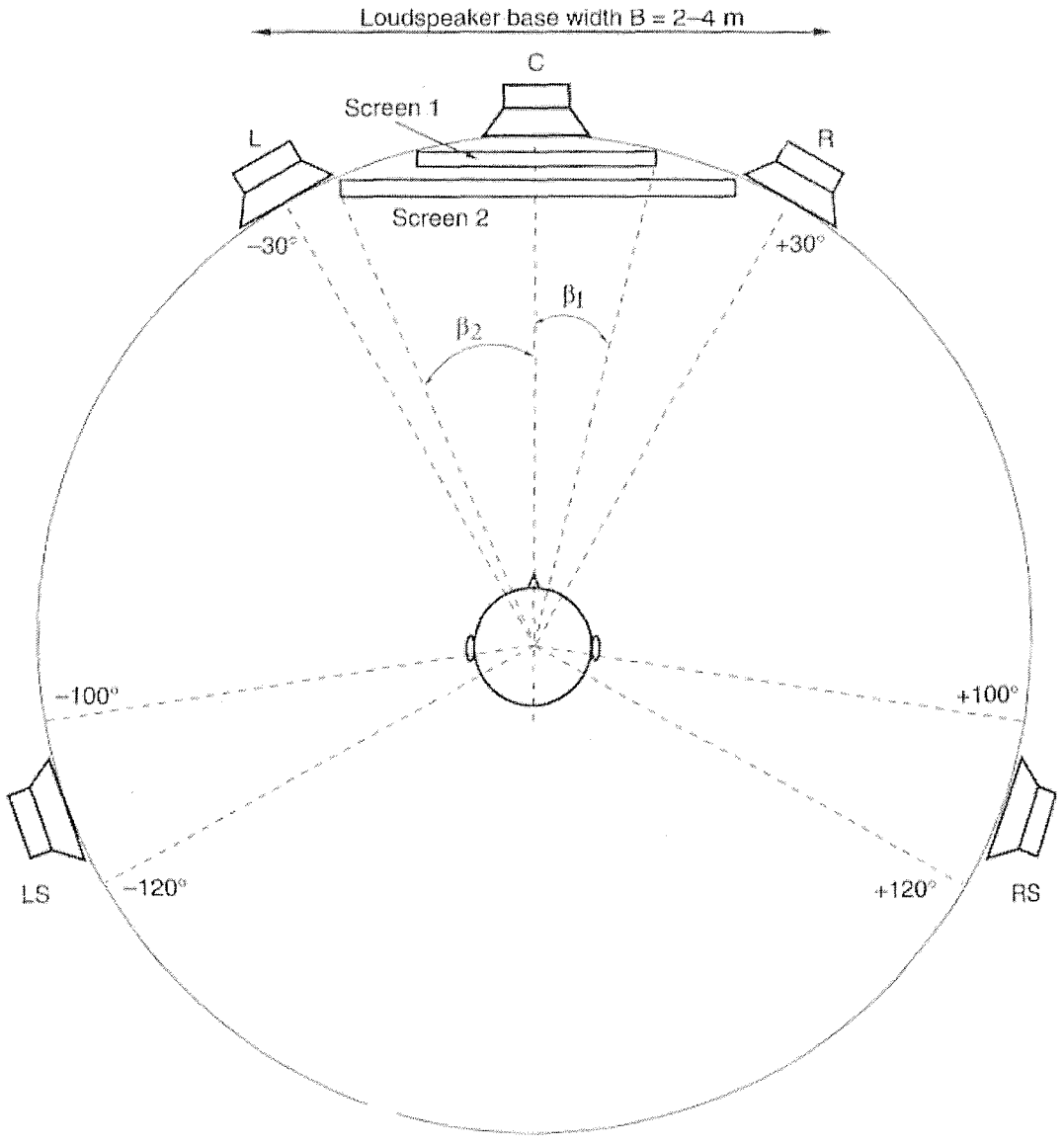

Screen 1: Listening distance = 3H (2 β_1 = 33°) (possibly more suitable for TV screen)
Screen 2: Listening distance = 2H (2 β_2 = 48°) (more suitable for projection screen)
H: Screen height

Figure 3.3 The loudspeaker layout and channel configuration in ITU-R BS.775-1.

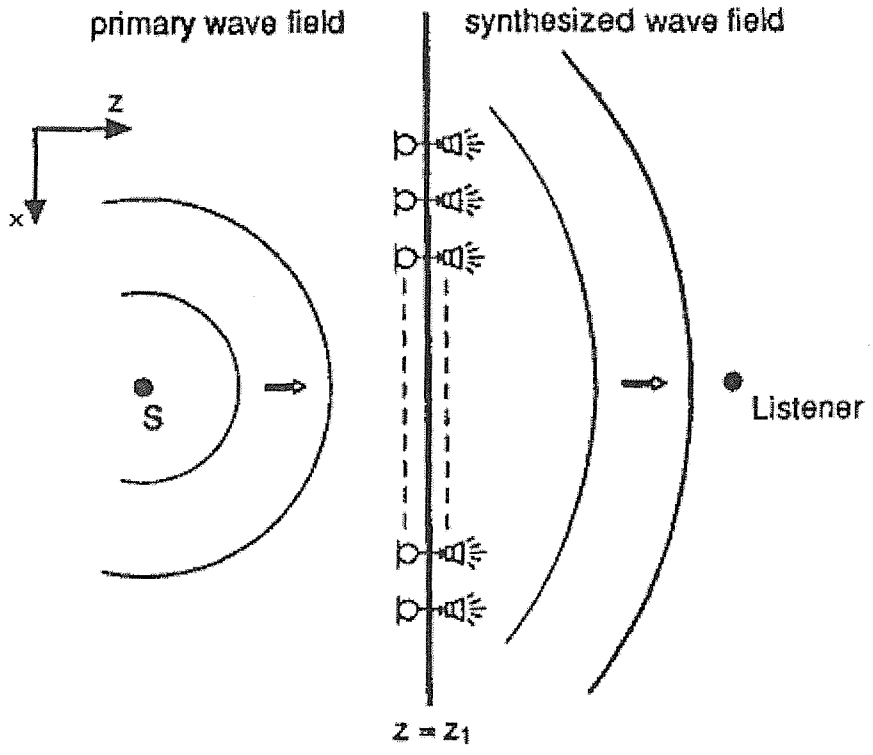

Figure 3.4 Implementation of wave field synthesis (after Berkhout, 1993).

CHAPTER 4
BOUNDARY ELEMENT ACOUSTICS

4.1 Introduction

In this chapter, the boundary element method is introduced and it is shown how acoustic fields are calculated by using the boundary element method. An introduction is given to the Kirchhoff-Helmholtz integral equation, on which the boundary element method is based. Then typical problems such as scattering problems are considered. The boundary element method is explained by using discretization and collocation, such that acoustic fields can be calculated numerically. The non-uniqueness problems for exterior problems are addressed and the number of over-determination points is discussed by undertaking some numerical calculations.

4.2 The Kirchhoff-Helmholtz integral equation

The acoustic pressure in an inviscid, quiescent, and homogeneous medium can be calculated by solving the linearized wave equation (Pierce, 1989). The wave equation for time-harmonic acoustic waves can be written as the Helmholtz equation. If there is no source in a given finite interior volume V bounded by a surface S, the solution of the inhomogeneous wave equation at a single frequency reduces to the Kirchhoff-Helmholtz integral equation that is given by (Nelson and Elliott, 1992)

$$C^0(\mathbf{x})\,p(\mathbf{x}) = \int_S \left(g(\mathbf{x}|\mathbf{y})\frac{\partial p(\mathbf{y})}{\partial n} - p(\mathbf{y})\frac{\partial g(\mathbf{x}|\mathbf{y})}{\partial n} \right) dS \qquad (4.1)$$

where **x** is a position vector, **y** is a position vector on the boundary surface S enclosing a given volume V, p is the complex acoustic pressure, and $g(\mathbf{x}|\mathbf{y})$ is the free space Green function which is given by

$$g(\mathbf{x}|\mathbf{y}) = \frac{e^{-jk|\mathbf{x}-\mathbf{y}|}}{4\pi|\mathbf{x}-\mathbf{y}|} \tag{4.2}$$

where k is the wavenumber. In this thesis, we use the letter j to stand for $\sqrt{-1}$ and the symbol $e^{j\omega t}$ to express simple-harmonic dependence on time. Note that some books on acoustical engineering use the symbol i instead of j and $e^{-i\omega t}$ with the negative sign in the exponential. The rate of change of a scalar function p at a point **y** in a direction given by a vector **n** is defined as a directional derivative of p at **y** in the direction of **n**, which is given by

$$\frac{\partial p(\mathbf{y})}{\partial n} = \nabla_y p(\mathbf{y}) \bullet \mathbf{n} \tag{4.3}$$

where ∇_y is the differential operator with respect to **y**, **n** is the unit outward normal on S (pointing into the external volume in this case), and n is the distance from a point **y** in the direction of **n**. The directional derivative of $g(\mathbf{x}|\mathbf{y})$ follows in the same manner. When a given acoustic domain is in a cavity V of finite dimensions, the coefficient $C^0(\mathbf{x})$ for an interior acoustic problem is given by (Wu, 2000a)

$$C^0(\mathbf{x}) = -\int_S \frac{\partial \psi_L(\mathbf{x}|\mathbf{y})}{\partial n} dS = -\int_S \frac{\partial}{\partial n}\left(\frac{1}{4\pi|\mathbf{x}-\mathbf{y}|}\right) dS . \tag{4.4}$$

where ψ_L is the fundamental solution of the Laplace equation. The coefficient $C^0(\mathbf{x})$ can be evaluated by integrating the normal derivative of the fundamental solution of the Laplace equation over the surface S numerically. For example, the coefficient $C^0(\mathbf{x})$ is equal to unity if **x** is within V, zero if **x** is outside V, and 0.5 if **x** is on a smooth boundary S (Wu, 2000a). The detailed explanation of the Kirchhoff-Helmholtz integral equation and the coefficient $C^0(\mathbf{x})$ can be found in Appendix. The

normal derivative of sound pressure is related to the normal particle velocity (Nelson and Elliott, 1992):

$$\frac{\partial p(\mathbf{y})}{\partial n} = -j\omega\rho_0 v_n(\mathbf{y}) \tag{4.5}$$

where ω is the angular frequency, ρ_0 is the mean density of the fluid, and v_n is the normal particle velocity. Then equation (4.1) becomes

$$C^0(\mathbf{x})p(\mathbf{x}) = -\int_S \left(j\omega\rho_0 v_n(\mathbf{y}) g(\mathbf{x}|\mathbf{y}) + p(\mathbf{y}) \frac{\partial g(\mathbf{x}|\mathbf{y})}{\partial n} \right) dS . \tag{4.6}$$

If there is no source in a given unbounded exterior volume V with a structure bounded by the surface S in a medium, the Kirchhoff-Helmholtz integral equation for an exterior acoustic problem can be written as

$$C(\mathbf{x})p(\mathbf{x}) = -\int_S \left(j\omega\rho_0 v_n(\mathbf{y}) g(\mathbf{x}|\mathbf{y}) + p(\mathbf{y}) \frac{\partial g(\mathbf{x}|\mathbf{y})}{\partial n} \right) dS \tag{4.7}$$

where the coefficient $C(\mathbf{x})$ for an exterior problem is given by (Wu, 2000a)

$$C(\mathbf{x}) = 1 - \int_S \frac{\partial \psi_L(\mathbf{x}|\mathbf{y})}{\partial n} dS = 1 - \int_S \frac{\partial}{\partial n} \left(\frac{1}{4\pi|\mathbf{x}-\mathbf{y}|} \right) dS = 1 - C^0(\mathbf{x}) . \tag{4.8}$$

For example, the coefficient $C(\mathbf{x})$ is equal to unity if $\mathbf{x}$ is within V, zero if $\mathbf{x}$ is outside V, and 0.5 if $\mathbf{x}$ is on a smooth boundary S.

The Kirchhoff-Helmholtz integral equation can be solved if the boundary conditions on the boundary surface S are given. The following three different boundary conditions are associated with the Kirchhoff-Helmholtz integral equation (Estorff, Coyette and Migeot, 2000):

- Dirichlet boundary conditions, where pressure values are imposed on some boundary segments

- Neumann boundary conditions, where normal particle velocity values are imposed on some boundary segments
- Robin or mixed boundary conditions, where a linear combination of pressure values and normal particle velocity values are imposed on some boundary segments

Note that only a single type of boundary condition may be prescribed on any part of the boundary. Let us consider an interior acoustic problem with each boundary condition on the assumption that the boundary surface S is smooth for simplicity.
The Kirchhoff-Helmholtz integral equation with the Dirichlet boundary condition is given by

$$\int_S j\omega\rho_0 v_n(\mathbf{y})\, g(\mathbf{x}|\mathbf{y})\, dS = -\frac{1}{2}p(\mathbf{x}) - \int_S p(\mathbf{y})\frac{\partial g(\mathbf{x}|\mathbf{y})}{\partial n} dS . \tag{4.9}$$

The unknown v_n has been moved to the left hand side and the known p has been moved to the right hand side. Then this integral equation can be solved numerically by using a discretization and collocation scheme (Wu, 2000b). Equation (4.6) with the Neumann boundary condition can be rewritten as

$$\frac{1}{2}p(\mathbf{x}) + \int_S p(\mathbf{y})\frac{\partial g(\mathbf{x}|\mathbf{y})}{\partial n} dS = -\int_S j\omega\rho_0 v_n(\mathbf{y})\, g(\mathbf{x}|\mathbf{y})\, dS . \tag{4.10}$$

Since the unknown variable is p, the right hand side of Eq. (4.9) becomes the left hand side and vice versa. The mixed boundary condition can be written in the following general form:

$$C_1(\mathbf{y})\, p(\mathbf{y}) + C_2(\mathbf{y})\, v_n(\mathbf{y}) = C_3(\mathbf{y}) \tag{4.11}$$

where C_1, C_2, and C_3 are coefficients. If C_2=0, it becomes the Dirichlet boundary condition and if C_1=0, it becomes the Neumann boundary condition. If $C_2 \neq 0$, equation (4.11) can be rewritten as

$$v_n(\mathbf{y}) = \frac{1}{C_2(\mathbf{y})}\left(C_3(\mathbf{y}) - C_1(\mathbf{y})\, p(\mathbf{y})\right). \tag{4.12}$$

By using Eq. (4.12), equation (4.6) with the mixed boundary condition can be rewritten as

$$\begin{aligned}&\frac{1}{2}p(\mathbf{x})+\int_S p(\mathbf{y})\left(\frac{\partial g(\mathbf{x}|\mathbf{y})}{\partial n}-j\omega\rho_0\frac{C_1(\mathbf{y})}{C_2(\mathbf{y})}g(\mathbf{x}|\mathbf{y})\right)dS\\&=-\int_S j\omega\rho_0\frac{C_3(\mathbf{y})}{C_2(\mathbf{y})}g(\mathbf{x}|\mathbf{y})dS\end{aligned} \tag{4.13}$$

where the unknown variable is p in this case.

4.3 Scattering problems

In a typical scattering problem, an incident sound wave is striking a solid obstacle V' in an unbounded exterior acoustic domain V, as shown in Fig. 4.1. The total sound field p may be composed of the incident sound field p_{in} and the scattered sound field p_{sc}:

$$p(\mathbf{x})=p_{in}(\mathbf{x})+p_{sc}(\mathbf{x}) \tag{4.14}$$

where $\mathbf{x}$ is a position vector in the volume V. The incident sound field can be interpreted as the sound field in the absence of the scatterer, and the scattered sound field can be interpreted as the sound field arising from the interaction of the incident sound field with the scatterer. The total normal particle velocity may also be composed of the incident normal particle velocity v_{nin} and the scattered normal particle velocity v_{nsc}:

$$v_n(\mathbf{y})=v_{nin}(\mathbf{y})+v_{nsc}(\mathbf{y}). \tag{4.15}$$

Both p_{in} and p_{sc} satisfy the Kirchhoff-Helmholtz integral equation, but only the scattered sound field p_{sc} should satisfy the Sommerfeld radiation condition (Wu, 2000a). For example, the plane wave from the sound source does not satisfy the

Sommerfeld radiation condition. The scattered sound field in an unbounded exterior domain V can be given by

$$C(\mathbf{x})p_{sc}(\mathbf{x}) = -\int_S \left(j\omega\rho_0 v_{nsc}(\mathbf{y})g(\mathbf{x}|\mathbf{y}) + p_{sc}(\mathbf{y})\frac{\partial g(\mathbf{x}|\mathbf{y})}{\partial n} \right) dS . \tag{4.16}$$

The interior Kirchhoff-Helmholtz integral equation can be applied to the incident sound field in the hypothetical interior acoustic domain V' where the Sommerfeld radiation condition is not required. If we keep the same direction of normal vector as in Eq. (4.16), that is, the direction of normal vector is pointing into the solid structure, equation (4.6) can be rewritten for an interior domain V' as:

$$C^0(\mathbf{x})p_{in}(\mathbf{x}) = \int_S \left(j\omega\rho_0 v_{nin}(\mathbf{y})g(\mathbf{x}|\mathbf{y}) + p_{in}(\mathbf{y})\frac{\partial g(\mathbf{x}|\mathbf{y})}{\partial n} \right) dS . \tag{4.17}$$

Note that the coefficient $C^0(\mathbf{x})$ becomes zero when the vector $\mathbf{x}$ is inside the exterior volume V, and then equation (4.17) becomes

$$\int_S \left(j\omega\rho_0 v_{nin}(\mathbf{y})g(\mathbf{x}|\mathbf{y}) + p_{in}(\mathbf{y})\frac{\partial g(\mathbf{x}|\mathbf{y})}{\partial n} \right) dS = 0 . \tag{4.18}$$

By substracting Eq. (4.17) from Eq. (4.16), equation becomes

$$\begin{aligned} & C(\mathbf{x})\{p(\mathbf{x}) - p_{in}(\mathbf{x})\} - C^0(\mathbf{x})p_{in}(\mathbf{x}) \\ & = -\int_S \left(j\omega\rho_0 v_n(\mathbf{y})g(\mathbf{x}|\mathbf{y}) + p(\mathbf{y})\frac{\partial g(\mathbf{x}|\mathbf{y})}{\partial n} \right) dS. \end{aligned} \tag{4.19}$$

Since $C(\mathbf{x}) + C^0(\mathbf{x}) = 1$, equation (4.19) becomes

$$C(\mathbf{x})p(\mathbf{x}) = p_{in}(\mathbf{x}) - \int_S \left(j\omega\rho_0 v_n(\mathbf{y})g(\mathbf{x}|\mathbf{y}) + p(\mathbf{y})\frac{\partial g(\mathbf{x}|\mathbf{y})}{\partial n} \right) dS . \tag{4.20}$$

This is the integral equation for a scattering problem in an unbounded medium. The boundary condition and geometry of the scatterer and the incident sound field determine the total sound field or scattered sound field. When the vector **x** is inside the exterior volume V, equation (4.20) can be rewritten as

$$\begin{aligned} p(\mathbf{x}) &= p_{in}(\mathbf{x}) - \int_S \left(j\omega\rho_0 v_{nsc}(\mathbf{y}) g(\mathbf{x}|\mathbf{y}) + p_{sc}(\mathbf{y}) \frac{\partial g(\mathbf{x}|\mathbf{y})}{\partial n} \right) dS \\ &= p_{in}(\mathbf{x}) + p_{sc}(\mathbf{x}). \end{aligned} \tag{4.21}$$

Note that this equation is the same as Eq. (4.14). With a given source strength distribution Q_{vol} per unit volume in an acoustic domain V, equation (4.20) is often rewritten as

$$\begin{aligned} C(\mathbf{x}) p(\mathbf{x}) = &- \int_S \left(j\omega\rho_0 v_n(\mathbf{y}) g(\mathbf{x}|\mathbf{y}) + p(\mathbf{y}) \frac{\partial g(\mathbf{x}|\mathbf{y})}{\partial n} \right) dS \\ &+ \int_V Q_{vol}(\mathbf{y}_v) g(\mathbf{x}|\mathbf{y}_v) dV \end{aligned} \tag{4.22}$$

where the position vector $\mathbf{y}_v$ is in the volume V.

4.4 Discretization and collocation

The Kirchhoff-Helmholtz integral equation with given boundary conditions can be solved numerically by using discretization and collocation. The boundary surface can be discretized into a number of boundary elements, such as four-node quadrilateral elements or three-node triangular elements in three-dimensional problems. The geometry of each boundary element can be represented by interpolation between the nodal points. If we choose an *xyz* Cartesian coordinate system in three-dimensional space, the components of the position vector $\mathbf{x} = [x, y, z]$ can be written as

$$x=\sum_{j=1}^{n_j} x_j N_j(\xi_1,\xi_2)$$
$$y=\sum_{j=1}^{n_j} y_j N_j(\xi_1,\xi_2) \tag{4.23}$$
$$z=\sum_{j=1}^{n_j} z_j N_j(\xi_1,\xi_2)$$

where x_j, y_j, and z_j are the coordinates at nodal points, $N_j(\xi_1, \xi_2)$ are the linear shape functions defined on a master element with a local coordinate $-1 \le \xi \le 1$, and n_j is the number of nodes (3 or 4) on the element. Figure 4.2 shows the mapping between a real element and its corresponding master element. The shape functions for four-node quadrilateral elements are given by (Wu, 2000b)

$$N_1=\frac{1}{4}(1-\xi_1)(1-\xi_2)\ , \qquad N_2=\frac{1}{4}(1+\xi_1)(1-\xi_2)$$
$$N_3=\frac{1}{4}(1+\xi_1)(1+\xi_2)\ , \qquad N_4=\frac{1}{4}(1-\xi_1)(1+\xi_2). \tag{4.24}$$

The shape functions for three-node triangular elements are given by

$$N_1=\xi_1\ ,\quad N_2=\xi_2\ ,\quad N_3=1-\xi_1-\xi_2\,. \tag{4.25}$$

For example, consider a scattering problem in an unbounded medium. If the surface S is divided into a set of n_e boundary elements, the integration of the Kirchhoff-Helmholtz equation over S in Eq. (4.20) is approximated by a sum of integrals over all boundary elements S_i, such that (Estorff *et al.*, 2000):

$$C(\mathbf{x})\,p(\mathbf{x})=-\sum_{i=1}^{n_e}\int_{S_i}\left(j\omega\rho_0 v_n(\mathbf{y})\,g(\mathbf{x}|\mathbf{y})+p(\mathbf{y})\frac{\partial g(\mathbf{x}|\mathbf{y})}{\partial n}\right)dS+p_{in}(\mathbf{x})\,. \tag{4.26}$$

With isoparametric elements, the sound pressure and normal particle velocity on each element can be approximated by a linear combination of shape functions:

$$p_i = \sum_{j=1}^{n_j} p_{ij} N_j(\xi_1, \xi_2)$$
$$v_{ni} = \sum_{j=1}^{n_j} v_{nij} N_j(\xi_1, \xi_2) \tag{4.27}$$

where p_{ij} and v_{nij} are the j-th nodal value of the sound pressure and the normal particle velocity on i-th element, respectively. Then equation (4.26) can be approxicated by

$$\begin{aligned} & C(\mathbf{x}) p(\mathbf{x}) - p_{in}(\mathbf{x}) \\ &= -\sum_{i=1}^{n_e} \int_{S_i} \left(j\omega\rho_0 g(\mathbf{x}|\mathbf{y}) \sum_{j=1}^{n_j} v_{nij} N_j(\mathbf{y}) + \frac{\partial g(\mathbf{x}|\mathbf{y})}{\partial n} \sum_{j=1}^{n_j} p_{ij} N_j(\mathbf{y}) \right) dS \\ &= -\sum_{i=1}^{n_e} \sum_{j=1}^{n_j} \left(j\omega\rho_0 v_{nij} \int_{S_i} g(\mathbf{x}|\mathbf{y}) N_j(\mathbf{y})\, dS + p_{ij} \int_{S_i} \frac{\partial g(\mathbf{x}|\mathbf{y})}{\partial n} N_j(\mathbf{y})\, dS \right) \end{aligned} \tag{4.28}$$

The nodal values are taken in front of the integral since they are independent of S_i. The two summations can be replaced by a sum of sound pressure or velocity over all nodes:

$$\begin{aligned} & C(\mathbf{x}) p(\mathbf{x}) - p_{in}(\mathbf{x}) \\ &= -\sum_{j=1}^{n_n} \left(j\omega\rho_0 v_{nj} \sum_{i=1}^{n_e} \int_{S_i} g(\mathbf{x}|\mathbf{y}) N_{ij}(\mathbf{y})\, dS + p_j \sum_{i=1}^{n_e} \int_{S_i} \frac{\partial g(\mathbf{x}|\mathbf{y})}{\partial n} N_{ij}(\mathbf{y})\, dS \right) \end{aligned} \tag{4.29}$$

where n_n is the total number of nodes in all the boundary element mesh and N_{ij} the shape function of node j of element i. Equation (4.29) can be rewritten as

$$C(\mathbf{x}) p(\mathbf{x}) + \sum_{j=1}^{n_n} p_j H_j(\mathbf{x}) - \sum_{j=1}^{n_n} v_{nj} G_j(\mathbf{x}) - p_{in}(\mathbf{x}) = 0 \tag{4.30}$$

where

$$\begin{aligned} H_j(\mathbf{x}) &= \sum_{i=1}^{n_e} \int_{S_i} \frac{\partial g(\mathbf{x}|\mathbf{y})}{\partial n} N_{ij}(\mathbf{y})\, dS \\ G_j(\mathbf{x}) &= -j\omega\rho_0 \sum_{i=1}^{n_e} \int_{S_i} g(\mathbf{x}|\mathbf{y}) N_{ij}(\mathbf{y})\, dS. \end{aligned} \tag{4.31}$$

The numerical integration on each element can be done by applying the standard Gaussian quadrature in both coordinate directions of the master element (Wu, 2000b). Then the position vector **x** can be collocated at each of the nodal points on each boundary element S_i successively. If the vector **x** is collocated at node k, equation (4.30) can be rewritten as

$$C_k p_k + \sum_{j=1}^{n_n} p_j H_{kj} - \sum_{j=1}^{n_n} v_{nj} G_{kj} - p_{ink} = 0, \tag{4.32}$$

or in compacted form

$$\sum_{j=1}^{n_n} p_j \left(H_{kj} + C_k \delta_{kj} \right) - \sum_{j=1}^{n_n} v_{nj} G_{kj} - p_{ink} = 0 \tag{4.33}$$

where δ_{kj} (δ_{kj} =0 for $j \neq k$ and δ_{kj} =1 for $j=k$) is the Kronecker symbol. The vectors H_{kj}, G_{kj}, and $C_k \delta_{kj}$ for each node k can be assembled into a global matrix **H′**, **G** and **C** respectively. For example, the matrix **H′** and **C** is given by

$$\mathbf{H}' = \begin{bmatrix} H_{11} & H_{12} & \cdots & H_{1n_n} \\ H_{21} & \ddots & & H_{2n_n} \\ \vdots & & H_{kj} & \vdots \\ H_{n_n 1} & H_{n_n 2} & \cdots & H_{n_n n_n} \end{bmatrix}, \quad \mathbf{C} = \begin{bmatrix} C_1 & 0 & \cdots & 0 \\ 0 & C_2 & & 0 \\ \vdots & & \ddots & \vdots \\ 0 & 0 & \cdots & C_{n_n} \end{bmatrix} \tag{4.34}$$

The matrix **G** has the same format as the matrix **H′**. Note that **C** is a diagonal matrix. This produces

$$\mathbf{H}'\mathbf{p} + \mathbf{C}\mathbf{p} = \mathbf{G}\mathbf{v}_n + \mathbf{p}_{in}. \tag{4.35}$$

Combining **C** and **H′** into one single matrix **H** produces

$$\mathbf{H}\mathbf{p} = \mathbf{G}\mathbf{v}_n + \mathbf{p}_{in}. \tag{4.36}$$

This gives a system of n_n equations with 2 n_n unknowns. If n_n unknowns are specified by the boundary conditions, this system of equations may be solved. If all the boundary unknowns stay on the left hand side, equation (4.36) becomes

$$\mathbf{Ax} = \mathbf{b} \tag{4.37}$$

where the unknown vector denotes **x**. Then, equation (4.37) can be solved by inverting the matrix **A**. Once the equation is solved, that is, the sound pressure and normal particle velocity on the boundary surface are known, the sound pressure at any point can be evaluated numerically from the discretized Kirchhoff-Helmholtz integral equation (4.30) in the acoustic domain, which is given by

$$C(\mathbf{x})\,p(\mathbf{x}) = -\sum_{j=1}^{n_n} p_j H_j(\mathbf{x}) + \sum_{j=1}^{n_n} v_{nj} G_j(\mathbf{x}) + p_{in}(\mathbf{x}). \tag{4.38}$$

4.5 The non-uniqueness problem

The non-uniqueness problem of the boundary element method can arise because the Helmholtz integral equation for an exterior acoustic radiation and scattering problem does not have a unique solution at certain characteristic eigenfrequencies associated with the corresponding interior problem (Wu, 2000a). The Helmholtz integral equation for an exterior Dirichlet problem is the same as Eq. (4.9) on the assumption that the boundary surface S is smooth and there is no sound source for simplicity. Note that the theory remains valid for non-smooth boundary surfaces and scattering problems. The directions of the normal vectors are pointing away from the exterior acoustic domain or into the solid body, in this case. Consider an auxiliary interior Dirichlet problem associated the same boundary surface. If we keep the same directions of normal vectors as used in the corresponding exterior problems, the Helmholtz equation for an interior Dirichlet problem is given by

$$\int_S j\omega\rho_0 v_n(\mathbf{y})\, g(\mathbf{x}|\mathbf{y})\, dS = \frac{1}{2} p(\mathbf{x}) - \int_S p(\mathbf{y}) \frac{\partial g(\mathbf{x}|\mathbf{y})}{\partial n} dS \tag{4.39}$$

where the normal vectors are pointing away from the exterior domain. The left hand side of Eq. (4.39) is the same as that of Eq. (4.9). Equation (4.39) can be written in matrix forms as $\mathbf{G}\mathbf{v}_n = (0.5\mathbf{I} - \mathbf{H}')\,\mathbf{p}$ as discussed in the previous section, and equation (4.9) can be also written as $\mathbf{G}\mathbf{v}_n = (-0.5\mathbf{I} - \mathbf{H}')\,\mathbf{p}$. The left hand side of both Eq. (4.39) and (4.9) determines the same coefficient matrix $\mathbf{G}$ as that in Eq. (4.36). It is well known that this integral equation establishes a unique relationship between the surface sound pressure and the surface normal particle velocity except at frequencies that are natural frequencies of the interior Dirichlet problem (Schenck, 1968). The coefficient matrix $\mathbf{G}$ thus becomes singular at eigenfrequencies of the interior Dirichlet problem. Therefore, although the exterior problem does not have any resonance at all, the Helmholtz integral equation for an exterior Dirichlet problem does not have a unique solution at eigenfrequencies associated with the corresponding interior problem. For an exterior Neumann problem or mixed problem, the non-uniqueness problem also occurs at eigenfrequencies of the interior Dirichlet problem (Wu, 2000a).

The possible solution of the non-uniqueness problem is the CHIEF (Combined Helmholtz Integral Equation Formulation) method, which collocates the Helmholtz integral equation at a few interior points inside the body as constraint equations (Benthien and Schenck, 1997). This CHIEF method is often used in the "direct" boundary element method using the collocation scheme. When the vector $\mathbf{x}$ is collocated inside the body, the CHIEF equations are given by

$$0 = -\int_S \left(j\omega\rho_0 v_n(\mathbf{y})\, g(\mathbf{x}|\mathbf{y}) + p(\mathbf{y}) \frac{\partial g(\mathbf{x}|\mathbf{y})}{\partial n} \right) dS \tag{4.40}$$

The left hand side is zero because the coefficient $C(\mathbf{x})$ for an exterior acoustic problem in Eq. (4.8) is zero. This leads to an over-determined system of equations for the surface pressures. These interior points are often called the CHIEF points or over-determination points. The choice of number and position of the over-determination

points can be a potential problem. If a chosen over-determination point is on a nodal point of the associated interior eigenmode, then the CHIEF method fails at the corresponding eigenfrequency. The number of over-determination points depends on the number of eigenfrequencies that must be eliminated. Because the number of eigenfrequencies is approximately proportional to cube of the frequency (Pierce, 1989), the non-uniqueness problem is hard to overcome at high frequencies. If too many over-determination points are collocated inside the body, the existing surface Helmholtz integral equation may be unstable. Therefore, the optimal number of the over-determination points should be evaluated, and this can be different for each case for which a solution is sought.

4.6 Number of over-determination points

The non-uniqueness problem of the boundary element method for an exterior problem can be solved by collocating the over-determination points inside the numerical model for the direct boundary element method. The required number of the over-determination points increases as frequency increases since the number of eigenfrequencies of the interior Dirichlet problem increases as frequency increases. Therefore, the optimal number of the over-determination points depends on frequency. The basic geometry of a sphere is studied for the optimal number of the over-determination points. When a plane wave is incident on a sphere from the front as shown in Fig. 4.3, the incident sound field can be written as (Morse and Ingrad, 1968)

$$p_i(r,\theta,\omega) = p_0 \exp(j\omega t)\left(\sum_{m=0}^{\infty}(2m+1)(-j)^m P_m(-\cos\theta) j_m(kr)\right) \qquad (4.41)$$

where p_i is the complex incident sound pressure, p_0 is an initial sound pressure, θ is a polar angle, r is a distance from the centre of the sphere, the function P_m is called the Legendre function of order m, and the function j_m is called the spherical Bessel function of order m. The scattered sound field is given by

$$p_s(r,\theta,\omega) = p_0 \exp(j\omega t)\sum_{m=0}^{\infty} A_m h_m^{(2)}(kr) P_m(-\cos\theta) \tag{4.42}$$

where A_m is a constant and the function $h_m^{(2)}$ is called the spherical Hankel function of the second kind of order m. If the surface of the sphere is rigid at $r=a$, we can evaluate A_m. Then the total sound field can be written as (Kahana, 1997)

$$\begin{aligned} &p_{tot}(r,\theta,\omega) \\ &= p_0 \exp(j\omega t)\sum_{m=0}^{\infty} (-j)^{m+1}(2m+1) P_m(-\cos\theta) \frac{j_m(kr) n_m'(ka) - n_m(kr) j_m'(ka)}{j_m'(ka) - j n_m'(ka)} \end{aligned} \tag{4.43}$$

where the function n_m is called the spherical Neumann function of order m, and n'_m and j'_m are derivatives with respect to kr. The total sound pressure on the surface of the sphere can be rewritten as

$$p_{tot}(a,\theta,\omega) = p_0 \exp(j\omega t)\sum_{m=0}^{\infty} \frac{(-j)^{m+1}(2m+1)(ka)^{-2} P_m(-\cos\theta)}{j_m'(ka) - j n_m'(ka)} \tag{4.44}$$

The numerical model of the sphere having a radius of 87.5 mm, which is an approximate model of human head, is used to compare the results of the numerical simulation with the analytical solution in Eq. (4.44). The radius is the same as that of the numerical head model shown in chapter 7. The source of the plane wave is placed at the front at the polar angle of zero, its direction is toward the centre of the sphere, and its complex amplitude is 1 at all frequencies, that is, 90.97 dB ref 2×10^{-5} Pa. The sound pressure on the surface of the sphere from the analytical solution is calculated by adding one hundred terms in the series of Eq. (4.44). The sound pressure on the surface of the numerical sphere model is calculated from 200Hz to 10000Hz with a constant frequency increment of 200Hz by using the direct boundary element method. The over-determination points are collocated inside the sphere randomly, and the number is changed from zero to two hundred. Figure 4.4 shows the differences between the sound pressure levels calculated for the theory and the sound pressure levels calculated in the numerical simulation when the measurement point is at the front of the sphere surface, that is, the polar angle $\theta = 0$. This figure shows that the

small number of the over-determination points produces numerical errors at high frequencies and the large number of over-determination points produces numerical errors at low frequencies. Therefore, a small number of them is required at low frequencies and a large number is required at high frequencies. Figure 4.5 shows the sum of the sound pressure level differences shown in Figure 4.4 over frequency. This figure shows that 130 of the over-determination points are the optimal value from 200Hz to 10kHz. Figure 4.6, 4.7, 4.8 and 4.9 shows the comparison between the sound pressure level for the theory and the simulation measured at the front of sphere surface for zero, 50, 130, and 200 over-determination points respectively. Figure 4.10 shows the sound pressure level differences between theoretical values and numerical values measured at the back of the sphere surface. The pattern of this figure is similar to Fig. 4.4 but there are more errors at high frequencies. Figure 4.11 shows the sum of the sound pressure level differences shown in Fig. 4.10 over frequency. This figure shows that 130 over-determination points are still nearly an optimal value from 200Hz to 10kHz. Figure 4.12, 4.13, 4.14 and 4.15 shows the comparison between the sound pressure level for the theory and the simulation at the back of sphere surface for zero, 50, 130, and 200 over-determination points respectively. Figure 4.14 shows there are some errors up to about 4kHz for 130 over-determination points. Figure 4.7 and 4.13 shows little error up to 4kHz for 50 over-determination points. In this thesis, 50 over-determination points are used for the numerical simulations up to 4kHz and 130 over-determination points are used between 4kHz and 10kHz from now on. Since the frequency increment of 200Hz is not small, some characteristic eigenfrequencies can be missed, so there may be more errors in these simulations.

4.7 Conclusion

This chapter explains how acoustic fields can be calculated by using the boundary element method that is based on the Kirchhoff-Helmholtz integral equation. The Kirchhoff-Helmholtz integral equation can be solved if the boundary conditions on the boundary surface are given. In a typical scattering problem, the total sound field can be decomposed into the incident sound field in the absence of the scatterer and the

scattered sound field arising from the interaction of the incident sound field with the scatterer. The boundary surface is discretized into a number of boundary elements and then this integral equation is solved numerically by using the collocation scheme. Once the equation is solved, the sound pressure at any point can be calculated numerically. The potential drawbacks of the boundary element method for an exterior acoustic radiation and scattering problem can be the non-uniqueness problem at characteristic eigenfrequencies associated with the corresponding interior Dirichlet problem. The non-uniqueness problem can be solved by collocating the over-determination points inside the numerical model for the direct boundary element method. The required number of the over-determination points depends on frequency. The number of over-determination points is discussed by studying the case of the approximate spherical head model. The study of the sphere suggests that 50 over-determination points are recommended for the numerical simulations with the spherical head model up to 4kHz and 130 over-determination points are recommended between 4kHz and 10kHz.

FIGURES

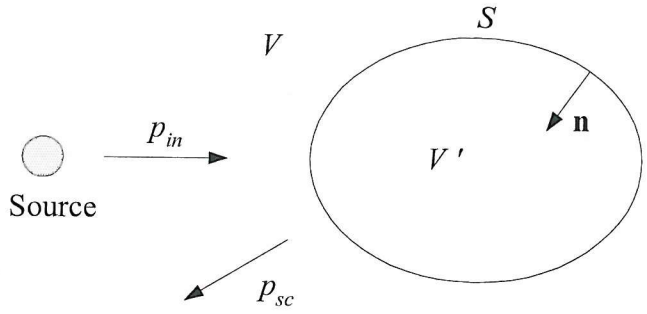

Figure 4.1 A scattering problem.

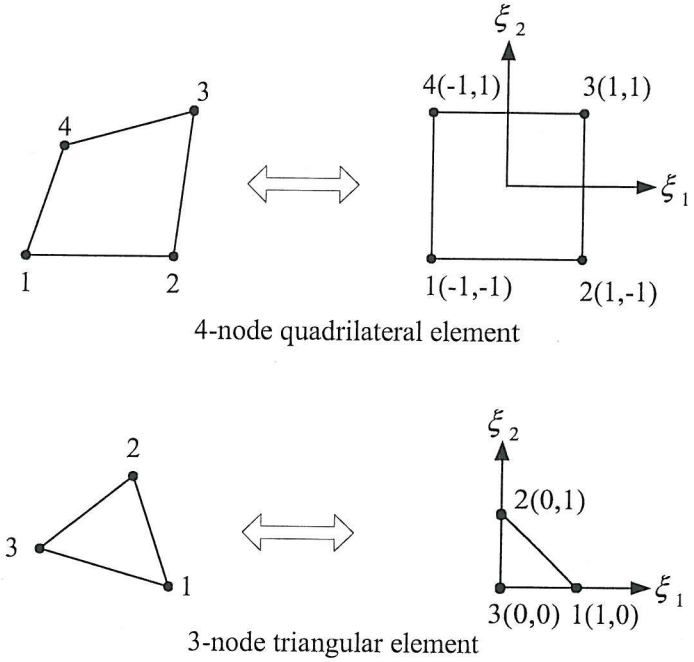

Figure 4.2 The mapping between a real element and its master element.

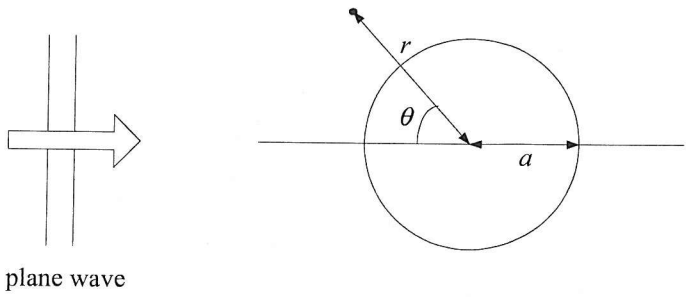

Figure 4.3 A plane wave is incident on the sphere.

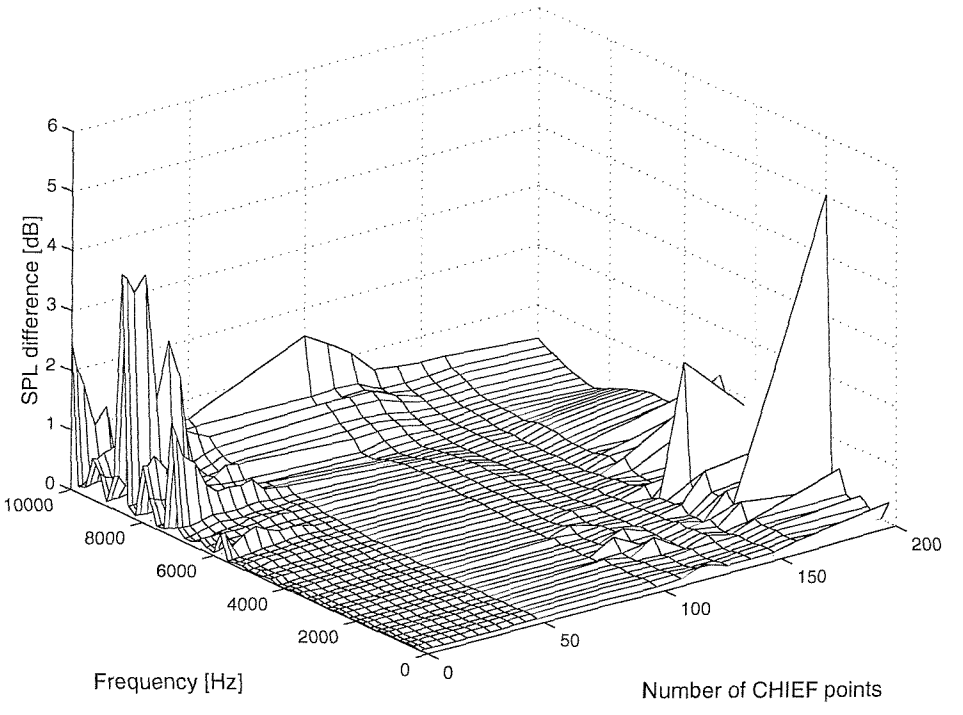

Figure 4.4 Sound pressure level difference between theoretical values and numerical values at the front of the sphere surface.

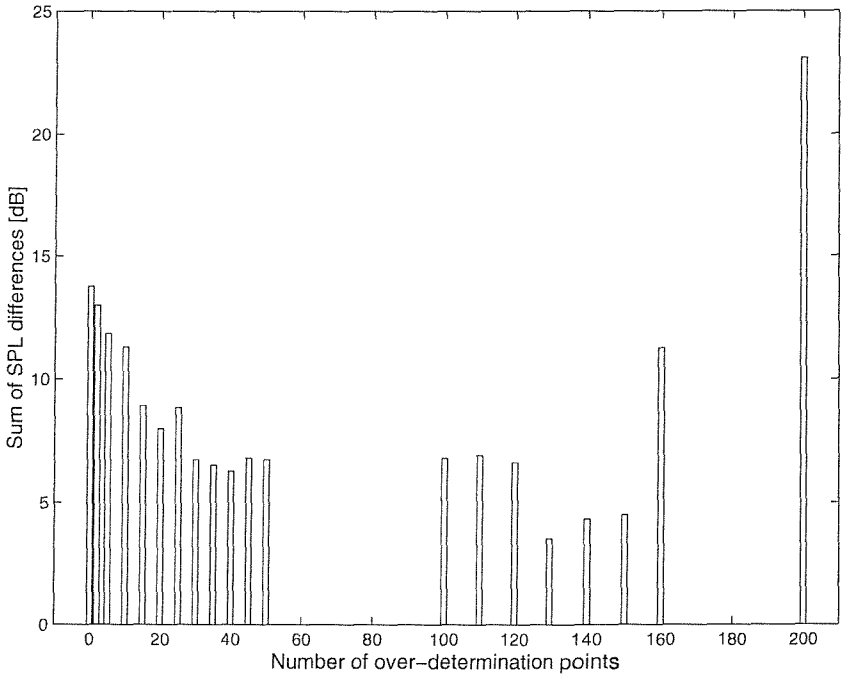

Figure 4.5 Sum of the sound pressure level differences over frequency at the front of the sphere surface.

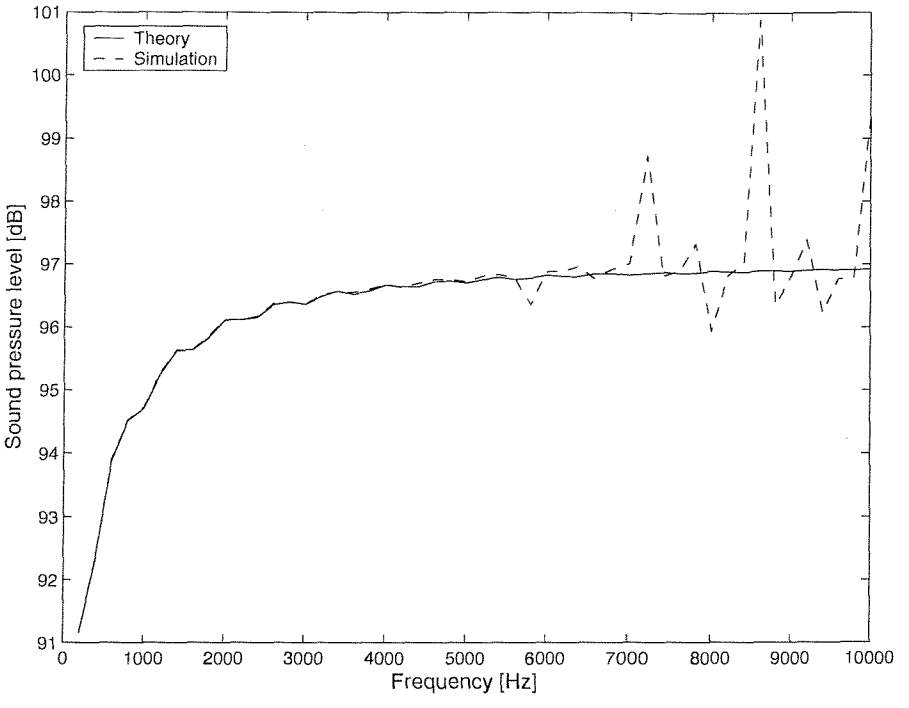

Figure 4.6 Comparison between theoretical values and numerical values for 0 over-determination point at the front of the sphere surface.

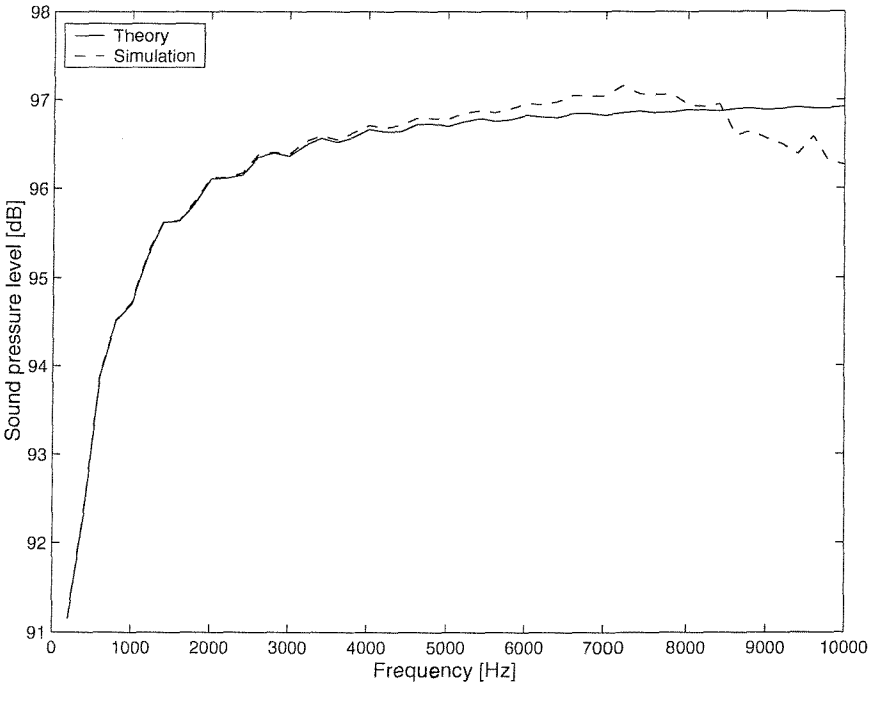

Figure 4.7 Comparison between theoretical values and numerical values for 50 over-determination point at the front of the sphere surface.

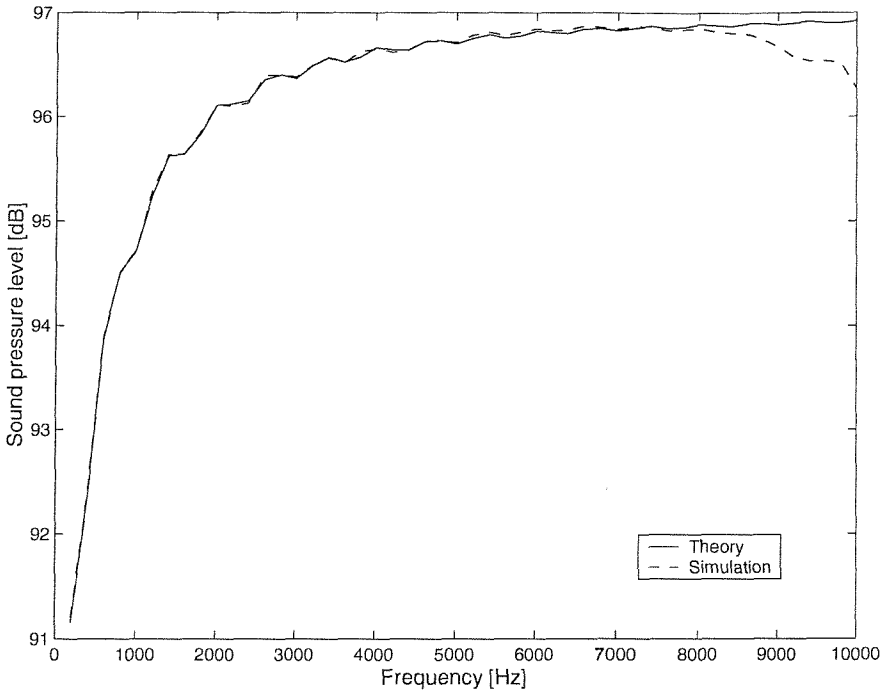

Figure 4.8 Comparison between theoretical values and numerical values for 130 over-determination points at the front of the sphere surface.

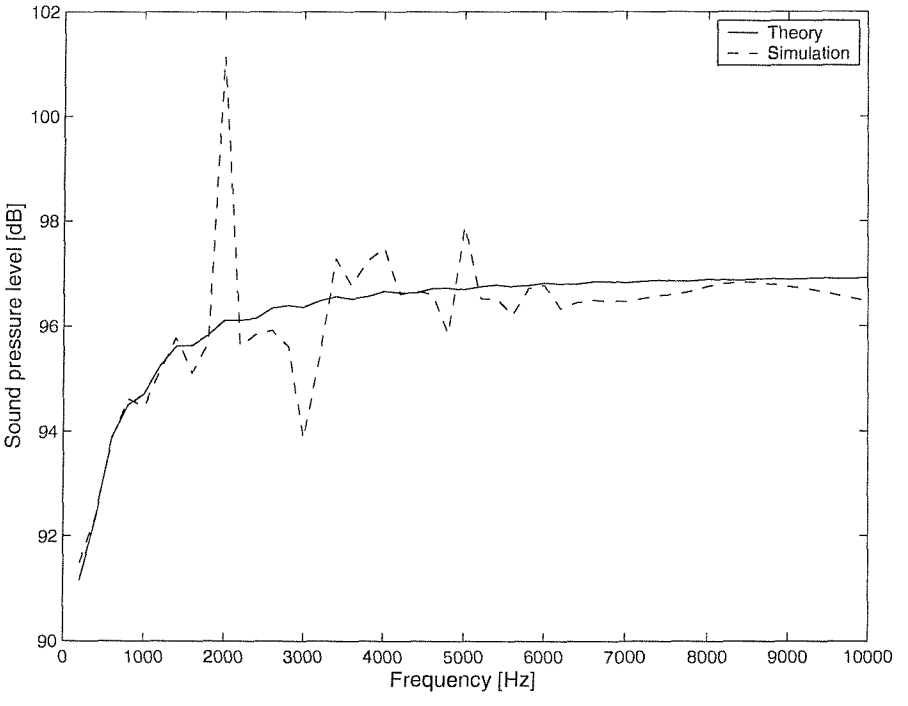

Figure 4.9 Comparison between theoretical values and numerical values for 200 over-determination points at the front of the sphere surface.

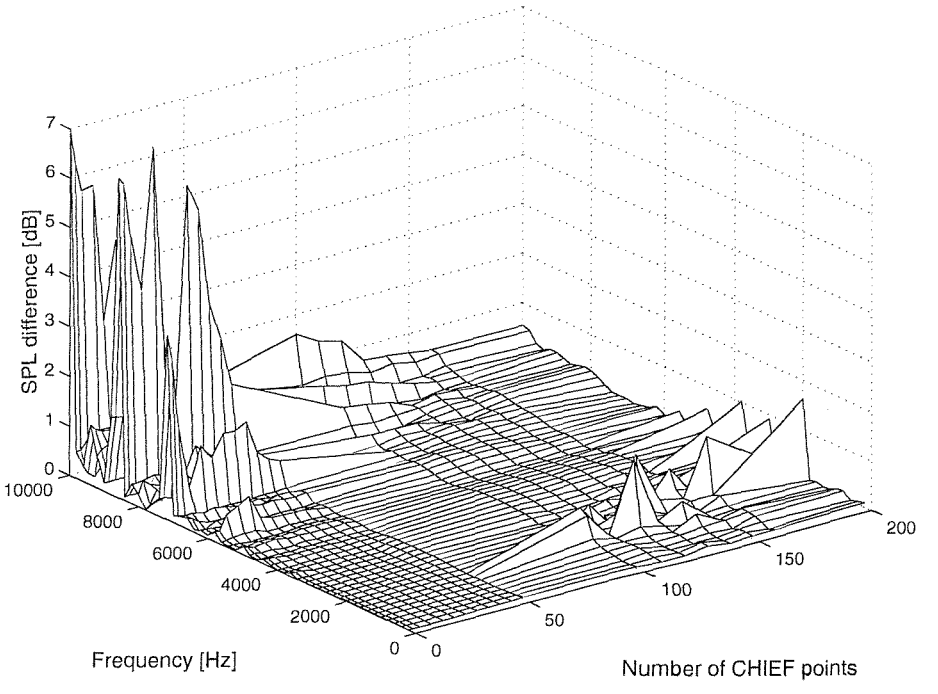

Figure 4.10 Sound pressure level difference between theoretical values and numerical values at the back of the sphere surface.

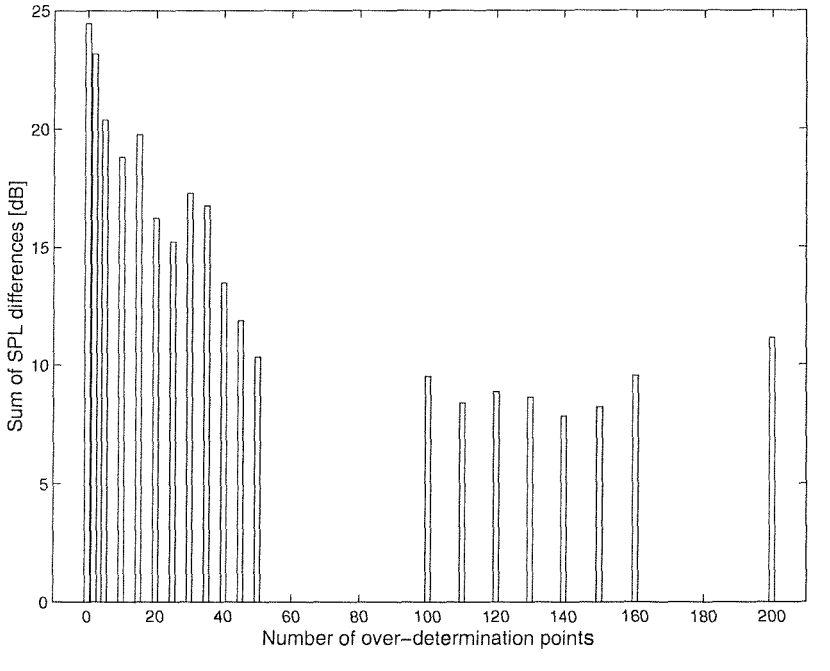

Figure 4.11 Sum of the sound pressure level differences over frequency at the back of the sphere surface.

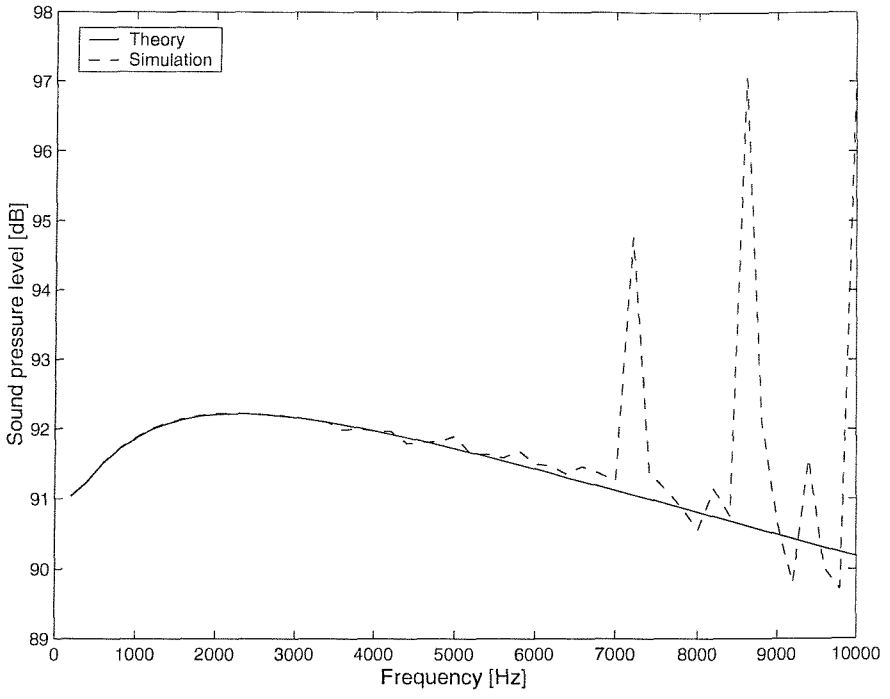

Figure 4.12 Comparison between theoretical values and numerical values for 0 over-determination points at the back of the sphere surface.

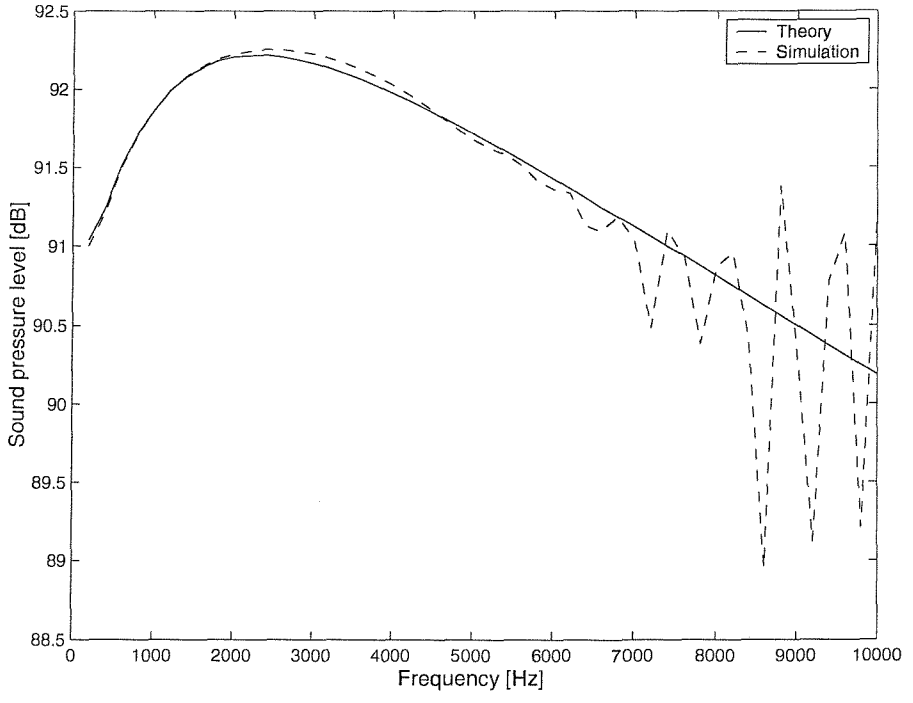

Figure 4.13 Comparison between theoretical values and numerical values for 50 over-determination points at the back of the sphere surface.

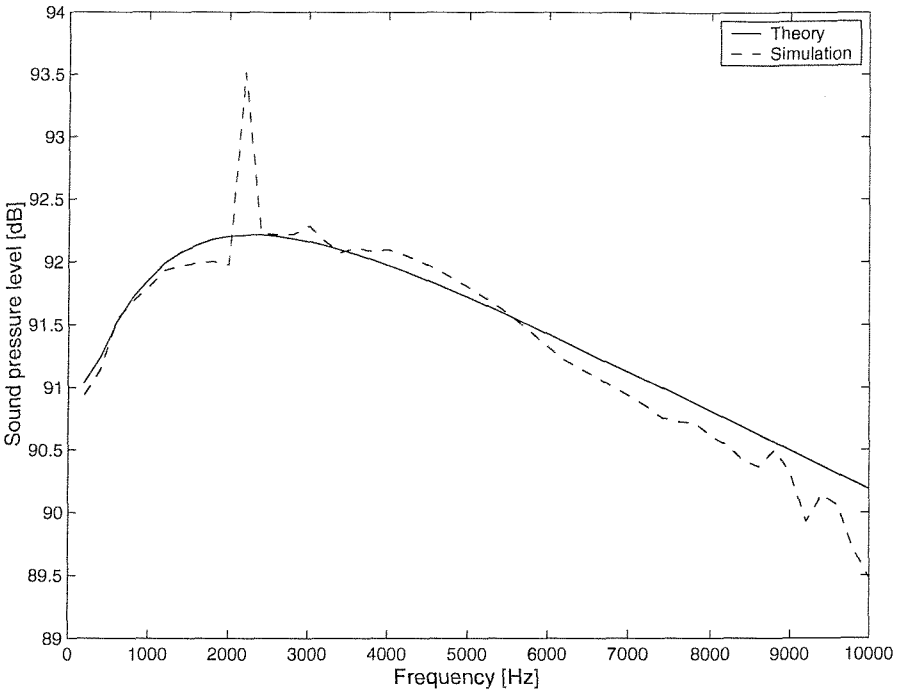

Figure 4.14 Comparison between theoretical values and numerical values for 130 over-determination points at the back of the sphere surface.

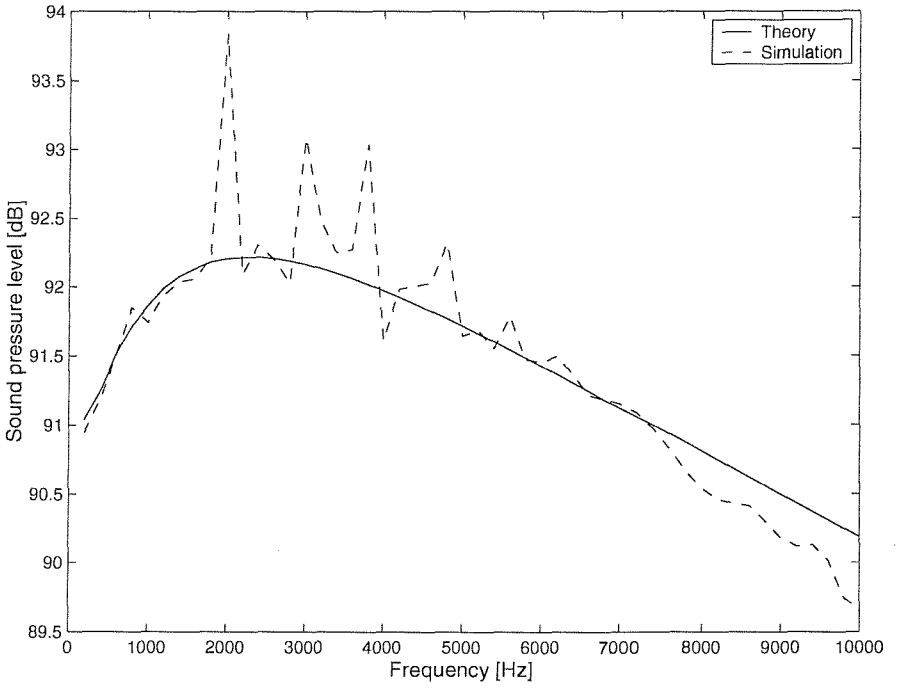

Figure 4.15 Comparison between theoretical values and numerical values for 200 over-determination points at the back of the sphere surface.

CHAPTER 5
INCIDENT SOUND FIELD REPRODUCTION

5.1 Introduction

The "incident sound field", when used in the context of the reflection or scattering of sound, can be defined as the sound field that would be present if the scatterer or boundary were removed to allow free field propagation (Morfey, 2001). Therefore, the incident sound field is not influenced by the scatterer or boundary, and so it is independent of the listener in a reproduced sound field. The incident sound field reproduction method attempts to create a virtual acoustic field by reproducing exactly the incident sound field within a control volume, where a listener may be located. This chapter describes the basic theory of the incident sound field reproduction method by studying simple cases. The theory is studied from the simplest case of a one-dimensional tube to the general three-dimensional case of a single scattering body. A clear understanding of the simple cases will help in understanding the more complicated cases explained in the next chapter. A study is also presented of the boundary surface control principle, which attempts to reproduce the incident sound field within a control volume by reproducing sound pressure and its gradient on the boundary surface of the control volume. The boundary surface is discretized and the transfer impedance matrix relating the pressure at a number of spatial positions to the strengths of a number of sources is introduced. An approach to virtual acoustics is explained by using this matrix. The least squares solution is used to calculate the optimal solution for a number of discrete sources used to generate a virtual acoustic field.

5.2 The one-dimensional tube

In order to understand the theory of the incident sound field reproduction method easily, the simplest case of one-dimensional sound field is studied first. Figure 5.1 (a) illustrates the generation of the primary sound field in a semi-infinite tube with a termination at $x = L_1$ and an anechoic termination at $x = -\infty$. The tube is assumed to be acoustically one-dimensional, that is, acoustic quantities are assumed to be the same across a cross-section of the tube. A plane monopole source is placed at $x = 0$, which emits a single frequency sound field. The source is assumed to be acoustically transparent, which means that there is no reflection at $x = 0$. L_1 is assumed to be a positive number. The specific acoustic impedance of the termination at $x = L_1$ is the complex value z_1. The sound pressure within the tube in a steady state is given by (Nelson and Elliott, 1992)

$$p(x) = \frac{\rho_0 c_0 q_{p1}}{2A} e^{-jkx} + R_1 \frac{\rho_0 c_0 q_{p1}}{2A} e^{jk(x-2L_1)} \tag{5.1}$$

where q_{p1} is the strength of the plane monopole source at $x = 0$ in the primary field, ρ_0 is a fluid density, c_0 is a speed of sound in a fluid, $\rho_0 c_0$ is the characteristic acoustic impedance of a fluid, A is the cross sectional area of the tube, and R_1 is the reflection coefficient of the termination at $x = L_1$. The first term on the right hand side of Eq. (5.1) can be interpreted as the incident sound field from the plane monopole source and the second term can be interpreted as the reflected sound field from the termination at the end of the tube. The term on the left hand side of Eq. (5.1) can be interpreted as the total sound field. The particle velocity is given by

$$v(x) = -\frac{1}{j\omega\rho_0} \frac{\mathrm{d}p(x)}{\mathrm{d}x} = \frac{q_{p1}}{2A} e^{-jkx} - R_1 \frac{q_{p1}}{2A} e^{jk(x-2L_1)}. \tag{5.2}$$

The specific acoustic impedance of the termination at $x = L_1$ is given by

$$z_1 = \frac{p(L_1)}{v(L_1)} = \rho_0 c_0 \frac{1+R_1}{1-R_1}, \tag{5.3}$$

and the reflection coefficient R_1 is given by

$$R_1 = \frac{z_1 - \rho_0 c_0}{z_1 + \rho_0 c_0}. \tag{5.4}$$

This sound pressure given in Eq. (5.1) is the desired sound field that we aim to reproduce in the secondary field.

Figure 5.1 (b) illustrates the generation of the secondary sound field in the same tube as that shown in Fig. 5.1 (a). The acoustically transparent plane monopole source is placed at $x = y$, where y is less than L_1. The specific acoustic impedance of the termination at $x = L_1$ is still z_1. The sound pressure within the tube in a steady state is given by

$$\begin{aligned} p(x) &= \frac{\rho_0 c_0 q_{s1}}{2A} e^{-jk(x-y)} + R_1 \frac{\rho_0 c_0 q_{s1}}{2A} e^{jk(x-2L_1+y)} \\ &= \frac{\rho_0 c_0 \left(q_{s1} e^{jky}\right)}{2A} e^{-jkx} + R_1 \frac{\rho_0 c_0 \left(q_{s1} e^{jky}\right)}{2A} e^{jk(x-2L_1)} \end{aligned} \tag{5.5}$$

where q_{s1} is the strength of the plane monopole source at $x=y$ in the secondary field. We should find out the secondary source strength to reproduce the primary sound field given in Eq. (5.1) in the secondary field given in Eq. (5.5). If $q_{s1} = q_{p1} e^{-jky}$, the secondary sound field is the same as the primary sound field, so the primary field can be successfully reproduced. In this case, the amplitude of the source in the secondary field is the same as that in the primary field, but the phase of the source in the secondary field is different from that in the primary field by the amount ky due to the propagation length y between the source in the primary field and the source in the secondary field.

Another pair of primary and secondary sound fields is studied to understand the characteristics of the incident sound field reproduction method more clearly. Figure

5.1 (c) illustrates the generation of another primary sound field in a semi-infinite tube with a different termination at $x = L_2$. The acoustically transparent plane monopole source is again placed at $x = 0$. L_2 is assumed to be a positive number and different from L_1. The specific acoustic impedance of the termination at $x = L_2$ is z_2, which is different from z_1. The sound pressure within the tube in a steady state is given by

$$p(x) = \frac{\rho_0 c_0 q_{p2}}{2A} e^{-jkx} + R_2 \frac{\rho_0 c_0 q_{p2}}{2A} e^{jk(x-2L_2)} \tag{5.6}$$

where q_{p2} is the source strength of the plane monopole source in this primary field. The reflection coefficient R_2 in this case is given by

$$R_2 = \frac{z_2 - \rho_0 c_0}{z_2 + \rho_0 c_0}. \tag{5.7}$$

This sound pressure given in Eq. (5.6) is the desired sound field that we aim to reproduce in the secondary field.

Figure 5.1 (d) illustrates the generation of the secondary sound field in the same tube as that shown in Fig. 5.1 (c). The acoustically transparent plane monopole source is again placed at $x=y$. The specific acoustic impedance of the termination at $x=L_2$ is still z_2. The sound pressure within the tube in the steady state is given by

$$\begin{aligned} p(x) &= \frac{\rho_0 c_0 q_{s2}}{2A} e^{-jk(x-y)} + R_2 \frac{\rho_0 c_0 q_{s2}}{2A} e^{jk(x-2L_2+y)} \\ &= \frac{\rho_0 c_0 \left(q_{s2} e^{jky}\right)}{2A} e^{-jkx} + R_2 \frac{\rho_0 c_0 \left(q_{s2} e^{jky}\right)}{2A} e^{jk(x-2L_2)} \end{aligned} \tag{5.8}$$

where q_{s2} is the strength of the plane monopole source in the secondary field. We should again find the secondary source strength to reproduce the primary sound field given in Eq. (5.6) in the secondary field given in Eq. (5.8). If $q_{s2} = q_{p2} e^{-jky}$, the secondary sound field is the same as the primary sound field, so the primary field can again be successfully reproduced.

If $q_{p1} = q_{p2}$, the incident sound fields in both the primary fields shown in Fig. 5.1 (a) and 5.1 (c) are the same, although the reflected sound fields in the primary fields are different. Then, the secondary source strengths to reproduce the corresponding primary sound field should be $q_{s1} = q_{s2}$. This suggests that the secondary source strength q_{s1} or q_{s2} is related only to the primary sound source and independent of the position and the boundary condition of the reflecting surface at the end of the tube. Therefore the secondary source only reproduces the incident sound field in the secondary field. This also suggests that the incident sound field from the source in the secondary field depends on only the incident sound field from the source in the primary field. The reflected sound field depends on only the boundary conditions of the reflecting termination and the sound field incident on the reflecting termination. The following hypothesis can be established from the above analysis of the one-dimensional case.

If the incident sound field from the source in the primary field is exactly reproduced in the secondary field, the total sound field is also exactly reproduced in the secondary field provided that the boundary conditions are the same as those in the primary field. Since the sound field incident on the scatterer is independent of the geometry and boundary condition of the scatterer, the total sound field is also exactly reproduced for a different geometry and boundary condition of the scatterer if the same incident sound field is exactly reproduced.

Numerical simulations for the one-dimensional tube are performed to verify the theory of the incident sound field reproduction method in one-dimensional case. The following conditions are given, for example: $L_1 = 0.8$ m, $y = 0.1$, $q_{p1} = 1$, $\rho_0 c_0 = 416.5$, $A = 1$, $R_1 = 1$, and $k = 2 \times \pi \times 1000\text{Hz} / 340\text{m/s}$. Figure 5.2 (a) shows the real and imaginary part of the primary sound pressure calculated from Eq. (5.1), and Figure 5.2 (b) shows that of the corresponding secondary sound pressure from Eq. (5.5). The secondary source strength necessary to reproduce the primary sound field is given by $q_{s1} = q_{p1} e^{-jky}$. The primary sound field is successfully reproduced in the secondary field. Another pair of primary and secondary sound fields is also numerically simulated with following conditions, for example: $L_2 = 0.6$ m and $R_2 = 0.5$. The position and boundary condition of the reflecting termination is changed. The same

strength of the primary sound source is applied ($q_{p2} = q_{p1} = 1$). Figure 5.3 (a) shows the real and imaginary part of the primary sound pressure calculated from Eq. (5.6). This primary sound field is different from that shown in Fig. 5.2 (a) since the reflected sound field from the different position and boundary condition of the reflecting termination is different even though the incident sound field is the same. Figure 5.3 (b) shows the real and imaginary part of the corresponding secondary sound pressure from Eq. (5.8). The same strength of the primary sound source is applied ($q_{s2} = q_{s1} = q_{p2}e^{-jky} = q_{p1}e^{-jky}$). The primary sound field is also successfully reproduced in the secondary field. This example confirms that the total sound field is exactly reproduced regardless of the geometry and boundary condition of the reflecting termination by reproducing exactly the incident sound field.

5.3 A single scattering body

This section will verify the hypothesis introduced in the previous section regarding the incident sound field reproduction method in the general three-dimensional case. The simple case of one arbitrary scattering body with sound sources in a free field is studied using the following procedure that is similar to that in the previous section. A sound field α, which simulates the real acoustic environment, represents the primary field produced by a sound source and a scatterer in an unbounded free field. The sound pressure inside the control volume is calculated. A sound field β, which simulates the virtual acoustic environment, represents the secondary field produced by different sound sources and the same scatterer as that in the sound field α. Optimal source strengths are deduced in order to reproduce the same sound field as the sound field α inside the control volume. A sound field γ represents another primary field produced by the same sound source as that in the sound field α but with a different scatterer. The sound pressure inside the control volume is also calculated. A sound field δ represents another secondary field produced by the same sound sources as those in the sound field β and the same scatterer as that in the sound field γ. If the same source strengths as those used to reproduce the sound field β are applied, the sound field δ turns out to be the same as the sound field γ inside the control volume.

(1) Sound field α

Figure 5.4 illustrates the primary field with a single scattering body and acoustic sources in an unbounded free field. Consider the unbounded exterior volume V outside the scattering body in an acoustic medium, of which the bounding surface is denoted by S_1. All surfaces in this thesis are assumed to be locally reacting surfaces (Pierce, 1989). The specific acoustic impedance z_1 of the surface S_1 is also assumed to be known, and is given by

$$z_1(\mathbf{y}) = \frac{p_{1\alpha}(\mathbf{y})}{v_{n1\alpha}(\mathbf{y})} \tag{5.9}$$

where the vector $\mathbf{y}$ is on the surface S_1, $p_{1\alpha}$ is the sound pressure on the surface S_1, and $v_{n1\alpha}$ is the normal particle velocity on the surface S_1. For example, the specific acoustic impedance of the rigid surface is infinite, that of the perfectly absorbent surface is equal to the characteristic acoustic impedance $\rho_0 c_0$ of the medium, and that of the soft surface or the pressure-release surface is zero (Morfey, 2001). The acoustic source strength distribution Q_{vol} in the volume V is assumed to be known and emit single frequency sound. The solution of the inhomogeneous Helmholtz equation at a single frequency in the exterior acoustic domain V can be written as

$$C(\mathbf{x})p(\mathbf{x}) = p_{in\alpha}(\mathbf{x}) - \int_{S_1}\left(j\omega\rho_0 v_{n1\alpha}(\mathbf{y})g(\mathbf{x}|\mathbf{y}) + p_{1\alpha}(\mathbf{y})\frac{\partial g(\mathbf{x}|\mathbf{y})}{\partial n}\right) dS \tag{5.10}$$

where symbols are the same as those used in chapter 4. This is an integral equation for a scattering problem in an unbounded medium of the type given in Eq. (4.21). Note that $C(\mathbf{x})$ is equal to one if $\mathbf{x}$ is within V, zero if $\mathbf{x}$ is outside V, and 0.5 if $\mathbf{x}$ is on a smooth boundary S_1. The sound pressure $p_{in\alpha}(\mathbf{x})$ is given by

$$p_{in\alpha}(\mathbf{x}) = \int_V Q_{vol}(\mathbf{y}_v)g(\mathbf{x}|\mathbf{y}_v)dV\,. \tag{5.11}$$

The sound field $p_{in\alpha}(\mathbf{x})$ denotes an incident sound field from the acoustic source strength distribution Q_{vol} and can be interpreted as the sound field in the absence of the scattering body. The second term on the right hand side of Eq. (5.10) can be regarded as the scattered sound field that is the additional sound field produced by the interaction of the incident sound field with the scattering body. For example, when only one point monopole source is located at the position $\mathbf{y}_s$ in the volume V, the incident sound field $p_{in\alpha}(\mathbf{x})$ can be written as

$$p_{in\alpha}(\mathbf{x}) = j\omega\rho_0 q g(\mathbf{x}|\mathbf{y}_s) = \frac{j\omega\rho_0 q\, \mathrm{e}^{-jk|\mathbf{x}-\mathbf{y}_s|}}{4\pi|\mathbf{x}-\mathbf{y}_s|} \tag{5.12}$$

where q is the complex strength of the monopole source. Two variables $p_{1\alpha}$, and $v_{n1\alpha}$ in the second term on the right hand side of Eq. (5.10) can be reduced into one variable by using Eq. (5.9) since the specific acoustic impedance z_1 of the surface S_1 is known. Therefore the second term of the right hand side of Eq. (5.10) can be rewritten as

$$-\int_{S_1}\left(j\omega\rho_0 v_{n1\alpha}(\mathbf{y})g(\mathbf{x}|\mathbf{y}) + p_{1\alpha}(\mathbf{y})\frac{\partial g(\mathbf{x}|\mathbf{y})}{\partial n}\right)dS = \begin{cases} \int_{S_1} H_1(\mathbf{x}|\mathbf{y})\, p_{1\alpha}(\mathbf{y})\, dS \\ \text{or} \\ \int_{S_1} H_1'(\mathbf{x}|\mathbf{y})\, v_{n1\alpha}(\mathbf{y})\, dS \end{cases} \tag{5.13}$$

where the transfer function $H_1(\mathbf{x}|\mathbf{y})$ from surface sound pressure to sound pressure at the field point is given by

$$H_1(\mathbf{x}|\mathbf{y}) = -\frac{j\omega\rho_0 g(\mathbf{x}|\mathbf{y})}{z_1(\mathbf{y})} - \frac{\partial g(\mathbf{x}|\mathbf{y})}{\partial n} \qquad (z_1(\mathbf{y})\neq 0), \tag{5.14}$$

and where another transfer function $H_1'(\mathbf{x}|\mathbf{y})$ from surface normal particle velocity to sound pressure at the field point is given by

$$H_1'(\mathbf{x}|\mathbf{y}) = -j\omega\rho_0 g(\mathbf{x}|\mathbf{y}) - z_1(\mathbf{y})\frac{\partial g(\mathbf{x}|\mathbf{y})}{\partial n} \qquad (z_1(\mathbf{y})<\infty). \tag{5.15}$$

Equation (5.14) can be used when the specific acoustic impedance is not equal to zero; that is, when the scattering surface is not a soft boundary. Equation (5.15) can be used when the specific acoustic impedance is finite; that is, when the scattering surface is not a rigid boundary. Throughout the thesis, the type of transfer function H such as those appearing in Eq. (5.14) will be used since most surfaces in this thesis are assumed to be rigid. This means that all surfaces are assumed not to be of the soft boundary type, that is, all the specific acoustic impedance is assumed to be non-zero in this thesis. Then the surface sound pressure of the scattering body is used rather than the surface normal particle velocity of the scattering body in equations representing the sound field outside the scattering body.

The control volume V_1 is considered to define the region where the sound field is supposed to be reproduced in the secondary field. The outer bounding surface of the control volume V_1 is denoted by S_c and the inner bounding surface of the volume V_1 is the surface S_1. In this case, the surface S_c is a transparent imaginary surface. The source strength distribution Q_{vol} is assumed to be located outside the volume V_1. When the position vector $\mathbf{x}$ is in the volume V_1, the sound pressure in the volume V_1 is denoted by p_α. Since the volume V_1 is inside the volume V, the sound pressure p_α can be written by using Eq. (5.10) as

$$p_\alpha(\mathbf{x}) = p_{in\alpha}(\mathbf{x}) + \int_{S_1} H_1(\mathbf{x}|\mathbf{y})\, p_{1\alpha}(\mathbf{y})\, dS \tag{5.16}$$

where the vector $\mathbf{x}$ is inside the volume V_1. Note that the coefficient $C(\mathbf{x})$ in Eq. (5.10) is equal to one in this case. This sound pressure p_α is the desired sound field that is supposed to be reproduced in the secondary field. When the vector $\mathbf{x}_1$ is on the surface S_1, the sound pressure $p(\mathbf{x})$ in Eq. (5.10) is equal to $p_{1\alpha}(\mathbf{x})$ on the surface S_1, and the coefficient $C(\mathbf{x})$ in Eq. (5.10) is equal to 0.5. Note that all the surfaces are assumed to be smooth boundaries in this thesis for simplicity. If the surface is not smooth, the coefficient $C(\mathbf{x})$ can be calculated from Eq. (4.8). Then the unknown variable $p_{1\alpha}$ in Eq. (5.16) can be evaluated by solving the following integral equation:

$$\frac{1}{2} p_{1\alpha}(\mathbf{x}_1) - \int_{S_1} H_1(\mathbf{x}_1|\mathbf{y})\, p_{1\alpha}(\mathbf{y})\, dS = p_{in\alpha}(\mathbf{x}_1). \tag{5.17}$$

(2) Sound field β

Figure 5.5 illustrates the secondary field with the same scattering body as that in the sound field α but with different sound sources that are intended to reproduce the primary sound field α within the control volume V_1. If continuous transparent monopole and dipole source layers are placed on the surface S_c and there is no other source in an unbounded free field, the sound pressure p_β at a single frequency in the volume V_1 can be written as

$$p_\beta(\mathbf{x}) = p_{in\beta}(\mathbf{x}) + \int_{S_1} H_1(\mathbf{x}|\mathbf{y}) p_{1\beta}(\mathbf{y})\, dS \tag{5.18}$$

where the vector $\mathbf{x}$ is inside the volume V_1 and $p_{1\beta}$ is the sound pressure on the surface S_1. Note that the coefficient $C(\mathbf{x})$ for an exterior problem is equal to one in this case since the control volume V_1 is inside the exterior acoustic domain V. The incident sound field $p_{in\beta}$ produced by the source layers on the surface S_c is given by

$$p_{in\beta}(\mathbf{x}) = -\int_{S_c} j\omega\rho_0 v_{nc\beta}(\mathbf{y}) g(\mathbf{x}|\mathbf{y}) + p_{c\beta}(\mathbf{y}) \frac{\partial g(\mathbf{x}|\mathbf{y})}{\partial n} dS \tag{5.19}$$

where $p_{c\beta}$ is the sound pressure on the surface S_c, and $v_{nc\beta}$ is the normal particle velocity on the surface S_c. The second term on the right hand side of Eq. (5.18) can be regarded as the scattered sound field produced from the scattering body. Note that equation (5.18) is still valid when the vector $\mathbf{x}$ is in the volume V. The distribution of the monopole source strength on the surface S_c is given by $Q_{m\beta}(\mathbf{y}) = -v_{nc\beta}(\mathbf{y})$ and the distribution of the dipole source strength on the surface S_c is given by $Q_{d\beta}(\mathbf{y}) = p_{c\beta}(\mathbf{y}) / j\omega\rho_0$ (Nelson and Elliott, 1992). The monopole and dipole source layers on the surface S_c are intended to reproduce the same sound field as the sound field α inside the control volume V_1. The following equation results from subtracting Eq. (5.18) from Eq. (5.16):

$$p_\alpha(\mathbf{x}) - p_\beta(\mathbf{x}) = p_{in\alpha}(\mathbf{x}) - p_{in\beta}(\mathbf{x}) + \int_{S_1} H_1(\mathbf{x}|\mathbf{y}) \left(p_{1\alpha}(\mathbf{y}) - p_{1\beta}(\mathbf{y}) \right) dS \tag{5.20}$$

If the secondary sound field β is assumed to be the same as the primary sound field α in the volume V_1, that is, $p_\alpha(\mathbf{x}) = p_\beta(\mathbf{x})$ when the vector $\mathbf{x}$ is inside V_1, and $p_{1\alpha}(\mathbf{y}) = p_{1\beta}(\mathbf{y})$ when the vector $\mathbf{y}$ is on the surface S_1, equation (5.20) becomes

$$p_{in\alpha}(\mathbf{x}) = p_{in\beta}(\mathbf{x}) \tag{5.21}$$

where the vector $\mathbf{x}$ is in the volume V_1. Therefore, the secondary source distribution $p_{c\beta}(\mathbf{y})$ and $v_{nc\beta}(\mathbf{y})$ on the surface S_c necessary to reproduce the same sound field as the sound field α inside the control volume V_1 can be determined by evaluating the sound pressure $p_{in\alpha}(\mathbf{y})$ and the sound pressure gradient $\partial p_{in\alpha}(\mathbf{y}) / \partial n$ on the surface S_c. Equation (5.21) shows that the monopole and dipole source layers on the surface S_c in the secondary field reproduce only the incident sound field produced by the source distribution in the primary sound field. This agrees with the one-dimensional case. If the incident sound field from the source distribution in the primary field is exactly reproduced and the scattering body is the same, the scattered sound field produced from the scattering body in the primary field is exactly reproduced from the scattering body itself in the secondary field. That means the virtual acoustic field produced from the source layers is independent of the geometry and boundary conditions of the scattering body. This principle is confirmed by considering another pair of primary and secondary fields with a different scattering body.

(3) Sound field γ

Figure 5.6 illustrates another primary field with the same sound source distribution as that in the sound field α, but with a different scattering body in an otherwise unbounded free field. Consider the unbounded exterior volume V' outside this different scattering body in an acoustic medium, of which the bounding surface is denoted by S_2. The specific acoustic impedance z_2 of the surface S_2 is assumed to be known, and is given by

$$z_2(\mathbf{y}) = \frac{p_{2\gamma}(\mathbf{y})}{v_{n2\gamma}(\mathbf{y})} \tag{5.22}$$

where the vector $\mathbf{y}$ is on the surface S_2, $p_{2\gamma}$ is the sound pressure on the surface S_2, and $v_{n2\gamma}$ is the normal particle velocity on the surface S_2. The impedance z_2 and the surface S_2 are assumed to differ from the impedance z_1 and the surface S_1 respectively. The acoustic source strength distribution Q_{vol} in the volume V' is assumed to be the same as that in the sound field α and emit single frequency sound. The solution of inhomogeneous wave equation in a single frequency exterior acoustic domain V' can be written as

$$C(\mathbf{x})\,p(\mathbf{x}) = -\int_{S_2} j\omega\rho_0 v_{n2\gamma}(\mathbf{y})\,g(\mathbf{x}|\mathbf{y}) + p_{2\gamma}(\mathbf{y})\frac{\partial g(\mathbf{x}|\mathbf{y})}{\partial n}\,dS + \int_{V'} Q_{vol}(\mathbf{y}_v)\,g(\mathbf{x}|\mathbf{y}_v)\,dV \tag{5.23}$$

The control volume V_2 is considered to define the region where the sound field is supposed to be reproduced in the secondary field. The outer bounding surface of the control volume V_2 is the surface S_c that is the same transparent surface as that in the sound field α, and the inner bounding surface of the volume V_2 is the surface S_2. The source strength distribution Q_{vol} is assumed to be located outside the volume V_2. When the vector $\mathbf{x}$ is in the volume V_2, the sound pressure is denoted by p_γ. The two variables $p_{2\gamma}$, and $v_{n2\gamma}$ in Eq. (5.23) can be reduced to one unknown variable by using Eq. (5.22). Since the volume V_2 is inside the volume V', the sound pressure p_γ can be written as

$$p_\gamma(\mathbf{x}) = p_{in\gamma}(\mathbf{x}) + \int_{S_2} H_2(\mathbf{x}|\mathbf{y})\,p_{2\gamma}(\mathbf{y})\,dS \tag{5.24}$$

where

$$H_2(\mathbf{x}|\mathbf{y}) = -\frac{j\omega\rho_0 g(\mathbf{x}|\mathbf{y})}{z_2(\mathbf{y})} - \frac{\partial g(\mathbf{x}|\mathbf{y})}{\partial n}, \tag{5.25}$$

and

$$p_{in\gamma}(\mathbf{x}) = \int_{V'} Q_{vol}(\mathbf{y}_v)\,g(\mathbf{x}|\mathbf{y}_v)\,dV, \tag{5.26}$$

and the vector $\mathbf{x}$ is inside the volume V_2. Note that the coefficient $C(\mathbf{x})$ in Eq. (5.23) is equal to one in this case. This sound pressure p_γ is the desired sound field that is supposed to be reproduced in the secondary field. The volume V' is assumed to differ

from the volume V due to the presence of the different scattering body. The sound field $p_{in\gamma}(\mathbf{x})$ in Eq. (5.26) is equal to the sound field $p_{in\alpha}(\mathbf{x})$ in Eq. (5.11) due to the same source strength distribution Q_{vol} when the vector $\mathbf{x}$ is in the intersection $V \cap V'$, i.e. when the vector $\mathbf{x}$ is inside both V and V'. However, the incident sound field is the sound field in the absence of the scattering body and so is not influenced by the scattered sound field or the scattering body. This means that the incident sound field in the sound field α is same as that in the sound field γ even though the scattered sound field in the sound field α is different from that in the sound field γ due to the presence of the different scattering body. Therefore, the incident sound field $p_{in\gamma}$ or $p_{in\alpha}$ can be extended to the domain in which either scattering body is located. Then the incident sound field $p_{in\gamma}(\mathbf{x})$ is equal to $p_{in\alpha}(\mathbf{x})$ where the vector $\mathbf{x}$ is in the union $V \cup V'$, i.e. when the vector $\mathbf{x}$ is inside V or V'. Since the union $V \cup V'$ includes the union $V_1 \cup V_2$, the incident sound field $p_{in}(\mathbf{x})$ produced by the acoustic source strength distribution Q_{vol} in either primary sound field α or γ can be rewritten as

$$p_{in}(\mathbf{x}) = p_{in\alpha}(\mathbf{x}) = p_{in\gamma}(\mathbf{x}) = \int_{V_1 \cup V_2} Q_{vol}(\mathbf{x}_v)\, g(\mathbf{x}|\mathbf{x}_v)\, dV \tag{5.27}$$

where the vector $\mathbf{x}$ is in the union volume $V_1 \cup V_2$. When the vector $\mathbf{x}_2$ is on the surface S_2, the sound pressure $p(\mathbf{x})$ in Eq. (5.23) is equal to $p_{2\gamma}(\mathbf{x})$ on the surface S_2, and the coefficient $C(\mathbf{x})$ in Eq. (5.23) is equal to 0.5. The unknown variable $p_{2\gamma}$ in Eq. (5.24) can be evaluated by solving the following equation:

$$\frac{1}{2} p_{2\gamma}(\mathbf{x}_2) - \int_{S_2} H_2(\mathbf{x}_2|\mathbf{y})\, p_{2\gamma}(\mathbf{y})\, dS = p_{in}(\mathbf{x}_2) \tag{5.28}$$

where the vector $\mathbf{x}_2$ is on the surface S_2.

(4) Sound field δ

Figure 5.7 illustrates another secondary field with the same scattering body as that in the sound field γ but with different sound sources that are intended to reproduce the primary sound field γ within the control volume V_2 in an otherwise unbounded free

field. If continuous transparent monopole and dipole source layers are placed on the surface S_c and there is no other source, the sound pressure p_δ at a single frequency in the volume V_2 can be written as:

$$p_\delta(\mathbf{x}) = p_{in\delta}(\mathbf{x}) + \int_{S_2} H_2(\mathbf{x}|\mathbf{y}) p_{2\delta}(\mathbf{y})\, dS \tag{5.29}$$

where the vector $\mathbf{x}$ is inside the volume V_2 and $p_{2\delta}$ is the sound pressure on the surface S_2. Note that the coefficient $C(\mathbf{x})$ for an exterior problem is equal to one in this case since the control volume V_2 is inside the exterior acoustic domain V'. The incident sound field $p_{in\delta}$ produced by source layers on the surface S_c is given by

$$p_{in\delta}(\mathbf{x}) = -\int_{S_c} j\omega\rho_0 v_{nc\delta}(\mathbf{y}) g(\mathbf{x}|\mathbf{y}) + p_{c\delta}(\mathbf{y}) \frac{\partial g(\mathbf{x}|\mathbf{y})}{\partial n} dS \tag{5.30}$$

where the position vector $\mathbf{x}$ is in the volume V_2, $p_{c\delta}$ is the sound pressure on the surface S_c, and $v_{nc\delta}$ is the normal particle velocity on the surface S_c. Note that equation (5.29) is still valid when the vector $\mathbf{x}$ is in the volume V'. The distribution of the monopole source strength on the surface S_c is given by $Q_{m\delta}(\mathbf{y}) = -v_{nc\delta}(\mathbf{y})$ and the distribution of the dipole source strength on the surface S_c is given by $Q_{d\delta}(\mathbf{y}) = p_{c\delta}(\mathbf{y}) / j\omega\rho_0$ (Nelson and Elliott, 1992). The monopole and dipole source layers on the surface S_c are intended to reproduce the same sound field as the sound field γ inside the control volume V_2. The following equation results from subtracting Eq. (5.30) from Eq. (5.19):

$$\begin{aligned} &p_{in\delta}(\mathbf{x}) - p_{in\beta}(\mathbf{x}) \\ &= -\int_{S_c} j\omega\rho_0 \left(v_{nc\delta}(\mathbf{y}) - v_{nc\beta}(\mathbf{y})\right) g(\mathbf{x}|\mathbf{y}) + \left(p_{c\delta}(\mathbf{y}) - p_{c\beta}(\mathbf{y})\right) \frac{\partial g(\mathbf{x}|\mathbf{y})}{\partial n} dS \end{aligned} \tag{5.31}$$

where the vector $\mathbf{x}$ is in the intersection $V_1 \cap V_2$. Because the incident sound field $p_{in\beta}$ or $p_{in\delta}$ can be extended to the domain in which either scattering body is located for the same reason as that discussed in the sound field γ, then the incident sound field $p_{in\delta}(\mathbf{x})$ is equal to $p_{in\beta}(\mathbf{x})$ where the vector $\mathbf{x}$ is in the union $V_1 \cup V_2$. If the same monopole

and dipole source strengths obtained in the sound field β are applied to the sound field δ, that is, $p_{c\delta}(\mathbf{y})= p_{c\beta}(\mathbf{y})$ and $v_{nc\delta}(\mathbf{y})= v_{nc\beta}(\mathbf{y})$ when the vector $\mathbf{y}$ on the surface S_c, the right hand side of Eq. (5.31) becomes zero. Then, the following equation results from Eq. (5.21) and Eq. (5.27):

$$p_{in\delta}(\mathbf{x}) = p_{in\beta}(\mathbf{x}) = p_{in\alpha}(\mathbf{x}) = p_{in\gamma}(\mathbf{x}) = p_{in}(\mathbf{x}) \tag{5.32}$$

where the vector $\mathbf{x}$ is in the union $V_1 \cup V_2$. This equation shows the monopole and dipole source layers on the surface S_c in the secondary field β or δ reproduces only the incident sound field produced by the sound source distribution in the primary sound field α or γ. All the incident sound fields on the scattering body inside the control volume, which is caused by the source strength distribution Q_{vol}, are the same. When the vector $\mathbf{x}_2$ is on the surface S_2, the sound pressure $p_\delta(\mathbf{x})$ in Eq. (5.29) is equal to $0.5 \times p_{2\delta}(\mathbf{x})$ on the surface S_2. The unknown variable $p_{2\delta}$ in Eq. (5.29) can be evaluated by solving the following integral equation:

$$\frac{1}{2} p_{2\delta}(\mathbf{x}_2) - \int_{S_2} H_2(\mathbf{x}_2|\mathbf{y}) p_{2\delta}(\mathbf{y})\, dS = p_{in}(\mathbf{x}_2) \tag{5.33}$$

where the vector $\mathbf{x}_2$ is on the surface S_2. By subtracting Eq. (5.33) from Eq. (5.28), the following equation results:

$$\frac{1}{2}\left(p_{2\gamma}(\mathbf{x}_2) - p_{2\delta}(\mathbf{x}_2)\right) - \int_{S_2} H_2(\mathbf{x}_2|\mathbf{y})\left(p_{2\gamma}(\mathbf{y}) - p_{2\delta}(\mathbf{y})\right) dS = 0\,. \tag{5.34}$$

If the surface sound pressure difference $p_{2\gamma}(\mathbf{x}) - p_{2\delta}(\mathbf{x})$ is substituted by $p_2(\mathbf{x})$ for simplicity, equation (5.34) can be rewritten as

$$\frac{1}{2} p_2(\mathbf{x}_2) - \int_{S_2} H_2(\mathbf{x}_2|\mathbf{y}) p_2(\mathbf{y})\, dS = 0\,. \tag{5.35}$$

Equation (5.35) is the same as Eq. (5.28) or Eq. (5.33) when $p_{in}(\mathbf{x}_2)$ is zero. This means that the surface sound pressure $p_2(\mathbf{x}_2)$ can be thought of as the sound pressure

on the scattering body S_2 without any incident sound from a sound source. Since the scattering body does not generate any sound without incident sound fields, the surface sound pressure $p_2(\mathbf{x}_2)$ should be zero. This integral equation is known as a homogeneous Fredholm equation of the second kind (Stakgold, 1998). The result that $p_2(\mathbf{x}_2) = 0$ can be confirmed by examining the solution of this equation numerically. If the surface S_2 is divided into a set of n_e boundary elements, the integral equation is approximated by a sum of integrals over all boundary elements S_i, as discussed in section 4.4. If the position vector $\mathbf{x}$ can be collocated at each of the nodal points on each boundary element S_i successively, then equation (5.35) can be approximated by

$$\sum_{j=1}^{n_n} p_j \left(\tilde{H}_{kj} - C_k \delta_{kj} \right) = 0 \tag{5.36}$$

where p_j is the j-th nodal value of the sound pressure on the discretized surface S_2, δ_{kj} is the Kronecker symbol, n_n is the total number of nodes, C_k is the coefficient evaluated from Eq. (4.8), and $\tilde{H}_{kj}$ is given by

$$\tilde{H}_{kj} = \sum_{i=1}^{n_e} \int_{S_i} H_2\left(\mathbf{x}_k \middle| \mathbf{y}\right) N_{ij}(\mathbf{y})\, dS \tag{5.37}$$

where the vector $\mathbf{x}$ is collocated at node k, and N_{ij} the linear shape function of node j of element i. Note that C_k is equal to 0.5 if the surface S_2 is smooth. The vectors $\tilde{H}_{kj}$, $C_k\ \delta_{kj}$ for each node k can be assembled into global matrices $\tilde{\mathbf{H}}$ and $\mathbf{C}$ respectively. This produces

$$\mathbf{Hp} = 0, \qquad \text{where } \mathbf{H} = \tilde{\mathbf{H}} - \mathbf{C}. \tag{5.38}$$

If the matrix $\mathbf{H}$ is not singular, this produces $\mathbf{p} = 0$ and the integral equation (5.35) has the unique solution $p_2(\mathbf{x}_2) = 0$. If the matrix $\mathbf{H}$ is singular, the integral equation (5.35) does not have a unique solution. Although the exterior problem does not have any resonance at all, the Helmholtz integral equation for an exterior problem does not have a unique solution at eigenfrequencies associated with the corresponding interior

problem as discussed in section 4.5. This non-uniqueness problem can occur only in numerical calculations. Therefore, it is reasonable to assume that the matrix **H** in Eq. (5.38) is non-singular matrix, and this produces **p**=0 and $p_2(\mathbf{x}_2) = 0$ in Eq. (5.35). Therefore, equation (5.34) shows that

$$p_{2\delta}(\mathbf{x}_2) = p_{2\gamma}(\mathbf{x}_2) \tag{5.39}$$

where the vector $\mathbf{x}_2$ is on the surface S_2. By subtracting Eq. (5.29) from Eq. (5.24), the following equation results:

$$\begin{aligned} p_\gamma(\mathbf{x}) - p_\delta(\mathbf{x}) &= p_{in}(\mathbf{x}) - p_{in}(\mathbf{x}) + \int_{S_2} H_2(\mathbf{x}|\mathbf{y})\left(p_{2\gamma}(\mathbf{y}) - p_{2\delta}(\mathbf{y})\right) dS \\ &= 0 \end{aligned} \tag{5.40}$$

This shows that

$$p_\gamma(\mathbf{x}) = p_\delta(\mathbf{x}) \tag{5.41}$$

where the position vector $\mathbf{x}$ is in the volume V_2. That means the secondary sound field δ is the same as the primary sound field γ. In fact, the secondary sound field $p_\beta(\mathbf{x})$ or $p_\delta(\mathbf{x})$ is same as the corresponding primary sound field $p_\alpha(\mathbf{x})$ or $p_\gamma(\mathbf{x})$ where $\mathbf{x}$ is in the union $V \cup V'$. But, in this case, we focused on the control region $V_1 \cup V_2$ to compare with the other cases studied in other sections.

The scattered sound field in the secondary sound field δ is different from that in the secondary sound field β due to the different geometry and boundary conditions of the scattering body within the control volume. However, the corresponding primary sound field is successfully reproduced in the secondary sound field β or δ by applying the same monopole and dipole source layers in the secondary field. This confirms that the total sound field for any scattering bodies within the control volume can be successfully reproduced if it is produced by the same sources that reproduce the same incident sound field on a given scattering body within the control volume.

5.4 A further interpretation of the incident sound field reproduction in the presence of a single scattering body

Typical scattering problems associated with a single solid body were discussed in section 4.3. The incident sound field reproduction can be better understood by studying this scattering problem more closely. Figure 5.8 shows a scattering problem with a single solid body having the solid surface S_s in an unbounded free field. The control volume V_c is considered. The outer bounding surface of the volume V_c is denoted by S_c and the inner bounding surface of the volume V_c is the surface S_s. The surface S_c is assumed to be a transparent surface. The unbounded exterior volume V_e outside the surface S_c and the interior volume V_s inside the surface S_s are also considered. Note that the normal vectors on the surface S_s are pointing into the volume V_s and the normal vectors on the surface S_c are pointing into the volume V_e. The source strength distribution Q_{vol} is assumed to be located inside the volume V_e. The total sound field p may be composed of the incident sound field p_{in} and the scattered sound field p_{sc} as discussed in section 4.3. Thus

$$p(\mathbf{x}) = p_{in}(\mathbf{x}) + p_{sc}(\mathbf{x}). \tag{5.42}$$

The interior Kirchhoff-Helmholtz integral equation can be applied to the incident sound field in the hypothetical interior acoustic domain V_s where the Sommerfeld radiation condition is not required. Since the incident sound field can be interpreted as the sound field in the absence of the scatterer, the incident sound field p_{in} can be written as

$$-\int_{S_s} H_s(\mathbf{x}|\mathbf{y})\, p_{in}(\mathbf{y})\, dS = \begin{cases} p_{in}(\mathbf{x}), & \mathbf{x} \text{ within } V_s \\ 0, & \mathbf{x} \text{ within } V_c \cup V_e \end{cases} \tag{5.43}$$

where $H_s(\mathbf{x}|\mathbf{y})$ is the transfer function for the surface associated with the specific acoustic impedance z_s of the surface S_s. Note that minus sign on the left hand side of the equation is caused by the direction of the normal vector on the surface S_s. Equation (5.43) corresponds to Eq. (4.17). If the same principle is applied, the

following Kirchhoff-Helmholtz integral equation for the hypothetical interior acoustic domain V_c can be also written:

$$\int_{S_c} H_c(\mathbf{x}|\mathbf{y})\, p_{in}(\mathbf{y})\, dS = \begin{cases} p_{in}(\mathbf{x}), & \mathbf{x} \text{ within } V_c \cup V_s \\ 0, & \mathbf{x} \text{ within } V_e \end{cases} \tag{5.44}$$

where $H_c(\mathbf{x}|\mathbf{y})$ is the transfer function for the surface S_c associated with the specific acoustic impedance z_c of the surface S_c.

The scattered sound field p_{sc} should satisfy the Sommerfeld radiation condition (Wu, 2000a). The scattered sound field in an unbounded exterior domain $V_c \cup V_e$ can be written as

$$\int_{S_s} H_s(\mathbf{x}|\mathbf{y})\, p_{sc}(\mathbf{y})\, dS = \begin{cases} p_{sc}(\mathbf{x}), & \mathbf{x} \text{ within } V_c \cup V_e \\ 0, & \mathbf{x} \text{ within } V_s \end{cases}. \tag{5.45}$$

If the same principle is applied, the following Kirchhoff-Helmholtz integral equation for the hypothetical exterior acoustic domain V_e can be also written:

$$-\int_{S_c} H_c(\mathbf{x}|\mathbf{y})\, p_{sc}(\mathbf{y})\, dS = \begin{cases} p_{sc}(\mathbf{x}), & \mathbf{x} \text{ within } V_e \\ 0, & \mathbf{x} \text{ within } V_c \cup V_s \end{cases} \tag{5.46}$$

Note that minus sign on the left hand side of the equation is caused by the direction of the normal vector on the surface S_c.

The total sound pressure inside the volume V_c is given by the following Kirchhoff-Helmholtz integral equation for the interior acoustic domain V_c:

$$C^0(\mathbf{x})\, p(\mathbf{x}) = \int_{S_s} H_s(\mathbf{x}|\mathbf{y})\, p(\mathbf{y})\, dS + \int_{S_c} H_c(\mathbf{x}|\mathbf{y})\, p(\mathbf{y})\, dS \tag{5.47}$$

where the coefficient $C^0(\mathbf{x})$ becomes unity when the vector $\mathbf{x}$ is inside the volume V_c and becomes zero when the vector $\mathbf{x}$ is outside the volume V_c. Since the total sound

pressure can be decomposed into the incident sound pressure and the scattered sound pressure, equation (5.47) can be rewritten as

$$\begin{aligned} C^0(\mathbf{x})p(\mathbf{x}) = &\int_{S_s} H_s(\mathbf{x}|\mathbf{y})p_{in}(\mathbf{y})\,dS + \int_{S_s} H_s(\mathbf{x}|\mathbf{y})p_{sc}(\mathbf{y})\,dS \\ &+ \int_{S_c} H_c(\mathbf{x}|\mathbf{y})p_{in}(\mathbf{y})\,dS + \int_{S_c} H_c(\mathbf{x}|\mathbf{y})p_{sc}(\mathbf{y})\,dS. \end{aligned} \tag{5.48}$$

When the vector $\mathbf{x}$ is inside the volume V_c, the following integral equation results from Eq. (5.43), (5.44), (5.45), and (5.46):

$$\begin{aligned} p(\mathbf{x}) &= \int_{S_s} H_s(\mathbf{x}|\mathbf{y})p_{sc}(\mathbf{y})\,dS + \int_{S_c} H_c(\mathbf{x}|\mathbf{y})p_{in}(\mathbf{y})\,dS \\ &= p_{sc}(\mathbf{x}) + p_{in}(\mathbf{x}). \end{aligned} \tag{5.49}$$

When the vector $\mathbf{x}$ is inside the volume V_c, the following equations thus result:

$$p_{in}(\mathbf{x}) = \int_{S_c} H_c(\mathbf{x}|\mathbf{y})p(\mathbf{y})\,dS \tag{5.50}$$

and

$$p_{sc}(\mathbf{x}) = \int_{S_s} H_s(\mathbf{x}|\mathbf{y})p(\mathbf{y})\,dS. \tag{5.51}$$

This means that the sound pressure produced from the surface S_c is only the incident sound field from the sound source distribution Q_{vol}, and the sound pressure produced from the surface S_s is only the scattered sound field from the solid body. The secondary sound sources on the surface S_c thus reproduce only the incident sound field from the sound source distribution Q_{vol}. This analysis confirms that the total sound field inside the control volume can be reproduced by reproducing only the incident sound field inside the control volume. Note that the surface sound pressure $p(\mathbf{y})$ on the right hand side of Eq. (5.50) and (5.51) is the total sound pressure. Therefore, when the optimal sound source strengths necessary to reproduce the incident sound field inside the control volume are evaluated from Eq. (5.50), the total sound pressures at the control points are measured and reproduced.

5.5 The boundary surface control principle

The sound pressure in a given volume can be calculated by solving the Kirchhoff-Helmholtz integral equation if there is no source in a given volume as discussed in chapter 4. The Kirchhoff-Helmholtz integral equation can be interpreted as the following boundary surface control principle (Ise, 1999): The pressure field within the volume V can be controlled by controlling the pressure and its gradient on the bounding surface S. In this case, the Green function and its gradient can be regarded as constants determined by the boundary shape. Ise (1999) suggested a sound field reproduction system based on the boundary surface control principle as shown in Figure 5.9. This system reproduces the sound pressure and its gradient on the boundary surface of the control volume in the secondary field so that they are identical to those in the primary field. It is impossible to realize a sound reproduction system with an infinite number of transparent monopole and dipole source layers on the boundary surface of the control volume in the secondary field as presented in the previous section. It is also impossible to realize the system with an infinite number of secondary sources reproducing perfectly the sound pressure and its gradient on the continuous boundary surface of the control volume. Therefore, the boundary surface of the control volume is discretized into a set of boundary elements as discussed in section 4.4, and then the sound pressure and its gradient at each node are reproduced. The pressure gradient can in practice be approximately calculated from the two point pressures, and this will be discussed in the next section. Therefore, the sound pressure and its gradient at finite number of discrete control points on the boundary surface can be approximately reproduced by multiple discrete secondary sources located at arbitrary positions outside the control volume rather than by using the continuous transparent monopole and dipole source layers on the boundary surface. The performance of this system is independent of a listener inside the control volume since the sound field from the source in the primary field incident on the control volume is reproduced as discussed in this chapter. However, there can be spatial aliasing above a certain frequency since the control surface in practice is divided into finite boundary elements. The distance between the control points must be less than half of the shortest wavelength of the reproduced sound. There can be an edge

problem when the control surface is not closed, so the control surface should be closed. There can be a non-uniqueness problem at the eigenfrequencies of the internal control volume and this problem can be serious at high frequencies when only the sound pressure on the control surface is reproduced. However, if both the sound pressure and its gradient on the control surface is reproduced, this non-uniqueness problem can be avoided since inner control points prevents the occurrence of the eigenfrequencies in the frequency range considered (Takane *et al.*, 1999). A great number of loudspeakers are needed if one wishes to control a sound field at high frequencies.

Virtual acoustic systems based on the incident sound field reproduction method using the boundary surface control principle should produce a performance that is not dependent upon the listener within the control volume. However, the number of loudspeakers is a critical problem in practice. For example, Ise (1999) showed that reasonably good reproduction could be made until about 1500Hz when the control field is a two-dimensional square with the side length of 0.5m and 16 sources are located in the secondary field. If the control volume is a three-dimensional cube with the side length of 0.5mm, which can cover one listener's head, 144 sources can make approximately similar performance until about 1500Hz. Since the human ear is, roughly speaking, sensitive up to frequencies of at least 10 kHz, thousands of loudspeakers may be needed to produce a reasonable performance up to 10 kHz in the volume of the cube with the side length of 0.5m. It is nearly impossible to make such system. Therefore, reducing the required number of sources is a most important task for a system based on the incident sound field reproduction method.

5.6 The transfer impedance matrix

A sound field reproduction system based on the boundary surface control principle attempts to reproduce the sound pressure and its gradient on the boundary surface S enclosing the controlled volume V in the secondary field so that these variables are identical to those in the primary field, as shown in Fig. 5.9. In practice, the control

surface S is divided into N control points $\mathbf{x}_i$ (i=1...N). Assume that a listener perceives an auditory event in a free-field environment and his head is fixed within the control region. The pressure gradient at the position vector $\mathbf{x}_i$ can be approximately calculated from the two point pressures at the vector $\mathbf{x}_i + c\mathbf{n}_i$ and $\mathbf{x}_i - c\mathbf{n}_i$ where c is coefficient that is much smaller than a half the wavelength and $\mathbf{n}_i$ is the unit outward normal vector on the control surface S at the vector $\mathbf{x}_i$. Then the sound pressure gradient at the vector $\mathbf{x}_i$ can be approximated by

$$\frac{\partial p(\mathbf{x}_i)}{\partial n} \simeq \frac{p(\mathbf{x}_i + c\mathbf{n}_i) - p(\mathbf{x}_i - c\mathbf{n}_i)}{2c}. \tag{5.52}$$

The sound pressure at the vector $\mathbf{x}_i$ can also be approximated by

$$p(\mathbf{x}_i) \simeq \frac{p(\mathbf{x}_i + c\mathbf{n}_i) + p(\mathbf{x}_i - c\mathbf{n}_i)}{2}. \tag{5.53}$$

Therefore, if the sound pressures at the $2N$ control points on the control surface S are recorded in the primary field and reproduced in the secondary field, the sound field inside the control volume V can be approximately reproduced. Now assume for simplicity that the sound sources generate a single frequency sound. In the primary field, the sound pressures on the boundary surface control points are given by

$$\mathbf{p}_p = \mathbf{g}\, q_p \tag{5.54}$$

where $\mathbf{g}$ is the acoustic transfer impedance vector relating the complex sound pressure vector $\mathbf{p}_p$ on the boundary surface control points to the complex strength q_p of the real source in the primary field. The number of elements of both vectors $\mathbf{g}$ and $\mathbf{p}_p$ equals the number of control points on the boundary surface. The vector $\mathbf{p}_p$ can be recorded with a given q_p in the primary field. In the secondary field, the sound pressures on the boundary surface control points can be written as

$$\mathbf{p}_s = \mathbf{G}\, \mathbf{q}_s \tag{5.55}$$

where $\mathbf{G}$ is the acoustic transfer impedance matrix relating the complex sound pressure vector $\mathbf{p}_s$ on the boundary surface control points to the complex strength vector $\mathbf{q}_s$ of the sources in the secondary field. If the number of control points is M and the number of secondary sources is N, then $\mathbf{G}$ is an $M \times N$ matrix. The n-th column of the matrix $\mathbf{G}$ can be calculated by recording the vector $\mathbf{p}_{sn}$ when only one secondary source produces sound with a given n-th element q_{sn} of the vector $\mathbf{q}_s$ in the secondary field. Then the matrix $\mathbf{G}$ is thus given by:

$$\mathbf{G} = [\mathbf{p}_{s1}/q_{s1} \quad \mathbf{p}_{s2}/q_{s2} \quad \cdots \quad \mathbf{p}_{sN}/q_{sN}] \tag{5.56}$$

In order to replicate the primary sound field with the secondary sound field, $\mathbf{p}_s$ must be equal to $\mathbf{p}_p$. If M equals N and the matrix $\mathbf{G}$ is not singular, we can find the exact $\mathbf{q}_s$ to match $\mathbf{p}_s$ with $\mathbf{p}_p$ by inverting the matrix $\mathbf{G}$. However, in practice, the number of secondary sources N is usually much smaller than the number of control points M and then the matrix $\mathbf{G}$ is not directly invertible. In this case, we can find the optimal $\mathbf{q}_s$ by using the least squares solution to minimize the following cost function:

$$J = \sum_{i=1}^{M} \left| p_{p,i} - p_{s,i} \right|^2 = \left(\mathbf{p}_p - \mathbf{G}\,\mathbf{q}_s \right)^{\mathrm{H}} \left(\mathbf{p}_p - \mathbf{G}\,\mathbf{q}_s \right) \tag{5.57}$$

where the subscript i denotes the ith element of pressure vector and the superscript H denotes the Hermitian transpose. The optimal strength $\mathbf{q}_{so}$ of headphone sources that minimizes J is given by (Nelson and Elliott, 1992)

$$\mathbf{q}_{so} = \left(\mathbf{G}^{\mathrm{H}}\mathbf{G} \right)^{-1} \mathbf{G}^{\mathrm{H}} \mathbf{p}_p \tag{5.58}$$

where it is assumed that the number of control points is greater than the number of secondary sources, and the minimum value of J corresponding $\mathbf{q}_{so}$ is given by

$$J_o = \mathbf{p}_p^{\mathrm{H}} \left(\mathbf{I} - \mathbf{G} \left(\mathbf{G}^{\mathrm{H}}\mathbf{G} \right)^{-1} \mathbf{G}^{\mathrm{H}} \right) \mathbf{p}_p . \tag{5.59}$$

Then, if the secondary sources whose strengths are given by Eq. (5.58) reproduces the sound pressure and its gradient on the control surface, the primary sound field within the control volume is assumed to be reproduced.

5.7 Numerical simulation in the case of a single body

Numerical simulations are performed to simulate virtual acoustic systems based on the incident sound field reproduction method using the boundary surface control principle. The simulations in a two-dimensional space are used for illustration since three-dimensional simulations need a much greater number of sources in the secondary field. Numerical models are created by using the ANSYS software package, and the sound pressure is evaluated by using the direct boundary element method in the SYSNOISE software package, and the optimal secondary source strengths are evaluated by using the MATLAB software package. A more detailed discussion of the numerical simulations can be found after Chapter 7 in this thesis. Figure 5.10 illustrates the two-dimensional primary sound field produced by a point source in an unbounded free field (a) without any scattering body, or (b) with a rigid cylinder, or (c) with a partly absorbent ellipsoid. The reflection coefficient of the ellipsoid from Eq. (5.4) is 0.5. In this case, a cylindrical source corresponds to a point source in a two-dimensional space, and the axis of a cylindrical source is perpendicular to the axes of a two-dimensional space. The sound pressure at a distance d from the axis of the cylindrical source is given by

$$p(d) = -j P_0 H_0^2(kd) \tag{5.60}$$

where P_0 is the peak complex sound pressure amplitude at a cylinder of unit radius and H_0^2 is the Hankel function of second type and zero order (SYSNOISE 5.5). In these simulations, the source amplitude P_0 is set to be unity at all frequencies. The control field is a two-dimensional square with the side length of 500 mm. Pairs of microphones are placed on the boundary surface of the square to measure the surface sound pressure and its gradient. The frequency range of interest is set to be from 100

Hz to 3000 Hz. The distance between a pair of microphones is 20 mm and the distance between two adjacent pairs of microphones is 100 mm as shown in Fig. 5.10. The number of control points is 40. The point source is 1000 mm away from the centre of the control field. The complex sound pressure vector $\mathbf{p}_p$ at the control points is evaluated in SYSNOISE, and it is the desired sound pressure that we aim to reproduce in the secondary field. Figure 5.11 illustrates the two-dimensional secondary sound field produced by multiple point sources in an unbounded free field (a) without any scattering body, or (b) with a rigid cylinder, or (c) with a partly absorbent ellipsoid. The 20 point sources are located on a square with the side length of 3000 mm outside the control volume in the secondary field. The acoustic transfer impedance matrix $\mathbf{G}$ from 20 point sources to 40 control points is evaluated by using the method presented in the previous section. Then, the optimal secondary source strengths necessary to reproduce the primary sound field within the control field are evaluated by using the least squares method. The optimal source strengths for all three cases are nearly the same and maximum amplitude difference of the optimal source strengths for different cases is less than 0.4 %. This verifies that the secondary sources reproduce all the same incident sound field from the primary source for different scattering bodies. The optimal secondary source strengths that are evaluated for the case of the free field are applied to secondary sources for all three cases. Figure 5.12 shows the sound pressure within the control field in the primary and corresponding secondary sound field at 1 kHz in various cases, for example. The secondary pressure fields are nearly identical with the corresponding primary fields. This good performance is a practical illustrator of the incident sound field reproduction method using the boundary surface control principle. However, the primary field is not always reproduced perfectly at all frequencies in limited conditions. Figure 5.13 shows the condition number of the transfer impedance matrices for various cases. The condition number is defined as the ratio of the largest singular value to the smallest singular value of the matrix (Kreyszig, 1993). A small condition number indicates well-conditioned and a large condition number indicates ill-conditioned regarding the matrix inversion. Figure 5.13 shows the condition numbers of the matrices for all cases are nearly the same, and the system is ill-conditioned at low frequencies (Nelson, 2001). Figure 5.14 shows the mean sound pressure level differences between the desired values and the reproduced values in various cases, which are averaged over the control points. It shows similar tendencies

for all cases. The reproduction is successfully performed between 300 Hz and 1500 Hz for all cases. A large reproduction error at low frequencies below 300 Hz results from an ill-conditioned system for the matrix inversion. A large reproduction error at high frequencies above 1500 Hz results from spatial aliasing effect due to spatial sampling. The 100 mm microphone spacing corresponds to half the wavelength of a 1700 Hz wave. These high reproduction errors at low and high frequencies may be applied to other incident sound reproduction systems generally. Therefore, there may be a middle frequency range in which the incident sound reproduction systems can successfully create virtual acoustic images.

5.8 Conclusion

A study has been presented of the incident sound field reproduction method that creates a virtual acoustic field by reproducing exactly the incident sound field within a control volume. The incident sound field from the source in the primary field is not influenced by changes of the scattering body. If the incident sound field in the primary field is exactly reproduced in the secondary field, the secondary sound field is always the same as the primary sound field regardless of the geometry and boundary condition of the scattering body within the control volume. The boundary surface control principle has also been studied to reproduce the incident sound field within a control volume by reproducing sound pressure and its gradient on the boundary surface of the control volume. The virtual acoustic system based on the incident sound field reproduction method using the boundary surface control principle has been suggested. The least squares solution is used to find the optimal secondary source strengths when the transfer impedance matrix is not invertible. The results of the numerical simulation for two-dimensional scattering body show the incident sound reproduction systems can successfully create virtual acoustic images over some useful range of frequencies.

FIGURES

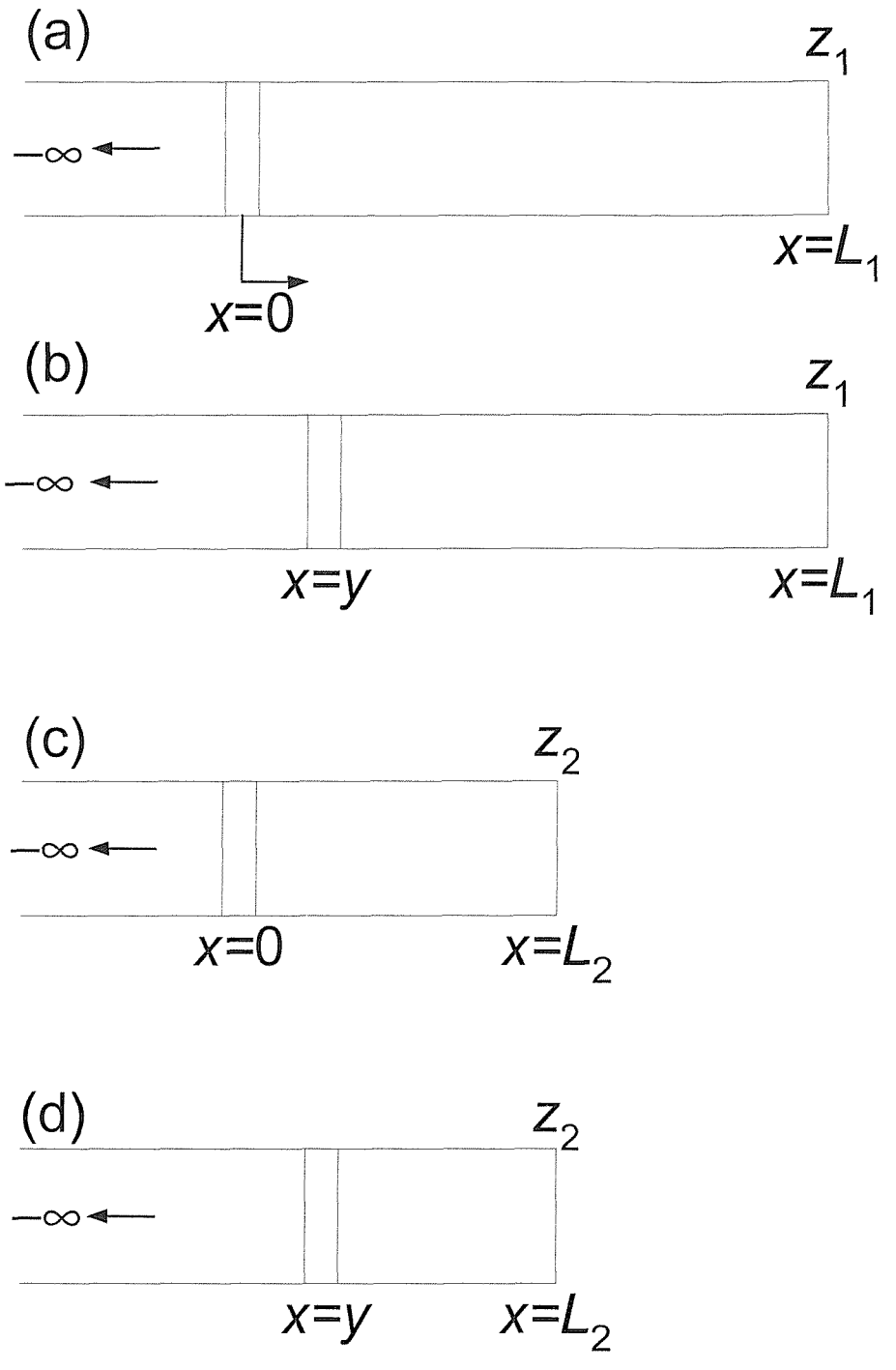

Figure 5.1 (a) Primary sound field in a tube with a termination at $x=L_1$

(b) Secondary sound field in a tube with a termination at $x=L_1$

(c) Primary sound field in a tube with a termination at $x=L_2$

(d) Secondary sound field in a tube with a termination at $x=L_2$.

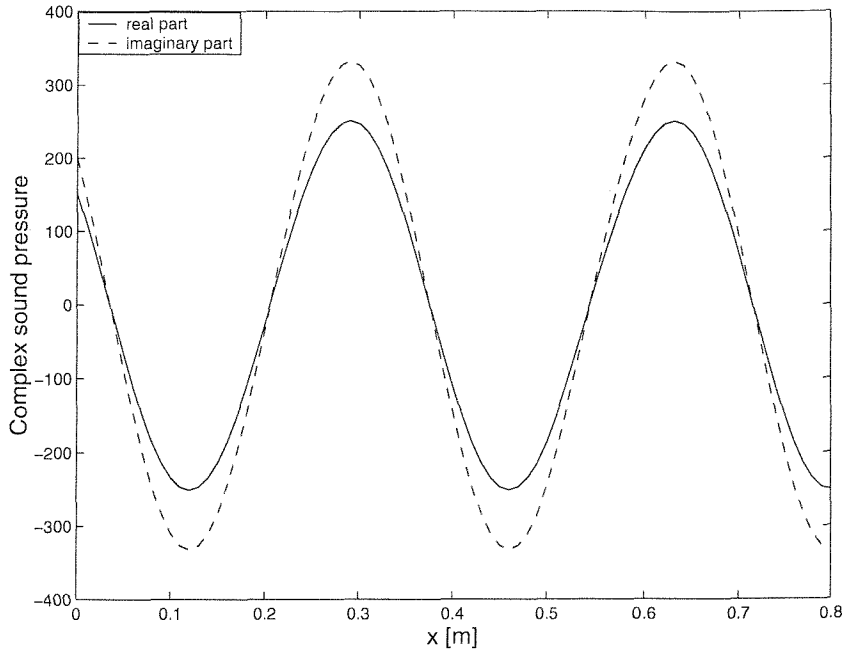

(a)

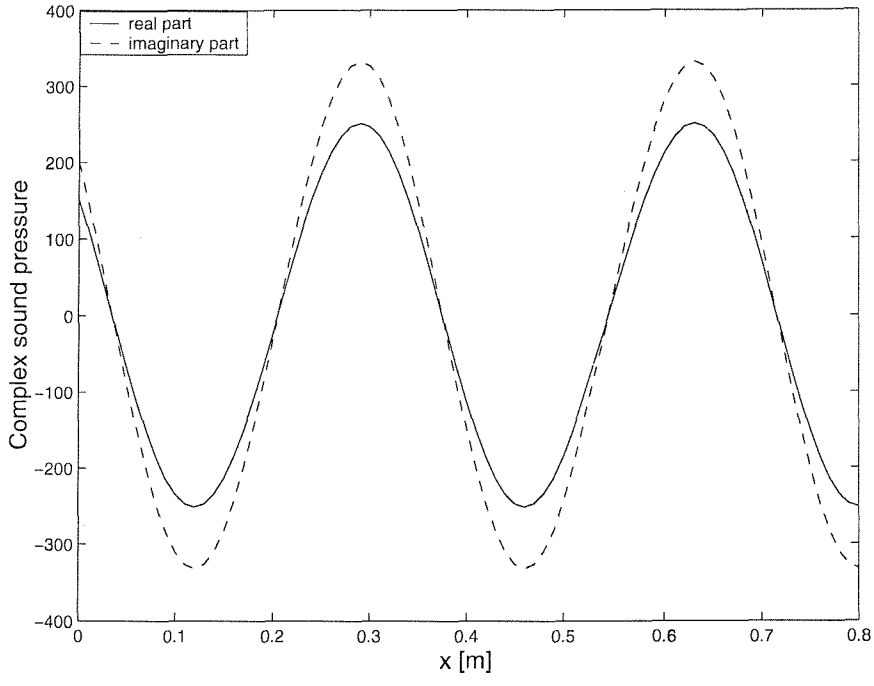

(b)

Figure 5.2 (a) Primary sound field in a tube at 1kHz with a termination of reflection coefficient one at x=0.8, (b) the corresponding secondary sound field.

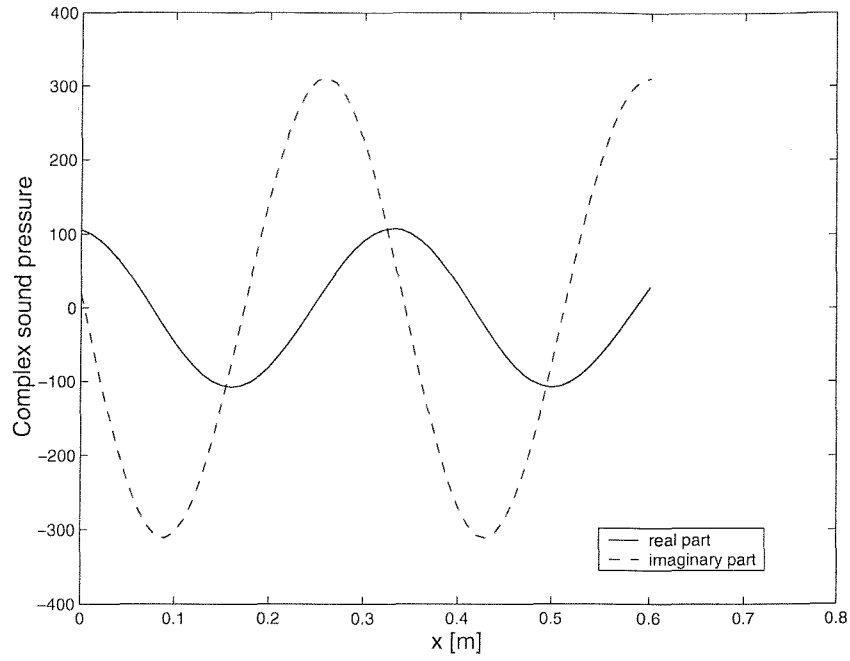

(a)

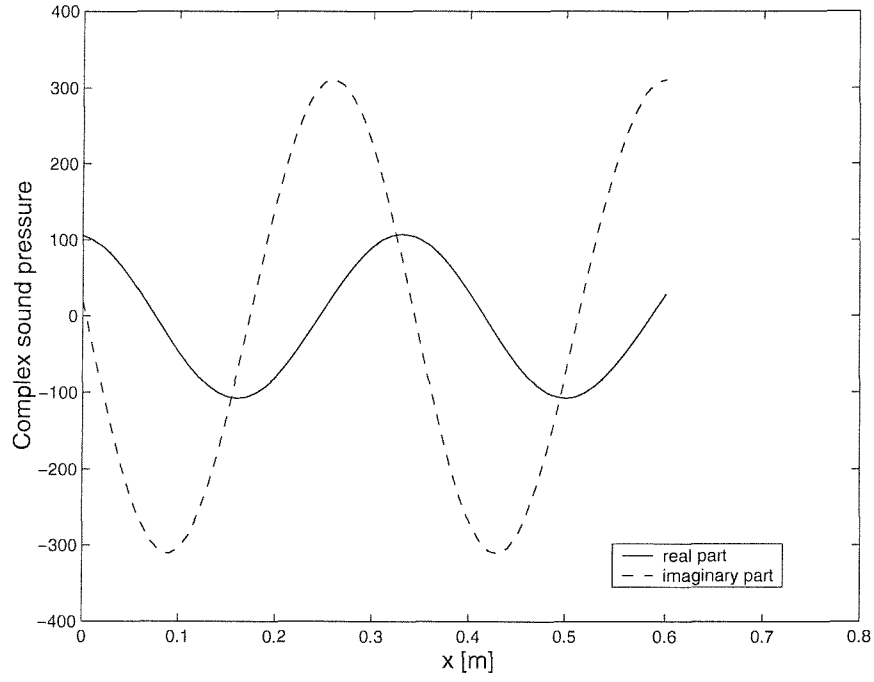

(b)

Figure 5.3 (a) Primary sound field in a tube at 1kHz with a termination of reflection coefficient 0.5 at x=0.6, (b) the corresponding secondary sound field.

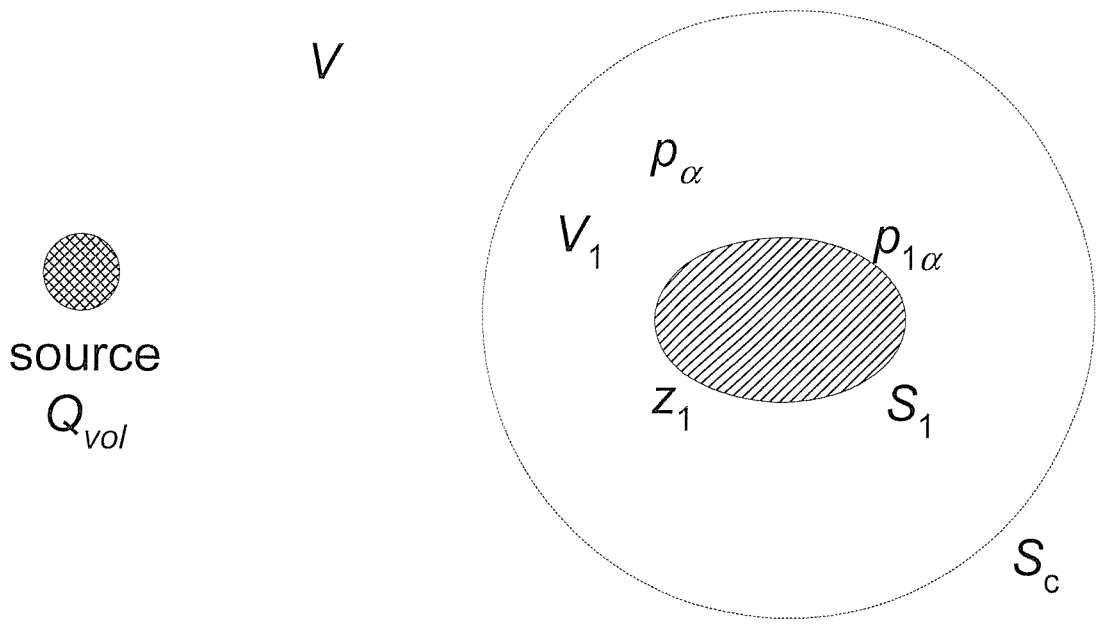

Figure 5.4 The sound field α in the case of a single scattering body.

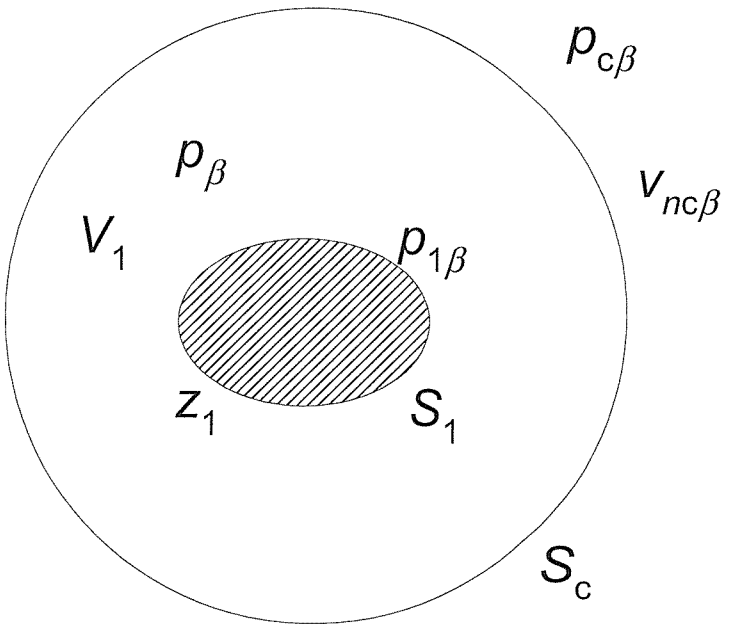

Figure 5.5 The sound field β in the case of a single scattering body.

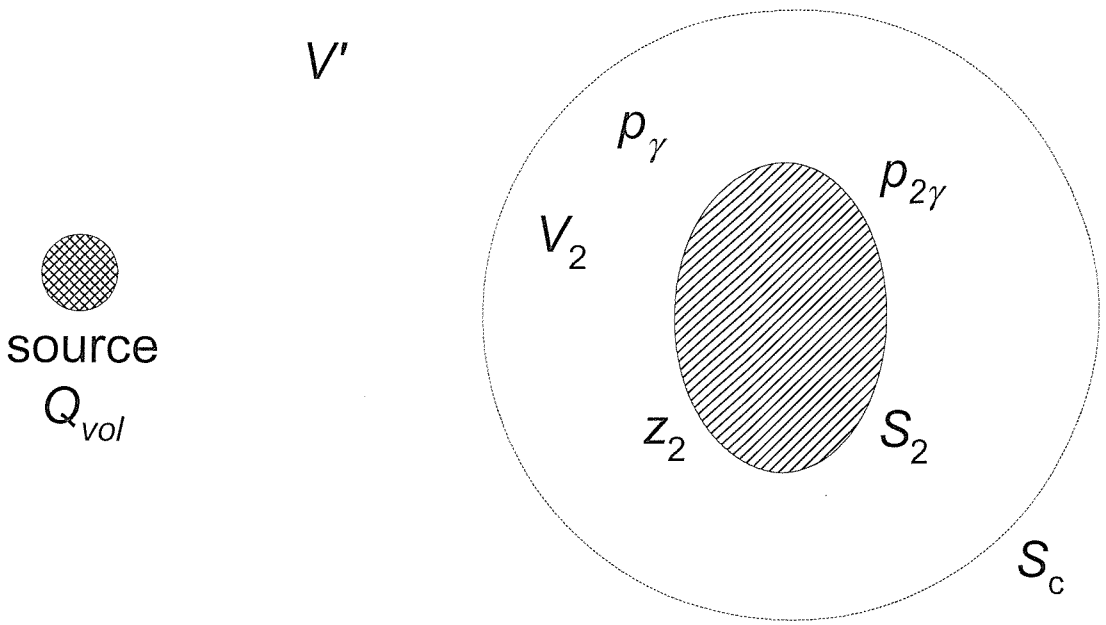

Figure 5.6 The sound field γ in the case of a single scattering body.

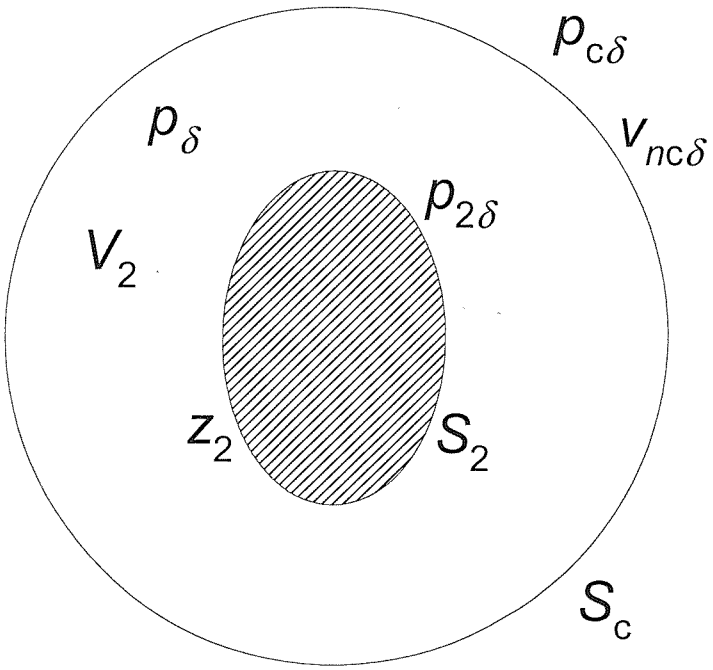

Figure 5.7 The sound field δ in the case of a single scattering body.

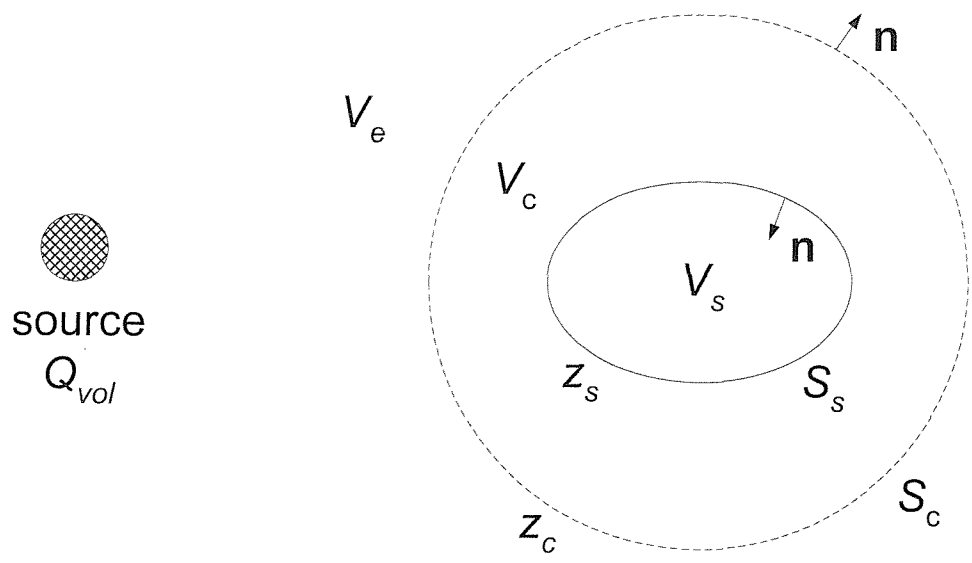

Figure 5.8 A scattering problem with a single solid body.

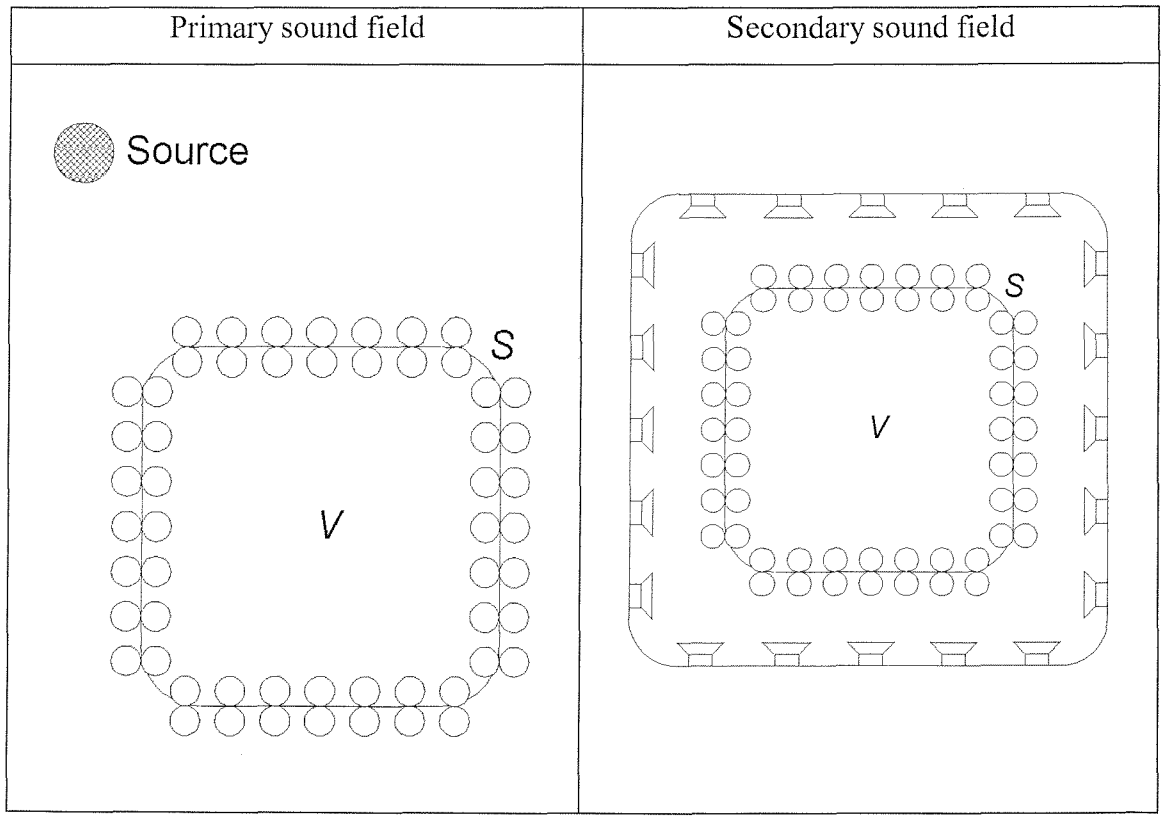

Figure 5.9 Sound field reproduction system based on the boundary surface control principle.

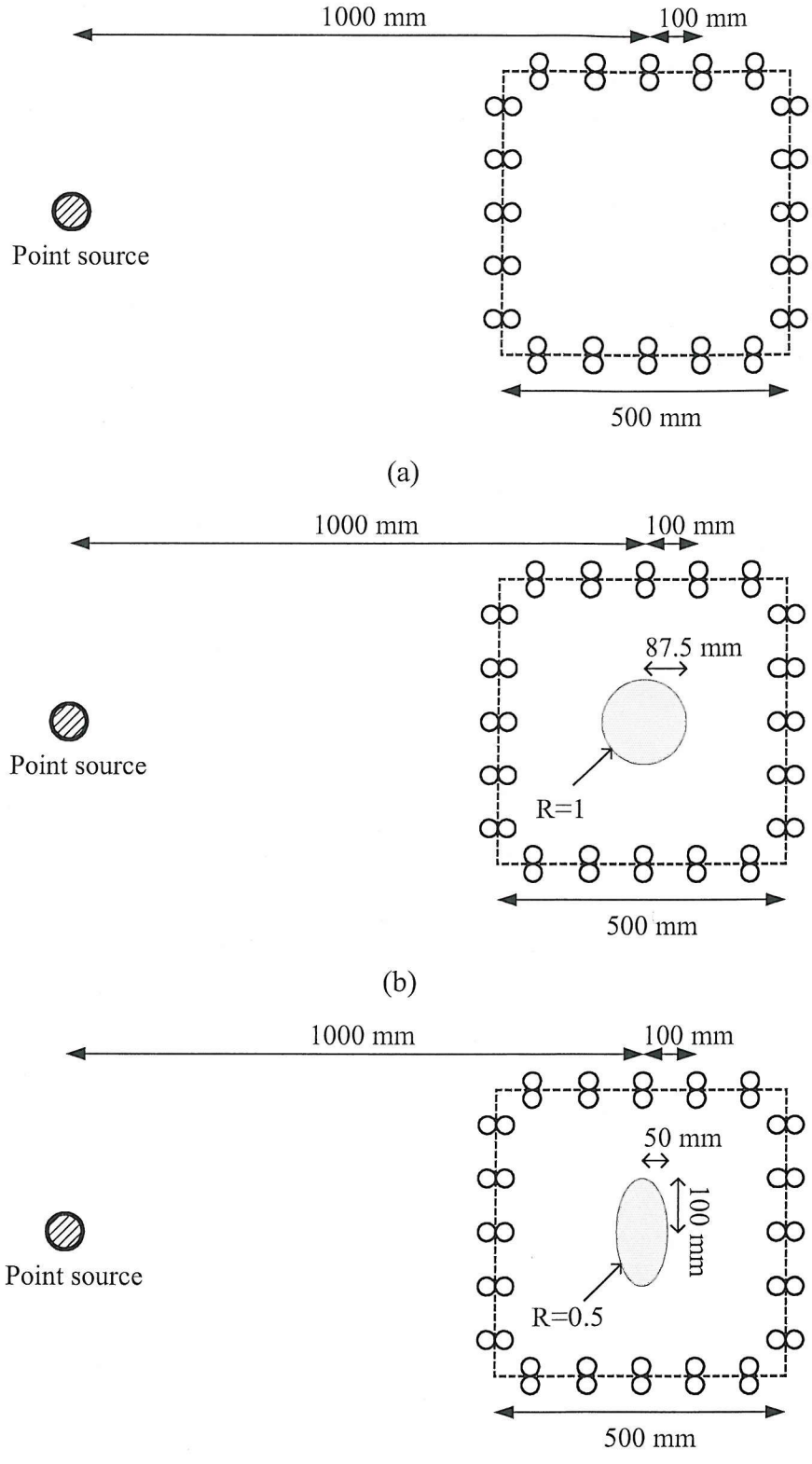

Figure 5.10 The two-dimensional primary sound field produced by a point source in an unbounded free field (a) without any scattering body, or (b) with a rigid cylinder, or (c) with a partly absorbent ellipsoid.

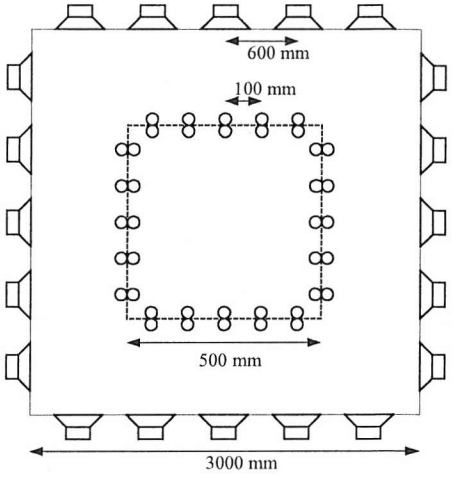

(a)

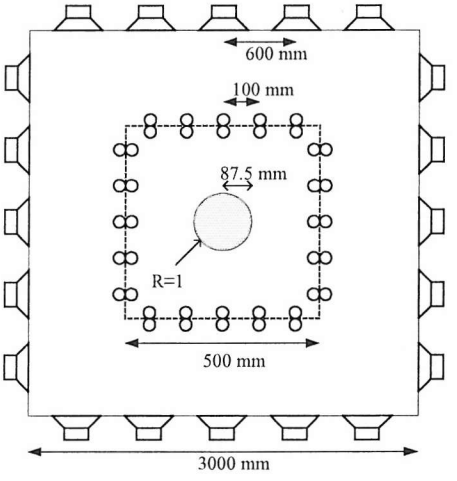

(b)

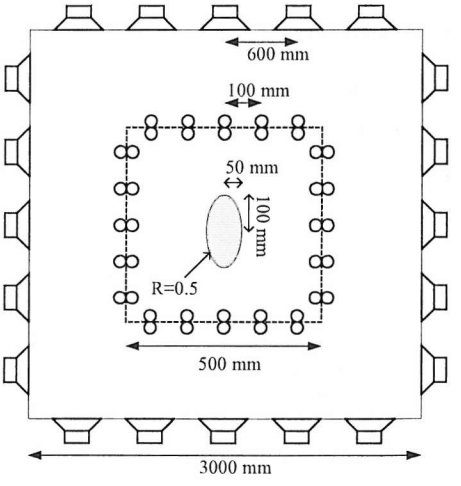

(c)

Figure 5.11 The two-dimensional secondary sound field produced by multiple point sources in an unbounded free field (a) without any scattering body, or (b) with a rigid cylinder, or (c) with a partly absorbent ellipsoid.

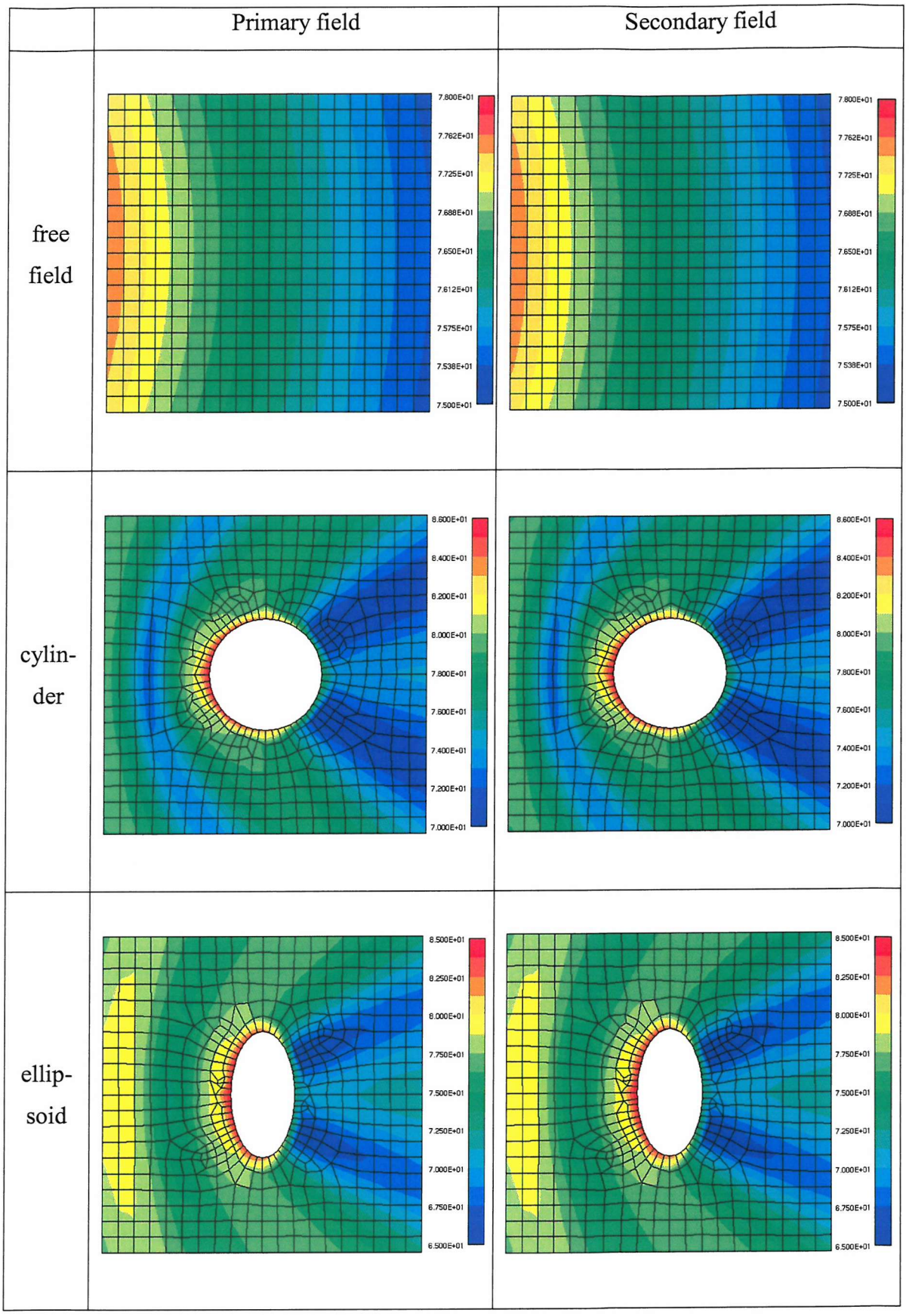

Figure 5.12 The primary and secondary sound field at 1 kHz in various cases.

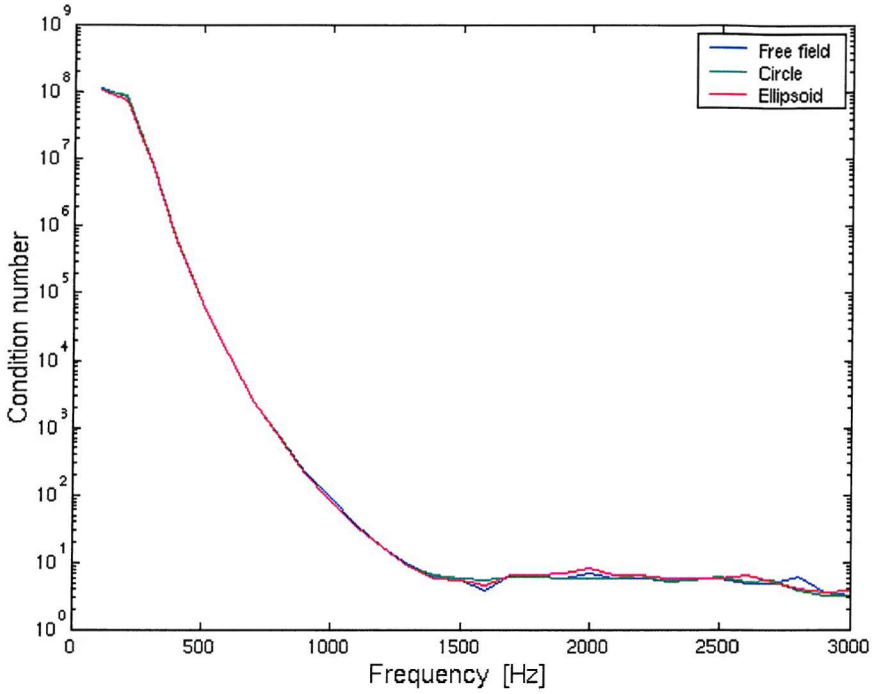

Figure 5.13 Condition number of the various transfer impedance matrices.

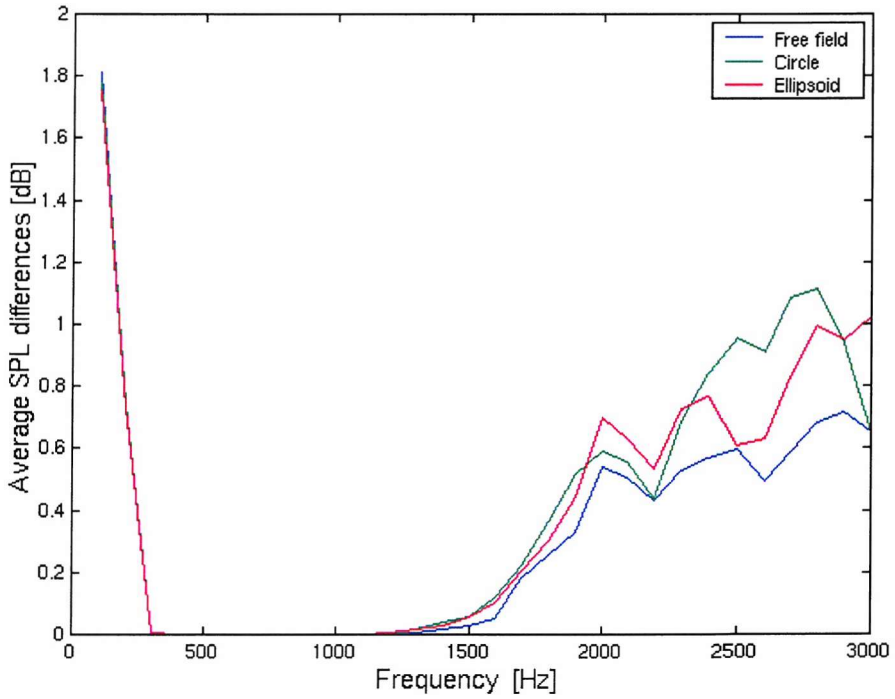

Figure 5.14 The sound pressure level differences averaged over control points in various cases.

CHAPTER 6
VIRTUAL ACOUSTIC SYSTEM WITH A MULTICHANNEL HEADPHONE

6.1 Introduction

Virtual acoustic systems based on binaural technology using non-individualized HRTFs may be useful for basic systems of low quality. However, they often give confusing and inaccurate information for sound localization since they often fail to give accurate monaural spectral cues and binaural spectral cues at high frequencies. This is because the HRTFs of the listener are sensitive to the geometry of the listener's ear at high frequencies. Virtual acoustic systems based on the incident sound field reproduction method may be a solution to this problem since their performance is independent of the listener within the control volume and so they may give accurate sound localization cues. They may be suitable for virtual acoustic systems of high quality that require pin-point accuracy of sound localization for broadband signals. Virtual acoustic images produced from such a system may be stable and obvious because loudspeakers located in the similar direction as that of a virtual source are used to make the virtual acoustic field. For example, frontal loudspeakers mainly make sound when a virtual source is frontal, and rear loudspeakers mainly make sound when a virtual source is to the rear. However, this kind of system has not been realized because it needs a potentially large number of loudspeakers and very strong processing power. During the past decade, numerical processing power has been amazingly improved and access to multimedia information is much more familiar to people. Since home theatre systems are now very popular due to a widespread use of DVD systems, multichannel sound systems have been widely spread quickly. If a reasonable number of loudspeakers can make a virtual acoustic field of reasonable quality, virtual acoustic systems of high quality using multichannel sound reproduction may be realized thanks to powerful modern processing technology.

The objective of this study is to evaluate the extent to which the incident sound field reproduction method might be used in practice. Of particular interest is the application where the sound field in the region of the ears of a listener is reproduced such that the field can be made independent of the geometry of the individual listener's ears. In such a case, an ear of the listener might be regarded as a scattering body inside a control volume, which the remaining part of the head of the listener can be regarded as another scattering body outside the control volume. It is then of interest to determine whether the first scattering body (the ear) influences the incident field produced by the second scattering body (the head). This chapter explains the theory of virtual acoustics reproducing the incident sound field on the ear with a multichannel headphone. The theory is studied first for the general three-dimensional case of two scattering bodies and secondly is applied to the case of the human head. The understanding of the case of two scattering bodies will help the understanding of the case of the human head.

6.2 The RISE system with a multichannel headphone

The previous chapter showed that the critical problem of virtual acoustic systems based on the incident sound field reproduction method is the number of loudspeakers. The required number of loudspeakers depends on the size of the control volume of the system for a given frequency range, and this should be as small as possible. If the size of the control volume is reduced from the volume covering a whole human head to the volume covering only an ear, the number of control points on the boundary surface can be substantially reduced and the number of loudspeakers can also be reduced. If just a few loudspeakers were enough to control the sound field around the ear using the boundary surface control principle, a virtual acoustic system based on the incident sound field reproduction method could be realizable using a multichannel headphone.

When we hear sounds, incoming sound waves are, for example, modified by a human body such as a listener's head, torso and pinna as shown in Figure 6.1. The acoustic

effect of the head, torso, and pinna is based on scattering, shadowing, reflection, diffraction, and resonance. The modification of the acoustic signal at the ear due to each body part can be considered to be the operation of a linear filter. The performance of the head, torso, and pinna filter differs among individuals. The performance of the pinna filter is the most sensitive to individual differences at high frequencies. However, if the incident sound field on the ear is reproduced, which may be independent of the geometry of the ear, the performance of a virtual acoustic system may be independent of the listener's ear. The incident sound field on the ear consists of the direct waves from the source, the waves scattered by objects and walls in a room, and the waves scattered by the listener's head and torso. When the incident sound field on the ear is reproduced, the listener hears virtual sound through the listener's own pinna filter. This means that the performance of a virtual acoustic system using this concept may be independent of the geometry of the listener's ear, and so one of the critical problems of virtual acoustic systems based on HRTF technology may be solved.

Figure 6.2 shows the basic concept of a virtual acoustic system reproducing the incident sound field on the ear within the control volume using a multichannel headphone. This system is called the "RISE (Reproduction of the Incident Sound on the Ear)" system in this thesis. The multichannel headphone reproduction of the RISE system is based on the boundary surface control principle. First, the head and headphone model without the ears is used to calculate the optimal strengths of the headphone sources to create the virtual acoustic field. In the primary field, the head model without the ears is placed in the sound field produced by a sound source having the strength of q_p in an arbitrary space, and the control volume is placed around the location where an ear is supposed to be located. The control volume is discretized into control points on double layer boundary surfaces. Then the sound pressures $\mathbf{p}_p$ at the control points are recorded. In the secondary field, the same control points on the double layer boundary control surfaces are placed on a headphone model without the ear. Then the acoustic transfer impedance matrix $\mathbf{G}$ is measured, which relates the sound pressures $\mathbf{p}_s$ at the control points to the strengths $\mathbf{q}_s$ of multiple headphone sources. Then the optimal headphone source strengths $\mathbf{q}_{so}$ necessary to best match $\mathbf{p}_s$ with $\mathbf{p}_p$ can be calculated using the least squares method explained in section 5.6. Second, the head and headphone model with the ears is used to confirm that the RISE

system is effective. The objective of any virtual acoustic system is to reproduce the same sound pressure at a listener's eardrum in the secondary field as the sound pressure at the eardrum in the primary field. In the primary field, the same sound source strength q_p in the same space is applied to the head model with the ears, and then the sound pressure at the eardrum is recorded. In the secondary field, the same headphone source strengths $\mathbf{q}_{so}$ are applied to the headphone model with the ear, and then the sound pressure at the eardrum is recorded. Then the sound pressure at the eardrum recorded in the primary field is compared with that in the secondary field to confirm that they are the same. If the sound pressures at the control points are recorded in the primary field and accurately reproduced in the secondary field, the sound pressure at the eardrum can be exactly replicated. This hypothesis will be verified and the detailed theory of the RISE system is explained in this chapter.

6.3 Two scattering bodies

This section studies the general case of two arbitrary scattering bodies with sound sources in a free field using the same procedure as that in case of one scattering body. This case will turn out to be closely related to the case of the human head and ear. The main difference between the case of one arbitrary scattering body and this case will be explained using the concept of "active" and "passive" sound sources. Note that the definition of the "active" and "passive" sound sources is applied only in this thesis.

(1) Active and passive sound sources

In case of ideal acoustic sources such as the point monopole source, the boundary conditions at the source such as sound pressure, particle velocity, and specific acoustic impedance are assumed not to be changed by the presence of scatterers and other sources. Therefore, the sound field emitted from the sound source is not changed regardless of the presence of scatterers and other sources. Such a source is called an "active sound source" in this thesis. Scattering can be defined as the sound

field arising from the interaction of the incident sound field with the scatterer. The acoustic field properties on the scatterer, such as the sound pressure or normal particle velocity on the surface of the scatterer, can be changed by the presence of other scatterers and other sources. although the specific acoustic impedance on the surface of the scatterer is not changed. Therefore, the sound field emitted from the scatterer can be changed by other scatterers. Since the scatterer does not generate any energy actively, the scatterer is not a sound source and it just reacts to the incident sound field. Nevertheless, since the additional sound field is produced by the scatterer, this scatterer can be regarded as some kind of "source" in a broad sense. Such a scatterer is called a "passive sound source" in this thesis. Those two different concepts of the sound source will help explain the theory of the RISE system.

(2) Sound field α

Figure 6.3 illustrates the primary field α with two scattering bodies and acoustic sources in an unbounded free field. The acoustic source strength distribution Q_{vol} in an unbounded acoustic domain V outside the scattering bodies is assumed to be known and emit a single frequency sound. Each bounding surface of the scattering bodies is denoted by S_1 or S_2. The specific acoustic impedance z_1 of the surface S_1 and z_2 of the surface S_2 are also assumed to be known and non-zero. Now consider the control volume V_1 bounded by the surface S_c and the surface S_2. The surface S_c is a transparent imaginary surface. The sound source distribution Q_{vol} is assumed to be located outside the volume V_1. When the vector $\mathbf{x}$ is in the volume V_1, the sound pressure in the volume V_1 is denoted by p_α. Then, the sound pressure p_α inside the volume V_1 can be written as

$$p_\alpha(\mathbf{x}) = p_{in\alpha}(\mathbf{x}) + \int_{S_1} H_1(\mathbf{x}|\mathbf{y})\, p_{1\alpha}(\mathbf{y})\, dS + \int_{S_2} H_2(\mathbf{x}|\mathbf{y})\, p_{2\alpha}(\mathbf{y})\, dS \qquad (6.1)$$

where the position vector $\mathbf{x}$ is inside the volume V_1, the sound field $p_{in\alpha}(\mathbf{x})$ from the source distribution is given by the same equation as Eq. (5.11), the transfer function $H_1(\mathbf{x}|\mathbf{y})$ is given by the same equation as Eq. (5.14), and $H_2(\mathbf{x}|\mathbf{y})$ is given by the same equation as Eq. (5.25). The sound field $p_{in\alpha}(\mathbf{x})$ is produced by the "active sound source". This sound pressure p_α is the desired sound field that is supposed to be

reproduced in the secondary field. The two unknown variables $p_{1\alpha}$ and $p_{2\alpha}$ in Eq. (6.1) can be calculated by solving the following two integral equations:

$$\frac{1}{2}p_{1\alpha}(\mathbf{x}_1)-\int_{S_1}H_1(\mathbf{x}_1|\mathbf{y})\,p_{1\alpha}(\mathbf{y})\,dS-\int_{S_2}H_2(\mathbf{x}_1|\mathbf{y})\,p_{2\alpha}(\mathbf{y})\,dS=p_{in\alpha}(\mathbf{x}_1) \quad (6.2)$$

where the vector $\mathbf{x}_1$ is on the surface S_1, and

$$\frac{1}{2}p_{2\alpha}(\mathbf{x}_2)-\int_{S_1}H_1(\mathbf{x}_2|\mathbf{y})\,p_{1\alpha}(\mathbf{y})\,dS-\int_{S_2}H_2(\mathbf{x}_2|\mathbf{y})\,p_{2\alpha}(\mathbf{y})\,dS=p_{in\alpha}(\mathbf{x}_2) \quad (6.3)$$

where the vector $\mathbf{x}_2$ is on the surface S_2. Note that all the boundary surfaces are assumed to be smooth boundaries in this chapter for simplicity.

(3) Sound field β

Figure 6.4 illustrates the secondary field β with the same scattering body having surface S_2 as that in the sound field α, but with different sound sources that are intended to reproduce the primary sound field α within the control volume V_1. If continuous transparent monopole and dipole source layers are placed on the surface S_c and there is no other source in an unbounded free field, the sound pressure p_β at a single frequency in the volume V_1 can be written as

$$p_\beta(\mathbf{x})=p_{in\beta}(\mathbf{x})+\int_{S_2}H_2(\mathbf{x}|\mathbf{y})p_{2\beta}(\mathbf{y})\,dS \quad (6.4)$$

where the vector $\mathbf{x}$ is inside the volume V_1 and the incident sound field $p_{in\beta}$ produced by source layers on the surface S_c is given by the same equation as Eq. (5.19). The monopole and dipole source layers on the surface S_c are intended to reproduce the same sound field as the sound field α inside the control volume V_1. If the sound field β is the same as the sound field α in the volume V_1, that is, $p_\alpha(\mathbf{x}) = p_\beta(\mathbf{x})$ when the vector $\mathbf{x}$ is inside the volume V_1 and $p_{2\alpha}(\mathbf{y}) = p_{2\beta}(\mathbf{y})$ when the vector $\mathbf{y}$ is on the surface S_2, then the following equation results from subtracting Eq. (6.4) from Eq. (6.1):

$$p_{in\beta}(\mathbf{x}) = p_{in\alpha}(\mathbf{x}) + p_{s\alpha}(\mathbf{x}) \tag{6.5}$$

where the vector $\mathbf{x}$ is in the volume V_1 and the scattered sound field $p_{s\alpha}(\mathbf{x})$ from the surface S_1 in the sound field α is given by

$$p_{s\alpha}(\mathbf{x}) = \int_{S_1} H_1(\mathbf{x}|\mathbf{y})\, p_{1\alpha}(\mathbf{y})\, dS\,. \tag{6.6}$$

This equation shows that the monopole and dipole source layers on the surface S_c reproduce only the "total" incident sound field on the volume V_1 which is composed of the sound field $p_{in\alpha}(\mathbf{x})$ produced by the "active sound source" and the sound field $p_{s\alpha}(\mathbf{x})$ produced by the "passive sound source" in the primary field α. The sound field $p_{s\alpha}(\mathbf{x})$ scattered from the scatterer S_1 can be regarded as another incident sound field that propagates into the volume V_1. This additional incident sound field is the main difference between the case of one scattering body and the case of two scattering bodies. However, this additional incident sound field $p_{s\alpha}(\mathbf{x})$ is dependent on the geometry and boundary condition of the scatterer S_2. The sound field scattered from the surface S_2 inside the control volume does not need to be reproduced by the source layers because it is determined only by the "total" incident sound field and it is reproduced or scattered by the surface S_2 itself. This will be discussed by studying another pair of primary and secondary fields.

(4) Sound field γ

Figure 6.5 illustrates another primary field γ in an otherwise unbounded free field with the sound sources and one scattering body that are the same as those in the sound field α but with one scattering body that differs from that in the sound field α. The bounding surface of the same scattering body is the surface S_1 and that of the different scattering body is denoted by S_3, and this different scattering body is assumed to be within the surface S_c. The specific acoustic impedance z_3 of the surface S_3 is assumed to be known and non-zero. The acoustic source strength distribution Q_{vol} is assumed to be the same as that in the sound field α. The outer bounding surface of the control volume V_2 is the surface S_c that is the same transparent surface as that in the sound

field α, and the inner bounding surface of the volume V_2 is the surface S_3. When the vector $\mathbf{x}$ is in the volume V_2, the sound pressure in the volume V_2 is denoted by p_γ. The sound pressure p_γ in the volume V_2 at a single frequency can be written as

$$p_\gamma(\mathbf{x}) = p_{in\gamma}(\mathbf{x}) + p_{s\gamma}(\mathbf{x}) + \int_{S_3} H_3(\mathbf{x}|\mathbf{y})\, p_{3\gamma}(\mathbf{y})\, dS \tag{6.7}$$

where the vector $\mathbf{x}$ is inside the volume V_2, the scattered sound field $p_{s\gamma}(\mathbf{x})$ from the surface S_1 in the sound field γ is given by

$$p_{s\gamma}(\mathbf{x}) = \int_{S_1} H_1(\mathbf{x}|\mathbf{y})\, p_{1\gamma}(\mathbf{y})\, dS\,, \tag{6.8}$$

and where the transfer function $H_3(\mathbf{x}|\mathbf{y})$ is given by

$$H_3(\mathbf{x}|\mathbf{y}) = -\frac{j\omega\rho_0 g(\mathbf{x}|\mathbf{y})}{z_3(\mathbf{y})} - \frac{\partial g(\mathbf{x}|\mathbf{y})}{\partial n}. \tag{6.9}$$

The incident sound field $p_{in\gamma}(\mathbf{x})$ from the source is given by the same equation as Eq. (5.26), which is produced by the "active sound source". The sound field $p_{s\gamma}(\mathbf{x})$ scattered from the scatterer S_1 is produced by the "passive sound source" in the primary sound field γ. This sound pressure p_γ is the desired sound field that is supposed to be reproduced in the secondary field. The sound field $p_{in\gamma}(\mathbf{x})$ is equal to the sound field $p_{in\alpha}(\mathbf{x})$ when the vector $\mathbf{x}$ is in the union $V_1 \cup V_2$, i.e. when the vector $\mathbf{x}$ is inside V_1 or V_2, for the same reasons as those in section 5.3.(3). Therefore, the incident sound field $p_{in}(\mathbf{x})$ produced by the acoustic source strength distribution Q_{vol} in either primary sound field α or γ can be rewritten as

$$p_{in}(\mathbf{x}) = p_{in\alpha}(\mathbf{x}) = p_{in\gamma}(\mathbf{x}) = \int_{V_1 \cup V_2} Q_{vol}(\mathbf{y}_v)\, g(\mathbf{x}|\mathbf{y}_v)\, dV \tag{6.10}$$

where the vector $\mathbf{x}$ is in the union volume $V_1 \cup V_2$. The two unknown variables $p_{1\gamma}$ and $p_{3\gamma}$ in Eq. (6.7) can be calculated by solving the following two integral equations:

$$\frac{1}{2}p_{1\gamma}(\mathbf{x}_1)-\int_{S_1}H_1(\mathbf{x}_1|\mathbf{y})p_{1\gamma}(\mathbf{y})\,dS-\int_{S_3}H_3(\mathbf{x}_1|\mathbf{y})p_{3\gamma}(\mathbf{y})\,dS=p_{in}(\mathbf{x}_1) \quad (6.11)$$

where the vector $\mathbf{x}_1$ is on the surface S_1, and

$$\frac{1}{2}p_{3\gamma}(\mathbf{x}_3)-\int_{S_1}H_1(\mathbf{x}_3|\mathbf{y})p_{1\gamma}(\mathbf{y})\,dS-\int_{S_3}H_3(\mathbf{x}_3|\mathbf{y})p_{3\gamma}(\mathbf{y})\,dS=p_{in}(\mathbf{x}_3) \quad (6.12)$$

where the vector $\mathbf{x}_3$ is on the surface S_3.

(5) Sound field δ

Figure 6.6 illustrates another secondary field δ with the scattering body having the surface S_3, which is the same as that in the sound field γ but with different sound sources that are intended to reproduce the primary sound field γ within the control volume V_2 in an otherwise unbounded free field. If continuous transparent monopole and dipole source layers are placed on the surface S_c and there is no other source, the sound pressure p_δ at a single frequency in the volume V_2 can be written as

$$p_\delta(\mathbf{x})=p_{in\delta}(\mathbf{x})+\int_{S_3}H_3(\mathbf{x}|\mathbf{y})p_{3\delta}(\mathbf{y})\,dS \quad (6.13)$$

where the vector $\mathbf{x}$ is inside the volume V_2 and the incident sound field $p_{in\delta}$ produced by source layers on the surface S_c is given by the same equation as Eq. (5.30). The monopole and dipole source layers on the surface S_c are intended to reproduce the same sound field as the sound field γ inside the control volume V_2. If the same monopole and dipole source strengths obtained in the sound field β are applied to the sound field δ, the following equation results from Eq. (6.5) and Eq. (6.10):

$$p_{in\delta}(\mathbf{x})=p_{in\beta}(\mathbf{x})=p_{in\alpha}(\mathbf{x})+p_{s\alpha}(\mathbf{x})=p_{in}(\mathbf{x})+p_{s\alpha}(\mathbf{x}) \quad (6.14)$$

where the vector $\mathbf{x}$ is in the union $V_1 \cup V_2$ for the same reasons as those discussed in section 5.3.(4). The unknown variable $p_{3\delta}$ in Eq. (6.13) can be calculated by solving the following integral equation:

$$\frac{1}{2} p_{3\delta}(\mathbf{x}_3) - \int_{S_1} H_1(\mathbf{x}_3|\mathbf{y})\, p_{1\alpha}(\mathbf{y})\, dS - \int_{S_3} H_3(\mathbf{x}_3|\mathbf{y})\, p_{3\delta}(\mathbf{y})\, dS = p_{in}(\mathbf{x}_3) \quad (6.15)$$

where the vector $\mathbf{x}_3$ is on the surface S_3. By subtracting Eq. (6.12) from Eq. (6.15), the following equation results:

$$\begin{aligned} &\frac{1}{2}\left(p_{3\gamma}(\mathbf{x}_3) - p_{3\delta}(\mathbf{x}_3)\right) - \int_{S_3} H_3(\mathbf{x}_3|\mathbf{y})\left(p_{3\gamma}(\mathbf{y}) - p_{3\delta}(\mathbf{y})\right) dS \\ &= \int_{S_1} H_1(\mathbf{x}_3|\mathbf{y})\left(p_{1\gamma}(\mathbf{y}) - p_{1\alpha}(\mathbf{y})\right) dS = p_{s\gamma}(\mathbf{x}_3) - p_{s\alpha}(\mathbf{x}_3) \end{aligned} \quad (6.16)$$

where the vector $\mathbf{x}_3$ is on the surface S_3. Strictly speaking, the sound field $p_{s\alpha}(\mathbf{x}_3)$ is different from the sound field $p_{s\gamma}(\mathbf{x}_3)$ on the surface S_3 since the sound field $p_{s\alpha}(\mathbf{x})$ or $p_{s\gamma}(\mathbf{x})$ is produced by the "passive sound source" and depends on the geometry and boundary condition of the scatterer S_3. However, $p_{s\gamma}(\mathbf{x}_3) - p_{s\alpha}(\mathbf{x}_3)$ will be nearly zero in certain cases. In such cases it may be assumed that the sound field incident on the control volume from scatterers outside the control volume is independent of the geometry and boundary conditions of the scatterer inside the control volume. This means that scatterers outside the control volume are "active sound sources". Therefore, the "total" incident sound field on the control volume in Eq. (6.14) is assumed to be produced from "active sound sources". This is an important assumption. This assumption is only reasonable if certain requirements are met. These requirements will be discussed in section 6.5. In this case, the scatterer having the bounding surface S_1 outside the control volume is assumed to be an "active sound source". This means that the acoustic properties such as the sound pressure on the surface S_1 is not changed when the geometry and boundary conditions of the scatterer having the bounding surface S_2 is changed into those of the scatterer S_2 having the bounding surface S_3 inside the control volume. Under these circumstances, the sound pressure on the surface S_1 in the sound field α is assumed to be the same as that in the sound field γ. That is

$$p_{1\alpha}(\mathbf{y}) = p_{1\gamma}(\mathbf{y}) \tag{6.17}$$

where the vector $\mathbf{y}$ is on the surface S_1. This assumption results in the following equation:

$$p_{s\gamma}(\mathbf{x}_3) - p_{s\alpha}(\mathbf{x}_3) = \int_{S_1} H_1(\mathbf{x}_3|\mathbf{y})\left(p_{1\gamma}(\mathbf{y}) - p_{1\alpha}(\mathbf{y})\right) dS = 0 \tag{6.18}$$

where the vector $\mathbf{x}_3$ is on the surface S_3. The assumption in Eq. (6.17) also causes the sound field $p_{s\alpha}(\mathbf{x})$ to be the same as the sound field $p_{s\gamma}(\mathbf{x})$ where the vector $\mathbf{x}$ is in the union $V_1 \cup V_2$ from Eq. (6.6) and (6.8). If the surface sound pressure difference $p_{3\gamma}(\mathbf{x}_3) - p_{3\delta}(\mathbf{x}_3)$ in Eq. (6.16) is replaced by $p_3(\mathbf{x}_3)$ for simplicity, equation (6.16) can be rewritten as

$$\frac{1}{2} p_3(\mathbf{x}_3) - \int_{S_3} H_3(\mathbf{x}_3|\mathbf{y})\, p_3(\mathbf{y})\, dS = 0. \tag{6.19}$$

If the surface S_3 is discretized into a set of boundary elements, equation (6.19) can be rewritten as $\mathbf{Hp} = 0$ in matrix form by using the same procedure as that in section 5.3.(4). It is reasonable to assume that the matrix $\mathbf{H}$ is non-singular matrix as discussed in section 5.3.(4), and so the integral equation (6.19) has the unique solution $p_3(\mathbf{x}_3)$=0. Then, equation (6.16) demonstrates that

$$p_{3\gamma}(\mathbf{x}_3) = p_{3\delta}(\mathbf{x}_3) \tag{6.20}$$

where the vector $\mathbf{x}_3$ is on the surface S_1. By subtracting Eq. (6.13) from Eq. (6.7), it follows that

$$\begin{aligned} & p_\gamma(\mathbf{x}) - p_\delta(\mathbf{x}) \\ &= p_{in}(\mathbf{x}) + p_{s\gamma}(\mathbf{x}) - p_{in}(\mathbf{x}) - p_{s\alpha}(\mathbf{x}) + \int_{S_3} H_3(\mathbf{x}|\mathbf{y})\left(p_{3\gamma}(\mathbf{y}) - p_{3\delta}(\mathbf{y})\right) dS \\ &= 0 \end{aligned} \tag{6.21}$$

where the vector $\mathbf{x}$ is on the surface S_3. This shows that

$$p_\gamma(\mathbf{x}) = p_\delta(\mathbf{x}) \tag{6.22}$$

where the position vector $\mathbf{x}$ is in the volume V_2. That means the secondary sound field δ is same as the primary sound field γ.

In this section, the case of two scattering bodies with sound sources has been studied. It is assumed that any kind of sound field incident on the control volume in the primary field is not influenced by the changes of the geometry and boundary condition of the scattering body inside the control volume. Under these conditions, it has been shown that the secondary sound field is always same as the primary sound field if the incident sound field on the control volume is exactly reproduced. Obviously the accuracy with which this can be achieved will depend upon the validity of the assumption made.

6.4 The human head and ear

To study the theory of the RISE system, simplified head and ear models are used. The case of the human head and ear is similar to the case of the two scattering bodies and acoustic sources in a free field. All the equations and the analysis are the same as the case of the two scattering bodies except for some terms. In this case, the surface of the human head is divided into two surfaces, an ear surface and a head surface excluding the ears. Each surface acts as a scattering body.

First, a pair of primary and secondary sound fields is studied in order to determine the required secondary source distribution. Figure 6.7 shows the primary field α produced by the sound source distribution Q_{vol} and a human head without ears in an unbounded free field. This simulates the real acoustic environment. S_1 and S_2 denote the bounding surfaces of the head. The surface S_1 is the surface of the head with the ear excluded. The surface S_2 is the flat surface of the dummy head in the absence of the ear. The surface S_c is a transparent imaginary surface as depicted in Figure 6.7. The sound pressure p_α inside the control volume V_1 at a single frequency can be written as

$$p_\alpha(\mathbf{x}) = p_{in\alpha}(\mathbf{x}) + p_{s\alpha}(\mathbf{x}) + \int_{S_2} H_2(\mathbf{x}|\mathbf{y})\, p_{2\alpha}(\mathbf{y})\, dS \tag{6.23}$$

which is same as Eq. (6.1). The scattered sound field $p_{s\alpha}(\mathbf{x})$ is produced by the head surface excluding the flat surface in the primary sound field α.

Figure 6.8 shows the secondary field β with the same scattering flat surface S_2 as that in the sound field α, which is produced by headphone sources that are intended to reproduce the primary sound field α within the control volume V_1. This simulates the virtual acoustic environment. The surface of the headphone is denoted by S_h and the specific acoustic impedance z_h of the surface S_h is assumed to be known. The sound pressure p_β at a single frequency in the volume V_1 can be written as

$$p_\beta(\mathbf{x}) = \int_{S_h} H_h(\mathbf{x}|\mathbf{y})\, p_{h\beta}(\mathbf{y})\, dS + \int_{S_2} H_2(\mathbf{x}|\mathbf{y}) p_{2\beta}(\mathbf{y})\, dS \tag{6.24}$$

where the vector $\mathbf{x}$ is inside the volume V_1, $p_{h\beta}$ denotes the sound pressure on the surface S_h, and $H_h(\mathbf{x}|\mathbf{y})$ is given by

$$H_h(\mathbf{x}|\mathbf{y}) = -\frac{j\omega\rho_0 g(\mathbf{x}|\mathbf{y})}{z_h(\mathbf{y})} - \frac{\partial g(\mathbf{x}|\mathbf{y})}{\partial n}. \tag{6.25}$$

The continuous source layer on the headphone surface is used to reproduce the sound field inside the control volume using the boundary surface control principle. For example, the continuous dipole source layer on the surface S_h having the strength of $Q_{h\beta} = p_{h\beta} / j\omega\rho_0$ is assumed to reproduce the sound pressure $p_{c\beta}$ and its gradient $-j\omega\rho_0 v_{nc\beta}$ on the surface S_c. Then, the sound field $p_{in\beta}(\mathbf{x})$ incident on the surface S_c, which is produced by the source layer on the surface S_h in the sound field β, is given by

$$p_{in\beta}(\mathbf{x}) = \int_{S_h} H_h(\mathbf{x}|\mathbf{y})\, p_{h\beta}(\mathbf{y})\, dS$$
$$= -\int_{S_c} j\omega\rho_0 v_{nc\beta}(\mathbf{y})\, g(\mathbf{x}|\mathbf{y}) + p_{c\beta}(\mathbf{y}) \frac{\partial g(\mathbf{x}|\mathbf{y})}{\partial n} dS \tag{6.26}$$

where the vector $\mathbf{x}$ is inside the volume V_1. In the ideal case of an infinite number of headphone sources, the impedance z_h can take any value. However, if the number of headphone sources is finite in practice, the specific acoustic impedance z_h of the headphone surface S_h should be perfectly absorbent to remove any cavity modes inside the headphone and absorb all the scattered sound from the ear. This will be discussed in section 7.5. If the sound field β is the same as the sound field α in the volume V_1, then the following equation results from subtracting Eq. (6.24) from Eq. (6.23):

$$p_{in\beta}(\mathbf{x}) = \int_{S_h} H_h(\mathbf{x}|\mathbf{y})\, p_{h\beta}(\mathbf{y})\, dS = p_{in\alpha}(\mathbf{x}) + p_{s\alpha}(\mathbf{x}) \tag{6.27}$$

This equation shows that the strengths of the continuous source layer on the headphone surface S_h must be obtained in order to reproduce the "total" incident sound field. The "total" incident sound field is composed of the incident sound field $p_{in\alpha}(\mathbf{x})$ produced by the source in the sound field α and another incident sound field $p_{s\alpha}(\mathbf{x})$ scattered from the head surface excluding the ear surface in the sound field α. This means the sound field scattered from the ear surface does not need to be reproduced by the headphone sources.

Second, another pair of primary and secondary sound fields are studied to confirm the performance of the RISE system and examine the conditions necessary for the production of the virtual sound field. Figure 6.9 shows another primary field γ in an otherwise unbounded free field with the sound source distribution and the human head surface which are the same as those in the sound field α but with an ear surface S_3 that differs from that in the sound field α. In this case, a realistic human ear surface is used. The specific acoustic impedance z_3 of the ear surface S_3 is assumed to be known. The sound pressure p_γ inside the control volume V_2 at a single frequency can be written as

$$p_\gamma(\mathbf{x}) = p_{in\gamma}(\mathbf{x}) + p_{s\gamma}(\mathbf{x}) + \int_{S_3} H_3(\mathbf{x}|\mathbf{y})\, p_{3\gamma}(\mathbf{y})\, dS \tag{6.28}$$

which is the same as Eq. (6.7). The scattered sound field $p_{s\gamma}(\mathbf{x})$ is produced by the head surface excluding the ear surface in the primary sound field γ. The incident sound field $p_{in\gamma}(\mathbf{x})$ is equal to $p_{in\alpha}(\mathbf{x})$ where $\mathbf{x}$ is in the union $V_1 \cup V_2$ for the same reason as that discussed in section 5.3.(3).

Figure 6.10 shows another secondary field δ produced by headphone sources with the same scattering ear surface S_3 as that in the sound field γ. The sound pressure p_δ at a single frequency in the volume V_2 can be written

$$p_\delta(\mathbf{x}) = \int_{S_h} H_h(\mathbf{x}|\mathbf{y})\, p_{h\delta}(\mathbf{y})\, dS + \int_{S_3} H_3(\mathbf{x}|\mathbf{y}) p_{3\delta}(\mathbf{y})\, dS \tag{6.29}$$

where the vector $\mathbf{x}$ is inside the volume V_2. The continuous source layer on the headphone surface is used to reproduce the sound pressure $p_{c\delta}$ and its gradient $-j\omega\rho_0 v_{nc\delta}$ on the surface S_c by using the boundary surface control principle. If the same headphone source strengths obtained in the sound field β are applied to those in the sound field δ, that is, $p_{h\delta}(\mathbf{y}) = p_{h\beta}(\mathbf{y})$ where the vector $\mathbf{y}$ on the surface S_h, the following equation results from Eq. (6.27):

$$\begin{aligned} \int_{S_h} H_h(\mathbf{x}|\mathbf{y})\, p_{h\delta}(\mathbf{y})\, dS &= \int_{S_h} H_h(\mathbf{x}|\mathbf{y})\, p_{h\beta}(\mathbf{y})\, dS \\ &= p_{in\alpha}(\mathbf{x}) + p_{s\alpha}(\mathbf{x}) = p_{in\gamma}(\mathbf{x}) + p_{s\alpha}(\mathbf{x}) \end{aligned} \tag{6.30}$$

where the vector x is in the intersection $V_1 \cap V_2$. This shows that the sound field reproduced by the headphone sources in the sound field δ is the same total incident sound field as that in the sound field β for the case of the flat surface S_2 in place of the ear surface S_3. By subtracting Eq. (6.29) from Eq. (6.28), it follows that

$$\begin{aligned} &p_\gamma(\mathbf{x}) - p_\delta(\mathbf{x}) - \int_{S_3} H_3(\mathbf{x}|\mathbf{y})\left(p_{3\gamma}(\mathbf{y}) - p_{3\delta}(\mathbf{y})\right) dS \\ &= p_{in\gamma}(\mathbf{x}) + p_{s\gamma}(\mathbf{x}) - \int_{S_h} H_h(\mathbf{x}|\mathbf{y})\, p_{h\delta}(\mathbf{y})\, dS \end{aligned} \tag{6.31}$$

where the vector $\mathbf{x}$ is inside the volume V_2. When the vector $\mathbf{x}_3$ is on the surface S_3, equation (6.31) can be modified to

$$\begin{aligned}&\frac{1}{2}\left(p_{3\gamma}(\mathbf{x}_3)-p_{3\delta}(\mathbf{x}_3)\right)-\int_{S_3}H_3(\mathbf{x}_3|\mathbf{y})\left(p_{3\gamma}(\mathbf{y})-p_{3\delta}(\mathbf{y})\right)dS\\&=p_{in\gamma}(\mathbf{x}_3)+p_{s\gamma}(\mathbf{x}_3)-\int_{S_h}H_h(\mathbf{x}_3|\mathbf{y})\,p_{h\delta}(\mathbf{y})\,dS=p_{s\gamma}(\mathbf{x}_3)-p_{s\alpha}(\mathbf{x}_3)\end{aligned}. \quad (6.32)$$

Now assume that the sound field incident on the control volume from the scatterers outside the control volume is independent of the geometry and boundary conditions of the scatterer inside the control volume. In this case, the head surface S_1 outside the control volume is assumed to be an "active sound source". This means that the acoustic properties such as the sound pressure on the head surface S_1 are not changed when the listener's ear inside the control volume is changed into another listener's ear or the flat surface. The requirements to make this assumption valid will be discussed in the next section. Therefore, the sound pressure on the head surface S_1 in the sound field α is assumed to be the same as that in the sound field γ. This means that $p_{s\alpha}(\mathbf{x}_3)$ is the same as $p_{s\gamma}(\mathbf{x}_3)$ and then equation (6.32) is equal to zero. Then, $p_{3\gamma}(\mathbf{x}_3)$ turns out to be the same as $p_{3\delta}(\mathbf{x}_3)$ as shown in the previous section. Then, the following equation results from Eq. (6.31):

$$p_\gamma(\mathbf{x})=p_\delta(\mathbf{x}) \quad (6.33)$$

where the position vector $\mathbf{x}$ is in the volume V_2. That means the secondary sound field δ is same as the primary sound field γ. This confirms that the RISE system can produce a virtual acoustic field under the assumption that any scattering bodies outside the control volume act not like "passive sound sources" but like "active sound sources".

6.5 Validity of the assumptions

The theory studied above has shown that the RISE system can successfully produce virtual acoustic fields only if the sound field incident on the control volume from the scatterers outside the control volume is independent of the geometry and boundary conditions of the scatterer inside the control volume. In the case of the two scattering bodies and the human head and ear, the sound pressure on the surface S_1 in the sound field α is assumed to be the same as that in the sound field γ as shown in Eq. (6.17). This assumption also implies that the sound field $p_{s\alpha}(\mathbf{x})$ scattered from the surface S_1 in the sound field α is assumed to be the same as the sound field $p_{s\gamma}(\mathbf{x})$ scattered from the surface S_1 in the sound field γ when the vector $\mathbf{x}$ is in the union $V_1 \cup V_2$. However, the sound field $p_{s\alpha}(\mathbf{x})$ may not be exactly same as the sound field $p_{s\gamma}(\mathbf{x})$ when the geometry and boundary condition of the scatterer inside the control volume in the sound field α is different from that in the sound field γ, that is, $S_2 \neq S_3$ and $z_2 \neq z_3$ as depicted in Figure 6.3 and 6.5 or in Figure 6.7 and 6.9. This is because the sound field produced by the one scatterer can be influenced by the sound field produced by the other scatterer. However, if *one* of the following requirements is met, the "total" incident sound field on the control volume can be assumed to be independent of the scattering body inside the control volume.

First, the geometry and boundary condition of the scatterer within the control volume in the sound field α is similar to that in the sound field γ, that is, $S_2 \approx S_3$ and $z_2 \approx z_3$. In the case of the human head, at low frequencies where wavelengths are much longer than the size of the ear, the detailed shape of the ear cannot influence the sound field around the ear very much, so this requirement can be fulfilled. However, at high frequencies where wavelengths are similar or shorter than the size of the ear, the detailed shape of the individual ear can influence the sound field around the ear significantly and interact with the incident waves, so this requirement may not be fulfilled.

Second, the sound pressure on the surface of the scattering body outside the control volume in the sound field α is similar to that in the sound field γ, that is, the sound

pressure $p_{1\alpha}(\mathbf{x}_1) \approx p_{1\gamma}(\mathbf{x}_1)$ on the surface S_1. By subtracting Eq. (6.2) from Eq. (6.11), the following equation results:

$$\begin{aligned}&\frac{1}{2}\left(p_{1\alpha}(\mathbf{x}_1)-p_{1\gamma}(\mathbf{x}_1)\right)-\int_{S_1} H_1(\mathbf{x}_1|\mathbf{y})\left(p_{1\alpha}(\mathbf{y})-p_{1\gamma}(\mathbf{y})\right)dS \\ &=\int_{S_2} H_2(\mathbf{x}_1|\mathbf{y})\,p_{2\alpha}(\mathbf{y})\,dS-\int_{S_3} H_3(\mathbf{x}_1|\mathbf{y})\,p_{3\gamma}(\mathbf{y})\,dS\end{aligned} \tag{6.34}$$

where the vector $\mathbf{x}_1$ is on the surface S_1. If the right hand side of the above equation is nearly zero, that is, if the sound pressures produced on the head surface scattered from the flat surface are similar to those scattered from the ear surface, the sound pressure $p_{1\alpha}(\mathbf{x}_1) - p_{1\gamma}(\mathbf{x}_1)$ on the surface S_1 is also near zero for the same reason as that discussed in section 5.3.(4). Then, this requirement can be satisfied. On the other hand, if the sound field produced on the head surface scattered from the ear surface is sufficiently weak compared to the sound pressure on the head surface, then this requirement can also be fulfilled. In the case studied above, this requirement can be written from Eq. (6.34) as

$$\begin{aligned}&\left|p_{1\alpha}(\mathbf{x}_1)\right| \gg \left|\int_{S_2} H_2(\mathbf{x}_1|\mathbf{y})\,p_{2\alpha}(\mathbf{y})\,dS\right| \\ &\qquad\text{and} \\ &\left|p_{1\gamma}(\mathbf{x}_1)\right| \gg \left|\int_{S_3} H_3(\mathbf{x}_1|\mathbf{y})\,p_{3\gamma}(\mathbf{y})\,dS\right|\end{aligned} \tag{6.35}$$

where the vector $\mathbf{x}_1$ is on the surface S_1. For example, at strong resonances of the listener's ear, the sound field scattered from the ear surface may influence the sound pressure on the head surface near the ear surface.

Third, the incident sound field inside the control volume produced from the scatterers outside the control volume may be sufficiently weak compared to the total sound pressure inside the control field. In the case studied above, this requirement can be written from Eq. (6.1) and (6.7) as

$$\left|p_\alpha(\mathbf{x})\right| \gg \left|\int_{S_1} H_1(\mathbf{x}|\mathbf{y})\, p_{1\alpha}(\mathbf{y})\, dS\right|$$
$$\text{and} \tag{6.36}$$
$$\left|p_\gamma(\mathbf{x})\right| \gg \left|\int_{S_1} H_1(\mathbf{x}|\mathbf{y})\, p_{1\gamma}(\mathbf{y})\, dS\right|$$

where the vector $\mathbf{x}$ is within the volume $V_1 \cup V_2$. Then, the sound pressure $p_{s\alpha}(\mathbf{x}) \approx p_{s\gamma}(\mathbf{x})$ within the volume $V_1 \cup V_2$. If the scattered sound field from the head surface inside the control volume is much weaker than the incident sound field from the sources or the scattered sound field from the ear surface in the control volume, this requirement may be fulfilled, for example, when the sound source in the primary field is placed on the same side of the ear.

If one of the above requirements is met, the "total" incident sound field on the control volume in the case of the head model without the ear is the same as that in case of the head model with the ear, and the head surface excluding the ears acts like an "active sound source". Some numerical simulations related to these requirements in the case of the head and ear will be presented in section 8.5.

6.6 Numerical simulation in the case of two scattering bodies

Numerical simulations in a two-dimensional space are performed to simulate virtual acoustic systems with two scattering bodies, which are based on the incident sound field reproduction method using the boundary surface control principle. Most numerical models and the procedure are the same as those described in section 5.7. Figure 6.11 illustrates the two-dimensional primary sound field produced by a point source in an unbounded free field with two rigid cylinders. In this case, one cylinder is located inside the control volume and the other cylinder is located outside the control volume. Figure 6.12 illustrates the two-dimensional primary sound field produced by a point source in an unbounded free field with a rigid cylinder and a rigid ellipsoid. In this case, the ellipsoid is located inside the control volume and the cylinder is located outside the control volume. The distance d between the two

scattering bodies is set to be 0.5 m, 1 m, or 2 m. The cylindrical source amplitude P_0 in Eq. (5.60) is set to be unity at all frequencies. The location of the source and the control field are the same as those in section 5.7. The frequency range of interest is set to be from 100 Hz to 3000 Hz. The complex sound pressure vector $\mathbf{p}_p$ at the control points, which we aim to reproduce in the secondary field, is evaluated in SYSNOISE. Figure 6.13 illustrates the two-dimensional secondary sound field produced by multiple point sources in an unbounded free field with a rigid cylinder. This figure is the same as Fig. 5.11 (b). This secondary field aims to reproduce the primary field inside the control volume shown in Fig. 6.11. The acoustic transfer impedance matrix $\mathbf{G}$ from 20 point sources to 40 control points is evaluated. Then, the optimal secondary source strengths necessary to reproduce the primary sound field within the control field are evaluated by using the least squares method. Figure 6.14 illustrates the two-dimensional secondary sound field produced by multiple point sources in an unbounded free field with a rigid ellipsoid. This figure is the same as Fig. 5.11 (c) except for the boundary condition of the ellipsoid. This secondary field aims to reproduce the primary field inside the control volume shown in Fig. 6.12. In this case, the optimal secondary source strengths evaluated for the case of two rigid cylinders are applied in this secondary field with the rigid ellipsoid. Figure 6.15 shows the sound pressure level differences averaged over the control points between the desired values and the reproduced values when the distance between two scatterers is 0.5 m. The solid line represents the case of two cylinders. This shows successful reproduction between 300 Hz and 1500 Hz and the performance is similar to that shown Fig. 5.14. Note that a large reproduction error results from an ill-conditioned system for the matrix inversion at low frequencies below 300 Hz and spatial aliasing effect at high frequencies above 1500 Hz. The dashed line represents the case of a cylinder and an ellipsoid. This shows inferior reproduction than that in the case of two cylinders. The secondary sources still reproduce the "total" incident sound field recorded in the case of two cylinders when the scatterer inside the control field is changed from the cylinder to the ellipsoid. The change of the geometry of the scatterer inside the control field can change the sound field scattered from the cylinder outside the control volume, which is a "passive sound source". Figure 6.16 shows the sound pressure level differences averaged over control points when the distance between two scatterers is 1 m, and Figure 6.17 shows those when the distance between two scatterers is 2 m. Figure 6.18 shows the comparison of the sound

pressure level differences averaged over control points for various distances between the ellipsoid and the cylinder. These figures show the performance of the system between 300 Hz and 1500 Hz gets better as the distance between two scatterers gets greater. This is because the sound field scattered from the cylinder outside the control volume becomes weaker than the sound field from the source and the scatterer inside the control volume in the primary field as distance between two scatterers gets greater. This is one of the requirements of the validity of the assumption discussed in the previous section. Figure 6.17 shows the reasonably successful reproduction between 300 Hz and 1500 Hz when the distance between two scatterers is 2 m. Therefore, in this case of 2 m distance, the assumption of the theory of the incident sound field reproduction system is reasonable. Figure 6.19 shows the sound pressure within the control field in the primary and corresponding secondary sound field at 1 kHz in both cases, for example. The secondary pressure fields are nearly identical with the corresponding primary fields. This good performance illustrates well the incident sound field reproduction method with two scattering bodies.

The theory of the RISE system in case of the human head and ear is almost identical to the theory of the incident sound field reproduction method with two scattering bodies as studied in this chapter. Numerical simulations of the RISE system will be presented in chapter 8. But, one example of the primary and secondary field in the RISE system is presented in advance. Numerical models used in the simulations described here are presented in chapter 7. The boundary conditions and procedure of the numerical simulation are presented in chapter 8. Figure 6.20 shows the sound pressure level at the eardrum of the DB65 artificial ear of the KEMAR dummy head. A point monopole source in the primary field is located 1 m away from the head model at 60° azimuth and 45 headphone sources are used. The solid line represents the desired sound pressure level at the eardrum measured in the primary sound field, and the dashed line represents the reproduced sound pressure level at the eardrum measured in the secondary sound field. This shows a good example of nearly perfect reproduction. Figure 6.21 shows the primary sound field around the DB65 artificial ear at 10 kHz on a dB scale when the monopole source is at 45° azimuth. Figure 6.22 shows the corresponding secondary sound field at 10 kHz on a dB scale. Those figures are nearly identical and show how well this system reproduces the virtual

sound field at such a high frequency. This good performance is a practical illustration of the RISE system with a multichannel headphone. The detailed results and explanation will be presented in chapter 8.

6.7 Conclusion

A virtual acoustic system that reproduces an incident sound field on the ear within a control volume using a multichannel headphone is suggested. This has been called the "RISE (Reproduction of the Incident Sound on the Ear)" system. The RISE system may produce any kind of virtual acoustic field that can be produced from arbitrary multiple phantom sources in full three-dimensional space of arbitrary shape and boundary condition. The theory of the RISE system is explained by introducing the case of two scattering bodies. The secondary sound field is always the same as the primary sound field even though the geometry and boundary condition of the ear inside the control volume is changed if the following conditions are met: The headphone sources in the secondary field reproduce exactly the sound field inside the control volume produced in the primary field for a given scattering body inside the control volume. All the conditions outside the control volume in both primary and secondary field remain same. It is assumed that all the incident sound field on the control volume is not changed when the geometry and boundary condition of the scattering body within the control volume is changed. This assumption can be valid when one of the following requirements is met: (1) the wavelengths of the incident waves are much longer than the size of the ear, (2) the sound pressure on the head surface outside the control volume is not significantly changed when the ear surface inside the control volume is changed, (3) the incident sound field inside the control volume produced from the head surface is sufficiently weak compared to the total sound pressure inside the control field. The results of the numerical simulations for two scattering bodies and for an example of a head scattered sound field show that the assumption of the theory of the incident sound field reproduction system may be reasonable and this system might successfully create virtual acoustic images.

FIGURES

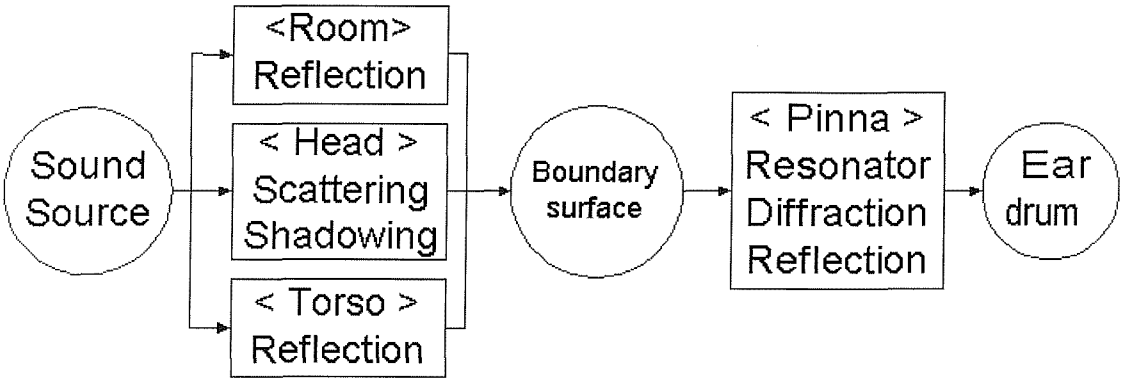

Figure 6.1 Sound modification by the human body.

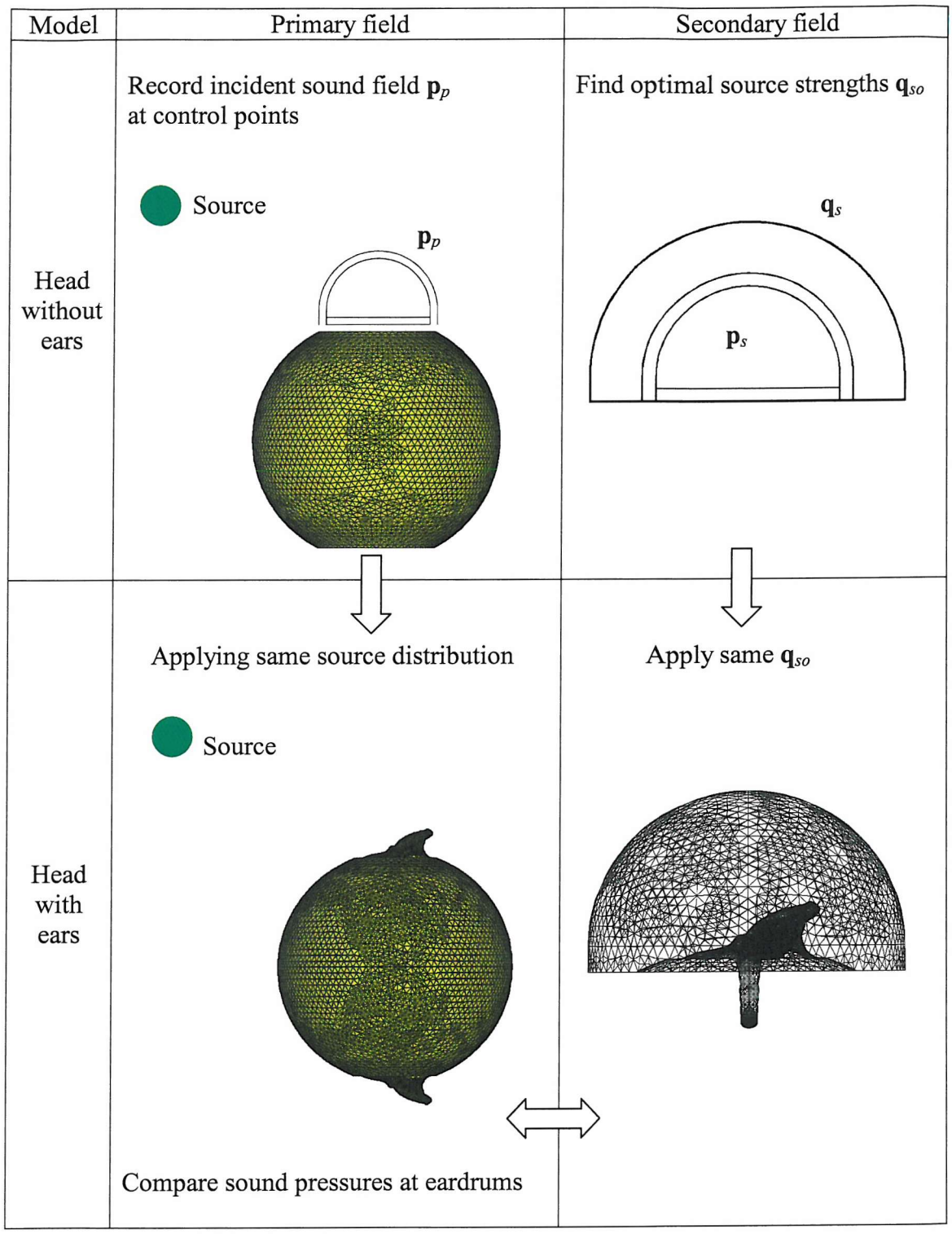

Figure 6.2 The basic concept of the RISE(Reproduction of the Incident Sound on the Ear) system.

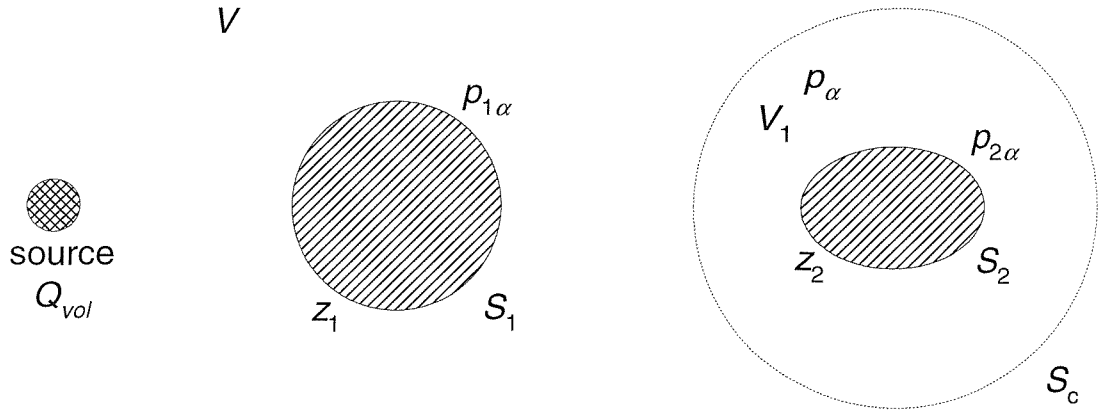

Figure 6.3 The sound field α in the case of two scattering bodies.

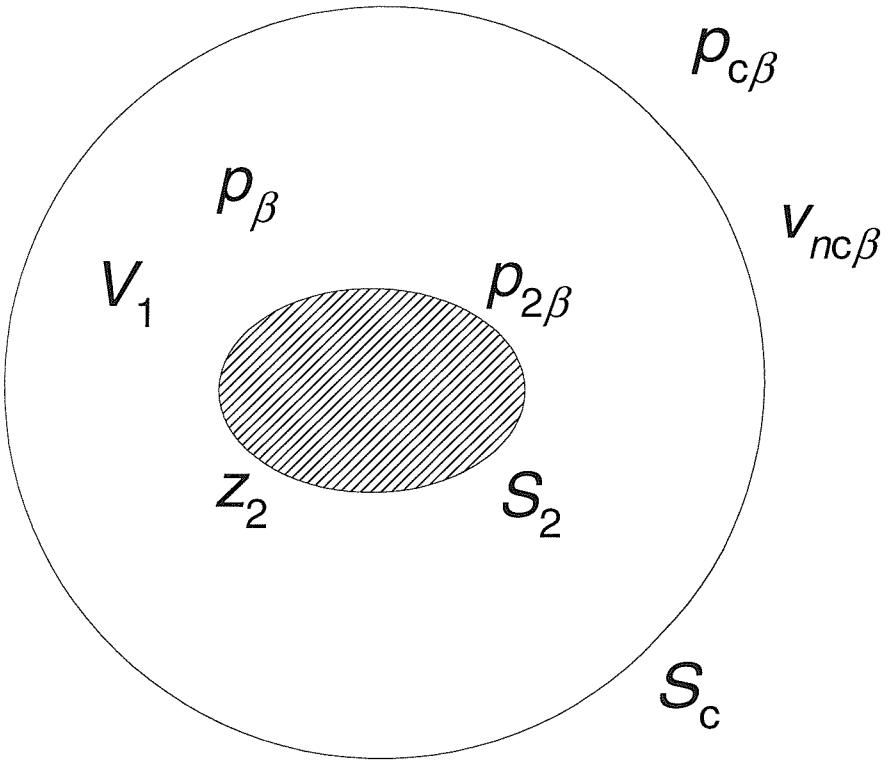

Figure 6.4 The sound field β in the case of two scattering bodies.

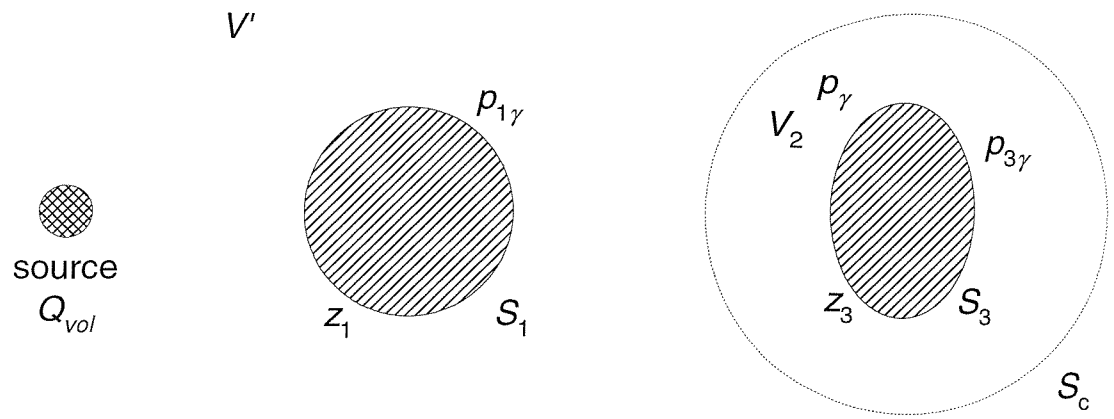

Figure 6.5 The sound field γ in the case of two scattering bodies.

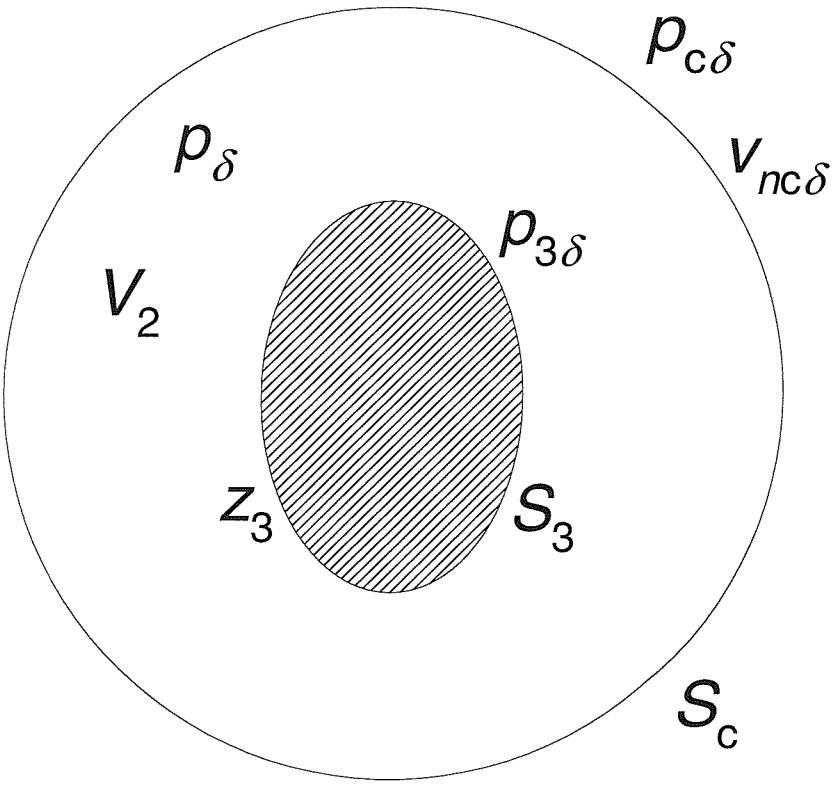

Figure 6.6 The sound field δ in the case of two scattering bodies.

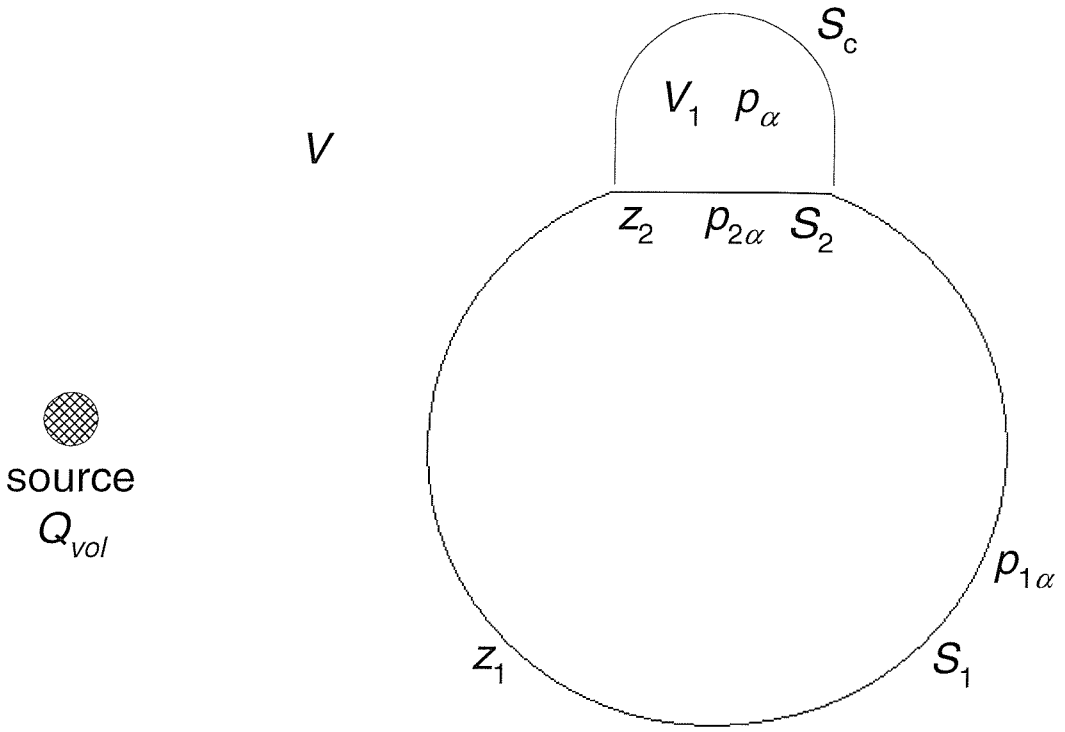

Figure 6.7 The sound field α in the case of the human head without an ear.

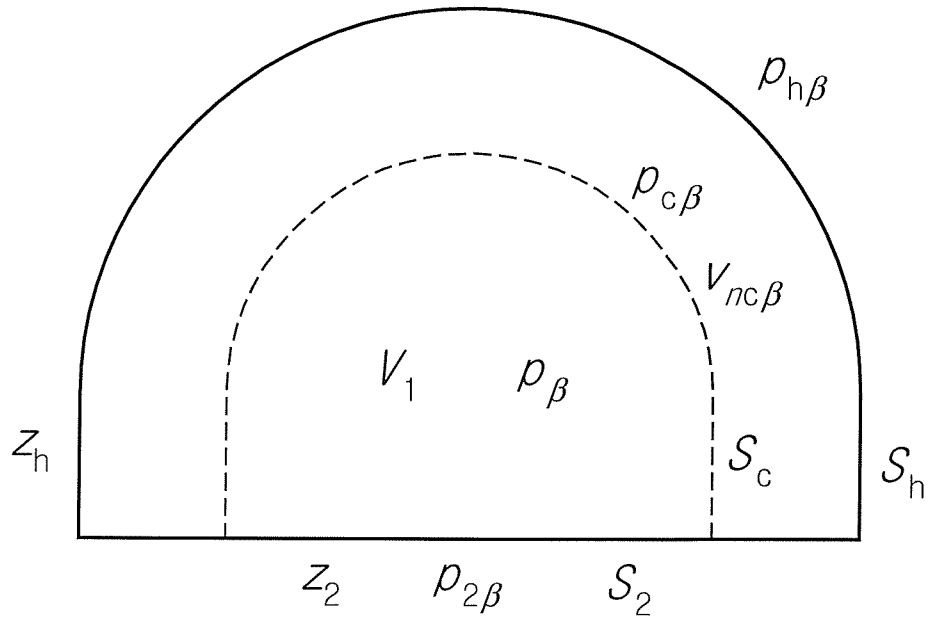

Figure 6.8 The sound field β in the case of the human head without an ear.

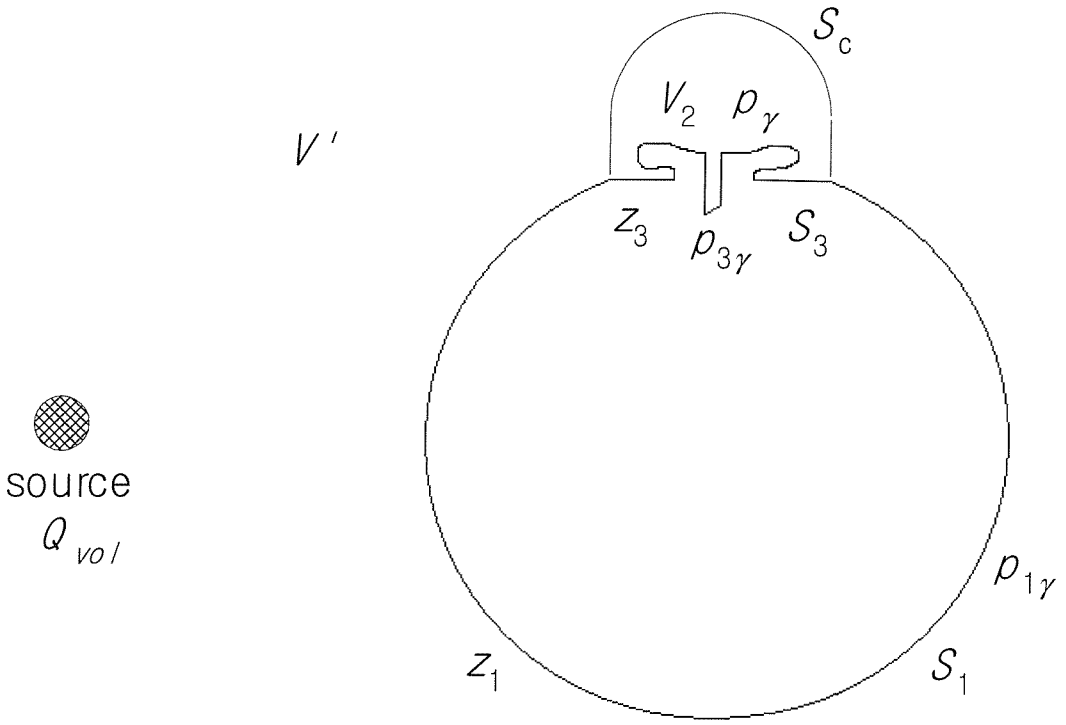

Figure 6.9 The sound field γin the case of the human head with an ear.

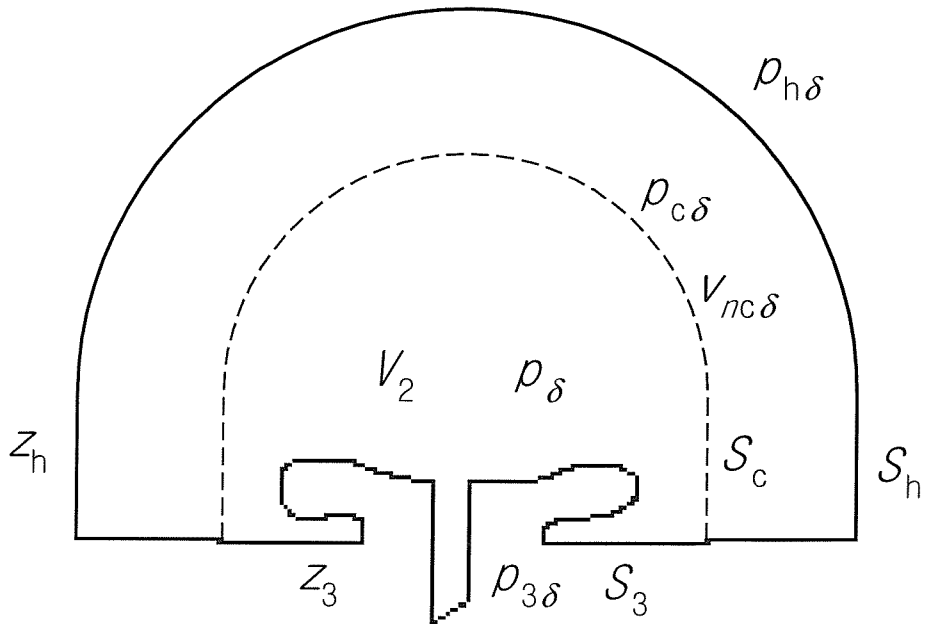

Figure 6.10 The sound field δin the case of the human head with an ear.

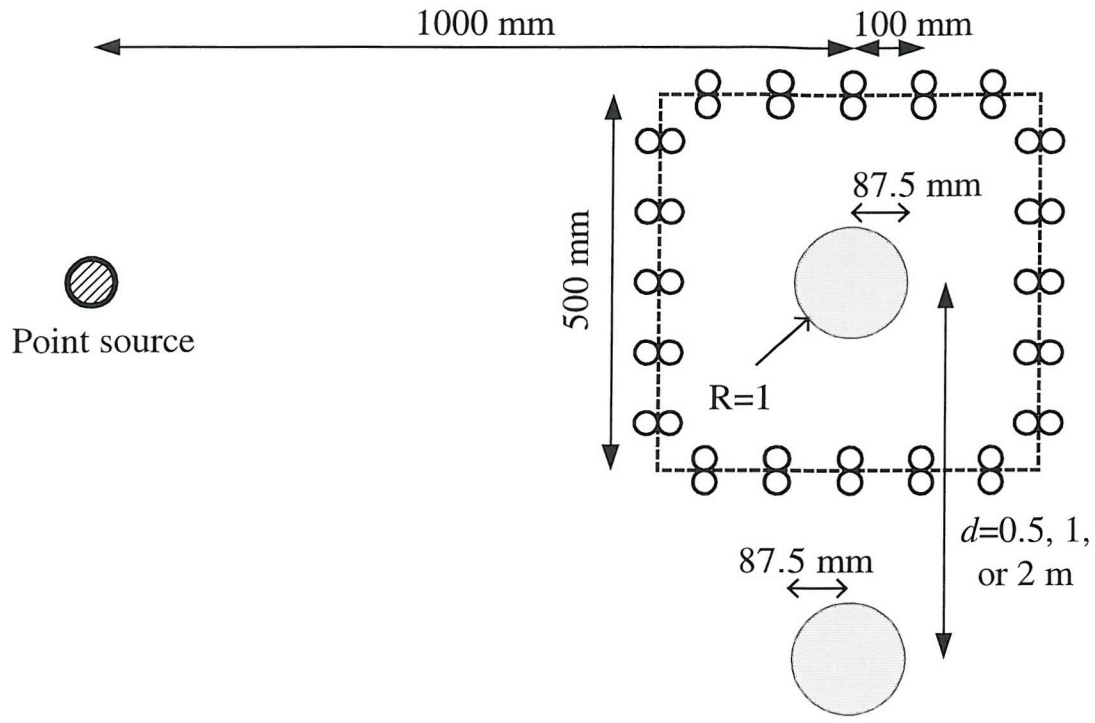

Figure 6.11 The two-dimensional primary sound field produced by a point source in an unbounded free field with two rigid cylinders.

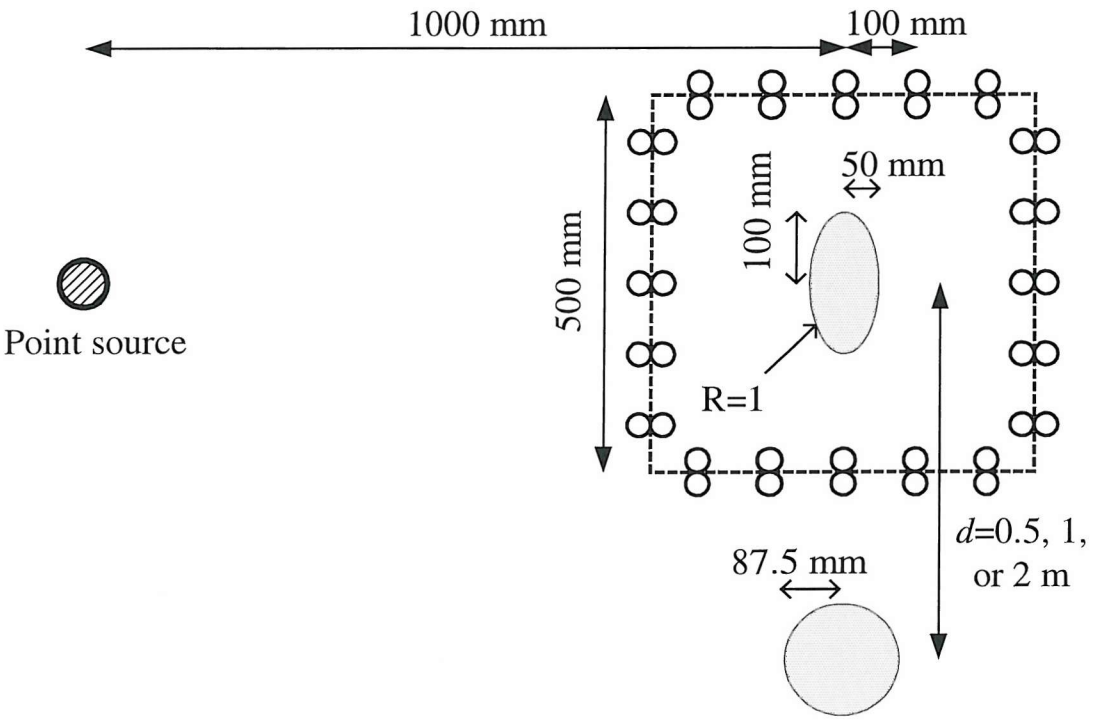

Figure 6.12 The two-dimensional primary sound field produced by a point source in an unbounded free field with a rigid cylinder and a rigid ellipsoid.

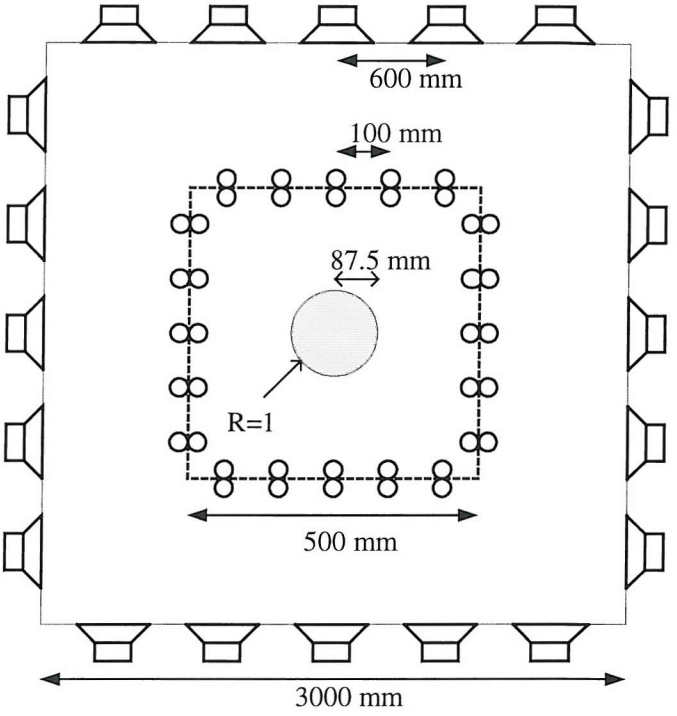

Figure 6.13 The two-dimensional secondary sound field produced by multiple point sources in an unbounded free field with a rigid cylinder.

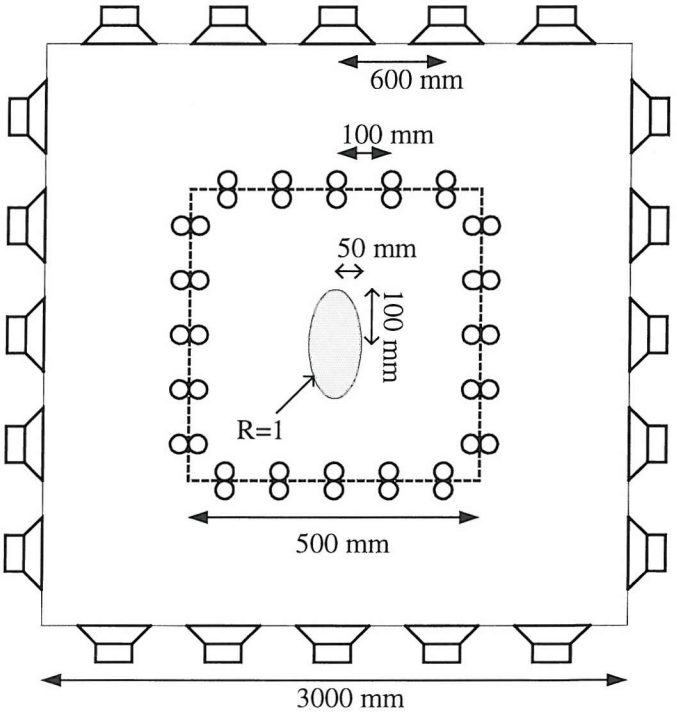

Figure 6.14 The two-dimensional secondary sound field produced by multiple point sources in an unbounded free field with a rigid ellipsoid.

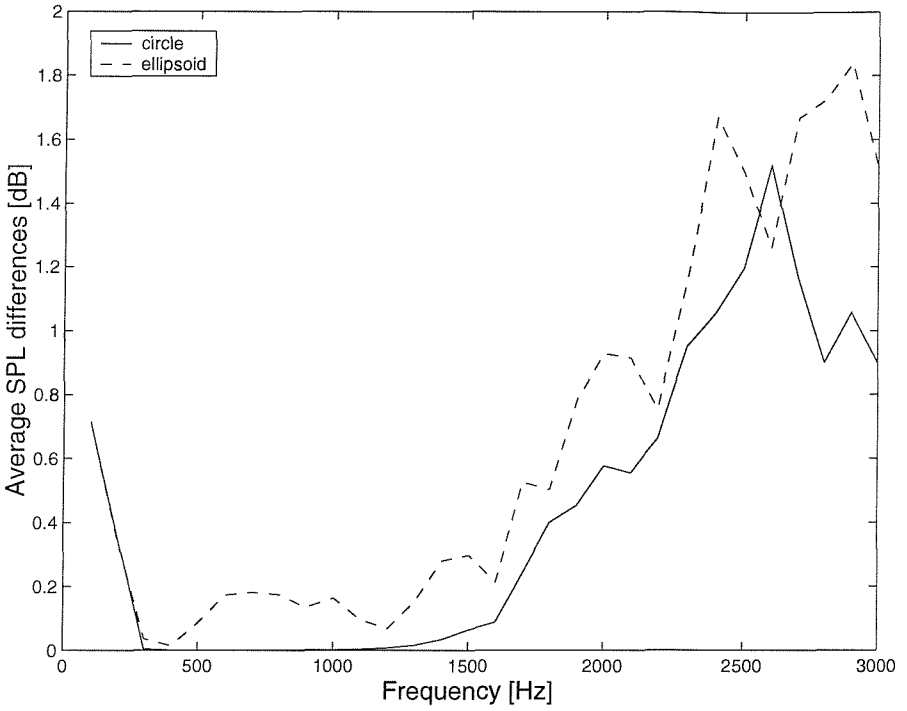

Figure 6.15 The sound pressure level differences averaged over control points when the distance between two scatterers is 0.5 m.

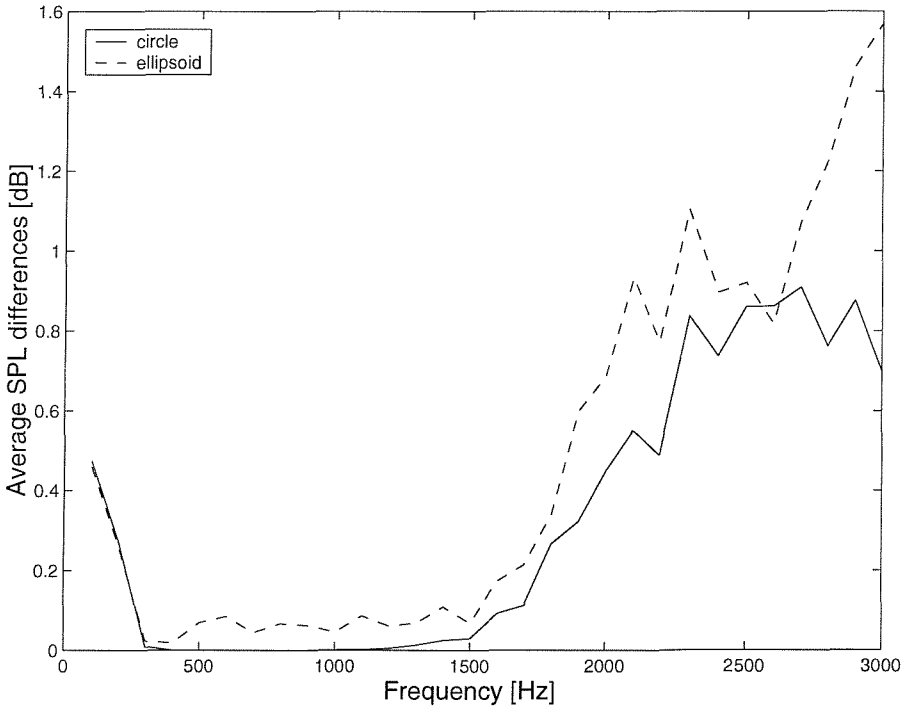

Figure 6.16 The sound pressure level differences averaged over control points when the distance between two scatterers is 1 m.

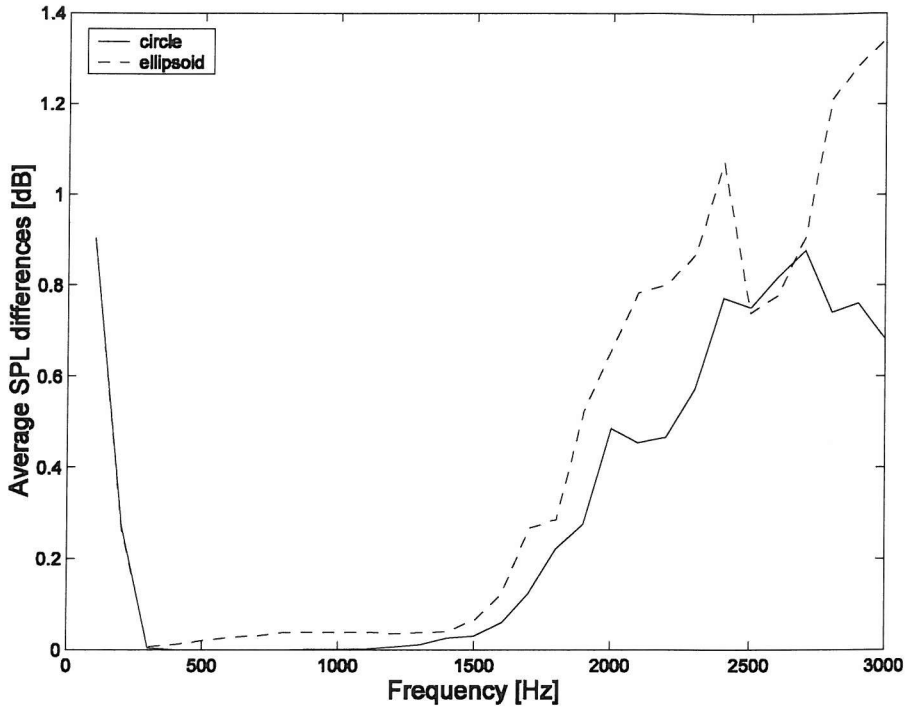

Figure 6.17 The sound pressure level differences averaged over control points when the distance between two scatterers is 2 m.

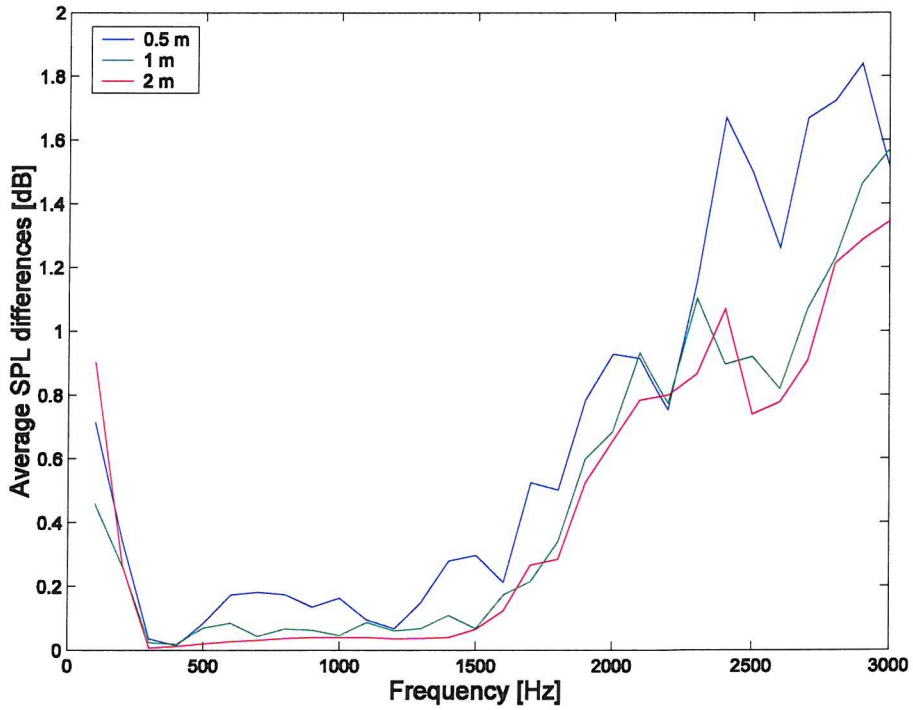

Figure 6.18 The sound pressure level differences averaged over control points for various distances between the ellipsoid and the cylinder.

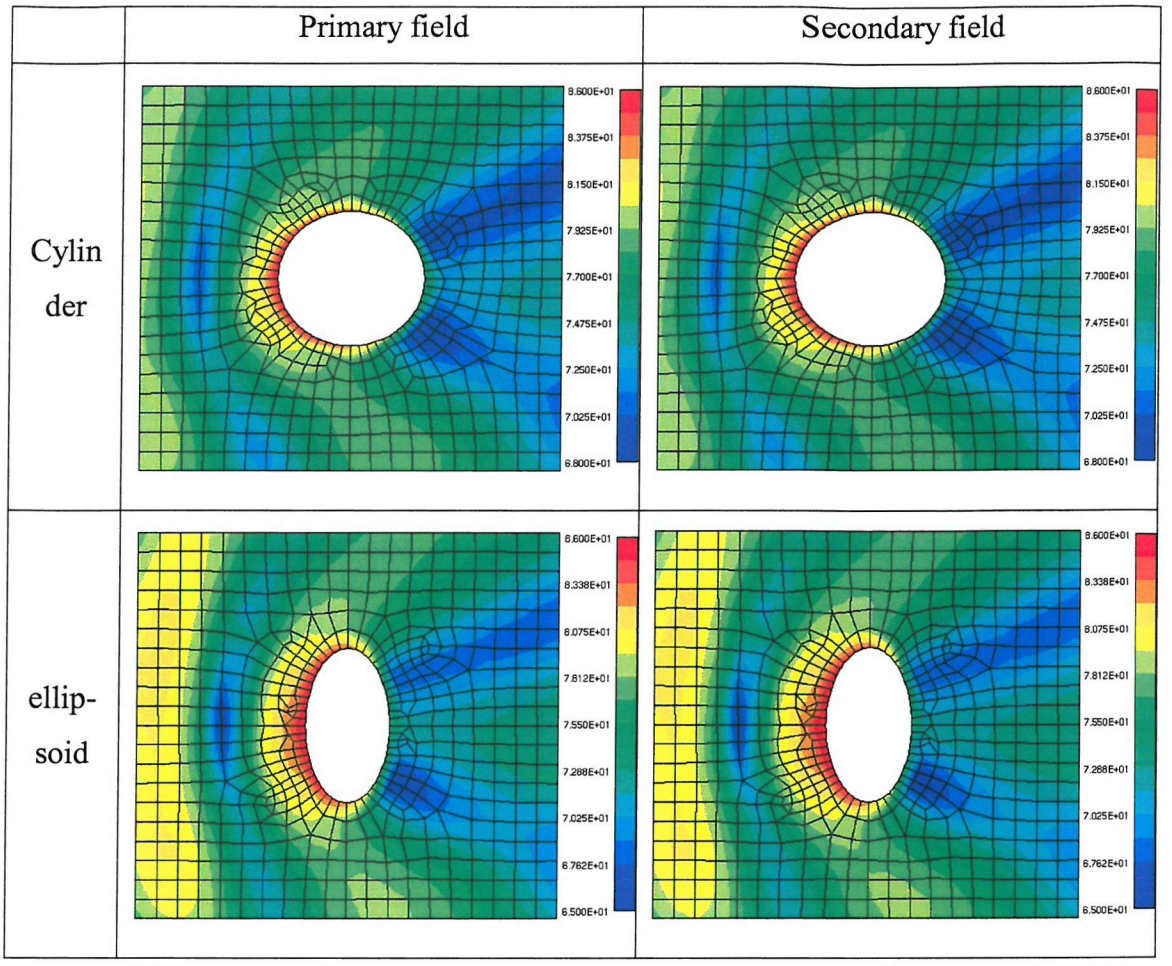

Figure 6.19 The primary and secondary sound field at 1 kHz for both cases.

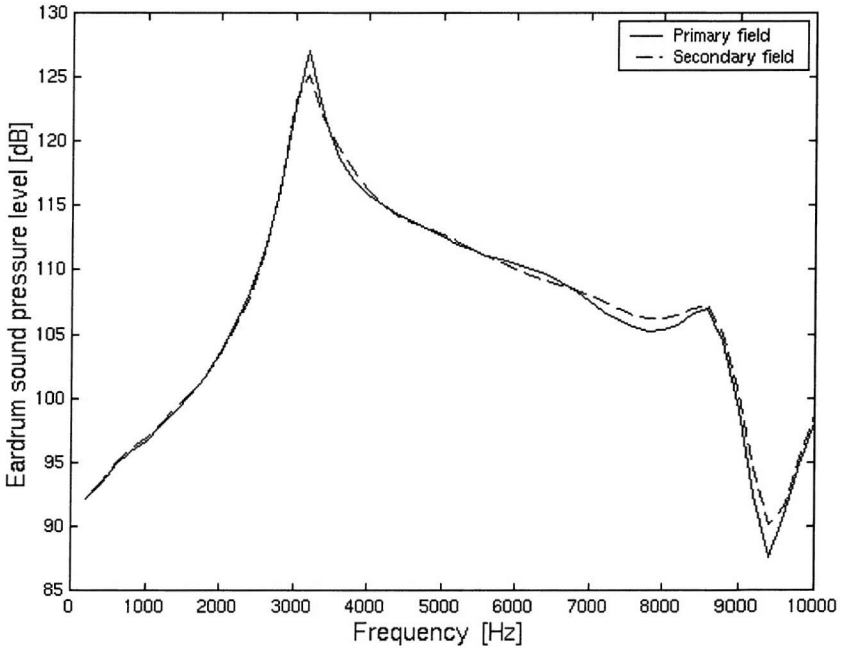

Figure 6.20 Sound pressure level at the DB65 eardrum for the source at 60° azimuth

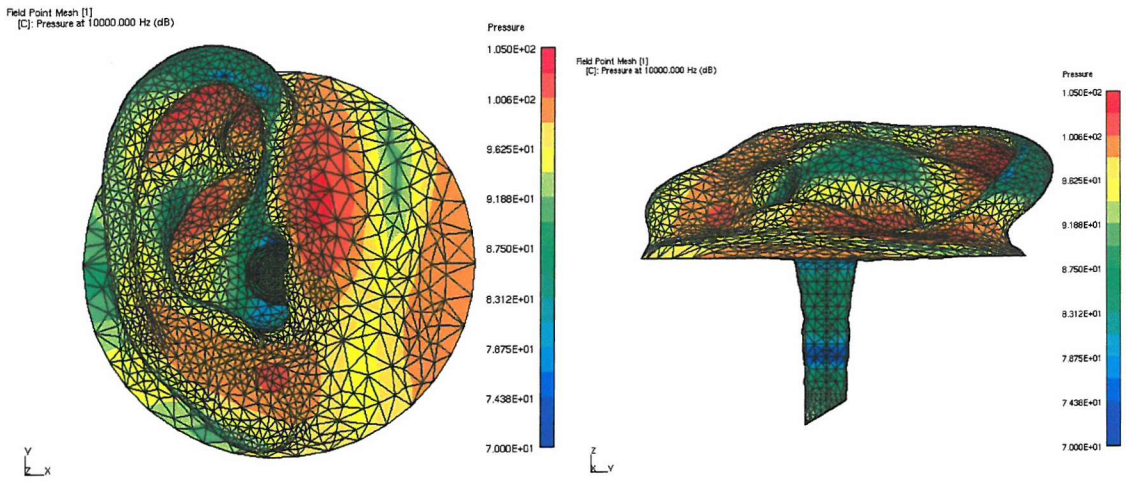

Figure 6.21 Primary sound field on the DB65 ear model at 10kHz for the source at 45° azimuth.

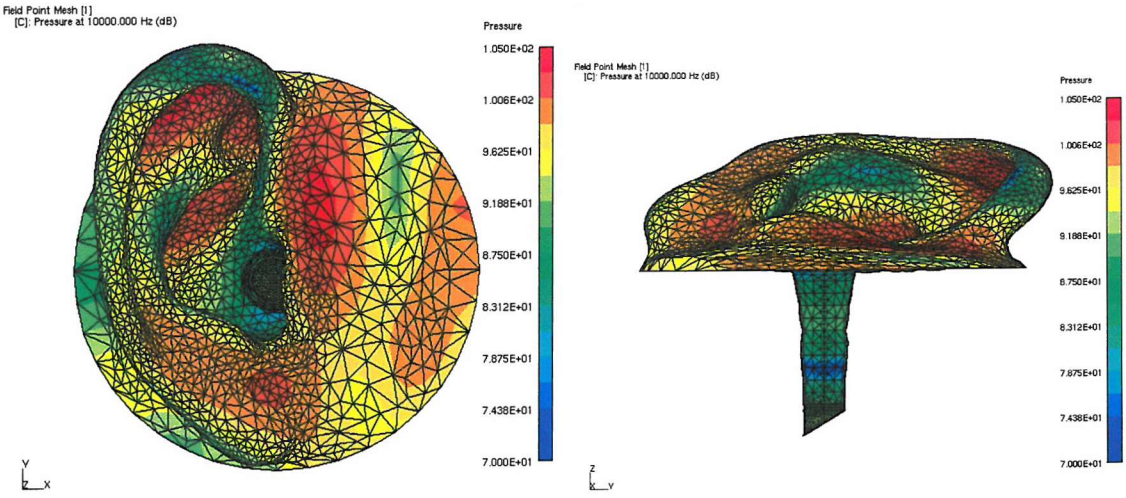

Figure 6.22 Secondary sound field on the DB65 ear model at 10kHz for the source at 45° azimuth.

CHAPTER 7
NUMERICAL MODELLING

7.1 Introduction

A virtual acoustic system with a multichannel headphone, called the RISE (Reproduction of the Incident Sound on the Ear) system, was suggested in Chapter 6. Various numerical models are designed to evaluate the performance of the RISE systems and the effects of important factors in designing multichannel headphones. Those numerical models are somewhat idealized to simplify modelling and the process of optimizing the headphone system. In this chapter, the numerical modelling procedure is discussed, and numerical models of ears, heads and headphones are presented. Five possibly important factors are suggested and their effects on the performance of the virtual acoustic system are discussed.

7.2 The numerical modelling procedure

Broadly speaking, two different kinds of numerical models are required to simulate the RISE system numerically. Numerical models of the human head are used to evaluate sound pressures produced in the primary sound field, and numerical models of the headphone are used to evaluate sound pressures produced in the secondary sound field. Each numerical model goes through the following procedure. First, basic geometrical figures are created by using the ANSYS software package (ANSYS, 6.1). In this step, only simple geometries such as a sphere or a hemisphere are used for simplicity rather than a more realistic complex geometry. This is because the objective of designing those simplified numerical models is to establish the important design factors and control those factors easily rather than designing practical systems.

Second, numerical meshes of all numerical models are generated by using the ANSYS software package (ANSYS, 6.1). The boundaries of numerical models are discretized into many shell elements since the direct boundary element method is used to simulate virtual acoustic systems. Most numerical models use three-node triangular linear elements although models of the control field use four-node quadrilateral linear elements. Triangular elements are chosen mostly because boundary element models using triangular elements show more detailed geometry than those using quadrilateral elements and the data format of the models using triangular elements can also be converted into other formats easily. It is no problem that the boundary element models using triangular elements have a greater number of elements than those using quadrilateral elements because they have a similar number of nodes to those using quadrilateral elements and the calculation time of the direct boundary element method depends mainly on the number of nodes of the model (SYSNOISE 5.5). The number of elements per wavelength depends on the required accuracy, the frequency range of interest, and the calculation time. The mesh resolution is defined as the median edge length of all edges in the mesh, and edge length is the distance between two nodes. As the mesh resolution increases, the accuracy of the numerical calculation increases but calculation time also increases. Therefore there should be some trade off between accuracy and calculation time. The maximum frequency at which numerical results can be calculated with reasonable accuracy is given by

$$\text{Maximum frequency} \leq \frac{\text{speed of sound}}{\begin{matrix}\text{maximum length} \\ \text{of elements}\end{matrix} \times \begin{matrix}\text{number of elements} \\ \text{per wavelength}\end{matrix}} \qquad (7.1)$$

At least six linear elements per wavelength are usually required to model acoustic wave propagation phenomena accurately by using the boundary element method and to thus identify the locations of peaks and troughs of sound pressure signal with reasonable accuracy (SYSNOISE 5.5). However, in some cases more elements per wavelength are required when the geometry is very complicated, or when sources or measurement points are located close to the boundary, or when boundary conditions are changing rapidly. The frequency range of interest is set to be 0 ~ 10 kHz throughout all numerical simulations because the calculation time was too long when

the frequency range of interest is set to be 0 ~ 20 kHz. The mesh resolution is set to be about 5 mm for the headphones and the spherical heads excluding the ear, and this equates roughly to seven elements per wavelength since the wavelength of a 10 kHz wave is 34 mm when the speed of sound is 340 metres per second. Since the shape of the ear is complicated and the important measurement point is located at the eardrum, a finer mesh is required in this case, and so the mesh resolution around the eardrum is set to be 0.5 mm, which equates roughly to 68 elements per wavelength, and that for the ear canal and pinna is set to be 2 mm, which equates roughly to 17 elements per wavelength.

Third, the mesh resolution is manipulated. When the mesh resolution is set and the surface mesh is generated in ANSYS, the distances between two nodes, that is, lengths of the mesh edges are distributed, but centered on the desired resolution. As discussed above, the maximum frequency at which numerical results can be calculated with reasonable accuracy is dependent on the maximum length of the mesh edge. For example, if the maximum frequency is set to be 10 kHz and the six elements criterion is used, the maximum length of the mesh edge is allowed to be up to 5.6 mm. Therefore, in order to minimize the number of nodes and calculation time, the desired mesh resolution should be near the allowed maximum edge length, and the edge length should be normalized to the desired mesh resolution while preserving model shape, and all edge lengths should not exceed the allowed maximum edge length. The surface mesh is controlled by using the algorithm developed and described by Johnson and Hebert (1997). The format of mesh data files is converted into VRML 1.0 format for using the mesh manipulation tools. This detailed procedure was also described by Kahana (2000). After the mesh has been controlled, the VRML format is converted into the format used in SYSNOISE.

Fourth, if necessary, the ear model is integrated to the head or headphone. This was undertaken by linking corresponding nodes manually. This manually integrated numerical model should be a closed mesh model because the direct boundary element method allows only closed mesh models. The above procedure of mesh manipulation is undertaken again if necessary.

Fifth, the validity and quality of the mesh are finally checked using tools in SYSNOISE. Those tools check whether the mesh is acceptable for the chosen numerical method, in which case the mesh model should be closed for the direct boundary element method. They also check the consistency of all the normal vectors of the elements, reorient them so they are consistent, merge superimposed nodes, and remove isolated nodes if there are any.

7.3 Numerical models of the ears

The human external ear is the most idiosyncratic part of the human hearing system at high frequencies as discussed in chapter 2. However, if the RISE system is used, the external ear should have nearly no effect on the performance of the virtual acoustic system. But, since it is necessary to confirm that the virtual sound field is successfully created, at least one human external ear should be modelled numerically in order to evaluate sound pressures at the eardrum in both the primary field and the secondary field. An arbitrary external ear model would be acceptable, but the numerical model of a realistic and typical ear is recommended in order to simulate the real case of a hearing experience.

First of all, the DB60 and DB65 pinnae were modelled numerically since these are the artificial ears of the KEMAR dummy head. The DB60 pinna model is typical of American and European female pinna size, and its ear length and ear breadth are 58.9mm and 34mm respectively (Burkhard and Sachs, 1975). The DB65 pinna model is typical of American and European male pinna size, and its ear length and ear breadth are 66mm and 37mm respectively (Maxwell and Burkhard, 1979). The numerical meshes of the DB60 and the DB65 pinna models were generated by using a laser scanning technique (Kahana, 2000). Figure 7.1(a) shows the numerical mesh model of the DB60 pinna and Figure 7.1(b) shows that of the DB65 pinna, and both models are attached to a finite baffle.

Second, the numerical ear canal and eardrum was modelled. To describe the canal geometry properly, a lumped element representation is sufficient below 1 kHz and a straight tube model of uniform cross section can be used below 8 kHz (Stinson and Lawton, 1989). But, the uniform tube approximation is not sufficient and intersubject differences of canal geometry can be important at frequencies above about 8 kHz. The eardrum (or the tympanic membrane) does not actually terminate the canal perpendicularly. Stinson and Lawton (1989) obtained an average ear canal length as 27 mm along a straight axis by studying the geometry of 15 human ear canals. They also showed how the sound pressure level difference from entrance to inner end of the canal reaches three peaks within a frequency range up to 20 kHz and intersubject variations are significant. Johansen (1975) took ten moulds of the complete ear canal from ten deceased people, six males and four females, and measured the incremental volume of the each mould at every 2 mm displacement along the axis of the ear canal and averaged them. The numerical model of the ear canal was made by using the data of Johansen. Figure 7.2 shows this mesh model of the ear canal. The canal length is 26 mm and the eardrum occupies a portion at the innermost 4 mm of the canal length. This model has 1482 elements and 750 nodes. Third, the ear canal model was attached to each of the DB60 and the DB65 pinna models respectively. This attachment was undertaken by linking corresponding nodes manually. Figure 7.3 shows the DB60 pinna model with the ear canal model, and Figure 7.4 shows the DB65 pinna model with the ear canal model. Both models are attached to a finite baffle of disk having a radius of 30 mm.

7.4 Numerical models of the heads and headphones

The primary field is modelled as that produced by a source in a free field whose sound field interacts with a human head. The human is modelled as just a head without a body and neck. Human body parts, especially the shoulders, reflect and scatter sound waves and so modify the sound pressure at the eardrum. However, since these reflecting or scattering boundaries are outside the control volume of interest here, the human body excluding the head can be regarded as one of the scattering bodies

outside the control volume, such as room boundaries, in terms of the incident sound field reproduction method. The human body excluding the head is consistently neglected throughout the numerical simulations for simplicity. The numerical human head was modelled as a sphere having a radius of 87.5 mm that corresponds to the average head radius for a number of individuals (Algazi *et al.*, 2001). Although the head size and shape vary substantially within the population, the radius of a spherical head model is fixed throughout the numerical simulations for simplicity and consistency. The head surface outside the control volume can also be regarded as one of the scattering surfaces outside the control volume in terms of the incident sound field reproduction method. Two different kinds of numerical head models were designed. First, the spherical head without the ear was modelled. Flat surfaces were placed at the locations where ears were supposed to be placed. Two different models were made. Figure 7.5 shows the spherical head model with the flat surfaces for the large control field presented in section 9.2. In this model, the flat surface having a radius of 41.56 mm is placed at a height of 77 mm from the centre of the sphere. This model has 12876 elements and 6440 nodes. Figure 7.6 shows the spherical head model with the flat surfaces for the small control field presented in section 9.2. In this model, the flat surface having a radius of 30.5 mm is placed at a height of 82 mm from the centre of the sphere. This model has 11656 elements and 5830 nodes. Second, the spherical head with the ear was modelled. Either the DB60 or the DB65 pinna model with the ear canal is placed at a height of 82 mm from the centre of the sphere respectively. Figure 7.7 shows the spherical head model with the DB60 ear model. This model has 27316 elements and 13660 nodes. Figure 7.8 shows the spherical head model with the DB65 ear model. This model has 25796 elements and 12900 nodes. Both the large and small control field models will be described in detail in section 9.2.

The secondary field is modelled as the sound field inside the headphone when the listener wears the headphone. This sound field is taken to be the close field enclosed by the headphone and the head surface, and it is also assumed that there is no leakage of air. Although a real headphone has a complicated structure, simplified numerical models of the headphone, for example, the hemisphere, are used since the objective of this thesis is not to design an actual commercial multichannel headphone but to verify the theory of the incident sound field reproduction method and to study the important

factors governing the multichannel headphone design. Two different kinds of numerical headphone models were designed. First, the headphone without the ear was modelled. The headphone was modelled as a hemisphere having a radius of 60 mm and an annulus having a thickness of 10 mm extended from the hemisphere as shown in Fig. 7.9. The bottom of the headphone should contain the surface of the head model where the headphone is supposed to be located, so part of the spherical head model without the ear where the headphone was supposed to be located was attached to the bottom of the headphone model. Figure 7.9 shows the headphone model with the flat surface for the large control field. This model corresponds to the head model shown in Fig. 7.5. Note that the bottom surface is flat. This model has 5316 elements and 2660 nodes. Figure 7.10 shows the headphone model with the flat surface for the small control field. This model corresponds to the head model shown in Fig. 7.6. This model contains part of the spherical head model between the height of 77 mm and 82 mm from the centre of the sphere. This model has 5276 elements and 2640 nodes. The headphone sources are modelled as piston-like flat vibrating surfaces having a radius of 5mm. Figure 7.11 shows 45 headphone sources that are distributed evenly, so two adjacent headphone sources spread at an angle of about 22.5°. Second, the headphone with the ear was modelled. The headphone surfaces are the same as those for the above models except for the bottom surface. Part of the spherical head model with the DB60 and the DB65 ear model where the headphone was supposed to be located was attached to the bottom of the headphone model. The axis of the ear canal is located at the centre of the bottom of the headphone model. Figure 7.12 shows the headphone model with the DB60 ear model with the same 45 headphone sources. This model corresponds to the head model shown in Fig. 7.7, and has 13110 elements and 6557 nodes. Figure 7.13 shows the headphone model with the DB65 ear model. This model corresponds to the head model shown in Fig. 7.8, and has 12134 elements and 6069 nodes.

7.5 Important factors

One of the main objectives of this thesis is to establish the important factors associated with the multichannel headphone design and how they affect the performance of the incident sound field reproduction system. There can be many factors associated with multichannel headphone design, but the following five major factors are assumed to be greatly influential to the performance of the virtual acoustic system. First of all, the number of headphone sources is a critical factor. The number of the control points depends on the frequency range of interest and the volume of the control field. However, in practice, the number of headphone sources is limited and is usually much less than the number of control points if the frequency range of interest is sufficiently broad for human hearing. The greater the number of headphone sources, the better the performance of the system is with a given frequency range, but the more difficult it becomes to make a practical system since the headphone becomes bigger, heavier, and more expensive, and the more system resources are needed. This is the critical factor in the design of the multichannel headphone because this is directly related and sensitive to the system performance and dominates other factors. This will be shown with the use of numerical simulations. Therefore, when a practical system is designed, the number of headphone sources should be a priority and maximized with given conditions of size and weight of the headphone and system resources, for example.

Second, the boundary condition at the headphone surface should be considered. This is a second important factor in the design. The inner surface of the ideal headphone model should be perfectly absorbent to remove any cavity modes inside the headphone and absorb all the scattered sound field from the ear and head surface. This means that the specific acoustic impedance of the inner headphone surface should be the same as the characteristic acoustic impedance $\rho_0 c_0$ of the medium. However, practical headphones cannot have perfectly absorbent boundaries. A strong scattered sound field from the ear surface and strong cavity resonances inside the headphone will degrade the system performance. When the scattered sound field from the ear is reflected back to the ear, the reflected sound field from the headphone

surface can be another incident sound field on the control volume and this is highly sensitive to the scattered sound field from the ear. However, the RISE system is based on the assumption that the incident sound field on the ear is independent of the scattered sound field from the ear. Therefore, the reflected sound field from the non-absorbent headphone surface will degrade the system performance. If the headphone is open, the so called the free field headphone, it has the same effect of absorbing but the ear on the other side of the head may hear the sound emitted from one side of the headphone and so cross-talk cancellation may be needed. Thus, the headphone is assumed to be closed in this thesis. Since the multichannel headphone has many transducers, a significant quantity of absorbent material may allow the interior to heat up and also make the headphone bigger and heavier. Even though a significant quantity of absorbent material is used, low frequency sound is difficult to absorb. However, the sound field is easily controlled at low frequencies, so the absorption may be needed only at middle and high frequencies. Therefore, when a practical system is designed, the boundary condition of headphone surface should be as absorbent as possible.

Third, the position of headphone sources determines the range of good performance of the system. As the angle of the incident sound wave approaches the angle of the headphone source, the performance of the system improves. The greater the number of headphone sources, the broader the range of good performance within a given frequency range of interest. To cover all angles of incident sound in three-dimensional space, the headphone sources should be distributed evenly. Figure 7.11 shows one example of the evenly distributed headphone sources. However, for example, if we focus on only the horizontal plane, the headphone sources could be placed only on the horizontal plane. For another example, if relatively good performance is wanted for frontal virtual sources and a lesser performance is allowed for rearward virtual sources, a greater number of headphone sources can be located at the front part of the multichannel headphone than that at its rear part. Therefore, the focus area should be determined before designing the practical multichannel headphone.

Fourth, the size and shape of the control field may be influential to the system performance. If the volume of the control field gets bigger, the system is more robust

for intersubject differences of pinna size and for different placements of the headphone on the head since the large control field can cover a large ear even though the placement of the headphone is slightly away from the ideal position. However, the larger control volume needs the larger headphone, and it needs a greater number of control points with a given frequency range of interest, which may make the performance of the virtual acoustic system worse with a given number of headphone sources. Therefore, when a practical system is designed, the volume of the control field should be as small as possible. The shape of the control field can be optimally designed with a given volume.

Fifth, the size and shape of the headphone may also be influential. The size and shape of the headphone depends on the size and shape of the control field because the headphone should be larger than the control field. If the headphone is too large, it is impractical to use. If the headphone is too small, that is, the distance from the headphone sources to the control points is too close, the performance of the system may be degraded when the number of headphone sources is much less than the number of control points and the headphone surface is not perfectly absorbent. The larger headphone can contain more headphone sources and absorbent material. Therefore, when the practical system is designed, the volume of the headphone should be as large as possible. These five major factors are interdependent, and optimization of those factors associated with the multichannel headphone design is needed to make an effective multichannel headphone system.

7.6 Conclusion

A number of numerical models are suggested for a virtual acoustic system implemented with a multichannel headphone. The numerical modelling procedure is explained. Some compromise for the mesh resolution should be made between the accuracy of the numerical calculation and the calculation time. The numerical ear models are made from the numerical ear canal model attached to the numerical models of the artificial ear of the KEMAR dummy head. The numerical head models

are based on the geometry of the sphere. The numerical headphone models are based on the geometry of the hemisphere. The head and headphone models without the ear use flat surfaces as substitutes for the ear surfaces. Five major factors affecting the performance of the virtual acoustic system are discussed. The number of the headphone sources should be maximized. The boundary condition of headphone surface should be made as absorbent as possible. Focusing the reproduction area may reduce the required number of headphone sources. The volume of the control field should be as small as possible. The volume of the headphone should be as large as possible.

FIGURES

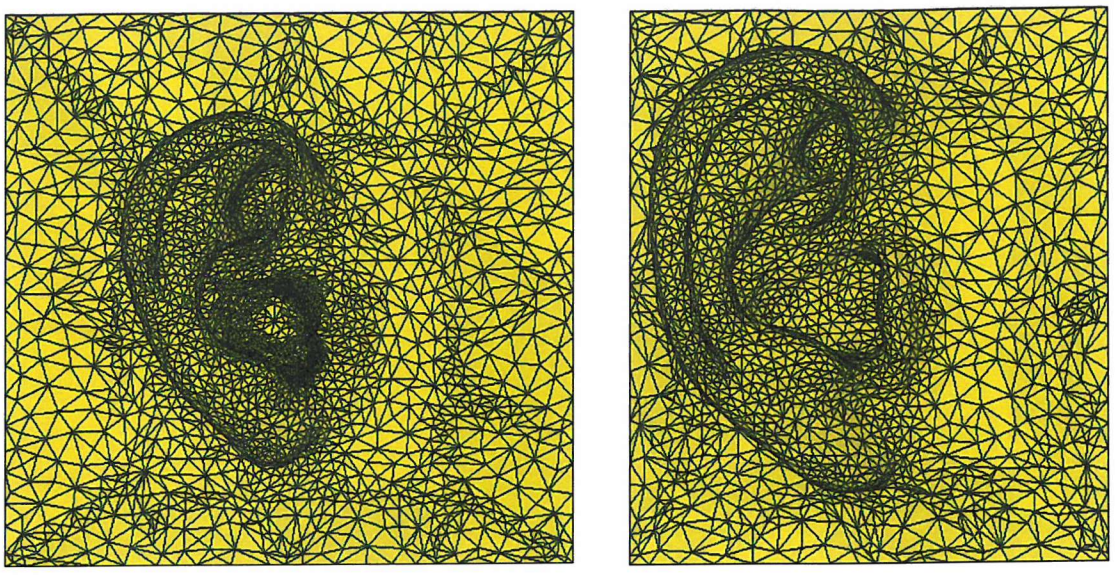

(a) (b)

Figure 7.1 (a) The mesh model of the DB60 pinna.
(b) The mesh model of the DB65 pinna.

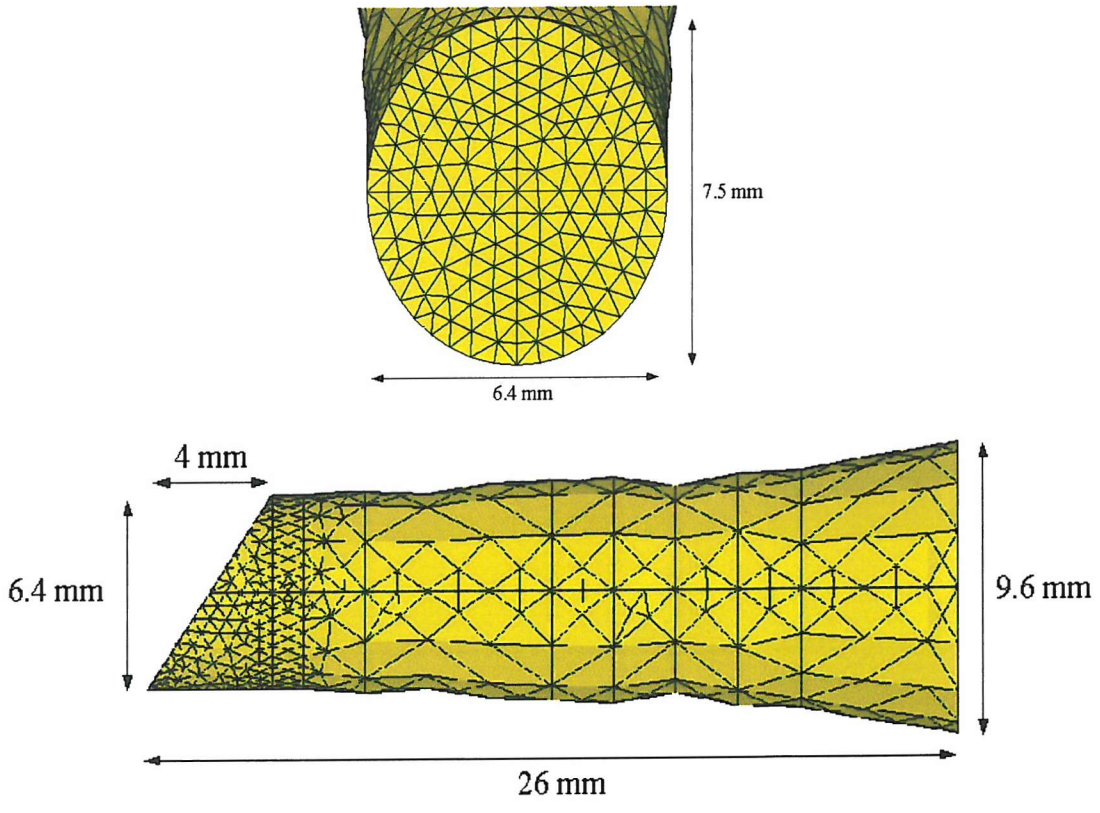

Figure 7.2 The mesh model of the ear canal.

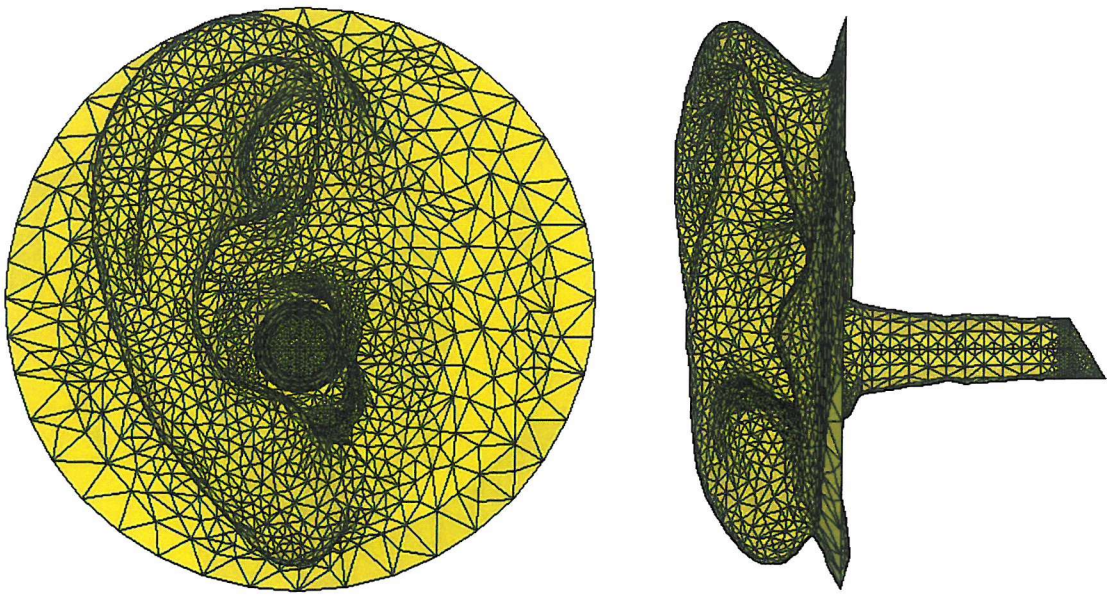

Figure 7.3 The DB60 pinna model with the ear canal model.

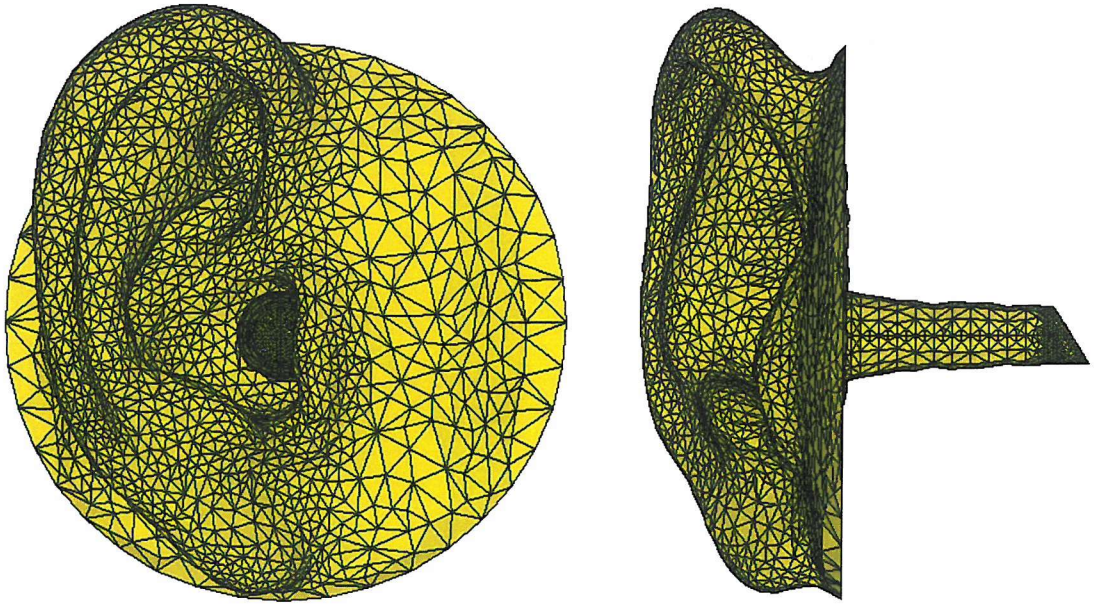

Figure 7.4 The DB65 pinna model with the ear canal model.

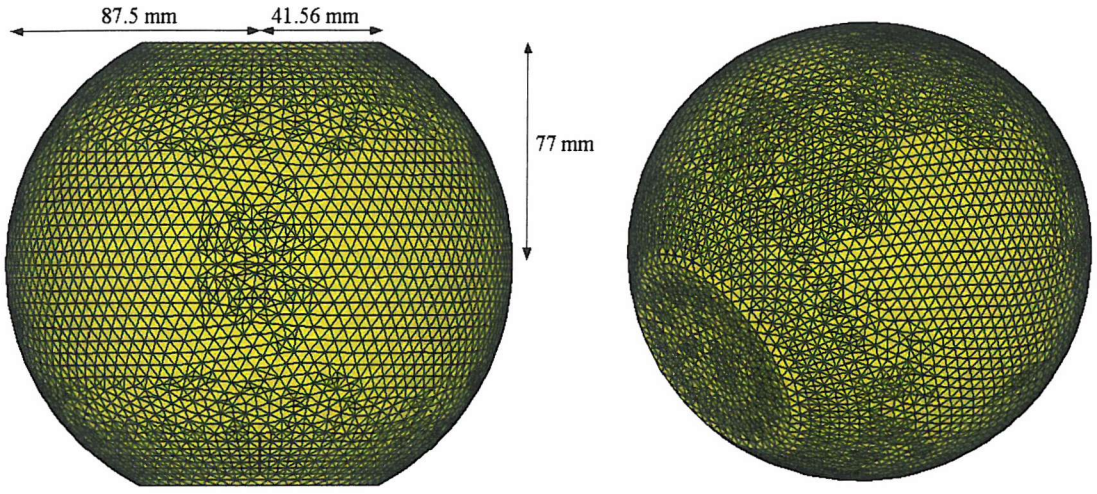

Figure 7.5 The spherical head model with the flat surfaces for the large control field.

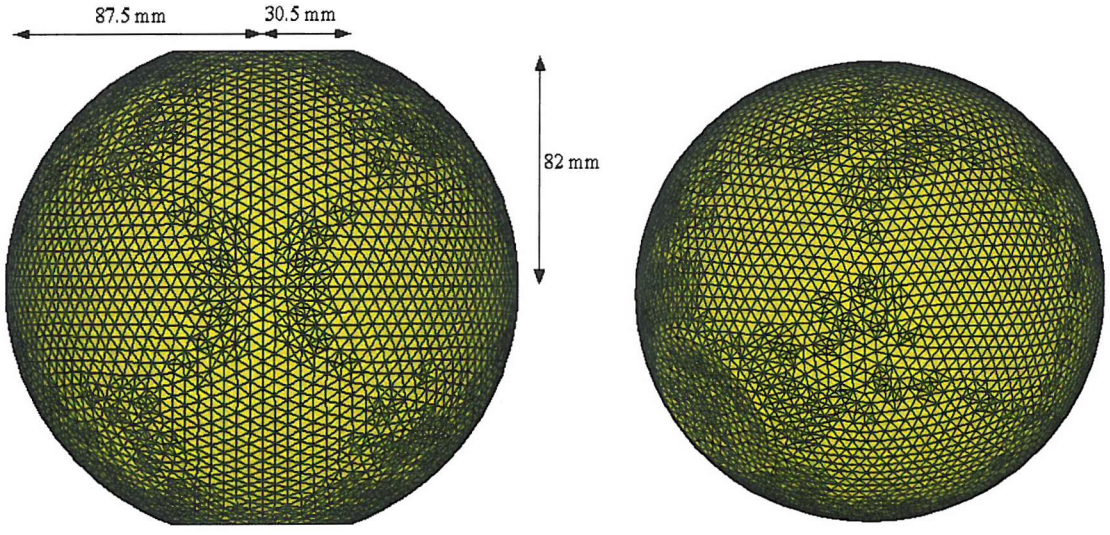

Figure 7.6 The spherical head model with the flat surfaces for the small control field.

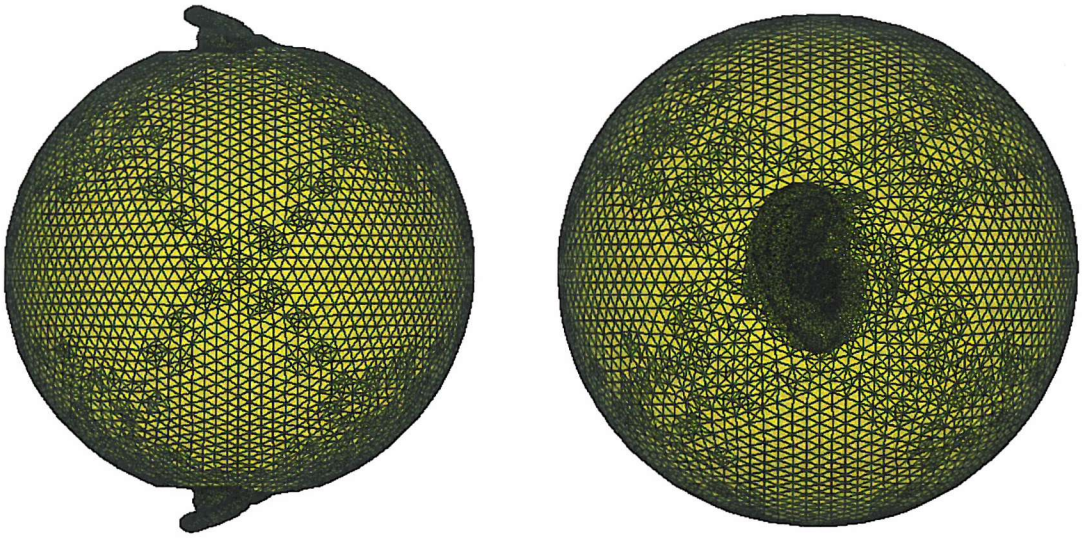

Figure 7.7 The spherical head model with the DB60 ear model.

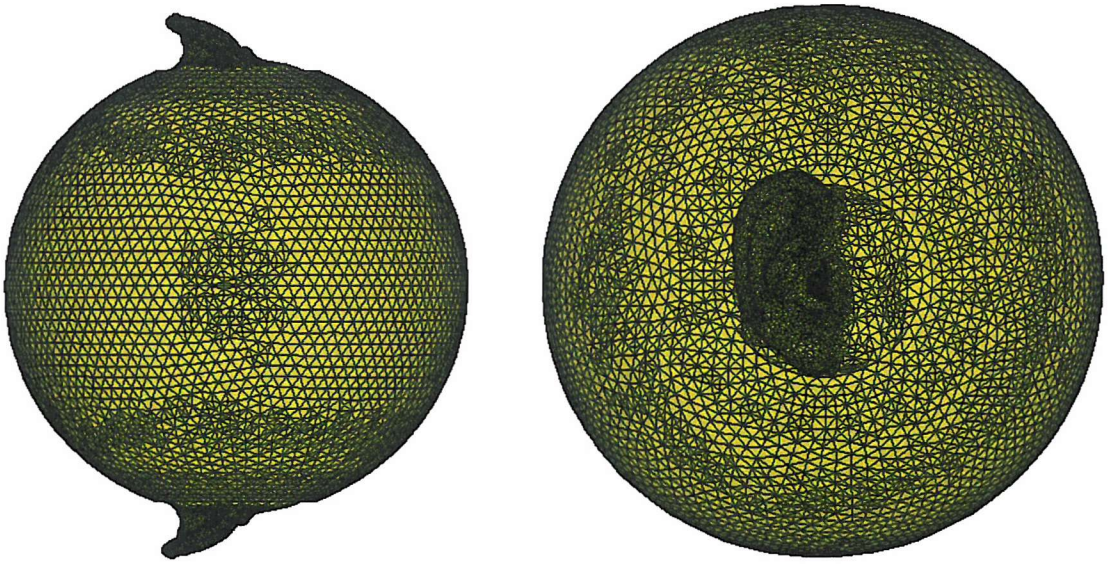

Figure 7.8 The spherical head model with the DB65 ear model.

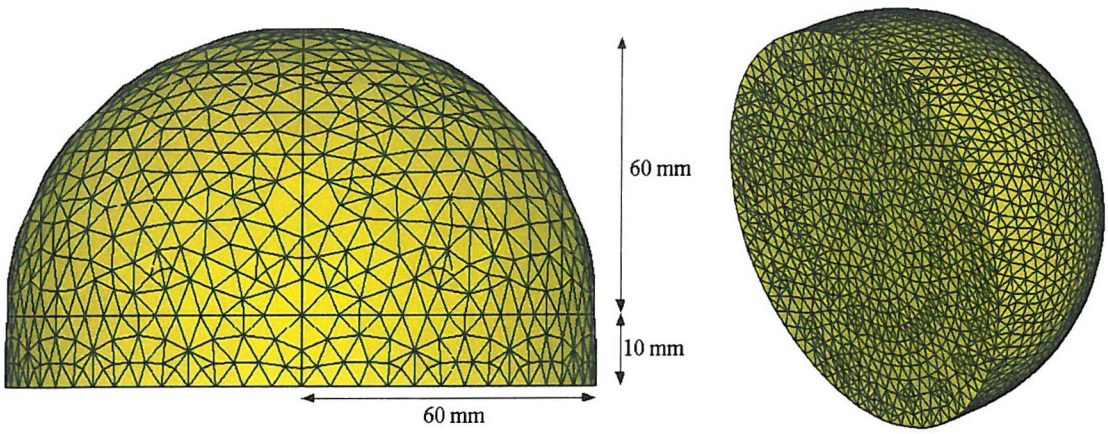

Figure 7.9 The headphone model with the flat surface for the large control field.

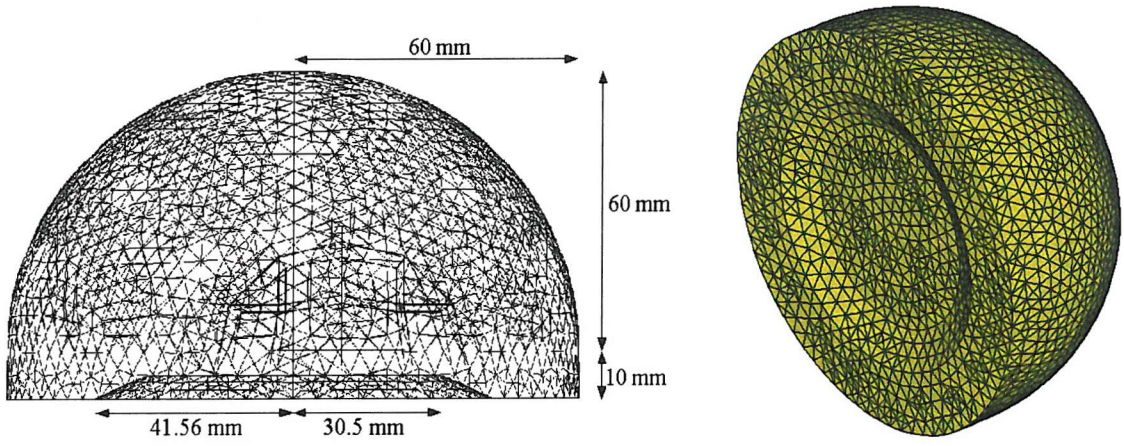

Figure 7.10 The headphone model with the flat surface for the small control field.

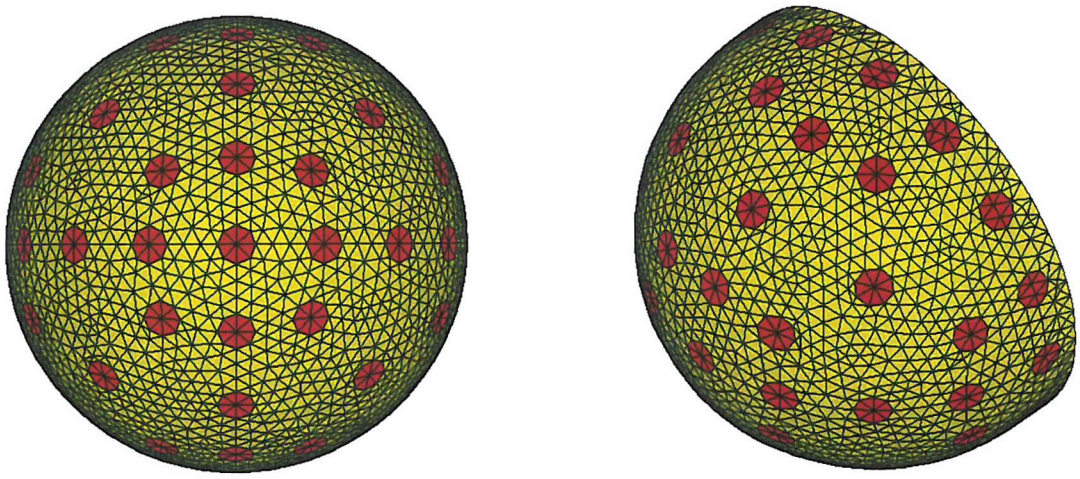

Figure 7.11 45 headphone sources

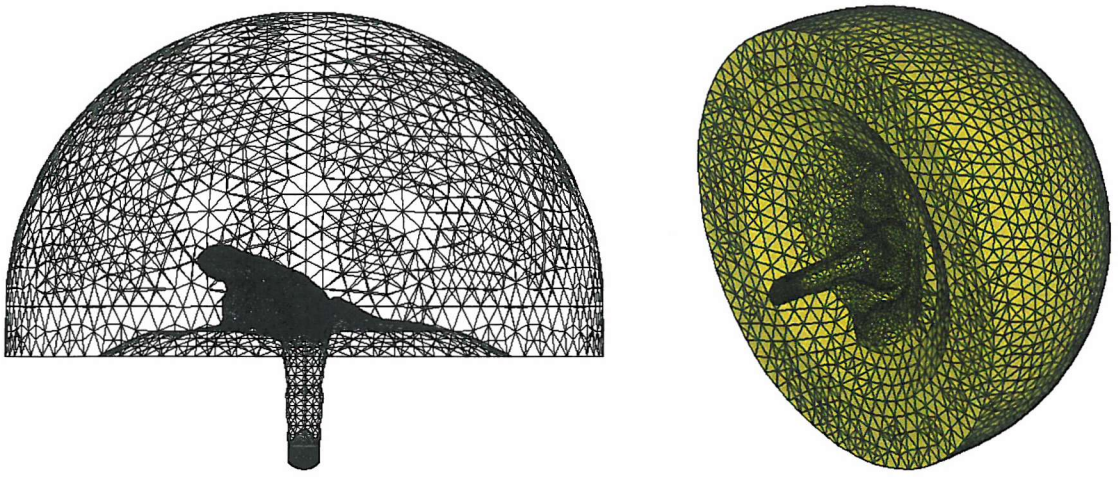

Figure 7.12 The headphone model with the DB60 ear model.

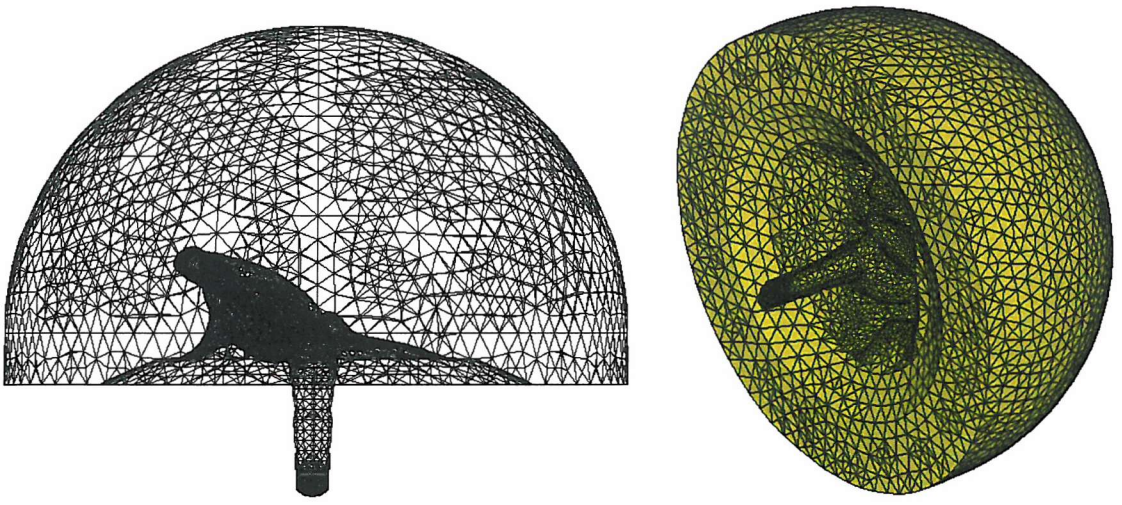

Figure 7.13 The headphone model with the DB65 ear model.

CHAPTER 8
NUMERICAL SIMULATION OF VIRTUAL ACOUSTICS

8.1 Introduction

Real sound fields can be produced and evaluated by undertaking experiments. However, experiment is not always the best way to find out what a given sound field will be. It is difficult to design the sound field freely because it can be very hard to control some factors. Experiments need proper facilities and equipment. In many cases, it is difficult to produce and evaluate the designed sound field due to the limited performance of experimental equipment. The presence of experimental equipment like microphones can alter the sound field. Therefore, in some cases, numerical simulation can be a better way to design and estimate a given sound field. Thanks to the rapid growth of computer performance, real sound fields can be precisely simulated. In this project, numerical simulations are preferred to experiment because some important factors associated with multichannel headphone design can be controlled easily. For example, several hundreds of transparent microphones and several tens of loudspeakers can be located within a hemisphere having a radius of 60 mm, and studied numerically. Such a task is very difficult to accomplish experimentally.

A number of numerical models have been introduced in the previous chapter in order to simulate the RISE (Reproduction of the Incident Sound on the Ear) system with the multichannel headphone. This chapter shows how to simulate the real sound field in the primary field and the corresponding virtual sound field in the secondary field. Some issues regarding numerical calculations are discussed. One example of the virtual acoustic system is suggested and results of the numerical simulations of that system are shown. Possible causes of error between the desired output and output produced are suggested and discussed. The validity of the assumption for the theory of the RISE system is also discussed.

8.2 Procedure for the numerical simulation

The objectives of the numerical simulations in this project are to simulate the sound field caused by a sound source in the primary field that interacts with a human head, and to simulate the sound field caused by multichannel headphone sources in the secondary field. The secondary field aims to create the same sound pressure at the eardrum as the corresponding sound pressure at the eardrum in the primary field. The optimal strengths of the headphone sources to create the virtual sound field are found and then the virtual sound field in the secondary field is compared with the desired sound field in the primary field. The related theory is explained in detail in chapters 4 and 6. To accomplish these objectives, the following procedure is used in the numerical calculations.

First, the primary field generated by a sound source with the numerical head model without the ear is created in an unbounded free field. Then the sound pressures at the control points are evaluated. These are the sound pressures that are desired to be reproduced in the secondary field. Second, the secondary field generated by the multichannel headphone placed on the head surface without the ear is created. The transfer impedance matrix between headphone sources and the same control points as those in the primary field is evaluated. Third, the optimal strengths of the headphone sources are calculated by using the least squares solution. The solution uses the transfer impedance matrix and the desired sound pressures at the control points. Fourth, the primary field generated by the same sound source as that in the first step with the numerical head model with the ear is created in an unbounded free field. Then the sound pressure at the eardrum is evaluated. This eardrum sound pressure is desired to be reproduced in the secondary field. Fifth, the secondary field generated by the same headphone as that in the second step placed on the head surface with the ear is created. Then the sound pressure at the eardrum is evaluated when the strengths of the headphone sources are applied, which are those calculated in the third step. If the sound pressure at the eardrum evaluated in the fifth step is same as that in the fourth step, the virtual acoustic field is successfully produced.

8.3 An example of numerical simulation

An example of the RISE system is suggested in order to illustrate the procedure for the numerical simulation. Figure 8.1 shows that the primary field produced by a monopole sound source in a free field with the numerical head model without the ear shown in Fig. 7.6. The monopole sound source is one metre away from the centre of the head model, and is located at 45 degree of azimuth in the horizontal plane. The detailed coordinate system will be shown in Fig. 9.8. The peak amplitude of the sound pressure one metre away from the source is set to be unity at all frequencies. This primary field is created in the SYSNOISE software package. The direct boundary element method for exterior uncoupled problems is used to solve the Helmholtz equation and evaluate sound field in the frequency domain (SYSNOISE, 5.5). The control field shown in Fig. 9.4 has 84 control points. The detailed explanation of the control field will be presented in section 9.2. Human skin is nearly rigid but hair is an absorbent material (Katz, 2000). To design the head model properly, the boundary condition of head model should be considered. However, the boundary surface of the spherical head model with or without the ear is assumed to be rigid for simplicity in this thesis. The density of the air is set to be 1.225 kg/m^3 and the speed of sound is set to be 340 m/s. After applying boundary conditions, fluid property, and source property, sound pressures at the control points are evaluated from 1 kHz to 10 kHz with a constant frequency increment of 1 kHz in SYSNOISE. The frequency increment is not small, so the detailed frequency response cannot be obtained in this simulation. Since the calculation time per single frequency was so long with the computing environment available, it was very time consuming to calculate the detailed frequency response.

The secondary field that uses a numerical model of the multichannel headphone without the ear shown in Fig. 7.10 is created in SYSNOISE. The same control points as those in Fig. 9.4 are used. The number of headphone sources of radius 5mm is assumed to be 45 as shown in Fig. 7.11. The headphone source is a piston-like flat vibrating surface and moves uniformly in phase. The boundary condition of the headphone surface is perfectly absorbent but the bottom of the headphone is rigid. In

this case, the rigid flat surface is a substitute of the ear. In order to calculate the transfer impedance matrix, the method explained in section 5.6 is used, so the sound pressures at the control points are evaluated one by one when only one headphone source is activated, which has unity velocity boundary condition. The data comprising the desired sound pressures evaluated in SYSNOISE are converted to the vector format suitable for the MATLAB software package (MATLAB, 5.3). Then the transfer impedance matrix is also created in MATLAB by combining data evaluated in SYSNOISE. Then the vector of the optimal strengths of the headphone sources is calculated by using the least squares solution in MATLAB.

Figure 8.2 shows that the primary field produced by the same monopole sound source as that in Fig. 8.1 in a free field with the numerical head model with the ear, and this is also created in SYSNOISE. The numerical head models with the DB60 ear shown in Fig. 7.7 and with the DB65 ear shown in Fig. 7.8 are used. Then, the sound pressure is evaluated at the eardrum in the primary field. The measurement point is set to be the point 2 mm away from the centre of the eardrum rather than the centre itself in order to avoid any miscalculation. If the field point is in an exterior field, the sound pressure at the field point is evaluated by integrating sound pressures and their gradients on the surface of the model, and this may be more stable numerically than evaluating the sound pressure at a single node of the eardrum surface, which may be influenced by some numerical error such as insufficiently suppressed internal resonances caused by the non-uniqueness problem.

The secondary field that uses a numerical model of the multichannel headphone with the ear is created in SYSNOISE. The numerical headphone models with the DB60 ear shown in Fig. 7.12 and with the DB65 ear shown in Fig. 7.13 are used. The same control points as those in Fig. 9.4 are used. The number of headphone sources of radius 5mm is also assumed to be 45. The boundary condition of the headphone surface is perfectly absorbent except for the ear. Then the sound pressure at the eardrum is evaluated when the optimal strengths of the headphone sources calculated in MATLAB are applied. The sound pressure is then evaluated at the eardrum in the secondary field. This sound pressure at the eardrum in the secondary field is thus compared with that in the primary field to assess the accuracy of reproduction of the virtual acoustic system.

Since the number of the headphone sources is less than the number of control points, there should be some control error when the optimal strengths of the headphone sources are calculated. To assess this control error, the following least squares error can be used:

$$E_{LS} = \sqrt{\frac{J_o}{\sum_{i=1}^{L} |p_{p,i}|^2}} \tag{8.1}$$

where J_o is the minimum value of the cost function given in Eq. (5.59), p_p is the complex sound pressure at the control point evaluated in the primary field and L is the number of control points. Note that the least squares error should be from 0 to 1 since it is normalized and it is non-dimensional. Figure 8.3 shows the least squares error. The control error is nearly negligible in this case since the 45 number of headphone sources are great enough to control the sound field at the 84 control points. Another assessment of the control error is suggested. The average sound pressure level difference at the control points between the desired sound pressure and the reproduced sound pressure is given by

$$E_{AD} = \frac{1}{L}\sum_{i=1}^{L}\left(20\log_{10}\frac{|\mathbf{p}_p|_i}{|\mathbf{G}\mathbf{q}_{so}|_i} \right) \quad [\text{dB}] \tag{8.2}$$

where $\mathbf{q}_{so}$ is the optimal headphone source strength in the secondary field and $\mathbf{G}$ is the acoustic transfer impedance matrix. Note that this measure of the control error has units of decibels. Figure 8.4 shows these average sound pressure level differences at the control points, and they are below 0.5 dB in this case, which are also nearly negligible.

Figure 8.5 shows the sound pressure levels at the eardrum of the DB60 ear in the primary and corresponding secondary field, and Figure 8.6 shows those at the eardrum of the DB65 ear. The solid line represents the desired sound pressure level evaluated in the primary sound field, and the dashed line represents the reproduced

sound pressure level evaluated in the secondary sound field. The agreements between the two sets of results are good for both ears. Since some measure is needed to assess the performance of the virtual acoustic systems, the following measure of reproductive accuracy is adopted as the sound pressure level difference at the eardrum between the desired values in the primary field and the reproduced values in the secondary field:

$$E_{ED} = \left| 20\log_{10}\left(\frac{|p_{ep}|}{|p_{es}|} \right) \right| = \left| 20\log_{10}\left(\frac{|p_{ep}|}{|\mathbf{g}^T\mathbf{q}_{so}|} \right) \right| \quad [\text{dB}] \tag{8.3}$$

where p_{ep} is the complex sound pressure evaluated at the eardrum in the primary field, p_{es} is the complex sound pressure evaluated at the eardrum in the secondary field, $\mathbf{g}$ is the acoustic transfer impedance vector between headphone source strengths and sound pressure at the eardrum in the secondary field. The term of $(\mathbf{g}^T\mathbf{q}_{so})$ equals the term (p_{es}) when the optimal strengths of the headphone sources are applied. Figure 8.7 shows these differences of sound pressure levels evaluated at the eardrum of the DB60 and DB65 between the desired values and the reproduced values shown in Fig. 8.5 and 8.6. This shows most eardrum sound pressure level differences are below 1dB except for two data points, which can be regarded as successful reproduction.

Figure 8.8 shows the corresponding phase differences at the eardrum between the desired complex sound pressure and the reproduced complex sound pressure, and these are below 10° except for one data point. However, the measure of the phase difference is not considered any further since the monaural phase information does not play an important role in sound localization as discussed in section 2.2. Note that there is not much difference between the DB60 and the DB65 in terms of the system performance if the same conditions are applied. Therefore, these results confirm that the performance of the RISE system is independent of the geometry of the individual ear.

8.4 Causes of differences

Two measures may be required to assess the performance of the virtual acoustic system. One of the measures is the reproductive accuracy given by the difference between the sound pressure level at the eardrum in the primary field and the sound pressure level at the eardrum in the secondary field. The other one is the robustness of the system performance, which means the degree to which the reproduction accuracy is changed when the ear is changed. If the RISE system for one arbitrary ear shows good reproductive accuracy, the system is robust automatically because the optimal source strengths are obtained from the system without the ear. Therefore, only the reproductive accuracy needs be considered to assess the performance of the RISE system for one typical ear.

There are the following three main sources of error, which are the control error caused by inverting non-square acoustic transfer impedance matrix, the numerical error caused by numerical calculation of the boundary element method, and the physical error caused for acoustical reasons. These three kinds of error may be interdependent. Control error mainly depends on the number and position of headphone sources and the size and shape of the control field. As discussed in section 7.5, in order to reduce control errors, the number of headphone sources should be as large as possible and the number of control points should be as small as possible. The control error increases as frequency increases since more control points are needed to reproduce shorter wavelengths accurately. The complexity of the incident sound field can raise the control error.

Numerical error can come from false modelling of the real case. This depends on mesh resolution, boundary condition and the shape of the model. It also depends on the numerical modelling method used. If the mesh resolution is increased, numerical errors can be reduced but calculation time is increased. Numerical errors increase as frequency increases due to decreased number of elements per wavelength. Numerical models should of course be made as similar as possible to real models. To compare various results of the numerical simulation, the modelling method is unified as the

direct boundary element method and same numerical models are used consistently because the sound pressure at some position using the direct boundary element method can be different from that using the indirect boundary element method. The non-uniqueness problem is one of the most critical problems. This also gets worse as frequency increases. The possible solution of the non-uniqueness problem is the CHIEF method, which collocates the over-determination points inside the numerical model as constraint equations. However, the non-uniqueness problem is difficult to overcome at high frequencies. The theoretical background to the non-uniqueness problem is explained in the section 4.5.

Even though the control error and numerical error is not significant, reproductive accuracy can be poor. If the boundary condition of headphone surface is not perfectly absorbent, the scattered sound field from the headphone surface can produce errors. If the angle of the incident sound wave matches the angle of the headphone source, the physical error can be reduced. As discussed in section 6.5, if the assumption that scatterers outside the control field act like an "active sound source" is not valid, the reproduction accuracy can be degraded. This validity of the assumption regarding the RISE system is discussed more in the next section.

8.5 Sound pressure on the head surface

Some numerical simulations were undertaken to check the validity of the assumption on the theory of the RISE system. This assumption is that the sound field incident on the control volume from the scatterers outside the control volume is independent of the geometry and boundary conditions of the scatterer inside the control volume. If the sound pressure on the head surface is not significantly changed for the change of the scatterer inside the control volume, the assumption is reasonably valid. Figure 8.9 (a) shows the primary sound field on the spherical head model with the flat surface shown in Fig. 7.6. Figure 8.9 (b) shows the primary sound field on the head model with the DB65 ears shown in Fig. 7.8. A point monopole source is located at 45 degree azimuth in the horizontal plane as shown Fig. 8.1 and 8.2, and generates 1kHz

single frequency sound. Figure 8.9 shows that both primary fields are very similar, so this is an example showing that sound pressure on the head surface is not strongly influenced by the geometry of the ear surface at low frequencies. Figure 8.10 (a) and (c) shows the primary sound field at 3200Hz produced by the same source at 45° azimuth on the head model with the flat surfaces, and Figure 8.10 (b) and (d) shows that on the head model with the DB65 ears in a free field. 3200Hz is an approximate first resonance frequency of the DB65 ear model, as shown in Fig. 9.22. The surface sound pressures around the ear surface are different from those around the flat surfaces due to the strong resonance of the DB65 ear. There can thus be some physical error at the resonance frequency of the ear. Figure 8.11 shows various primary sound fields at 7 kHz produced by the same source but located at (a) 45° or 135° azimuth, (b) 225° or 315° azimuth, (c) 45° azimuth, (d) 315° azimuth, (e) 135° azimuth, (f) 225° azimuth in the horizontal plane. These angles are relative azimuth angles to the ear, for example, when the source is at 45° azimuth for the right ear, the same source is at 315° azimuth for the left ear. 7 kHz is an example of a high frequency that is not a resonance frequency of the DB65 ear model. The influence of the ear surface is not totally negligible since 7 kHz is a relatively high frequency in this case. In all cases, the patterns of the surface sound pressures are similar and the differences between the primary fields may not be serious. The cases at 135° and 225° azimuth where the source is at the rear is slightly worse than the cases at 45° and 315° azimuth where the source is in front because, if the ear is regarded as a wedge, the steep "wall" of the wedge reflects incident waves more and so influences the surface sound pressure around the ear more.

The following measure is suggested in order to evaluate the physical error caused by the false assumption of the theory of the RISE system. This is the difference between the sound pressure levels on the head surface excluding the flat surfaces in the primary field α and those on the head surface excluding the ear surfaces in the primary field γ:

$$E_{DH} = \left| 20 \log_{10} \left(\frac{|p_\alpha(\mathbf{x})|}{|p_\gamma(\mathbf{x})|} \right) \right| \tag{8.4}$$

where the vector **x** is on the head surface, $p_\alpha(\mathbf{x})$ is the sound pressure in the primary field with the flat surface, and $p_\gamma(\mathbf{x})$ is the sound pressure in the primary field with the ear. Figure 8.12 shows the differences between the sound pressure levels on the head surfaces with and without the scattering by the ear in the primary sound fields produced by the same source at 45° azimuth for the right ear or 315° azimuth for the left ear. Figure 8.13 shows those differences with a source at 135° azimuth for the right ear or 225° azimuth for the left ear. All colour figures are scaled from 0 to 6dB and the monopole source is at the right hand side of all figures. The figures show the differences at 1 kHz are below 1dB, and confirm that the physical error is nearly negligible at low frequencies. The differences at 3200 Hz are slightly larger than those at 7 kHz due to the effect of the resonance of the ear. Figures show the tails of errors on the left hand side caused by scattering sound waves from the ear, and the rippling errors on the right hand side caused by the reflected sound waves from the ear. The case of sources at 315° and 225° azimuth is slightly worse than the case of sources at 45° and 135° azimuth because the sound field scattered from the ear is more influential to the surface sound pressure near the ear when the ear is in the shadow zone of the spherical head.

Figure 8.14 shows the average difference of the sound pressure levels on the head surfaces in the primary sound fields with a source at 45° or 315° azimuth, and Figure 8.15 shows that with a source at 135° or 225° azimuth. These are the average differences at all nodes on the head surface between the sound pressure levels on the head surfaces with and without the scattering by the ear in the primary sound fields. These figures show the error is maximum at the resonance frequency of 3200Hz that is probably due to the resonance of the ear. These figures also show that most errors are below 1dB, which are reasonably low. Therefore, these results of the numerical simulations show that the assumption of the theory of the RISE system is reasonably acceptable even at high frequencies up to at least 10kHz.

8.6 Conclusion

Numerical simulations have been undertaken in order to calculate the sound field in the primary field and the secondary field for a virtual acoustic system with a multichannel headphone. The procedure used in the numerical calculation is explained. The optimal strengths of the headphone sources are calculated from the acoustic transfer impedance matrix calculated in the secondary field and the desired sound pressures at the control points evaluated in the primary field by using the numerical models without the ear. In order to assess the performance of the RISE system, the sound pressure level at the eardrum of the numerical head model in the primary field is compared with the sound pressure level at the eardrum in the secondary field with the multichannel headphone when the same optimal source strengths calculated before are applied to the headphone.

Three main sources of error between the desired output and reproduced output are the control error, numerical error, and the physical error. The control error and numerical error increase as frequency increases for given conditions. The control error can be reduced by increasing the number of headphone sources for a given number of control points. The absorbent surface of the headphone can reduce the physical error. The numerical error should be minimized to give credibility to the results of the numerical calculations by applying suitable over-determination points and increasing mesh resolution, for example. The physical error caused by the false assumption of the theory of the RISE system can be negligible if the differences between the sound pressure levels on the head surfaces with and without the scattering by the ear in the primary sound fields are sufficiently small.

FIGURES

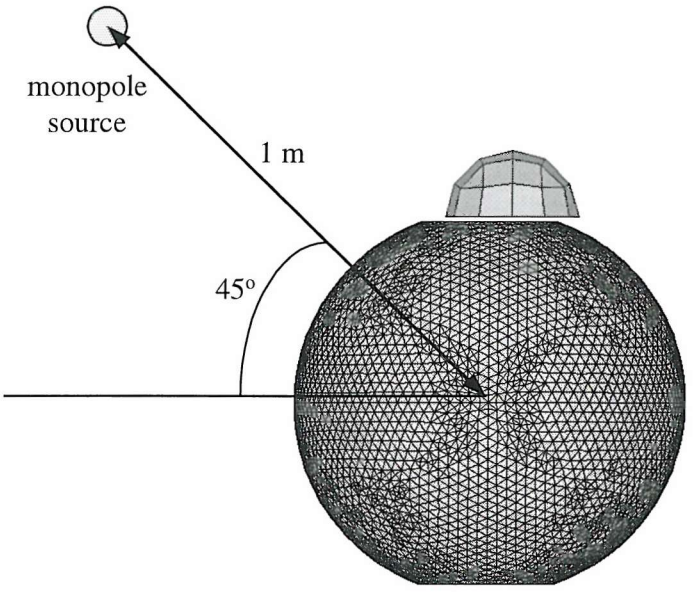

Figure 8.1 The primary field produced by a monopole sound source in a free field with the numerical head model without the ear.

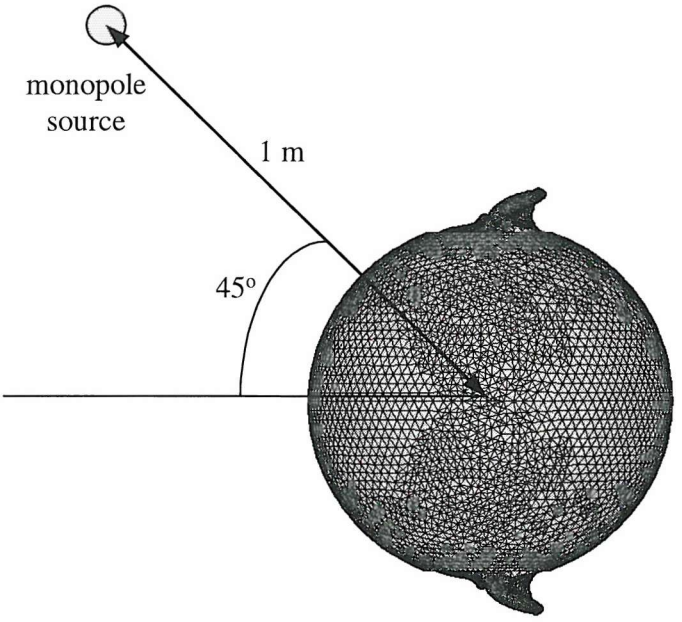

Figure 8.2 The primary field produced by a monopole sound source in a free field with the numerical head model with the ear.

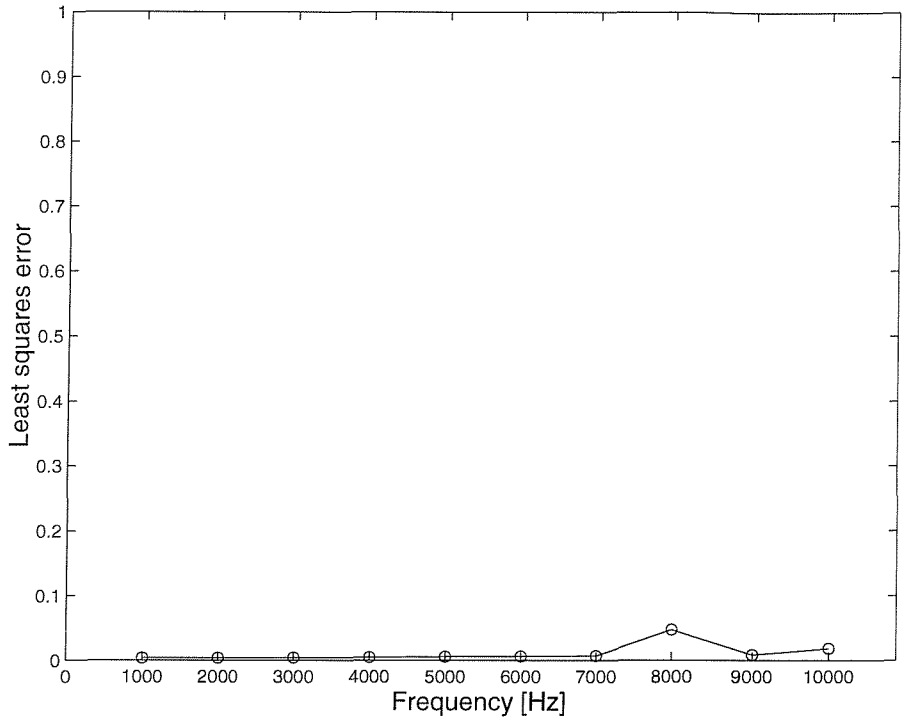

Figure 8.3 Least squares error.

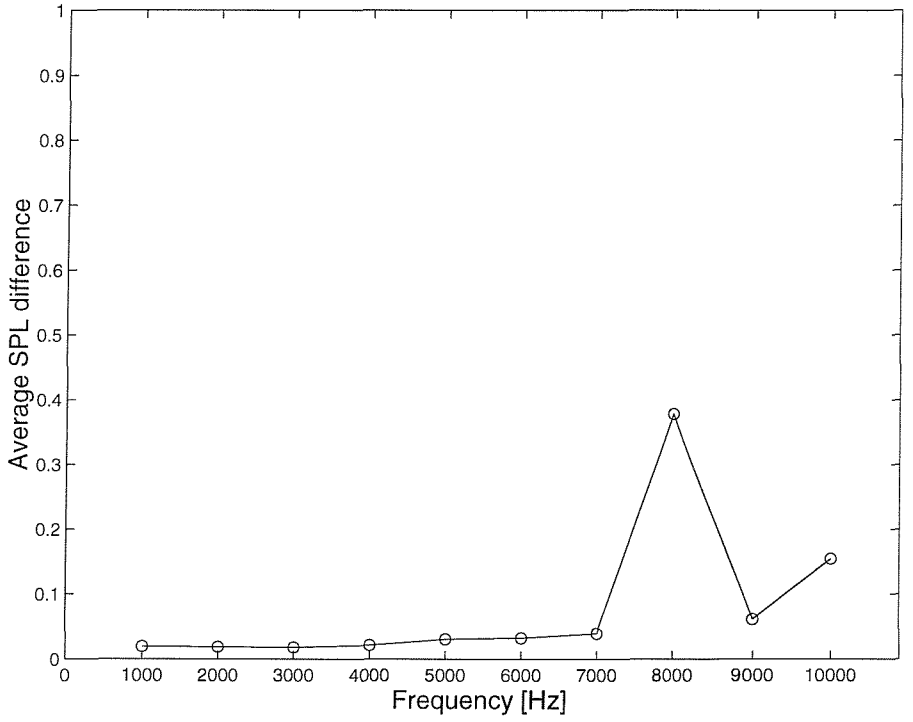

Figure 8.4 Average sound pressure level difference at the control points.

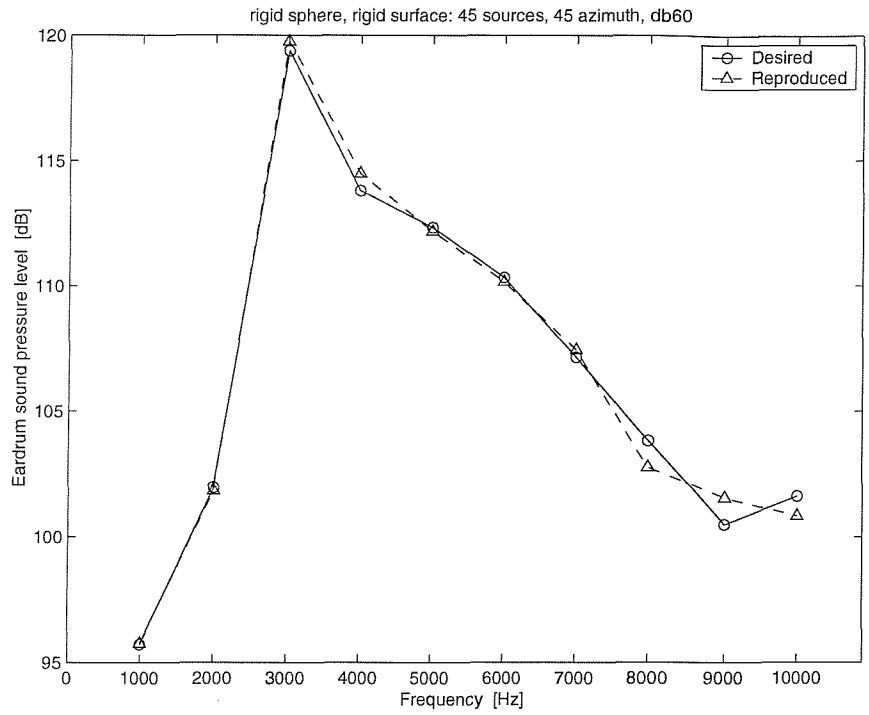

Figure 8.5 Sound pressure level at the eardrum of DB60.

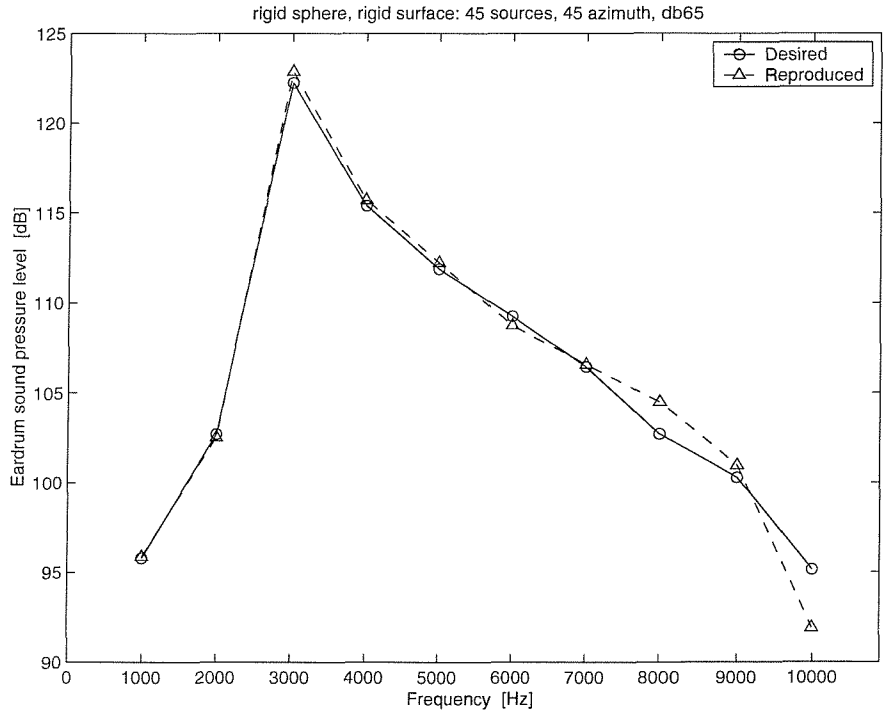

Figure 8.6 Sound pressure level at the eardrum of DB65.

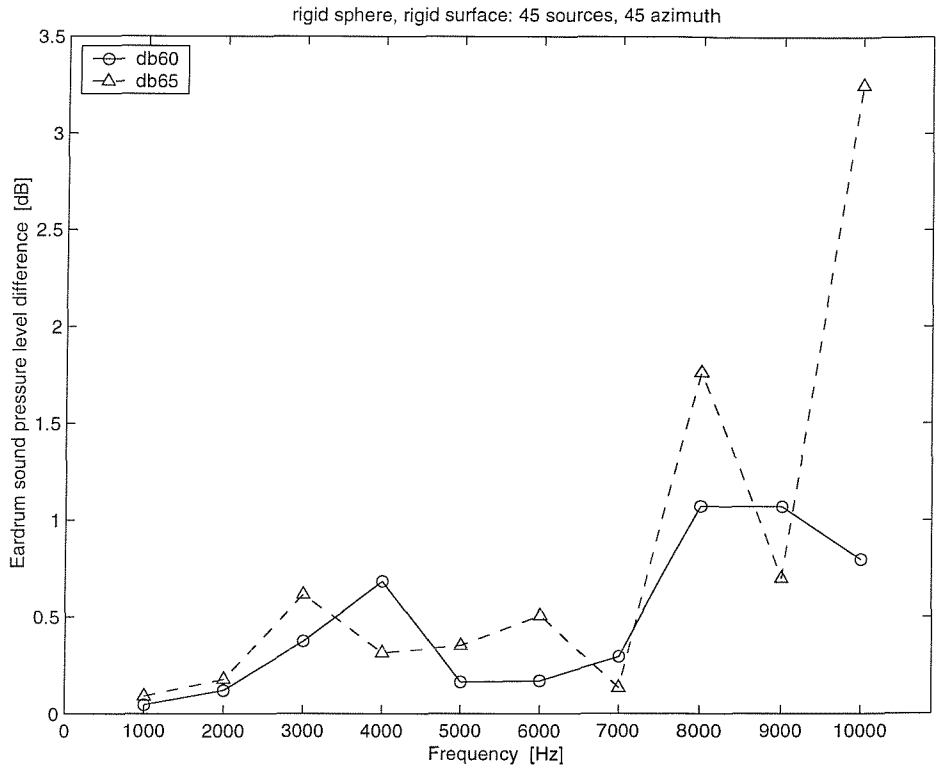

Figure 8.7 Sound pressure level difference at the eardrum.

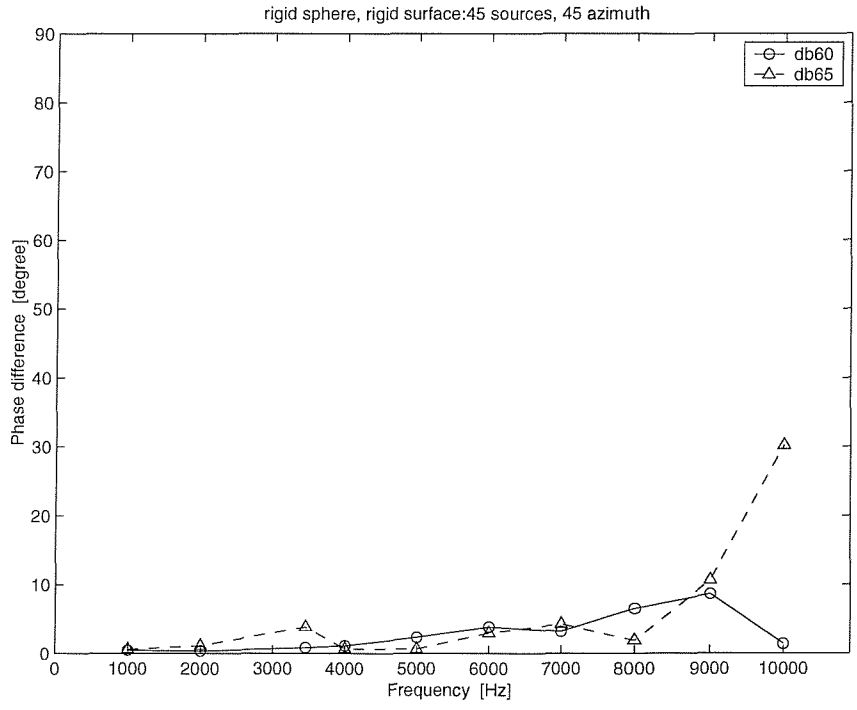

Figure 8.8 Phase difference at the eardrum.

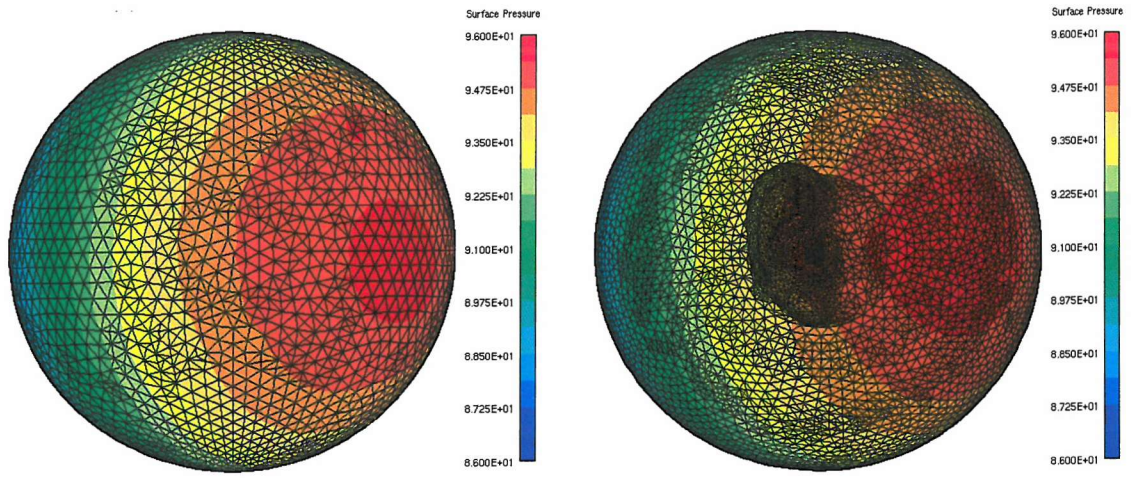

(a) (b)

Figure 8.9 Primary sound fields at 1 kHz with a monopole source at 45° azimuth, 1m away. (a) the head model with flat surfaces (b) the head model with the DB65 ears.

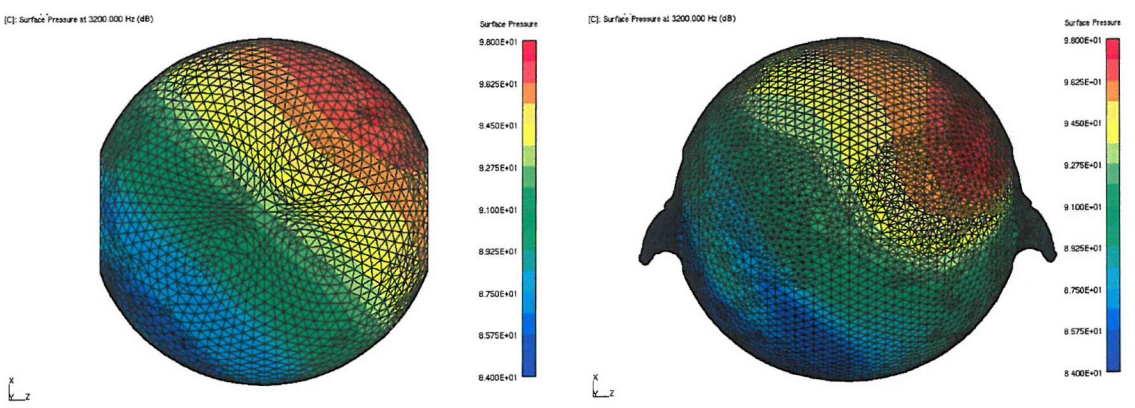

(a) (b)

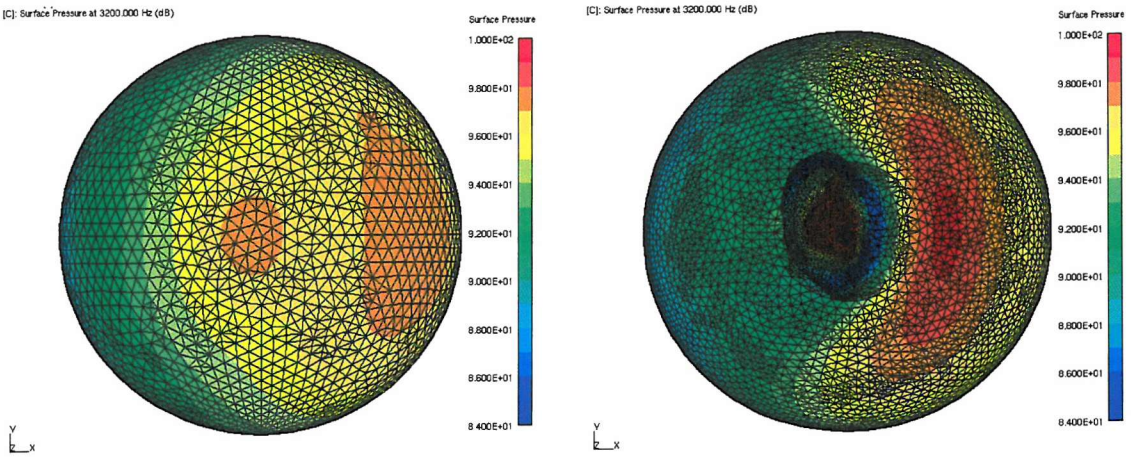

(c) (d)

Figure 8.10 Primary sound fields at 3200 Hz with a source at 45° azimuth. (a), (c) the head model with flat surfaces (b),(d) the head model with the DB65 ears.

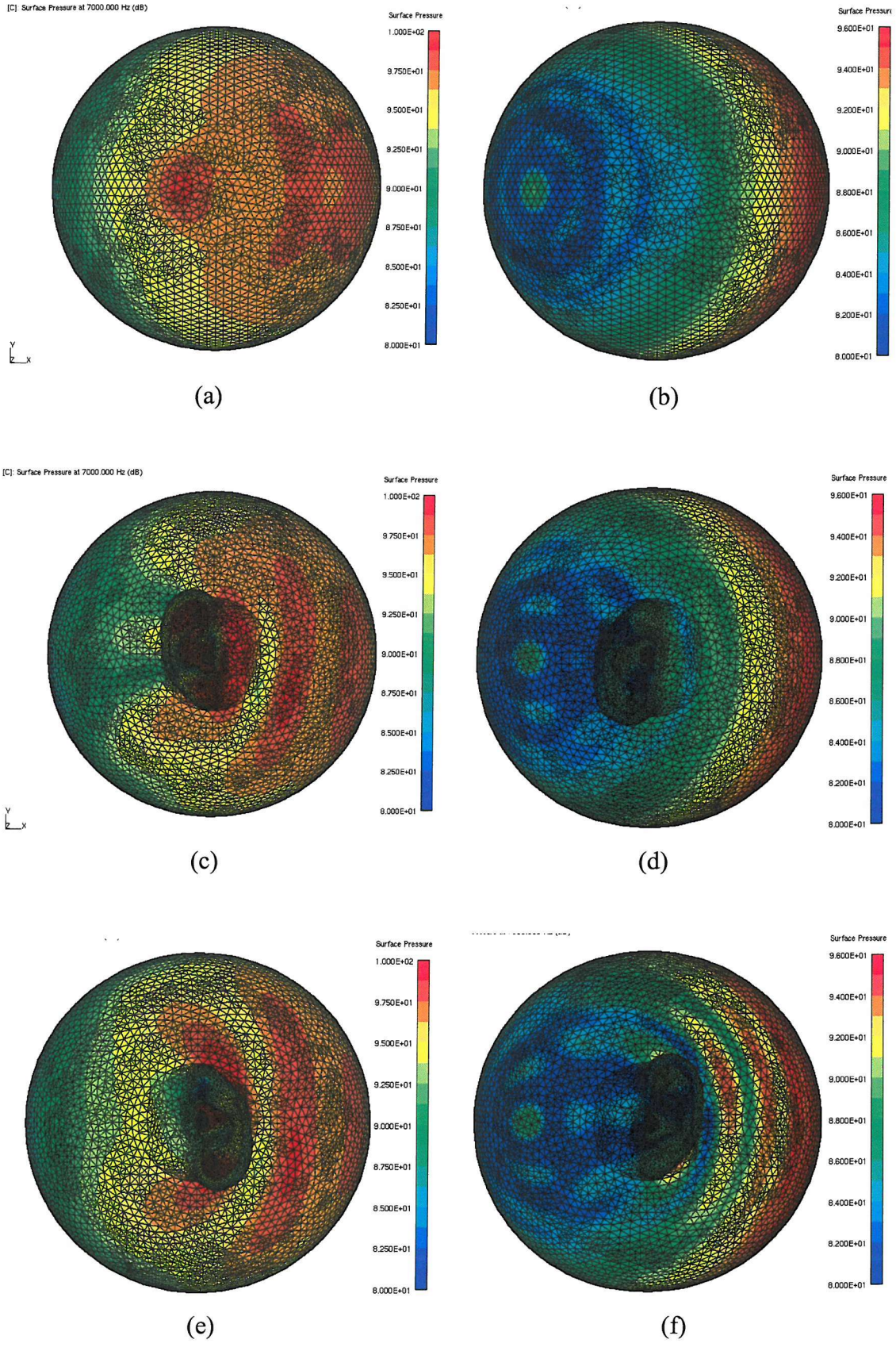

Figure 8.11 Primary sound fields at 7 kHz with a source at (a) 45° or 135° azimuth, (b) 225° or 315° azimuth, (c) 45° azimuth, (d) 315° azimuth, (e) 135° azimuth, (f) 225° azimuth.

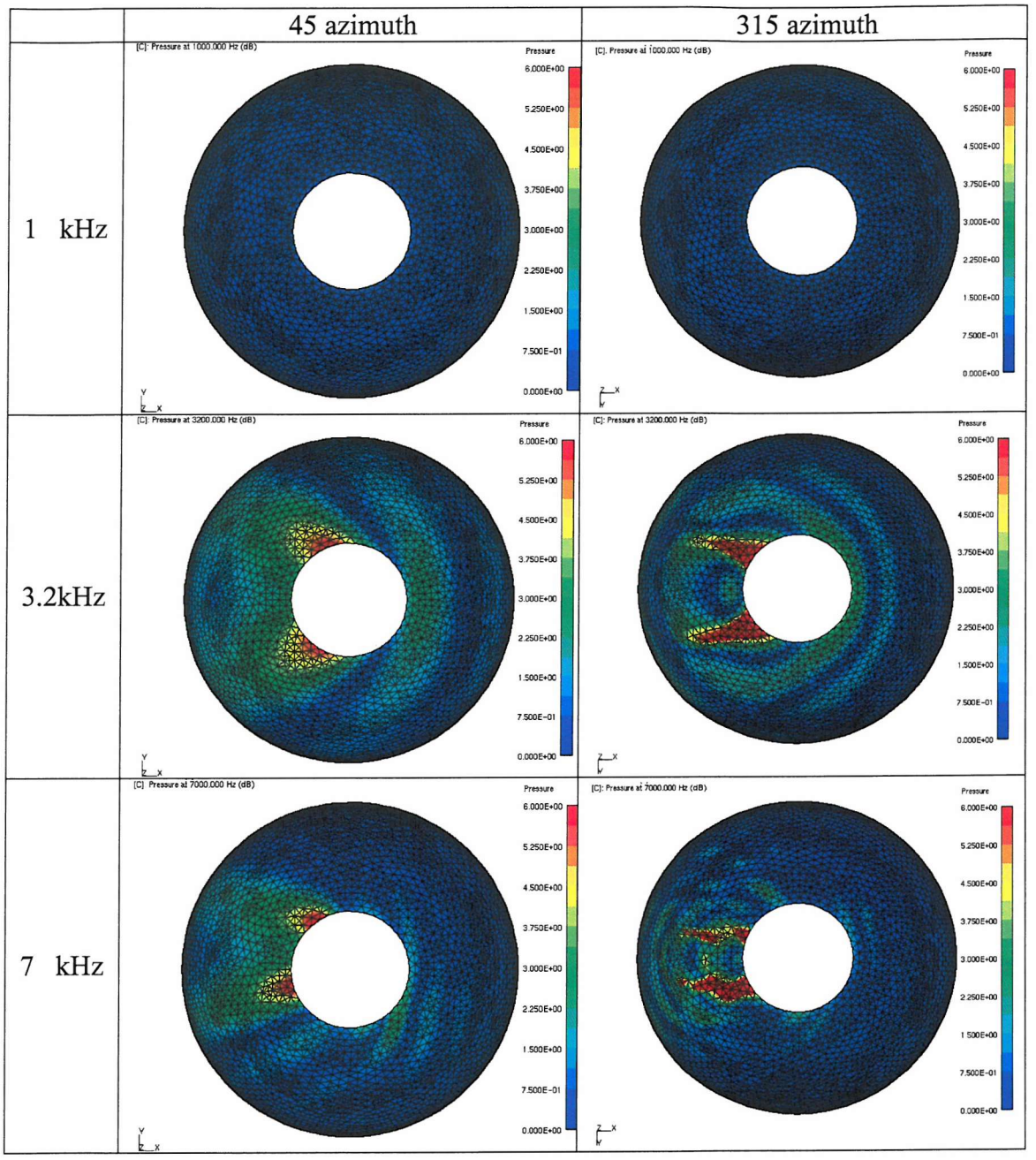

Figure 8.12 Differences between the sound pressure levels on the head surfaces with and without the scattering by the ear in the primary sound fields produced by a source at 45° or 315° azimuth.

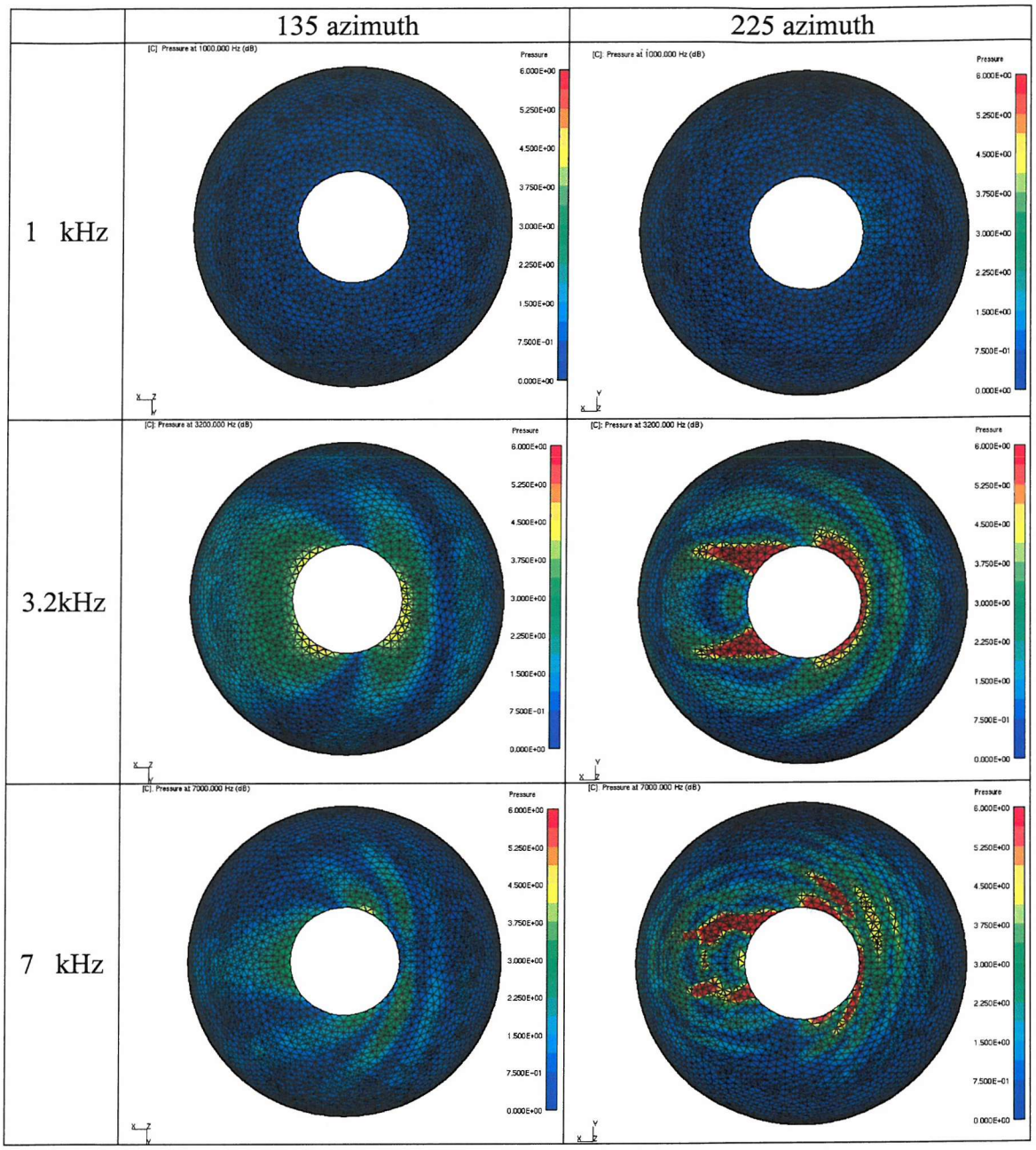

Figure 8.13 Differences between the sound pressure levels on the head surfaces with and without the scattering by the ear in the primary sound fields produced by a source at 135° or 225° azimuth.

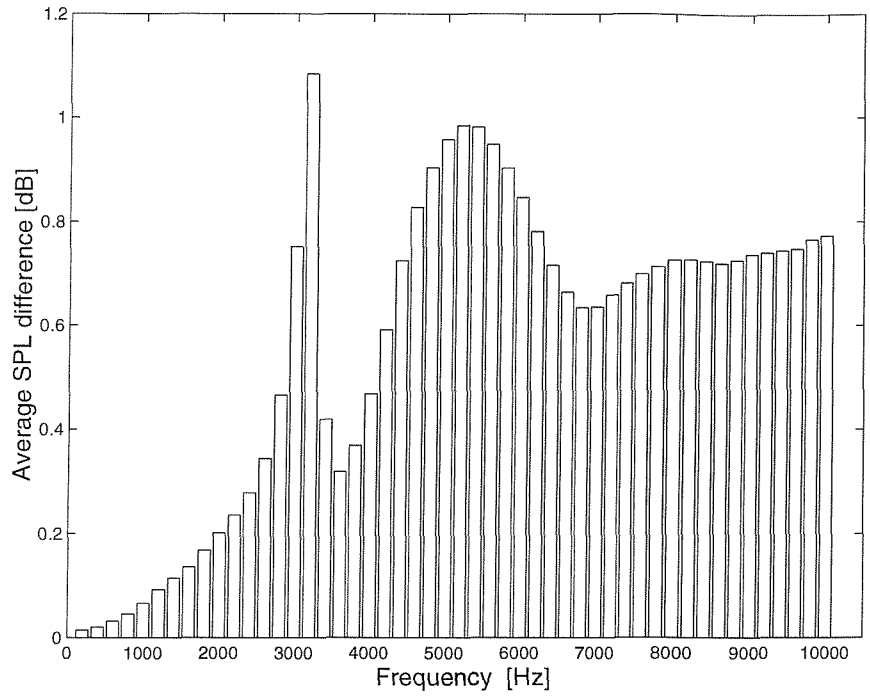

Figure 8.14 Average difference of the sound pressure levels on the head surfaces in the primary sound fields with a source at 45° or 315° azimuth.

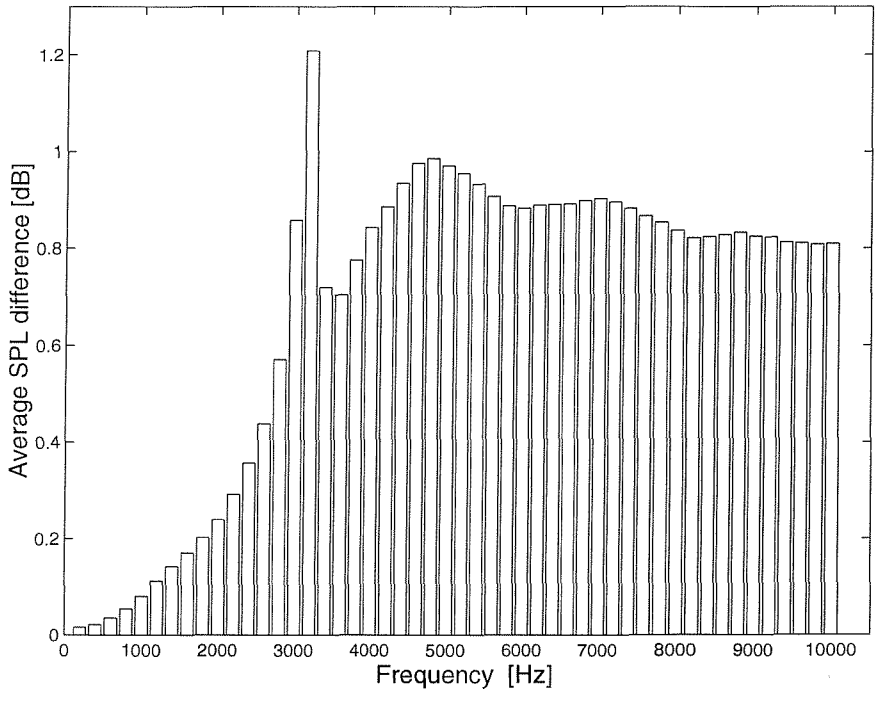

Figure 8.15 Average difference of the sound pressure levels on the head surfaces in the primary sound fields with a source at 135° or 225° azimuth.

CHAPTER 9
PERFORMANCE OF
THE VIRTUAL ACOUSTIC SYSTEM

9.1 Introduction

In principle, the RISE system could use either multichannel loudspeakers or multichannel headphones. However, since the control volume is small, the "sweet spot" produced by the loudspeakers would be narrow. Therefore, the creation of the virtual acoustic images by the loudspeakers would be very difficult for a natural listening environment since the illusion would be destroyed if the listener moves his or her head slightly from the "sweet spot". However, the "sweet spot" for the RISE system with multichannel loudspeakers may be broader than that for the binaural system using the HRTF technology with two-channel loudspeakers. If the listener's head is guaranteed to be fixed relative to the loudspeakers, the production of virtual acoustic images may be feasible. Cross-talk cancellation among multichannel loudspeakers is needed and this would not be easy. It would be difficult to find the physical locations for the multiple loudspeakers in practical listening rooms. It would be slightly more difficult to place the loudspeakers above or below the listener for the reproduction of source elevation.

On the other hand, multichannel headphones can solve many of the problems of multichannel loudspeakers. Since the location of transducers relative to the ear is not significantly variable, the listener's ear can be easily placed within the control volume. Cross-talk cancellation is also not required. If it is feasible, multiple transducers can be placed on the headphone and transducers can be placed above or below the listener's ear for the reproduction of source elevation. If possible, a head tracking device could be attached to the multichannel headphone, and then the listener can rotate the head. Therefore, the multichannel headphone is preferred as a device for the implementation of the RISE system.

Chapter 6 showed the theory of the RISE system and proved that the system can produce any kind of virtual acoustic field regardless of the geometry of the ear. This chapter will show the performance of the RISE system for various source angles and verify the theory of the RISE system. Somewhat idealized and simplified systems are studied in order to minimize the control and numerical errors.

9.2 Design of the geometry of the control field

Various kinds of control field where the sound pressures were recorded and reproduced have been modelled. The geometry of the control field, such as the size or shape, should be carefully designed to optimize the performance of the virtual acoustic system. Three different geometries of the control field are suggested. The volume of the control field can be converted into bounding surfaces according to the boundary surface control principle discussed in section 5.5. Those control surfaces are modelled as double layers to evaluate sound pressures and their normal gradients. The direction from nodes on the inner layer to corresponding nodes on the outer layer is normal to the tangential plane of the inner layer. The distance between the inner and outer layer is 3.4 mm that is one tenth of the wavelength at a frequency of 10 kHz.

First of all, Figure 9.1 shows the large and sparse control field that is modelled as a hemisphere and a cylinder with 10 mm width extended from the hemisphere. The radius of the outer layer is 41.56 mm, which is the same as the radius of the flat surface of the corresponding head model shown in Fig. 7.5. The radius of the inner layer is 38.16 mm. The total height of the control field is 51.56 mm. This control field may be large enough to cover the entire volume of most human ears. The control surfaces are discretized and the distance between two adjacent control points, that is, the resolution of the control points is about 10 mm, which is about one third of the wavelength at a frequency of 10 kHz. The number of control points is 512. This is much larger than the number of headphone sources which are at most 45 in this case. Figure 9.2 shows the placement of the large control field on the spherical head model

with the flat surface, and the corresponding head model is shown in Fig. 7.5. Figure 9.3 shows the placement of the large control field on the hemispherical headphone model with the flat surface, and the corresponding headphone model is shown in Fig. 7.9. The control field is located 2 mm away from the flat surface of the head or headphone model in order to avoid any miscalculation. When the control field is placed on the surface of the numerical model, the sound pressure at some control points can be miscalculated as a zero pressure. This is because some control points can be regarded as points inside the numerical model if those points are misplaced in only a minute amount below the surface of the model.

Second, Figure 9.4 shows the small and sparse control field that is modelled as a hemisphere. The radius of the outer layer is 30 mm and the radius of the inner layer is 26.6 mm. The height of the control field is of course 30 mm. The distance between the inner and outer layers is also 3.4 mm. This control field may not cover the entire volume of some large human ears like the DB65 but may be large enough to cover a great portion of most human ears. The control surfaces are discretized and the resolution of the control points is about 15 mm, which is about half the wavelength at a frequency of 10 kHz. The number of control points is 84 and this is much less than that of other control fields. Figure 9.5 shows the placement of the small control field on the spherical head model with the flat surface, and the corresponding head model is shown in Fig. 7.6. Figure 9.6 shows the placement of the small control field on the hemispherical headphone model with the flat surface, and the corresponding headphone model is shown in Fig. 7.10. The control field is located 2 mm away from the flat surface of the head or headphone model and 10 mm off-centered rearward since the greater portion of the pinna model is located in the rear of the axis of ear canal as shown in Fig. 7.8 or 7.13 for example. Third, Figure 9.7 shows the small and dense control field. Its geometry and the placement of this control field are the same as that of the previous small and sparse control field. The resolution of the control points is about 5mm, which is about one sixth of the wavelength at a frequency of 10 kHz. The number of points of the control field is 730.

In this thesis, a head-related system of coordinates shown in Figure 9.8 is assumed (Blauert, 1997). The origin of the system of coordinates lies halfway between the entrances to the two ear canals. The angle ϕ is the azimuth, and the angle θ is the

elevation. The distance between the source and the origin of the coordinates system is one metre unless otherwise noted. The source is in front of the listener at $(\phi,\theta)=(0,0)$, the source is to the right ear at $(\phi,\theta)=(90°,0)$, the source is at the rear at $(\phi,\theta)=(180°,0)$, the source is to the left ear at $(\phi,\theta)=(270°,0)$, the source is above the listener at $(\phi,\theta)=(0,90°)$, and the source is below the listener at $(\phi,\theta)=(0,-90°)$.

The performance of virtual acoustic systems is studied when the three different geometries of the control field suggested above are used respectively. The boundary surface of the spherical head model with or without the ear is assumed to be rigid. In this chapter, the boundary condition of the headphone including surface of the headphone sources is set to be perfectly absorbent, that is, of which the specific acoustic impedance is 416.5 Pa s m^{-1}. Note that the flat surface or the ear surface with some part of the spherical head on the bottom of the headphone is still rigid. Figure 9.9 shows the red area where the perfectly absorbent condition is set. The single monopole sound source in the primary sound field is located on the horizontal plane with the azimuth angle of 45°, 135° degrees for the right ear or 225°, and 315° degrees for the left ear. The monopole sound source is one metre away from the centre of the head model, and the peak amplitude of sound pressure one metre away from the source is set to be unity at all frequencies, that is, 90.97 dB ref 2×10^{-5} Pa. The numerical ear of the DB65 is preferred, which is larger than the DB60, in order to study the case of the small control field that cannot cover the entire volume of the DB65. If the RISE system works for a large ear, the system should work for smaller ears with the same control volume. The numerical models for the DB65 shown in Fig. 7.8 and 7.13 are used. The number of headphone sources of radius 5mm is assumed to be 45, which are distributed evenly as shown in Fig. 7.11 to cover every angle of incident wave equally in three-dimensional space. The sound pressures at the control points are calculated from 1 kHz to 10 kHz with a constant frequency increment of 1 kHz. Figure 9.10, 9.11, 9.12 and 9.13 shows the sound pressure level differences at the eardrum between the desired values and the reproduced values for the monopole source at 45°, 135°, 225°, and 315° respectively when 45 headphone sources are used. All three control fields show similar patterns, but the large and sparse control field gives slightly worse performance in the case of 135° and 315° azimuth. Figure 9.14, 9.15, 9.16 and 9.17 shows the eardrum sound pressure level

differences for the monopole source at 45°, 135°, 225°, and 315° azimuth respectively when 9 headphone sources are used. The 9 headphone sources are distributed evenly as shown in Fig. 10.1. Both the small and sparse control field and the small and dense control field show similar patterns, but the large and sparse control field causes worse performance in the case of 45° and 315° azimuth. Those results of the numerical simulation imply that the small control field is better than the large control field. This agrees with the discussion presented in section 7.5. The increase in resolution of the control points does not change the system performance very much. This means that the size of the control field is more important that the number of control points. Since the use of the smaller number of control points reduces the calculation time of the numerical simulations, the small and sparse control field is preferred in the following numerical simulations.

9.3 Horizontal plane

The angle of incidence of the sound wave from the source in the primary field may affect the performance of the virtual acoustic system since it is related to the assumption of the theory of the incident sound field reproduction method that has been discussed in the section 6.5. The horizontal plane in the head-related coordinates system shown in Fig. 9.8 is the *x-z* plane where the elevation angle is zero. In this section, the single monopole sound source in the primary sound field is located in the horizontal plane at every 15° angle of azimuth. The source is one metre away from the centre of the coordinate system, and the peak amplitude of the sound pressure one metre away from the source is set to be unity at all frequencies. This numerical simulation uses the numerical models for the small control field shown in Fig. 7.6 and 7.10, and the numerical models for the DB65 shown in Fig. 7.8 and 7.13. The small and sparse control field is used, which has 84 control points as shown in Fig. 9.4. The number of headphone sources of radius 5mm is assumed to be 45 as shown in Fig. 7.11. The boundary condition of the surface of the spherical head model both with and without the ears is rigid, and that of the headphone surface is perfectly absorbent. The sound pressures at the control points are calculated from 200 Hz to 10 kHz with a

constant frequency increment of 200 Hz. The highest frequency is set to be 10 kHz since the computing ability is limited and human hearing reduces in sensitivity at frequencies roughly over 10 kHz.

Figure 9.18 shows the sound pressure level evaluated at the eardrum of the DB65 produced in the primary field for various source directions in the horizontal plane. It shows that the heights of peaks and dips of the frequency response curve varies with the source direction. Figure 9.19 shows the corresponding sound pressure level at the eardrum of the DB65 in the secondary field reproduced by the 45 headphone sources in the perfectly absorbent headphone. Those two figures show similar patterns of the curves. If those two curves are identical, the performance of the RISE system is successful. Figure 9.20 shows the sound pressure level differences at the eardrum between the desired values in the primary field shown in Fig. 9.18 and the reproduced values in the secondary field shown in Fig 9.19. These are evaluated for every 15° azimuth of the monopole source direction in the horizontal plane using Eq. (8.3) to illustrate the performance of the system. In the colour filled contour figure scaled from 0 to 6 dB, roughly speaking, the blue area means the eardrum sound pressure level difference or reproduction error is below about 3 dB and the red area means the reproduction error is above about 3 dB. The criterion of 3 dB is somewhat arbitrary. These figures show that most eardrum sound pressure level differences except for a few data are below 1 dB for most azimuth angles up to frequencies of at least 10 kHz, which can be regarded as successful reproduction. The results also show that the good reproduction might be extended to frequencies above 10 kHz. Roughly speaking, the sound pressure level of 1 dB is arguably the just noticeable difference in sound intensity for the human ear (Backus, 1977). This good performance is a practical illustration of the RISE system and it demonstrates that the assumption of the theory is reasonable and does not give rise to significant problems. Figure 9.21 shows the eardrum sound pressure level differences averaged over frequency for each source direction in the horizontal plane. This also shows most values are below 1 dB, and the worst value is below 2 dB. The performance is slightly worse when the source is at the rear-left side to the right ear. This is likely to arise since the sound field scattered from the ear is more influential to the surface sound pressure near the ear when the ear is in the shadow zone of the spherical head, and the back side of the ear

gives significant reflection of incident waves, as discussed in section 6.5. Figure 9.22 shows the eardrum sound pressure level differences averaged over various source directions in the horizontal plane. Two sharp peaks are observed at 3200 Hz and 9400 Hz. Figure 9.18 shows these are resonance or anti-resonance frequencies of the DB65 artificial ear. At resonance or anti-resonance, the sound field scattered from the ear surface may be influential to the sound pressure on the head surface near the ear surface as discussed in section 6.5. Moreover, the sound field near the eardrum can be sensitive to any tiny numerical errors at the anti-resonance because low sound pressures near the eardrum become more vulnerable to numerical errors. For example, numerical errors may be due to the non-uniqueness problem, or insufficiently suppressed internal resonance of the head. The numerical simulation at very high frequencies can be unstable due to the non-uniqueness problem. The non-uniqueness problem is very difficult to eliminate completely at very high frequencies as discussed in section 4.6, and other numerical errors and control errors increase as frequency increases. Therefore, all kinds of errors increase as frequency increases, so these result in high errors around 9400Hz at the anti-resonance of the ear.

Figure 9.23 shows that the least squares error of control points for various source directions in the horizontal plane using Eq. (8.1). Note that the maximum possible value of the least squares error is unity. Figure 9.24 shows the corresponding average sound pressure level differences at control points using Eq. (8.2). These two figures show the same patterns. This shows that the control error is below 0.3 dB, which is nearly negligible. If the control errors are assumed to be negligible in this numerical simulation, the main source of error is likely to be the numerical error, or the physical error that comes only from the false assumption of the theory since the perfectly absorbent headphone is used. This means that the assumption of the theory of the RISE system is reasonable and does not give rise to significant problems.

Figure 9.25 shows an example of the sound pressure level evaluated at the DB65 eardrum for the source at 60° azimuth and Figure 9.26 shows that for the source at 240° azimuth. The solid line represents the desired sound pressure level at the eardrum evaluated in the primary sound field, and the dashed line represents the reproduced sound pressure level at the eardrum evaluated in the secondary sound

field. Figure 9.25 shows good example of nearly perfect reproduction. There is a small error around the resonance near 3200Hz and the anti-resonance near 9400Hz. Figure 9.26 shows more errors at high frequencies (around 9400Hz) than the errors shown in Fig. 9.25. This occurs because the numerical errors are likely to be more influential to the sound pressure levels around the eardrum that are about 20 dB lower at high frequencies. Therefore, the numerical errors can be increased at anti-resonances when the ear is in the shadow region of the head.

It is time consuming to evaluate the HRTF database numerically produced by discrete positions of sound sources in the far field. Kahana (2000) suggested an alternative efficient method of numerical calculation by using the principle of reciprocity: The acoustic pressure p_A at point A in a fluid produced by a source at another point B is the same as the acoustic pressure p_B at point B produced by the same source at point A (Pierce, 1989). This means that the sound pressure at the eardrum produced by the source at a given field point in the far field is assumed to be the same as the sound pressure at the given field point in the far field produced by the same source at the eardrum. The sound pressure levels at the eardrum of the DB65 ear in the primary sound field shown in Fig. 9.18 are evaluated at the field points located in the horizontal plane at every 15° angle of azimuth and one metre away from the centre of the coordinate system, when a monopole sound source is located 2 mm away from the centre of the eardrum as discussed in section 8.3. Figure 9.27 shows an example of the principle of reciprocity in the case of 45° azimuth. The solid line represents the sound pressure levels evaluated at the eardrum of the DB65 produced by the source at the far field point, and the dashed line represents those evaluated at the same far field point produced by the same source at the eardrum. Figure 9.28, 9.29, and 9.30 corresponds to the case of 135°, 225°, and 315° azimuth respectively. Figure 9.31 shows differences between values on the solid lines and corresponding values on the dashed lines in Fig. 9.27, 9.28, 9.29, and 9.30. These figures show that the principle of reciprocity is reasonably applied when the source is in the same side of the ear. However, there is some mismatch above 8kHz when the ear is in the shadow zone of the head. This may be because the sound field near the eardrum can be sensitive to any tiny numerical errors at the anti-resonance as discussed previously. Therefore, the numerical errors can be increased at high frequencies above 8kHz when the ear is

in the shadow region of the head. Figure 9.32 shows the condition number of the acoustic transfer matrix in this case evaluated in the secondary sound field without the ear. Note that this matrix has a dimension of 84 (the number of control points) × 45 (the number of headphone sources). The maximum condition number is 8.6×10^5 at 200Hz in this case. Although the high condition number implies the system could be ill-conditioned, Figure 9.23 and 9.24 show nearly negligible control error at low frequencies because in these numerical simulations it is assumed that noise does not exist. If there is noise, the system may be ill-conditioned. However, when the number of headphone sources is reduced, the condition number is reduced, and this will be presented in section 10.2. Even when an inverse problem may be poorly conditioned, useful results can still be found by using methods aimed at "regularising" the solution (Nelson, 2001).

The interaural level difference can be obtained by subtracting the sound pressure levels at the left eardrum from those at the right eardrum when the source is on the right hand side of the head. Figure 9.33 shows the interaural level differences between the sound pressure levels at both the DB65 ears of the head in the primary field and Figure 9.34 shows the corresponding interaural level differences in the secondary field reproduced by the 45 headphone sources in the perfectly absorbent headphone. These two figures look similar. Figure 9.35 shows the differences of interaural level differences between the desired ILD in the primary field shown in Fig. 9.33 and the reproduced ILD in the secondary field shown in Fig 9.34 for every 15° azimuth of the monopole source directions in the horizontal plane. The colour filled contour figure is scaled from 0 to 6 dB. Note that azimuth angles are from 15° to 165° since the ILD is a binaural quantity and does not exist at 0 and 180° azimuths. These figures show that the greatest difference of ILDs is less than 1 dB. As in the case of Figure 9.20, this can also be regarded as successful reproduction. Note that the good reproduction of the sound pressure levels at both ears is sufficient to produce a good reproduction of the ILD. This good performance again verifies the theory of the RISE system. Figure 9.36 shows the average differences of the ILDs over frequency for various source directions in the horizontal plane. The performance is slightly worse when the source is at the rear side of the head, again possibly due to the errors caused by the reflected sound waves from the rear side of the ear. Figure 9.37

shows the average differences of the ILDs over various source directions in the horizontal plane. One sharp peak is observed at 9400Hz. This error at anti-resonance was discussed before. However, the error at resonance of 3200Hz is suppressed. This implies that the errors at both eardrums are similar at resonance and are different at anti-resonance. This also implies that the numerical errors are small at 3200Hz since it is a relatively low frequency and the errors resulting from the assumption are similar at both ears. The numerical errors can also result in large reproduction errors of the ILDs at 9400Hz since it is a relatively high frequency at which the sound field around either eardrum may change differently. Figure 9.38 shows the interaural level differences for the source at 30° azimuth and Figure 9.39 shows that for the source at 135° azimuth, for example. The solid line represents the desired ILDs evaluated in the primary sound field, and the dashed line represents the reproduced values evaluated in the secondary sound field. Figure 9.38 shows a good example of nearly perfect reproduction, and Figure 9.39 shows more errors at high frequencies around 9400Hz than the errors shown in Fig. 9.38 as discussed before.

The interaural phase difference can be obtained by subtracting the phase of the sound pressure at the left eardrum from that at the right eardrum when the source is at the right hand side of the head. Figure 9.40 shows that the interaural phase differences in the primary field for every 15° azimuth of the monopole source directions in the horizontal plane. The interaural phase difference shows the pure group delay of the signal due to the difference of the propagation length of the incident waves. Figure 9.41 shows the differences of the interaural phase difference between the desired IPD in the primary field and the reproduced IPD in the secondary field. Most differences are small, less than about 10°. The IPD is only important at low frequencies as discussed in chapter 2, and its difference is less than 3° up to a frequency of 3 kHz. The interaural time difference can be obtained from the group delay of the signal that is given by

$$\mathrm{ITD} = -\frac{\mathrm{d}\phi(\omega)}{\mathrm{d}\omega} = -\frac{\mathrm{IPD}}{360\Delta f} \tag{9.1}$$

where the ITD is in seconds, the IPD is in degrees, and ϕ is the phase in radians. The IPD up to a frequency of 1 kHz is used to calculate the ITD. Figure 9.42 shows the interaural time difference in the primary field in microseconds for every 15° azimuth of the monopole source directions in the horizontal plane. Figure 9.43 shows the error of the ITD in percentage for various source directions in the horizontal plane, which is the differences of the ITD between the desired ITD in the primary field and the reproduced ITD in the secondary field divided by the desired ITD in the primary field. This shows that the error in the ITD is below 0.18%, which is nearly negligible. Since the interaural time difference is nearly frequency independent, it is nearly perfectly reproduced in the secondary field.

These results show the RISE system with a multichannel headphone can work very well over any angle of incident waves at least on the horizontal plane if 45 headphone sources are used and the boundary condition of the headphone is perfectly absorbent. The system should work over any incident waves in three dimensional space since the headphone sources are distributed evenly. The good performance might be extended to frequencies above 10 kHz. The dominant source of error in these numerical simulations is assumed to be the numerical error since the creation of virtual acoustic images in the horizontal plane uses binaural cues dominantly. Note that the numerical errors only exist in numerical simulations and do not exist in real systems

9.4 Median and frontal plane

The median plane in the head-related coordinate system shown in Fig. 9.8 is the x-y plane where the azimuth angle is zero. The frontal plane is the z-y plane where the azimuth angle is 90°. In this section, the single monopole sound source in the primary sound field is located on the median or frontal plane for every elevation angle in increments of 15°. The elevation angle is usually from −90° to 90°, but in this section the elevation angle ranges from −165° to 180° on the basis of the positive x axis for the median plane and the positive z axis for the frontal plane. The source is in front of the listener at $(\phi,\theta)=(0,0)$ and the source is at the rear at $(\phi,\theta)=(0,180°)$ in the

median plane. The source is to the right ear at $(\phi,\theta)=(90°,0)$ and the source is to the left ear at $(\phi,\theta)=(90°,180°)$ in the frontal plane. The source is one metre away from the centre of the coordinate system, and the peak amplitude of sound pressure one metre away from the source is set to unity at all frequencies.

Figure 9.44 shows the sound pressure levels at the eardrum of the DB65 in the primary field for every 15° elevation of the monopole source directions in the median plane, and Figure 9.45 shows the corresponding sound pressure levels at the eardrum of the DB65 in the secondary field reproduced by the 45 headphone sources in the perfectly absorbent headphone. Those two figures show similar patterns of the curves. Figure 9.46 shows the sound pressure level differences at the eardrum between the desired values in the primary field shown in Fig. 9.44 and the reproduced values in the secondary field shown in Fig 9.45. The colour filled contour figure is scaled from 0 to 6 dB. This shows nearly all eardrum sound pressure level differences are below 1 dB for all elevation angles up to a frequency of 10 kHz. This can be regarded as successful reproduction. This performance is even better than that in the horizontal plane shown in Figure 9.20. This good performance again verifies the theory of the RISE system again and the good reproduction might be extended above 10 kHz. Figure 9.47 shows the eardrum sound pressure level differences averaged over frequency for each source direction in the median plane. This also shows that nearly all values are below 1 dB. The performance is similar for all source angles but just slightly worse when the source is at the rear side to the head due to reflected waves from the back side of the ear. Figure 9.48 shows the eardrum sound pressure level differences averaged over various source directions in the median plane. One sharp peak is observed at 3200 Hz at the resonance frequency of the DB65 artificial ear. Note that there are far fewer errors at the anti-resonance around 9400Hz than those in the horizontal plane shown in Fig. 9.22.

Figure 9.49 shows the average sound pressure level differences between the desired sound pressure levels at control points in the primary field and the reproduced values in the secondary field. This shows that the control error is below 0.1 dB, which is nearly negligible. Figure 9.50(a) shows the sound pressure level at the DB65 eardrum for the source at 90° elevation and Figure 9.50(b) shows that for the source at 15°

elevation in the frontal plane, for example. The solid line represents the desired sound pressure levels at the eardrum evaluated in the primary sound field, and the dashed line represents the reproduced values evaluated in the secondary sound field. Figure 9.50(a) shows good example of nearly perfect reproduction. There is a small error around the anti-resonance of 9400Hz in Fig. 9.50(b). Figure 9.44 shows the anti-resonance at 9400Hz is activated at some particular angles of incident waves in the median plane. When the source is located in the median plane, binaural cues do not exist under the assumption that the head is symmetric in the median plane. Therefore, only the monaural spectral cue gives information regarding sound localization. Figure 9.46 shows the monaural spectral response can be successfully reproduced by using the RISE system with the multichannel headphone.

Figure 9.51 shows the sound pressure levels at the eardrum of the DB65 in the primary field for every 15° elevation of the monopole source directions in the frontal plane, and Figure 9.52 shows the corresponding sound pressure levels at the eardrum in the secondary field reproduced by the 45 headphone sources in the perfectly absorbent headphone. Those two figures also show similar patterns of curves. Figure 9.53 shows the sound pressure level differences at the eardrum between the desired values in the primary field shown in Fig. 9.51 and the reproduced values in the secondary field shown in Fig 9.52. The colour filled contour figure is scaled from 0 to 3 dB. It shows nearly all eardrum sound pressure level differences are below 1 dB for all elevation angles up to a frequency of 10 kHz, which can again be regarded as successful reproduction. This performance is even better than that in the horizontal plane shown in Figure 9.20 and the median plane shown in Figure 9.46. This good performance again verifies the theory of the RISE system and the good reproduction might be extended over 10 kHz. Figure 9.54 shows the eardrum sound pressure level differences averaged over frequency for each source direction in the frontal plane. This shows nearly all values are below 0.7 dB, which is also better than other cases of the horizontal or median plane. The performance is similar for all source angles but just slightly worse when the source is in the shadow zone of the head. Figure 9.55 shows the eardrum sound pressure level differences averaged over various source directions in the frontal plane. One sharp peak is observed at 3200Hz at the resonance frequency and there is no peak is at 9400Hz. These results show the same tendency

as that shown in the case of the median plane. Figure 9.56 shows the average sound pressure level differences at the control points between the desired values and the reproduced values. This shows that the control error is below 0.2 dB, which is nearly negligible. Figure 9.57(a) shows the sound pressure level at the DB65 eardrum for the source at 30° elevation and Figure 9.57(b) shows that for the source at 150° elevation in the frontal plane, for example. Figure 9.57(a) shows a good example of nearly perfect reproduction. Figure 9.57(b) shows the error of the reproduction is not great since the eardrum sound pressure levels are not much lower at high frequencies compared with other cases of the horizontal and median plane, even though the ear is in the shadow zone.

Figure 9.58 shows the interaural level differences at both the DB65 ears of the head in the primary field and Figure 9.59 shows the corresponding ILDs in the secondary field reproduced by the 45 headphone sources in the perfectly absorbent headphone for every 15° elevation of the monopole source directions in the frontal plane. Figure 9.60 shows the differences of the ILDs between the desired ILD in the primary field shown in Fig. 9.58 and the reproduced ILD in the secondary field shown in Fig 9.59. The colour filled contour figure is scaled from 0 to 3 dB. Note that elevation angles are from −75° to 75° since the ILD is a binaural quantity and does not exist at ±90° elevations. Those figures shows most differences of ILDs are less than 1 dB as in the case of the results shown in Figure 9.53. This can again be regarded as successful reproduction. This performance is better than that in the horizontal plane shown in Figure 9.35. This good performance again verifes the theory of the RISE system again. Figure 9.61 shows the average differences of the ILDs over frequency for various source directions in the frontal plane. This shows all values are below 0.8 dB. The performance is roughly symmetrical for 0 elevation. Figure 9.62 shows the average differences of the ILDs over various source directions in the frontal plane. This shows all values are below 1.1 dB and there is no peak. This confirms the better performance in the frontal plane. Figure 9.63 shows the interaural level differences for the source at 30° elevation and this example shows how well the system works in the frontal plane. Figure 9.64 shows the differences of the interaural phase differences between the desired IPD in the primary field and the reproduced IPD in the secondary field. Most differences are small, less than about 10°. Figure 9.65

shows the interaural time differences in the primary field in microseconds for various source directions in the frontal plane. This figure looks same as Fig. 9.42 since the head is spherical. Figure 9.66 shows the error of the ITD in percentage, and it is below 2.2 %. Those results show the RISE system with a multichannel headphone can work better over any angle of incident waves in the frontal plane than other cases of the horizontal and median plane because there is no sharp great dip in the frequency response of the ear at high frequencies up to 10 kHz.

9.5 Conclusion

Various kinds of control field are tested to find out which one is the best for the RISE system by undertaking numerical simulations. The small and sparse control field is optimal and efficient among three different control fields since the performance of the RISE system depends on the size of the control fields more than the number of control points. A particular ideal RISE system is examined for various incident angles. The results of the numerical simulations show that the performance of the RISE system with a multichannel headphone is reasonably good over any angle of incident waves in three-dimensional space up to a frequency of at least 10 kHz if 45 headphone sources are used and the boundary condition of the headphone is perfectly absorbent. Most errors of the reproduction of the monaural and binaural spectral cues are less than 1 dB. This confirms that the theory of the RISE system is valid. The elevated source is usually difficult to reproduce in other virtual acoustic systems such as the system using non-individualized HRTFs. But, the RISE system has in principle no limit to the direction of the source relative to listener's head.

FIGURES

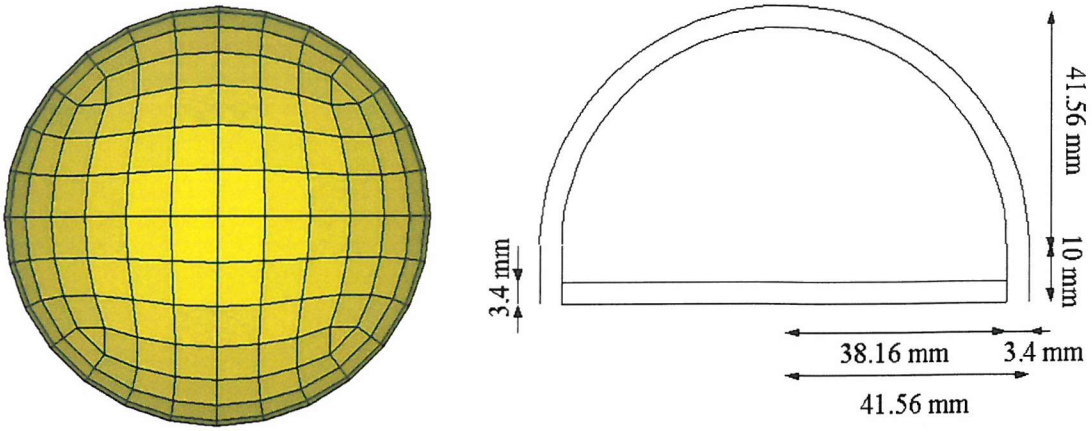

Figure 9.1 Large and sparse control field

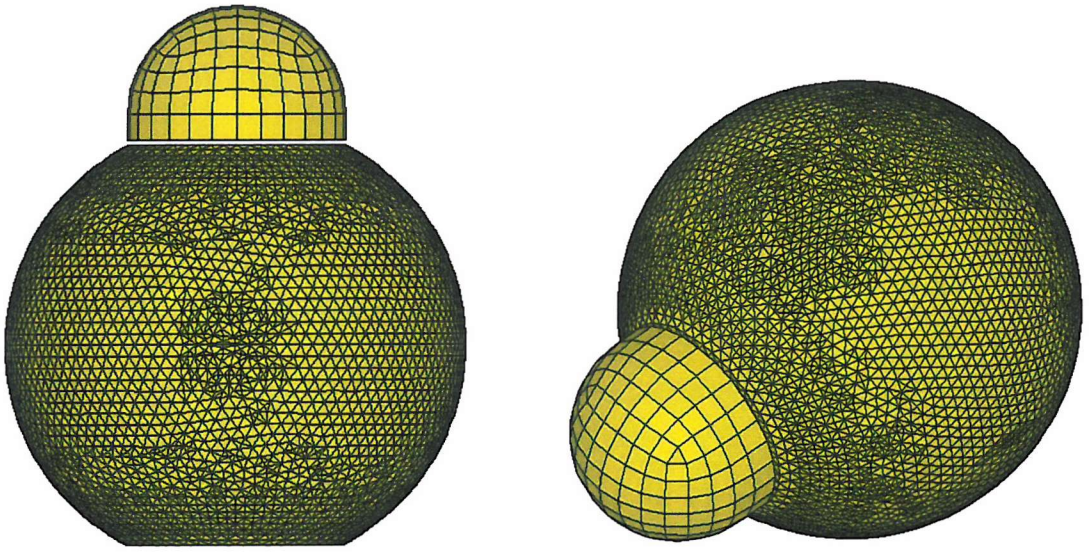

Figure 9.2 The placement of the large control field on the spherical head model.

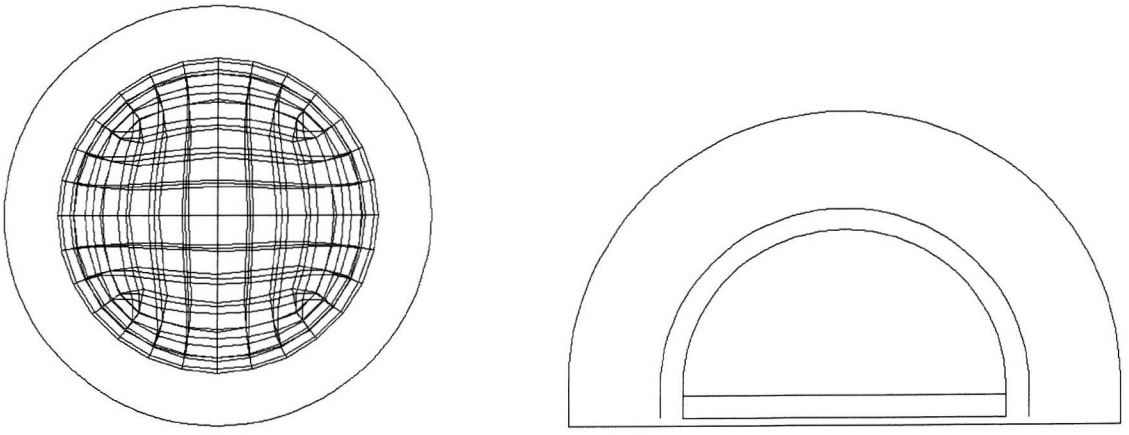

Figure 9.3 The placement of the large control field on the headphone model.

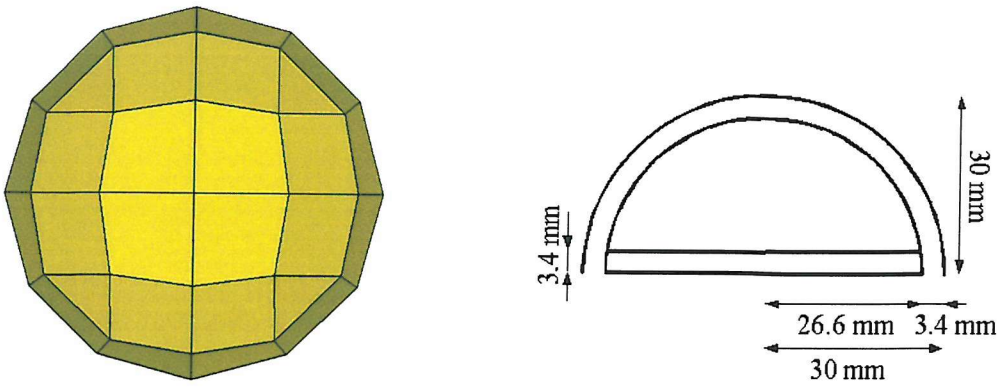

Figure 9.4 Small and sparse control field

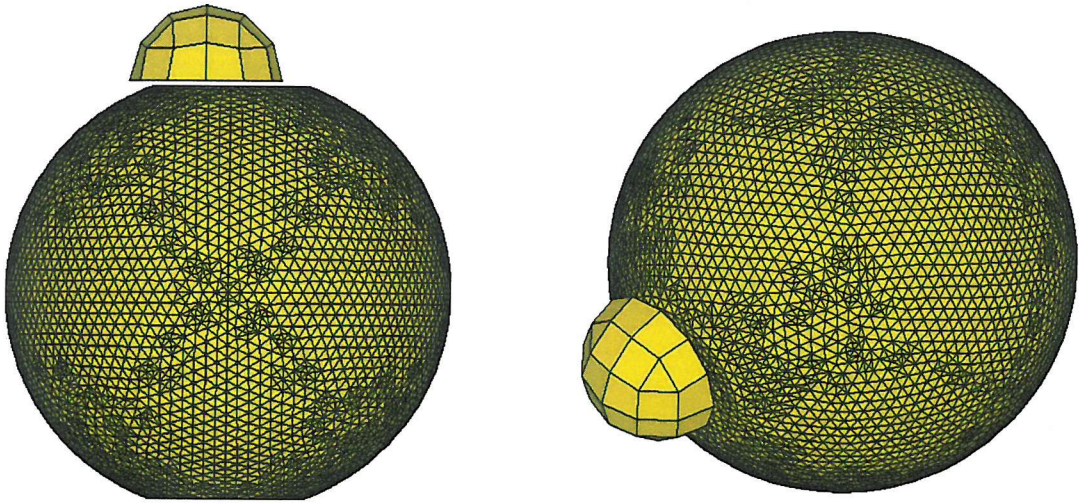

Figure 9.5 The placement of the small control field on the spherical head model.

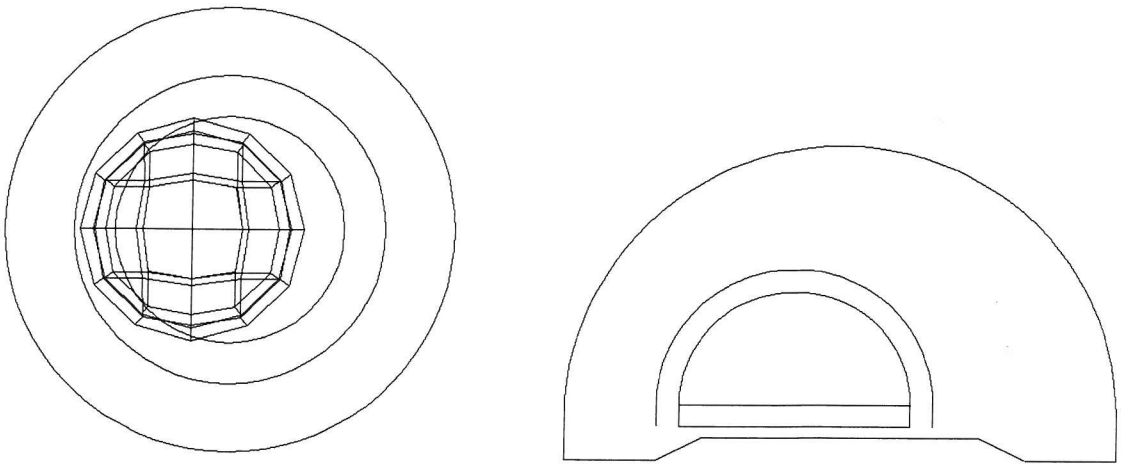

Figure 9.6 The placement of the small control field on the headphone model.

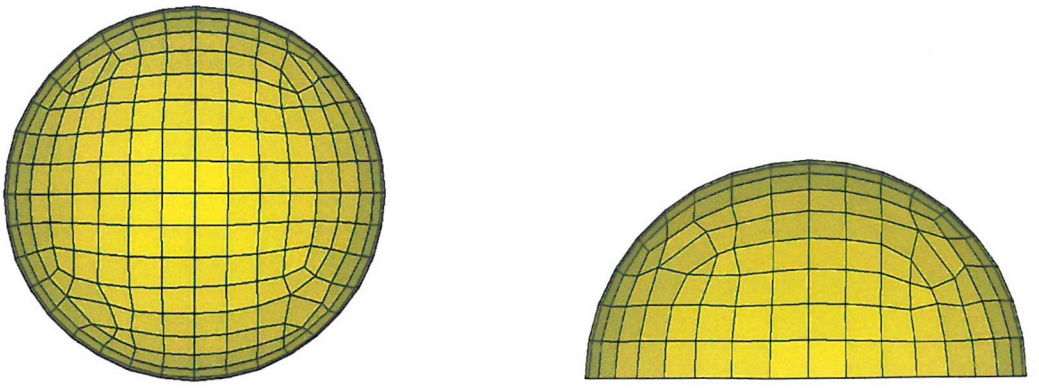

Figure 9.7 Small and dense control field

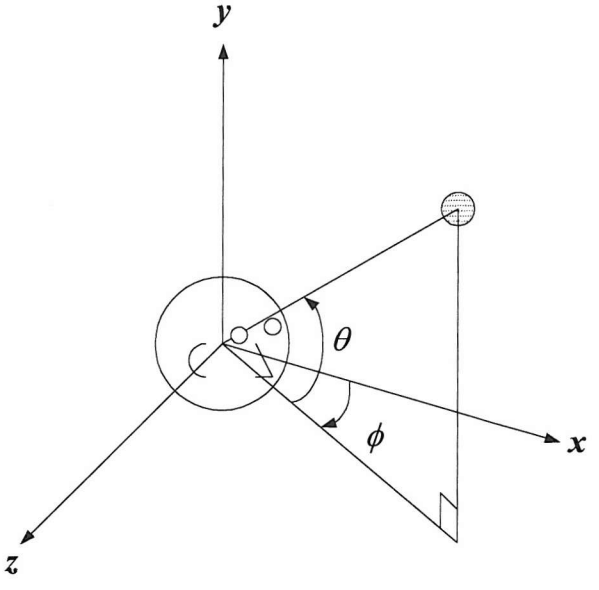

Figure 9.8 A head-related system of coordinates.

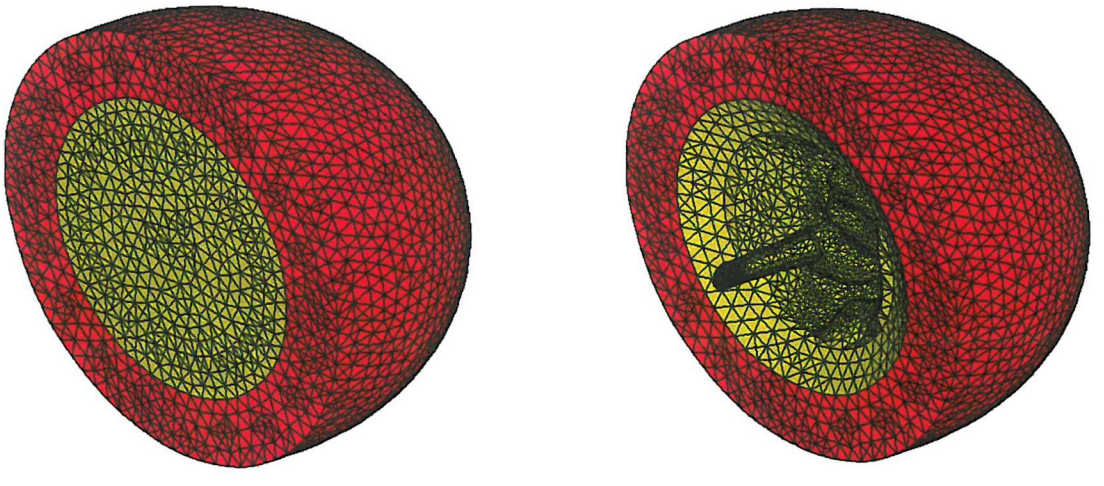

Figure 9.9 The boundary condition of the headphone.

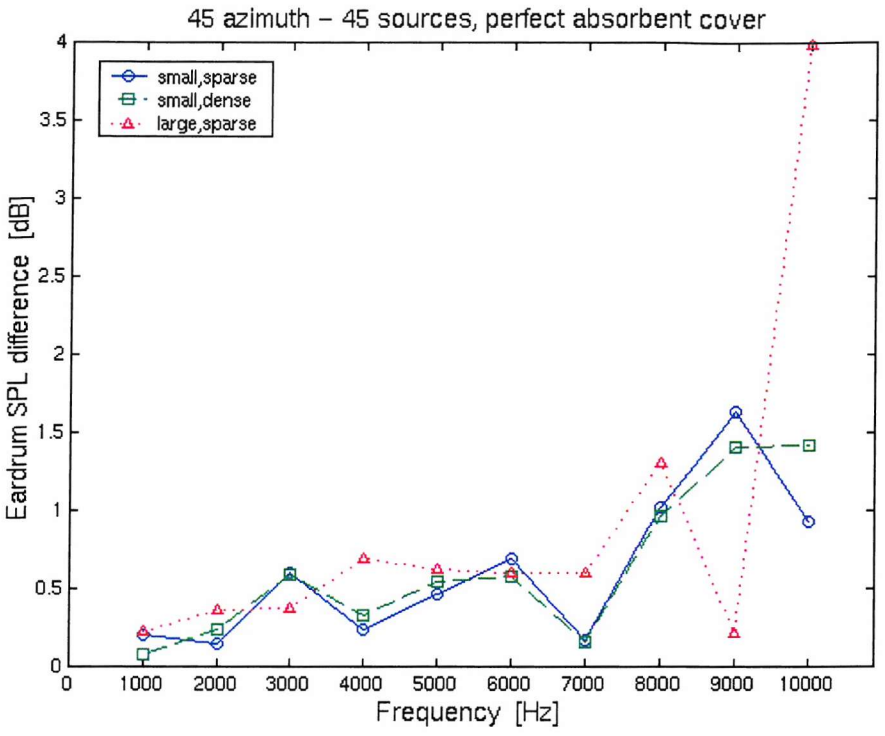

Figure 9.10 Eardrum sound pressure level differences for 45 headphone sources and the monopole source at 45° azimuth.

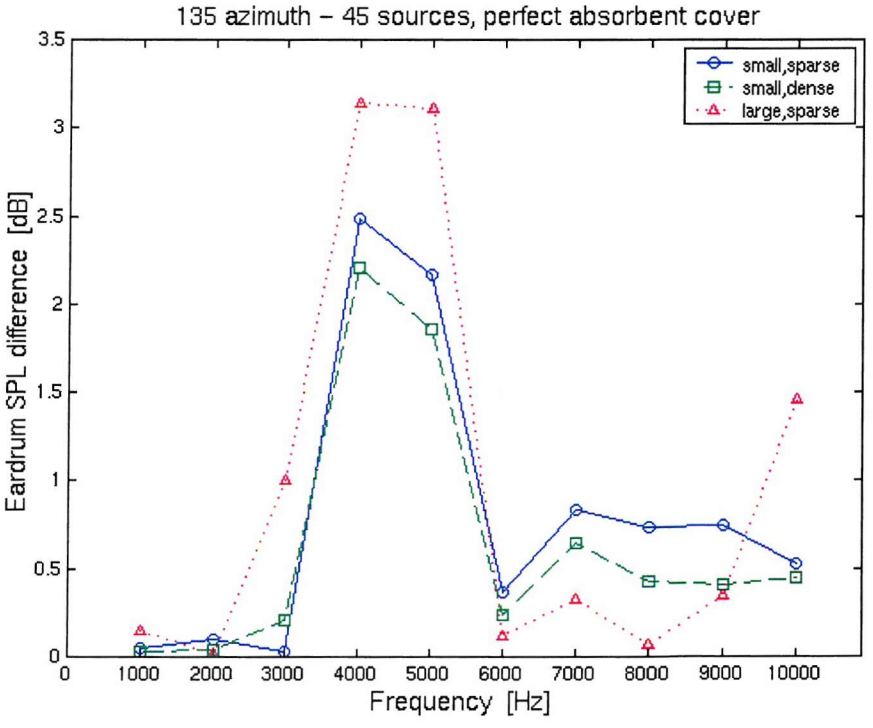

Figure 9.11 Eardrum sound pressure level differences for 45 headphone sources and the monopole source at 135° azimuth.

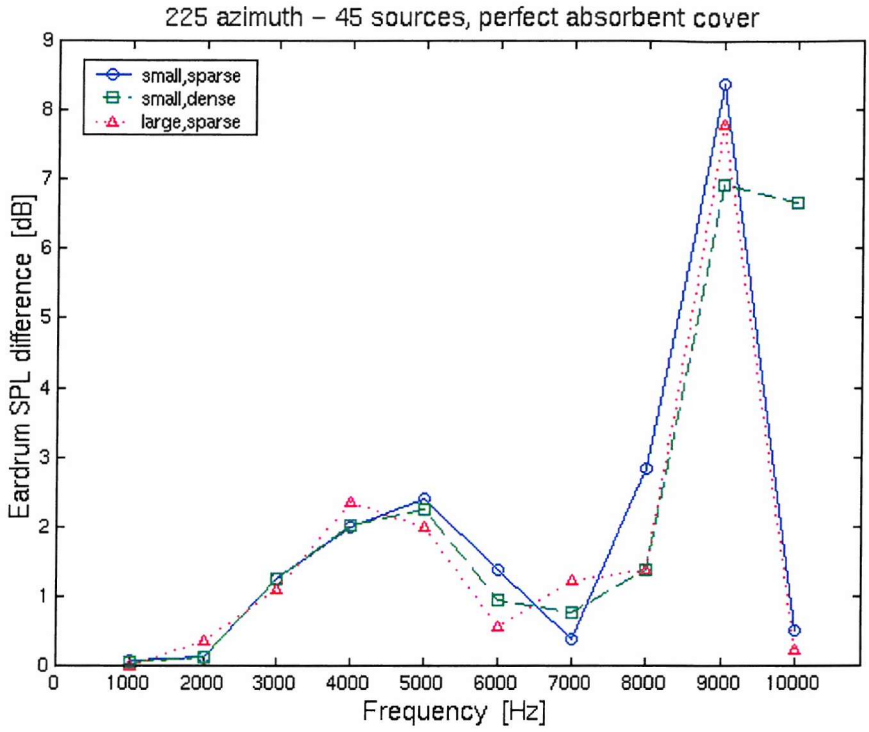

Figure 9.12 Eardrum sound pressure level differences for 45 headphone sources and the monopole source at 225° azimuth.

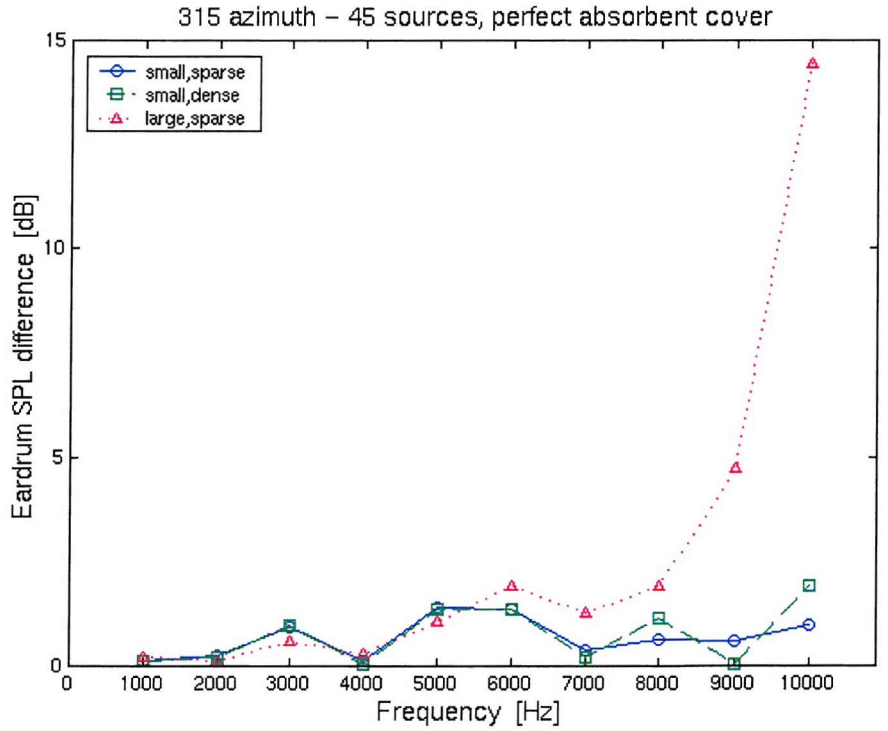

Figure 9.13 Eardrum sound pressure level differences for 45 headphone sources and the monopole source at 315° azimuth.

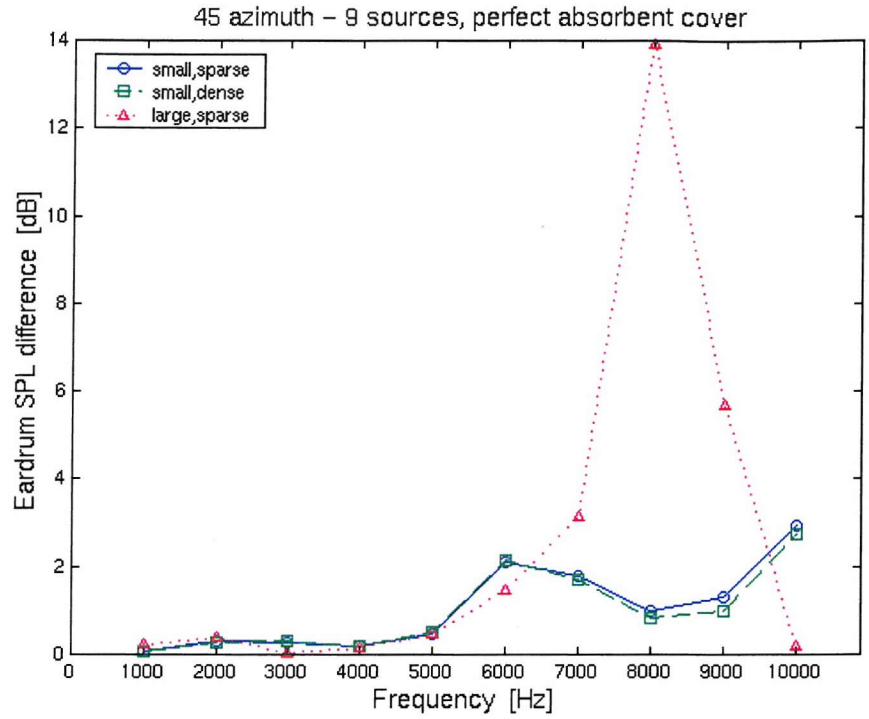

Figure 9.14 Eardrum sound pressure level differences for 9 headphone sources and the monopole source at 45° azimuth.

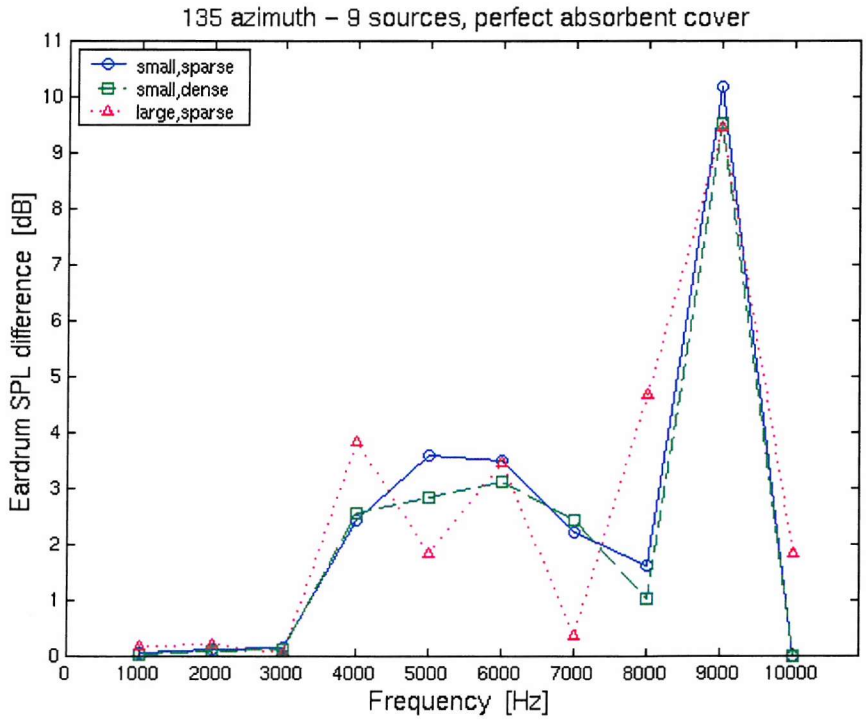

Figure 9.15 Eardrum sound pressure level differences for 9 headphone sources and the monopole source at 135° azimuth.

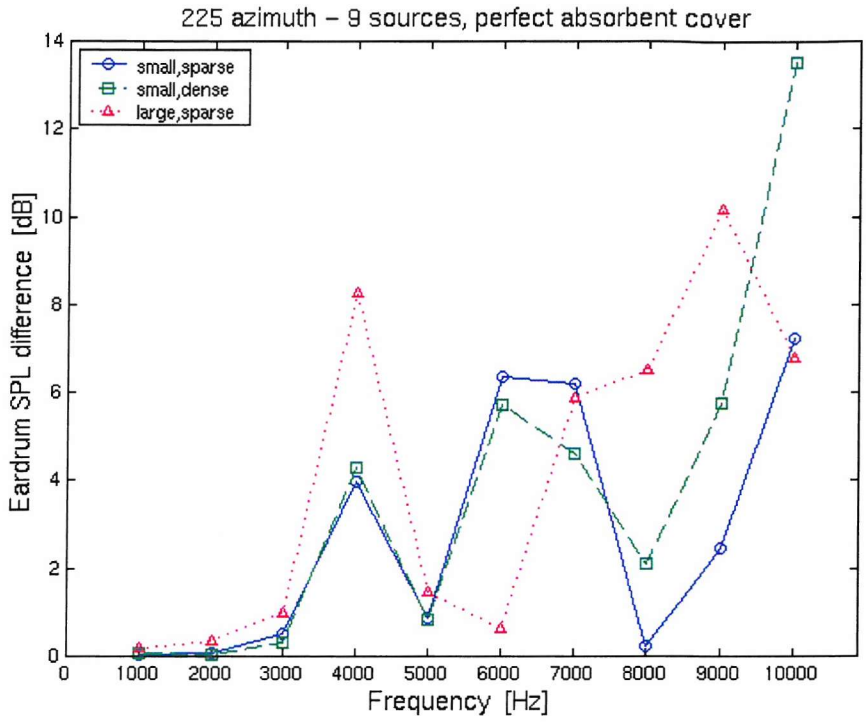

Figure 9.16 Eardrum sound pressure level differences for 9 headphone sources and the monopole source at 225° azimuth.

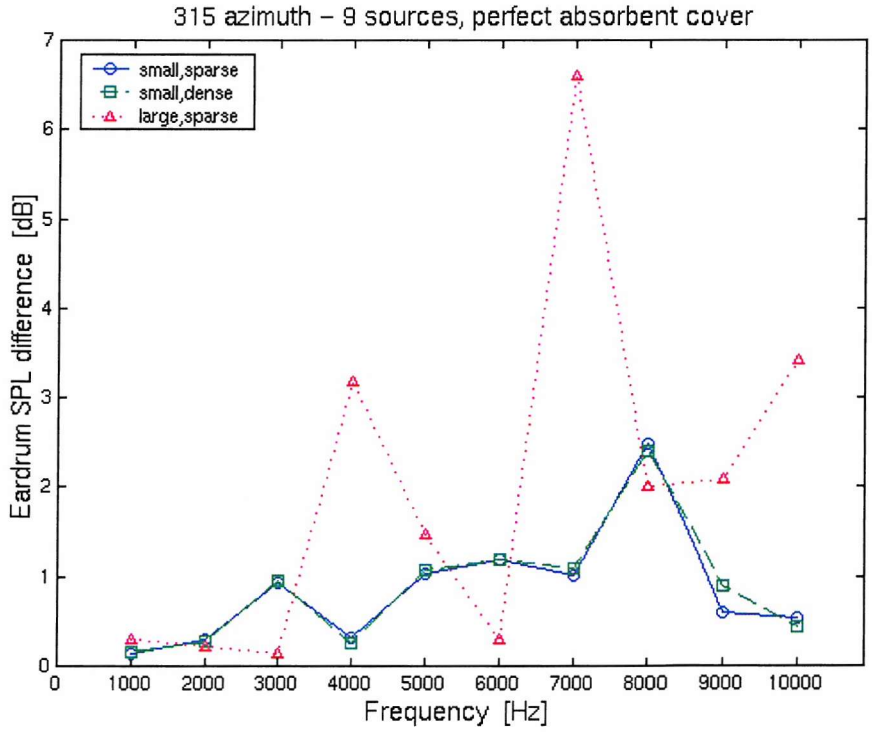

Figure 9.17 Eardrum sound pressure level differences for 9 headphone sources and the monopole source at 315° azimuth.

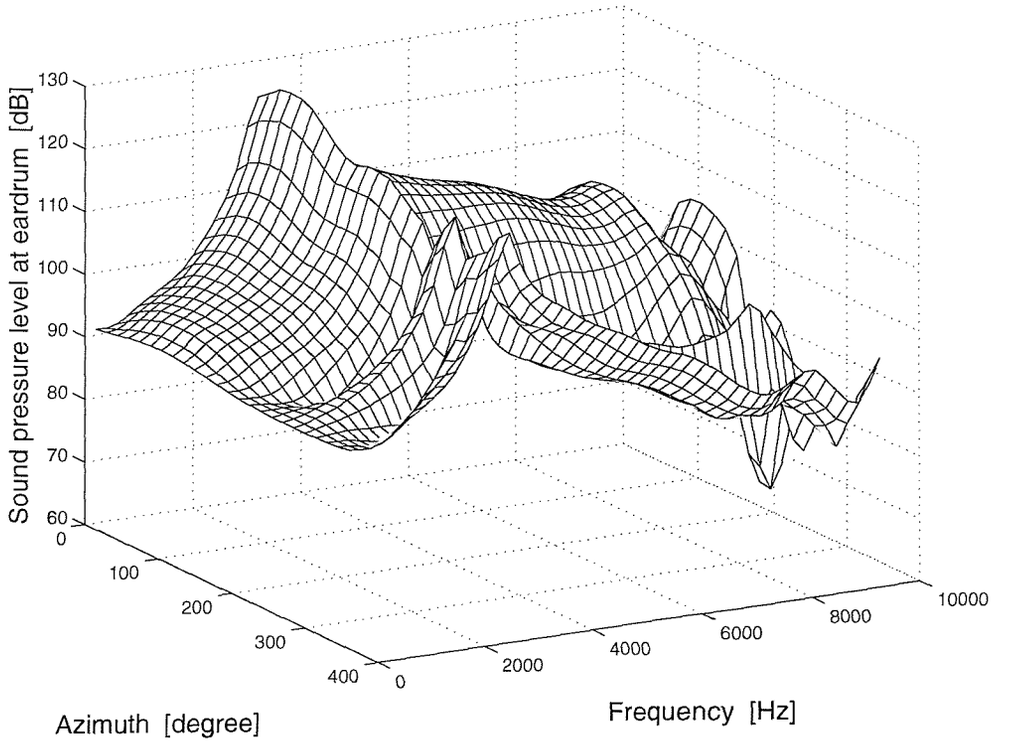

Figure 9.18 Sound pressure level at the eardrum of the DB65 in the primary field for various source directions in the horizontal plane.

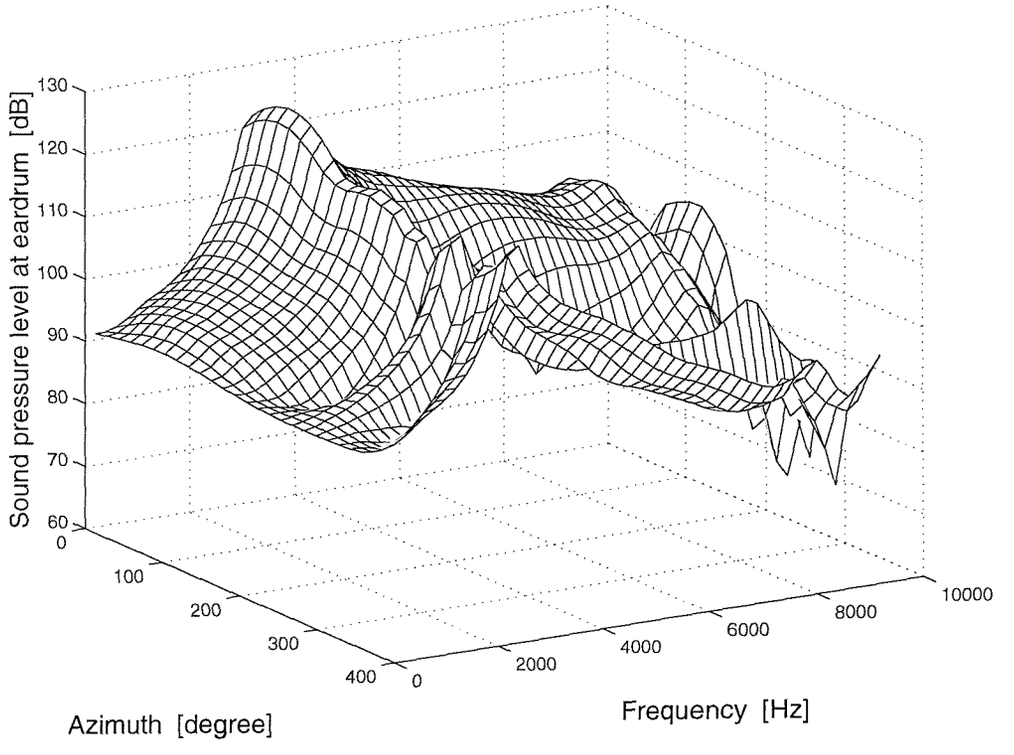

Figure 9.19 Sound pressure level at the eardrum of the DB65 in the secondary field for various source directions in the horizontal plane.

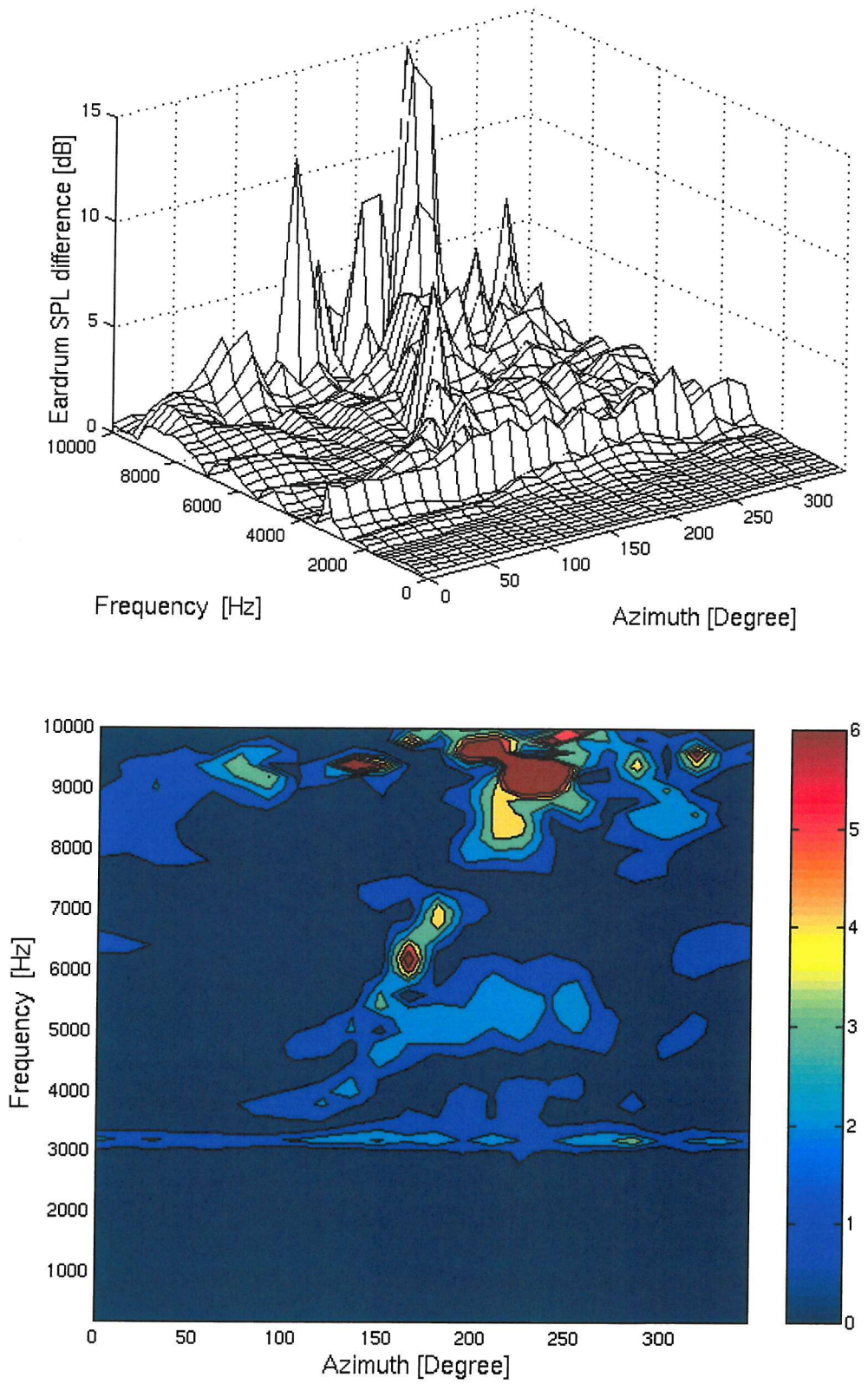

Figure 9.20 The eardrum sound pressure level differences for various source directions in the horizontal plane, 45 headphone sources, and perfectly absorbent headphone.

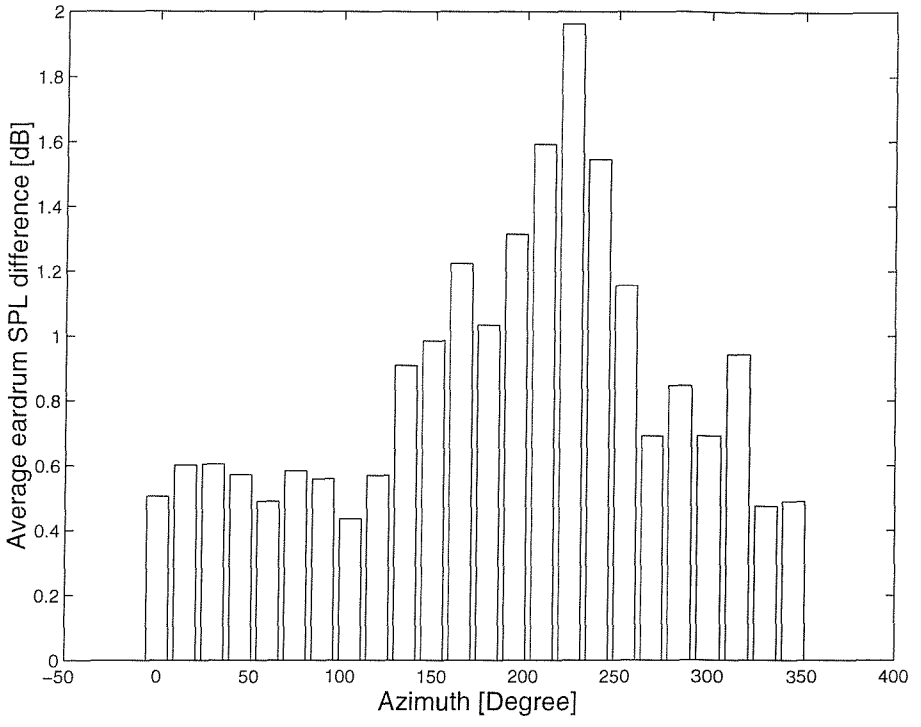

Figure 9.21 The eardrum sound pressure level differences averaged over frequency for each source direction in the horizontal plane.

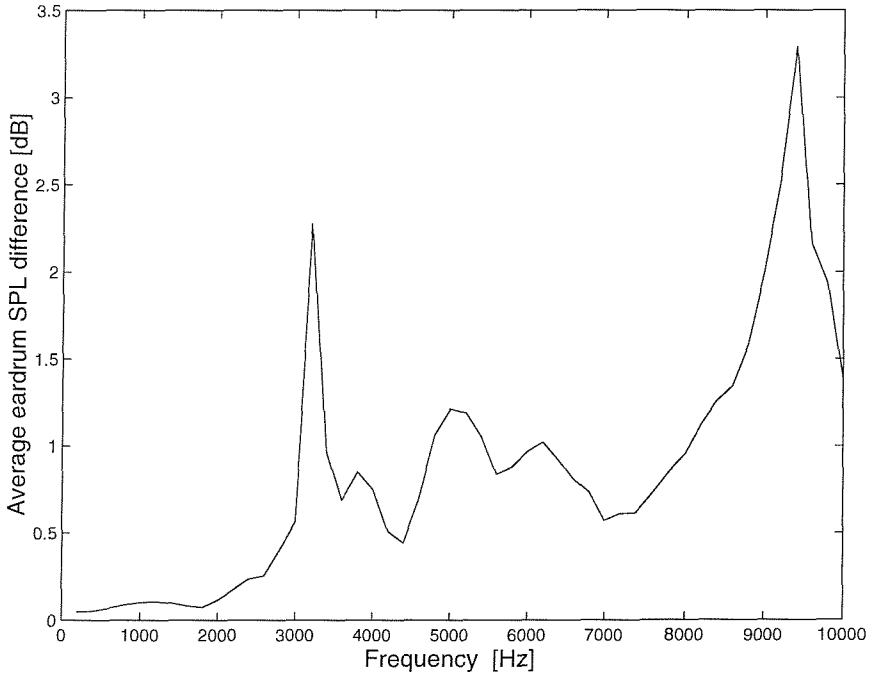

Figure 9.22 The eardrum sound pressure level differences averaged over various source directions in the horizontal plane.

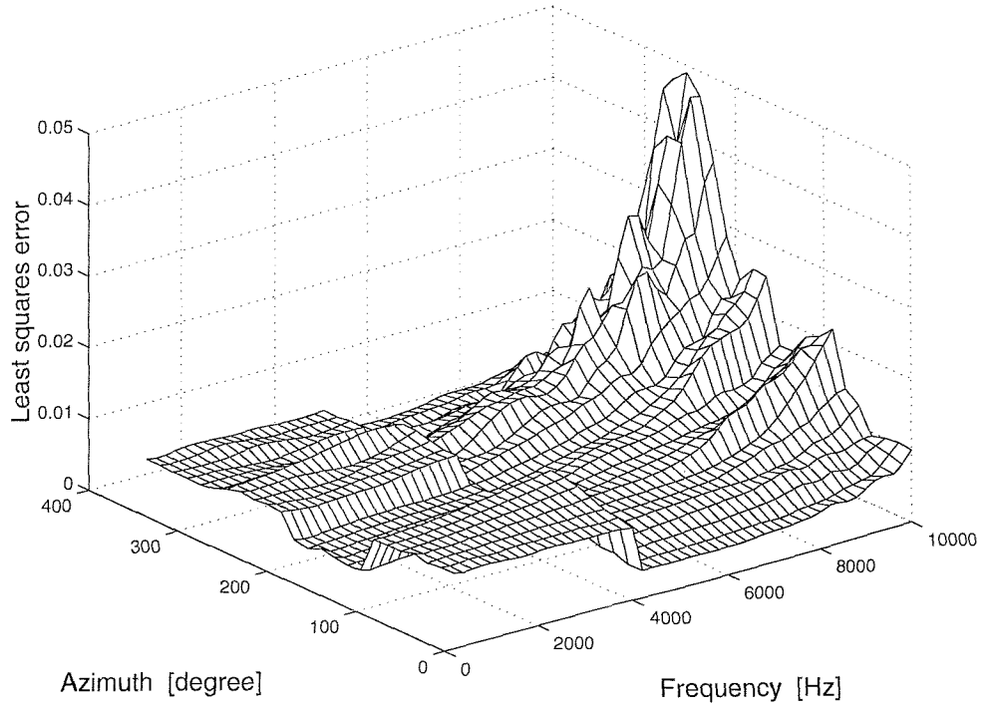

Figure 9.23 Least squares error of control points for various source directions in the horizontal plane.

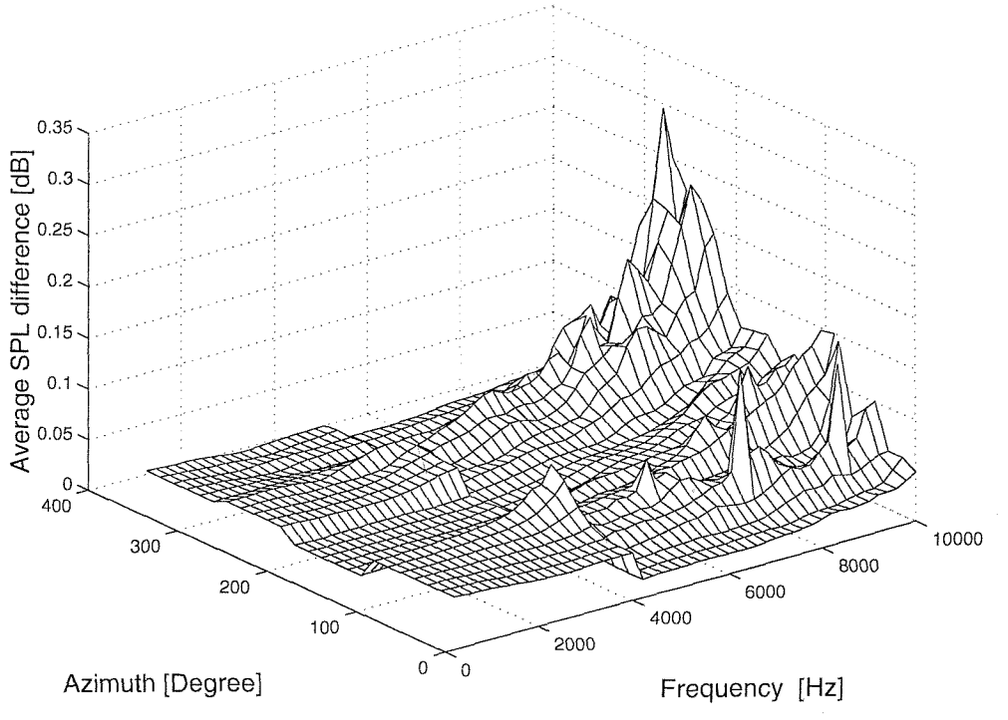

Figure 9.24 Average sound pressure level differences at control points for various source directions in the horizontal plane.

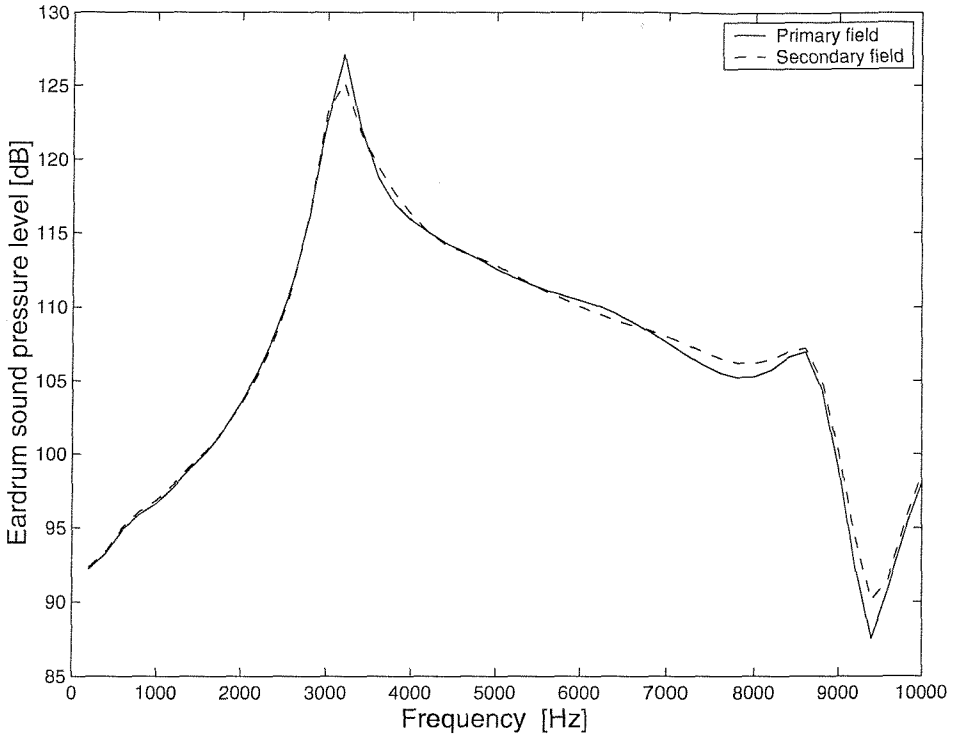

Figure 9.25 Sound pressure level at the DB65 eardrum for the source at 60° azimuth

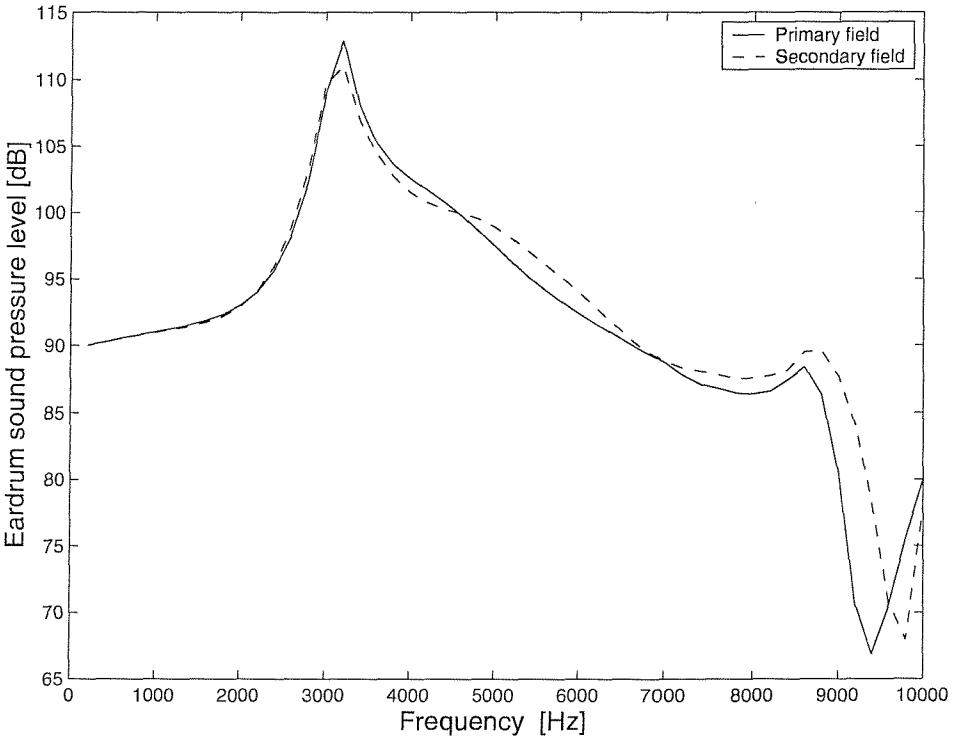

Figure 9.26 Sound pressure level at the DB65 eardrum for the source at 240° azimuth

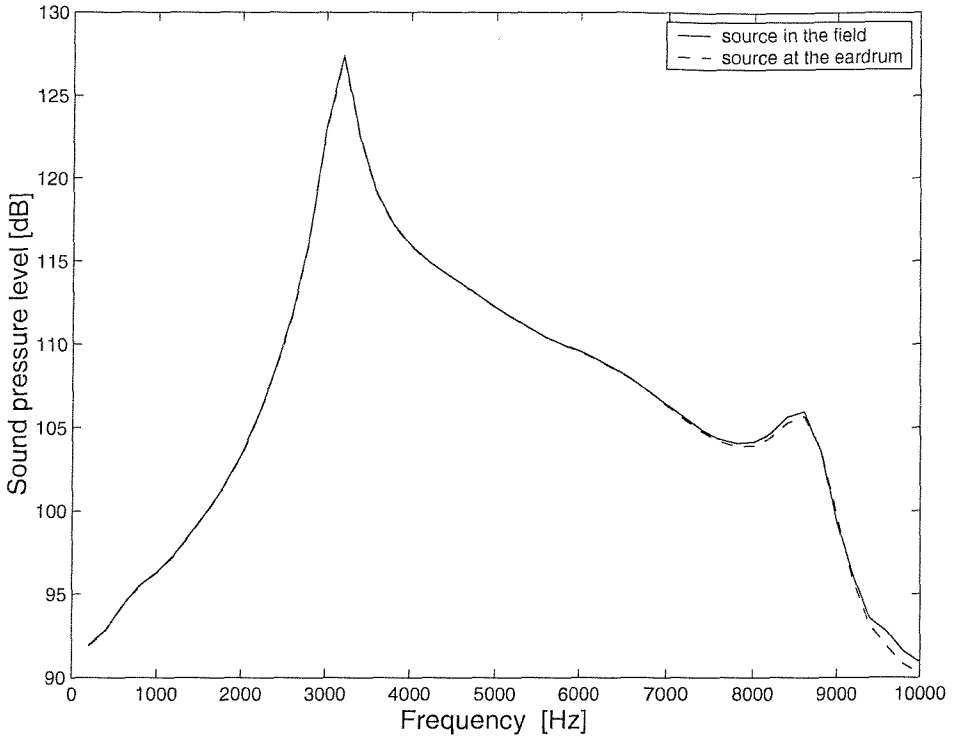

Figure 9.27 Reciprocity in the case of 45 azimuth of source direction.

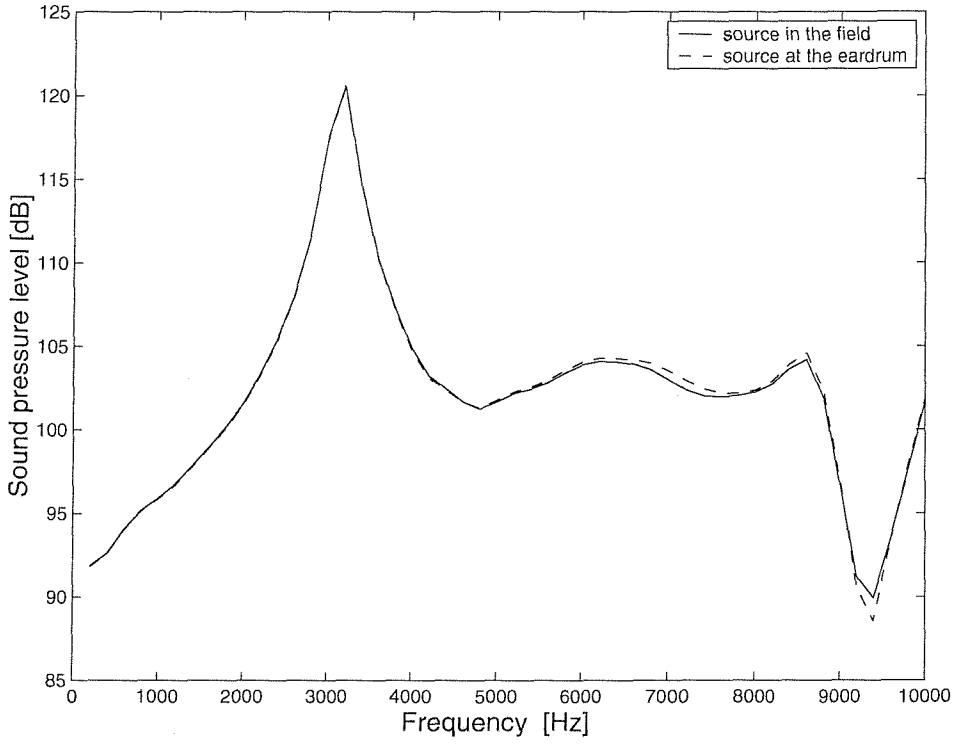

Figure 9.28 Reciprocity in the case of 135 azimuth of source direction.

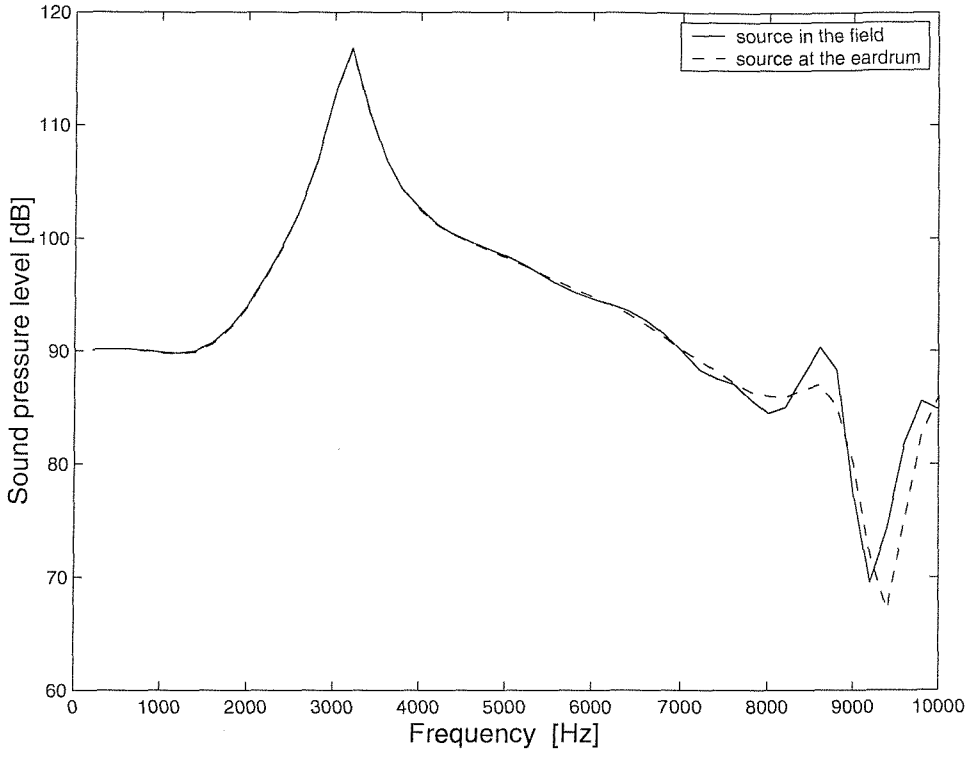

Figure 9.29 Reciprocity in the case of 225 azimuth of source direction.

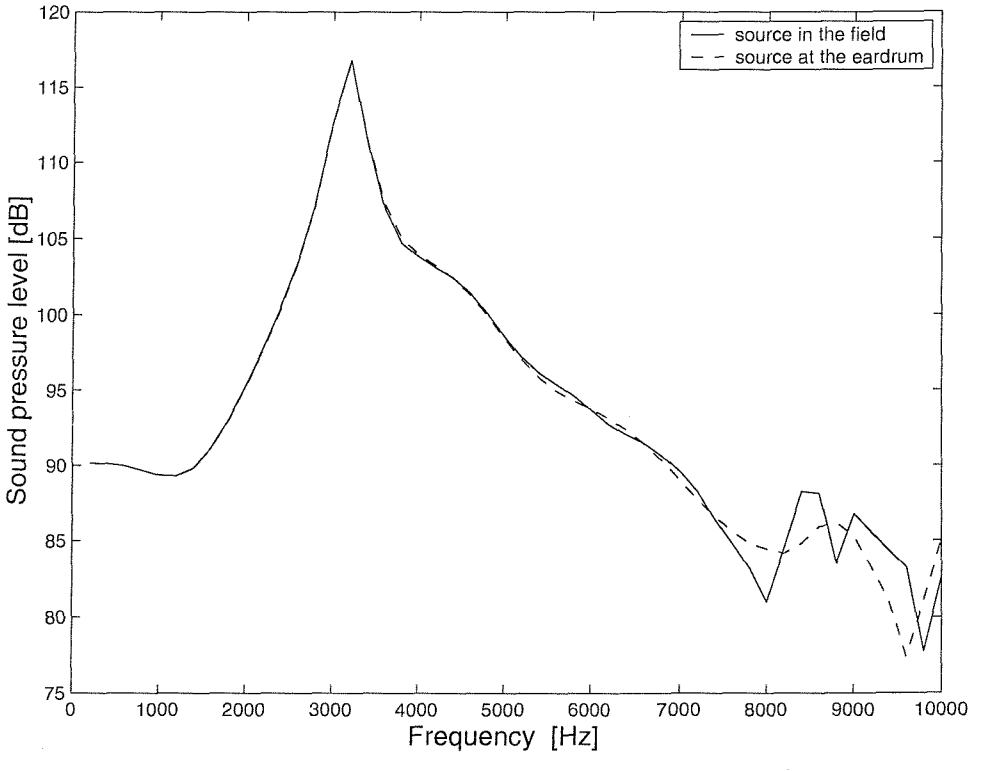

Figure 9.30 Reciprocity in the case of 315 azimuth of source direction.

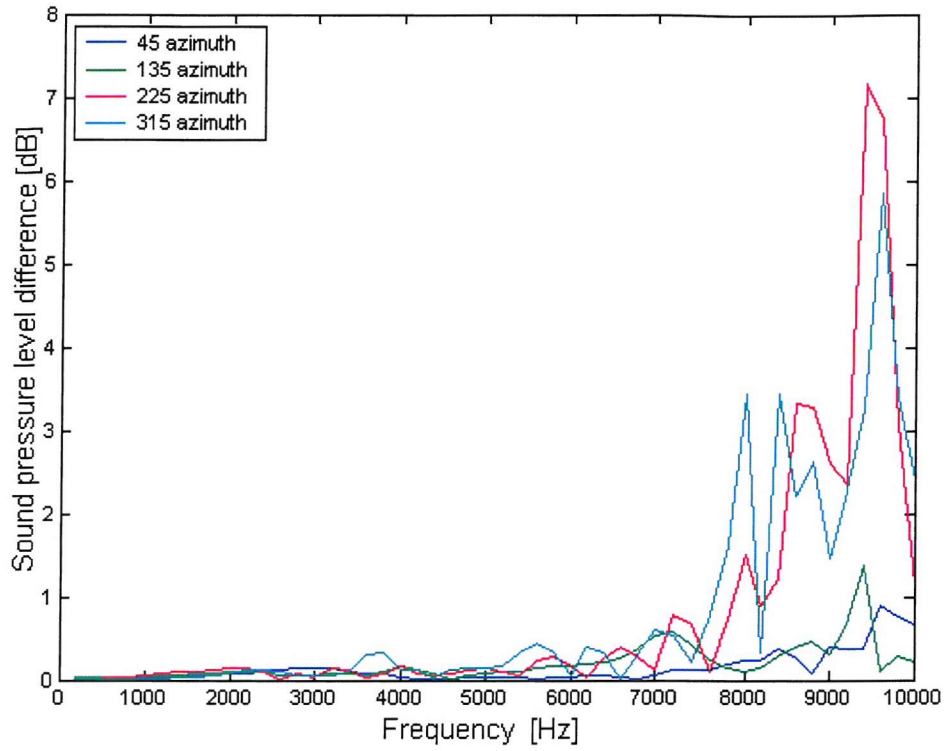

Figure 9.31 Reciprocity for various source directions.

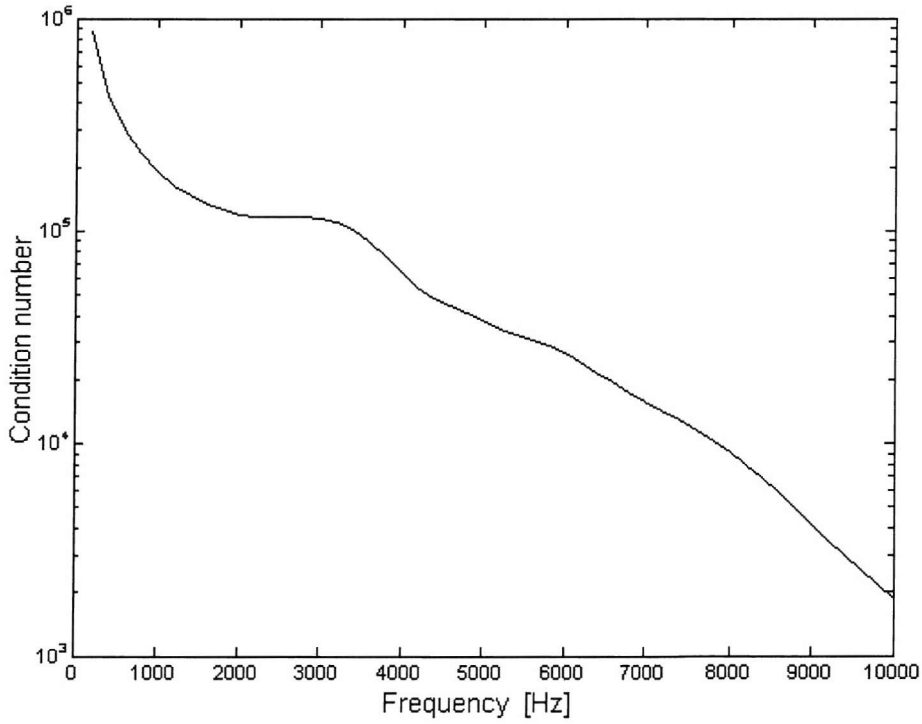

Figure 9.32 Condition number of the acoustic transfer impedance matrix.

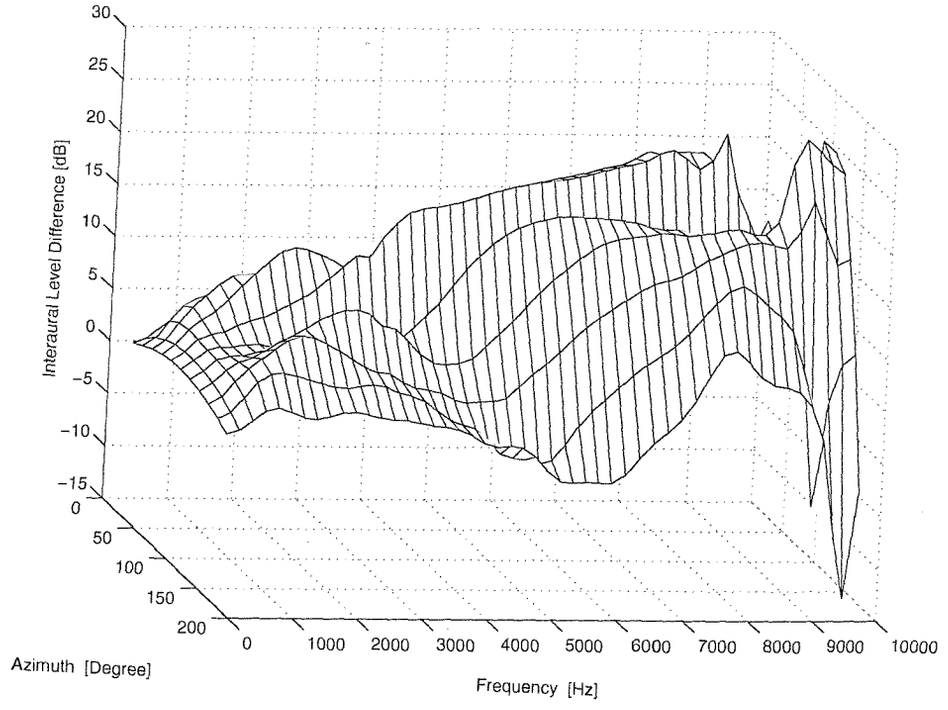

Figure 9.33 Interaural level differences in the primary field for various source directions in the horizontal plane.

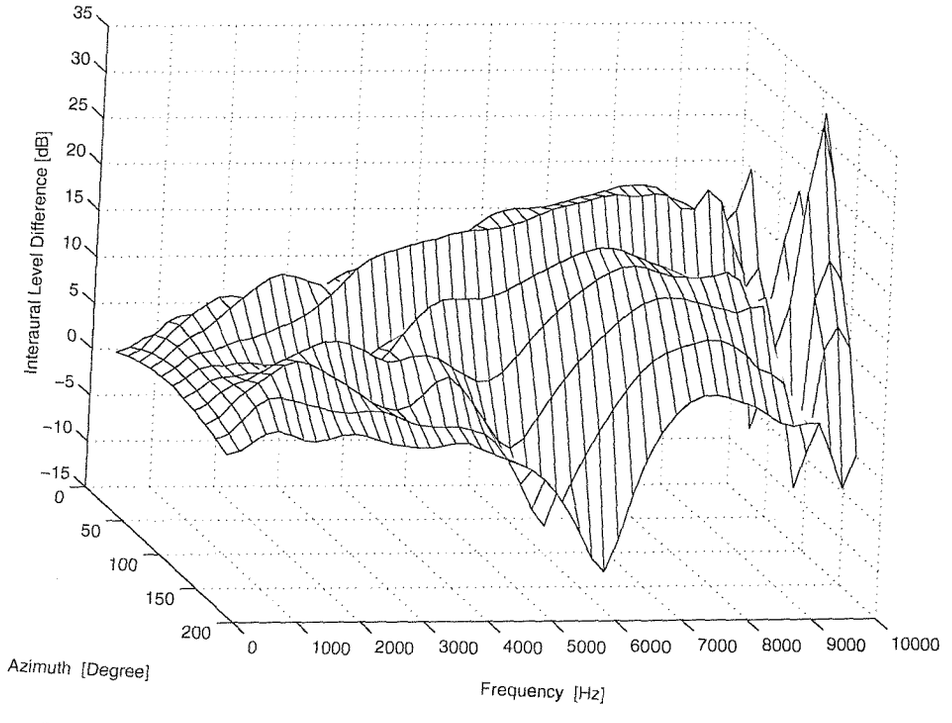

Figure 9.34 Interaural level differences in the secondary field for various source directions in the horizontal plane.

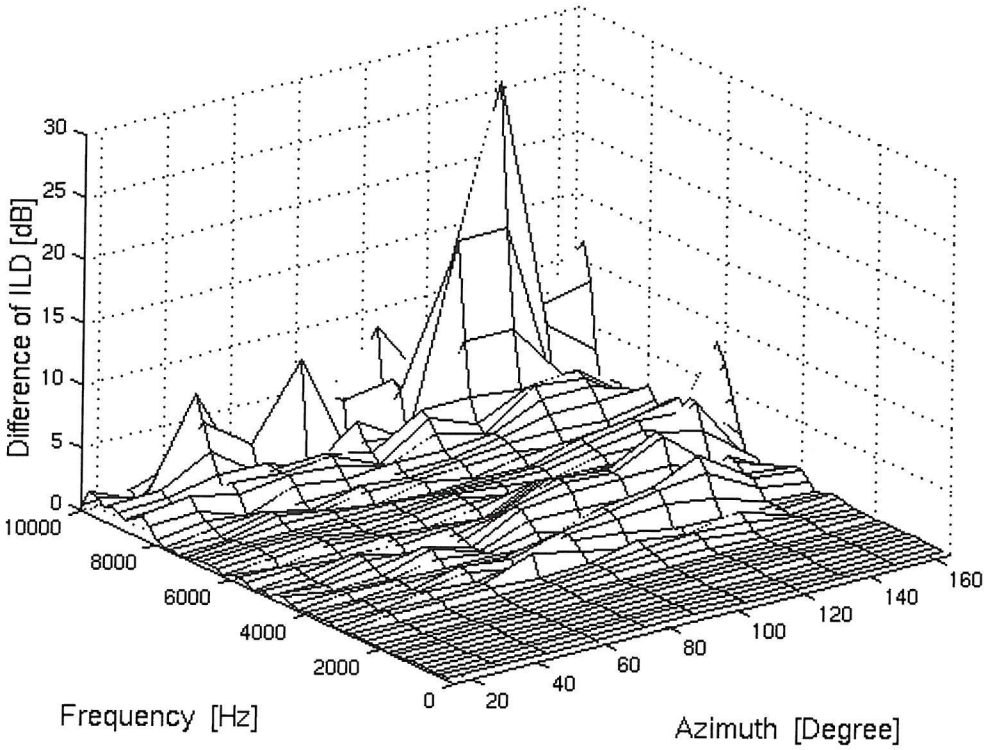

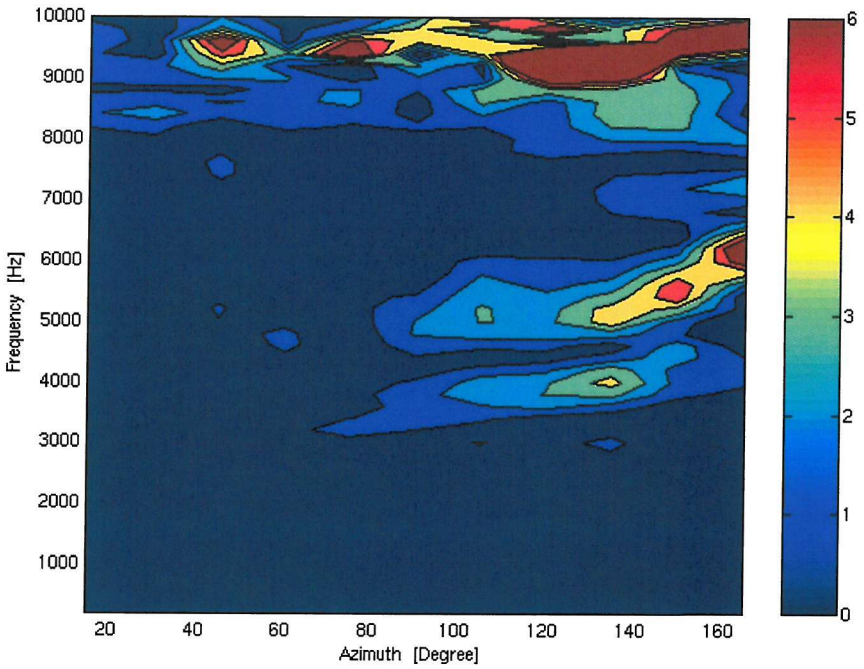

Figure 9.35 Differences of interaural level differences for various source directions in the horizontal plane, 45 headphone sources, and perfectly absorbent headphone.

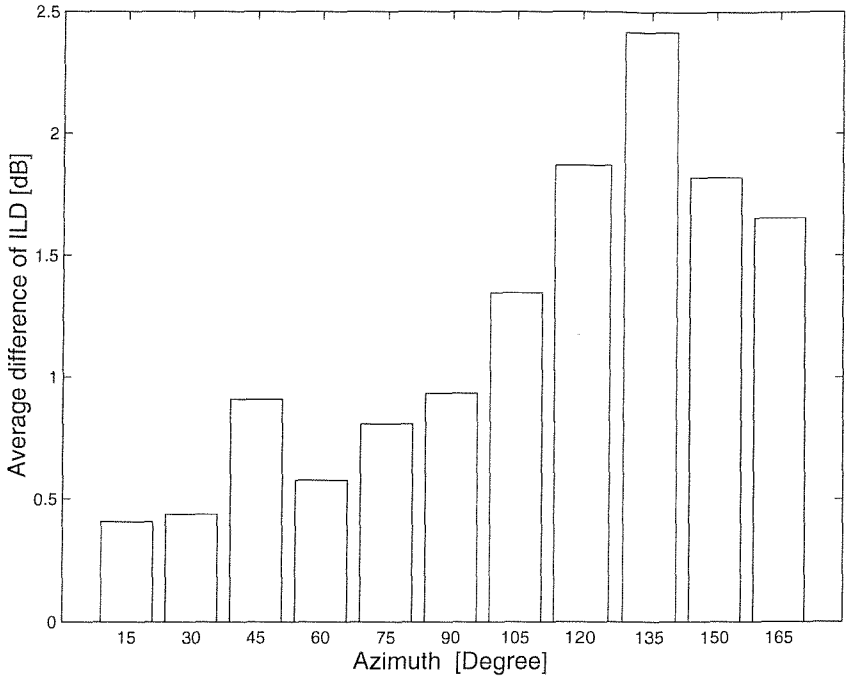

Figure 9.36 Average differences of the ILDs over frequency for various source directions in the horizontal plane.

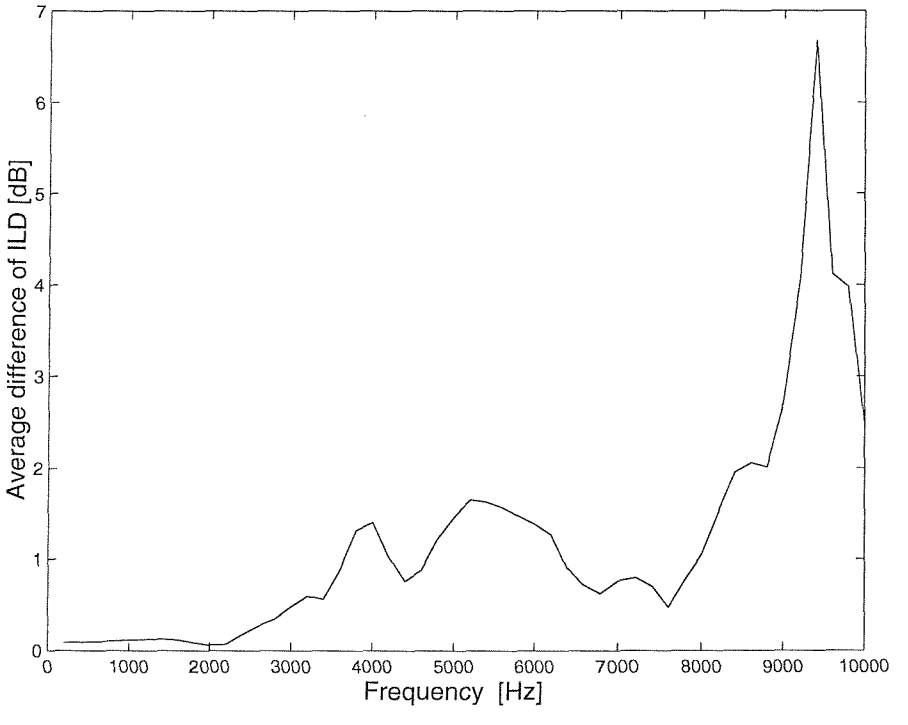

Figure 9.37 Average differences of the ILDs over various source directions in the horizontal plane.

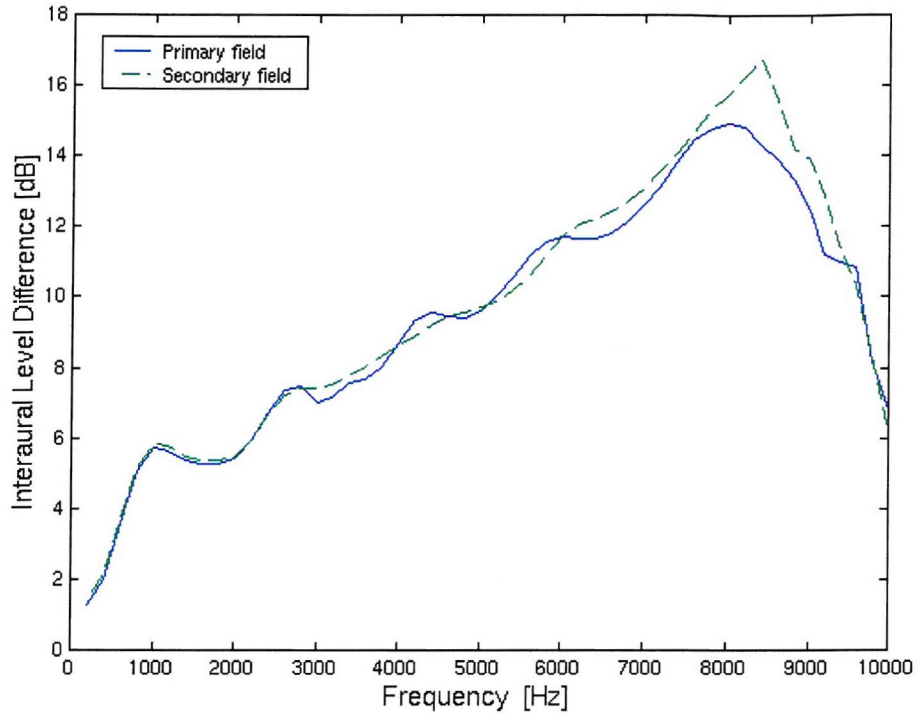

Figure 9.38 Interaural level differences for the source at 30° azimuth

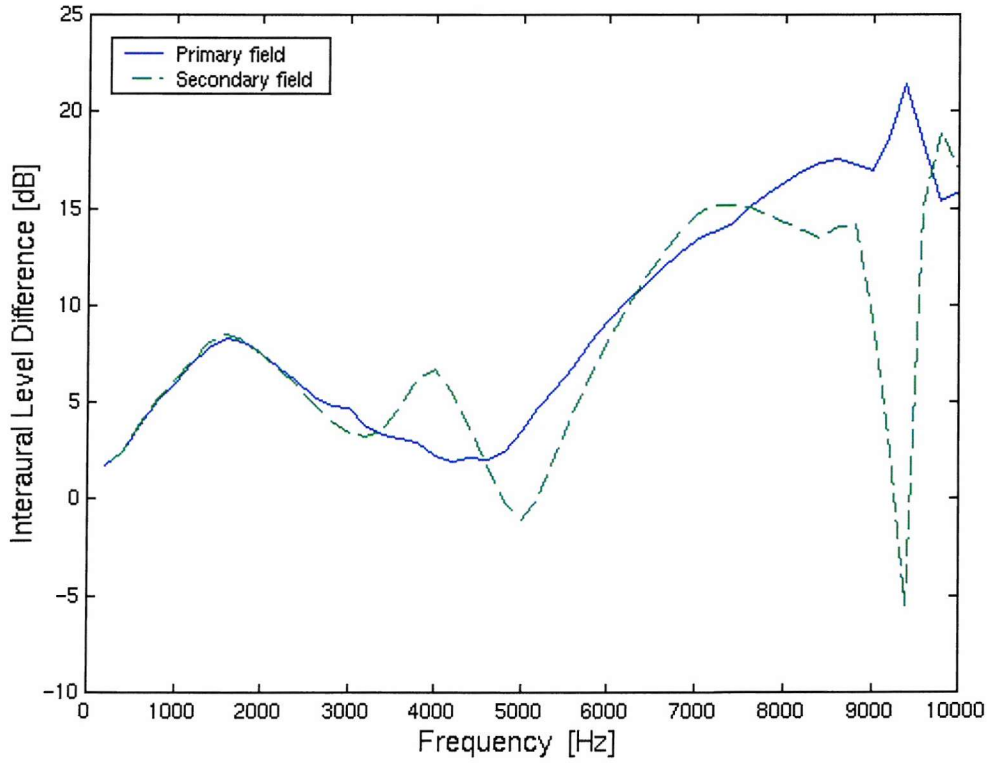

Figure 9.39 Interaural level differences for the source at 135° azimuth

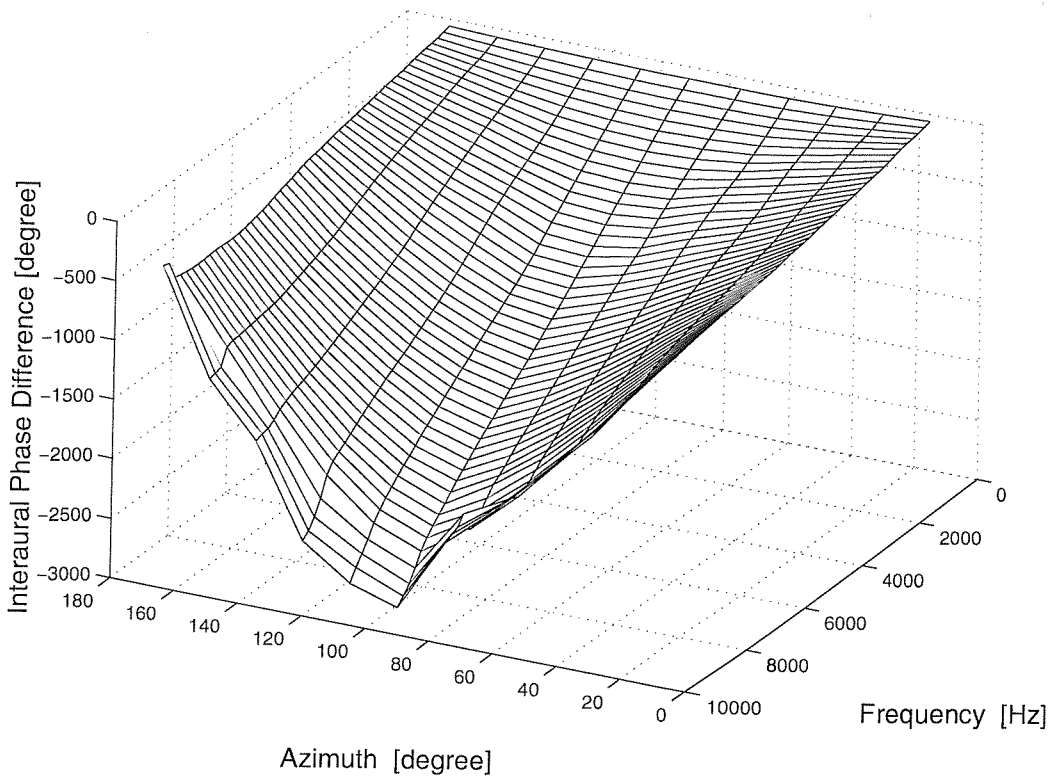

Figure 9.40 Interaural phase differences in the primary field in the horizontal plane.

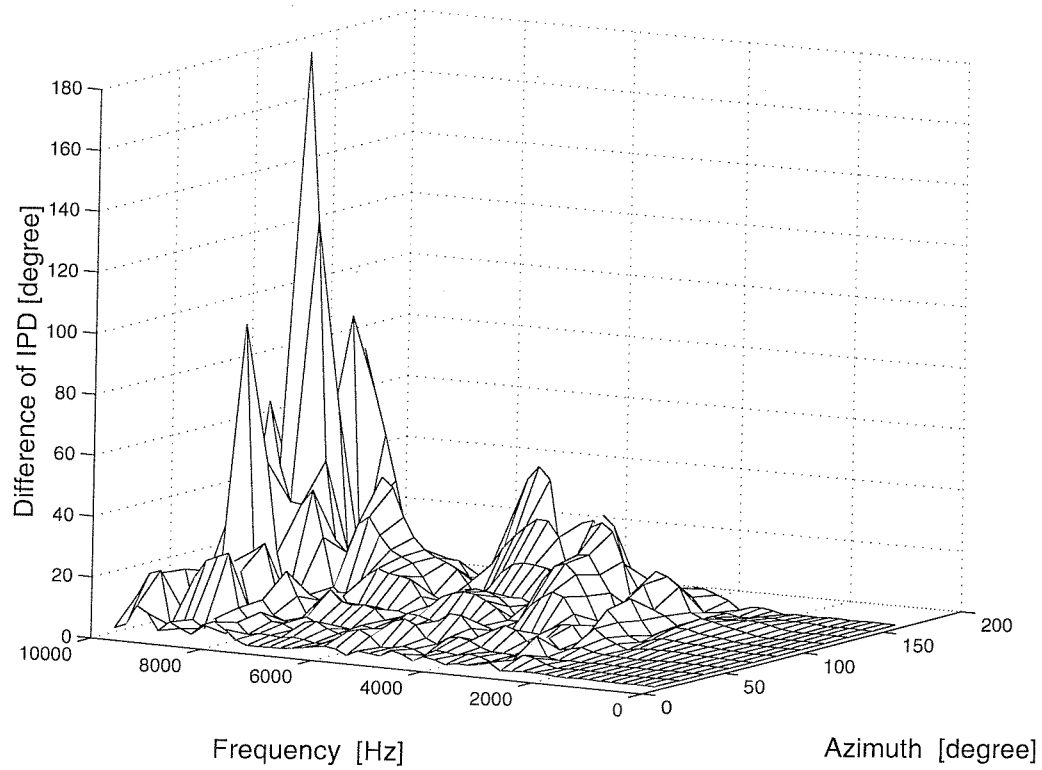

Figure 9.41 Differences of the IPDs for various source directions in the horizontal plane.

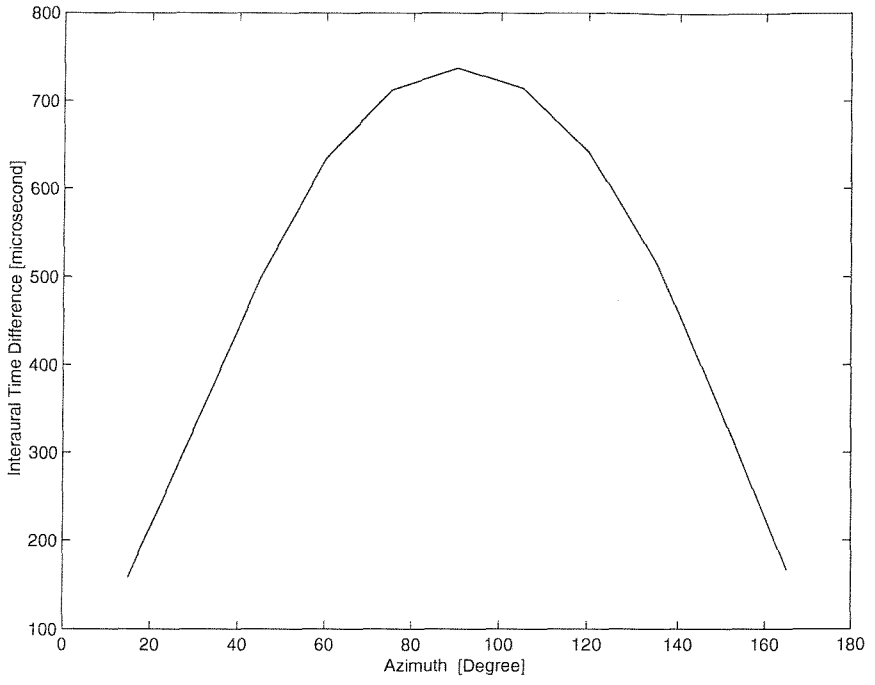

Figure 9.42 Interaural time differences in the primary field for various source directions in the horizontal plane.

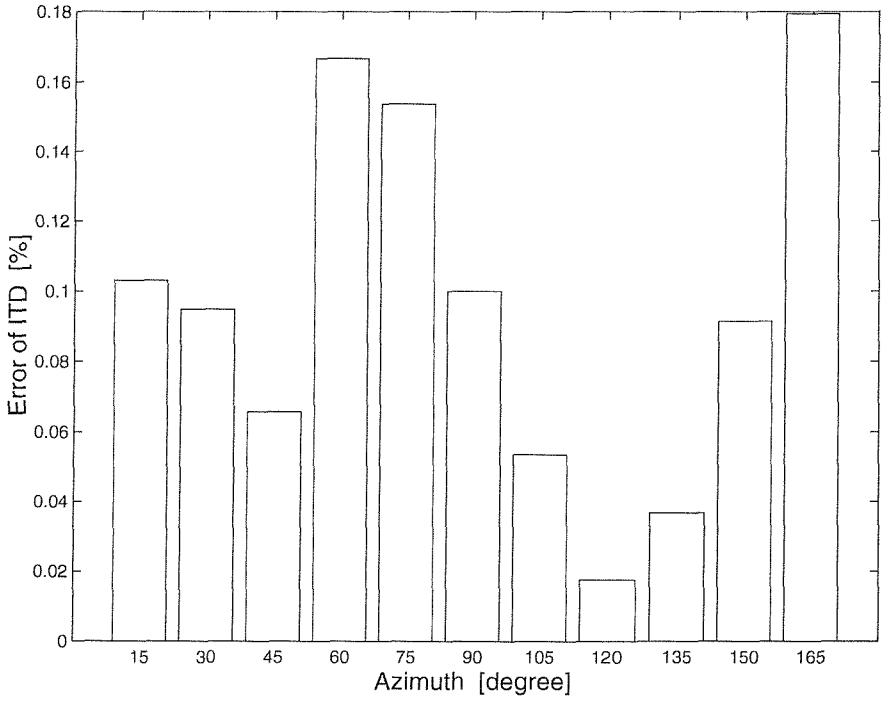

Figure 9.43 Error of the ITD for various source directions in the horizontal plane.

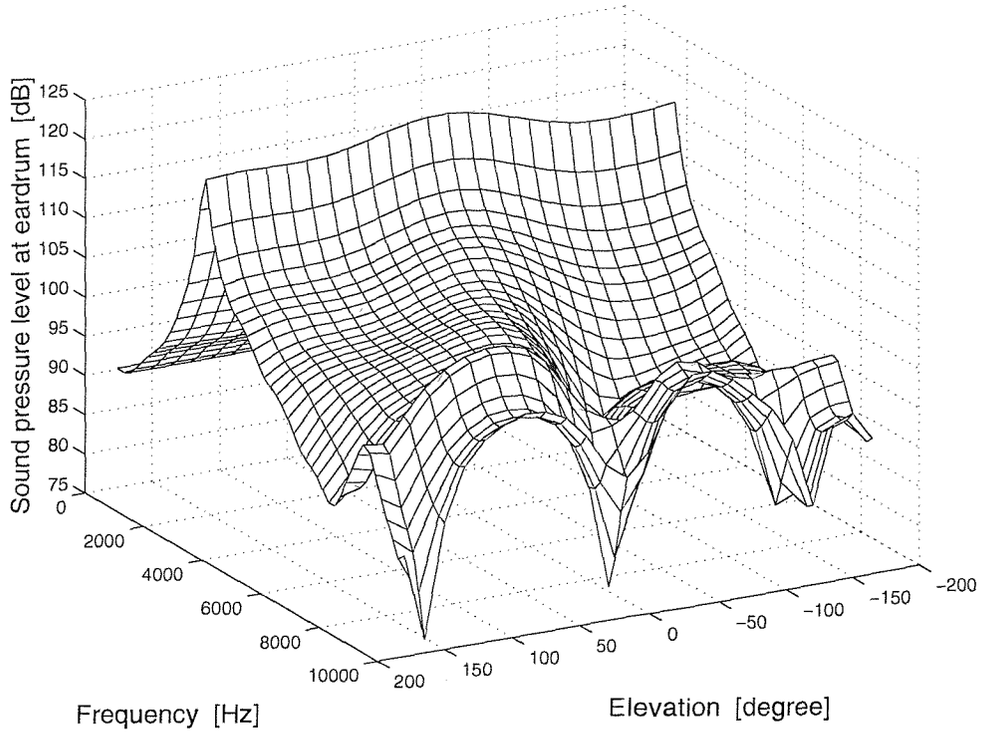

Figure 9.44 Sound pressure level at the eardrum of the DB65 in the primary field for various source directions in the median plane.

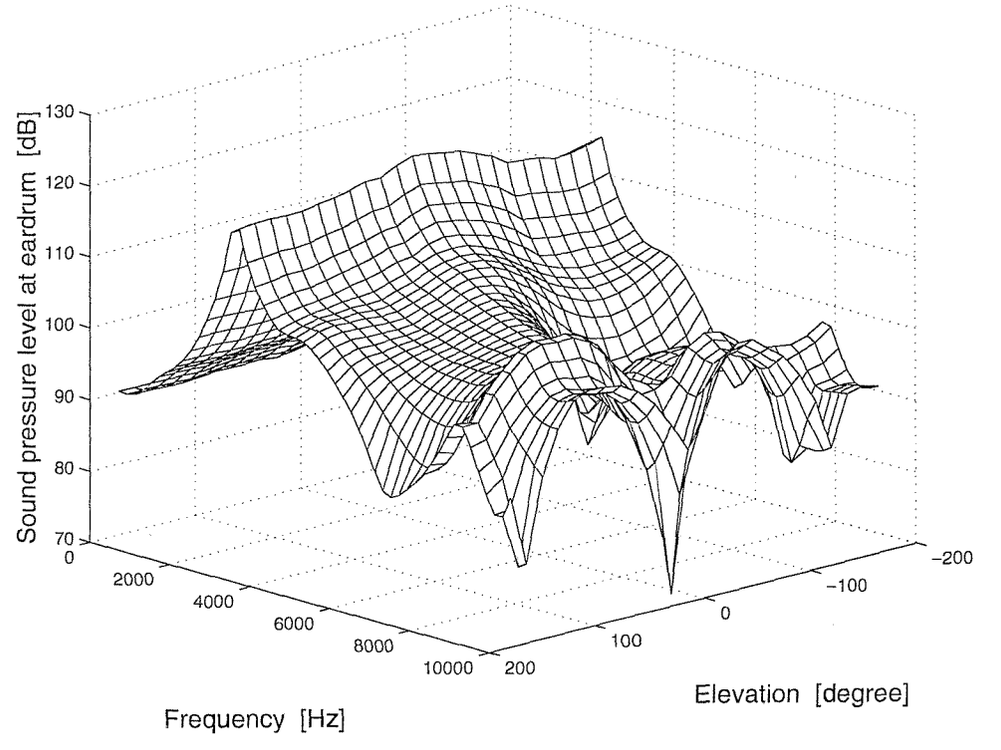

Figure 9.45 Sound pressure level at the eardrum of the DB65 in the secondary field for various source directions in the median plane.

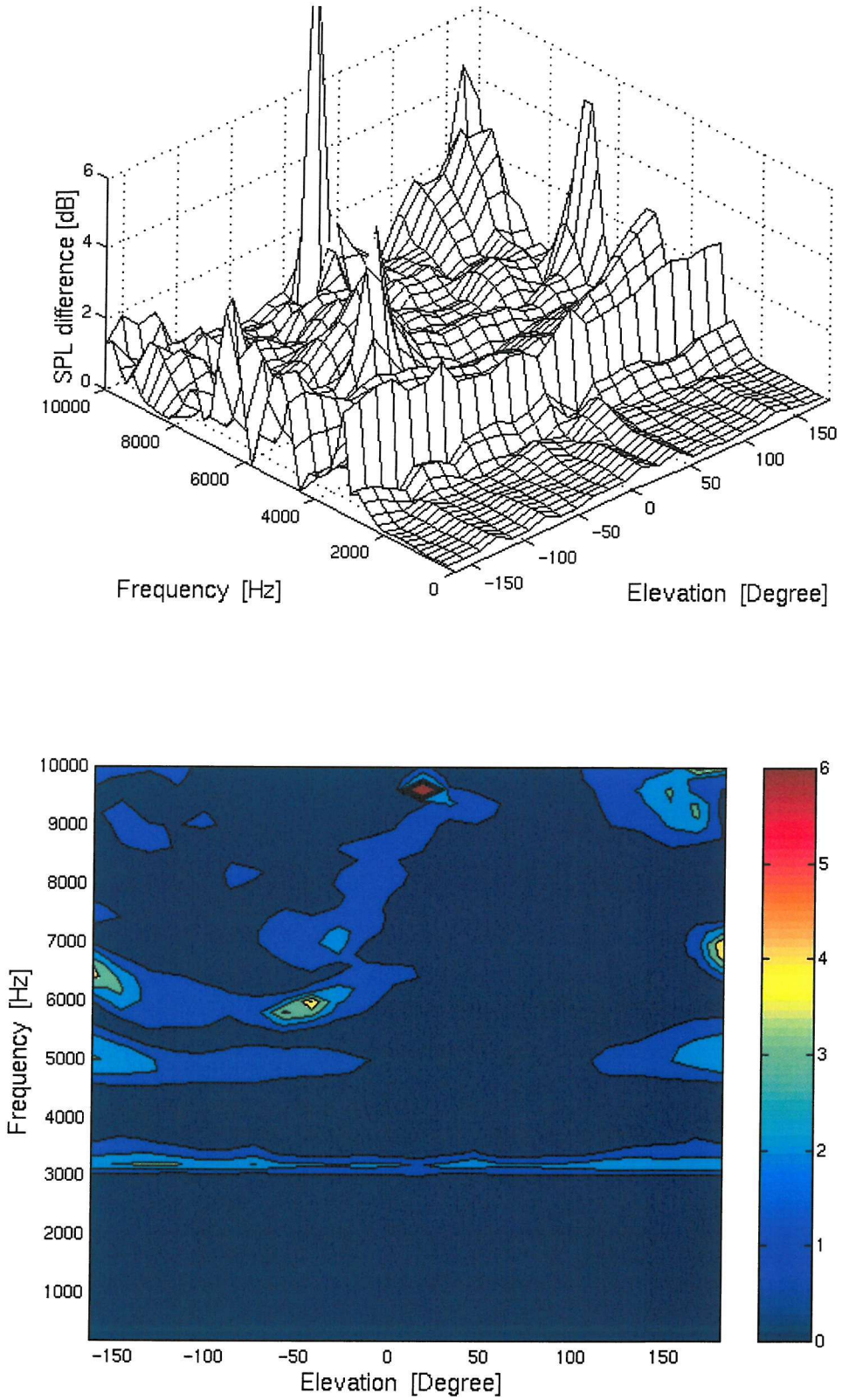

Figure 9.46 The eardrum sound pressure level differences for various source directions in the median plane, 45 headphone sources, and perfectly absorbent headphone.

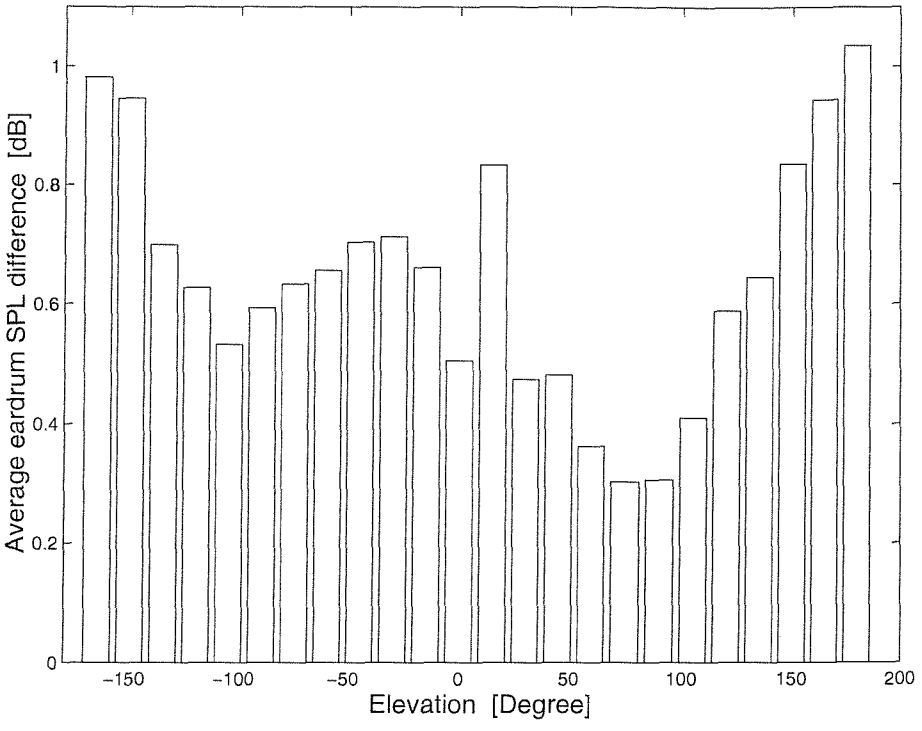

Figure 9.47 The eardrum sound pressure level differences averaged over frequency for each source direction in the median plane.

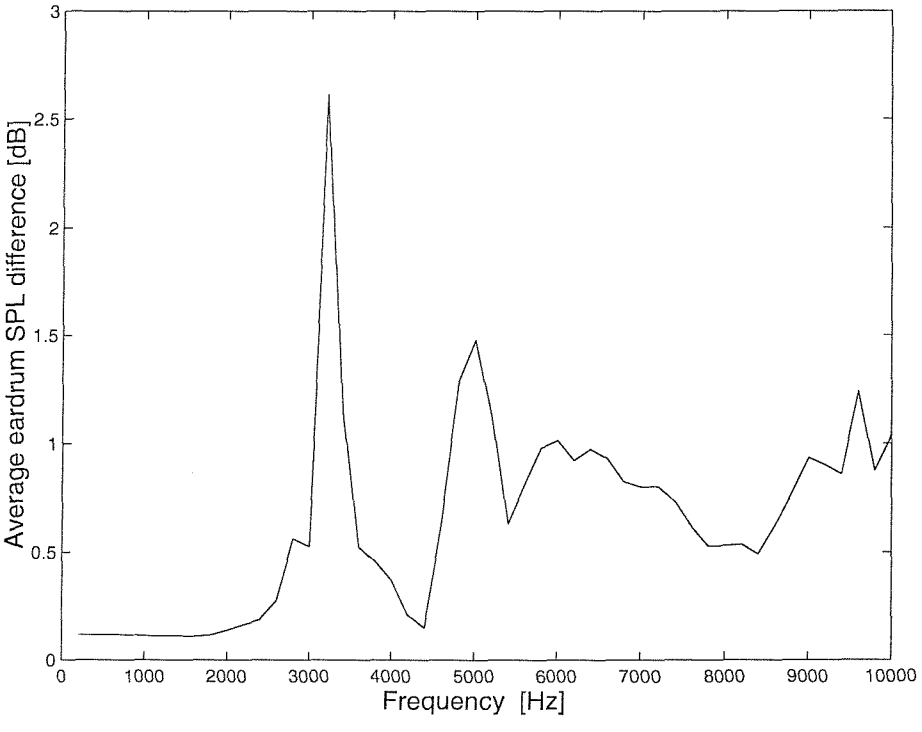

Figure 9.48 The eardrum sound pressure level differences averaged over various source directions in the median plane.

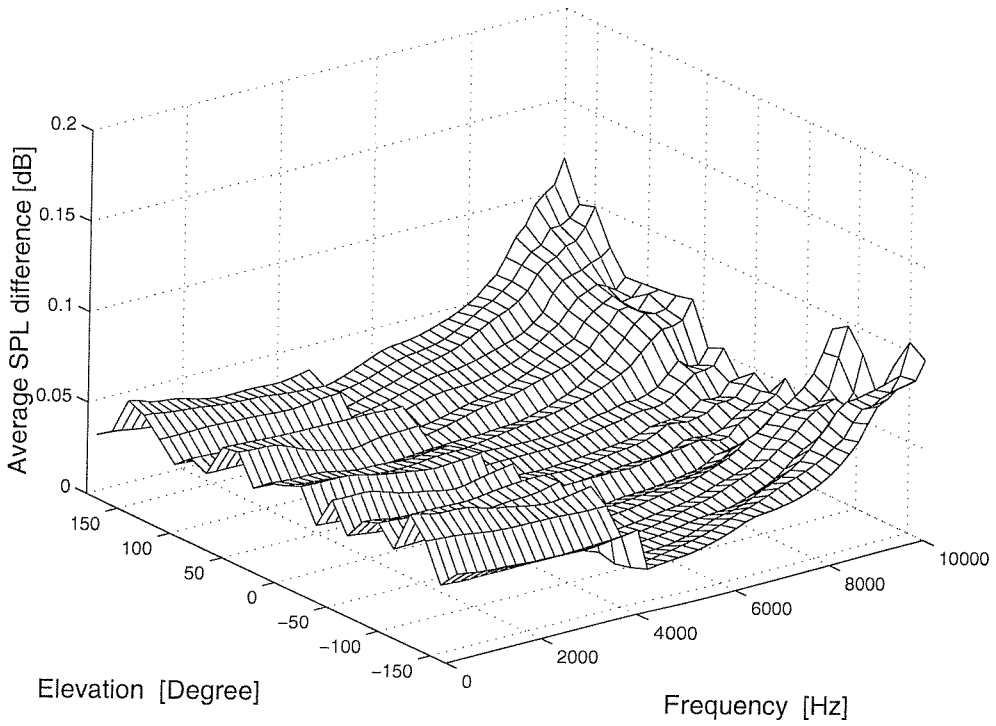

Figure 9.49 Average sound pressure level differences at control points in the median plane.

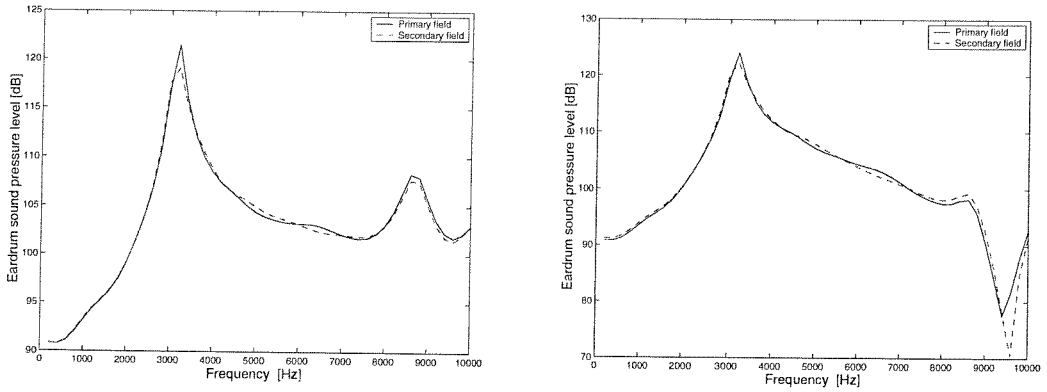

(a) (b)

Figure 9.50 Sound pressure level at the DB65 eardrum for the source (a) at 90° elevation (b) at 15° elevation in the median plane.

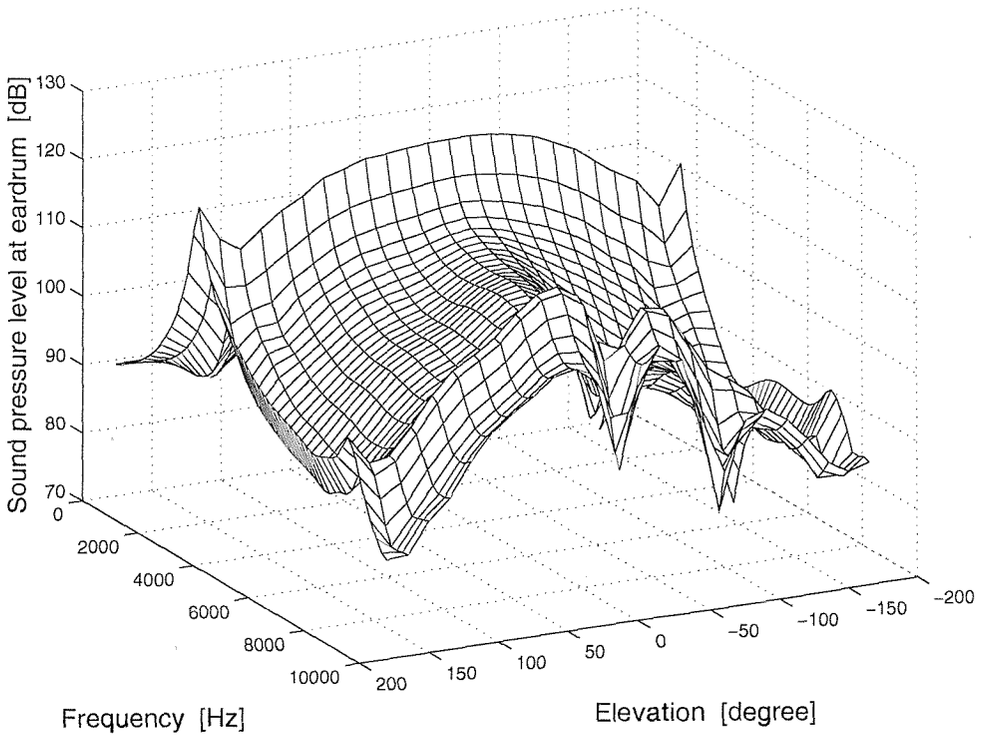

Figure 9.51 Sound pressure level at the eardrum of the DB65 in the primary field for various source directions in the frontal plane.

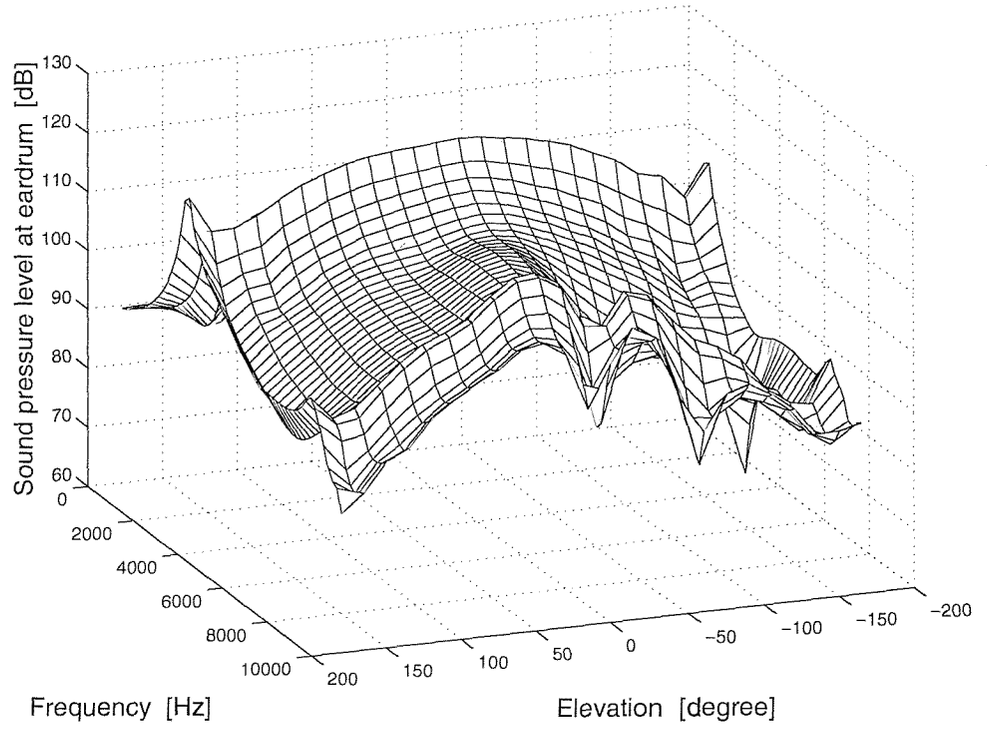

Figure 9.52 Sound pressure level at the eardrum of the DB65 in the secondary field for various source directions in the frontal plane.

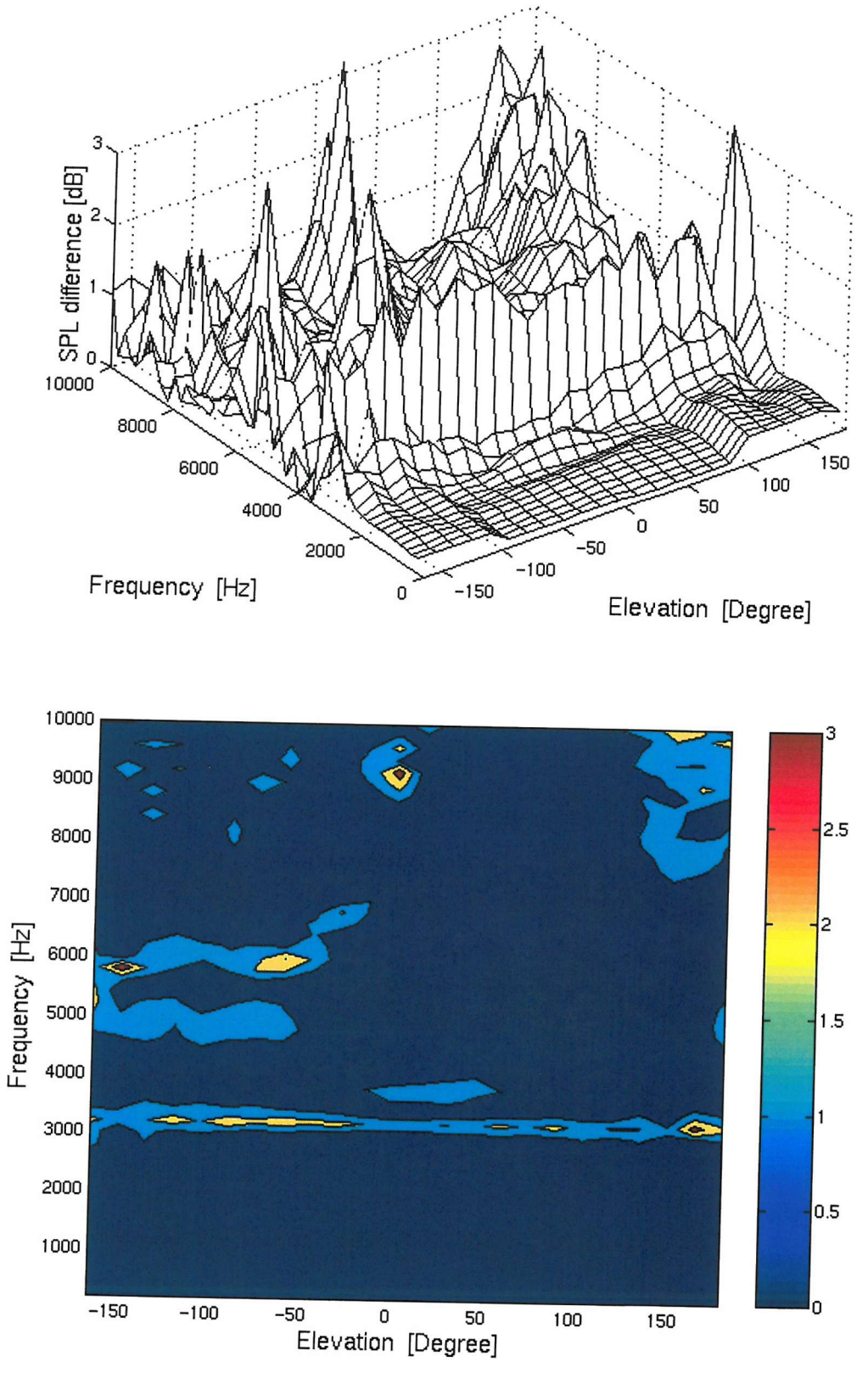

Figure 9.53 The eardrum sound pressure level differences for various source directions in the frontal plane, 45 headphone sources, and perfectly absorbent headphone.

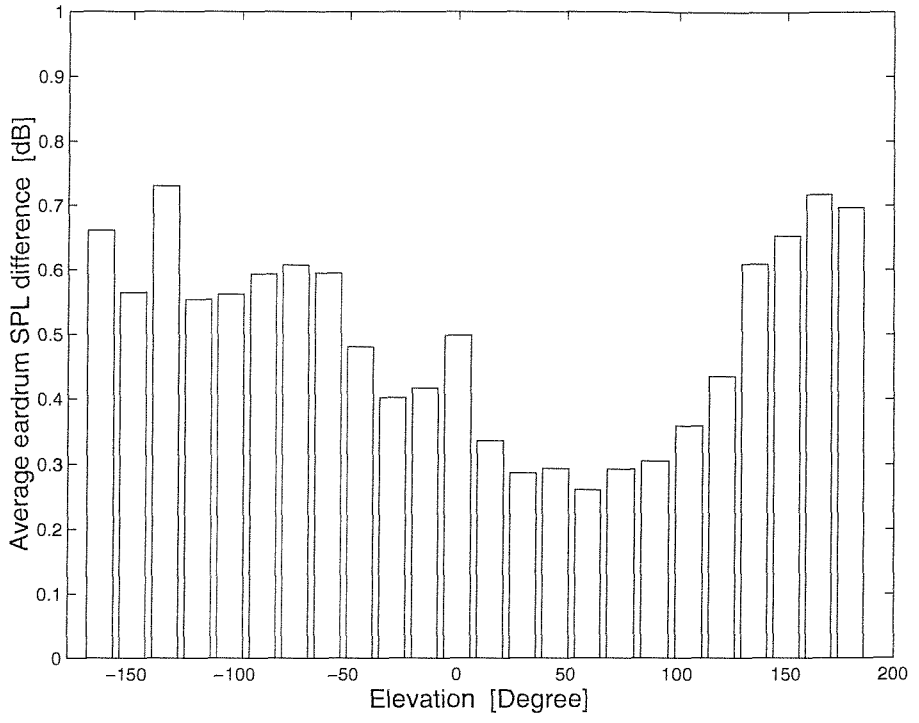

Figure 9.54 The eardrum sound pressure level differences averaged over frequency for each source direction in the frontal plane.

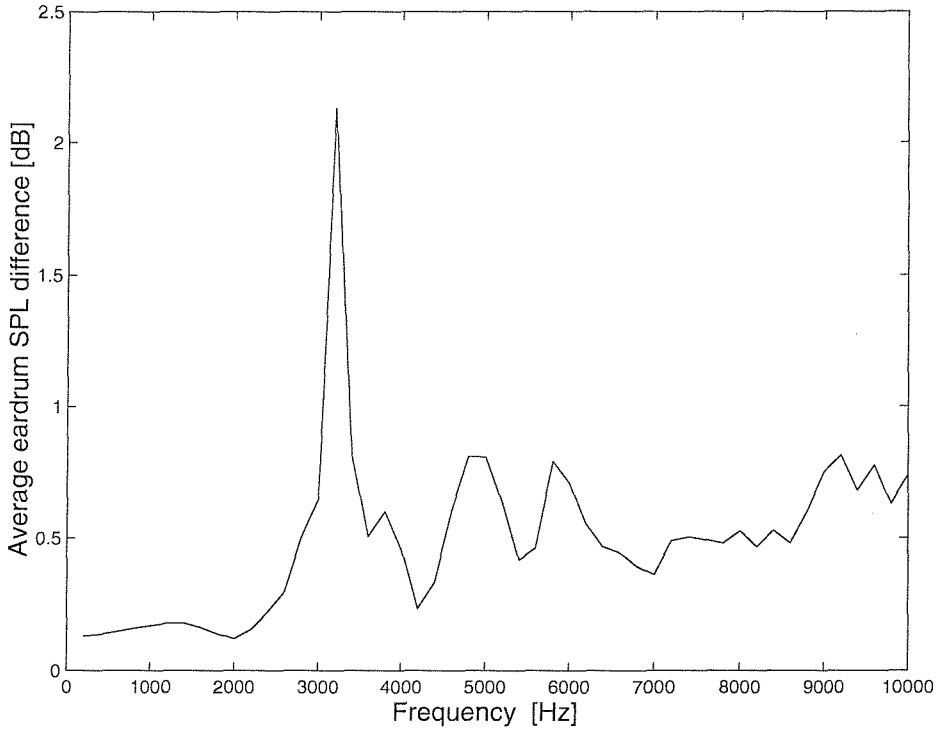

Figure 9.55 The eardrum sound pressure level differences averaged over various source directions in the frontal plane.

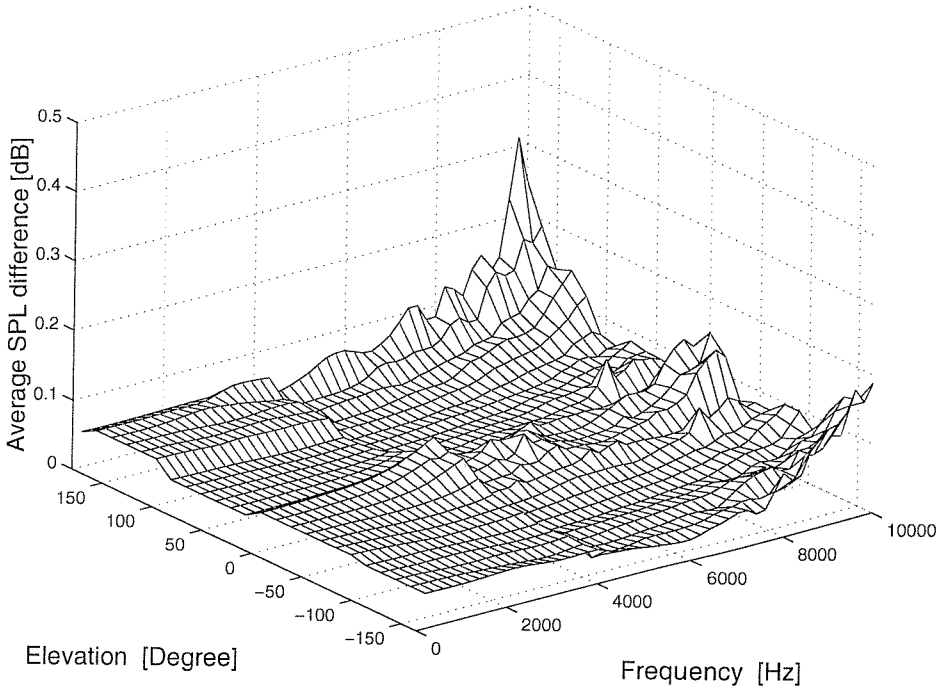

Figure 9.56 Average sound pressure level differences at control points in the frontal plane.

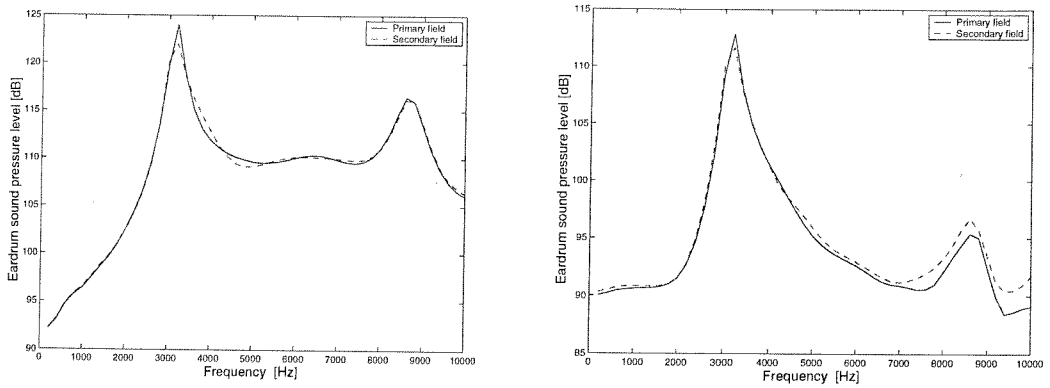

Figure 9.57 Sound pressure level at the DB65 eardrum for the source (a) at 30° elevation (b) at 150° elevation in the frontal plane.

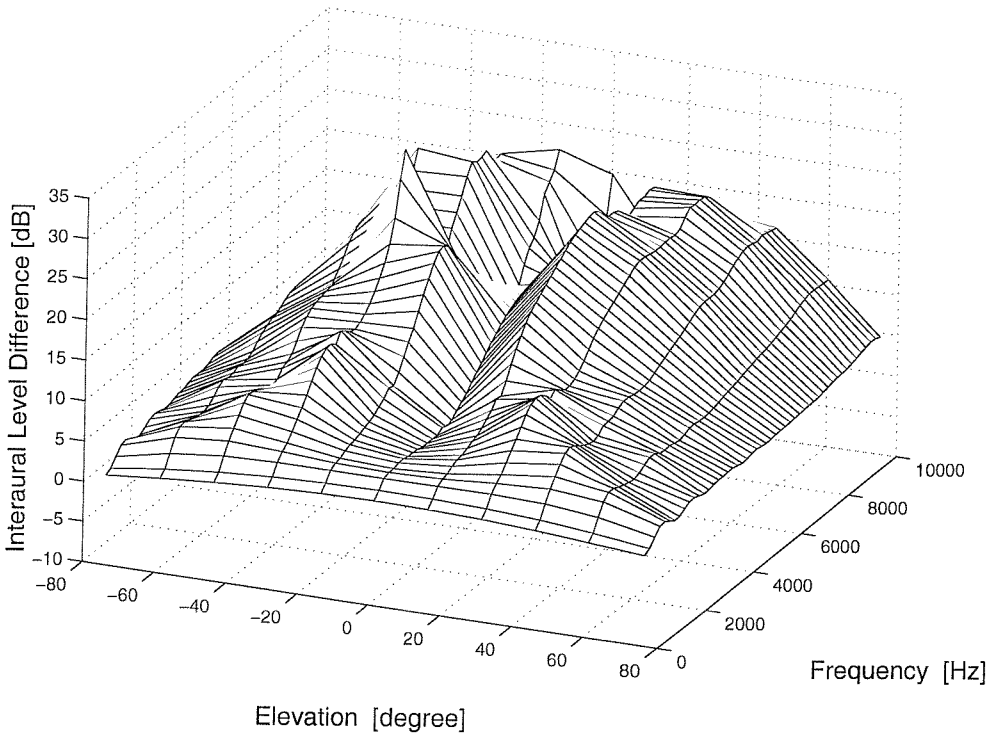

Figure 9.58 Interaural level differences in the primary field for various source directions in the frontal plane.

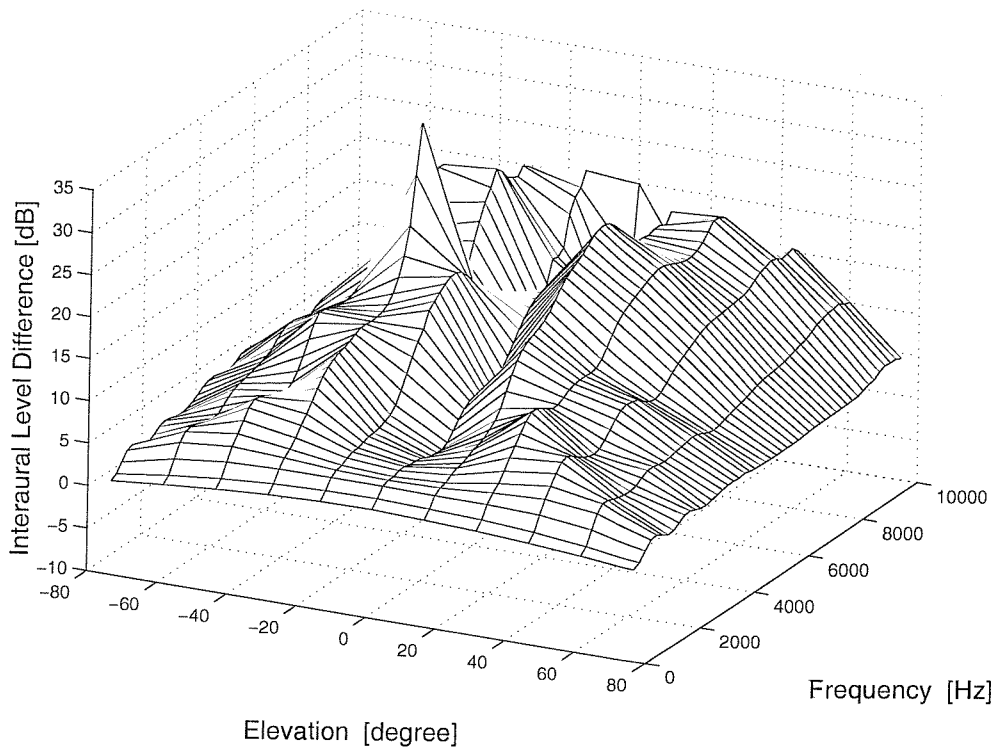

Figure 9.59 Interaural level differences in the primary field for various source directions in the horizontal plane.

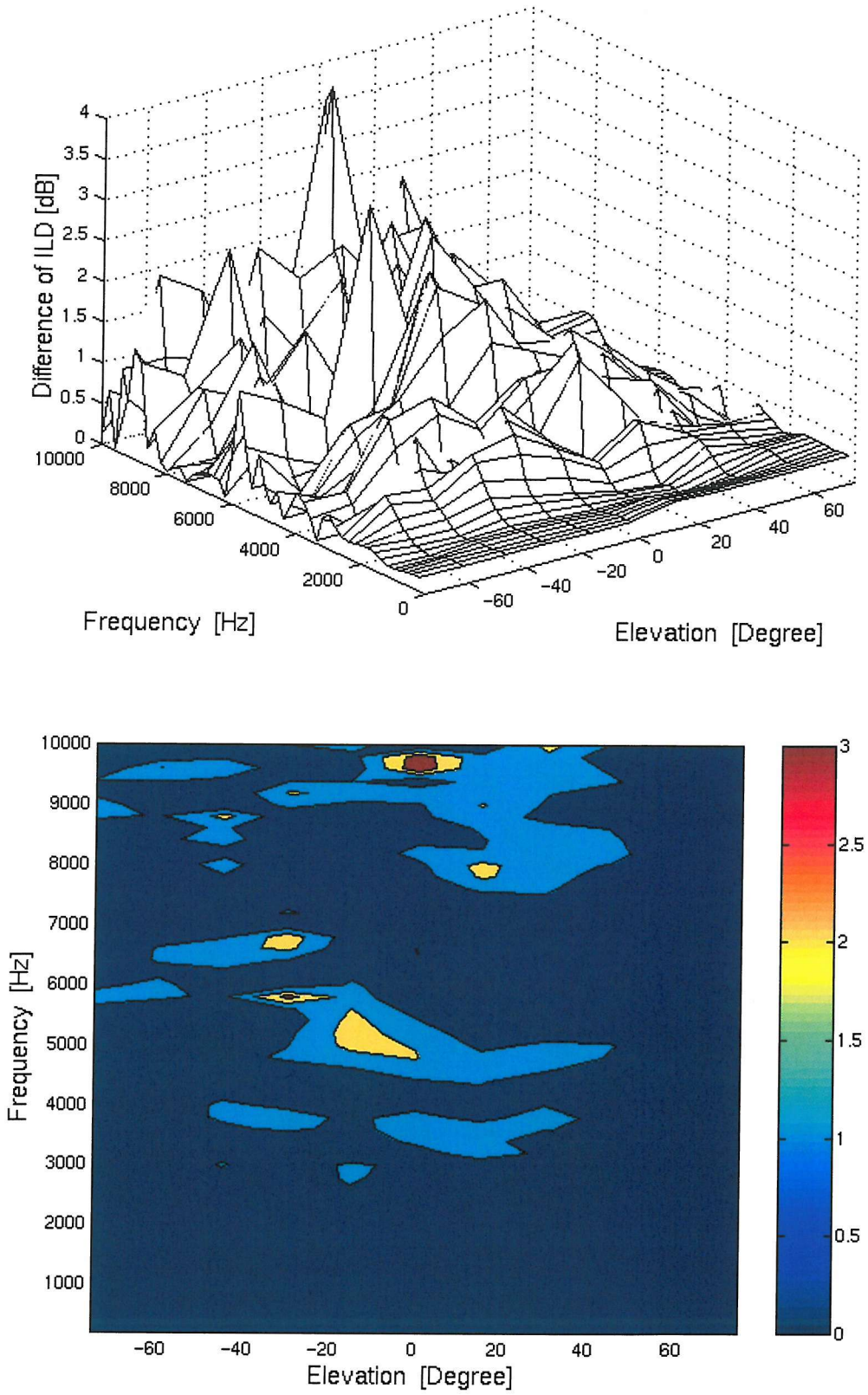

Figure 9.60 Differences of interaural level differences for various source directions in the frontal plane, 45 headphone sources, and perfectly absorbent headphone.

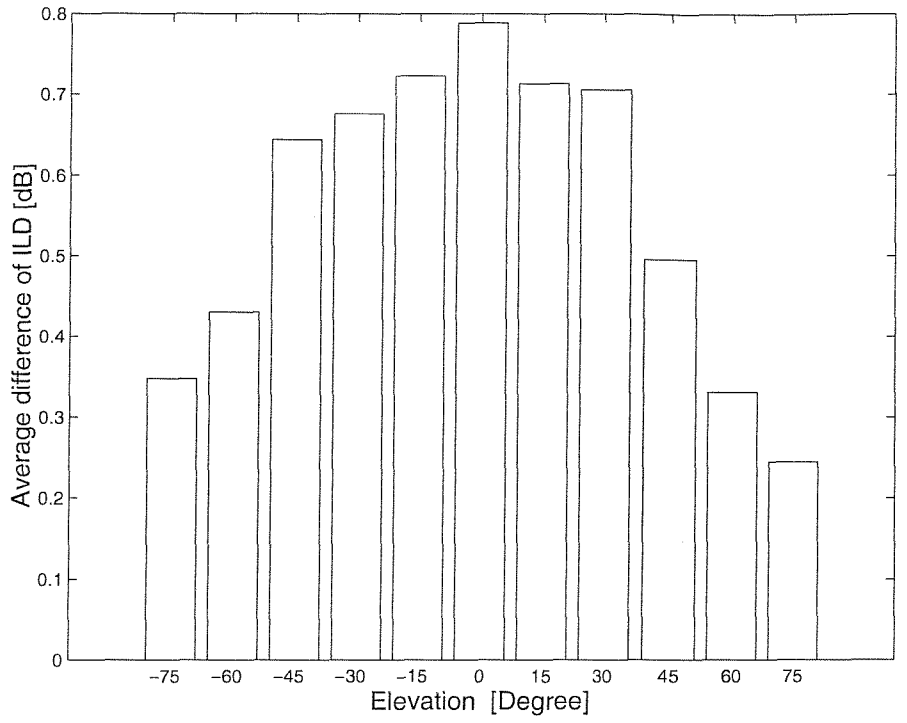

Figure 9.61 Average differences of interaural level difference over frequency for various source directions in the frontal plane.

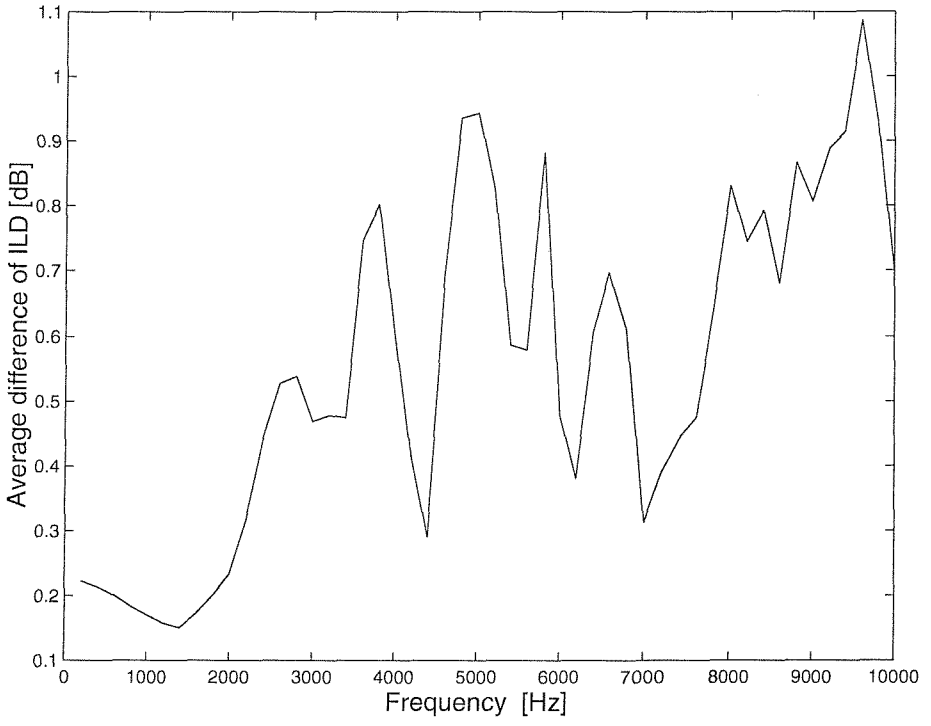

Figure 9.62 Average differences of interaural level difference over various source directions in the frontal plane.

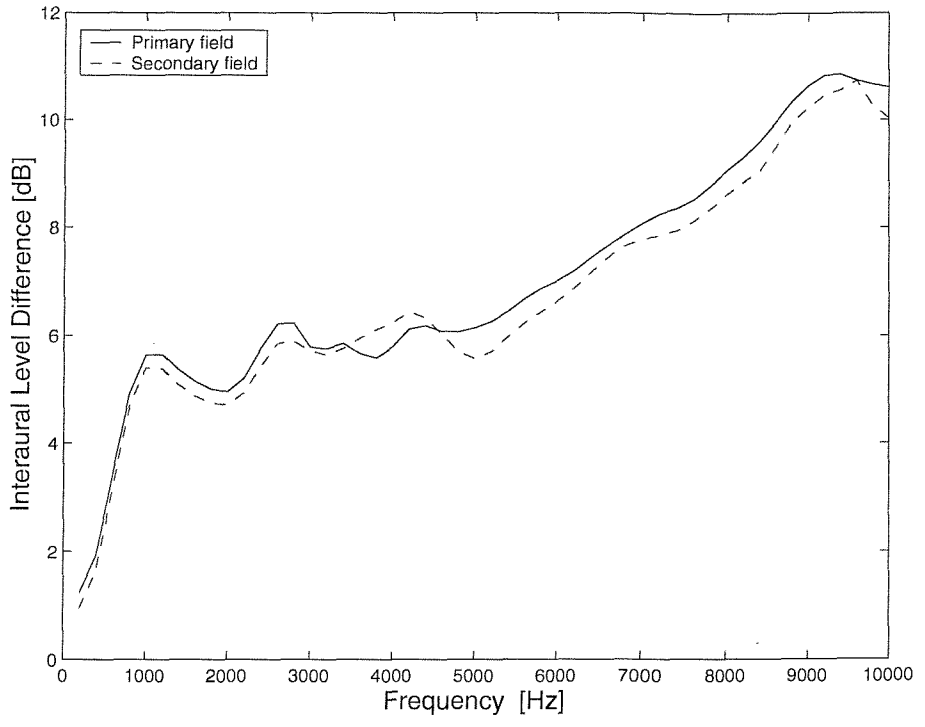

Figure 9.63 Interaural level differences for the source at 30° elevation in the frontal plane.

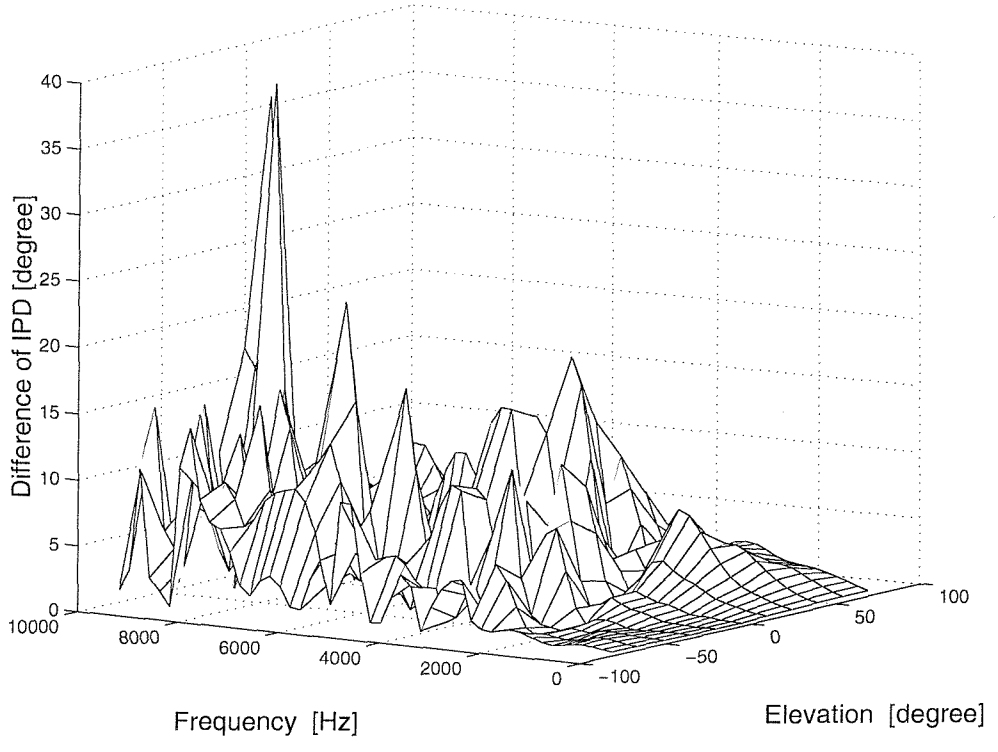

Figure 9.64 Differences of interaural phase differences for various source directions in the frontal plane.

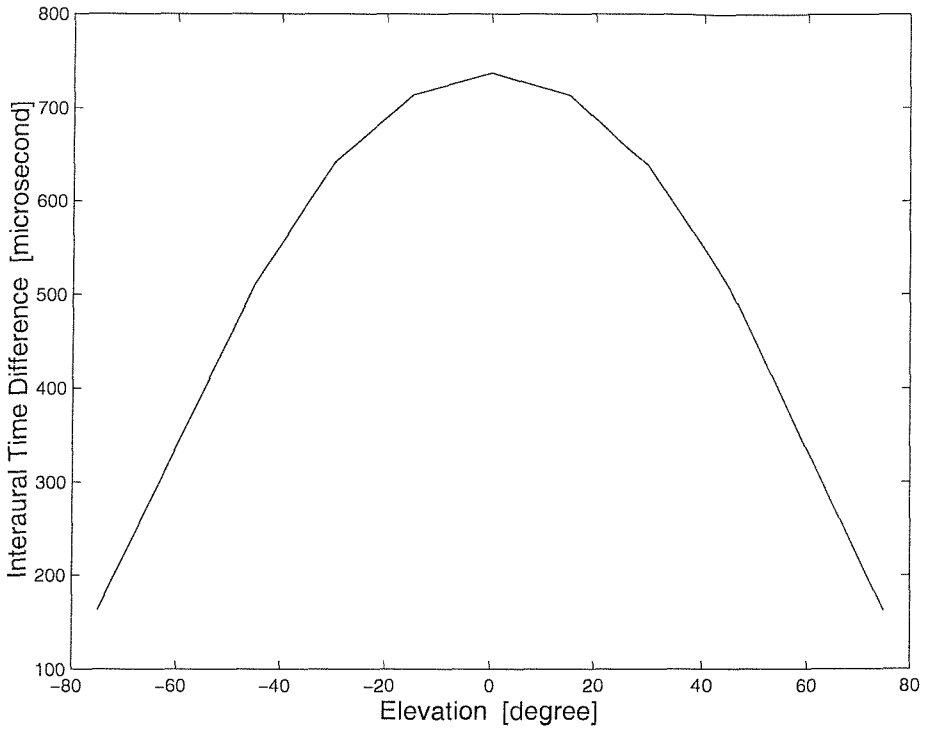

Figure 9.65 Interaural time differences in the primary field for various source directions in the frontal plane.

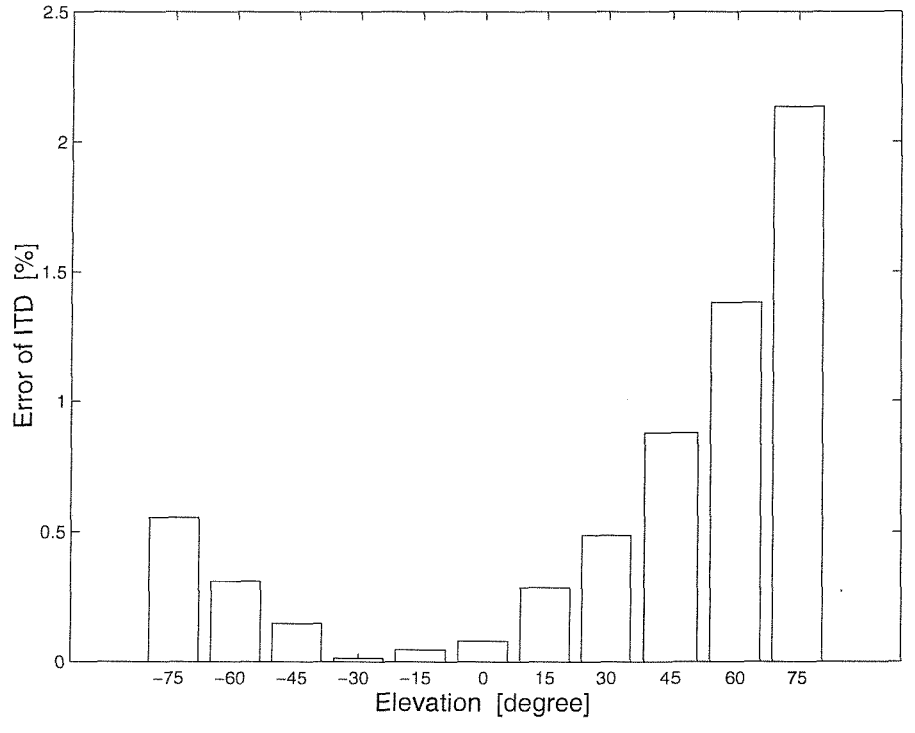

Figure 9.66 Error of the ITD for various source directions in the frontal plane.

CHAPTER 10
OPTIMIZATION OF THE HEADPHONE

10.1 Introduction

Since the ideal headphone, which has an infinite number of sources, cannot be made in practice, the RISE system should be optimized under given restrictions. As discussed in section 7.5, there are many parameters that affect the performance of a virtual acoustic system. In this chapter, the performances are compared of virtual acoustic systems with different numbers of headphone sources. The geometry and boundary conditions of headphones are also optimized. The performance of a system using different sizes of the headphone is investigated. Although such design parameters are interdependent, they are assumed to be independent or weakly interdependent for simplicity. In most cases, results of numerical simulations suggest that this is a reasonable assumption.

10.2 Comparison of headphones with different numbers of sources

The number of headphone sources is the critical factor affecting the performance of the virtual acoustic system since the number of sources is far less than the number of control points at high frequencies and it is very difficult in practice to make headphones with a large numbers of sources. The number of headphone sources should be as large as possible in terms of the system performance, but it should also be as small as possible in terms of commercialization. Since only a limited number of headphone sources are used, the position of headphone sources should be designed. The position of headphone sources will influence the range of performance of the virtual acoustic system. The performance of the system depends on the difference

between the angle of the incident sound wave and the angle of the close headphone source relative to the wavelength of the incident waves. In this section, the headphone sources are distributed almost evenly to cover all angles of incident sound waves in three-dimensional space. However, if the area of production of the virtual acoustic fields is focused, the placement of the headphone sources can be also focused.

Figure 10.1 shows the position of the headphone sources for the number of (a) 45, (b) 17, (c) 9, or (d) 5. The diagram shows the upper-right part of the headphone. Figure 10.2 shows the schematic representation of the number of headphone sources. They show the headphone sources are distributed almost evenly in all cases. Roughly speaking, the angular interval between two adjacent sources is 22.5° in case of 45 sources, 45° in case of 17 sources, 55° in case of 9 sources, and 90° in case of 5 sources. The headphone sources are modelled as the idealized piston-like flat vibrating round surfaces having a radius of 5mm. All the numerical models and conditions are the same as those in section 9.3 or 9.4 except for the headphone sources. The single point monopole sound source in the primary sound field is located in the horizontal, median, or frontal plane for every 15° angle, and the source is one metre away from the centre of the coordinate system. The peak amplitude of sound pressure one metre away from the source is set to be unity at all frequencies. The numerical simulations use the numerical models shown in Fig. 7.6, 7.8, 7.10 and 7.12(b). The small and sparse control field is used, which has 84 control points and which is shown in Fig. 9.4. The boundary condition of the spherical head surface of models is rigid, and that of the headphone surface is perfectly absorbent. The sound pressures at the control points are calculated from 200 Hz to 10 kHz with a constant frequency increment of 200 Hz. The highest frequency is set to be 10 kHz.

Figure 10.3 shows the sound pressure level differences at the eardrum of the DB65 artificial ear between the desired values and the reproduced values for every 15° azimuth of the monopole source direction in the horizontal plane using the 17 headphone sources with the perfectly absorbent headphone surface. In this chapter, all the colour filled contour figures are scaled from 0 to 6 dB. This shows that most of the eardrum sound pressure level differences except for a few data are below 1 dB

and this is almost similar to Fig. 9.20. This can be regarded as successful reproduction even though the number of headphone sources is reduced to about one third of 45 sources. Figure 10.4 shows the eardrum sound pressure level differences in the median plane using the 17 headphone sources and Figure 10.5 shows those in the frontal plane. Figure 10.6 shows the differences between the desired ILDs in the primary field and the reproduced ILDs in the secondary field for various source directions in the horizontal plane using the 17 headphone sources with the perfectly absorbent headphone surface. Figure 10.7 shows the differences of the ILDs for various source directions in the frontal plane using the 17 headphone sources. They all show that most of the reproduction errors except for a few data are below 1 dB and they are not much different from the corresponding figures in the case of 45 headphone sources. These results imply that the 17 headphone sources can be a maximum number of sources to produce a good performance of the RISE system covering whole range of incident angles, and the 45° of angular interval of every two sources is sufficient to gives a good performance. For example, if the desired reproduction focus area is limited to horizontal plane, 5 headphone sources in the horizontal plane may be sufficient.

Figure 10.8 shows the eardrum sound pressure level differences for various source directions in the horizontal plane using the 9 headphone sources with the perfectly absorbent headphone surface. This shows that accuracy of reproduction is good up to about 8 kHz when the source in the primary field is in the front of the listener and up to about 6 kHz when the source in the primary field is in the rear. Figure 10.9 shows the eardrum sound pressure level differences in the median plane using the 9 headphone sources. This shows that accuracy of reproduction is good up to about 9 kHz when the source in the primary field is in the upward frontal side, that is, elevation angles from 0 to 90°, and good up to about 5 kHz in other angles. Figure 10.10 shows the eardrum sound pressure level differences in the frontal plane using the 9 headphone sources. This shows many reproduction errors except for some data that are below 1 dB and these are not much worse than those in case of the 17 headphone sources. The performance of the system is better than that in case of the horizontal and median plane, particularly when the source is to the rear of the head. Figure 10.11 shows the differences of the ILDs for various source directions in the

horizontal plane using the 9 headphone sources. The reproduction of the ILDs is very accurate up to at least 10 kHz for the azimuth angles from 15° to 45°. The reproduction is reasonably accurate up to about 8 kHz for the azimuth angles from 45° to 90° and 135° to 165°, but the reproduction is inaccurate for the azimuth angles of 105° and 120° from 3 kHz. Figure 10.12 shows the differences of the ILDs in the frontal plane using the 9 headphone sources. The reproduction of the ILDs is reasonably accurate when the source is above the head, but there are some severe errors around 6 kHz when the source is below the head in the frontal plane.

These results show that the performance of the RISE system using the 9 headphone sources is reasonable for most angles of incident wave in the upper hemispheric range up to about 8 kHz. Although a system using 17 headphone sources may produce better performance for any source in three-dimensional space, the headphone using the 17 sources is still difficult to manufacture for commercial products. However, the headphone using the 9 headphone sources is easier to make and it produces reasonable performance with some limits in terms of value for a headphone source. If the 3 headphone sources located in lower part of the headphone are removed, which are relatively inefficient for generating virtual acoustic fields, the number of headphone sources could be reduced to 6 and the reproduction area is focused to the upper hemispheric region.

Figure 10.13 shows the eardrum sound pressure level differences for various source directions in the horizontal plane using the 5 headphone sources with the perfectly absorbent headphone surface. This shows that accuracy of reproduction is good up to about 7 kHz when the source in the primary field is in the front of the listener and up to about 5 or 6 kHz when the source is in the rear. Figure 10.14 shows the eardrum sound pressure level differences in the median plane using 5 headphone sources. This shows that accuracy of reproduction is good up to about 5 kHz for most elevation angles. The reproduction is more accurate when the angle of the incident wave matches the angle of one of the headphone sources, such as at 0 or 90° elevation. Figure 10.15 shows the eardrum sound pressure level differences in the frontal plane using the 5 headphone sources. The reproduction is accurate up to at least 10 kHz for the elevation angles from 75° to 150°, and up to about 5 kHz at other angles. Figure

10.16 shows the differences of the ILDs for various source directions in the horizontal plane using the 5 headphone sources. The reproduction of the ILDs is accurate up to about 7 kHz for the azimuth angles from 15° to 90°, but the reproduction is inaccurate for the azimuth angles of 105° and 165° from 3 kHz. Figure 10.17 shows the differences of the ILDs in the frontal plane using the 5 headphone sources. The reproduction of the ILDs is reasonable up to about 7 kHz when the source is above the head, and up to about 5 kHz when the source is below the head in the frontal plane. Those results shows that the performance of the RISE system using the 5 headphone sources is reasonably good for only limited incident angles up to about 5 kHz or 7 kHz. This limited performance is mainly due to the small number of headphone sources and broad angular interval of 90° between every two adjacent sources.

Figure 10.18 shows, as an example, the sound pressure levels measured at the eardrum of the DB65 for the primary source at 45° azimuth in the horizontal plane. Figure 10.19 shows equivalent results for the source at 135° azimuth. These two figures show the breakdown in performance at high frequencies when 5 headphone sources are used. They also show the performance is better for any number of headphone sources when the primary source is frontal, and the 9 headphone source may be optimal. The 9 headphone sources fail to reproduce the anti-resonance at 9400 Hz for the primary source at 135° azimuth. As a further example, Figure 10.20 shows the sound pressure levels at the eardrum for the primary source at 45° elevation in the median plane. Figure 10.21 shows equivalent results for the source at 45° elevation in the frontal plane. Figure 10.22 shows the interaural level differences for the primary source at 45° azimuth in the horizontal plane, and Figure 10.23 shows the ILDs for the source at 45° elevation in the frontal plane. They also show the breakdown at high frequencies when the 5 headphone sources are used, and again, the 9 headphone sources may be optimal.

Figure 10.24 shows the eardrum sound pressure level differences averaged over frequency for different numbers of headphone sources in the horizontal plane. The case of the 17 headphone sources is not too different from the case of the 45 headphone sources, and most average values are below 1 dB and the worst value is

below 2 dB. In the case of 9 headphone sources, most average values are below 3 dB, and they are about 1 dB when the primary source is in the front. In the case of 5 headphone sources, the headphone sources are located at 0, 90°, 180°, and 270° azimuth in the horizontal plane and the performance of the system is good only when the angle of the primary source matches the location of the headphone source. The 9 headphone sources may be optimal in the horizontal plane particularly for the reproduction of frontal sound.

Figure 10.25 shows the eardrum sound pressure level differences averaged over frequency in the median plane. The case of the 17 headphone sources is also not very different from the case of the 45 headphone sources, and most average values are below 1 dB and the worst value is below 2 dB. In cases of the 9 and 5 headphone sources, the headphone sources are located at 0, ±90°, and 180° elevation in the median plane and the performance of the system is good when the angle of the primary source matches the location of the headphone source. However, the 9 headphone sources produce a good performance for the elevation angles from 0 to 90°. The 17 headphone sources may be optimal in the median plane, but the 9 headphone sources can be chosen for the reproduction of upper frontal sound. Figure 10.26 shows the eardrum sound pressure level differences averaged over frequency in the frontal plane. The 9 headphone sources show possibly optimal performance in the frontal plane. Figure 10.27 shows the average differences of the ILDs over frequency for different numbers of headphone sources in the horizontal plane. The 17 headphone sources show similar performance to the 45 headphone sources. The 9 headphone sources show good performance from 15° to 60° azimuth, but most average values are below 3 dB. Figure 10.28 shows the average differences of the ILDs over frequency in the frontal plane. They show the 9 headphone sources may be the best choice if a relatively poor performance for the rear primary source is accepted.

The eardrum sound pressure level differences averaged over various source directions in the horizontal, median, or frontal plane for different number of headphone sources are shown in Fig. 10.29, 10.30, or 10.31 respectively. The average differences of the ILDs over various source directions in the horizontal or frontal plane for different

number of headphone sources are shown in Fig. 10.32 and 10.33. They show similar performance for any number of headphone sources up to about 5 kHz and from about 5 kHz the reproduction error increases more rapidly as frequency increases when a smaller number of headphone sources are used. Figures 10.34 and 10.35 show the errors of the ITD over various source directions for different numbers of headphone sources in the horizontal and frontal plane respectively. Most errors of the ITD are less than 0.5 %, which is nearly negligible.

Figure 10.36 shows the average sound pressure level differences at control points in the horizontal plane for different number of headphone sources. This shows the control error is radically increased from about 8 kHz in case of the 17 sources, from about 6 kHz in case of the 9 sources, and from about 5 kHz in case of the 5 sources. Figure 10.37 shows those in the median plane and Figure 10.38 shows those in the frontal plane. Figure 10.37 and 10.38 shows similar patterns to those in Fig. 10.36. These high control errors at high frequencies can be a major source of error of reproduction of the system and that is why the performance of the system is poor at high frequencies in cases of 9 and 5 headphone sources. Note that the control errors are low when the angle of the primary source matches the location of the headphone source.

Figure 10.39 shows the condition numbers of the acoustic transfer matrices for various number of headphone sources, which are evaluated in the secondary sound fields without the ear. It shows that when the number of headphone sources is reduced, the condition number is reduced and the system becomes better-conditioned. In an ideal noise-free condition, the number of headphone sources should be as large as possible in terms of the system performance. However, in practice, the more the headphone sources, the poorer the condition of the system would be. Therefore, there should be an optimized number of headphone sources. As discussed in section 9.3, there are some methods to overcome ill-conditioned problems such as "Tikhonov regularisation" (Nelson, 2001).

The 17 headphone sources appears to be the maximum number of headphone sources to produce an overall good performance of the RISE system with a multichannel headphone covering the whole range of three-dimensional space. However, if a

performance error of up to 3 dB is accepted, the 9 headphone sources may be the optimal value to give a reasonably good performance of the system with some limitations.

10.3 Design of the boundary condition of the headphone

The production of the virtual acoustic field from the multichannel headphone of the RISE system is based on the boundary surface control principle. The headphone sources try to reproduce the sound pressure and its gradient on the surface of the control volume. One of the main assumption of the theory of the RISE system is that the scattered sound field from the ear surface does not change the incident sound field on the ear. Therefore, the scattered sound field from the ear surface should be absorbed completely within the headphone. However, if the surface of the headphone is not perfectly absorbent, the scattered sound waves from the ear surface are reflected from the headphone surface. This reflected sound field from the headphone surface acts as another incident sound field on the control volume. Moreover, some eigenmodes of the closed volume of the headphone can occur, which can make this situation worse and thus destroy the virtual acoustic field. Therefore the theory of the RISE system cannot be applied because the incident sound field on the control volume is changed due to the scattered sound field from the ear surface. The perfectly absorbent headphone surface is obviously an ideal condition. However, it is not perfectly realizable although highly absorbent material at high frequency is available. A large volume of absorbent material can also make a headphone heavier and larger. Therefore, some compromise in the performance with other factors should be made. Most absorbent material often fails to absorb low frequency waves, but this is not problematic because the production of virtual acoustic images at low frequencies is straightforward due to the dominance of the ITD cue as discussed in chapter 2.

All the numerical models and most conditions are the same as those in the previous section. The point monopole source in the primary sound field is located in the horizontal plane at every 15° angle, one metre away from the centre, and has the same

amplitude. The sound pressures at the control points are calculated from 200 Hz to 10 kHz with a constant frequency increment of 200 Hz. The highest frequency is again set to be 10 kHz. The number of headphone sources is fixed at 45. The boundary condition of the spherical head surface of the models is rigid. Figure 10.40 shows the eardrum sound pressure level differences averaged over frequency for various reflection coefficients of the headphone surface with the 45 headphone sources. Reflection coefficients of the surface of the headphone are assumed to be real numbers. Zero reflection coefficient implies perfect absorption and unit reflection coefficient implies rigid condition as given in Eq. (5.4). This clearly shows that the perfect absorbent headphone surface produces the best performance of the RISE system, and the performance error is proportional to the reflection coefficient regardless of the angle of incident waves in the horizontal plane. Therefore, the performance of the system will probably show a similar tendency in case of the median or frontal plane. Figure 9.20 shows the case of zero reflection coefficient of the headphone surface. Figure 10.41 shows the eardrum sound pressure level differences for various source directions in the horizontal plane with the 45 headphone sources and the following reflection coefficients of the headphone surface: (a) R=0.1, (b) R=0.2, (c) R=0.3, (d) R=0.4, (e) R=0.5, (f) R=0.6, (g) R=0.7, (h) R=0.8, (i) R=0.9, (j) R=1. The scales of all the colour filled contour figures are identical from 0 to 6 dB. Figure 10.42 shows the example of the eardrum sound pressure level for the source at 180° azimuth. The solid line shows the desired eardrum sound pressure levels and dashed line shows the reproduced values when the reflection coefficient of the headphone surface is 0.5. This shows the interference of the eigenmodes of the enclosed headphone volume. A reasonable performance is shown overall up to the case of R=0.2 and the performance becomes poorer from the case of R=0.3. Generally the accuracy of reproduction is slightly better when the source in the primary field is in the frontal side than when the source is in the rear.

Figure 10.43 shows the average differences of the interaural level differences over frequency for various reflection coefficients of the headphone surface with the 45 headphone sources in the horizontal plane. This also shows that the best value of the boundary condition of the headphone is perfect absorption. Figure 10.44 shows the differences in the ILDs for various source directions in the horizontal plane with the

45 headphone sources and the following reflection coefficients of the headphone surface: (a) R=0.1, (b) R=0.2, (c) R=0.3, (d) R=0.4, (e) R=0.5, (f) R=0.6, (g) R=0.7, (h) R=0.8, (i) R=0.9, (j) R=1. These results show a similar tendency to those shown in Figure 10.41 but are somewhat improved. For example, the reproduction error of the ILD is under about 3 dB up to 7 kHz in the case of R=0.5 when the source in the primary field is in the front. This is quite a promising result for frontal reproduction. Figure 10.45 shows the error in the interaural time differences for various reflection coefficients of the headphone surface over frequency with 45 headphone sources in the horizontal plane. Even the worst error is below 0.7%, which is almost negligible. Therefore, the ITD can be reasonably reproduced regardless of the boundary conditions of the headphone surface.

10.4 A headphone of smaller size

The size and geometry of the headphone is one of major factors affecting the design of a virtual acoustic system. The hemispheric numerical headphone models having a radius of 60 mm have been used up to now. However, that headphone is somewhat large for practical use. Since there is a gap from the surfaces of the small control field having a radius of 30 mm to surfaces of the 'large' headphone, the simplified numerical model of the multichannel headphone of smaller size is suggested. The headphone of smaller size was modelled as a hemisphere having a radius of 40 mm and a cylinder with 10 mm width extended from the hemisphere. The flat surface or the DB65 ear surface was located at the bottom of the headphone. Figure 10.46 shows this hemispheric headphone model of smaller size with the flat surface. This model has 2694 elements and 1349 nodes. The headphone sources are modelled as piston-like flat vibrating surfaces having a radius of 5mm, and they are placed in the same way as those of the large headphone shown in Fig. 10.1. The small and sparse control field shown in Fig. 9.4. is used. This figure also shows the placement of the small control field on this small headphone model. Figure 10.47 shows the small headphone model with the DB65 artificial ear model. This model has 9496 elements and 4750 nodes. The axis of the ear canal is off-centered by 10mm from the centre to

locate the whole pinna at the centre of the headphone model. Since the length of the ear is longer than the breadth of the ear, this round type of headphone has just a tiny gap from the upper ear surface to the headphone surface. The numerical simulations use the numerical models of the head shown in Fig. 7.6 and 7.8. The point monopole source in the primary sound field is located in the horizontal, median, or frontal plane for every 15° angle, one metre away from the centre, and has the same amplitude as that in previous section. The sound pressures at the control points are calculated from 200 Hz to 10 kHz with a constant frequency increment of 200 Hz. The highest frequency is set to be 10 kHz. The boundary condition of the spherical head surface of models is rigid.

First, the performance of the RISE system using the headphone of smaller size is examined by changing the number of headphone sources. The boundary condition of the surface of the headphone including the headphone sources is assumed to be perfectly absorbent. Figure 10.48 shows the red area is where the perfectly absorbent boundary condition of the headphone is applied. Figure 10.49 shows the filled contour figure of the eardrum sound pressure level differences for 17 headphone sources in the horizontal plane, scaled from 0 to 6 dB. Figure 10.50 shows those in the median plane and Figure 10.51 shows those in the frontal plane. Figure 10.52 shows the differences of interaural level differences for 17 headphone sources in the horizontal plane with the small headphone, and Figure 10.53 shows those in the frontal plane. They show that many reproduction errors are below 1 dB, and they show similar trends to the cases of the large headphone shown in section 10.2, although the errors are slightly worse for a few angles at high frequencies.

Figure 10.54 shows the eardrum sound pressure level differences for 9 headphone sources in the horizontal plane. Figure 10.55 shows those in the median plane and Figure 10.56 shows those in the frontal plane. Figure 10.57 shows the differences of interaural level differences for 9 headphone sources in the horizontal plane, and Figure 10.58 shows those in the frontal plane. Figure 10.59, 10.60, 10.61, 10.62, or 10.63 shows the corresponding differences of the eardrum sound pressure level or ILDs for the 5 headphone sources in the horizontal, median or frontal plane. They all show similar trends to the cases of the large headphone described in section 10.2.

Figure 10.64 shows the errors of the ITD over various source directions for different number of headphone sources in the horizontal plane, and Figure 10.65 shows those in the frontal plane. Most of the errors in the ITD are less than 1%, which is almost negligible. Figure 10.66 shows the mean value of the average sound pressure level differences at control points over various source directions in the horizontal plane. This shows the control error increases as frequency increases and more rapidly for a smaller number of headphone sources. For example, this control error becomes over 3 dB from about 9 kHz for 17 sources, 7 kHz for 9 sources, and 5 kHz for 5 sources.

Figure 10.67 shows the average differences of the eardrum sound pressure levels or the ILDs over frequency or various source directions in the horizontal, median, or frontal plane for the 17 headphone sources. The performance of the large headphone is better than that of the small headphone in most cases. So the headphone should be large enough for the 17 headphone sources. Figure 10.68 shows the corresponding average differences for the 9 headphone sources. The performance of the large headphone is better than that of the small headphone for some angles and some frequencies, but it is worse for other angles and frequencies. So, in case of the 9 headphone sources, neither size of headphone shows clear superiority in terms of performance. Figure 10.69 shows the corresponding average differences for the 5 headphone sources. Similarly, in the case of 5 headphone sources, neither size of headphone shows superior performance.

Second, the performance of the RISE system using the headphone of smaller size is examined by changing the boundary condition of the surface of the headphone. The number of headphone sources is assumed to be 17. Reflection coefficients of the surface of the headphone are assumed to be real numbers. Figure 10.70 shows the eardrum sound pressure level differences averaged over frequency in the horizontal plane for various reflection coefficients of the small headphone surface. This shows a similar tendency to that of the large headphone. Figure 10.71 shows those in the median plane, and Figure 10.72 shows those in the frontal plane. Figure 10.73 shows the average differences of the ILDs over frequency in the horizontal plane, and Figure 10.74 shows those in the frontal plane. They show that the perfectly absorbent headphone surface produces the best performance of the RISE system, and the performance error in general is roughly proportional to the reflection coefficient at

each angle. However, as the reflection coefficient goes from 0 to 1, the reproduction errors increase less rapidly at some angles and more rapidly at other angles. For example, the performance of the system is better for high reflection coefficients when the primary source is frontal than that when the source is in the rear. Therefore, the optimal boundary condition of the headphone depends on the focused reproduction area of the system. Figure 10.75 shows the errors of the interaural time differences over frequency in the horizontal plane for various reflection coefficients of the small headphone surface. Most errors are below 1 % and the maximum is below 2 %, which is nearly negligible. Therefore, the ITD can be reasonably reproduced regardless of the boundary conditions of the headphone surface.

10.5 Conclusion

The RISE system is optimized for various system design factors by undertaking numerical simulations. A somewhat idealized multichannel headphone is examined for various numbers of headphone sources. The results of the numerical simulations show that the performance of the RISE system with a multichannel headphone is reasonably good over any angle of incident sound in three-dimensional space if 17 headphone sources are used and the boundary condition of the headphone is perfectly absorbent. The 9 headphone sources can produce a reasonable performance up to about 8 kHz when the source in the primary field is to the front of the listener. The headphone of smaller size does not produce a much lesser performance than the headphone of bigger size in the case of the 9 or 5 headphone sources. The results of numerical simulations show that the perfect absorbent headphone surface results in the best performance of the RISE system, and the performance error is proportional to the reflection coefficient for each angle of incident sound. The performance of the system is better for high reflection coefficients when the primary source is frontal than that when the source is to the rear. A reasonable performance is shown overall up to the reflection coefficient of 0.2. Therefore, the multichannel headphone of smaller size having 9 sources with the reflection coefficient of 0.2 of its surface might be the optimal headphone for a practical virtual acoustic system.

FIGURES

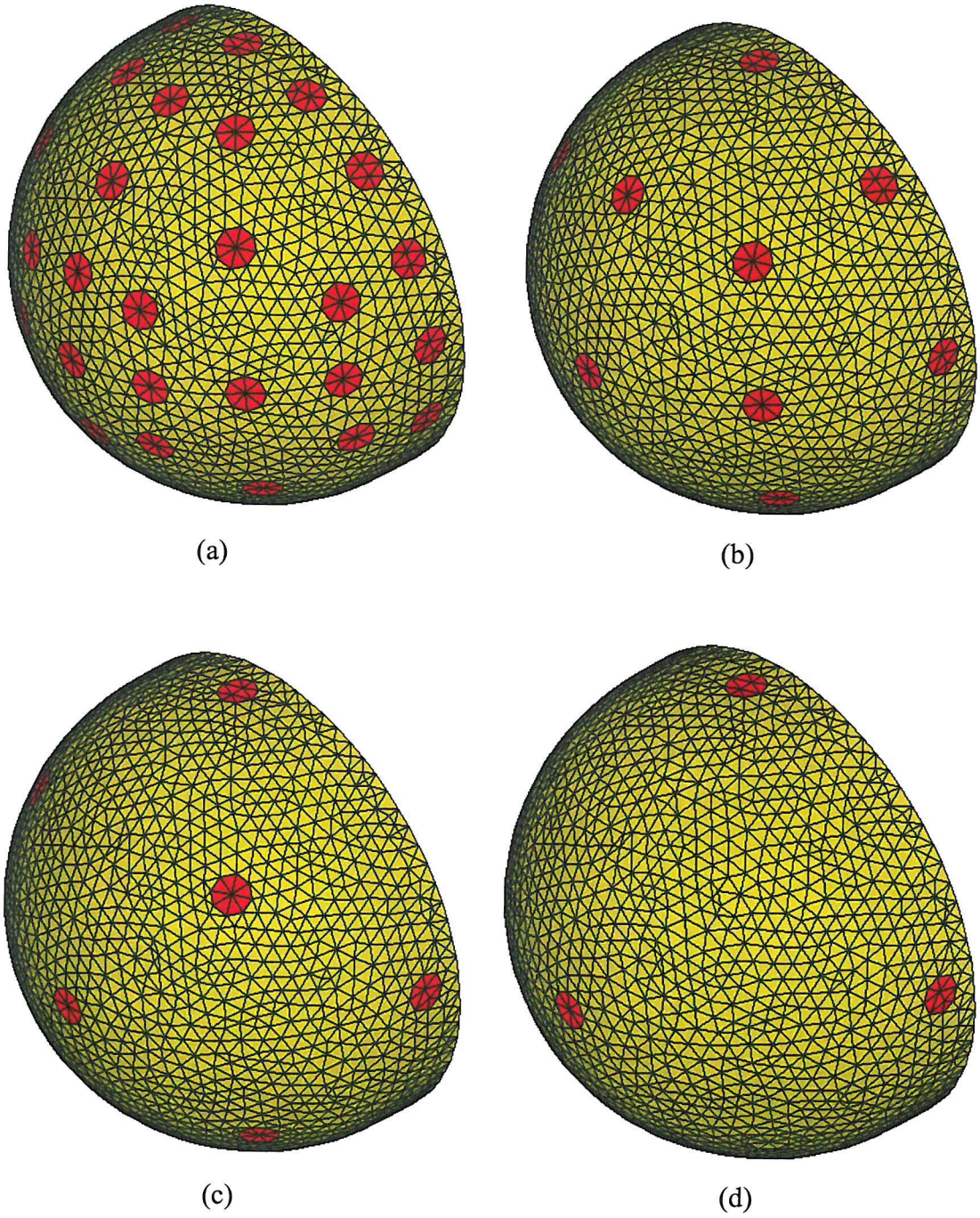

Figure 10.1. Different number of headphone sources. (a) 45 (b) 17 (c) 9 (d) 5.

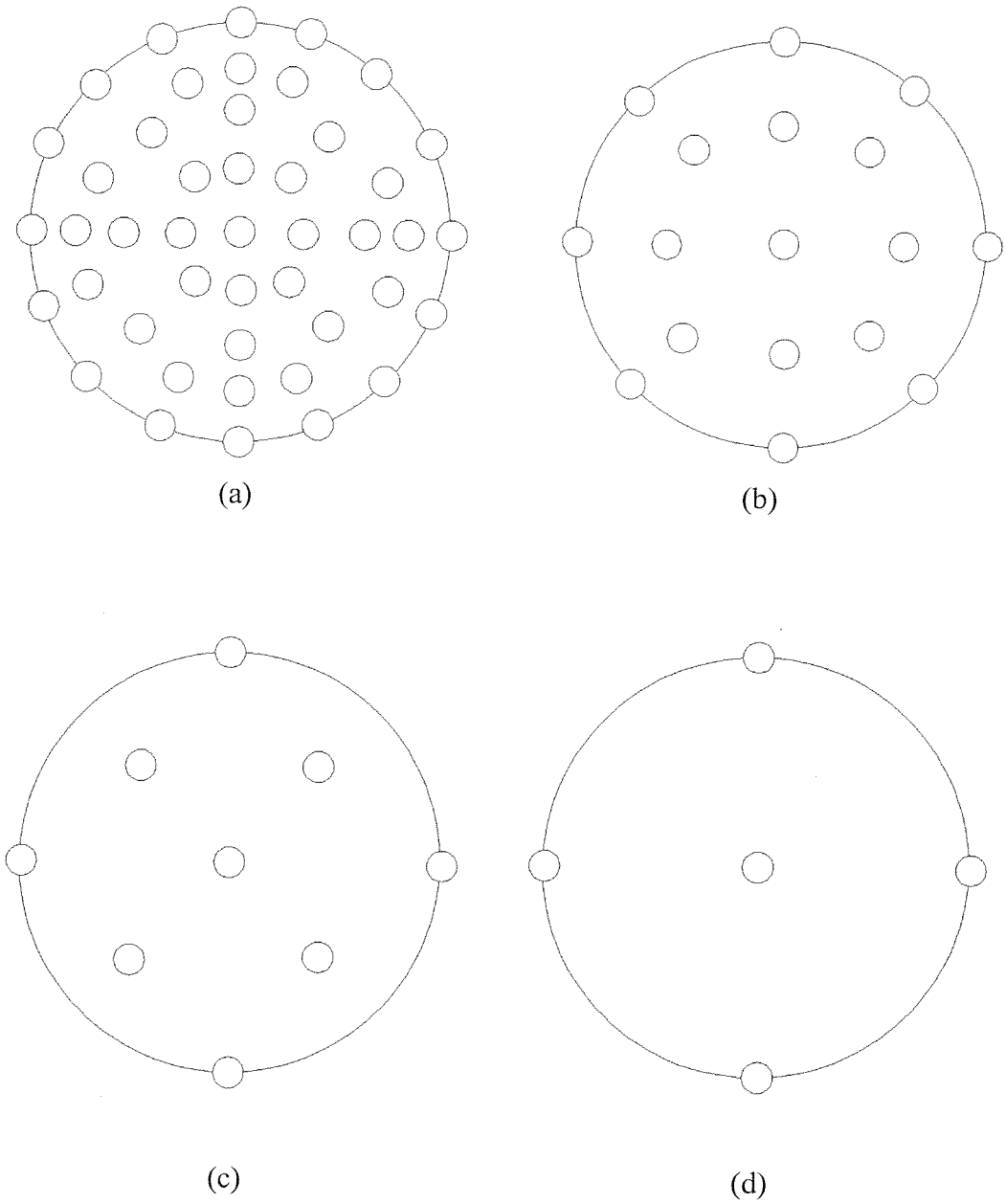

Figure 10.2. Schematic representation of the number of headphone sources. (a) 45 (b) 17 (c) 9 (d) 5.

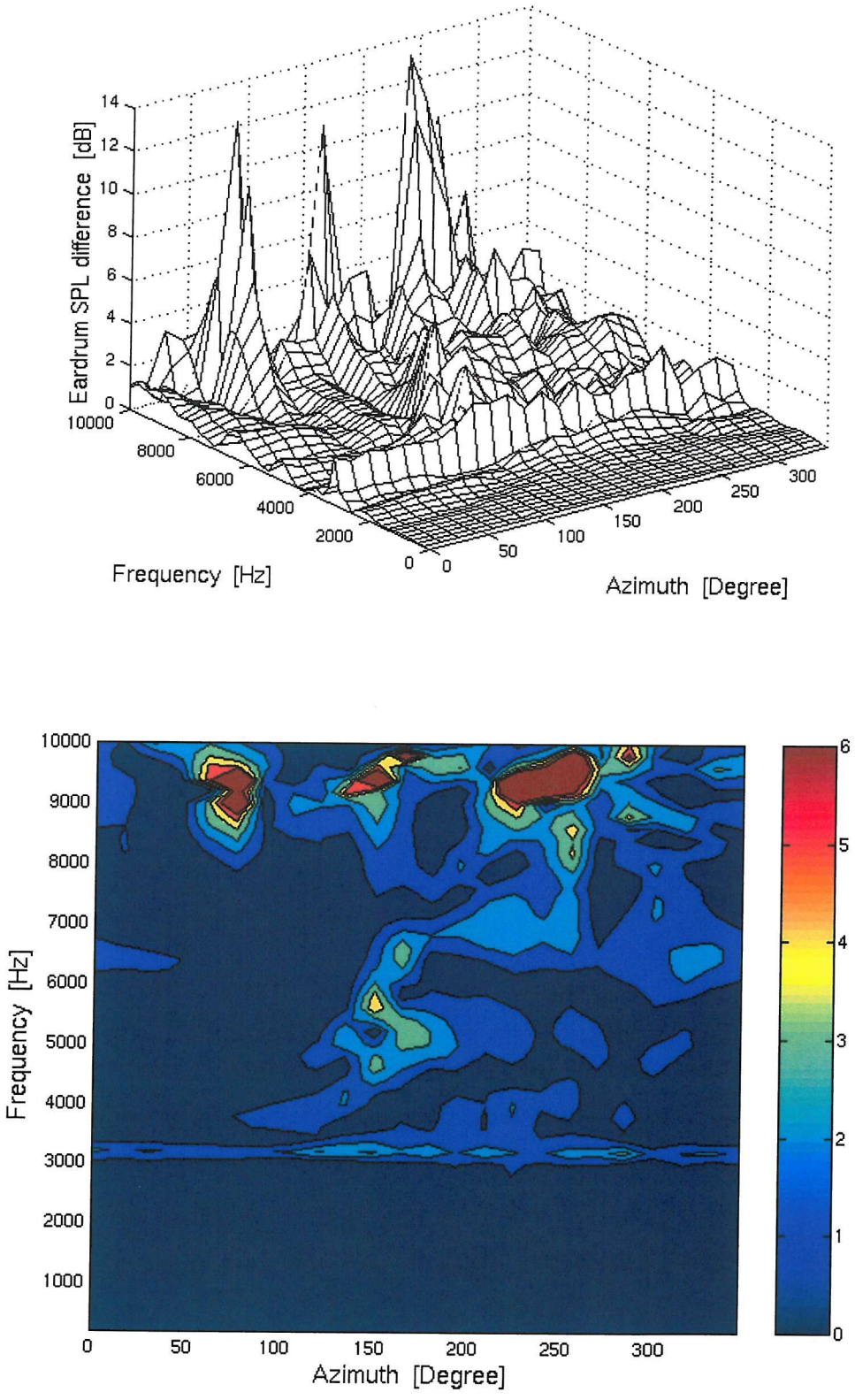

Figure 10.3 The eardrum sound pressure level differences for 17 headphone sources in the horizontal plane with the perfectly absorbent headphone.

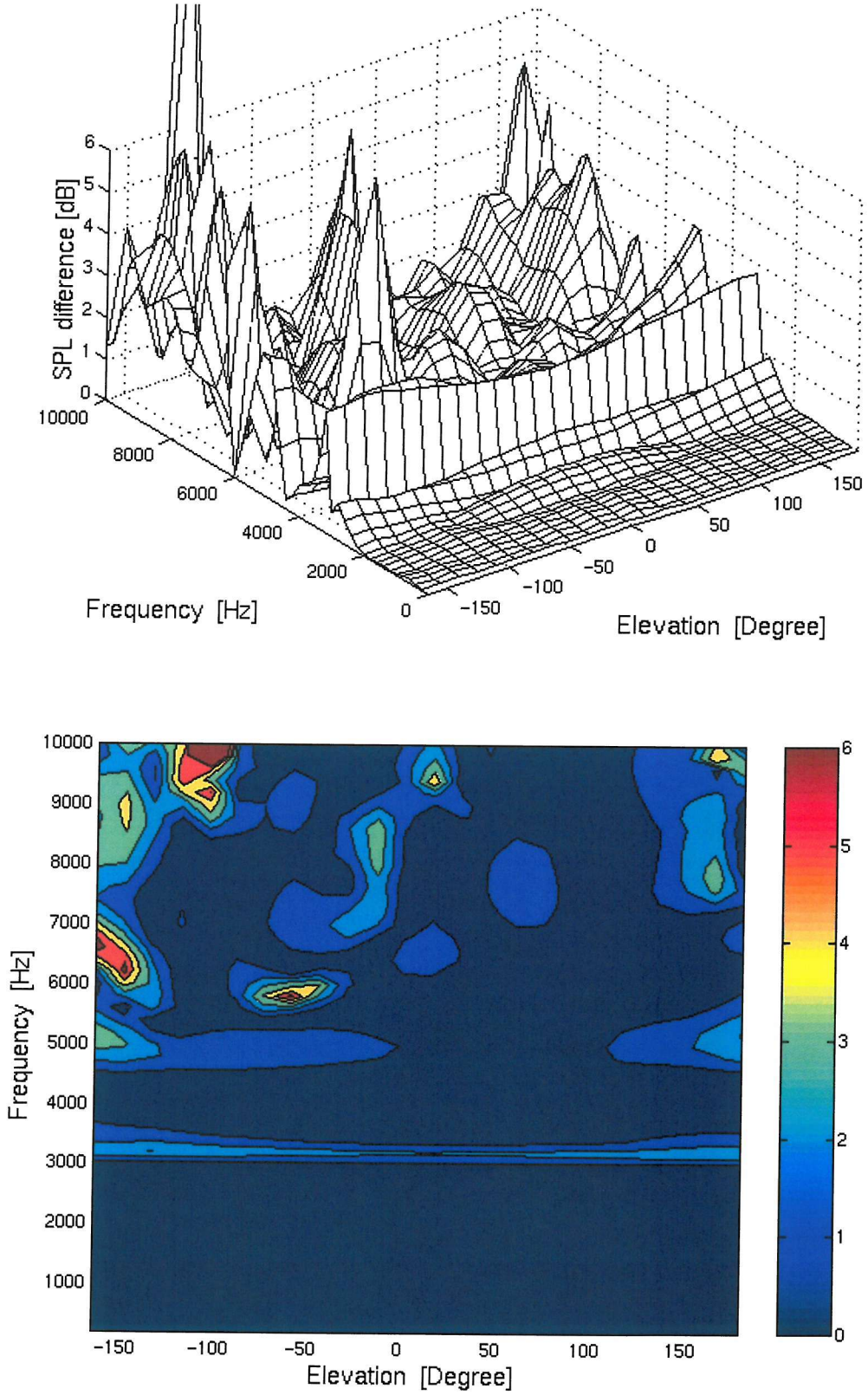

Figure 10.4 The eardrum sound pressure level differences for 17 headphone sources in the median plane with the perfectly absorbent headphone.

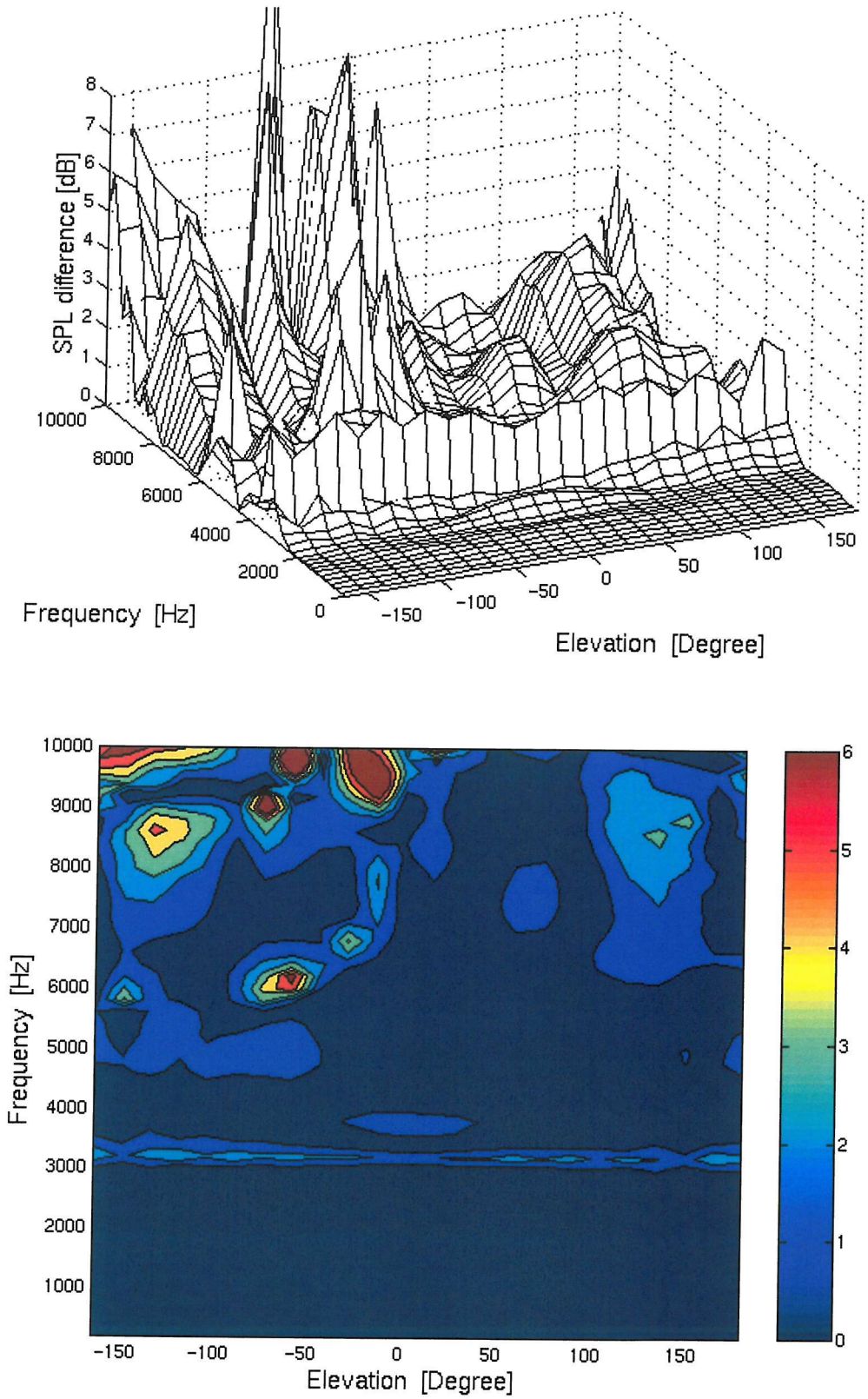

Figure 10.5 The eardrum sound pressure level differences for 17 headphone sources in the frontal plane with the perfectly absorbent headphone.

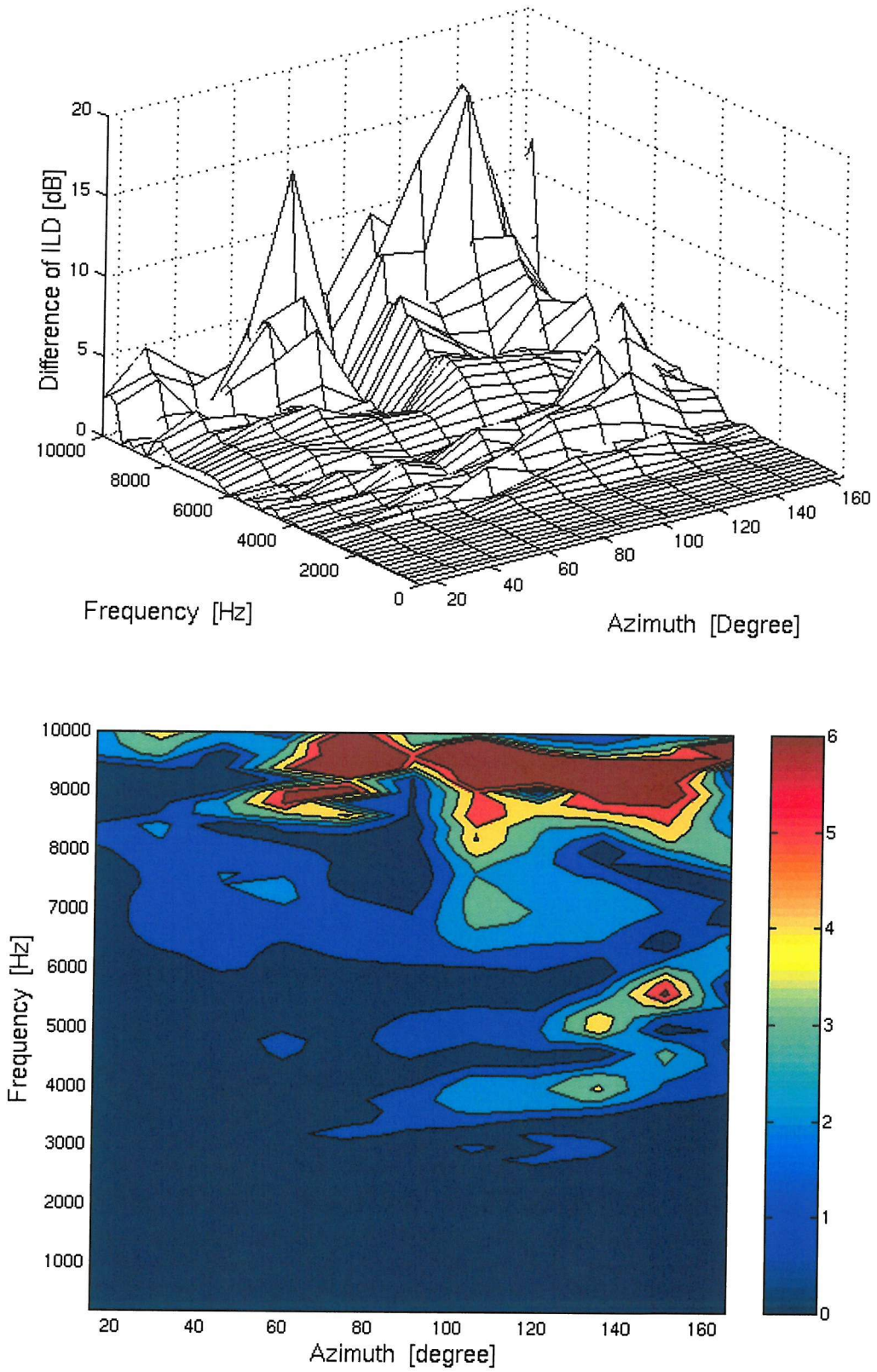

Figure 10.6 Differences of interaural level differences for various source directions in the horizontal plane, 17 headphone sources with the perfectly absorbent headphone.

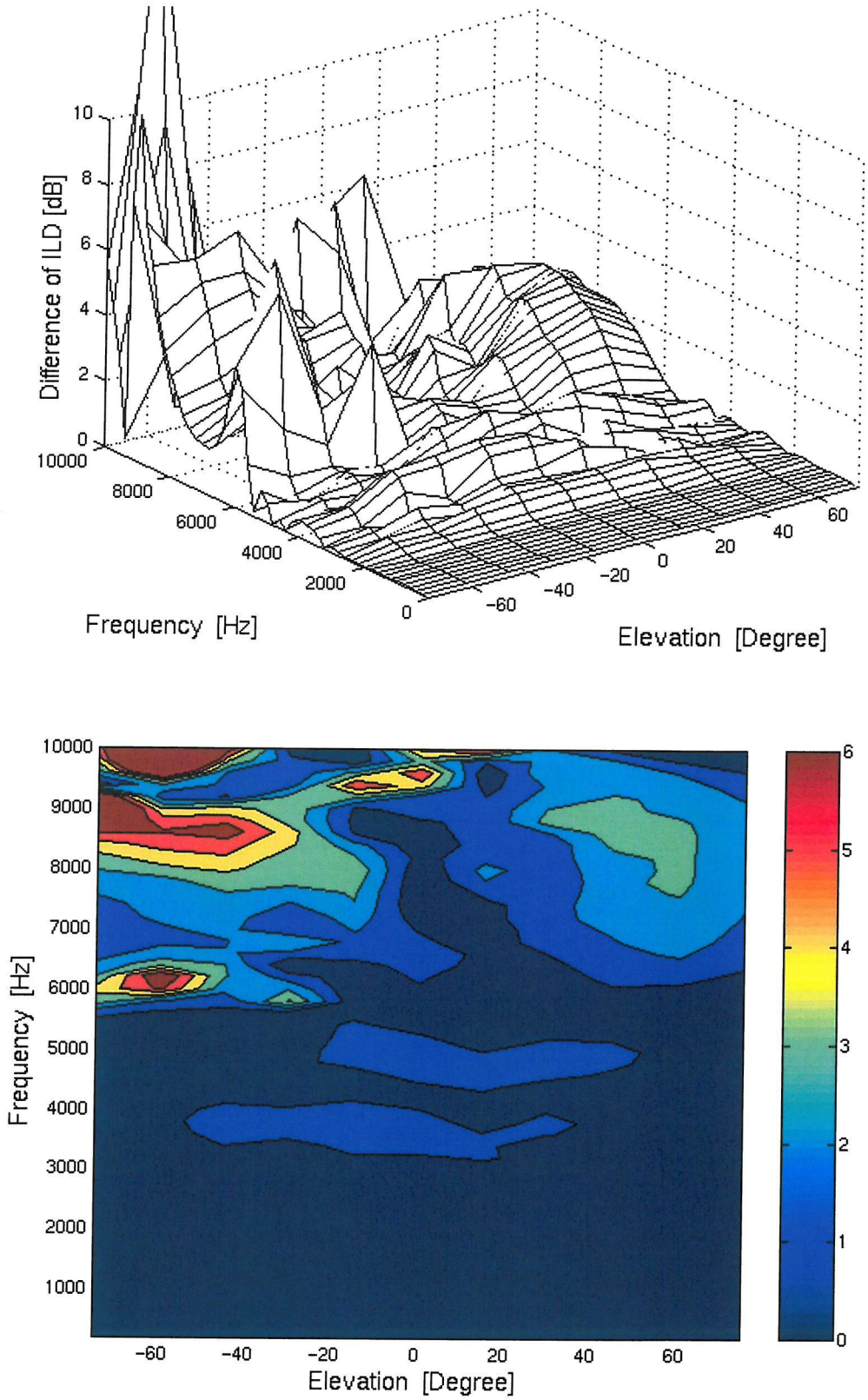

Figure 10.7 Differences of interaural level differences for various source directions in the frontal plane, 17 headphone sources with the perfectly absorbent headphone.

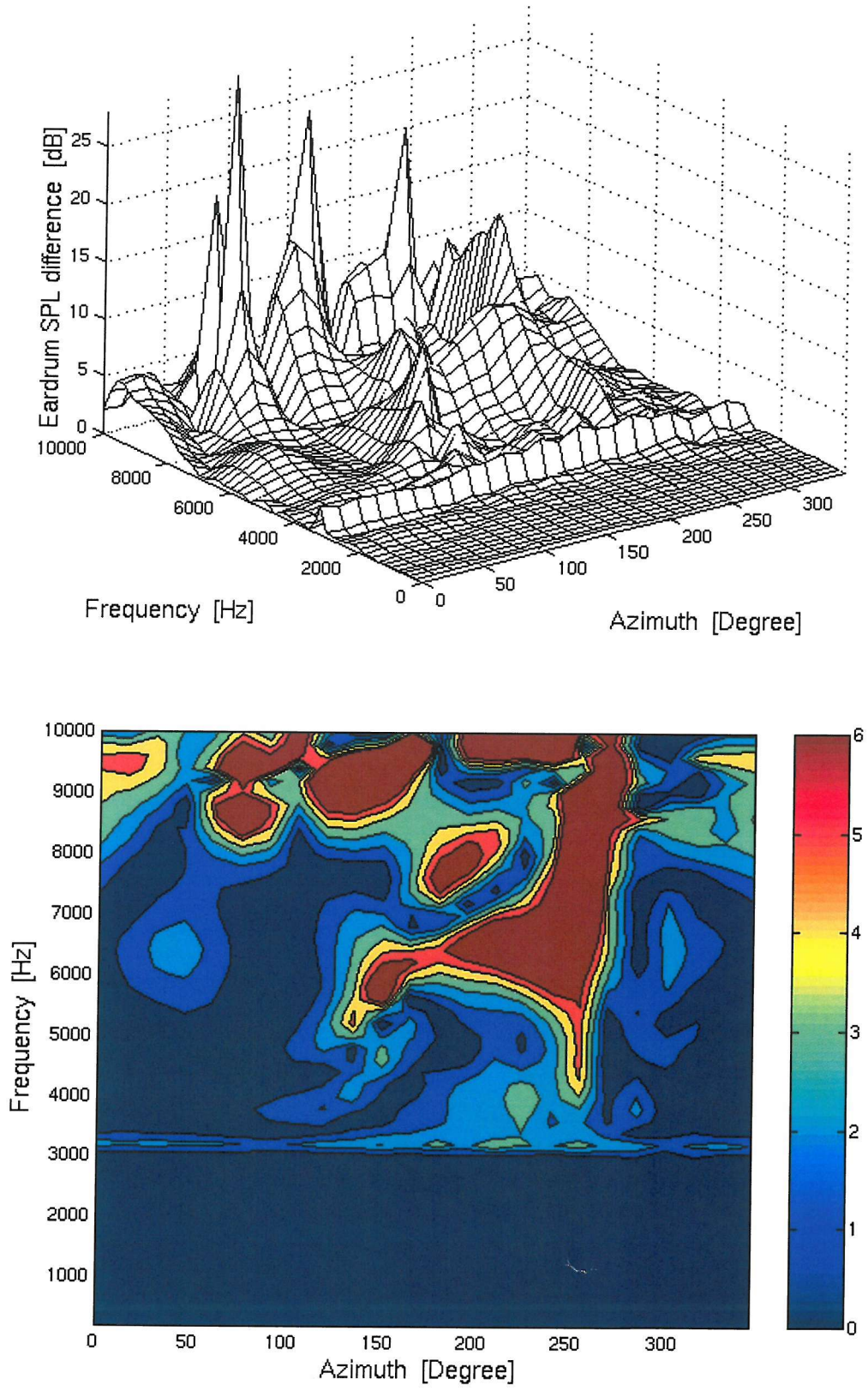

Figure 10.8 The eardrum sound pressure level differences for 9 headphone sources in the horizontal plane with the perfectly absorbent headphone.

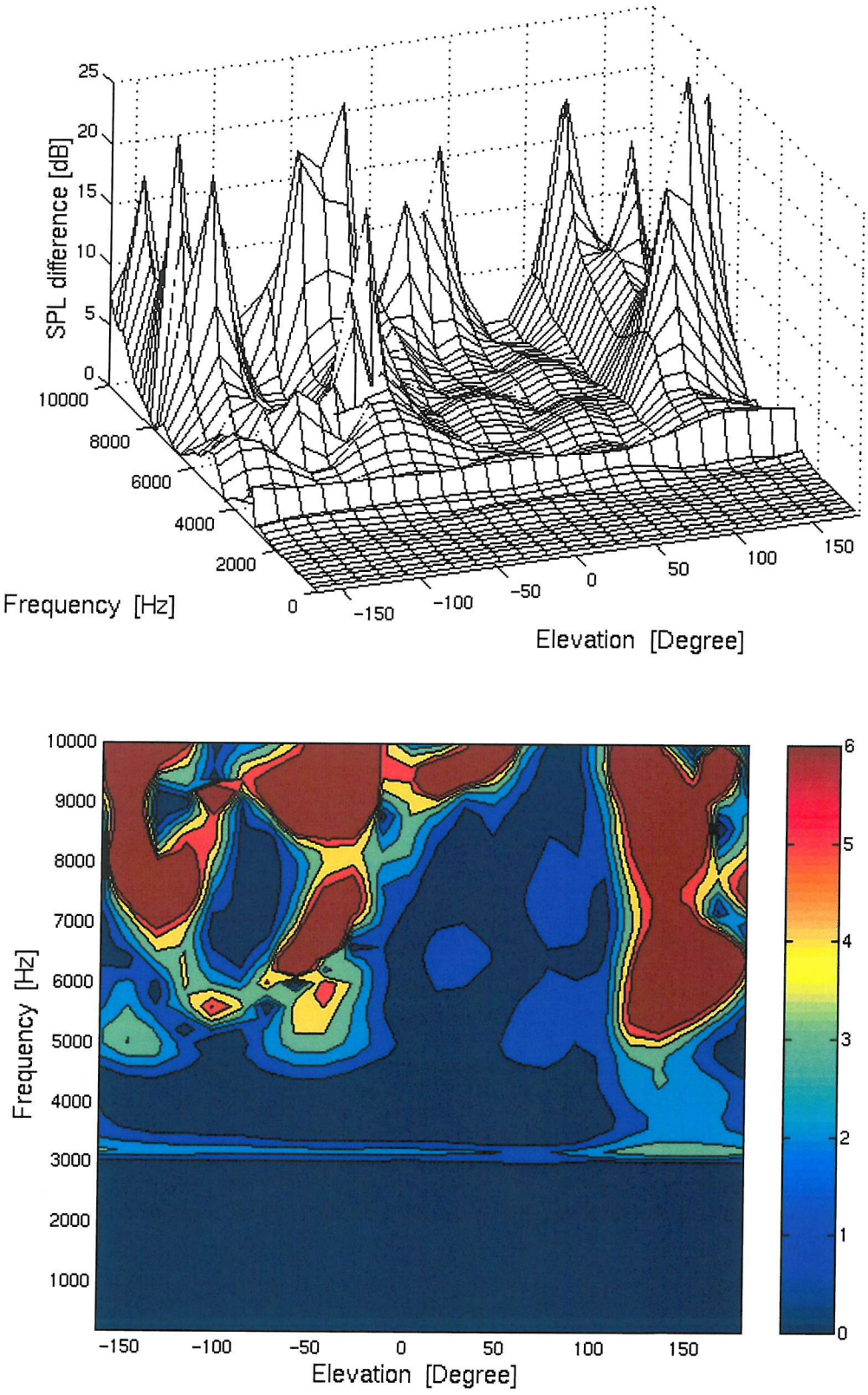

Figure 10.9 The eardrum sound pressure level differences for 9 headphone sources in the median plane with the perfectly absorbent headphone.

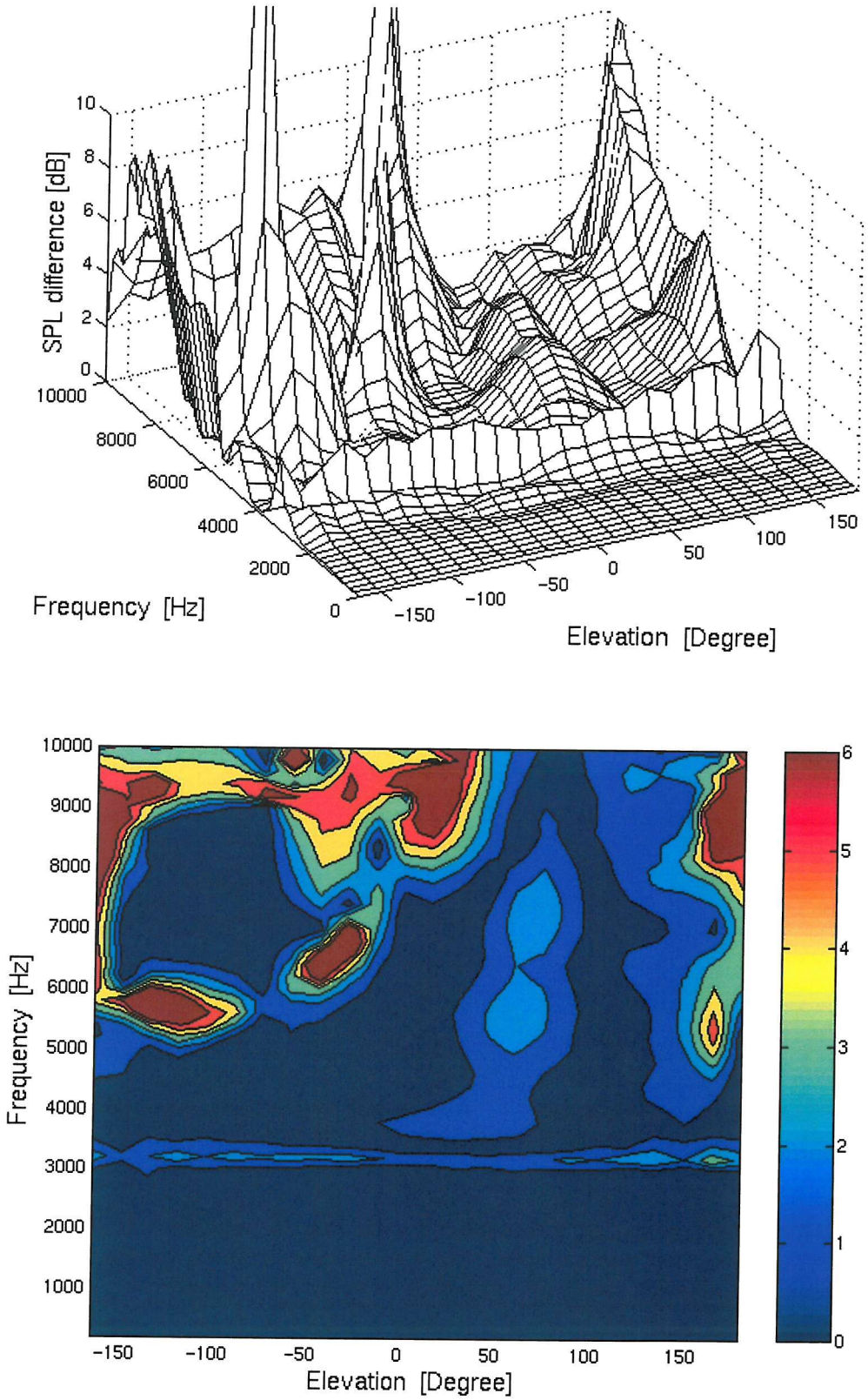

Figure 10.10 The eardrum sound pressure level differences for 9 headphone sources in the frontal plane with the perfectly absorbent headphone.

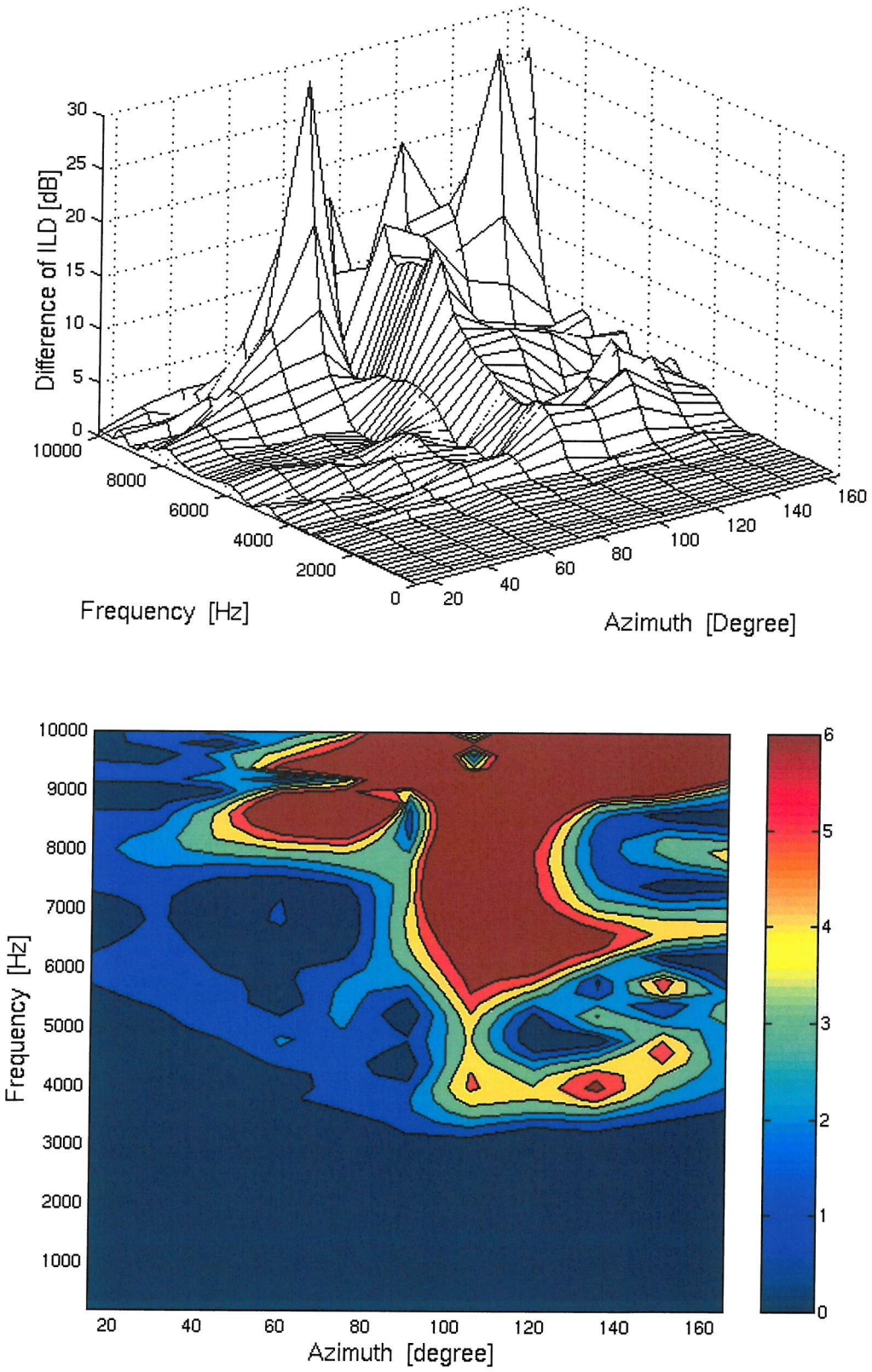

Figure 10.11 Differences of interaural level differences for various source directions in the horizontal plane, 9 headphone sources with the perfectly absorbent headphone.

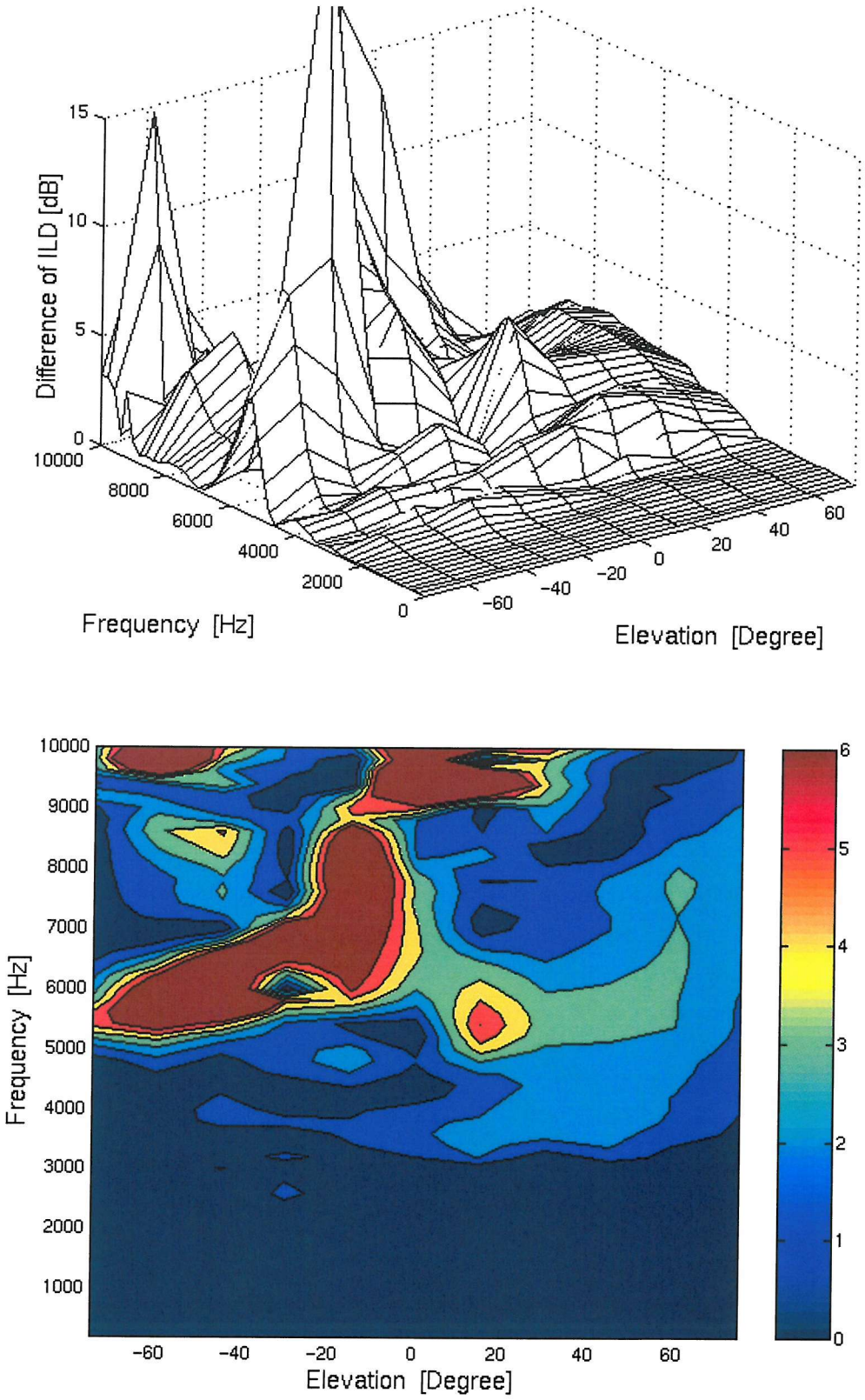

Figure 10.12 Differences of interaural level differences for various source directions in the frontal plane, 9 headphone sources with the perfectly absorbent headphone.

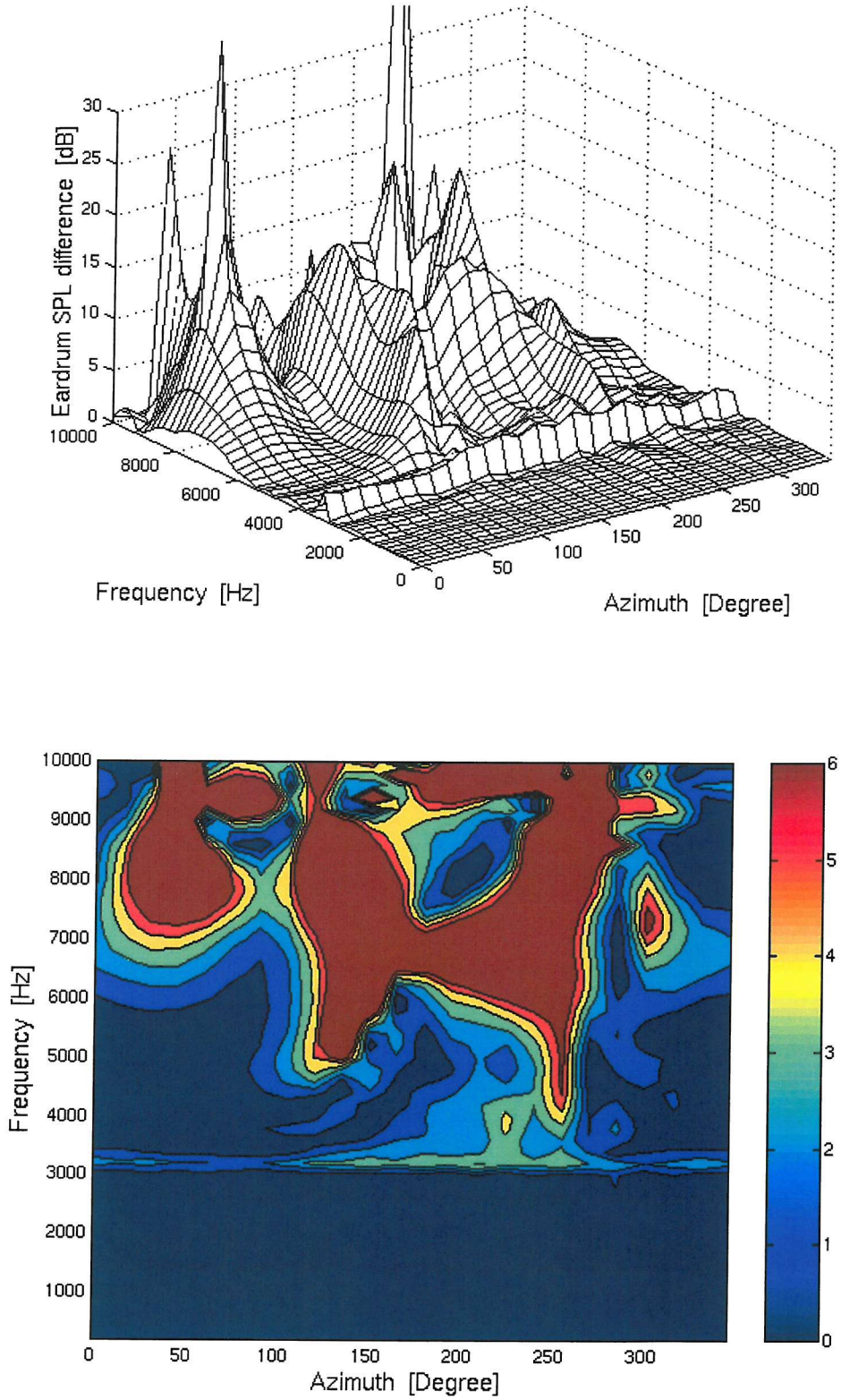

Figure 10.13 The eardrum sound pressure level differences for 5 headphone sources in the horizontal plane with the perfectly absorbent headphone.

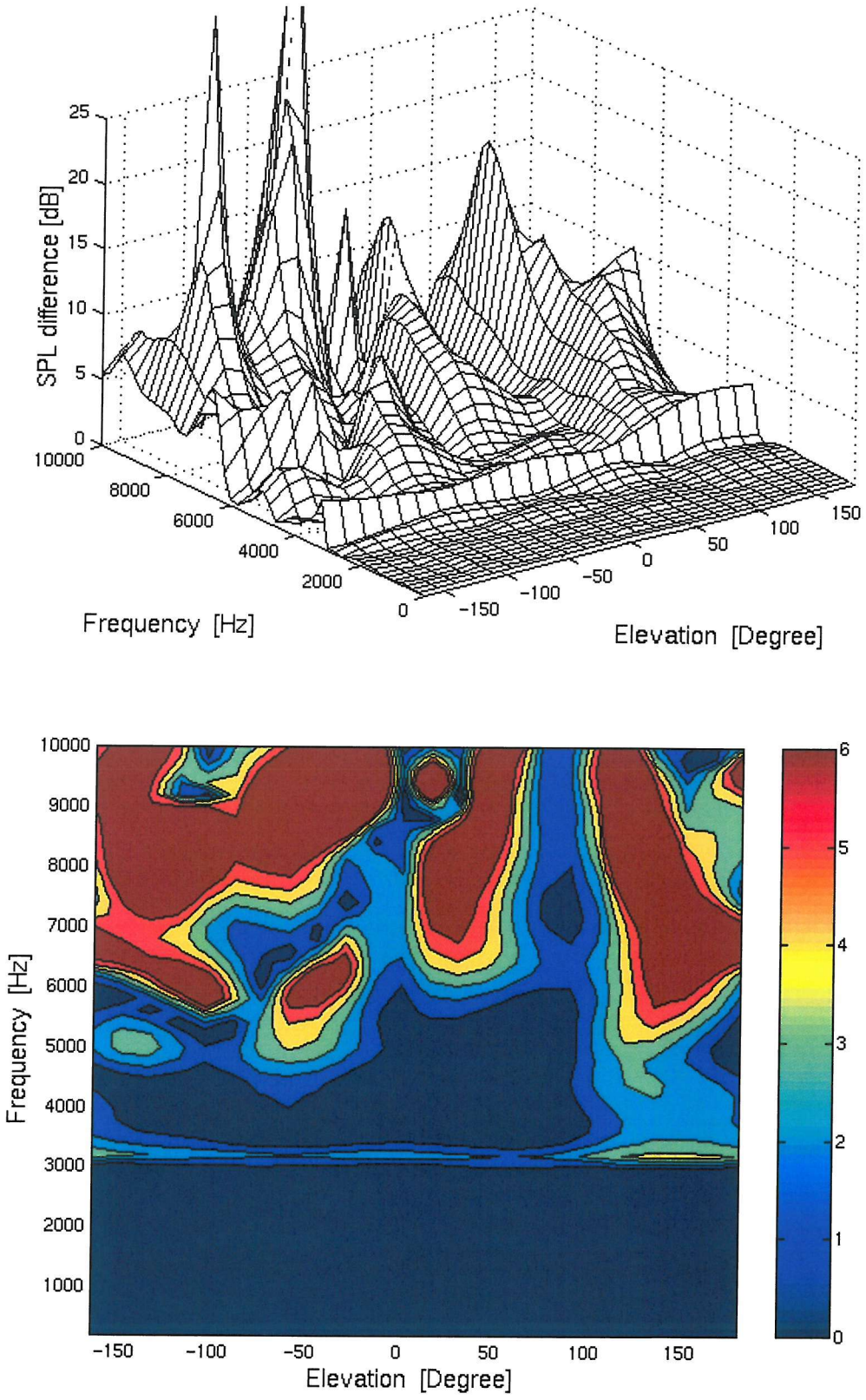

Figure 10.14 The eardrum sound pressure level differences for 5 headphone sources in the median plane with the perfectly absorbent headphone.

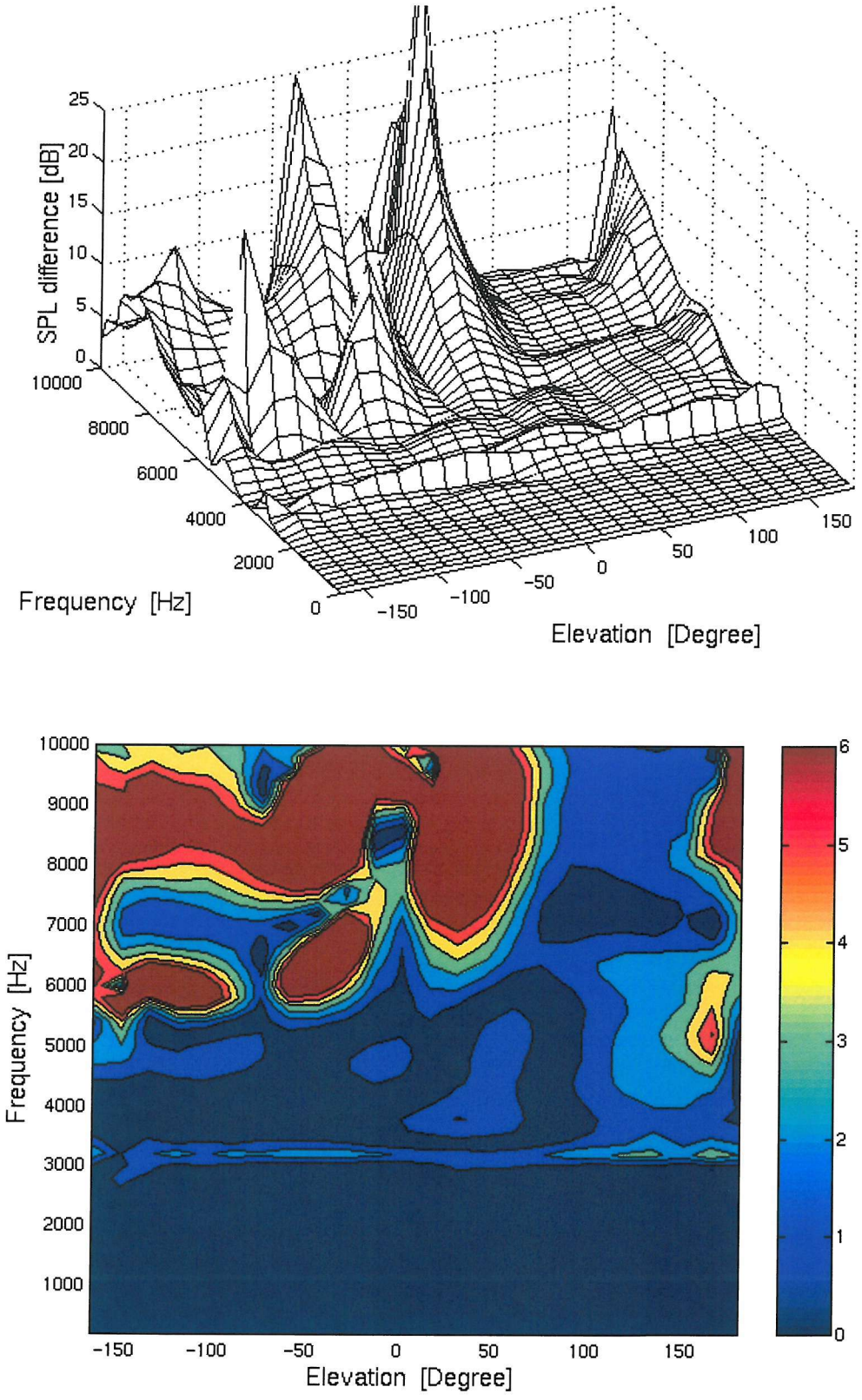

Figure 10.15 The eardrum sound pressure level differences for 5 headphone sources in the frontal plane with the perfectly absorbent headphone.

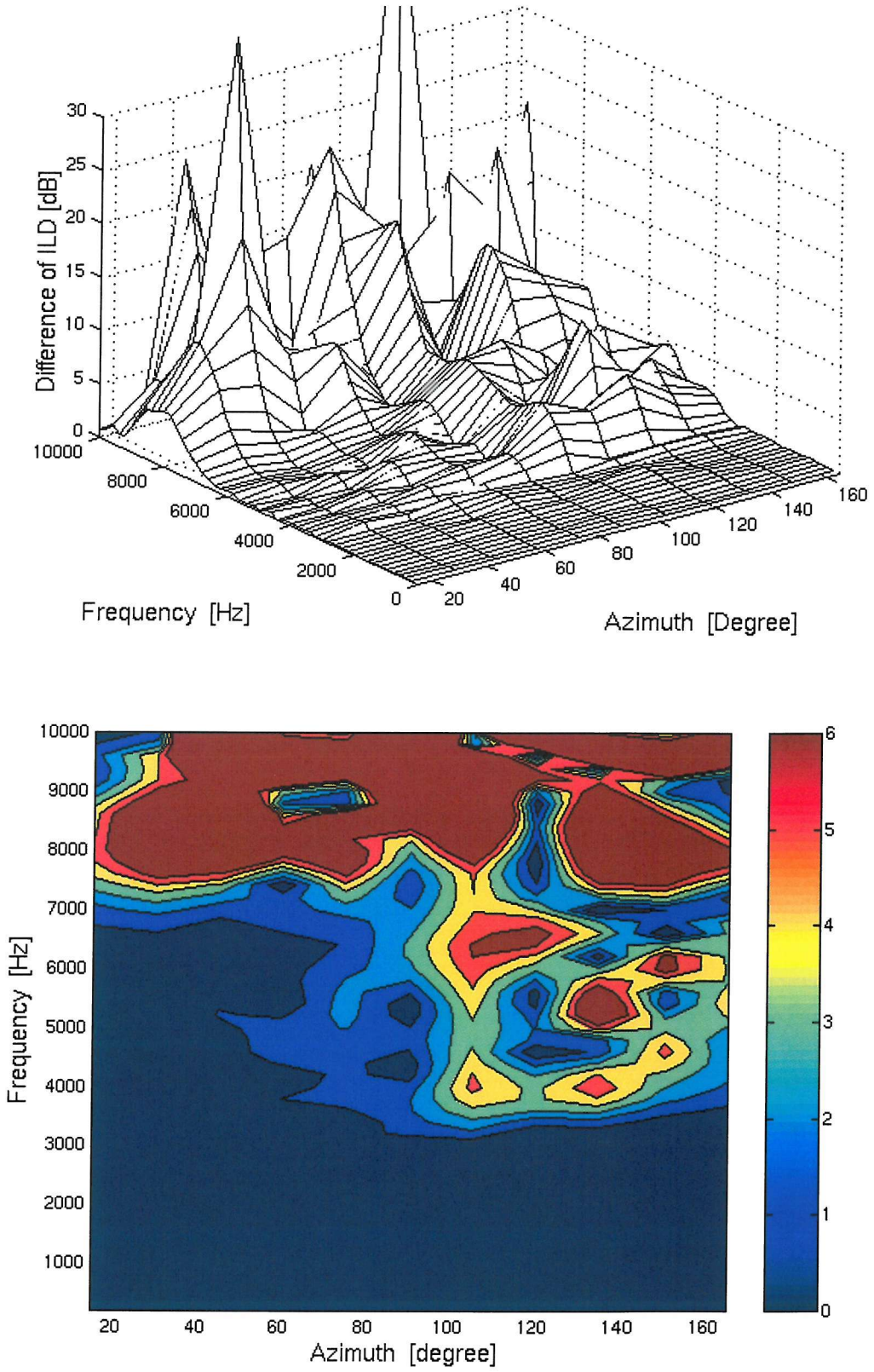

Figure 10.16 Differences of interaural level differences for various source directions in the horizontal plane, 5 headphone sources with the perfectly absorbent headphone.

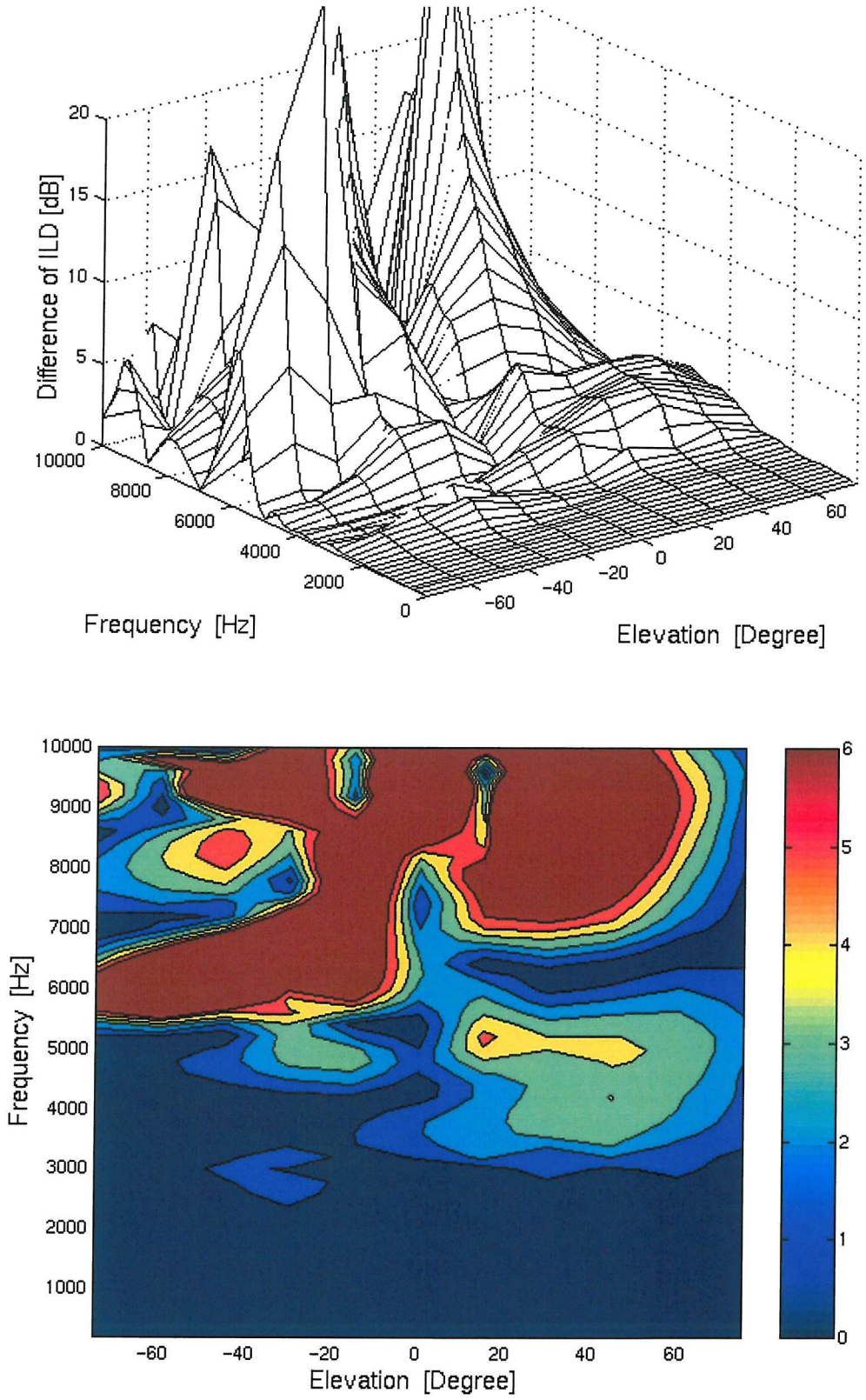

Figure 10.17 Differences of interaural level differences for various source directions in the frontal plane, 5 headphone sources with the perfectly absorbent headphone.

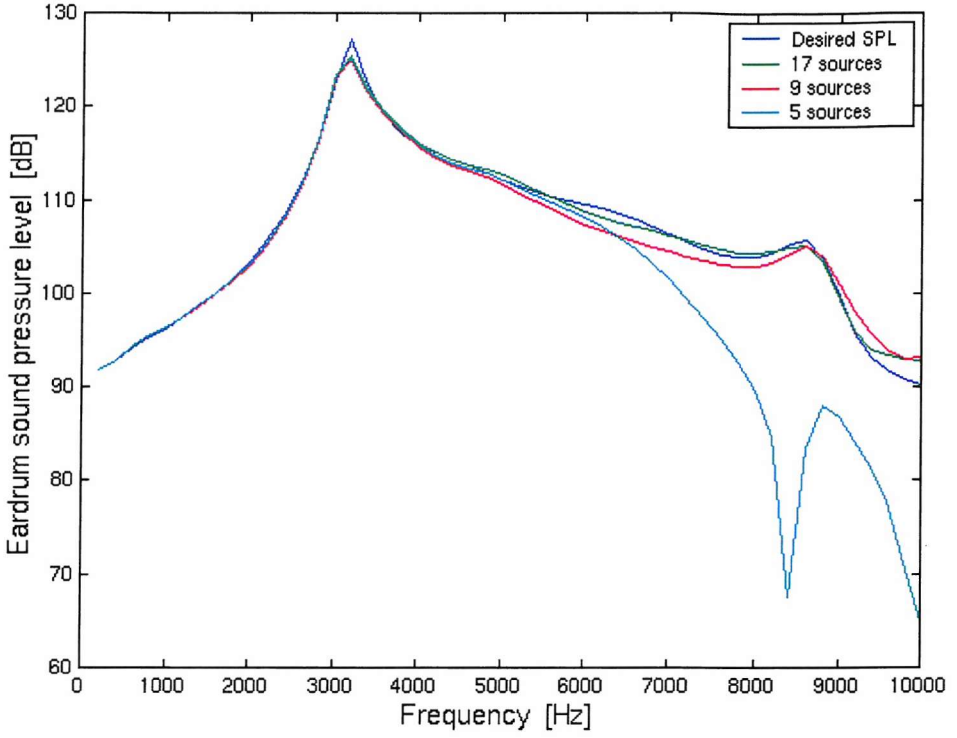

Figure 10.18 Eardrum sound pressure level for the source at 45° azimuth in the horizontal plane.

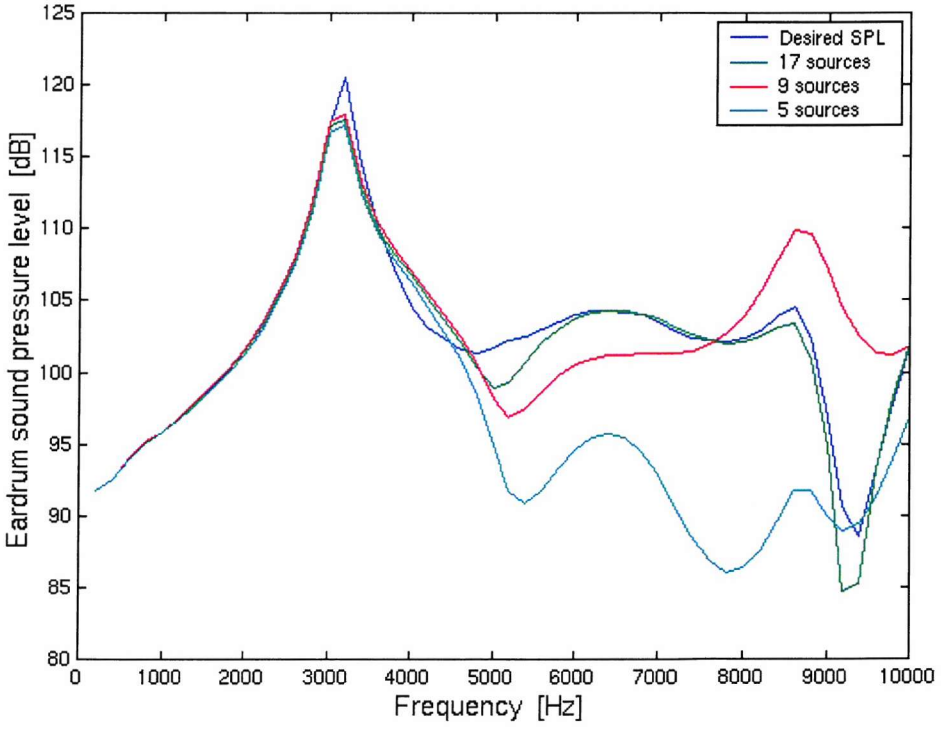

Figure 10.19 Eardrum sound pressure level for the source at 135° azimuth in the horizontal plane.

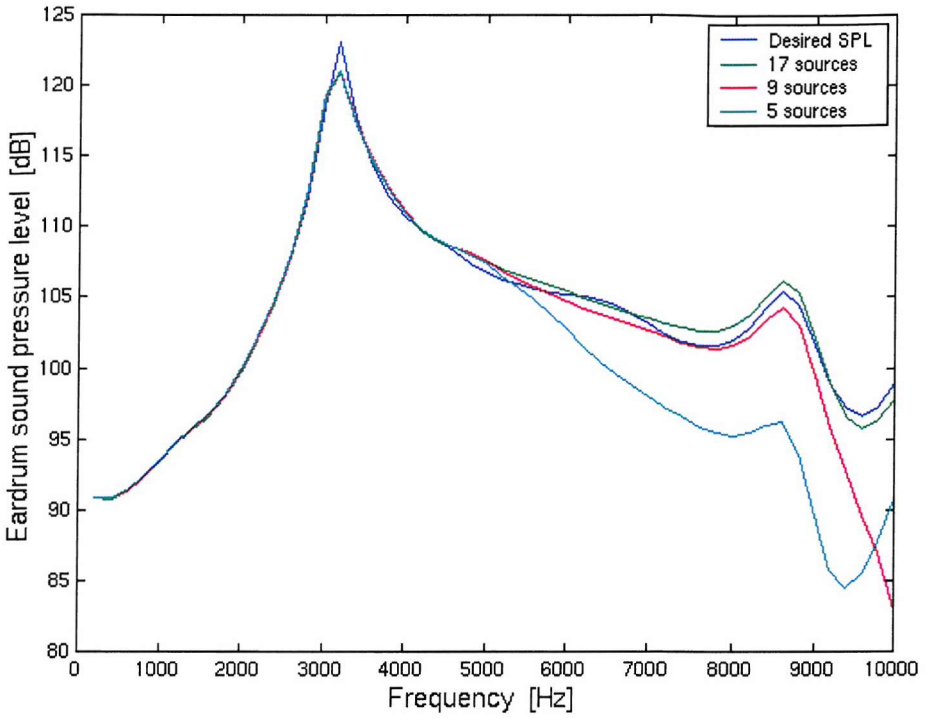

Figure 10.20 Eardrum sound pressure level for the source at 45° elevation in the median plane.

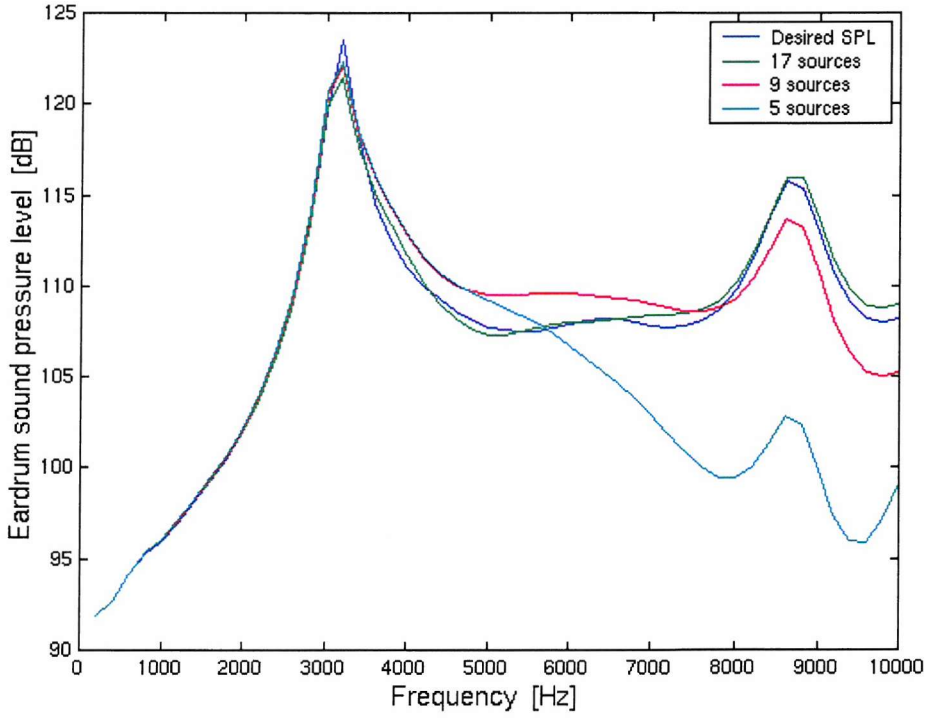

Figure 10.21 Eardrum sound pressure level for the source at 45° elevation in the frontal plane.

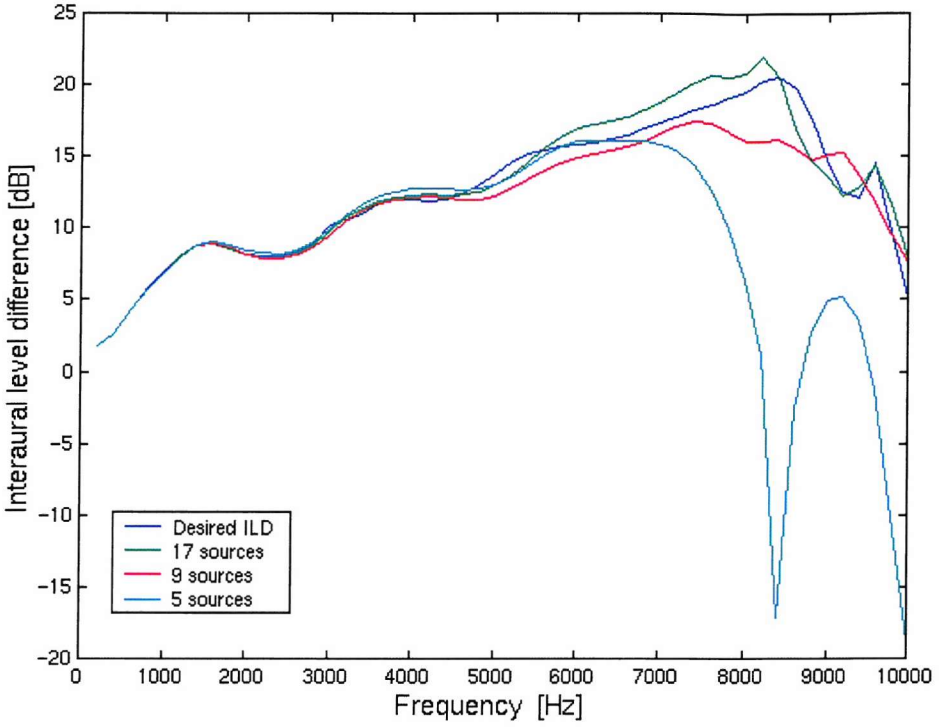

Figure 10.22 Interaural level differences for the source at 45° azimuth in the horizontal plane.

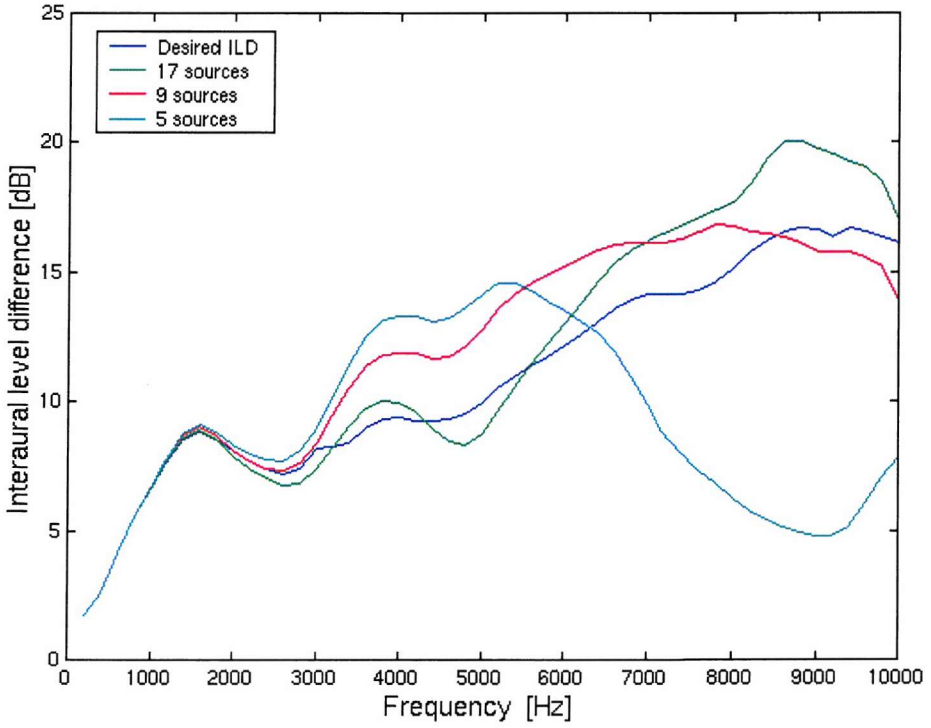

Figure 10.23 Interaural level differences for the source at 45° elevation in the frontal plane.

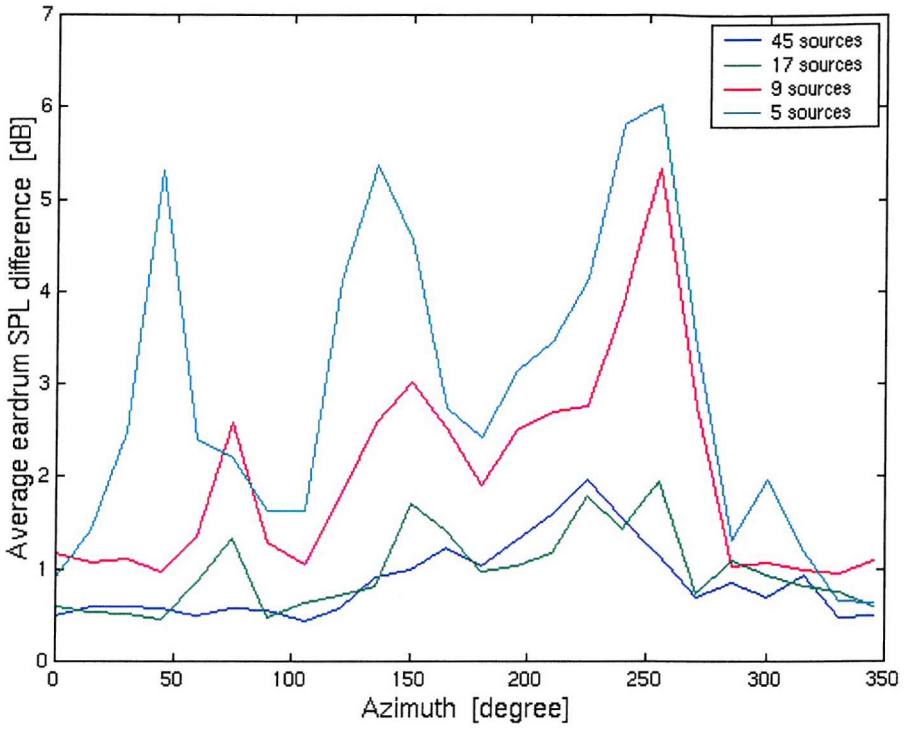

Figure 10.24 The eardrum sound pressure level differences averaged over frequency for different number of headphone sources in the horizontal plane.

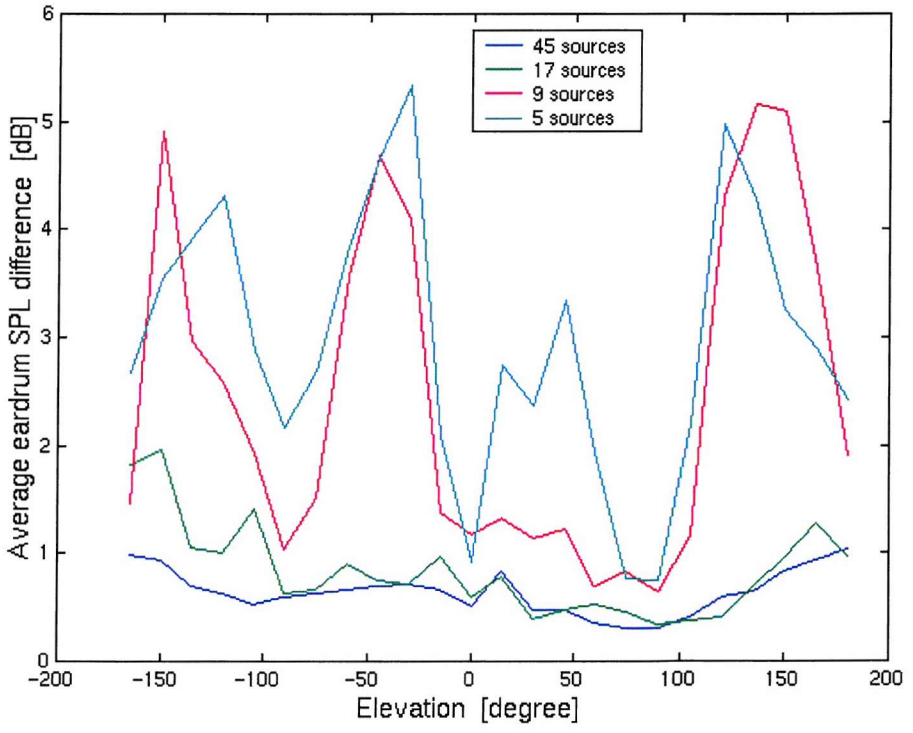

Figure 10.25 The eardrum sound pressure level differences averaged over frequency for different number of headphone sources in the median plane.

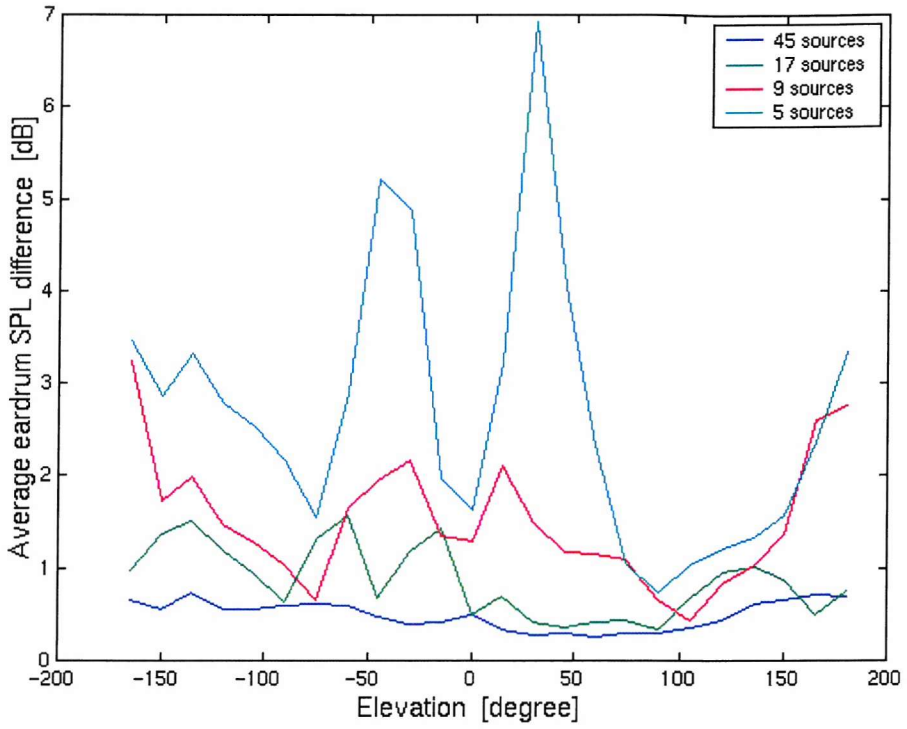

Figure 10.26 The eardrum sound pressure level differences averaged over frequency for different number of headphone sources in the frontal plane.

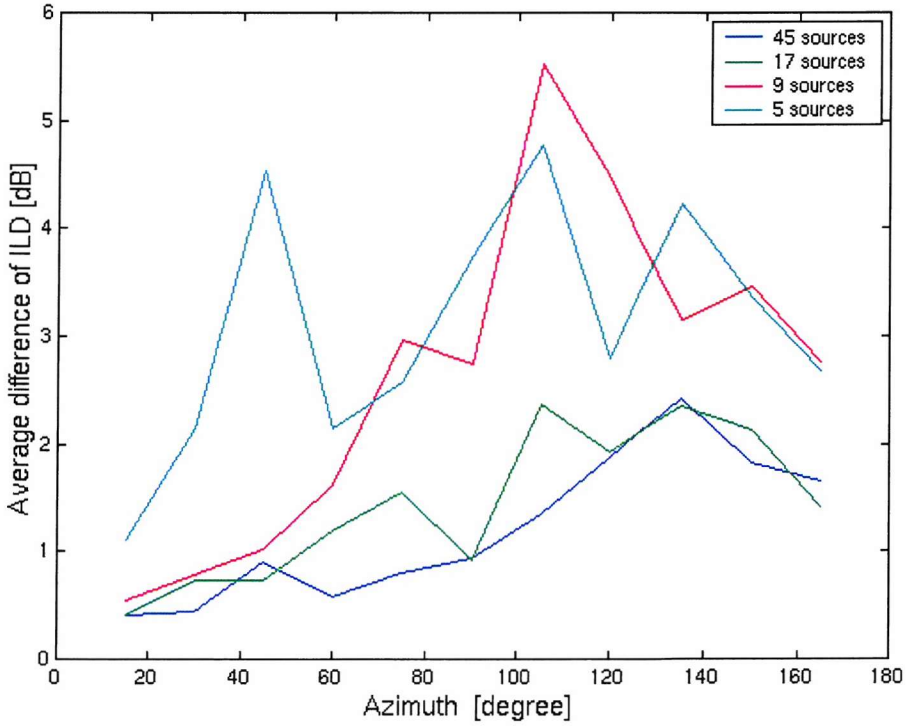

Figure 10.27 Average differences of the ILDs over frequency for different number of headphone sources in the horizontal plane.

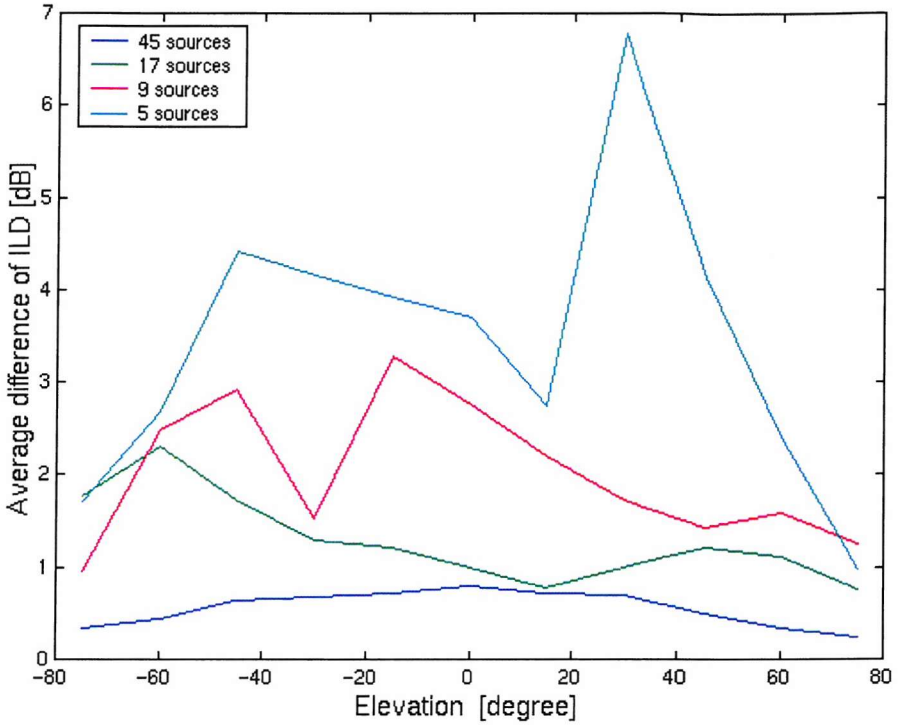

Figure 10.28 Average differences of the ILDs over frequency for different number of headphone sources in the frontal plane.

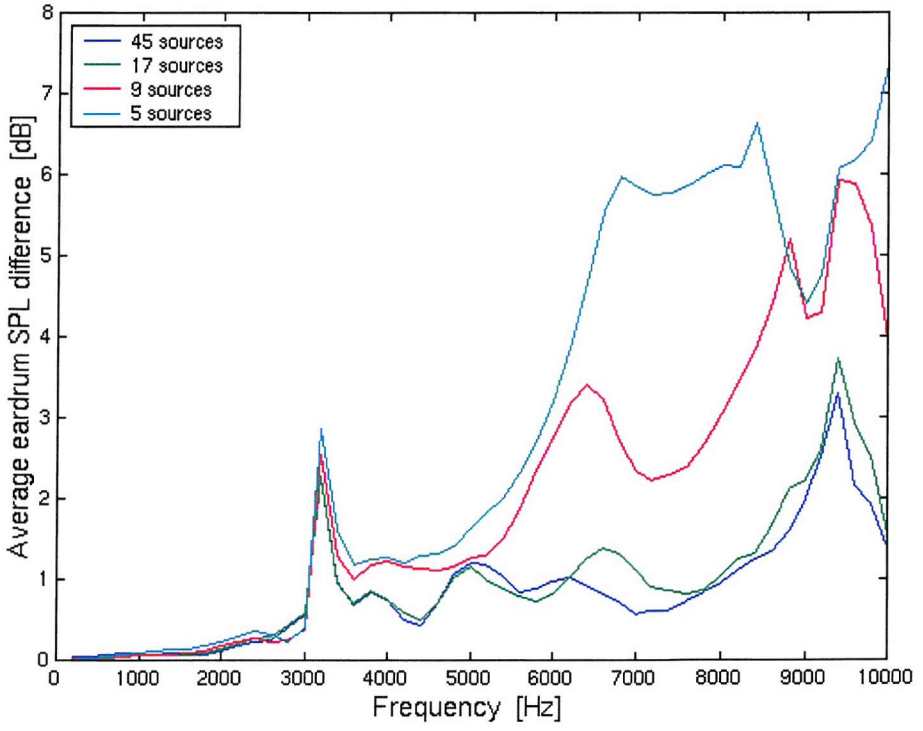

Figure 10.29 The eardrum sound pressure level differences averaged over various source directions in the horizontal plane for different number of headphone sources.

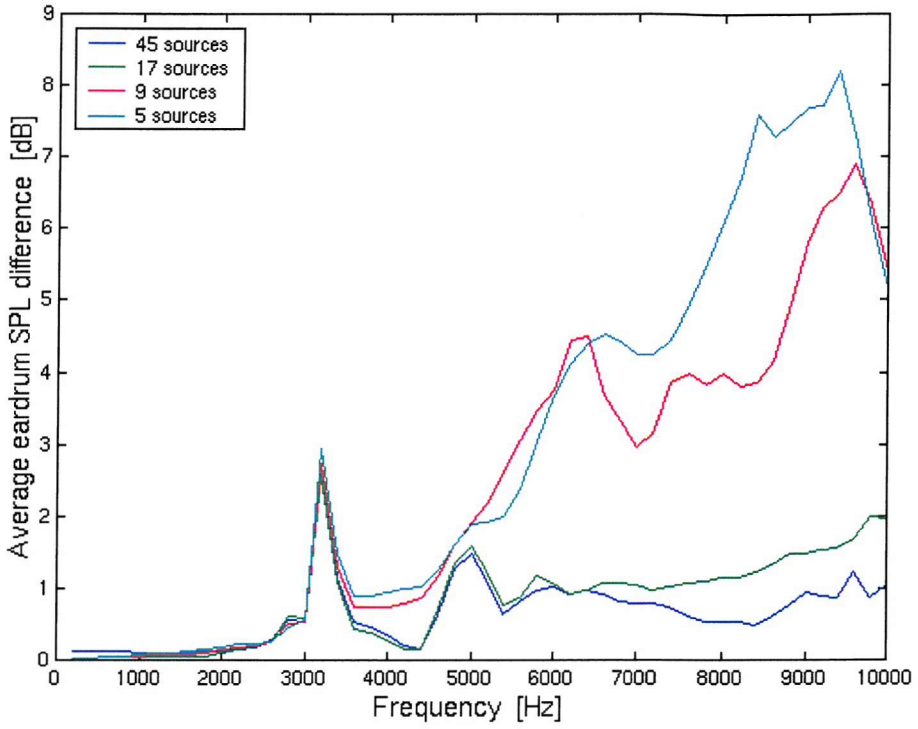

Figure 10.30 The eardrum sound pressure level differences averaged over various source directions in the median plane for different number of headphone sources.

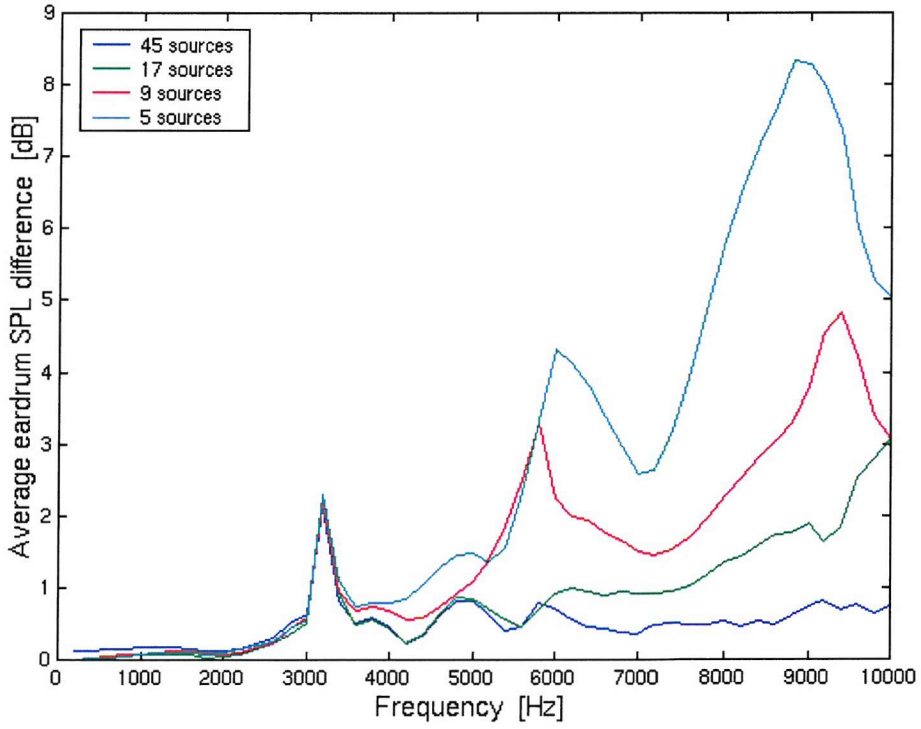

Figure 10.31 The eardrum sound pressure level differences averaged over various source directions in the frontal plane for different number of headphone sources.

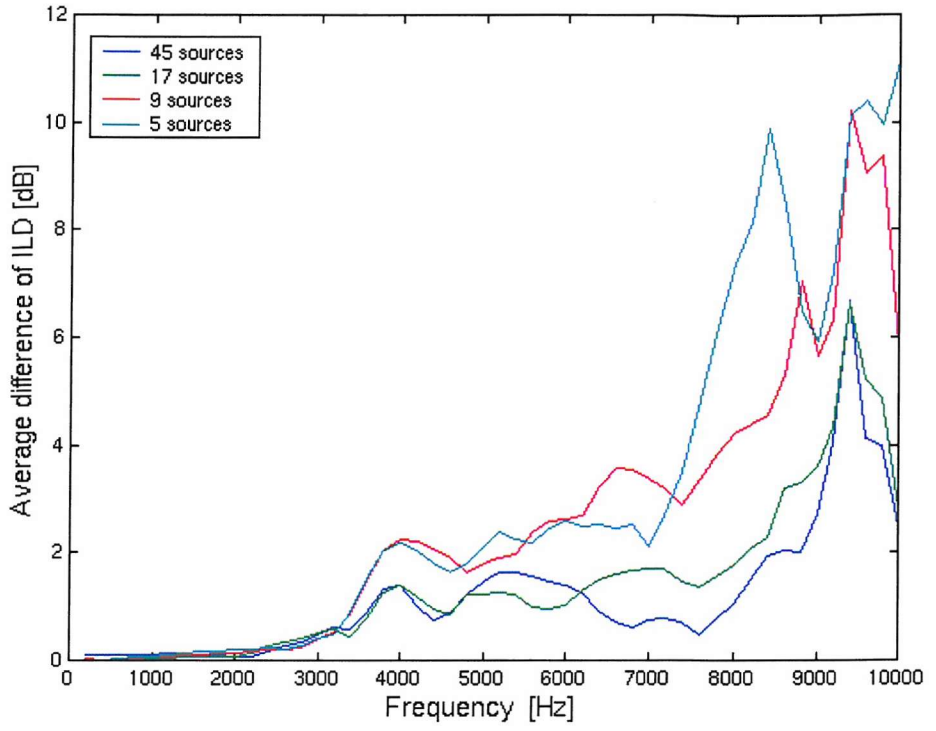

Figure 10.32 Average differences of the ILDs over various source directions in the horizontal plane for different number of headphone sources.

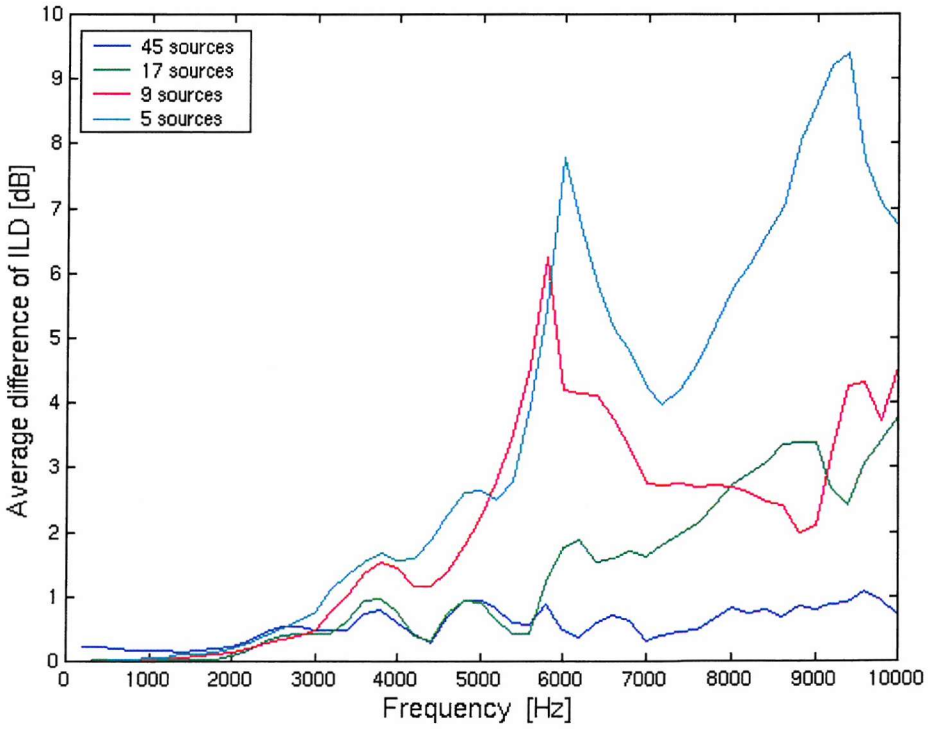

Figure 10.33 Average differences of the ILDs over various source directions in the frontal plane for different number of headphone sources.

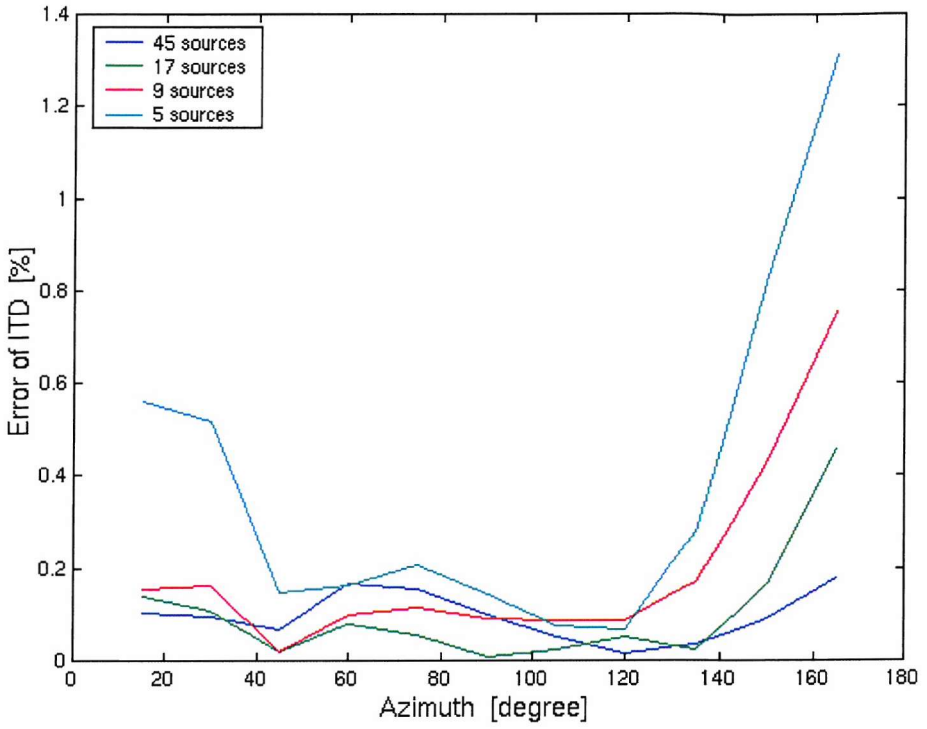

Figure 10.34 Error of the ITD over various source directions in the horizontal plane for different number of headphone sources.

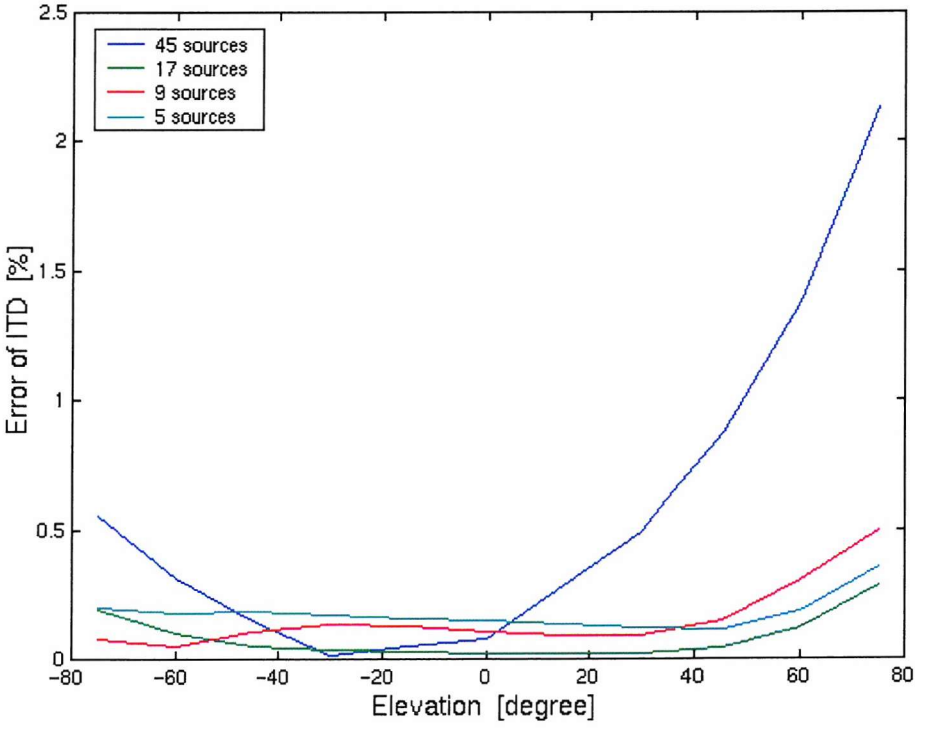

Figure 10.35 Error of the ITD over various source directions in the frontal plane for different number of headphone sources.

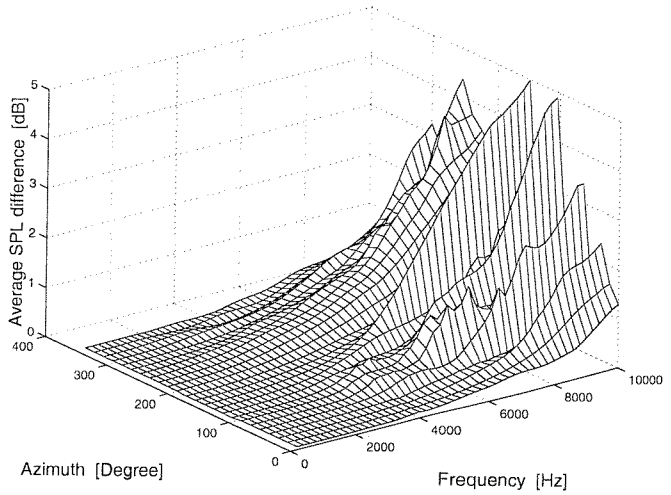

(a)

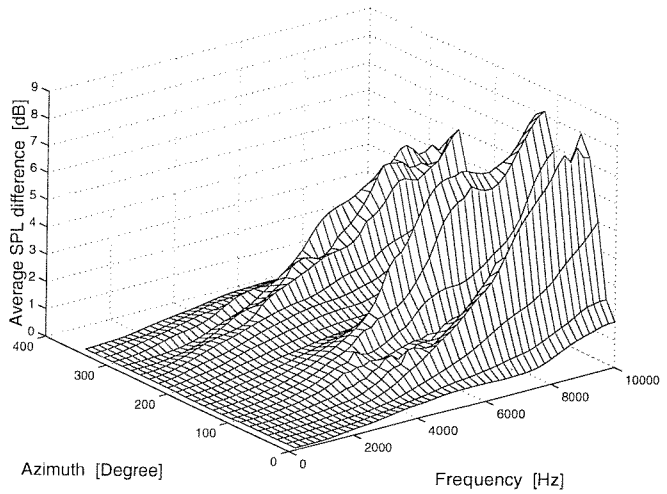

(b)

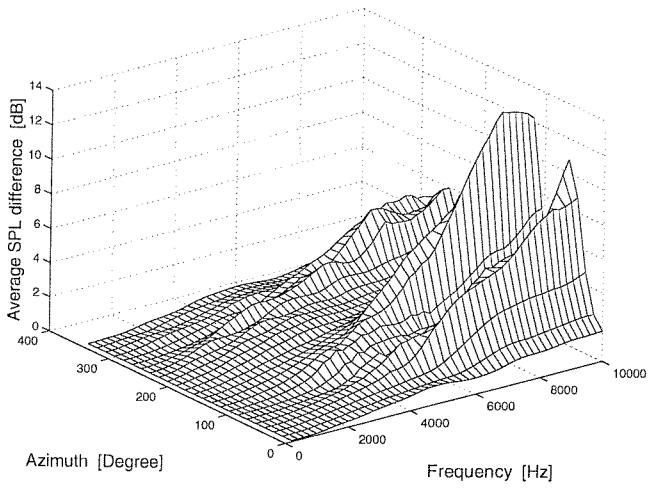

(c)

Figure 10.36 The average sound pressure level differences at control points in the horizontal plane for (a) 17 (b) 9 (c) 5 headphone sources.

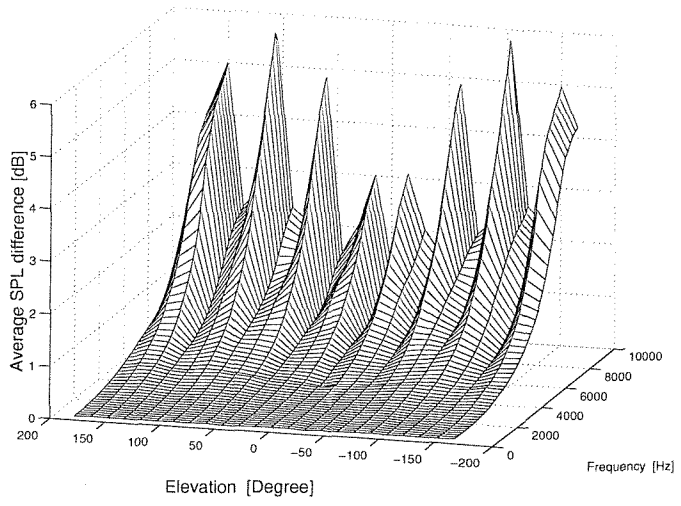

(a)

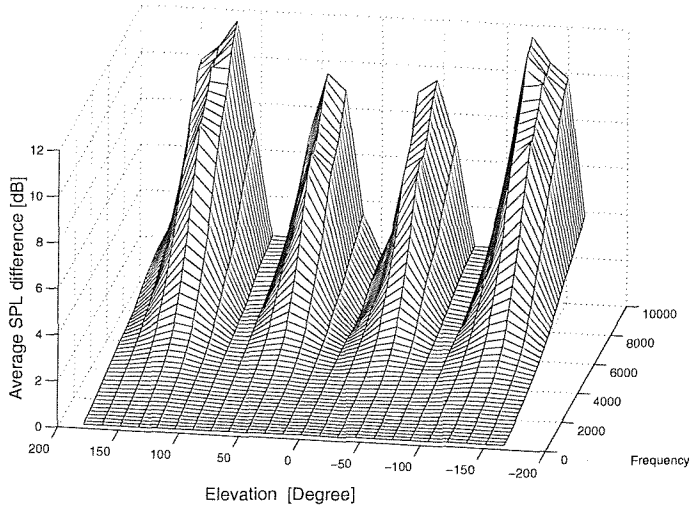

(b)

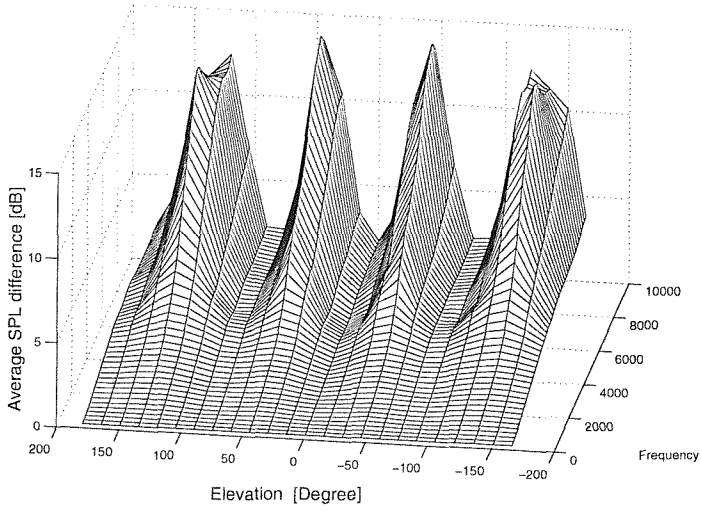

(c)

Figure 10.37 The average sound pressure level differences at control points in the median plane for (a) 17 (b) 9 (c) 5 headphone sources.

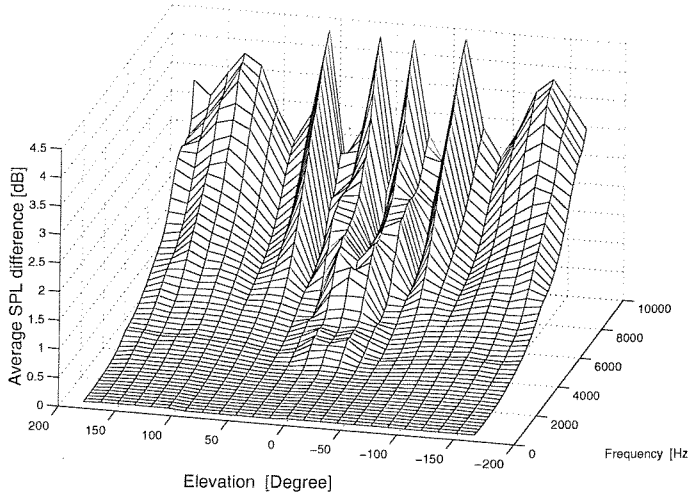

(a)

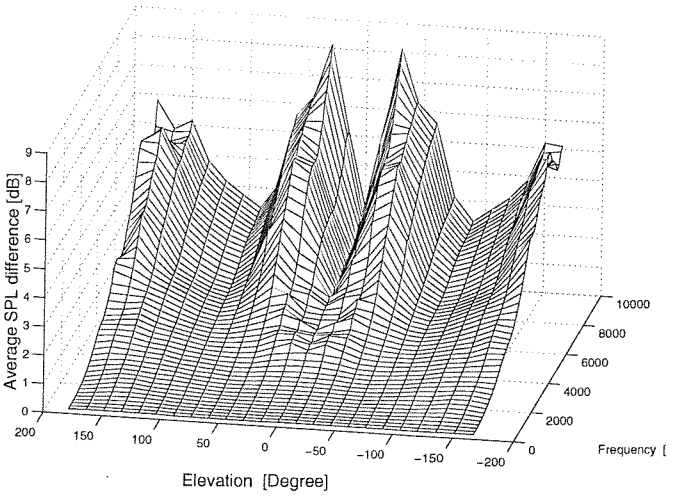

(b)

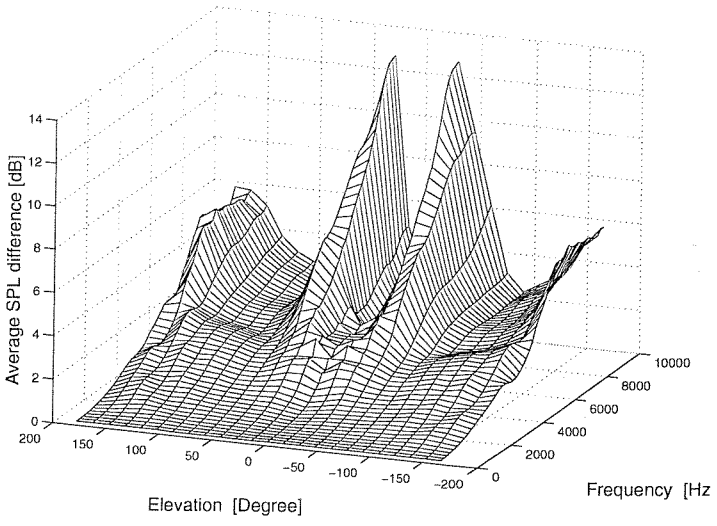

(c)

Figure 10.38 The average sound pressure level differences at control points in the frontal plane for (a) 17 (b) 9 (c) 5 headphone sources.

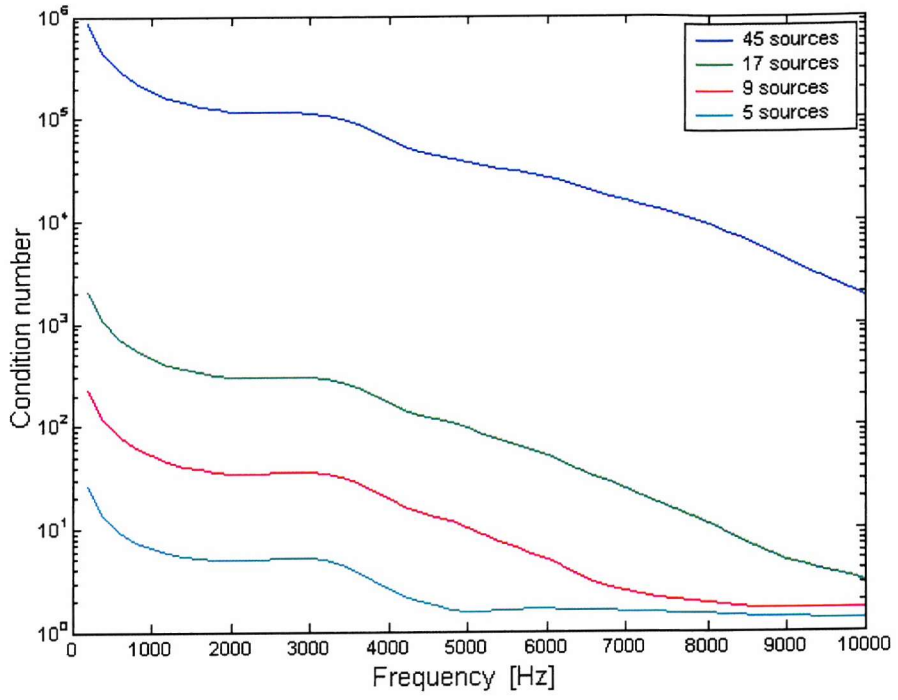

Figure 10.39 Condition number of the acoustic transfer impedance matrix.

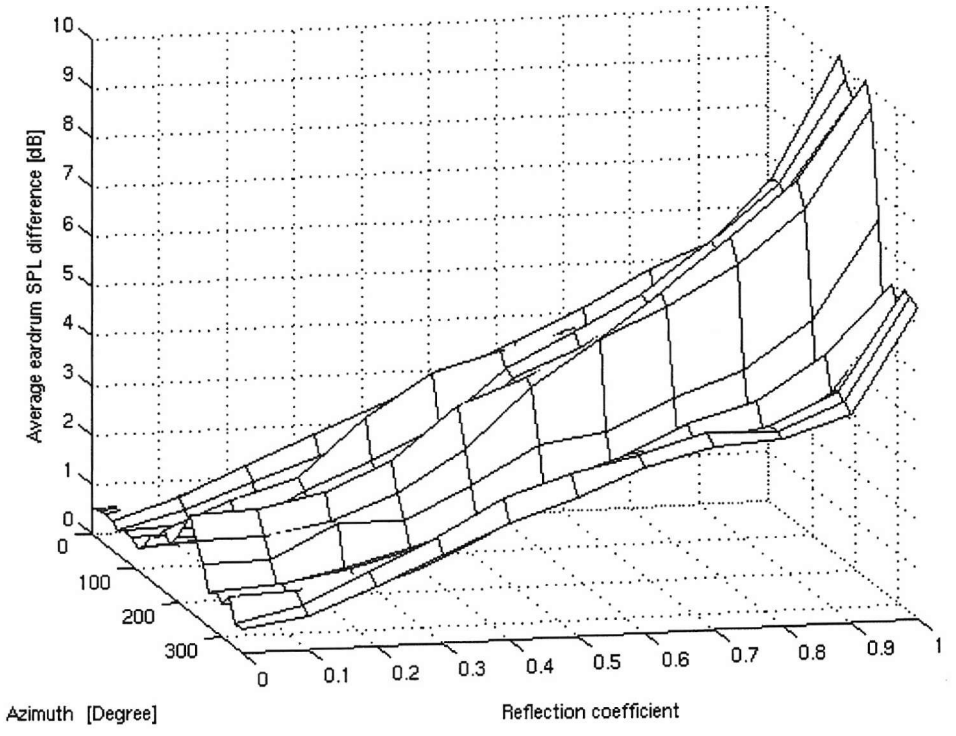

Figure 10.40 The eardrum sound pressure level differences averaged over frequency for various reflection coefficients of the headphone surface with 45 headphone sources.

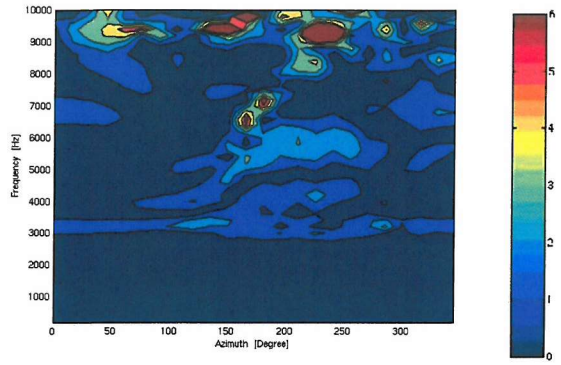

(a)

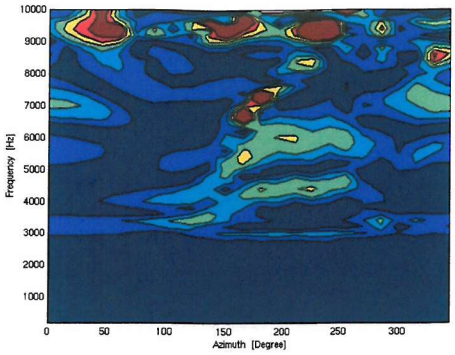

(b)

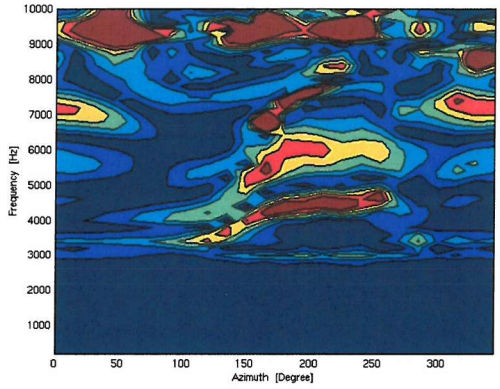

(c)

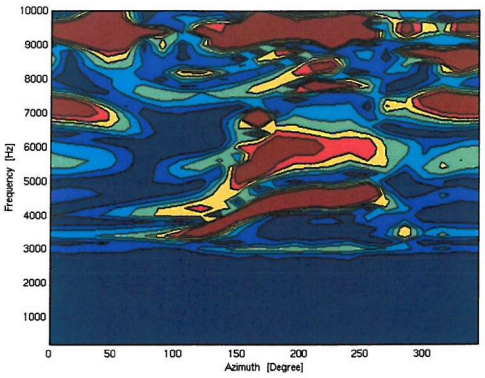

(d)

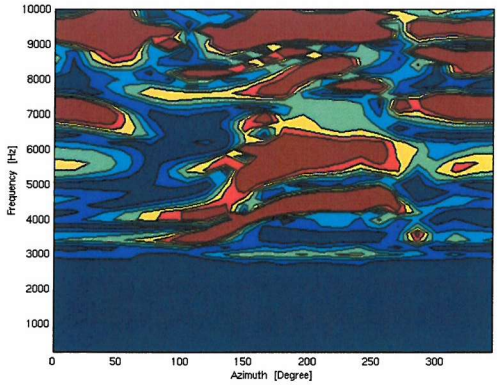

(e)

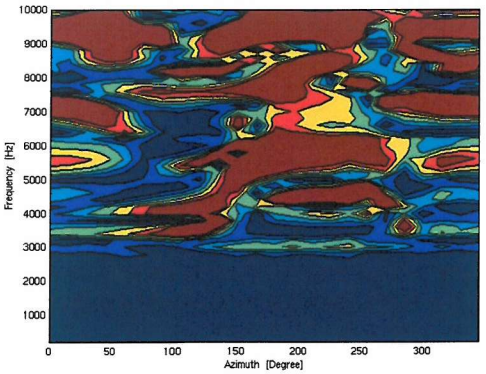

(f)

(continued on next page)

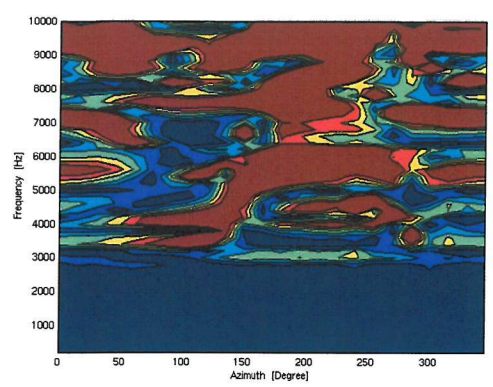

(g)

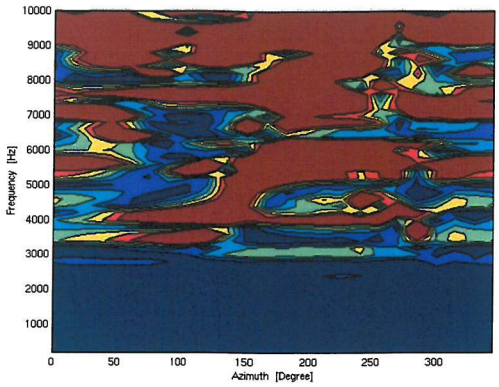

(h)

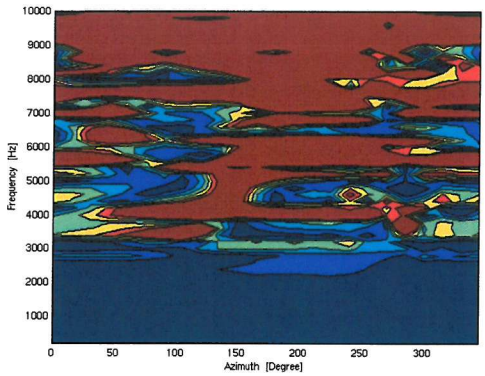

(i)

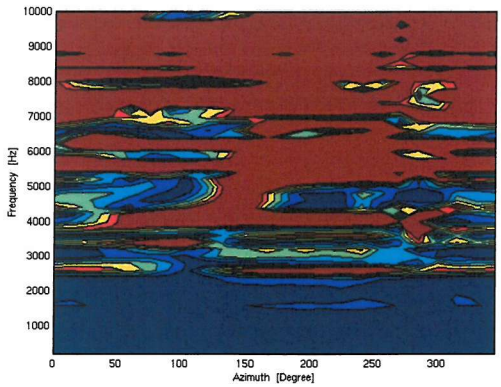

(j)

Figure 10.41 The eardrum sound pressure level differences for various source directions with 45 headphone sources and the following reflection coefficient of the headphone surface: (a) R=0.1, (b) R=0.2, (c) R=0.3, (d) R=0.4, (e) R=0.5, (f) R=0.6, (g) R=0.7, (h) R=0.8, (i) R=0.9, (j) R=1.

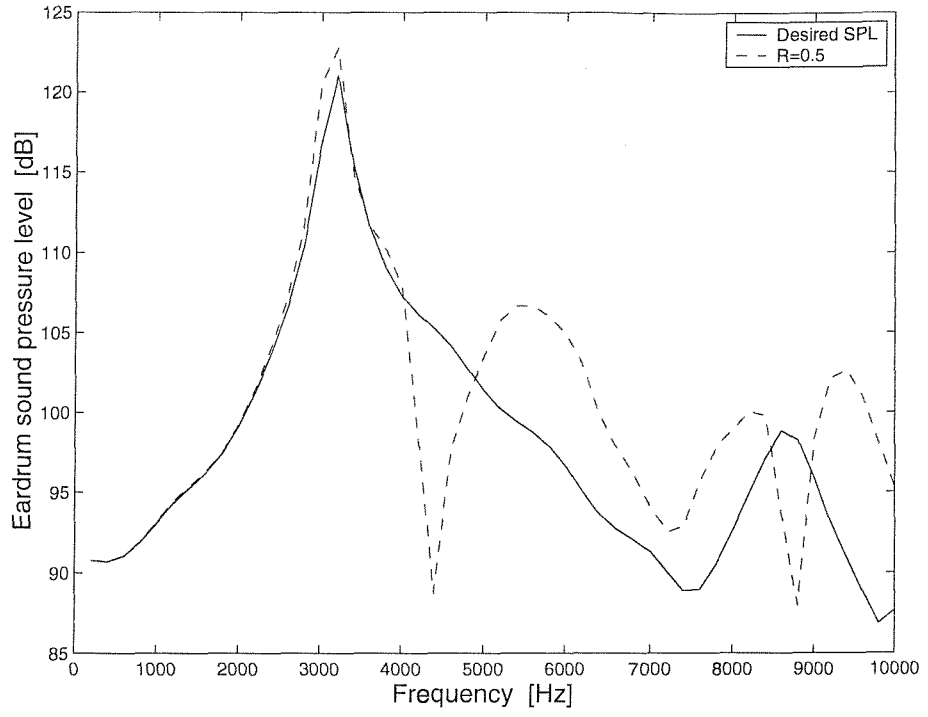

Figure 10.42 Eardrum sound pressure level for the source at 180 azimuth.

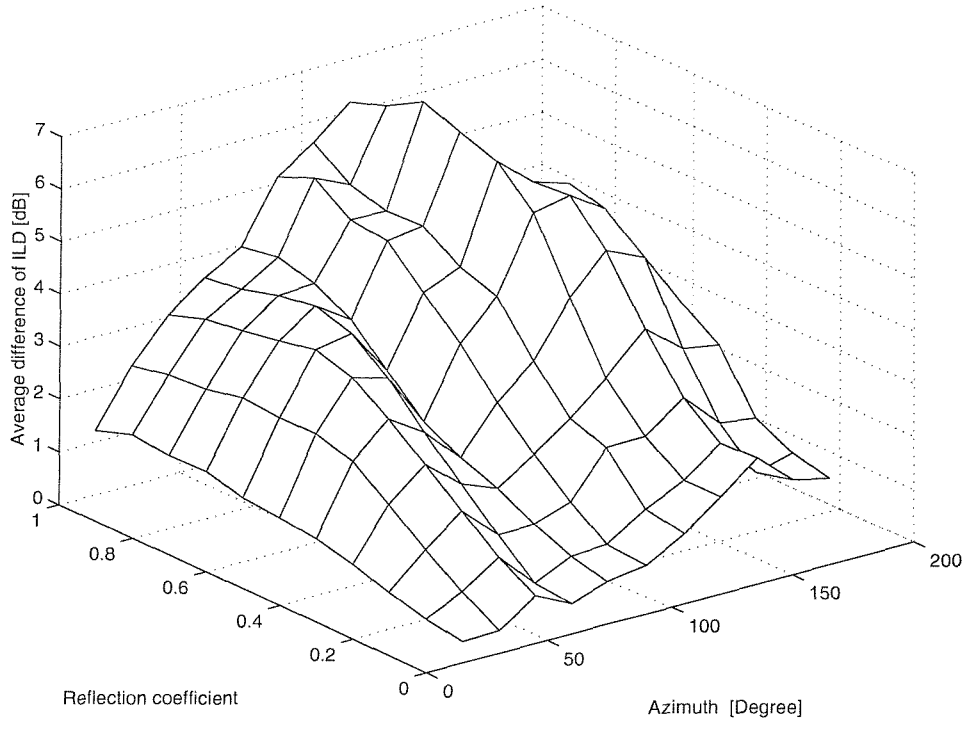

Figure 10.43 Average differences of the ILDs over frequency for various reflection coefficients of the headphone surface with 45 headphone sources

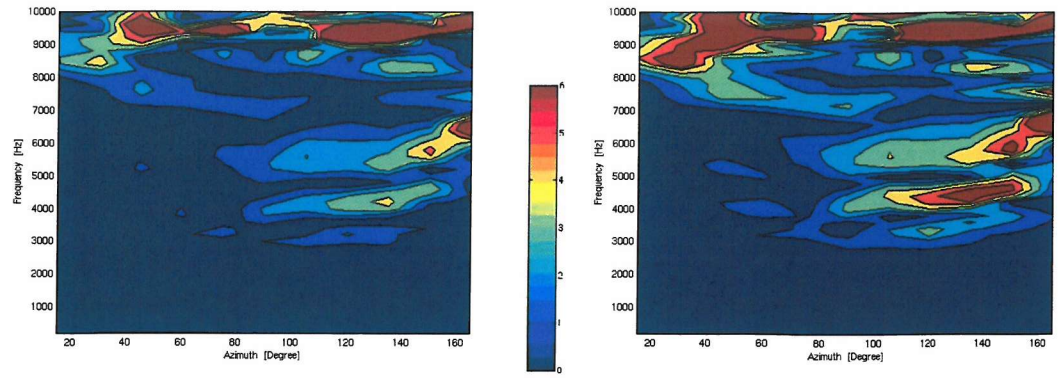

(a) (b)

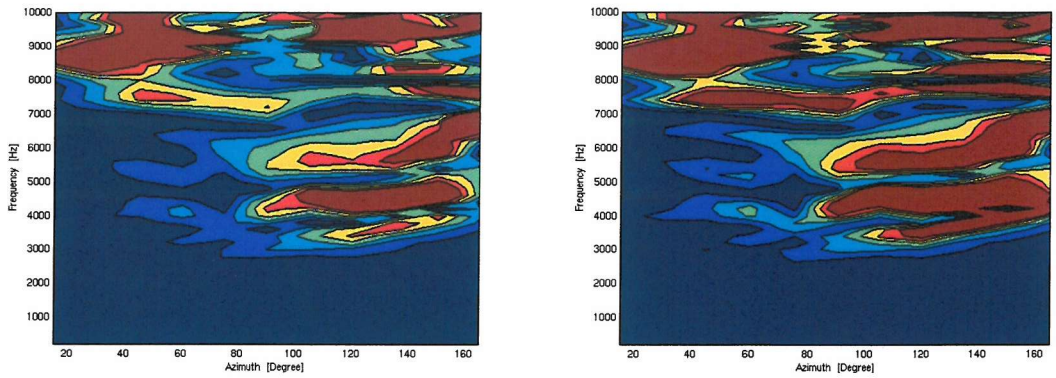

(c) (d)

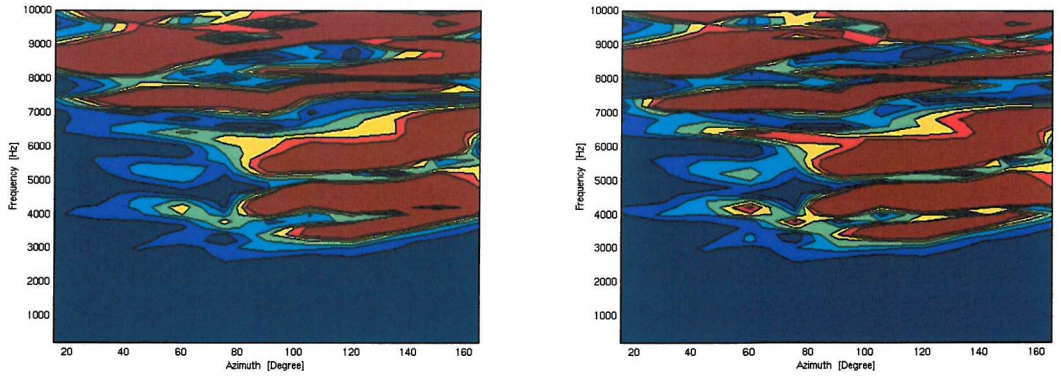

(e) (f)

(continued on next page)

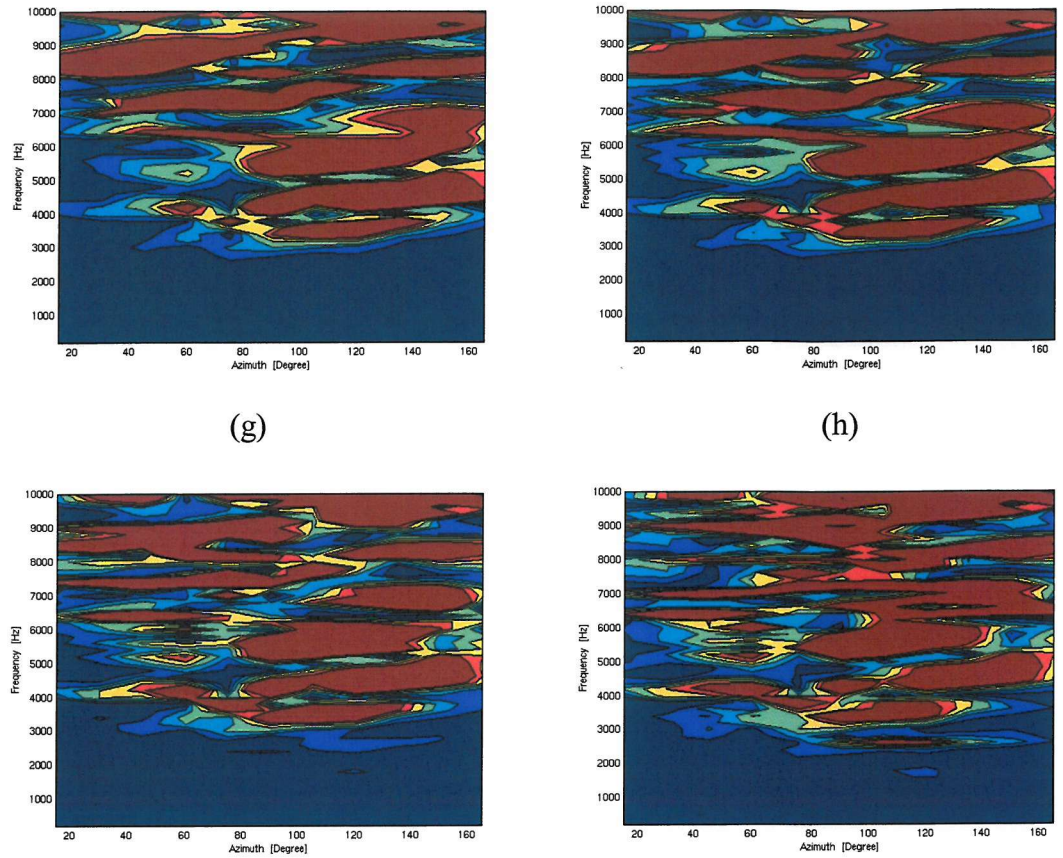

Figure 10.44 The differences of the ILDs with 45 headphone sources and the following reflection coefficient of the headphone surface: (a) R=0.1, (b) R=0.2, (c) R=0.3, (d) R=0.4, (e) R=0.5, (f) R=0.6, (g) R=0.7, (h) R=0.8, (i) R=0.9, (j) R=1.

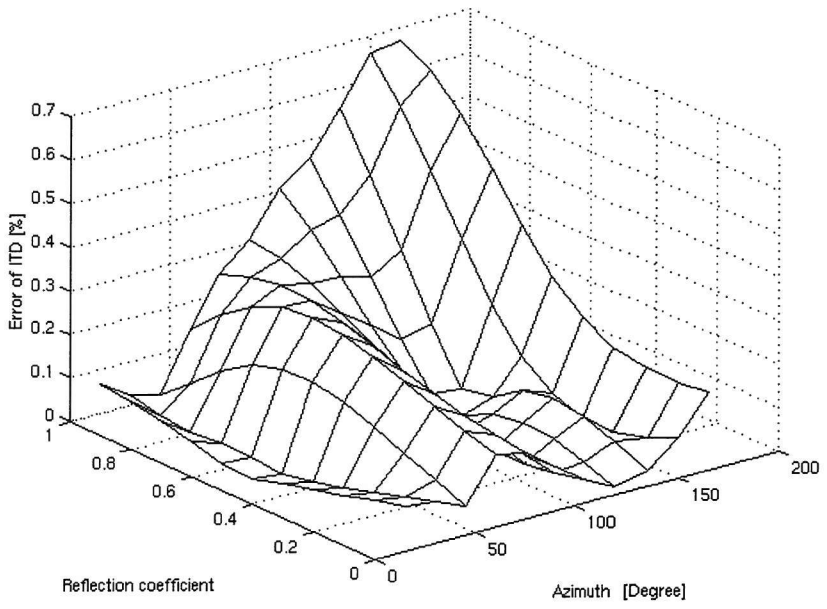

Figure 10.45 Error of ITD over frequency for various reflection coefficients.

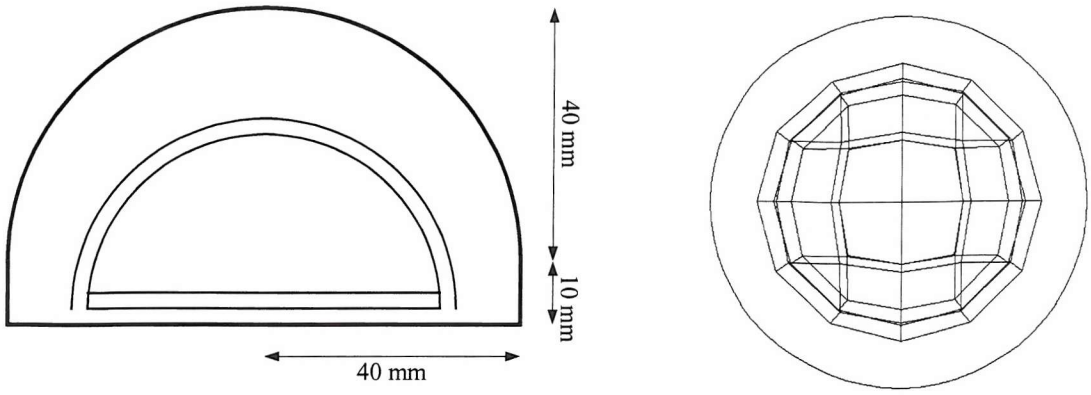

Figure 10.46 The small headphone model with the flat surface.

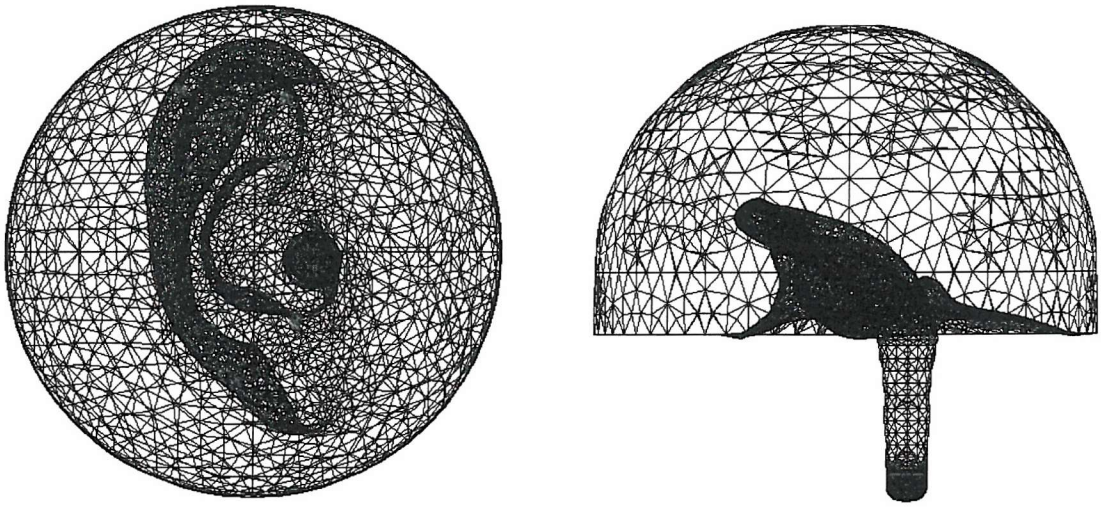

Figure 10.47 The small headphone model with the DB65 ear model.

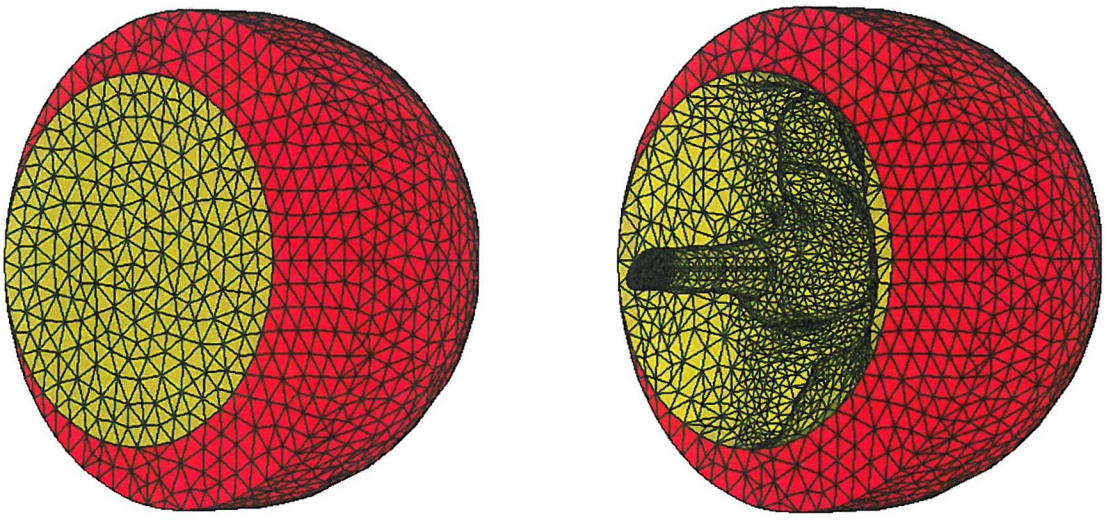

Figure 10.48 The boundary condition of the surface of the small headphone.

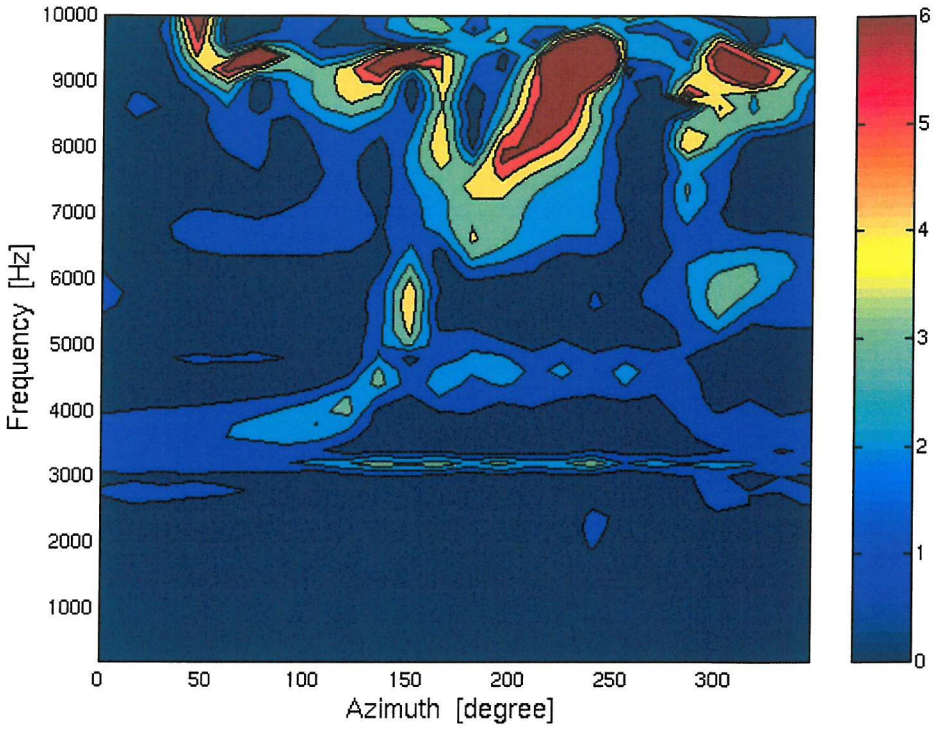

Figure 10.49 The eardrum sound pressure level differences for 17 headphone sources in the horizontal plane with the perfectly absorbent surface of the small headphone.

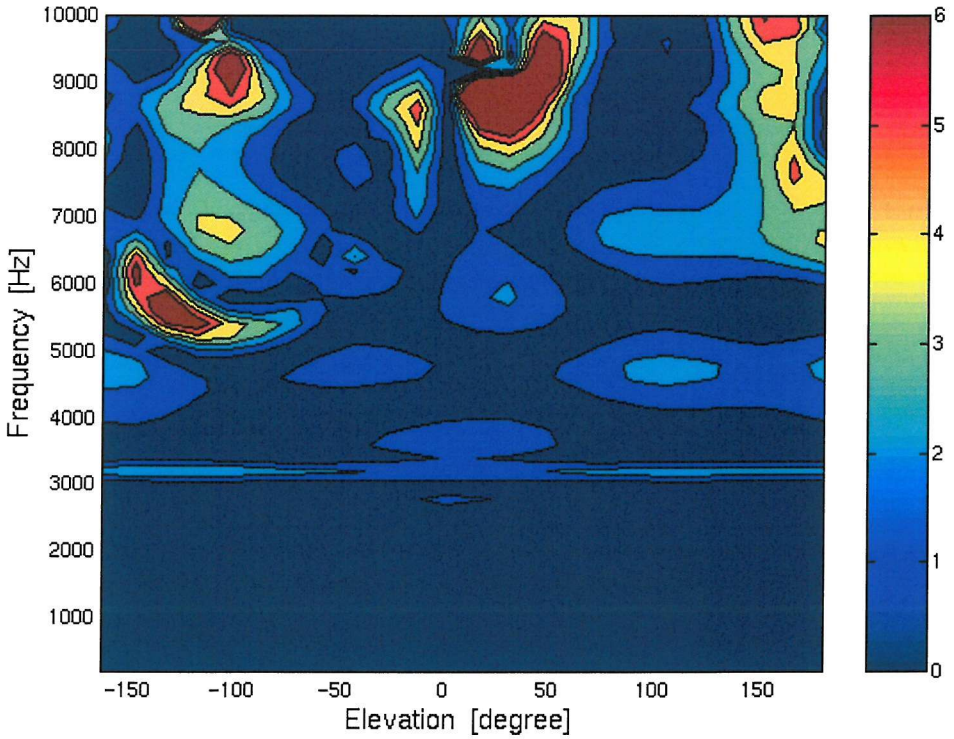

Figure 10.50 The eardrum sound pressure level differences for 17 headphone sources in the median plane with the perfectly absorbent surface of the small headphone.

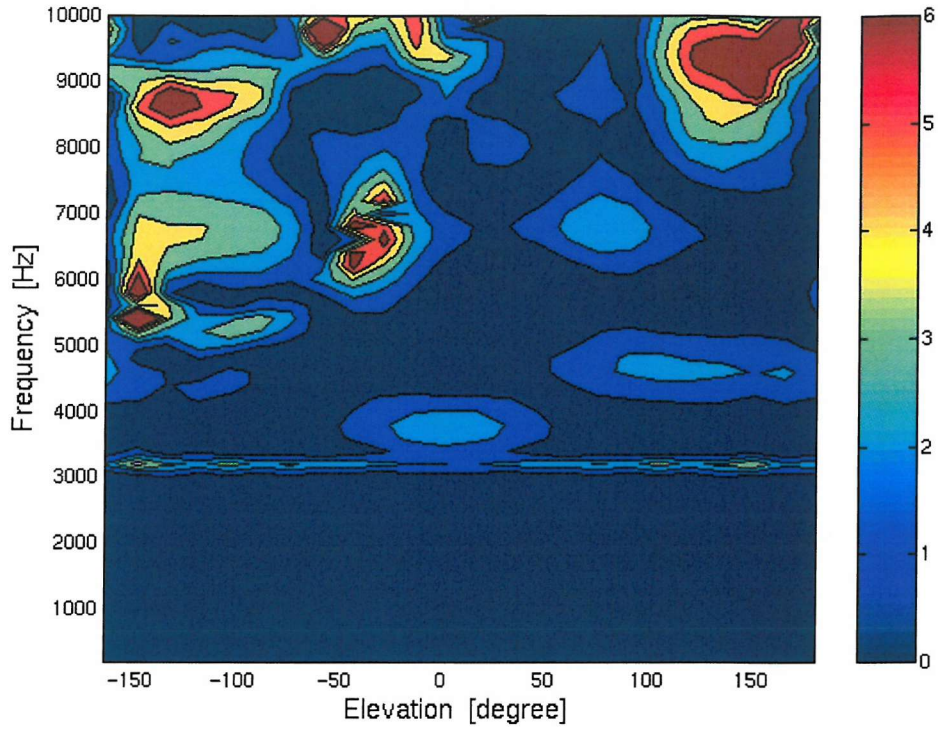

Figure 10.51 The eardrum sound pressure level differences for 17 headphone sources in the frontal plane with the perfectly absorbent surface of the small headphone.

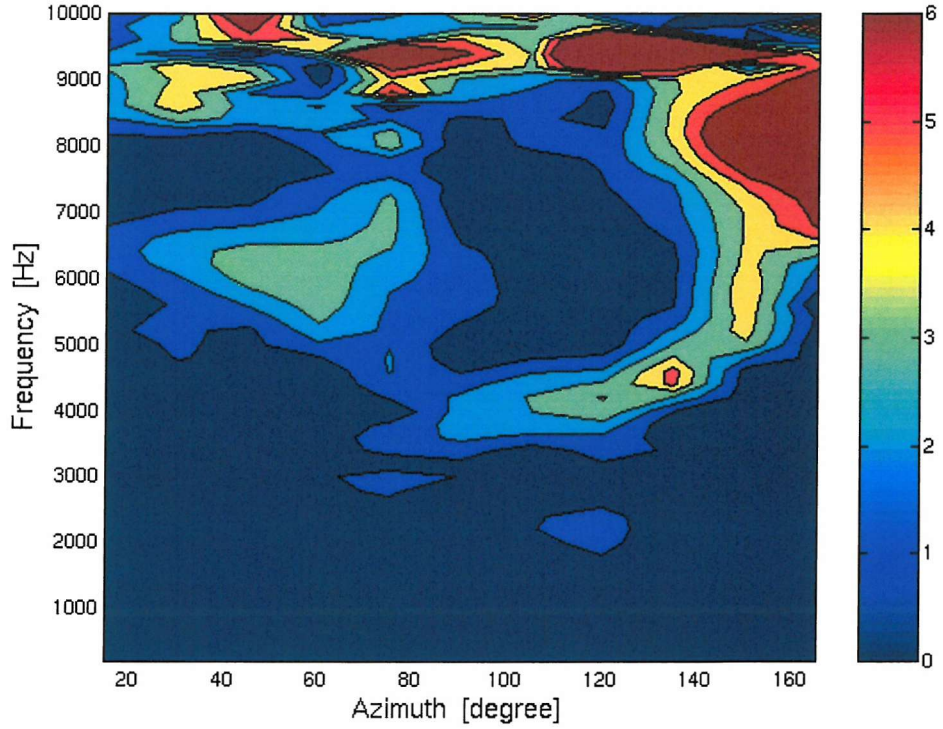

Figure 10.52 Differences of interaural level differences for 17 headphone sources in the horizontal plane with the perfectly absorbent surface of the small headphone.

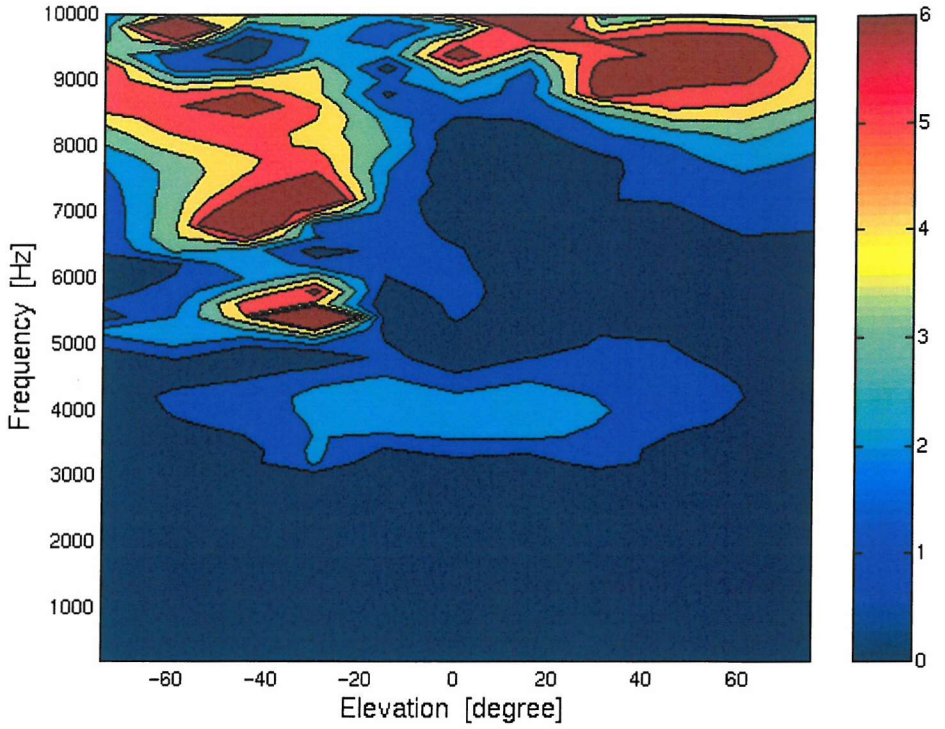

Figure 10.53 Differences of interaural level differences for 17 headphone sources in the frontal plane with the perfectly absorbent surface of the small headphone.

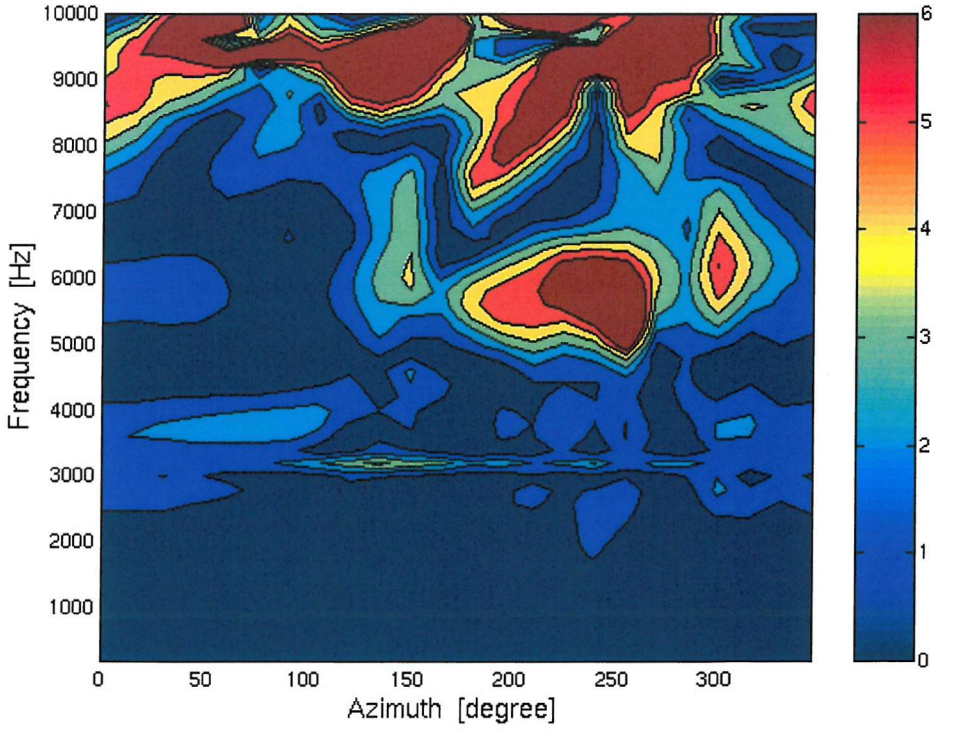

Figure 10.54 The eardrum sound pressure level differences for 9 headphone sources in the horizontal plane with the perfectly absorbent surface of the small headphone.

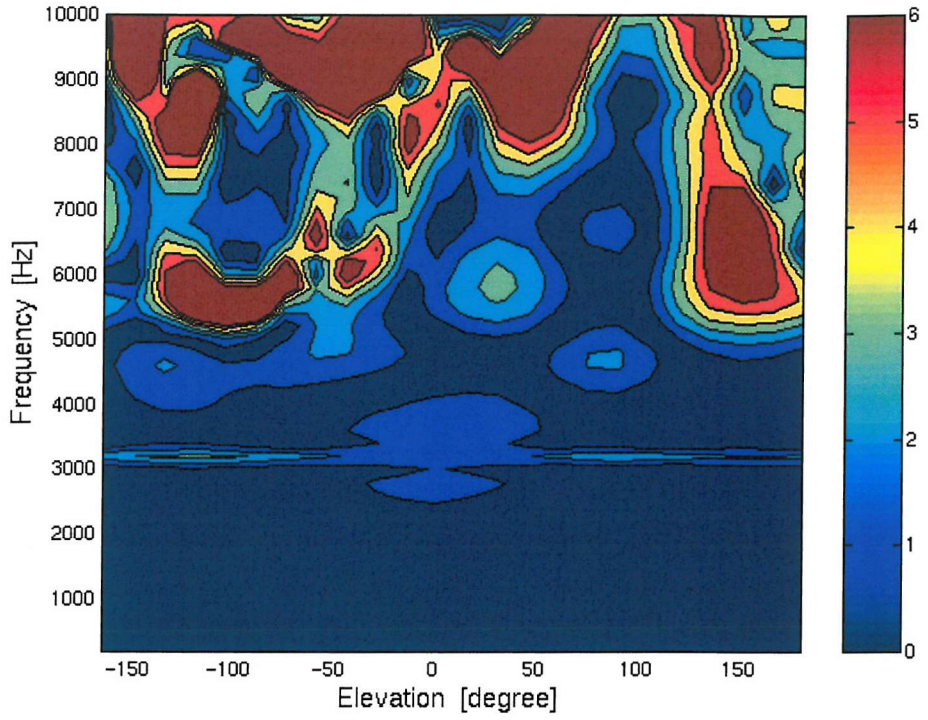

Figure 10.55 The eardrum sound pressure level differences for 9 headphone sources in the median plane with the perfectly absorbent surface of the small headphone.

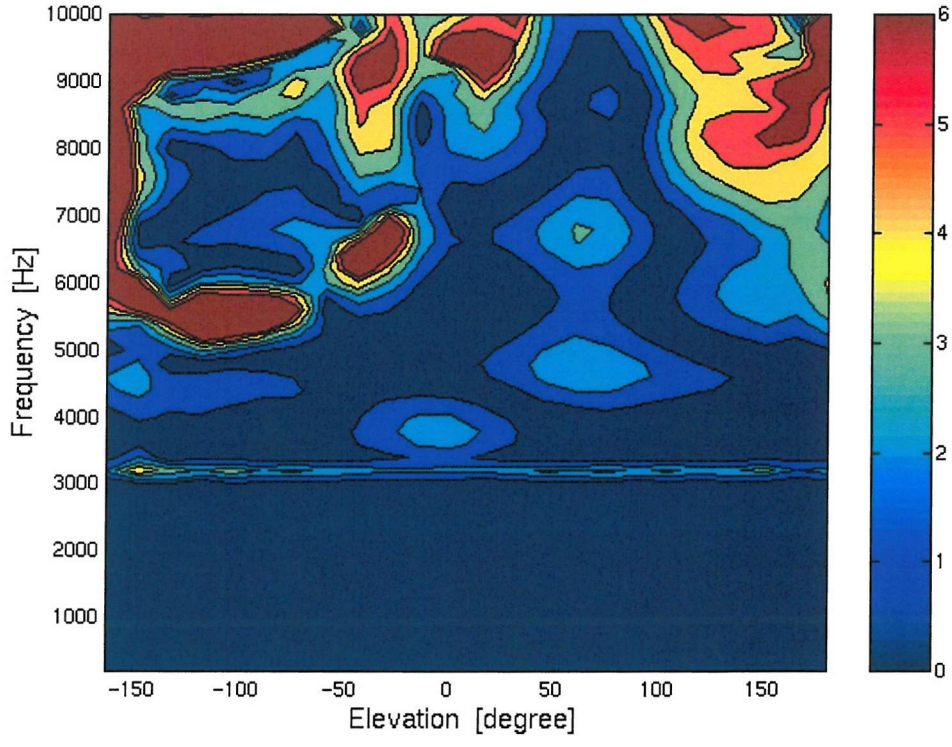

Figure 10.56 The eardrum sound pressure level differences for 9 headphone sources in the frontal plane with the perfectly absorbent surface of the small headphone.

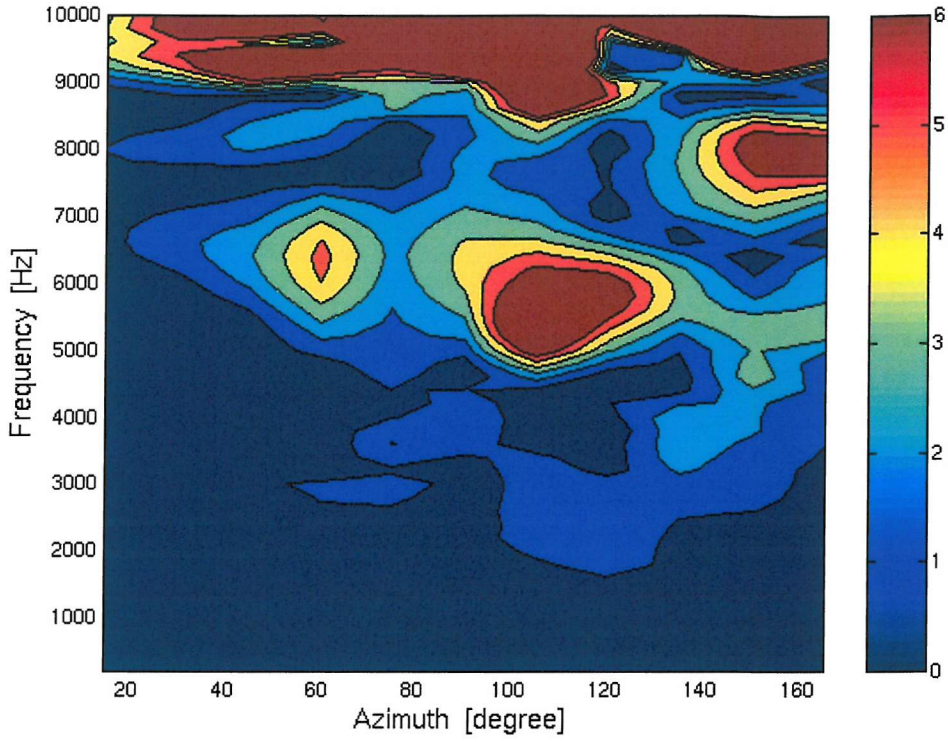

Figure 10.57 Differences of interaural level differences for 9 headphone sources in the horizontal plane with the perfectly absorbent surface of the small headphone.

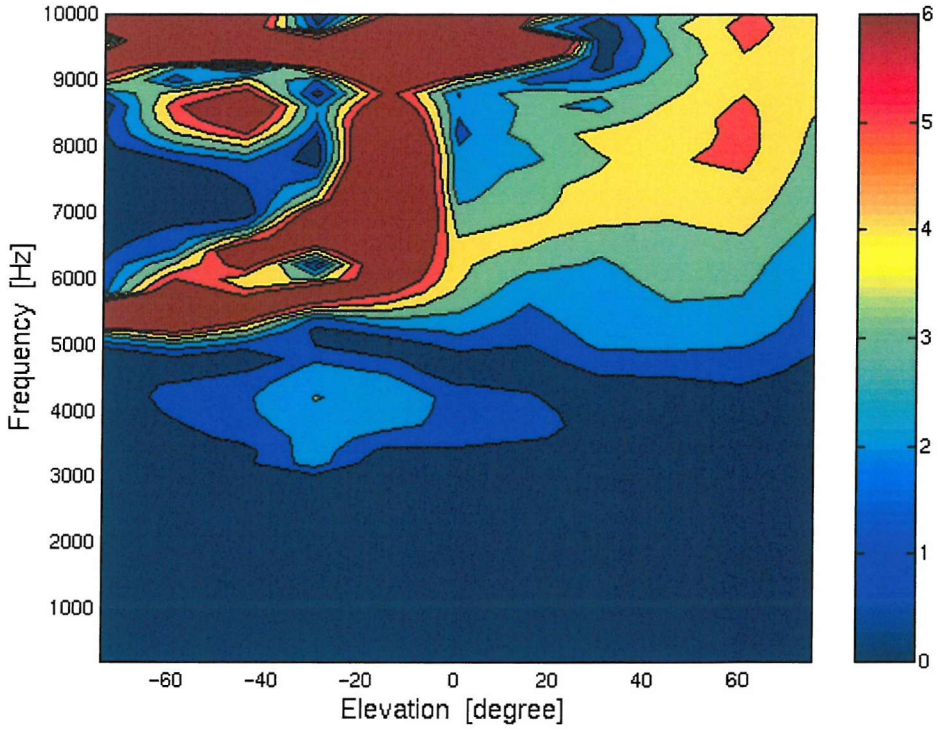

Figure 10.58 Differences of interaural level differences for 9 headphone sources in the frontal plane with the perfectly absorbent surface of the small headphone.

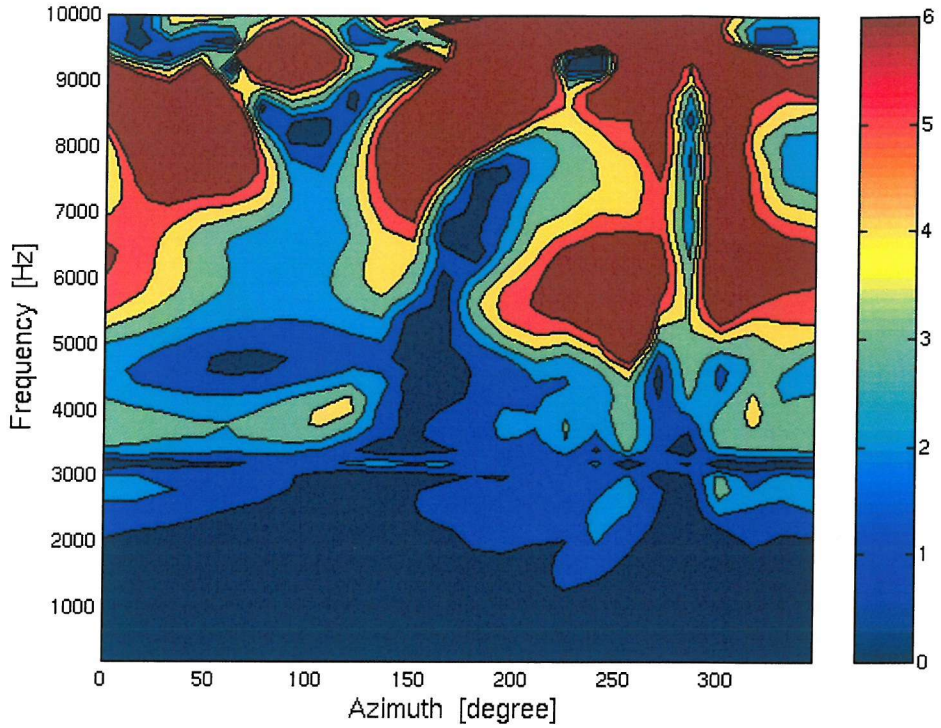

Figure 10.59 The eardrum sound pressure level differences for 5 headphone sources in the horizontal plane with the perfectly absorbent surface of the small headphone.

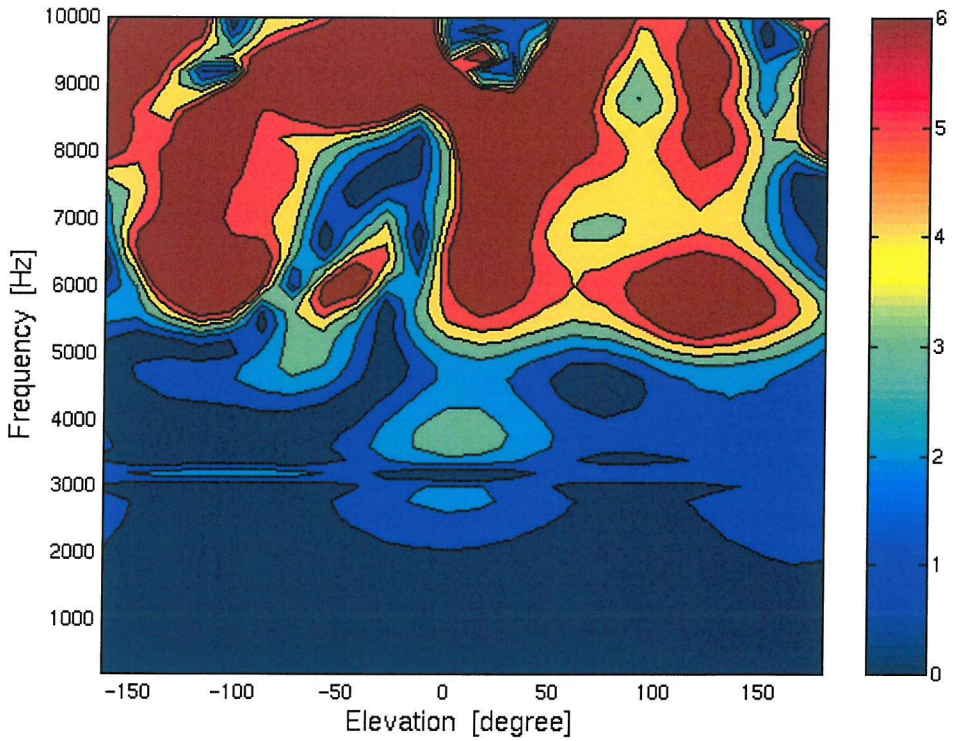

Figure 10.60 The eardrum sound pressure level differences for 5 headphone sources in the median plane with the perfectly absorbent surface of the small headphone.

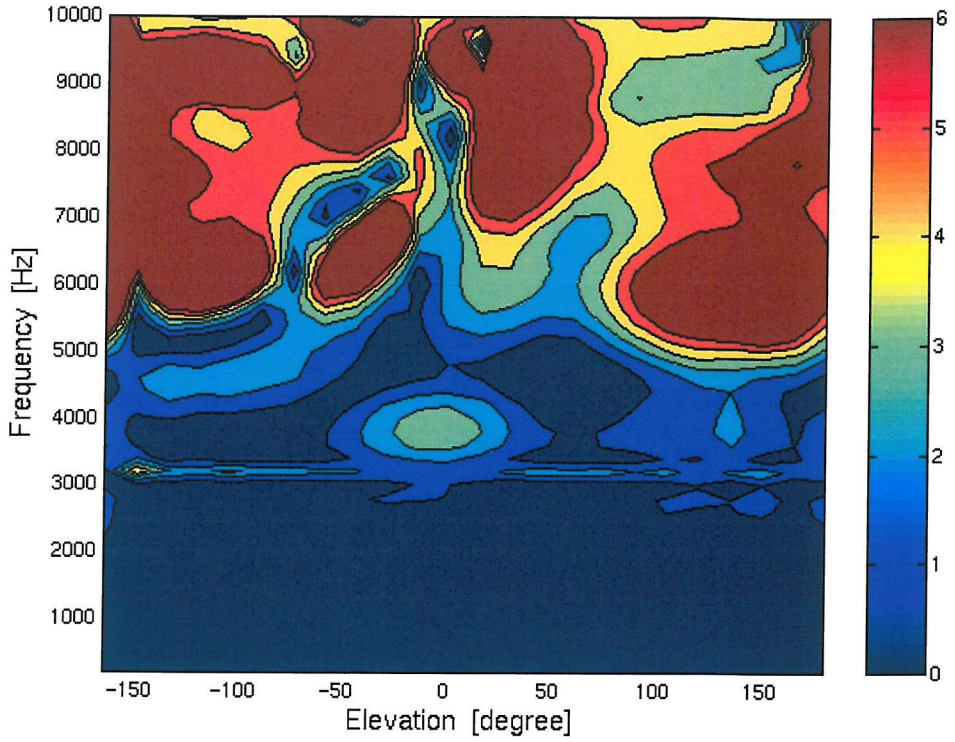

Figure 10.61 The eardrum sound pressure level differences for 5 headphone sources in the frontal plane with the perfectly absorbent surface of the small headphone.

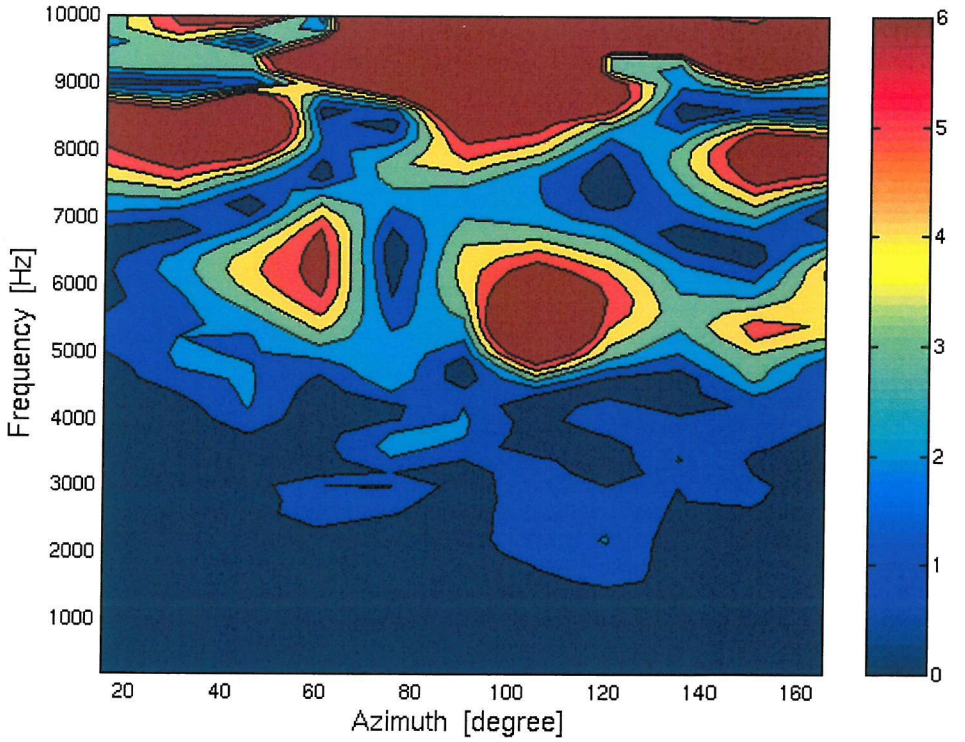

Figure 10.62 Differences of interaural level differences for 5 headphone sources in the horizontal plane with the perfectly absorbent surface of the small headphone.

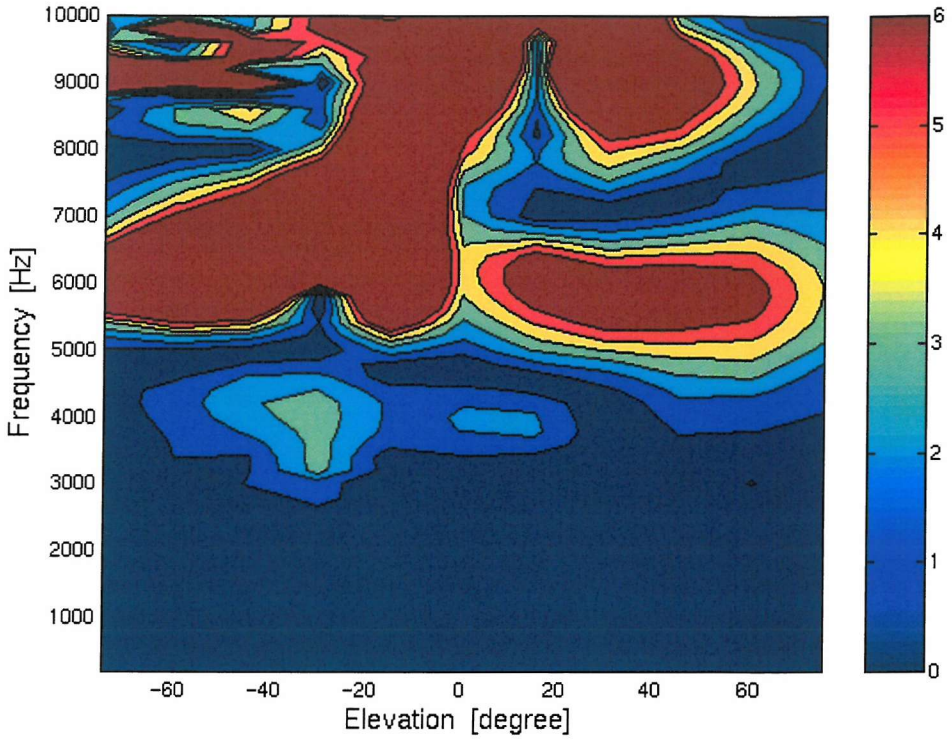

Figure 10.63 Differences of interaural level differences for 5 headphone sources in the frontal plane with the perfectly absorbent surface of the small headphone.

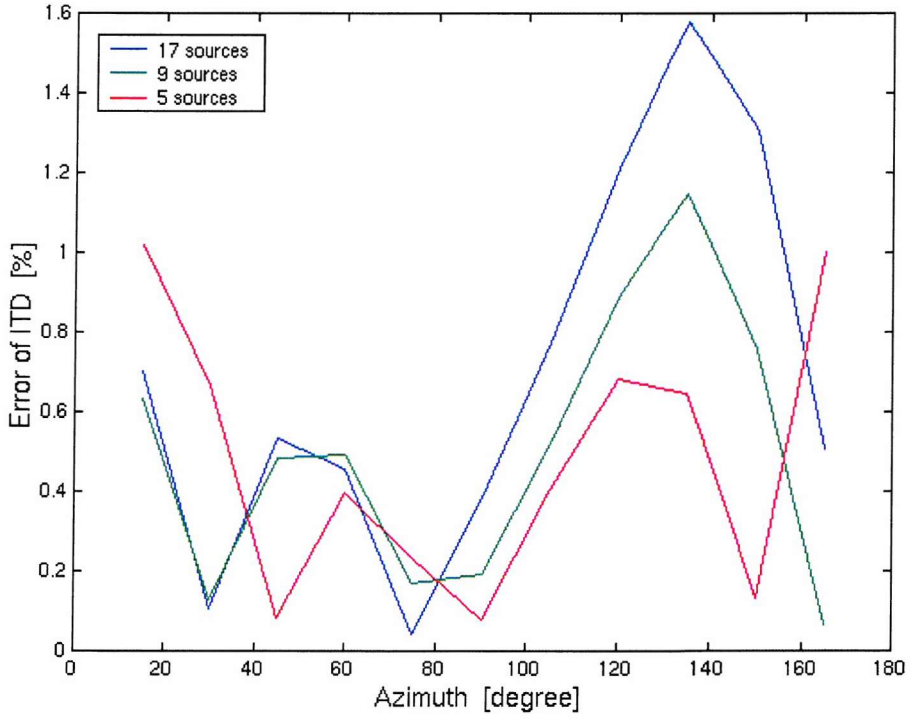

Figure 10.64 Error of the ITD over various source directions in the horizontal plane with the perfectly absorbent surface of the small headphone.

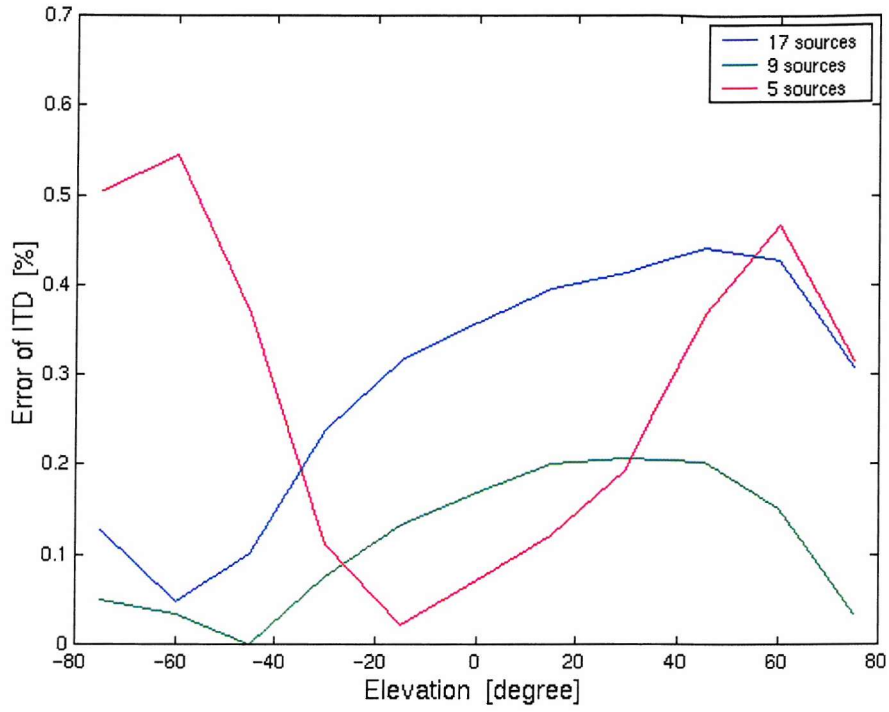

Figure 10.65 Error of the ITD over various source directions in the frontal plane with the perfectly absorbent surface of the small headphone.

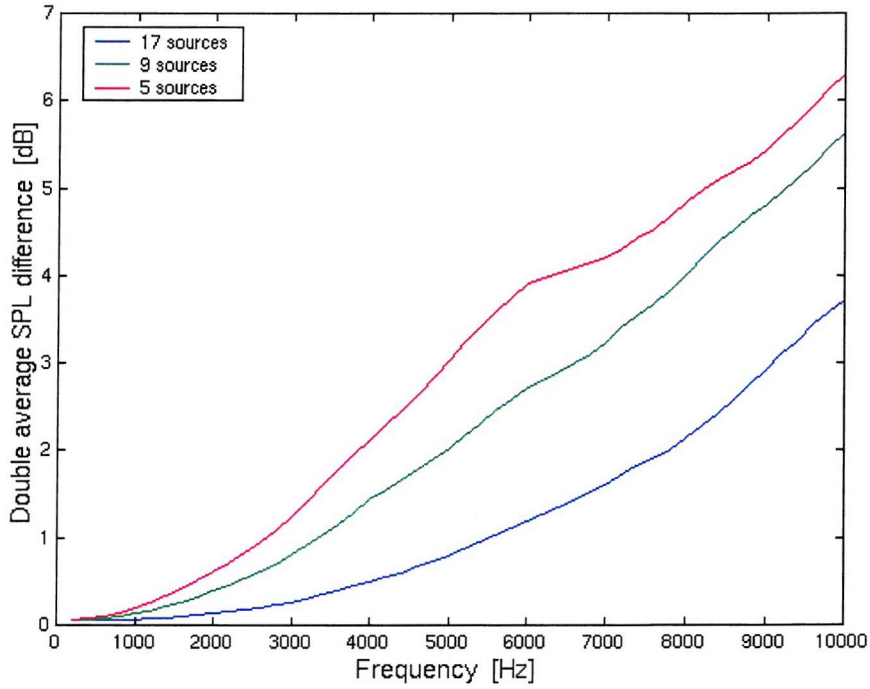

Figure 10.66 The mean value of the average sound pressure level differences at control points over various source directions in the horizontal plane with the small headphone.

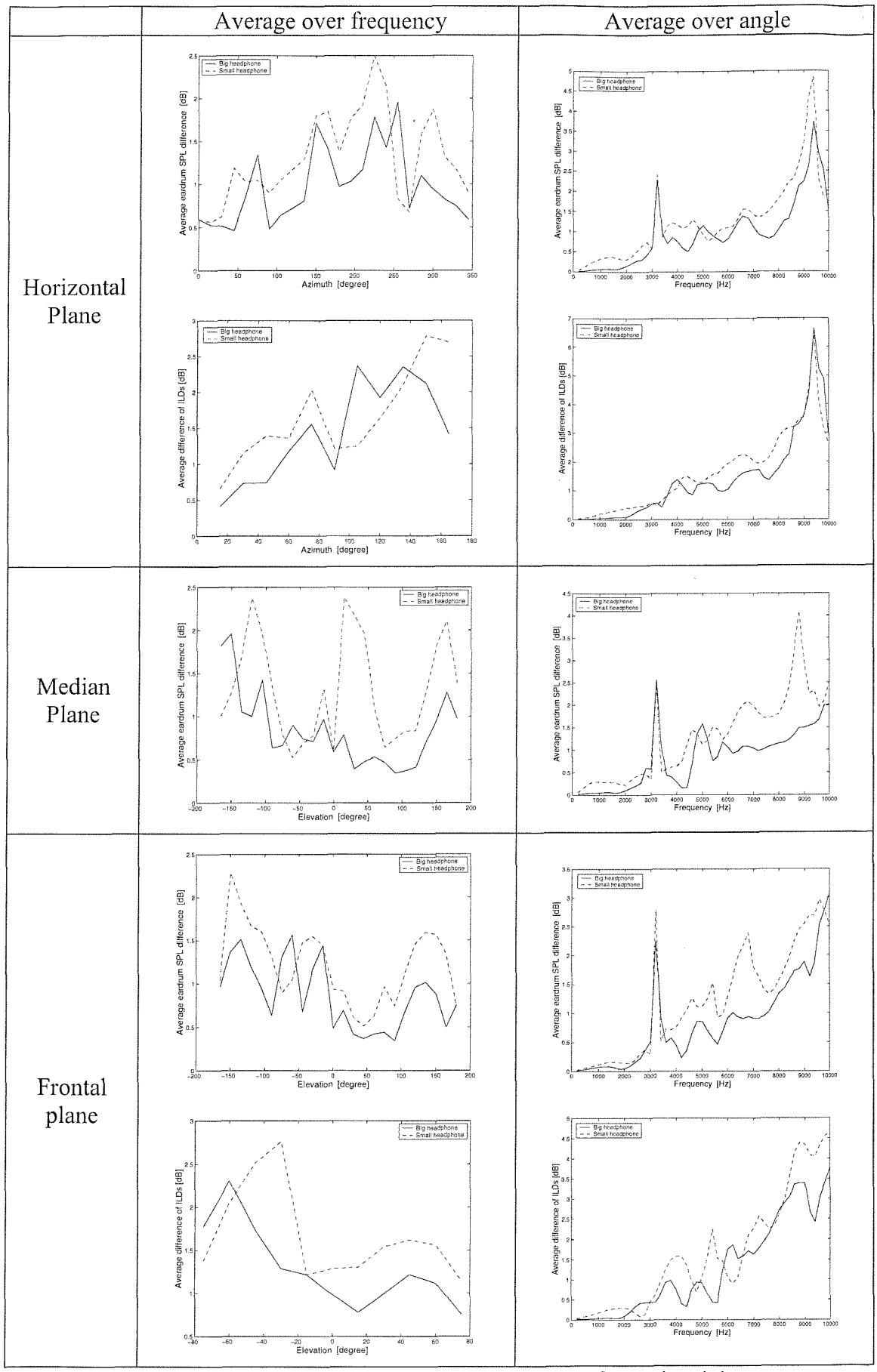

Figure 10.67 Average differences of eardrum SPL or ILD for 17 headphone sources.

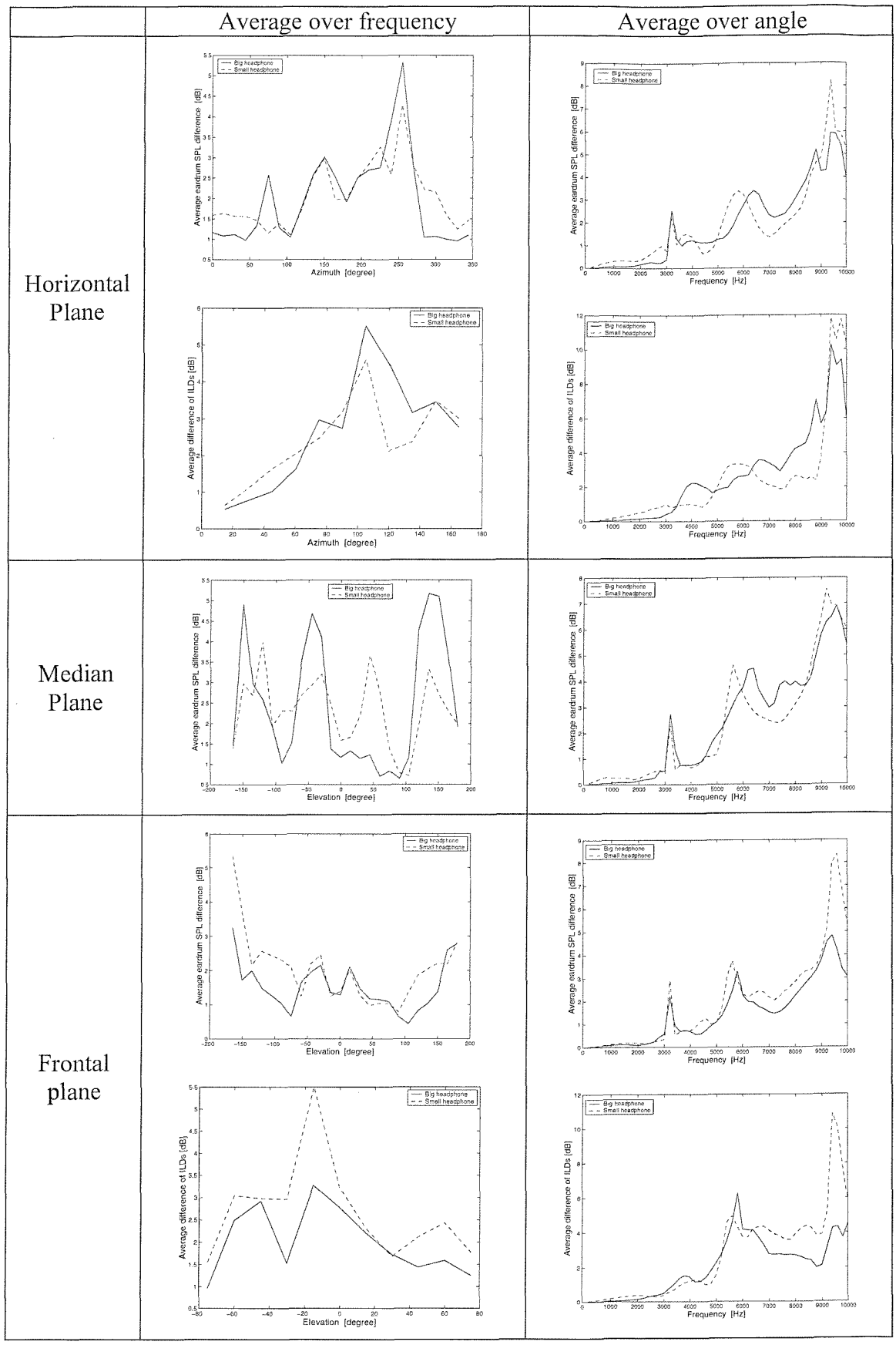

Figure 10.68 Average differences of eardrum SPL or ILD for 9 headphone sources.

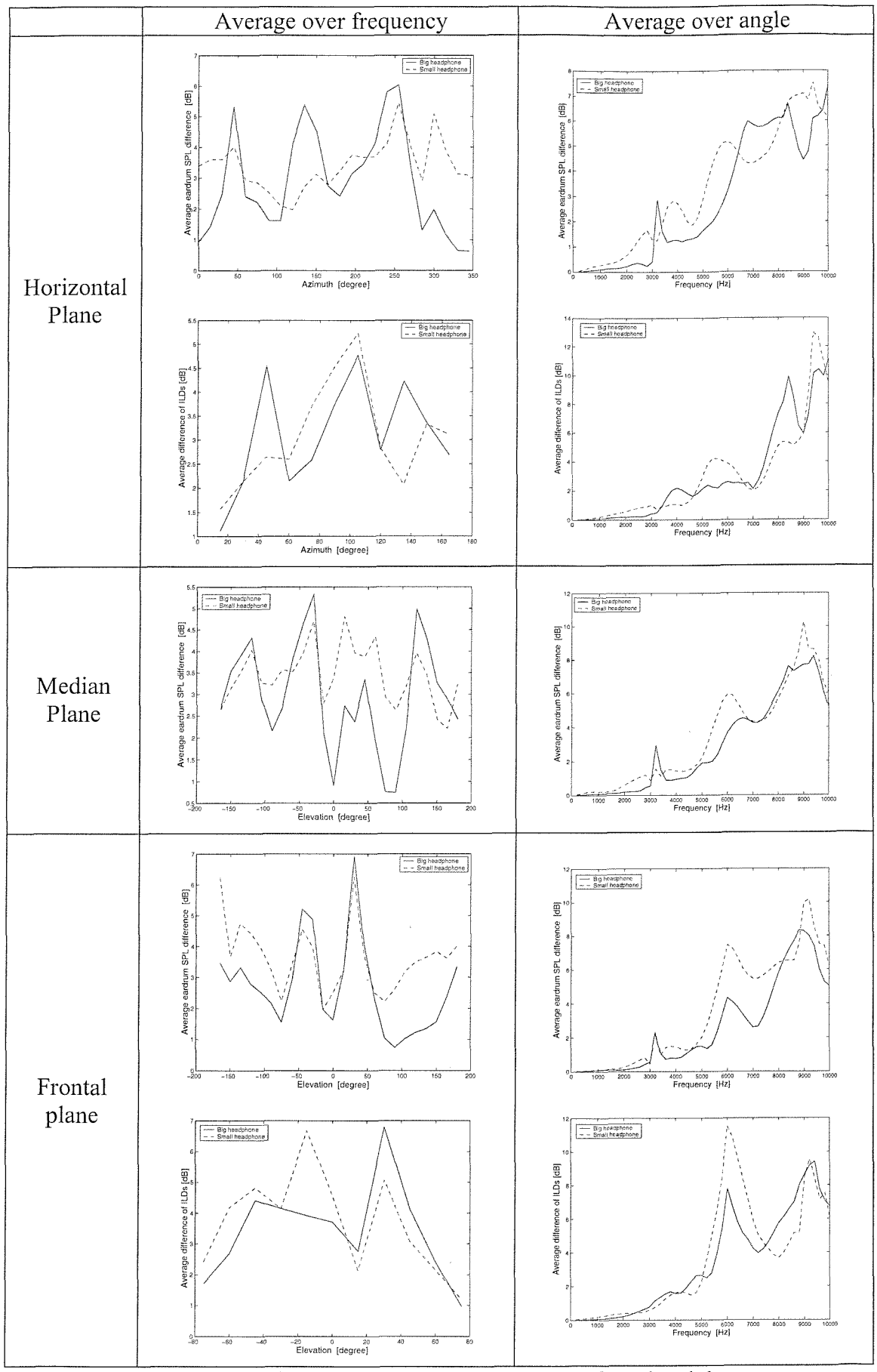

Figure 10.69 Average differences of eardrum SPL or ILD for 5 headphone sources.

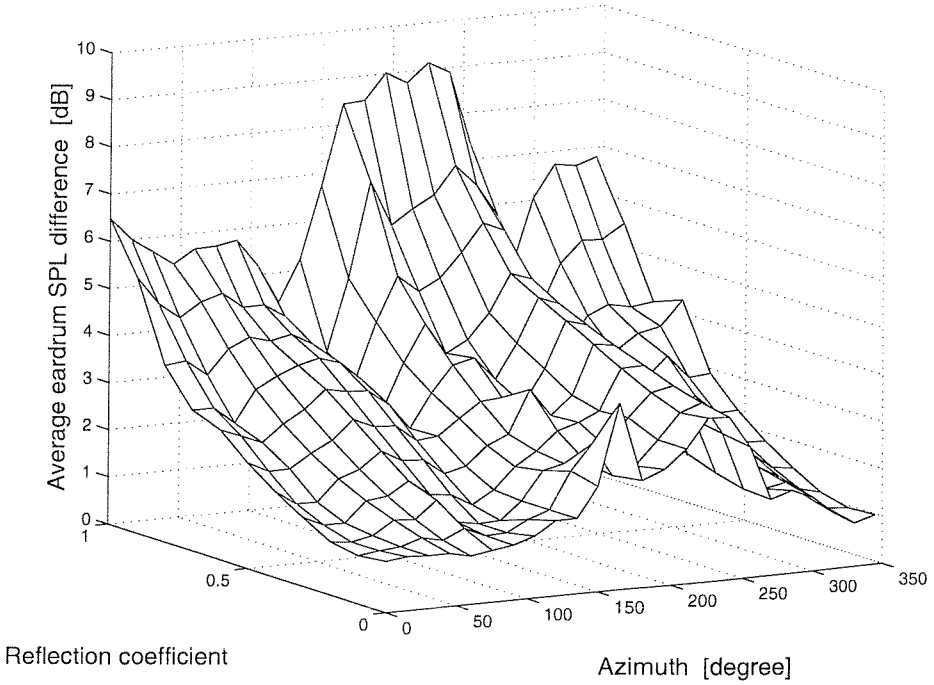

Figure 10.70 The eardrum sound pressure level differences averaged over frequency in the horizontal plane for various reflection coefficients of the small headphone surface using 17 headphone sources.

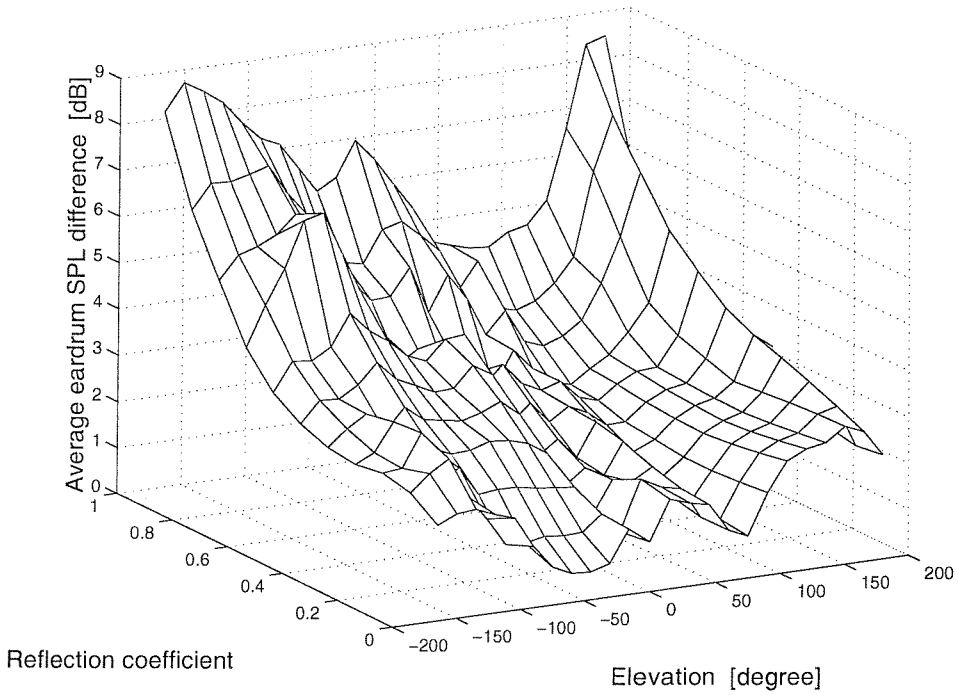

Figure 10.71 The eardrum sound pressure level differences averaged over frequency in the median plane for various reflection coefficients of the small headphone surface.

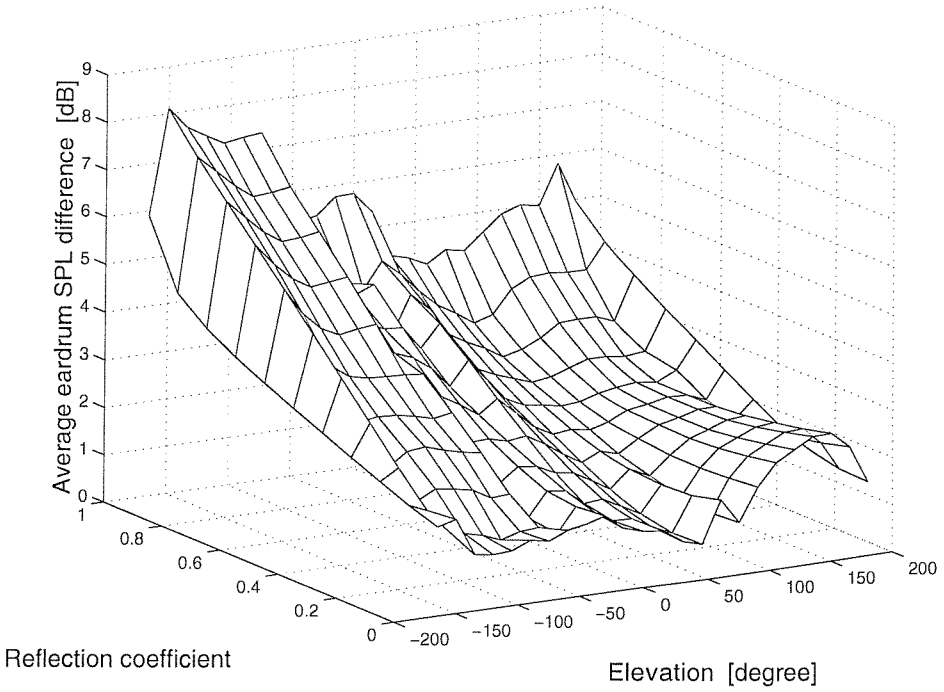

Figure 10.72 The eardrum sound pressure level differences averaged over frequency in the frontal plane for various reflection coefficients of the small headphone surface.

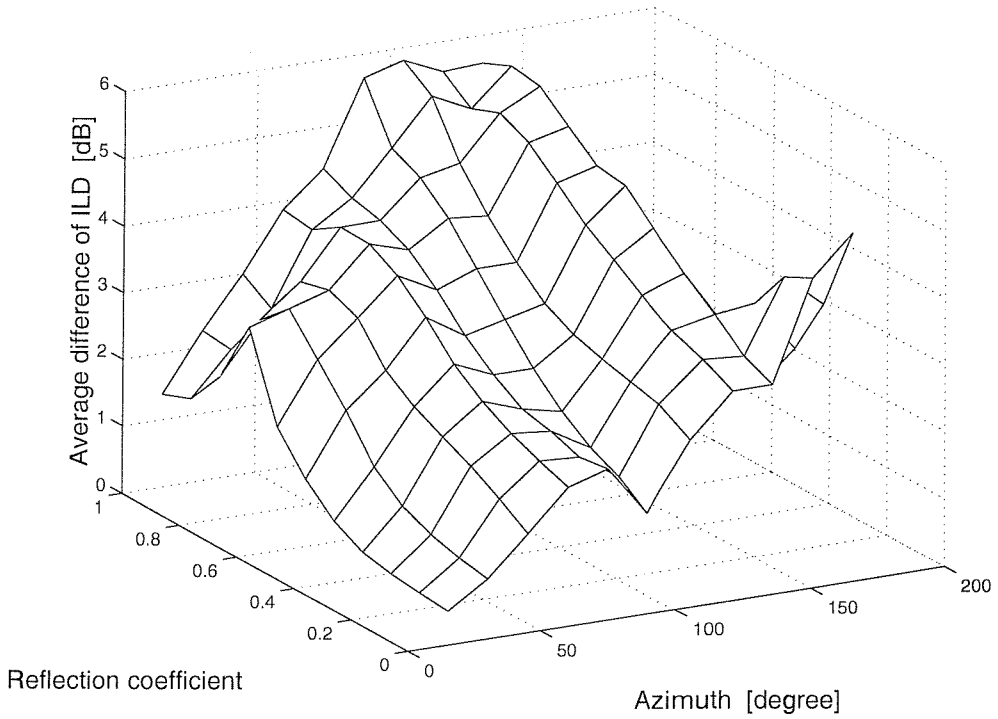

Figure 10.73 Average differences of the ILDs over frequency in the horizontal plane for various reflection coefficients of the small headphone surface.

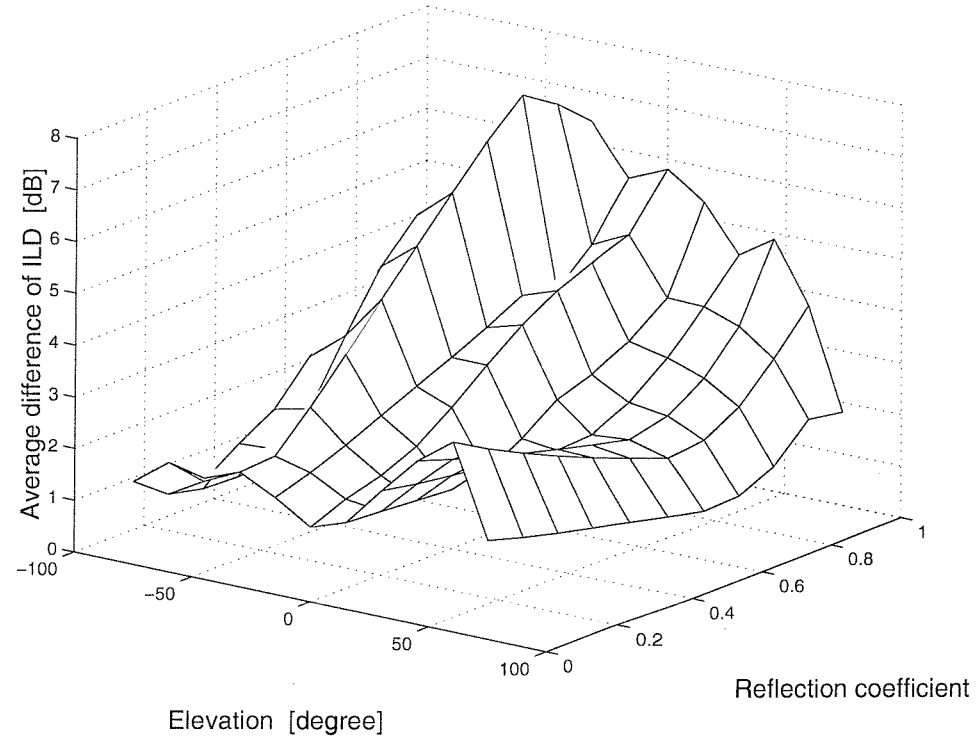

Figure 10.74 Average differences of the ILDs over frequency in the frontal plane for various reflection coefficients of the small headphone surface.

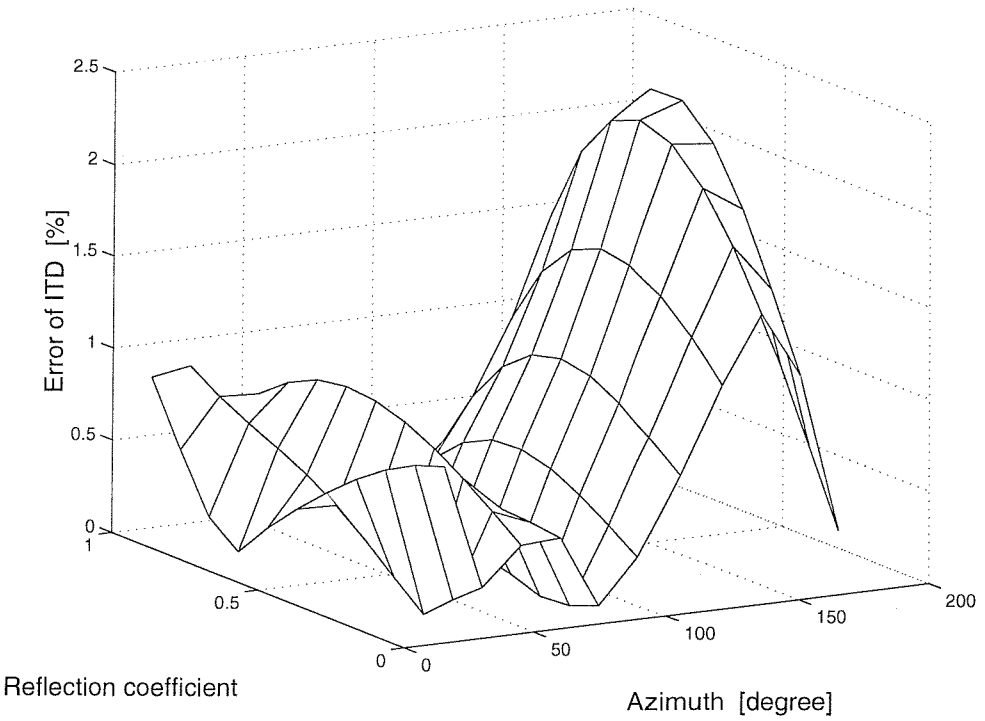

Figure 10.75 Error of the ITDs over frequency in the horizontal plane for various reflection coefficients of the small headphone surface.

CHAPTER 11
CONCLUSIONS

The most critical problem associated with systems for virtual acoustic imaging using binaural technology is the high sensitivity of the performance of the system to the individual differences in the frequency response of the pinna. To solve this problem, a new virtual acoustic imaging system has been proposed, which uses a multichannel headphone. This is called the RISE (Reproduction of the Incident Sound on the Ear) system. The multichannel headphone reproduction of the RISE system is based on the boundary surface control principle derived from the Kirchhoff-Helmholtz integral equation. The sound field outside the control region is assumed to be the incident sound in the primary field, which will not be changed regardless of the scattering body within the control volume. The primary sound field within the control volume can be exactly reproduced in the secondary sound field by reproducing the pressure and its gradient on the boundary surface of the control volume. To minimize the difference between the desired sound field and the reproduced sound field, the least squares solution is used. The performance of this system is independent of the geometry and boundary condition of the scattering body within the control volume. Therefore, this analysis implies that anyone can experience the same quality of the virtual sound field that can be created inside the multichannel headphone of the RISE system by reproducing the sound field that is recorded using a dummy head without the ears.

The results of the numerical simulation using the boundary element method imply that the virtual acoustic field can be successfully produced by using the RISE system with large numbers of headphone sources and a perfectly absorbent headphone surface. The multichannel headphone is optimized in terms of the control field, number of headphone sources, the boundary condition of the headphone surface, and the size of the headphone. The small and sparse control field is preferred since the performance of the system is more sensitive to the size of the control field than the number of control points. Evenly distributed 17 headphone sources can reproduce incident sound on the ear from any angle in three-dimensional space with reasonably good

precision up to frequency of at least 10 kHz. An even distribution of 9 headphone sources can reproduce sound from frontal angles, which is incident on the ear reasonably well in three-dimensional space up to frequency of about 8 kHz. The performance error is proportional to reflection coefficient of the headphone surface for each angle of incident waves. The performance of the multichannel headphone having a radius of 40 mm is not worse than that of the headphone having a radius of 60 mm in case of the 9 headphone sources. The work of this thesis has produced practical guidelines for the design of a multichannel headphone.

Further work is now required on the digital signal processing techniques necessary to implement a practical system. More study would be needed for designing practical multichannel headphones. The acoustical properties of absorbent material on the headphone surface need to be investigated. Since there is some noise in practice, the poor conditioning of the system at very low frequencies could be a problem. The methods to overcome ill-conditioned problems for practical multichannel headphones also need to be studied further. Psychoacoustical experiments are also required to confirm the performance of the RISE system. Feedback from the psychoacoustical experiments may help improving the design of the RISE system. Some suitable software to control the RISE system would need to be developed. Possible applications using the RISE systems such as 3-D games could be investigated.

APPENDIX

In this Appendix, an introduction is given to the Kirchhoff-Helmholtz integral equation, on which the boundary element method is based. The homogeneous wave equation for time-harmonic acoustic waves in an inviscid, quiescent, and homogeneous medium can be written as the following homogeneous Helmholtz equation:

$$\left(\nabla^2 + k^2\right) p(\mathbf{x}) = 0 \tag{A.1}$$

where $\mathbf{x}$ is a position vector, p is the complex acoustic pressure, and k is the wavenumber. We shall now find the fundamental solution of the Helmholtz equation by using the Green function $G(\mathbf{x}|\mathbf{y})$, which satisfies

$$\nabla_y^2 G(\mathbf{y}|\mathbf{x}) + k^2 G(\mathbf{y}|\mathbf{x}) = -\delta(\mathbf{y} - \mathbf{x}) \tag{A.2}$$

where $\mathbf{y}$ is a position vector, ∇_y is the differential operator with respect to $\mathbf{y}$, and $\delta(\mathbf{y}-\mathbf{x})$ is a three-dimensional Dirac delta function. The Green function describes the spatial dependence of the complex pressure field produced by a harmonic point monopole source. The Green function satisfies the principle of reciprocity, and therefore that $G(\mathbf{x}|\mathbf{y}) = G(\mathbf{y}|\mathbf{x})$ (Nelson and Elliott, 1992). Consider a finite interior volume V enclosed by a boundary S in a medium with a singular point $\mathbf{x}$, as shown in Fig. A.1. This singular point is enclosed by a tiny spherical volume V_ε to exclude a singular point from the domain V. Application of Green's theorem (Nelson and Elliott, 1992) shows that

$$\begin{aligned} &\int_{V-V_\varepsilon} \left(G(\mathbf{x}|\mathbf{y}) \nabla^2 p(\mathbf{y}) - p(\mathbf{y}) \nabla_y^2 G(\mathbf{x}|\mathbf{y}) \right) dV \\ &= \int_{S+S_\varepsilon} \left(G(\mathbf{x}|\mathbf{y}) \frac{\partial p(\mathbf{y})}{\partial n} - p(\mathbf{y}) \frac{\partial G(\mathbf{x}|\mathbf{y})}{\partial n} \right) dS \end{aligned} \tag{A.3}$$

where the position vector **y** is on the surface S. The rate of change of a scalar function p at a point **y** in a direction given by a vector **n** is defined as a directional derivative of p at **y** in the direction of **n**, which is given by

$$\frac{\partial p(\mathbf{y})}{\partial n} = \nabla_y p(\mathbf{y}) \bullet \mathbf{n} \tag{A.4}$$

where **n** is the unit outward normal on S (pointing into the external volume in this case), and n is the distance from a point **y** in the direction of **n**. The directional derivative of $G(\mathbf{x}|\mathbf{y})$ follows in the same manner. Since the singular point **x** is excluded from the domain V, we have $\nabla^2 p = -k^2 p$ and $\nabla^2 G(\mathbf{x}|\mathbf{y}) = -k^2 G(\mathbf{x}|\mathbf{y})$ from Eq. (A.1) and (A.2). Therefore, the left hand side of Eq. (A.3) is zero. Then equation (A.3) can be rewritten as

$$\int_{S+S_\varepsilon} \left(G(\mathbf{x}|\mathbf{y}) \frac{\partial p(\mathbf{y})}{\partial n} - p(\mathbf{y}) \frac{\partial G(\mathbf{x}|\mathbf{y})}{\partial n} \right) dS = 0 . \tag{A.5}$$

This integral equation can be evaluated on the surface S and the tiny surface S_ε enclosing the singular point **x**. If the radius ε of the volume V_ε goes to zero, equation (A.5) becomes

$$\begin{aligned} &\lim_{\varepsilon \to 0} \int_{S_\varepsilon} \left(p(\mathbf{y}) \frac{\partial G(\mathbf{x}|\mathbf{y})}{\partial n} \right) dS - \lim_{\varepsilon \to 0} \int_{S_\varepsilon} \left(G(\mathbf{x}|\mathbf{y}) \frac{\partial p(\mathbf{y})}{\partial n} \right) dS \\ &= \int_S \left(G(\mathbf{x}|\mathbf{y}) \frac{\partial p(\mathbf{y})}{\partial n} - p(\mathbf{y}) \frac{\partial G(\mathbf{x}|\mathbf{y})}{\partial n} \right) dS. \end{aligned} \tag{A.6}$$

The second term of the left hand side of Eq. (A.6) becomes zero since the Green function is in the order of $1/\varepsilon$ and dS is in the order of ε^2 as ε goes to zero (Wu, 2000a). The Green function is chosen to be the free space Green function $g(\mathbf{x}|\mathbf{y})$ that is given by

$$g(\mathbf{x}|\mathbf{y}) = \frac{e^{-jk|\mathbf{x}-\mathbf{y}|}}{4\pi|\mathbf{x}-\mathbf{y}|}. \tag{A.7}$$

Then, equation (A.6) can be rewritten as

$$\lim_{\varepsilon\to 0}\int_{S_\varepsilon}\left(p(\mathbf{y})\frac{\partial g(\mathbf{x}|\mathbf{y})}{\partial n}\right)dS = \int_S\left(g(\mathbf{x}|\mathbf{y})\frac{\partial p(\mathbf{y})}{\partial n} - p(\mathbf{y})\frac{\partial g(\mathbf{x}|\mathbf{y})}{\partial n}\right)dS. \tag{A.8}$$

The left hand side of Eq. (A.8) can also be rewritten as

$$\lim_{\varepsilon\to 0}\int_{S_\varepsilon}\left(p(\mathbf{y})\frac{\partial g(\mathbf{x}|\mathbf{y})}{\partial n}\right)dS = \lim_{\mathbf{y}\to\mathbf{x}}\int_{S_\varepsilon}\left(p(\mathbf{y})\frac{\partial g(\mathbf{x}|\mathbf{y})}{\partial n}\right)dS = C^0(\mathbf{x})\,p(\mathbf{x}) \tag{A.9}$$

where the coefficient $C^0(\mathbf{x})$ for an interior acoustic problem is given by (Wu, 2000a)

$$\begin{aligned} C^0(\mathbf{x}) &= \lim_{\varepsilon\to 0}\int_{S_\varepsilon}\frac{\partial g(\mathbf{x}|\mathbf{y})}{\partial n}dS = \lim_{\mathbf{y}\to\mathbf{x}}\int_{S_\varepsilon}\frac{\partial}{\partial n}\left(\frac{e^{-jk|\mathbf{x}-\mathbf{y}|}}{4\pi|\mathbf{x}-\mathbf{y}|}\right)dS \\ &= \lim_{\mathbf{y}\to\mathbf{x}}\int_{S_\varepsilon}\frac{\partial}{\partial n}\left(\frac{1}{4\pi|\mathbf{x}-\mathbf{y}|}\right)dS = \lim_{\mathbf{y}\to\mathbf{x}}\int_{S_\varepsilon}\frac{\partial \psi_L(\mathbf{x}|\mathbf{y})}{\partial n}dS \end{aligned} \tag{A.10}$$

where $\psi_L(\mathbf{x}|\mathbf{y}) = 1/(4\pi|\mathbf{x}-\mathbf{y}|)$ is the fundamental solution of the Laplace equation. Equation (A.10) is not useful since it is impractical to evaluate an integral over an infinitesimal surface S_ε numerically. Now consider an imaginary Laplace problem $\nabla^2\phi = 0$ occupying the same domain V as the acoustic problem shown Fig. A.1. For example, the gravitational force at the singular point $\mathbf{x}$ produced by the distribution of masses in the region V is given by a vector function that is the gradient of the scalar function ϕ (Kreyszig, 1993). Application of Green's theorem also shows that

$$\begin{aligned} &\int_{V-V_\varepsilon}\left(\psi_L(\mathbf{x}|\mathbf{y})\nabla^2\phi(\mathbf{y}) - \phi(\mathbf{y})\nabla_y^2\psi_L(\mathbf{x}|\mathbf{y})\right)dV \\ &= \int_{S+S_\varepsilon}\left(\psi_L(\mathbf{x}|\mathbf{y})\frac{\partial\phi(\mathbf{y})}{\partial n} - \phi(\mathbf{y})\frac{\partial\psi_L(\mathbf{x}|\mathbf{y})}{\partial n}\right)dS. \end{aligned} \tag{A.11}$$

By following same procedure as shown above, the following equation can be derived:

$$\begin{aligned}&\lim_{\mathbf{y}\to\mathbf{x}}\int_{S_\varepsilon}\left(\psi_L(\mathbf{x}|\mathbf{y})\frac{\partial\phi(\mathbf{y})}{\partial n}-\phi(\mathbf{y})\frac{\partial\psi_L(\mathbf{x}|\mathbf{y})}{\partial n}\right)dS\\&=-\int_S\left(\psi_L(\mathbf{x}|\mathbf{y})\frac{\partial\phi(\mathbf{y})}{\partial n}-\phi(\mathbf{y})\frac{\partial\psi_L(\mathbf{x}|\mathbf{y})}{\partial n}\right)dS\end{aligned} \tag{A.12}$$

Note that right hand side of Eq. (A.12) is the integral over the surface S. If a particular solution $\phi=1$ of the Laplace problem $\nabla^2\phi=0$ is substituted into Eq. (A.12), $\partial\phi(\mathbf{y})/\partial n$ becomes zero, and equation (A.12) becomes (Wu, 2000a)

$$\lim_{\mathbf{y}\to\mathbf{x}}\int_{S_\varepsilon}-\frac{\partial\psi_L(\mathbf{x}|\mathbf{y})}{\partial n}dS=\int_S\frac{\partial\psi_L(\mathbf{x}|\mathbf{y})}{\partial n}dS\,. \tag{A.13}$$

Then, equation (A.10) thus becomes

$$C^0(\mathbf{x})=-\int_S\frac{\partial\psi_L(\mathbf{x}|\mathbf{y})}{\partial n}dS=-\int_S\frac{\partial}{\partial n}\left(\frac{1}{4\pi|\mathbf{x}-\mathbf{y}|}\right)dS\,. \tag{A.14}$$

The coefficient $C^0(\mathbf{x})$ can be evaluated by integrating the normal derivative of the fundamental solution of the Laplace equation over the surface S numerically. For example, the coefficient $C^0(\mathbf{x})$ is equal to unity if $\mathbf{x}$ is within V, zero if $\mathbf{x}$ is outside V, and 0.5 if $\mathbf{x}$ is on a smooth boundary S (Wu, 2000a). Then, equation (A.8) becomes the Kirchhoff-Helmholtz integral equation for the interior problem, which is given by

$$C^0(\mathbf{x})p(\mathbf{x})=\int_S\left(g(\mathbf{x}|\mathbf{y})\frac{\partial p(\mathbf{y})}{\partial n}-p(\mathbf{y})\frac{\partial g(\mathbf{x}|\mathbf{y})}{\partial n}\right)dS\,. \tag{A.15}$$

Consider unbounded exterior volume V with a structure bounded by the surface S in a medium with a singular point $\mathbf{x}$, as shown in Fig. A.2. A far field boundary surface S_R of radius R is temporarily constructed to bind the acoustic domain V. The singular

point $\mathbf{x}$ is enclosed by a tiny spherical volume V_ε of radius ε to exclude a singular point from the domain V. Application of Green's theorem produces

$$\begin{aligned}&\int_{V-V_\varepsilon}\left(G(\mathbf{x}|\mathbf{y})\nabla^2 p(\mathbf{y})-p(\mathbf{y})\nabla_y^2 G(\mathbf{x}|\mathbf{y})\right)dV\\&=\int_{S+S_\varepsilon+S_R}\left(G(\mathbf{x}|\mathbf{y})\frac{\partial p(\mathbf{y})}{\partial n}-p(\mathbf{y})\frac{\partial G(\mathbf{x}|\mathbf{y})}{\partial n}\right)dS\end{aligned} \tag{A.16}$$

Due to the Sommerfeld radiation condition (Nelson and Elliott, 1992), it can be shown that

$$\lim_{R\to\infty}\int_{S_R}\left(G(\mathbf{x}|\mathbf{y})\frac{\partial p(\mathbf{y})}{\partial n}-p(\mathbf{y})\frac{\partial G(\mathbf{x}|\mathbf{y})}{\partial n}\right)dS=0. \tag{A.17}$$

By following same procedure as the corresponding interior problem, the Kirchhoff-Helmholtz integral equation for the exterior acoustic problem can be written as

$$C(\mathbf{x})p(\mathbf{x})=\int_S g(\mathbf{x}|\mathbf{y})\frac{\partial p(\mathbf{y})}{\partial n}-p(\mathbf{y})\frac{\partial g(\mathbf{x}|\mathbf{y})}{\partial n}dS \tag{A.18}$$

where the coefficient $C(\mathbf{x})$ for an exterior problem is given by (Wu, 2000a)

$$C(\mathbf{x})=1-\int_S\frac{\partial\psi_L(\mathbf{x}|\mathbf{y})}{\partial n}dS=1-\int_S\frac{\partial}{\partial n}\left(\frac{1}{4\pi|\mathbf{x}-\mathbf{y}|}\right)dS=1-C^0(\mathbf{x}). \tag{A.19}$$

For example, the coefficient $C(\mathbf{x})$ is equal to unity if $\mathbf{x}$ is within V, zero if $\mathbf{x}$ is outside V, and 0.5 if $\mathbf{x}$ is on a smooth boundary S.

FIGURES

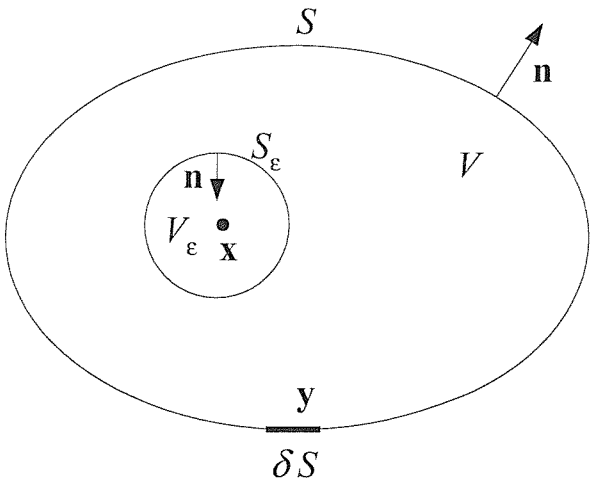

Figure A.1 An interior volume V enclosed by a boundary S in a medium.

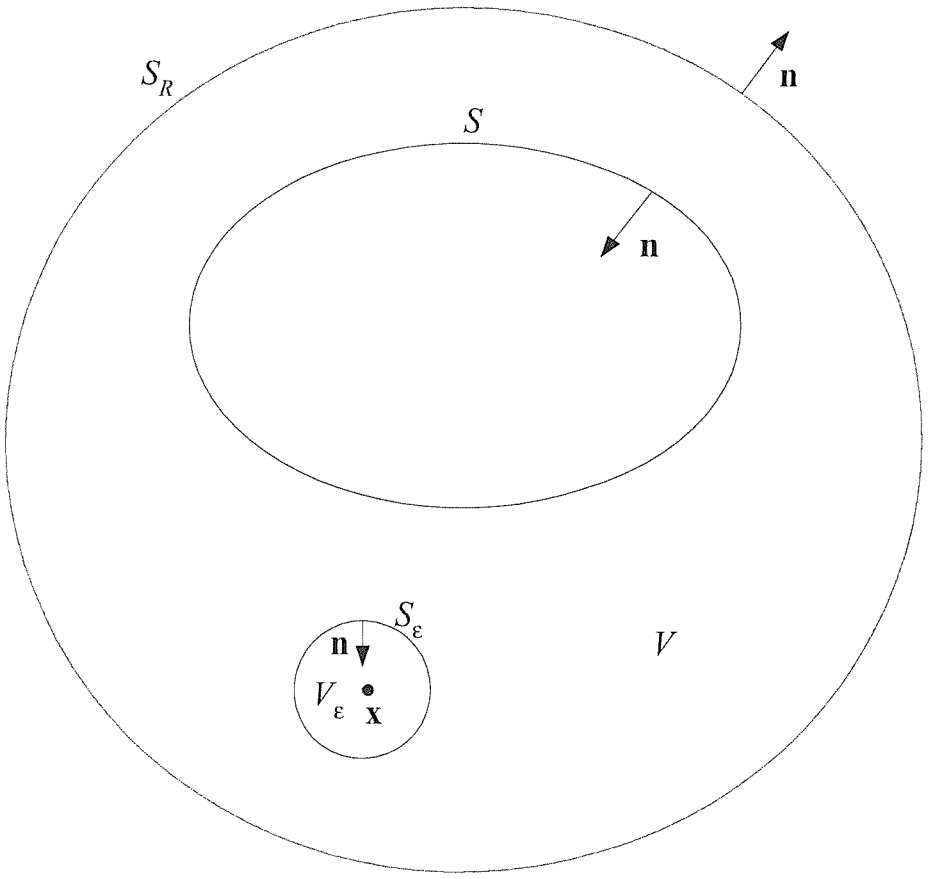

Figure A.2 An exterior volume V with a structure bounded by the surface S.

REFERENCES

Algazi, V. R., Avendano, C. and Duda, R. O. (2001). Estimation of a spherical-head model from anthropometry. *J. Audio Eng. Soc.*, **49**, 472–479.

ANSYS 6.1. *Users manual.* ANSYS Inc., Canonsburg.

Backus, J. (1977). *The Acoustical Foundations of Music.* Norton, New York.

Begault, D. R. (1991). Challenges to the successful implementation of 3-D sound. *J. Audio Eng. Soc.*, **39**, 864–870.

Begault, D. R. (1999). Virtual acoustic displays for teleconferencing: intelligibility advantage for telephone-grade audio. *J. Audio Eng. Soc.*, **47**, 824–828.

Begault, D. R., Wenzel, E. M., Lee, A. S. and Anderson, M. R. (2000). Direct comparison of the impact of head tracking, reverberation, and individualized head-related transfer functions on the spatial perception of a virtual speech source. In *Audio Engineering Society 108th Convention*, Paris, prepint 5134.

Benthien, W. and Schenck, A. (1997). Nonexistence and nonuniqueness problems associated with integral equation methods in acoustics. *Computers & structures*, **65**, 295–305.

Berkhout, A. J., de Vries, D. and Vogel, P. (1993). Acoustic control by wave field synthesis. *J. Acoust. Soc. Am.*, **93**, 2764–2778.

Blauert, J. (1997). *Spatial Hearing – The Psychophysics of Human Sound Localization, Revised edition.* The MIT Press, London.

Blauert, J., Lehnert, H., Sahrhage, J. and Strauss, H. (2000). An interactive virtual-environment generator for psychoacoustic research. I: architecture and implementation. *Acustica*, **86**, 94–102.

Blumlein, A. (1931). Improvements in and relating to sound transmission, sound recording and sound reproducing systems. *British Patent Specification 394325.*

Boone, M. M., Verheihen, E. N. G. and Van Tol, P. F. (1995). Spatial sound-field reproduction by wave-field synthesis. *J. Audio Eng. Soc.*, **43**, 1003–1011.

Burkhard, M. D. and Sachs, R. M. (1975). Anthropometric manikin for acoustic research. *J. Acoust. Soc. Am.*, **58**, 214–222.

Djelani, T., Pörschmann, C., Sahrhage, J. and Blauert, J. (2000). An interactive virtual-environment generator for psychoacoustic research II: collection of head-related impulse responses and evaluation of auditory localization. *Acustica*, **86**, 1046–1053

Estorff, O. V., Coyette, J-P. and Migeot J-L. (2000). Governing formulations of the BEM in acoustics. In *Boudnary Elements in Acoustics – Advances & Applications*, (O. V. Estorff ed). WITpress, Southampton.

Gerzon, M. (1977). Criteria for evaluating surround sound systems. *J. Audio Eng. Soc.*, **25**, 400–408.

Green, D. M. (1971). Temporal auditory acuity. *Psych. Rev.*, **78**, 540–551.

Hertz, B. (1981). 100 years with stereo: the beginning. *J. Audio Eng. Soc.*, **29**, 368–372.

Hill, P. A., Nelson, P. A. and Kirkeby, O. (2000). Resolution of front-back confusion in virtual acoustic imaging systems. *J. Acoust. Soc. Am.*, **108**, 2901–2910.

Ise, S. (1999). A principle of sound field control based on the Kirchhoff-Helmholtz integral equation and the theory of inverse systems. *Acustica*, **85**, 78–102.

ITU-R (1994). Recommendation BS. 775-1: Multi-channel stereophonic sound system with or without accompanying picture. *International Telecommunications Union.*

Johansen, P. A. (1975). Measurement of the human ear canal. *Acustica*, **33**, 349–351.

Johnson, A. E. and Hebert, M. (1997). Control of polygonal mesh resolution for 3-D computer vision. Carnegie Mellon University, School of Computer Science, Tech. Report (CMU-RI-TR-96-20).

Kahana, Y. (1997). *Multi-channel Sound Reproduction with a Four-ear Dummy-head.* M.Sc. thesis. Institute of Sound and Vibration Research, University of Southampton, Southampton.

Kahana, Y. (2000). *Numerical Modelling of the Head Related Transfer Function.* Ph.D. thesis, Institute of Sound and Vibration Research, University of Southampton, Southampton.

Katz, B. F. G. (2000). Acoustic absorption measurement of human hair and skin within the audible frequency range. *J. Acoust. Soc. Am.*, **108**, 2238–2242.

Kistler, D. J. and Wightman, F. L. (1992). A model of head-related transfer functions based on principal components analysis and minimum-phase reconstruction. *J. Acoust. Soc. Am.*, **91**, 1637–1647.

Kreyszig, E. (1993). *Advanced Engineering Mathmatics, 7th Edition*. John Wiley & Sons, New York.

Kulkarni, A. and Colburn, H. S. (2000). Variability in the characterization of the headphone transfer function. *J. Acoust. Soc. Am.*, **107**, 1071–1074.

MATLAB 5.3. *Users manual*. The MathWorks, Inc., Natick.

Maxwell, R.J. and Burkhard, M. D. (1979). Larger ear replica for KEMAR manikin. *J. Acoust. Soc. Am.*, **65**, 1055–1058.

Møller, H. (1992). Fundamentals of binaural technology. *Applied Acoustics*, **36**, 171–218.

Møller, H., Sørensen, M. F., Hammershøi, D. and Jensen, C. B. (1995a). Head-related transfer functions of human subjects. *J. Audio Eng. Soc.*, **43**, 300–321.

Møller, H., Jensen, C. B., Hammershøi, D. and Sørensen, M. F. (1995b). Design criteria for headphones. *J. Audio Eng. Soc.*, **43**, 218–232.

Morfey, C. L. (2001). *Dictionary of Acoustics*. Academic Press, London.

Morse, P.M. and Ingard, K.U. (1968). *Theoretical Acoustics*. Princeton University Press, Princeton.

Nelson, P. A. and Elliott, S. J. (1992). *Active Control of Sound*. Academic Press, London.

Nelson, P. A. (2001). A review of some inverse problems in acoustics. *International Journal of Acoustics and Vibration*, **6**, 118–134.

Pierce, A. D. (1989). *Acoustics-An Introduction to Its Physical Principles and Application*. The Acoustical society of America, New York.

Perrett, S. and Noble, W. (1997). The contribution of head motion cues to localization of low-pass noise. *Percept. Psychophys.* **59**, 1018–1026.

Pralong, D. and Carlile, S. (1996). The role of individualized headphone calibration for the generation of high fidelity virtual auditory space. *J. Acoust. Soc. Am.*, **100**, 3785–3793.

Rumsey, F. (2001). *Spatial Audio*. Focal Press, Oxford.

Schenck, H. A. (1968). Improved integral formulation for acoustic radiation problems. *J. Acoust. Soc. Am.*, **44**, 41–58.

Shaw, E. A. G. and Thiessen, G. J. (1962). Acoustics of circumaural earphones. *J. Acoust. Soc. Am.*, **34**, 1233–1246.

Shaw, E. A. G. (1966). Ear canal pressure generated by circumaural and supra-aural earphones. *J. Acoust. Soc. Am.*, **39**, 471–479.

Shaw, E. A. G. (1974). The external ear. In *Handbook of Secsory Physiology, Vol. V/2: Auditory System* (Keidel, W.D. and Neff, W.D. eds). Springer-Verlag, Berlin.

Shaw, E. A. G. (1997). Acoustical features of the human external ear. In *Binaural and Spatial Hearing in Real and Virtual Environments* (Gilkey, R.H. and Anderson, T.R. eds). Lawrence Erlbaum Associates, New Jersey.

Shinn-Cunningham, B. G., Durlach, N. I., and Held, R. M. (1998). Adapting to supernormal auditory localization cues. I. Bias and resolution. *J. Acoust. Soc. Am.*, **103**, 3656–3666.

Stakgold, I. (1998). *Green's Functions and Boundary Value Problems, 2nd Edition.* John Wiley & Sons, New York.

Stinson, M. R. and Lawton, B. W. (1989). Specification of the geometry of the human ear canal for the prediction of sound pressure level distribution. *J. Acoust. Soc. Am.*, **85**, 2492–2503.

SYSNOISE 5.5. *Users manual.* LMS International, Leuven.

Takane, S., Suzuki, Y., Sone, T. (1999). A new method for global sound field reproduction based on Kirchhoff's integral equation. *Acustica*, **85**, 250–257.

Wenzel, E. M., Arruda, M., Kistler, D. J., and Wightman, F. L. (1993). Localization using nonindividualized head-related transfer function. *J. Acoust. Soc. Am.*, **94**, 111–123.

Wightman, F. L. and Kistler, D. J. (1992). The dominant role of low-frequency interaural time differences in sound localization. *J. Acoust. Soc. Am.*, **91**, 1648–1661.

Wightman, F. L. and Kistler, D. J. (1997). Factors affecting the relative salience of sound localization. In *Binaural and Spatial Hearing in Real and Virtual Environments* (Gilkey, R.H. and Anderson, T.R. eds). Lawrence Erlbaum Associates, New Jersey.

Wu, T. W. (2000a). The Helmholtz integral equation. In *Boundary Element Acoustics – Fundamentals and Computer Codes*, (T. W. Wu ed). WITpress, Southampton.

Wu, T. W. (2000b). Three-dimensional problems. In *Boundary Element Acoustics – Fundamentals and Computer Codes*, (T. W. Wu ed). WITpress, Southampton.